A numerical study of damage mechanisms in the CAI of laminated composites for aerospace applications

by

Yu Yang

DOCTORAL THESIS

Submitted in partial fulfilment of the
requirements for the award of

Doctor of Philosophy

of the University of Nottingham

October 2015

Abstract

Compression after impact (CAI) is one of the crucial factors affecting material selection and determination of allowable design values in aircraft design process for fibre reinforced composite laminates. The major objectives of this thesis are to investigate the damage mechanism of CAI and to obtain a practical prediction method accordingly.

Through literature review, it has been found that current perceptions of CAI damage mechanism are too categorical as they conceive either of two possible failure modes only, delamination propagation and in-plane compressive failure due to stress concentration. A finite element (FE) modelling method has been presented, which takes both potential failure modes into account simultaneously. Through a substantial parametric study employing this FE modelling method, it has been found that these two failure modes co-exist in the damage process, and compete to be the dominant failure mode favoured by various factors, among which the delamination multiplicity is one of the major factors dictating the damage mechanism.

Further investigation has been carried out with more realistic FE models of CAI, which take all major damage modes due to impact into account, such as delamination distribution, transverse matrix cracks and fibre breakage. Especially, a method of determining the delamination distribution over laminate thickness direction based on the result of double-sided ultrasonic scan has been presented, which has been extremely helpful to preserve the key features of delamination distribution in corresponding FE models. Through the investigation, the damage mechanism of CAI has been concluded as in-plane failure due to stress concentration at

delamination front and large extent of delamination propagation is unlikely to take place during the loading process. This conclusion is fully justified for material systems with toughened matrix as employed in aerospace widely nowadays. In the meantime, a practical strategy of applying the CAI prediction method employing this FE modelling is presented, which overcomes the deficiency of other similar methods that require extremely refined and often unaffordable mesh as for the FE modelling.

Based on the conclusion of CAI damage mechanism obtained above, a simplified CAI prediction method has been presented, which takes advantage of the results from ultrasonic scan. It is computationally efficient, numerically accurate and physically sound. In order to investigate the degrading tendency of stiffness over the delaminated area, an improved inverse method has been developed, through which it has been found that the stiffness degradation is neither uniform over the delaminated area nor constant during compression process in CAI cases.

In addition, a deficiency of cohesive element has been spotted. It roots from the discrepancy of coordinate systems of cohesive elements and crack propagation direction, and may bring additional numerical error if used improperly.

All the outcomes of this project, modelling strategies and prediction methods as presented in this thesis are highly valuable in CAI evaluation from experimental, theoretical and practical perspectives. After further validation, they should be applicable to most CAI cases faced in the aerospace industry currently.

Acknowledgements

I am sincerely grateful to my supervisor, Prof. Shuguang Li. He imparted me knowledge, methodology, enthusiasm and morality of academic research. I thank him for his friendship, guidance, support and all the expertise he has shared with me.

Prof. Xiasheng Sun, the former president of my employer, The Aircraft Strength Research Institute of China (ASRI) has made huge benign impacts on my career at ASRI. Inspired by his trust, expectation and encouragement, I embarked on this precious opportunity of PhD study.

ASRI, the Aviation Industry Corporation of China (AVIC) and China Scholarship Council (CSC) provided me with funding for the duration of my PhD. Without these supports, it would not have been possible for me to have completed my PhD course at Nottingham.

Dr. Jianhong Lin from Airbus gave me many valuable suggestions based on his expertise. He also inspired me continuously during my PhD. His cross-age friendship is greatly valued.

My wife, Ling Liang, sacrificed a great deal to support my PhD study. She gave up her own business in China in order to stay together with me in this foreign country. She went out to work laboriously to alleviate the financial tension. Her understanding, tenacity and inclusiveness motivated me to strive through the challenging period. Most importantly, she gave me the most precious gift, my baby son Joshua. In the meantime, I would like to express my deep gratitude to

my parents for their support throughout the years and, in particular, in caring for the demanding baby.

Finally, I thank a large number of friends I met here who inspired me to walk forward firmly. Their selflessly supports, mentally and physically, will leave me eternal source of motivations.

Contents

List of Figures

List of Tables

List of Abbreviations

ASRI	Aircraft Strength Research Institute	**ENF**	End notched flexure
CAI	Compression after impact	**ERR**	Energy release rate
CERR	Critical energy release rate	**FD**	Fibre damage
DCB	Double cantilever beam	**FE**	Finite element
DI	Damage influence	**FOI**	Foreign object impact
DIC	Digital image correlation	**MMB**	Mixed mode bending
DSF	Damaging state function	**NDI**	Nondestructive inspection
DSP	Digital Speckle Photogrammetry	**VCCT**	Virtual closure crack technique

Chapter 1 Introduction

1.1 Current issue

Advanced fibre reinforced composite laminates have been successfully used in primary structures of aircrafts in recent years. However, there still remains quite a few issues which impair the full exploitation of their great potentials, the susceptibility to low-velocity impact being one of them.

Low-velocity impacts compromises structure integrity, which could render 60% loss of compressive strength without obvious visibility. Therefore, substantial research has been devoted to this field and the residual strength of compression after impact (CAI) has become one of the critical measures for material selection and structural design in the aerospace industry.

For the purpose of reduction of cost and design cycle period, theoretical prediction method of CAI has been pursued over the past decades. However, a unanimous prediction method is still not yet available. One of the reasons is that the damage mechanism of CAI is not yet clearly understood. Therefore, attempt to understand the damage mechanisms of CAI is identified as the core concern of this thesis.

1.2 Aim and objectives

The aim and objectives of the research summarized in this thesis are presented in this section.

1.2.1 Aim

The aim of this thesis is to explore the damage mechanisms of CAI of composite laminate which is consisted of unidirectional laminae, and to seek for an effective prediction method based on this mechanism accordingly.

1.2.2 Objectives

The objectives of this research are as follows. Firstly, a comprehensive method to model the CAI cases is to be established, which can overcome the deficiency of being biased to a particular mode of damage as exposed in previous studies and unravel the damage mechanisms of CAI objectively. Secondly, an appropriate approach will be investigated to predict the CAI strength, which captures the physical damage mechanism while being computationally efficient.

1.3 Major research work in this thesis

Firstly, extensive parametric study was performed to investigate the damage mechanism of delaminated plates through detailed FE models, and the dominating factors were identified. Secondly, the thoroughly modelling method of damaged laminate subjected to low-velocity impact was presented, which simulated the delamination distribution, transverse matrix cracks and fibre breakage in CAI samples by taking advantage of C-scan results as well as other experimental information. Through investigating these detailed FE models, the damage mechanism of CAI was concluded finally. Afterwards, based on the confirmed damage mechanism, a simplified method to predict CAI strength was presented. Finally, the degraded stiffness distribution over the delaminated area of the plate when subjected to compression was demonstrated through the improved inverse method, which was presented by the author.

1.4 Research contribution

The CAI damage mechanism of laminates using toughened material systems have been studied systematically. It can be concluded that in most cases impacted laminate fails due to in-plane failure initiating around the delamination front, and delamination propagation is unlikely to take place, in particular, when delaminations are found on most of the interfaces. This is the underlying justification for developing a computationally efficient method to predict CAI which only takes in-plane failure into account.

A method of detailed FE modelling of CAI is presented. This model takes all major damage modes induced by low-velocity impact, such as delaminations, transverse matrix cracks and fibre breakage, into account. It incorporates two possible failure modes simultaneously, delamination propagation and in-plane failure, and allows them to compete with each other to dominate the damage process. It employs C-scan result as damage input. This modelling method is more realistic than previous methods. In the meantime, the application strategy of this method is also presented.

A method to predict CAI strength based on soft inclusion assumption is presented. It overcomes some crucial weaknesses of previous methods, employs C-scan result as damage input, and it is effective in problem solving and efficient in computation.

An improved inverse method is presented, which has the potential to efficiently simulate the mechanical behaviour of a complex structure containing a zone of damage through a simplified FE model.

A deficiency of cohesive element is spotted. It roots from the discrepancy of coordinate systems of cohesive elements and crack propagation direction, and may bring additional numerical error if used improperly.

1.5 Originality of research

CAI has been a well-attended topic for decades. However, the present work can still claim originalities and novelties in the following aspects.

Firstly, the damage mechanism of CAI is investigated and it is found that toughened laminates bearing barely visible impact damage usually fail due to in-plane failure initiating around the delamination front, and delamination propagation is unlikely to take place. This conclusion is of high significance because it implies that the demanding and expensive simulation work of delamination propagation for CAI strength prediction is actually unnecessary. Oppositely, improving the strategy to calculate the stress distribution around the impact damage of the plate would be more practical and efficient.

Secondly, some key factors dominating the damage mechanisms in delaminated laminates subjected to in-plane compression are identified through an extensive parametric study. They are found to play an important role in promoting one CAI damage mechanism subsequently.

Thirdly, a practical method to idealize the detailed delamination distribution in impact-damaged laminates is presented based on double-sided scan data, which is capable of capturing the key features of damage state. With this method, a strategy of CAI modelling is also proposed, which

can simulate the impact-induced damage comprehensively by taking all relevant failure modes into account. This is essential for understanding the damage mechanisms of CAI.

Fourthly, a method to predict CAI strength in a computationally efficient way is proposed. It is based on the conclusion of damage mechanisms of CAI established in this thesis. Although similar method had been presented by other researchers, some crucial weaknesses are addressed and fundamentally improved.

Fifthly, an improved inverse method is presented, and through this method the tendency of stiffness degradation over delaminated area is investigated. This method is useful for simulating the mechanical behaviour of complex structures containing damage zones through a simplified FE model. However, it is proved not to be the most efficient approach for CAI strength prediction.

Lastly, a deficiency of cohesive elements is spotted. Although the final solution is not presented in this thesis, the reason identified clearly and corresponding measure is recommended.

1.6 Thesis layout

A brief background of the research is presented in the beginning of Chapter 2, which set the scene for the specific topic of CAI. Afterwards, the history of development in the CAI-related problems is reviewed in detail, and the critical issues of current CAI study is identified. Based on those, the objectives of current research are determined.

The process and analysis of the experimental data is presented in Chapter 3. The experimental work was conducted by the candidate during his employment while work at his sponsoring institute, which has not been counted as a part of the presented project. However, the process

and analysis of the experimental data is performed during the PhD project, and the most significant outcome is that the way to determine the detailed delamination distribution in impact-damaged laminates. Meanwhile, the analysing results provide the data as reference and resource for present investigation.

Chapter 4 reports the process of an extensive parametric study and the outcomes. From this study, key factors dominating the damage mechanisms of delaminated laminates subjected to in-plane compression are unravelled.

A method for detailed CAI modelling is developed in Chapter 5. Through analysing models associated with the cases as involved in the experimental programme, the damage mechanisms of CAI are revealed. Based on those, a practical strategy for CAI prediction is proposed and demonstrated.

Chapter 6 consists of two parts. In the first part, a CAI strength prediction method of high computational efficiency is presented. Then, an improved inverse method is proposed to demonstrate the tendency of stiffness degradation over the delaminated area.

The outcomes of the present research project are concluded in Chapter 7. Contributions to this researching area are summarised and suggestions for future work are presented.

Some highly relevant information is presented in appendixes. The experimental work done at the author's sponsoring institute before the PhD project, including the drop-weight impact test and the compression after impact test, are introduced in detail in Appendix A. The final experimental work is also presented in this part. In Appendix B, an engineering prediction method of CAI

proposed by Chen, Shen [1] is evaluated based on the experimental data presented in Appendix A. Similarly, another prediction method proposed by Tang, Shen [2] is evaluated in Appendix C.

Chapter 2 Literature review

The historical development on the research of CAI is reviewed, the weaknesses in the current research of CAI are identified and the impeding factors are revealed. Based on this review, the objectives of the investigations in this thesis are presented.

2.1 The originality of CAI-related problem

As a great achievement, high performance composite laminates have been successfully used in primary structures of both military and commercial airplanes in recent years. For example, 35% of structural weight of the fifth generation fighter Lockheed Martin F-35 is contributed using carbon fibre composites and the entire upper wing skin is made of a single piece of composite panel. In the latest and most advanced commercial airplanes, Boeing 787 Dreamliner, composite materials account for 50% by structure weight and 80% by structure volume. They formed in the fuselage, wings and tail plates. However, the wide application of composite laminates doesn't mean all major technical cruxes have been solved. Actually, there still remains quite a few critical problems, which impede exploiting their full potential. Among these problems, their susceptibility to foreign object impact (FOI) is one of the key issues. FOI is a frequently encountered type of incidents during the service life of airplanes, such as tool dropping during the maintenance process or runway debris hitting when taking-off and landing. The damage of such impact could be a serious threat to the flight safety, as large extent of delaminations as well as transverse matrix cracks and fibre breakage would result from such impact which compromise the mechanical properties of these laminates significantly. Another reason is that such damage

usually submerges inside the laminates and is difficult to be detected. This may lead unsuccessful detection of such damage before it develops into a fatal failure.

Among the mechanical properties impaired by impact, the compression strength is of the most significance. Relevant studies revealed that up to 60% loss of compressive strength could have been inflicted when no obvious defect is observed from exterior [3]. Because the residual compressive strength significantly influences material selection and structural design, it is always highly concerned and a substantial studying efforts have been devoted to it in the past three decades, which will be reviewed in this chapter.

2.2 Classification of foreign object impact

The residual compressive strength of impact damaged composites is dominated by many factors, such as impacting velocity and angle, mass and texture of the impacting object, etc. Customarily, “low” or “high” velocity impact is adopted as an institutive description of impact characteristic. However, this kind of description is ambiguous before a specific field is specialized. For example, according to classic dynamics, the distinction between low and high velocity impact is whether dynamic behaviour and stress wave effects are negligible. In the field of aeronautics and aerospace, Craven [4] classified FOI into low velocity, high velocity and hypervelocity impact based on different speed ranges (Table 2.1). Low velocity impact is typically introduced by dropping tool or runway debris with the upper velocity limit of 100m/s. High velocity impact refers to bullets or missile fragments, and the velocity ranges from 100m/s to 1km/s. Above 1km/s is considered as hypervelocity impact which is usually only associated with dust or debris colliding with spacecrafts and satellites. In the practice of aircraft structural design, the range of

low velocity mentioned above is partitioned further. Prichard [5] defined the low-velocity impact as the incident like tool dropping of which the impact speed was about 5m/s, while the high-velocity impact as runway debris hitting of which the impact speed was about 70m/s. Olsson [6] found that when the impact times was in the order of the transition time for through-the-thickness waves, the response was dominated by three-dimensional wave propagation (Figure 2.1a), which was usually associated with ballistic impact. For longer impact times, the response is governed by flexural waves and shear waves (Figure 2.1b), which was typical for impact by hail and runway debris. For times much longer than the times needed by these waves to reach the plate boundaries the lowest vibration mode of the impactor–plate system predominates (Figure 2.1c), which was typical for dropping of heavy tools. He proposed that the impact response was not governed by impact velocity but the impactor-plate mass ratio. Furthermore, [7] derived a mass criterion for small mass impact. For the case of central impact on quasi-isotropic plates this criterion is sufficient when the impactor weighs less than 1/4 of the plate.

Table 2.1 Classification of FOI by Craven [4]

Definition	Velocity range	Example
Low velocity	<100m/s	Drop tool, runway debris
High velocity	100m/s-1 km/s	Bullet missile fragment
Hypervelocity	>1km/s	Dust debris colliding in space

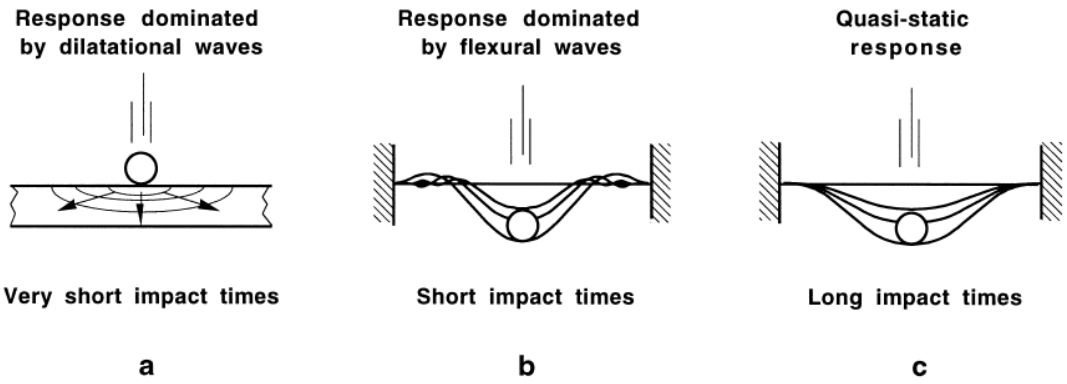

Figure 2.1 Response types during impact on plates (Olsson [6])

2.3 Significance of CAI

In this thesis the investigation will focus on the relevant issues induced by tool dropping, which is categorised as low-velocity impact by Prichard [5] and Olsson [6].

During the service life, the body of the aircraft may suffer from many kinds of impact, for example, tool dropping during the maintenance, runway debris hitting during the take-off, ground vehicle hitting, bird strike, uncontained engine failure, etc.. The damage severity can differ significantly among these impact incidents. For more severe impact incidents, such as bird strike or engine burst, they are supposed to be known by the flight crew or easily observed from ground inspection. Those less severe incidents, such as tool dropping, usually leave only tiny dents on the structure surface. Therefore, in the process of structural design, different levels of residual structural strength are required on account of different severities of impact events. For example, certification FAA [8] requires that structure must be designed to sustain ultimate load, limit load and continuing safe flight when bearing barely visible impact damage (BVID), visible impact damage (VID) and discrete source damage, respectively, which is illustrated in Figure 2.2.

It can be found that, in this specification (actually in almost all current design specifications and guidelines of composite aircraft structures), the detectability of impact damage through visual inspection methods rather than some advanced approaches, for example, the ultrasound inspection, are emphasized regarding the determination of design load. This is "purely economic"[1] consideration.

The low-velocity impacts usually produce insignificant impact dent, of which the depth varies from invisibility to minor VID. From the design guidelines mentioned above, it is seen that this level of impact matters as the damaged structures are expected to sustain ultimate load and limit load of the structure. Moreover, the form of damage induced at this impact level usually consists of delaminations, matrix cracks and, sometimes, limited fibre breakage [4, 9, 10], which is shown in Figure 2.3 and Figure 2.4. As a result, compressive strength of the overall structure is impaired most seriously due to the delamination. Therefore, as a measure of residual compressive strength, CAI becomes one of the most important parameters influencing the material selection and structure design in the aerospace industry.

[1] Quoted from 7.2.2 Methods of compliance to aviation regulations, MIL-HDBK-17-3F, 2002

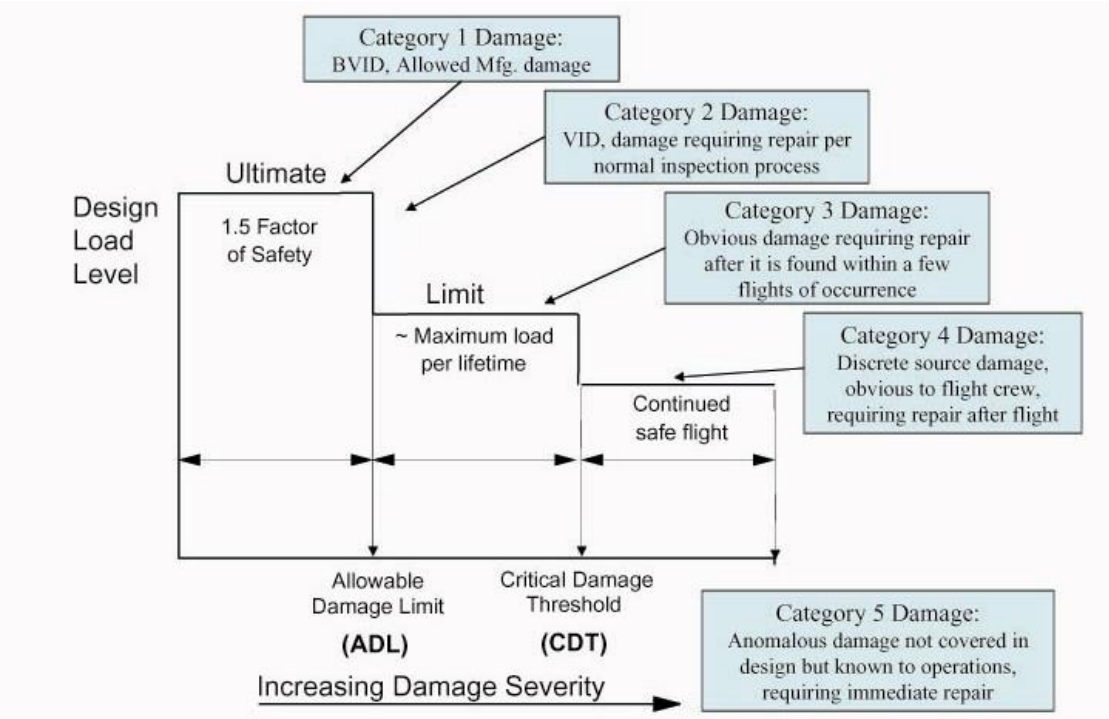

Figure 2.2 Schematic diagram of design load levels versus categories of damage severity [8]

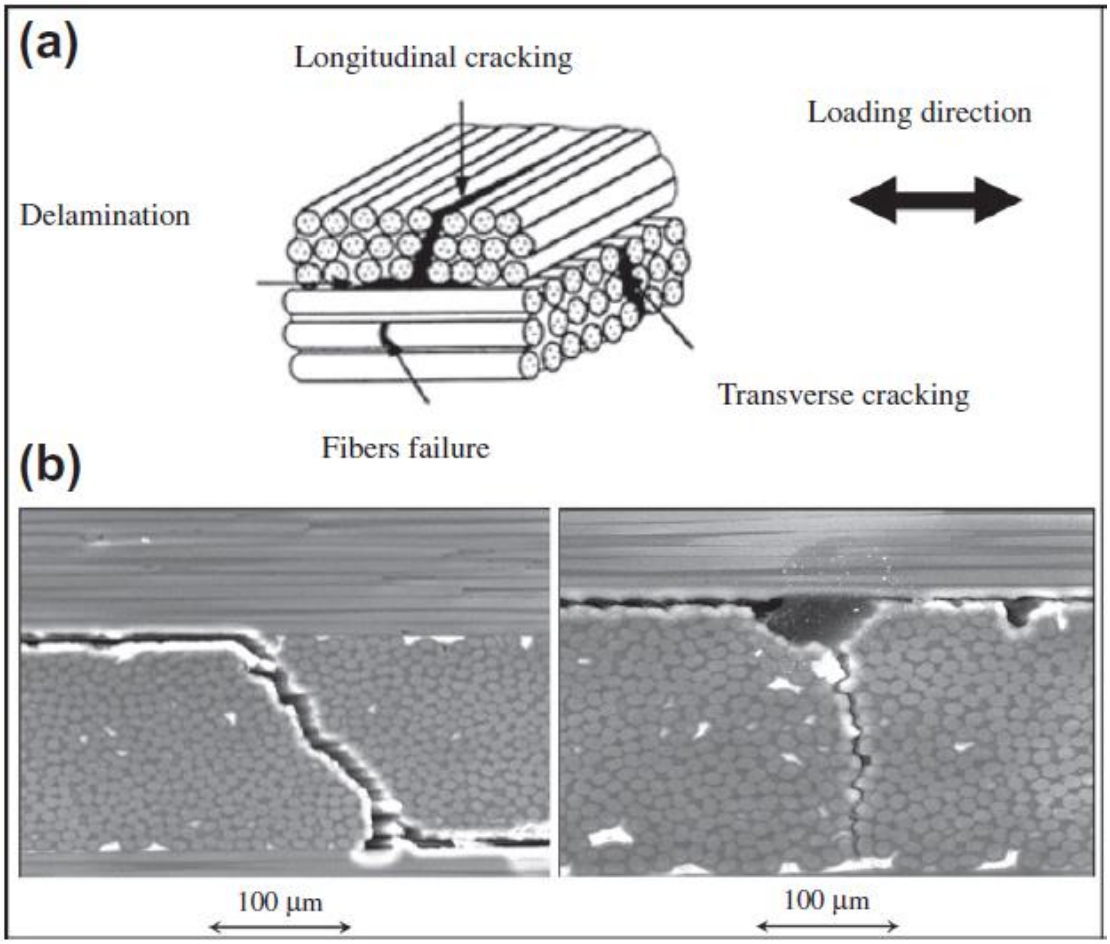

Figure 2.3 Different damage types induced by impact [10]

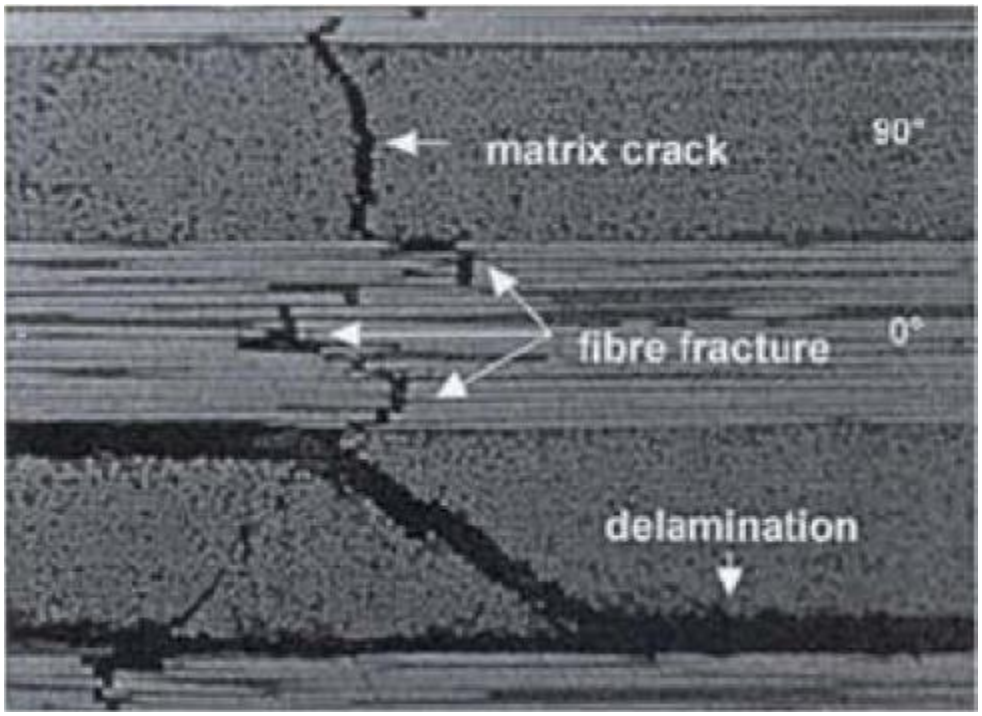

Figure 2.4 Damage modes induced by impact [11]

2.4 Experimental approaches for CAI study

So far, the common approach to investigate CAI is through experiments which consist of two steps: introducing impact damage to the specimen and subsequent compression to the specimen until it collapses, based on respective test standards ASTM D7136 [12] and ASTM D7137 [13], for instance.

2.4.1 Impact

Based on the classification of foreign object impact above, high velocity impact such as runway debris is usually simulated by gas gun test, while for low-velocity impact the most common way to introduce impact damage is through drop-weight impact. The specific process may vary one another, but the basic mechanism is to simulate diverse impact incidents by adjusting the shape,

mass and texture of the projectile as well as the impact velocity. In this thesis, the test standard ASTM D7136 [12] is employed and the device shown in Figure 2.5 is used for impact damage introduction. Generally speaking, the test fixture consisted of three major components: impactor, tube and support.

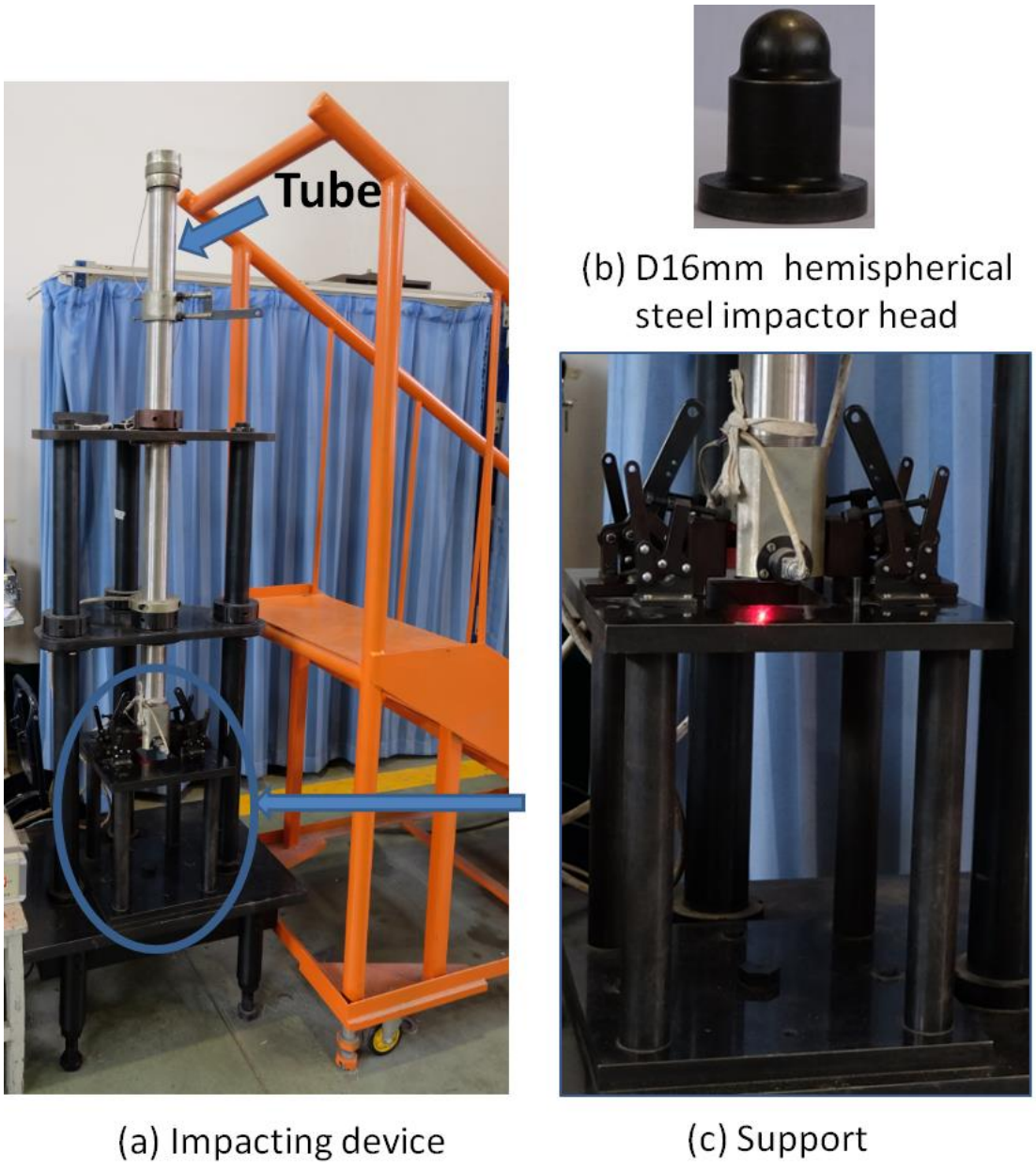

Figure 2.5 Impacting device

Impactor was the device used to impact laminates. It was made of metal, with a hemispherical tip. The weight, texture and size of striker tip could be customised for specific requirements. A steel striker with a hemispherical head of diameter 16mm was employed for all specimens.

Tube was the device for tubing the impactor. At the lower end of the tube when the tube was erected upright for test, a velocity detector was allocated to read the impacting speed. With the impactor weight and impacting speed, the impact energy could be calculated. By adjusting the drop height and/or mass of the impactor, the impact energy could be adjusted to the prescribed values.

The support was the device to hold the specimen, which is schematically illustrated in Figure 2.6. In the centre of the fixture base, there was a square hole of 125mm×75mm. A square groove on the top face of the fixture base was made, which was 150mm×100mm and 6mm in depth. The groove and the square hole were co-centred. Therefore, the specimen could be accommodated in the groove and partly supported around the perimeter. Four toggle clamps were installed on the fixture base to restrain the specimen from bouncing during impact. Furthermore, a piece of metal plate was slide in between the impactor and the specimen after the first impact. This was for the purpose of preventing rebouncing hits.

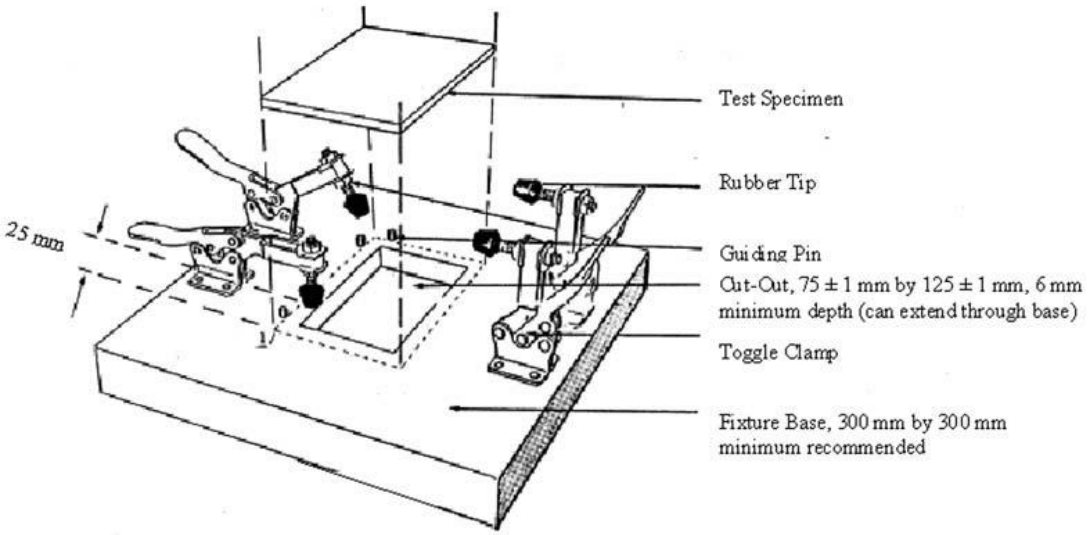

Figure 2.6 Impact support fixture (cited from Fig. 2 of ASTM [12])

Meanwhile, it is worth mentioning that some researchers [14] found that drop-weight impact test could be replaced with quasi-static indentation test, because the damaging states in terms of damage area and dent depth from these two different approaches were similar. However, for quasi-static indentation test the measure describing the severity of impact damage is indentation force rather than impact energy, which induces inconvenience in analogising with real impact incident.

2.4.2 Compression

At early stages of development, individual researchers employed specimens with different in-plane sizes, and several companies and organisations also had developed their own test standards, for example, ASTM D7137 [13], Boeing BSS 7260 [15], Airbus AITM1-0010 [16], SACAMA SRM 2R-94 [17] and NASA Reference Publication 1092 [18]. In the first four test standards, specimen sizes are prescribed similar to each other, about 150mm in length and 100mm in width. In the fifth, the required size is about 254mm in length and 127mm in width. As

the last one requires more material than the previous four, it becomes less commonly used now. In this thesis, the test standard ASTM D7137 is referred to in the CAI test, which will be described in detail in the following. It is worth mentioning that the compression test standards apply mainly to specimen with thickness thicker than 3mm. If the specimen is too thin, additional devices, for example, anti-buckling plates, are needed [9].

Compression tests in this thesis were conducted according to the test standard ASTM D7137 [13], of which the testing configuration is shown in Figure 2.7. The specimen was placed in a test fixture which was schematically shown in Figure 2.8 and compressed along the length direction. In order to prevent global buckling during the compressing process, the standard employs two pairs of sliding plates with knife edges, one on each side along the length direction of the specimen, approximately 4mm away from the edge (Figure 2.9(a)). On each surface of the specimen two strain gauges were attached at two symmetric points respectively, each of which was 25mm away from the length edge as well as the width edge (Figure 2.10). That is to say, on either of the two selected points on the specimen two gauges were attached back to back. This was done for the purpose of monitoring integral deformation of the specimen and avoiding global buckling in the early stage of experimental process. Because once bending takes place, two strains measured on the same point but opposite faces of the specimen would be divergent gradually. Once this divergence was observed, unloaded the specimen, adjusted the test fixture slightly and reloaded. Repeated this operation until obvious divergence of gauge readings vanished. The specimen was loaded until catastrophic failure by a universal test machine in displacement control mode, and the failure load was recorded as CAI strength.

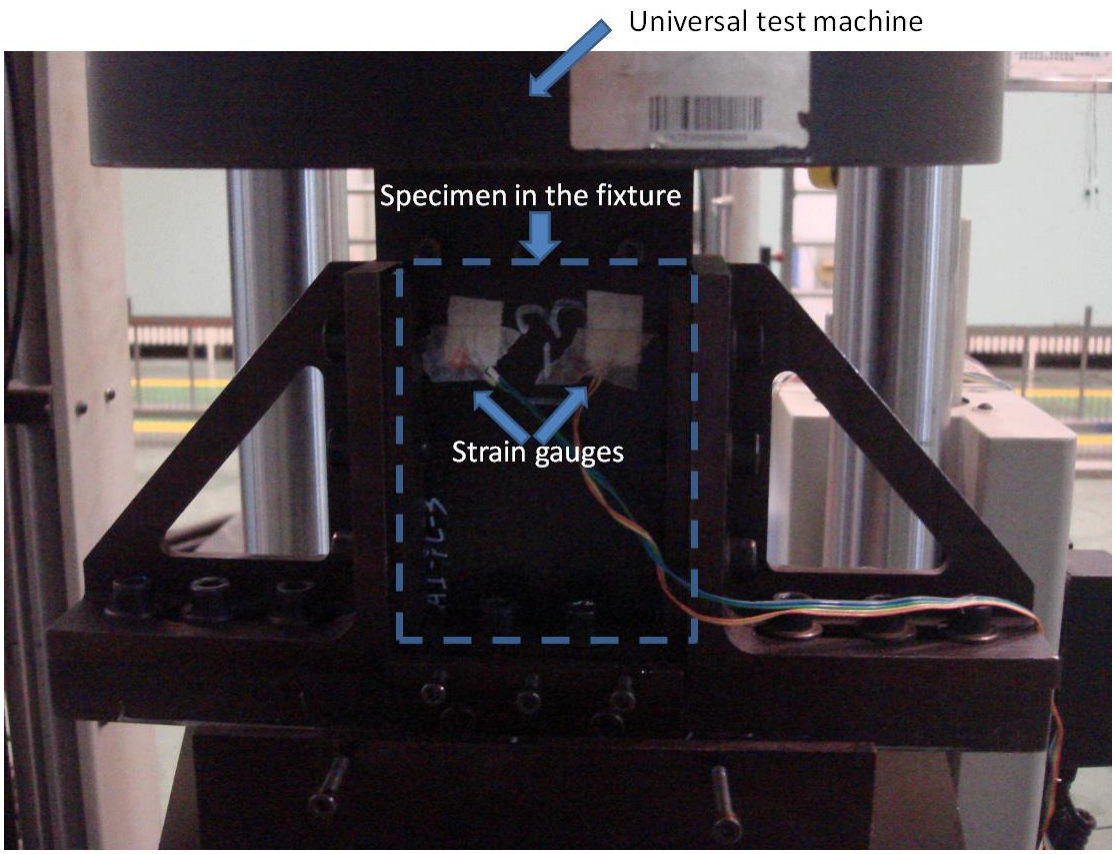

Figure 2.7 Testing configuration of CAI

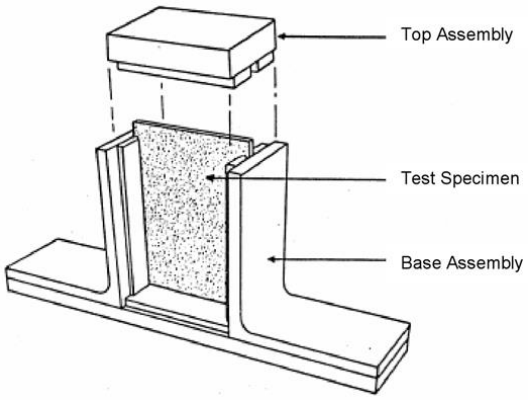

Figure 2.8 Schematic of compressive residual strength support fixture with specimen in place (cited from Fig. 1 of [13])

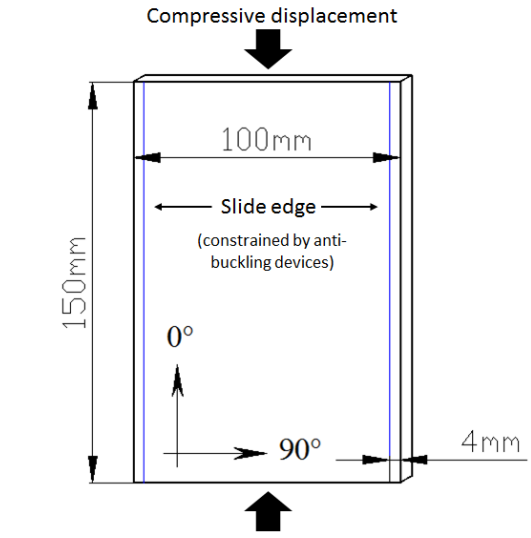

(a) Front view

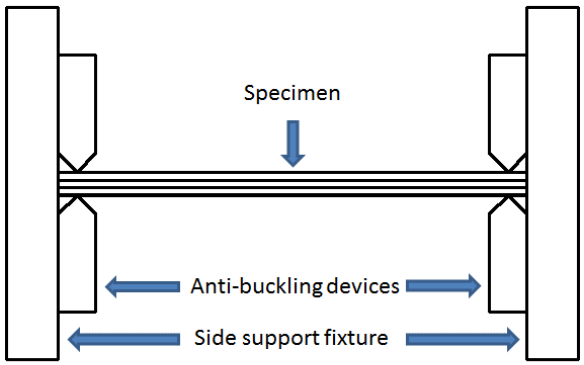

(b) Top view with side fixtures

Figure 2.9 Schematic of specimen details of the CAI model based on test standard ASTM D7137

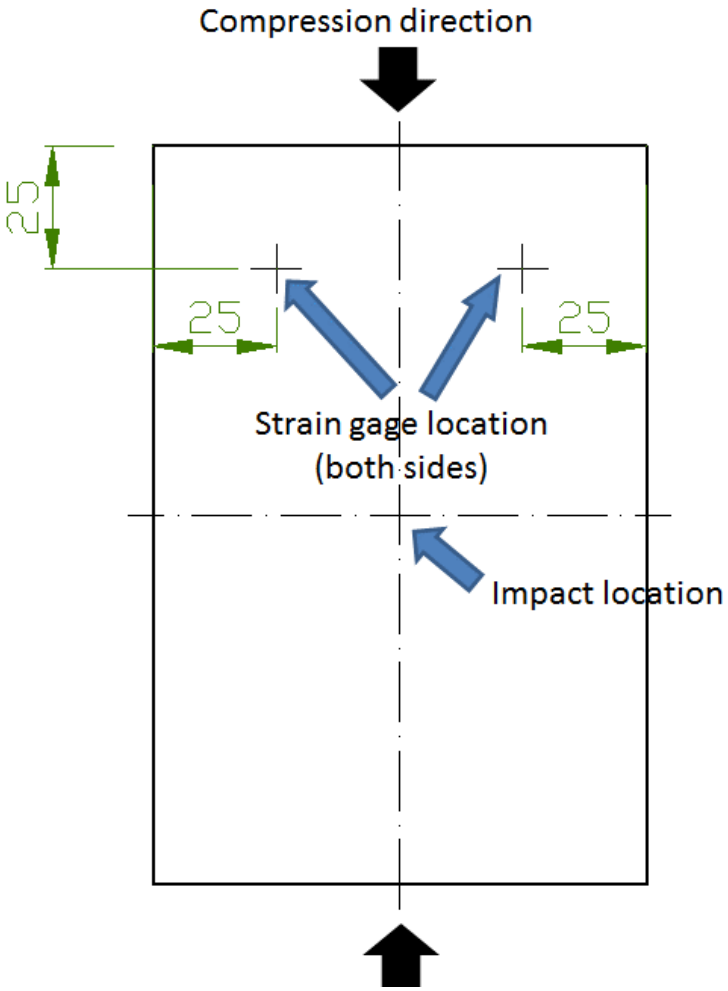

Figure 2.10 Locations of strain gauge on specimen (unit: mm)

2.5 Damage mechanism

Although experiments are the most reliable approach to investigate CAI currently, it is time consuming and expensive. For the purpose of reduction of cost and design cycle period, theoretical prediction method of CAI has been pursued over the past decades [3]. However, a unanimous prediction method is still not yet available. One of the reasons is that the damage mechanism is not clearly understood. In this section, the issues of current CAI study are reviewed and the objective of the PhD project is set out accordingly.

2.5.1 Two perceptions

There are mainly two perceptions of damage mechanism of CAI. In this thesis, they are referred as “delamination propagation” and “stress concentration”, respectively, which will be introduced in detail below. It is worth explaining the physical obstacle for studying the damage mechanism of CAI through experiments. This is because the damage development progresses mainly inside the laminate. Although some instruments, such as infrared camera and acoustic emission, are capable of detecting the occurrence of damage inside, they can hardly distinguish between different failure modes. As an alternative, the damage mechanism can also be investigated theoretically based on available experimental observations. However, the truth is that different emphases lead to different perceptions.

2.5.1.1 The perception of delamination propagation

Based on the damage characteristic that large area of delaminations are observed after the low-velocity impact, one commonly accepted perception of the damage mechanism is delamination propagation. When the delaminated laminate is subjected in-plane compressive load, sublaminates lose stability and deform into the post-buckling regime. Consequently, a tendency of relative movements of neighbouring sublaminates arises, rendering energy release rate (ERR) at delamination front increasing. Therefore, it is expected naturally that once ERR exceeds its critical value, delamination propagation takes place and the whole laminate collapses due to this unstable and catastrophic propagation. To the best of the author’s knowledge, a few cases had been reported on the observation of delamination propagation successfully, which are shown in Table 2.2. C-scan was employed by these researchers to monitor the delamination

propagation process. The process was generally like this: (1) before CAI test, the impacted specimen was scanned to obtain the delamination image as a baseline; (2) then the specimen was loaded in the test rig and compressed to some extent before catastrophic failure; (3) the specimen was unloaded and scanned again for comparison. Step (2) and (3) were repeated until the specimen collapsed finally.

With this perception, Chai, Babcock [19] presented an analytical model to predict the failure load, in which a single one-dimensional delamination or also referred as through-width delamination was assumed. Afterwards, many other researchers [20-23] followed and developed the problem from single delamination to multiple delaminations. For example, [20] proposed an analytical method to predict the buckling load of a one-dimensional delamination. [21] calculated the buckling load of evenly-spaced and uniform multiple delaminations through Rayleigh-Ritz method in one-dimensional problem. [23] employed numerical method to investigate the delamination buckling for slender composite panels in three-dimensional problem. However, in through-width delamination case, the delamination can only propagate along the loading direction which is not in accordance with practical CAI cases in which delaminations are of limited sizes in both longitudinal and width directions. Even if the failure was dictated by delamination propagation, it would not be in the longitudinal direction alone. Failure occurs over the cross section perpendicular to the loading direction. Therefore, models with two-dimensional delaminations have been developed. Initially, the assumption of a circular or elliptical shape was widely adopted [24-28] due to its relative ease for analytical and numerical simulation.

However, experimental evidence suggested that circular or elliptical delamination assumption was not as accurate as peanut shaped or double spiral fan-shaped ones, [3, 28-31]. Additionally, delamination propagation simulation is not the only intractable issue, geometric nonlinearity with structural instability, the contact condition between delaminating sublaminates, and the damage growth at multiple sites [27] need to be considered simultaneously. Taking all of them into account, analytical method is impractical and numerical approaches such as finite element (FE) method demonstrate their versatility. Thanks to the fast developing computation capability and newly developed models in FE method for simulating delamination propagation [32], fairly complex FE models can be analysed on small-scale workstations or even desktop PCs, and this promotes extensive investigations on this subject in recent years. Even though, the computation cost is still high and a typical job can easily take days or longer to run [29].

Table 2.2 Reported cases of delamination propagation (In column "Type", A for artificially induced delamination, I for impact-induced delamination)

Material system	Referring	Specimen size Length*width (mm*mm)	Lay-up	Delamination		
				Type	Numbers	Radius (mm)
HTA/6376C	Nilsson, Asp [23]	150*150	$[(90/0)_{17}/90]$	A	3, 5, 7	30
IM7/977-2 T800/5245C	De Freitas and Reis [33]	150*100	$[-45_4/45_4/0_3/90]_S$ $[-45_3/45_3/0_5/90]_S$	I	6	unknown
IM600/133	Aoki, Kondo [31]	150*100	$[45/0/-45/90]_{4S}$	A	7	8-20
HTA7/6376C	Nilsson, Thesken [34]	300*150	$[90/0/90]_{16}$	A	15	10
HS160/REM	Ruan, Aymerich [35]	87.5*65	$[0_3/90_3]_S$	I	2	unknown

2.5.1.2 The perception of stress concentration

On the other hand, although delamination propagation is widely accepted as the damage mechanism of CAI, there are researchers [1, 36-41] inclining to an alternative damage mechanism,. Their considerations were that delaminated area of an impacted damaged laminate was easy to buckle when it was subjected to compression and could only sustain a reduced amount of compressive load afterwards. It was conceivable that stresses would redistribute as the delaminated sublaminates buckle, given the reduced effective stiffness of the buckled zone.

Stress concentration arose around the delaminated area, which led to catastrophic failure of the whole laminate when the concentrated stress level exceeded the material strength. An evidence to support this perception is as follows. At the beginning, engineers endeavoured to increase the matrix toughness of the laminate to enhance the interlaminar strength against delamination propagation, and expected that the CAI strength would increase as a consequence. However, experimental results [1, 41-44] demonstrated that the CAI strengths of impact damaged laminates tended to be the same as toughness has increased to a certain level provided that delaminated areas in both sample types were of similar sizes. This negates delamination propagation as the relevant damage mechanism for laminates of sufficiently high toughness as normally used in aerospace industry. If the mechanism of stress concentration is tenable, the CAI prediction method can be significantly simplified compared with that based on the perception of delamination propagation, because the damage mode of delamination propagation is avoided, expensive computation cost for simulation of delamination propagation can be waived.

2.5.2 Techniques associated with CAI

In the past three decades at least [3], substantial researching work has been performed in order to understand CAI behaviour. It is amazing that a significant wide range of knowledge and techniques are involved to solve this problem, such as structure stability, fracture mechanics, failure criteria of composite material, finite element techniques, non-destructive inspection techniques, optical observation techniques, etc.. the subject areas involved in the investigation of CAI can be presented a problem tree, as shown in Figure 2.11. They are reviewed below in their

logical order although it proves beneficial to present the states of developments in a chronological order.

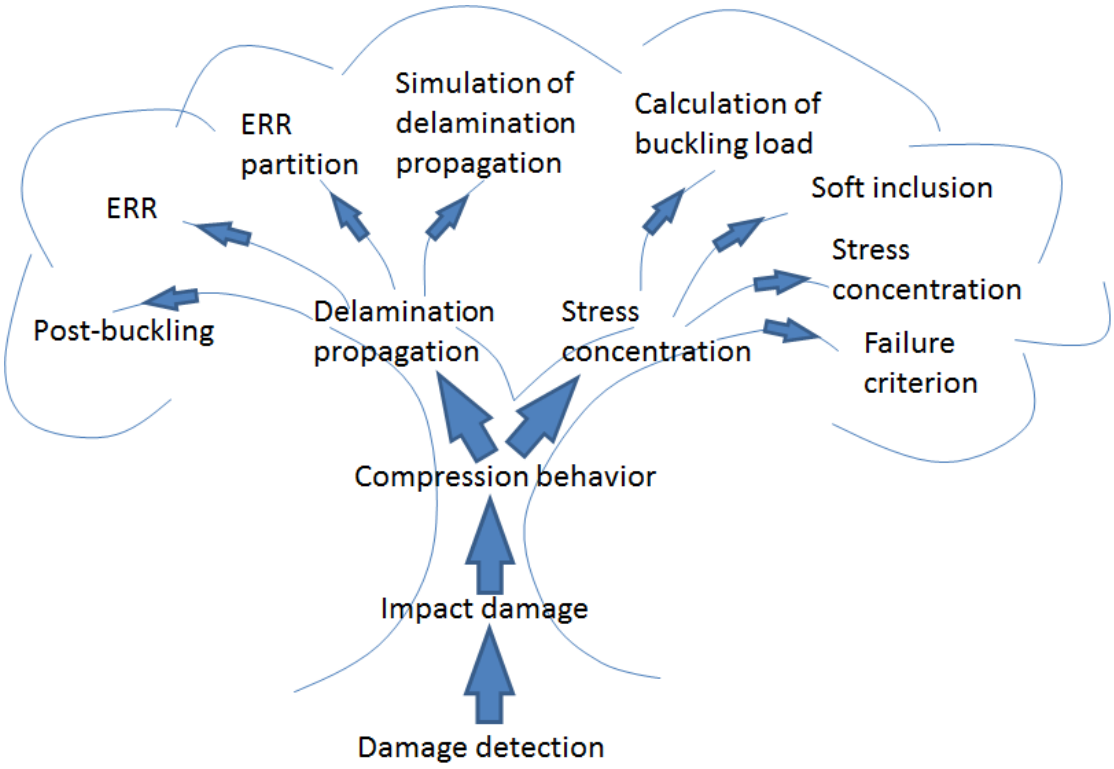

Figure 2.11 Hierarchy tree of CAI-related subjects

2.5.2.1 Damage detection

Once laminate is subjected to low-velocity impact, impact damage is generated over the laminate thickness in mainly three forms: delaminations, transverse matrix cracks and fibre breakage. As these damages submerge inside, they cannot be detected and evaluated by naked eyes directly. Therefore, many inspection methods have been employed, which are divided into destructive and non-destructive inspection (NDI) approaches. Destructive inspection methods mainly include

sectioning and polishing technique [45] and deply technique [46]. The first one is to section the specimen along the interesting area followed by polishing and microscopy. The second one is to mark the damage by using a dye penetrant, then put the specimen into a heated oven to degrade the matrix material. Afterwards, separate the specimen ply by ply with extreme care. The state of transverse matrix cracks and fibre breakage on each individual ply can be examined directly. The stain of dye penetrant remained on the ply reveals the shape of delamination. So far, deply technique is the best approach to reveal impact damage precisely and comprehensively compared with NDI approaches. Although Prichard [5] claimed that transverse matrix cracks could not be seen because most of the matrix material had been removed through deply. The transverse matrix crack actually could be identified as in un-cracked part fibres remained aligned while over the cracks fibres become slightly untidy [47]. NDI approaches include ultrasound scan, X-radiography and acoustic emission, etc.. Ultrasound scan, such as C-scan, may be the most widely used one, which makes use of ultrasound to detect the defect underneath the specimen surface. The mechanism is that the ultrasound wave transmits through a medium and reflects when it meets the interface to the neighbouring medium (for example the void or impurity). According to the speed of ultrasound wave transmitting through this medium and the time taken for the wave emitting and reflecting back, the depth of that defect can be worked out. Although C-scan is the most widely used technique nowadays, it has an intrinsic weakness that the delamination closest to the scanning sensor prevent delaminations further away from the sensor to be detected, of which the reason is schematically shown in Figure 3.1.

2.5.2.2 Impact damage

As mentioned above, impact damage consists of three forms mainly: delaminations, transverse matrix cracks and fibre breakage. In this section, they will be reviewed respectively.

When subjected to low-velocity impact, as a laminate bends, the tendency of relative sliding between neighbouring laminae produces delamination due to significant mismatch of the in-plane elastic properties across interlaminar interfaces and the relatively weak inter-laminar shear strengths. Through NDI, such as C-scan or X-radiography, it can be found that the projected image of delaminations through laminate thickness usually resembles a circle or an ellipse roughly [3, 10]. However, through deply technique it has been confirmed that the shape of delamination on each individual interface is peanut shaped or double-fan shaped bounded by the fibre orientations of the laminae on both sides of the delamination in acute angle [47], which is shown in Figure 2.12 [3], Figure 2.13 [10], Figure 2.14 [48] and Figure 2.15 [49], schematically. It is found both analytically and experimentally that delaminations tend to appear almost on all interfaces through laminate thickness except between plies of the same fibre orientation [50], and the outline of delamination distribution in a section view is not cylindrical but conical or spindle depending on many factors.

From section/polishing technique it can be found that the transverse matrix cracks extend through laminae and connect delaminations of upper and lower interfaces [37, 44, 45]. In the meantime, from deply technique it is found transverse matrix cracks in each lamina mainly locate at the co-boundary of upper and lower delaminations [47]. The transverse matrix cracks are

generated during the impact process as a path to transfer fracture energy between delaminations of upper and lower interfaces.

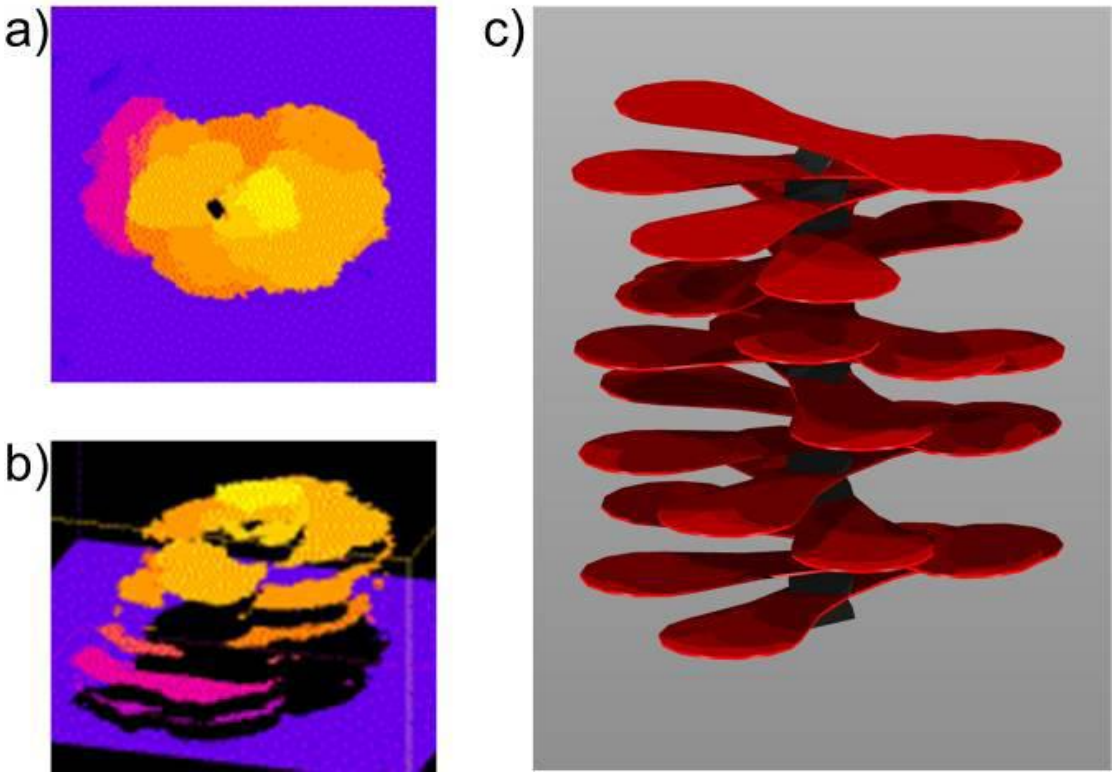

Figure 2.12 2D C-scan, (b) 3D C-scan and (c) computer generated idealised model of delaminations [3]

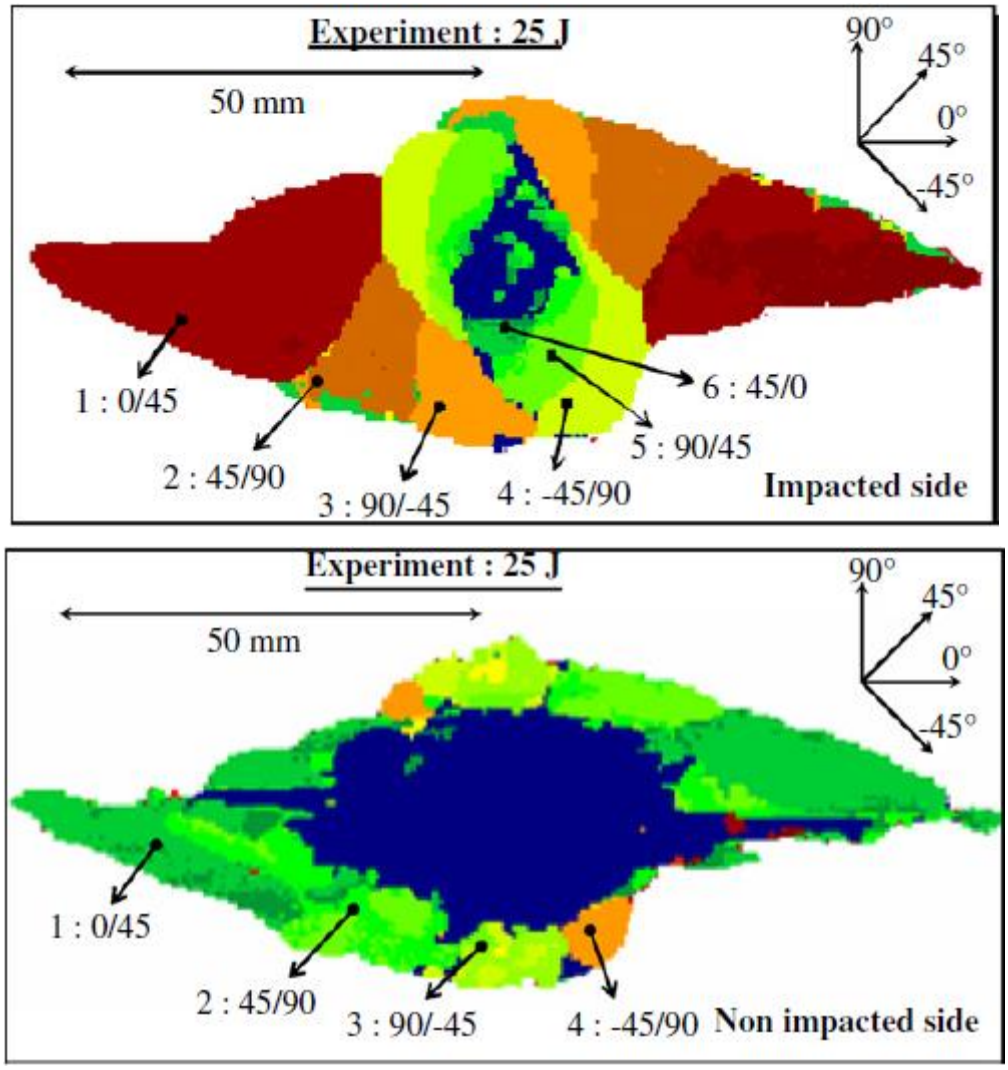

Figure 2.13 2D C-scan images of delaminations [10]

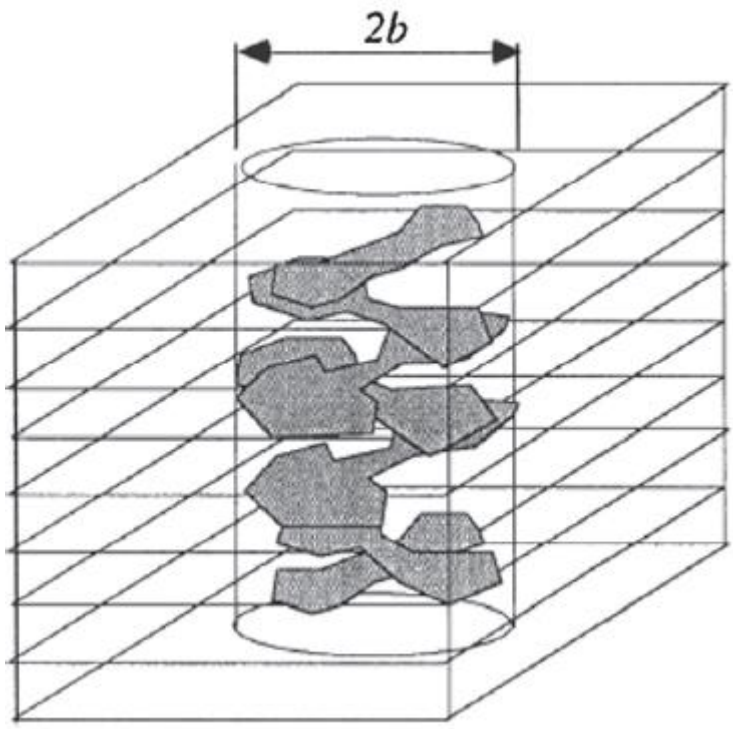

Figure 2.14 Schematic demonstration of delamination distribution due to impact [48]

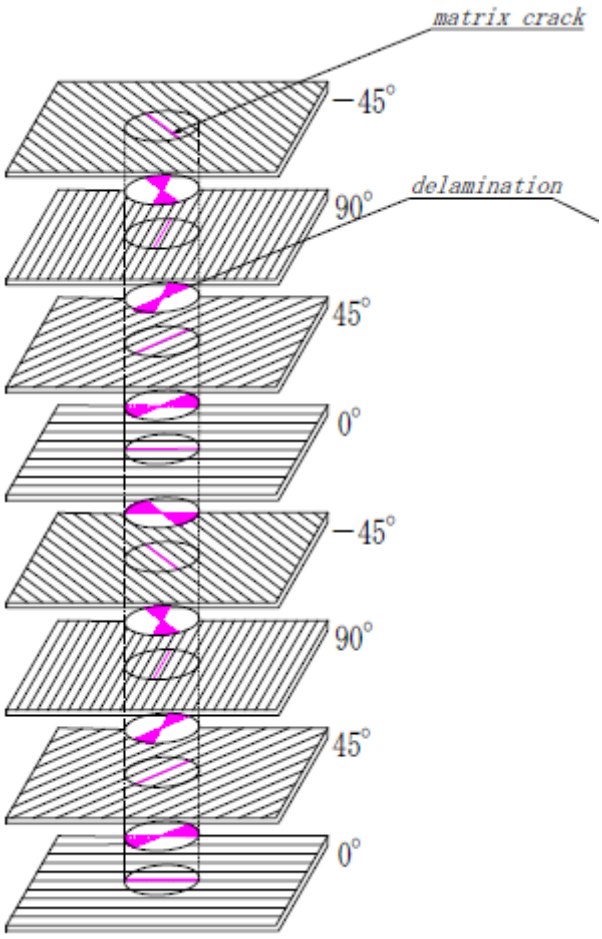

Figure 2.15 Analytical model with spiral delaminations [49]

Fibre breakage mainly concentrates at the central zone of impact-induced damage where impacting object contacts. Its significance is not as important as delaminations because in compression cases stability is affected by the extent of delaminations. Moreover, Shen, Yang [47] argued that fibre breakage was not definitely present due to impact, but only appeared when impact energy was greater than a threshold. He attributed this to different damage mechanisms of impact, which could be identified by impacting dent depth.

2.5.2.3 Compression behaviour

When an impacted laminate is subjected to compression before final collapse, one of the most significant observations is the local buckling of delaminated area. This phenomenon can be observed through a number of approaches experimentally, such as Moire fringes [51], deflection sensor [52] and digital image correlation (DIC) measurement [53]. After buckling, the delaminated area will enter the post-buckling regime and its capability to sustain compressive load will be impaired severely. Usually, it is assumed that the load-bearing capability remains constantly as its buckling load, but Gu and Chattopadhyay [54] reported that the ultimate load was as high as three times of its critical buckling load in through-width delamination cases experimentally. As the compressive load increases continuously, the plate collapses due to fibre kinking failure which is the consequence of small misalignments of fibres in composite when subjected compression[55].

The presence of buckling is the common ground of the two perceptions, as shown in Figure 2.11. However, they bifurcate from there and develop in respective directions. For the perception of delamination propagation, the core issue is how to simulate delamination propagation. However, before reaching this goal, there are some other hurdles lying ahead, for example, post-buckling simulation, energy release rate (ERR) calculation and ERR partition. On the other hand, the perception of stress concentration is not easily assessed either. The problems of calculation of critical buckling load, stiffness degradation method and in-plane failure criterion, etc. are the hurdles which must be overcome.

2.5.2.4 Post-buckling simulation of delaminated sublaminates

The problem of post-buckling covers an extremely wide range. In this thesis, it is only limited to the case of delaminated sublaminates, of which the geometry is 150mm in length and 100mm in width. Most damage development of CAI occurs at the stage when sublaminates enter the post-buckling regime. Since the deformation configuration will directly affect the stress state at the delamination front and consequent delamination propagation, simulation of post-buckling deformation is essential to the CAI prediction in the delamination propagation perception.

Solving post-buckling problem is not easy as it involves geometrical non-linearity. Gaudenzi, Perugini [56] investigated the post-buckling behaviour of composite laminates with through-width, equal-size, equally-spaced multiple delaminations on the basis of Rayleigh-Ritz method. Contact problem was also considered at the time. The post-buckling paths of delaminated laminates were solved through Newton-Raphson iterated method. However, this strategy is only applicable to some simple cases since the assumption of the deflection function for the Rayleigh-Ritz method will become extremely difficult when complex delamination pattern is encountered. FE method is a more effective approach for post-buckling analysis of complex structure. For example, Whitcomb [25] employed a three-dimensional, geometrically nonlinear FE program to calculate the equilibrium state in the post-buckling regime. The equilibrium state is determined by minimizing the total potential energy, and Newton-Raphson iterated method was used to solve the nonlinear equations. Contact problem was also considered. Aoki, Kondo [31] employed ABAQUS to solve the post-buckling process. In their FE model, the initial imperfection resembled the buckling mode which was obtained from linear buckling analysis.

Even in FE method, there still have been a few alternatives, such as implicit method using Newton-Raphson iterated method or using Riks method, or explicit method using direct integration based on central difference. Newton-Raphson iterated method is the well-known approach to solve non-linear problems. However, when it encounters unstable problems like the one here of which load and/or the displacement may decrease as the solution evolves, severe convergence problem may arise and the calculation may fail. In contrast, Riks method is more suitable as the equilibrium path is searched within a circle rather than a fixed increment size. However, if too many factors need to take into account, such as contact, material failure and delamination propagation, both Newton-Raphson iterated method and Riks method become incompetent. This is because both methods need to calculate the inverse of stiffness matrix which usually leads to severe convergence problem. As an alternative, explicit method is adopted which is mainly used to cope with dynamic problems. Because this avoids the inverse of stiffness matrix, the analysis can usually be carried out successfully. However, as CAI problem is considered as a quasi-static simulation, the time period and/or mass need to be set properly in explicit method to balance the simulation precision and calculation cost.[2]

2.5.2.5 ERR calculation

Referring to the fracture mechanics on composite laminates, ERR is the quantity to dominate delamination propagation. ERR is defined as the energy dissipated during delamination growth per unit of newly created delamination surface area, which is expressed as

[2] Details seen in "Computation cost", 6.3.3 Explicit dynamic analysis, Abaqus analysis user's manual, Version 6.11

$$G = -\frac{\partial(\Pi)}{\partial A} \tag{2.1}$$

where Π is the total potential energy and *A* is the area of delamination growth [57].

Employing this equation to calculate ERR in CAI, post-buckling deformation configuration must be known for the calculation of the potential energy of the whole structure. In the early stage of development, limited by computation capability, iterative methods were not always employed to obtain the nonlinear deformation path. Instead, some assumptions were adopted to simplify the problem. For example, Chai, Babcock [19] studied various types of through-width delamination cases such as thin film and general case. He assumed the length of the delaminated section remained unchanged after it buckled and the membrane stress in buckled laminate was the same as buckling stress. Based on these assumptions, the total potential energy was calculated. Williams [57] employed the similar strategy. He presented the expression of ERR at delamination tip in a plate containing through-width delamination in terms of bending moment, shear force and axial force acting on two individual sublaminates. The section forces and moments at the post-buckling configuration were then calculated based on the assumption that the compressive load kept constant and equalled to the critical load. Obviously, these assumptions mentioned above cannot describe the post-buckling deformation precisely and brings in significant error. As ERR is a local quantity, it is affected only by the forces at the crack tip [57, 58]. In compression cases, a small turbulence of compressive displacement may affect the deflection of post-buckled sublaminate significantly, and the stress state around the delamination front consequently. Therefore, calculating the post-buckling configuration accurately is essential for ERR evaluation, and advanced approach involving nonlinear analysis must be adopted. For example, Gaudenzi,

Perugini [56] investigated the case of through-width, equal-size, equally-spaced multiple delaminations and presented the expression of ERR analytically. The stress state around the delamination front was obtained by solving the nonlinear governing equations through the use of Newton-Raphson iterated method. Chai and Babcock [59] investigated the case of thin-film, circular delamination with self-similar growth assumption. The nonlinear governing equations were solved numerically by Newton-Raphson iterated method as well.

Benefited from the fast developing computation capability, FE method gradually became one of the most popular approaches to solve mechanical problems of such complex structures. In the meantime, virtual closure crack technique (VCCT) was developed to calculate ERR, which is highly efficient through FE method. It is worth claiming clearly that although VCCT is widely mentioned in the literature, there are two methods: two-step VCCT and modified VCCT [60]. Two-step VCCT is based on the assumption that the energy released when the crack is extended by Δa from a (Figure 2.16(a)) to a+Δa (Figure 2.16(b)) is identical to the energy required to close the crack between location l and i (Figure 2.16(a)). Here, index “1” denotes the first step depicted in Figure 2.16(a) and index “2” the second step as shown in Figure 2.16(b). X1 and Z1 are the shear and opening forces at nodal point l to be closed (Figure 2.16(a)) and u2 and w2 are the differences in shear and opening nodal displacements at node l as shown in Figure 2.16(b).

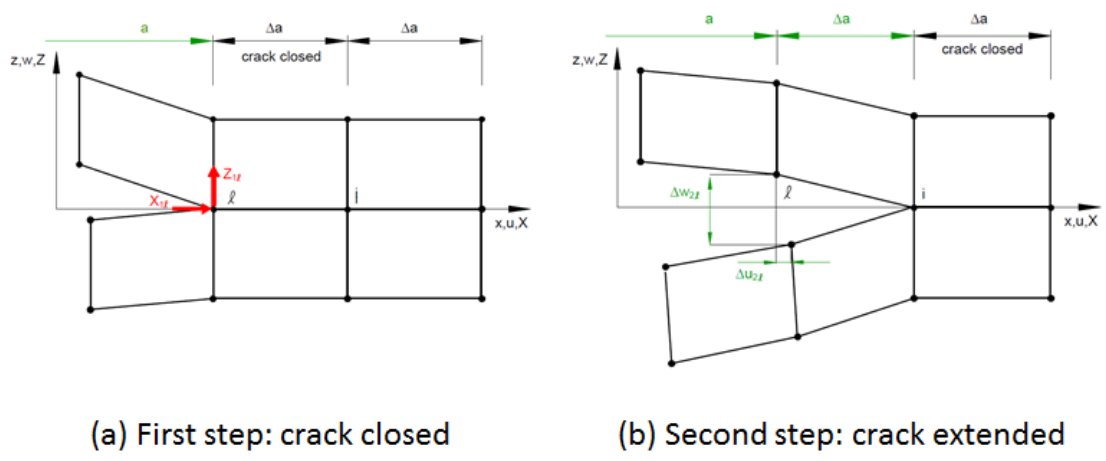

Figure 2.16 Two-step VCCT [60]

However, the calculating efficiency of two-step VCCT is relatively low as two steps of analysis are required. Therefore, modified VCCT is developed, which is based on the same assumptions as the crack closure method described above. Additionally, it is assumed that a crack extension of Δa from a+Δa (node i) to a+2Δa (node k) does not significantly alter the state at the crack tip (Figure 2.17). Therefore the displacements behind the crack tip at node i are approximately equal to the displacements behind the original crack tip at node l. Further, the energy released when the crack is extended by a from a+Δa to a+2Δa is identical to the energy required to close the crack between location i and k. Xi and Zi are the shear and opening forces at nodal point i and u and w are the shear and opening displacements at node i as shown in Figure 2.17.

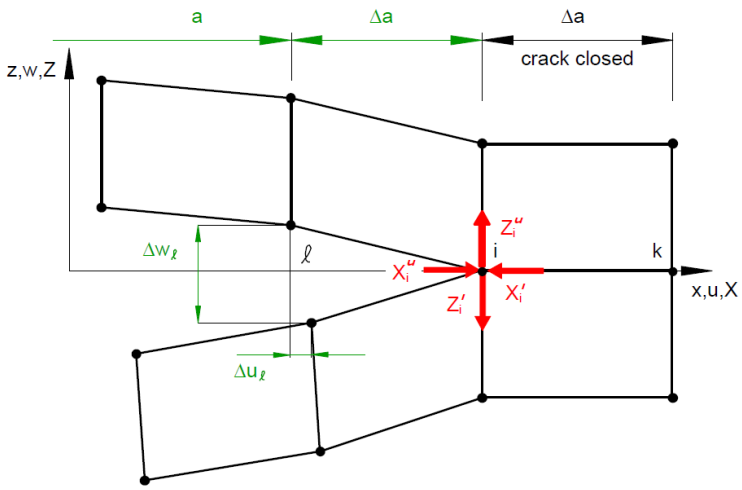

Figure 2.17 Modified VCCT [60]

Compared with earlier approaches to calculate ERR based on the definition, VCCT brought a remarkable significance. Through Equation (2.1), only an average ERR can be obtained through the derivation of dissipated energy with respect to increased crack area based on the assumption of self-similar growth. However, ERR is proved to vary significantly along the delamination front and delamination propagates rarely in self-similar pattern. Therefore, approaches of obtaining the ERR distribution and simulating local delamination propagation are essential. VCCT, based on FE method, meets these requirements. With VCCT, Whitcomb and Shivakumar [24] investigated the distribution of ERR around the perimeter of a rectangular delamination in a plate. Klug, Wu [61] investigated the sensitivity of ERR to the configuration of delamination front around an embedded circular delamination, and found that the bending stiffness of the sublaminate in the delamination zone governed the delamination growth.

2.5.2.6 ERR partition

Through diverse methods mentioned above, the ERR can be obtained. However, the ERR cannot be used directly for delamination propagation simulation through the following criterion

$$\frac{G}{G_{\mathrm{C}}} \leq 1 \tag{2.2}$$

where G is the current ERR and G_C is the critical energy release rate (CERR). The reason is that G_C is not a material property which may vary with the loading conditions. In fracture mechanics, a crack can be in one of three modes or any combinations of them (Figure 2.18): (1) opening displacement or tensile cracks (Mode I cracks); (2) transverse shear cracks (Mode II cracks); and (3) longitudinal shear cracks (Mode III cracks). It is impossible to measure the CERR through experiments at all mode ratios. The feasible approach is to obtain some characteristic CERRs (for example, CERR of Mode I, II and some CERRs at specific mixed ratios) and then to propose a mathematical expression to best fit these crucial CERR points. There are two most commonly used criteria. One is referred as power law, which is given in Eq. (2.3).

$$\left(\frac{G_{\mathrm{I}}}{G_{\mathrm{IC}}}\right)^{\mathrm{a}} + \left(\frac{G_{\mathrm{II}}}{G_{\mathrm{IIC}}}\right)^{\mathrm{a}} + \left(\frac{G_{\mathrm{III}}}{G_{\mathrm{IIIC}}}\right)^{\mathrm{a}} \leq 1 \tag{2.3}$$

where G_{I}, G_{II} and G_{III} are the current ERR in Mode I, II and III, G_{IC}, G_{IIC} and G_{IIIC} are the CERR in Mode I, II and III, respectively. The power α is usually determined through experiments.

The other one is referred as BK law [62], of which the expression is shown in

$$G_{\mathrm{IC}} + (G_{\mathrm{IIC}} - G_{\mathrm{IC}})\left(\frac{G_{II}}{G_I}\right)^{m} = G_{\mathrm{TC}} \tag{2.4}$$

where G_{TC} and m are the total CERR and material property, respectively.

There are already mature test standards for measuring CERRs at Mode I, II and any given mixed mode ratios, respectively. For example, DCB (double cantilever beam test, such as ASTM D5528), ENF (end notched flexure, such as Chinese aviation industry standard HB 7043-96 [63]) and MMB (mixed mode bending test, such as ASTM D6671) test for Mode I, II and mixed mode, respectively. Usually, it is found the CERR of Mode II is significantly higher than that of Mode I [64]. Table 2.3 lists some CERRs of Mode I and II as quoted from literature. In the meantime, there is still not a unanimous testing method for measuring CERR of Mode III, and the value is usually designated equivalent to that of Mode II [23].

Before Equation (2.3) can be used, ERR must be partitioned into separate modes. Regarding ERR partition, substantial publications were devoted through diverse approaches. For delaminated plates, an analytical partition method is usually defined by the relative deformation of the upper and lower sublaminates at the delamination front. For example, Williams [57] suggested that Mode I crack was presented by a pair of moments and transverse shear forces, which applied to the opposite sides of delamination and acted in opposite directions. Mode II was obtained when the curvatures of the upper and lower sublaminates at the delamination front were the same. The underlying justification for this approach was associated with the relative displacements between the surfaces of the delamination around its tip. The opening displacement produced Mode I while Mode II corresponded to an in-plane sliding displacement. However, a pair of moments acting in opposite directions applied to a split beam with two arms of different thicknesses, for example, results in non-zero relative sliding displacement. This means that it is a

mixed mode rather than a pure mode I problem (quoted from Zou, Reid [65]). Therefore, in order to modify it, Bazhenov [66] presented an adaptive expression of CERR of Mode I, which considered the individual bending angles of upper and lower sublaminates for the case of DCB opening mode with different thickness of sublaminates.

Table 2.3 Collection of CERR values of some material systems

Material system (fibre/matrix)	Referring	G_{IC} (J/m^2)	G_{IIC} (J/m^2)
IM7/8551-7	[49]	200	610
E-glass/epoxy	[49]	240	1500
Unknown	[32]	514	1014
T300/913	[32]	188	416
Unknown	[32]	250	1080
Unknown	[32]	275	300
T300/946	[67]	88	315
HTA/6376C	[68]	200	570
T800h/924C	[69]	300	580

Unknown	[70]	306	632
IM600/133	[31]	440	1860
Unknown	[34]	196	596
Unknown	[56]	200	570

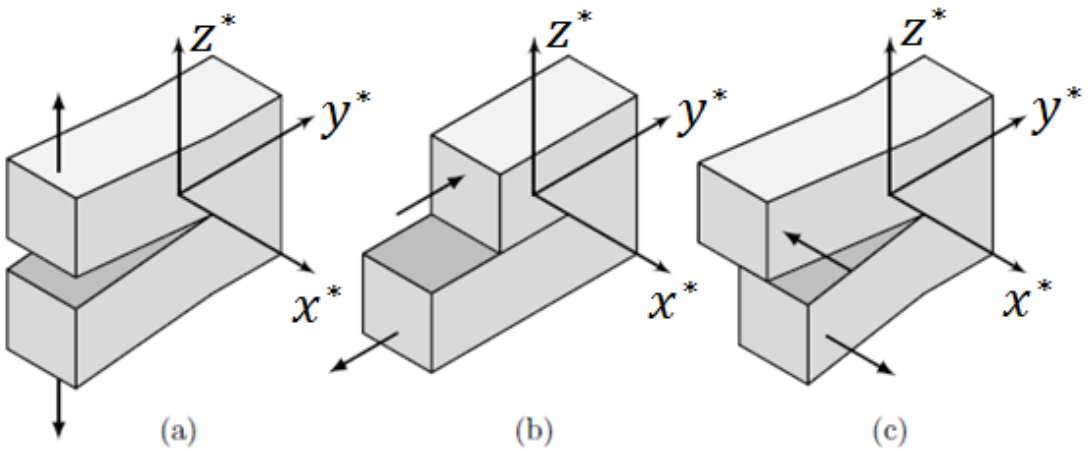

Figure 2.18 The three basic modes of fracture [58]. (a) Mode I. (b) Mode II. (c) Mode III

Wang and Harvey [58] developed a new partition method based on Euler and Timoshenko beam theories. Firstly, they presented a strategy to divide the crack mode globally and locally. By "globally pure" it meant that the pureness was defined with respect to the whole region mechanically affected by the presence of the crack tip. The global partition of ERR was calculated by considering this whole region. Further, the globally pure modes were divided into two pairs. In one pair Mode I was defined as the resultant shearing force over the whole region in front of the crack tip equalled to zero, while in the other pair Mode II was defined as the resultant moment equalled to zero. Referring to "locally" it meant that the pureness was defined with respect only to the crack tip. The local partition of ERR was therefore calculated by considering the near crack-tip region only. Similarly, the locally pure modes were divided into two pairs as well. The first pair was referred as DF pairs, of which zero crack tip relative shearing displacement was

defined as Mode I, and zero crack tip opening force as Mode II. The second pair was referred as FD pairs, of which zero crack tip shearing force was defined as Mode I, and zero crack tip relative opening displacement was defined as Mode II. Then they applied Euler and Timoshenko beam theories to above partition rules respectively for investigation. A detailed account discriminating diverse beam theories and mode partition assumptions were presented. However, this partition method only applies to one-dimensional fracture so far. When it comes to CAI problems, two-dimensional fracture would be the norm.

VCCT is considered as a potential tool solving ERR related problems. For a solid FE model, Zou, Reid [71] gave the representation of mode partition in terms of nodal force and displacements at nodes on the upper and lower surfaces of the delamination when it grew virtually by a length of one element size Δa. According to fracture mechanics, size Δa of delamination tip elements should approach zero to obtain the exact energy release rate. The nodal forces X_{cd}, Y_{cd} and Z_{cd} were actually the resultants of the interlaminar stresses behind the delamination tip over the length Δa. However, due to the physically inadmissible oscillation around the interfacial crack tip encountered in a two-dimensional or three-dimensional elastic theory, the displacement and interlaminar stresses (and therefore the nodal displacements and forces) changed their value and sign dramatically as Δa decreased. The individual components of ERR were not well defined and showed oscillatory behaviour [72], although a definite value of total ERR could be obtained at the crack tip.

For delaminations in composite laminates, it is preferable to use laminate theory rather than three-dimensional elasticity theory. It is computationally expensive to use solid finite elements

because a large number of elements through laminate thickness are required, especially in the case of multiple delamination problems. However, when laminate theory is used, the laminate is considered to be comprised of two sublaminates in the delaminated region and a single intact laminate in the undelaminated region. The moments contributing to both Mode I and Mode II will inevitably be involved in the expression for total ERR. Individual components cannot be separated directly. Zou, Reid [65] tactfully solved this problem. The laminate was divided into sublaminates not only in delaminated region as described above but also in undelaminated region. Transverse shear-deformable laminate theory was adopted for each of the sublaminates, and the displacement continuity through the interface of sublaminates was guaranteed. It was found that the actions and reactions between the sublaminates in the undelaminated region consisted of only three interfacial forces acting on the interface and the interfacial moments was not present. Moreover, stress singularity and the oscillatory behaviour involved in linear elastic fracture mechanics theory were eliminated. Instead, discontinuities of stress resultant across the delamination tip arose to reflect the interfacial stress singularity. Therefore, terms of interfacial moments vanished in the expression of total ERR, and individual components of ERR can be obtained through the mode partition of VCCT. Zou, Reid [71] found that VCCT imposed special requirements on the element mesh, namely that the elements behind and ahead of the delamination front should be orthogonal to the delamination front. The two-step VCCT was employed requiring two separate analyses of two consecutive configurations to obtain nodal forces and relative displacements. For the modified VCCT [71, 73], elements behind and ahead of the delamination were usually required to be of the same size, i.e. the method required self-similarity, to enable a single analysis to be performed on one configuration. These limitations

imposed strict requirements on the mesh, for example that an adaptive mesh be used when applying the VCCT to a progressive delamination growth problem. Therefore, Zou, Reid [71] developed an alternative approach which didn't suffer from the mesh limitation. The ERRs were expressed explicitly in the terms of stress resultant jumps and the derivatives of the relative displacements between the upper and lower surfaces of the delamination at its tip. They could be calculated directly, provided the displacements of the delaminated laminate had been determined.

2.5.2.7 Simulation of delamination propagation

For through-width delamination cases, a two-dimensional model is applicable. However, for embedded delamination cases, a three-dimensional model is essential [33]. Chai and Babcock [59] perhaps were the pioneers to investigate the delamination propagation in three-dimensional problems. They presented an analytical method to simulate the case that a plate bore an elliptical delamination and was compressed to enter post-buckling regime. Delamination propagation took place when the ERR exceeded specified CERR. However, this primitive analysis had limitations for practical use. For example, firstly, their model was only applicable to the case that a single delamination located between a thick isotropic plate and a thin orthotropic layer, of which the material axes coincided with the elliptical axes. Secondly, a self-similar disbonding growth was assumed which meant a concentric but larger elliptical delamination was generated after propagation. Actually, in most cases delamination does not propagate self-similarly, which has been confirmed experimentally and theoretically. Thirdly, based on self-similar disbonding growth assumption, only average total ERR around the delamination front was calculated, rather

than the components on individual crack modes. Later, Whitcomb [74] demonstrated that the delamination propagation in embedded delamination cases were mixed-mode problems and the ERR varied significantly around the delamination front. Hence, self-similar growth was not a correct assumption [24].

Compared with the self-similar growth method which employed a general governing function to describe the deformation of the entire model, FE method is much more versatile which is capable to simulate delamination propagating locally. At the beginning, a node-moving technique was employed to deal with the delamination propagation problem. In the work done by Klug, Wu [61], the ERR along delamination front was calculated through crack closure integral method. When at some points the ERR exceeded the critical value, corresponding nodes were moved outwards along the normal direction of the delamination front to generate a new mesh. However, the total ERR was not partitioned into three components, and compared with an assumed CERR. Nilsson, Thesken [34] employed the similar method, and he was not able to partition the total ERR either. Employing this method, the distance of propagation must be sufficiently small. Large values may induce spurious variations in the ERR distribution [23]. Nilsson, Thesken [34] chose 20% of the typical element length at the delamination front region as the recommended moving distance to balance the accuracy and computation cost. In the meantime, load increments needed to be adjusted so that the growth load was reached rapidly without jeopardizing post-buckling stability. Nonetheless, both approaches above revealed that delamination only propagated towards the direction perpendicular to compressive load, which was in good agreement with the experimental observations.

The node-moving technique, being able to simulate the local delamination propagation, is of low computation efficiency. Every time nodes are moved, the whole model has to be re-meshed and the nonlinear calculation has to be repeated from the very beginning to determine post-buckling configuration of a newly increased delamination [61]. Additionally, the mesh will distort significantly if the delamination propagates a relatively long distance.

VCCT, as a potential tool for delamination propagation simulation in FE method, was firstly presented about forty years ago [73]. However, it had not been implemented in any of the commercial general purpose FE packages until quite recently [60]. Therefore, to the best of the author's knowledge, the simulation of delamination propagation employing VCCT is not seen widely in publications. Aoki, Kondo [31] employed built-in VCCT function of ABAQUS to simulate delamination propagation, but no more details had been revealed.

On the other side, the demand for studying on delamination-related problems has explosively increased as a consequence of wide application of composite laminate. Engineers crave for a convenient tool to simulate and analyse the delamination propagation process, especially based on FE method. The implementation of VCCT in an FE analysis requires accessing and transmitting information between elements in the neighbourhood of the delamination front, which is intractable in almost all available commercial FE codes as the access is not available to users.

2.5.2.8 Cohesive elements

Therefore, cohesive element method, as an alternative, is devised timely for this purpose. At the beginning, this kind of element was also referred as interface element [70]. However, since it was

implemented in ABAQUS which named it as cohesive element at the beginning of this century, it has been used all around and this name has also been accepted widely.

Cohesive element is an alternative approach based on continuum mechanics to solve the problem in fracture mechanics realm. The cohesive elements in-between two neighbouring sublaminates resemble the resin rich zones, of which the mechanical behaviour is demonstrated in Figure 2.19. The upwards slope of this curve from the origin represents the increasing loading state of the cohesive element before damage initiates. However, once the traction exceeds its "peak value of nominal stress" (t_{n}^{0}, t_{s}^{0} or t_{t}^{0}, where n, s and t represent the normal, first and second shear direction, respectively), the traction-separation curve drops downwards to reflect the damage process. When the traction of the cohesive element degrades to zero (equivalently, separation exceeds corresponding$\delta_{\mathrm{n}}^{\mathrm{f}}$, $\delta_{\mathrm{s}}^{\mathrm{f}}$ or $\delta_{\mathrm{t}}^{\mathrm{f}}$), it means this cohesive element fails completely and delamination propagates through it.

Therefore, the value of the area enclosed by the traction-separation curve and the separation axis can be considered as the energy required to break this cohesive element and to produce a new fracture surface, which is equivalent to the projected area of the cohesive element along normal direction with respect to the fracture surface. Furthermore, the quotient of the enclosed area of the traction-separation curve with respect to projected area of corresponding cohesive element is considered as a material property. In ABAQUS it is referred as "fracture energy", and its dimension can be derived as N/m. The "fracture energy" does not have an appropriate explanation of physical meaning so far. Nevertheless, it is similar to the concept of CERR in fracture mechanics, of which the physical meaning is the energy needed to generate a new unit

area of fracture surface ahead of the crack front. The dimension of ERR is J/m^2 or N/m, which is equivalent to the dimension of “fracture energy”. Therefore, when the “fracture energy” is required as an input for simulation of delamination propagation, it is usually assigned with equivalent value of CERR which is obtained through standard tests.

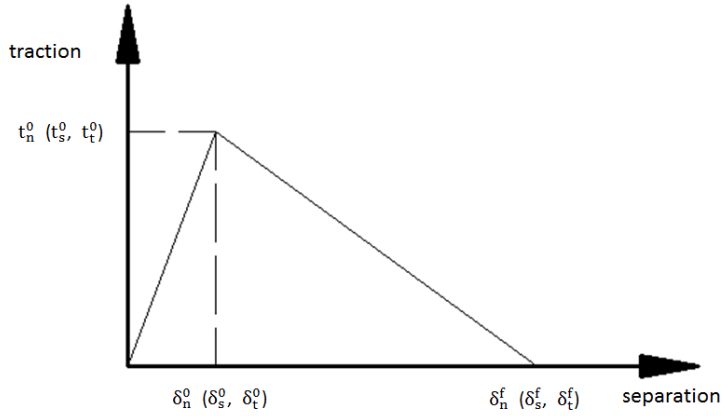

Figure 2.19 Typical traction-separation response of cohesive element[3]

Similarly, the failure of cohesive element can be partitioned into three modes as well. The normal direction z of cohesive element is defined as from bottom side to top side of the delamination based on the node ordering (Figure 2.20(a))[4]. The remaining two in-plane directions x and y are determined by the projection of corresponding axes of global coordinate system[5]. Accordingly, Mode I fracture is dominated by the relative opening displacement in the normal direction

[3] Cited from Figure 28.5.6-1, Abaqus analysis user’s manual, Version 6.11

[4] Details seen in “Element thickness direction definition”, 28.5.4 Defining the cohesive element’s initial geometry, Abaqus analysis user’s manual, Version 6.11

[5] Details seen in “Local directions in surface space”, 1.2.2 Coventions, Abaqus analysis user’s manual, Version 6.11

(Figure 2.20(b)), and Mode II and III are dominated by the transverse shearing displacement in x-z plane and y-z plane, respectively (Figure 2.20(c) and (d)). For mixed mode, the response of cohesive elements is illustrated in

Before cohesive element was implemented in commercial FE packages, its functionality had been fulfilled through subroutines. Lots of researchers developed their own subroutines to simulate the delamination propagation behaviour [32, 49, 70]. Although these subroutines were distinctive to each other in detail, the general rationale was the same.

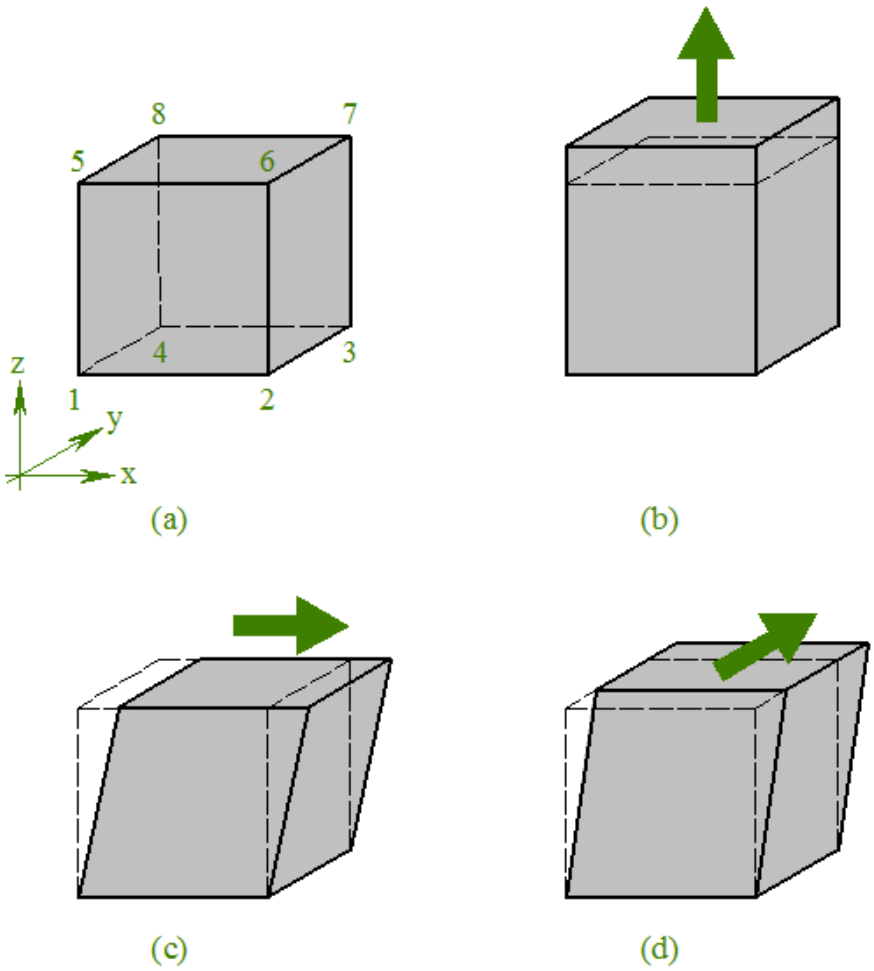

Figure 2.20 (a) Default coordinates and node ordering of three-dimensional cohesive element. (b) Mode I displacement. (c) Mode II displacement. (d) Mode III displacement

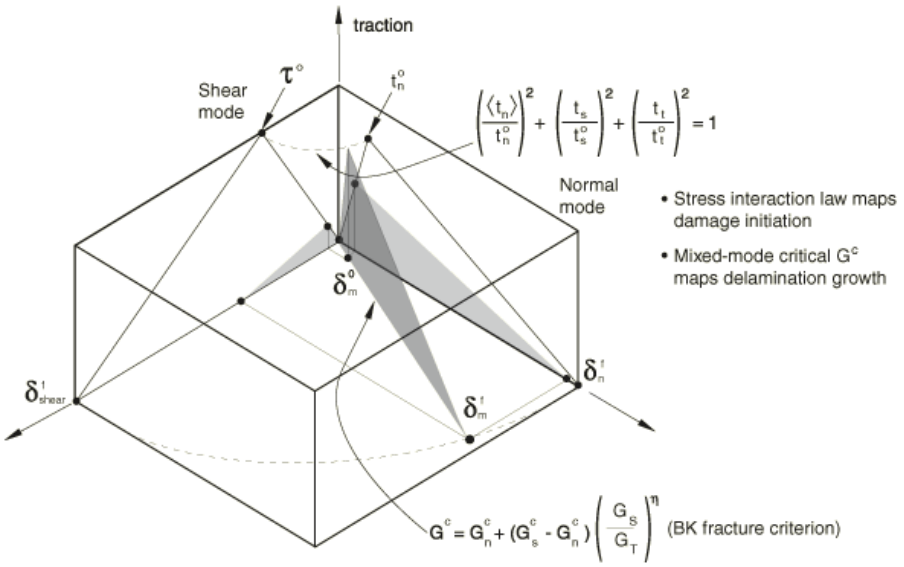

Figure 2.21 Illustration of mixed-mode response in cohesive elements[6]

The oscillatory behaviour of stress and displacement, which is mentioned in Section 2.5.2.6 when VCCT is employed to deal with delamination propagation at crack tip, did not appear in cohesive elements. Instead, the individual components as well as total ERR remain unchanged in terms of fracture energy when the size of cohesive element at crack tip decreases. Of course, there are some weaknesses of cohesive elements. For example, it requires extremely refined mesh at the delamination front. It is reported that only when the element size is as fine as 0.1mm, the simulating effect is authentic [75]. This is unaffordable in many investigations with complex structures. Therefore, some approaches were proposed to alleviate this issue. [75] found that by reducing the maximum interfacial strength the mesh could be ten times coarser than by using the nominal interface strength with the same accurate results. However, the drawback is that the stress concentrations near the crack tip are less accurate in using a reduced interfacial strength value is through. While, [76] criticized that the method from [75] only worked well with the mode I delamination propagation but was not as successful in mode II. [76] proposed using enriched interface finite element as user-defined elements in the commercial finite element code ABAQUS/Explicit to simulate delaminations. Through this approach, the mesh size could be extended to 5mm while still in excellent agreement with experimental findings. However, it was found that the computational savings in mode I was significant but was not always the case for mode II delamination.

[6] Details seen in "Damage evolution", 31.5.6 Defining the constitutive response of cohesive element elements using a traction-separation description, Abaqus analysis user's manual, Version 6.11

Additionally, it is verified in this thesis that the mode partition algorithm developed by ABAQUS is of deficiency and will lead numerical error if used improperly. This will be discussed in detail in Section 4.2.

2.5.2.9 Practical issues

There are two critical deficiencies of the above work regarding delamination simulation alone. The first issue is that the number of delaminations over the laminate thickness direction considered in the above work is far insufficient to represent reality. As composite laminates are more and more used in primary structures of aircraft, the ply number can be quite high, varying over a range from 10 to over 100 plies. Because of the basic principle that plies with same fibre orientation should avoid stacking together [77], almost all interfaces through the laminate will be vulnerable against delaminations when the laminate is subjected to low velocity impact and delamination is unlikely to be introduced between plies with same fibre orientation [3, 4, 78]. In contrast, the delamination number seldom exceeds 8 in the literature so far [49, 79, 80], and rarely reaches 15 [81]. However, the delamination number is a critical factor affecting damage mechanism of CAI, which will be demonstrated in the following chapters. The issue is mainly due to costly computation. Currently, the most common FE modelling is to partition the laminate into several sublaminates in the thickness direction, each of which is meshed with one layer of shell or solid elements. In the meantime, between any pair of neighbouring sublaminates, an interface is introduced to allow potential delamination propagation employing some special techniques, such as cohesive elements, surface-based cohesive behaviour, VCCT, etc.. Therefore, the model size depends on the interface number by large. Moreover, in order to simulate delamination

propagation precisely, extremely refined mesh is required over the propagation zone. The length of cohesive zone l_{cz} is determined through equation Eq. (2.5) by [75]

$$l_{cz} = ME\frac{G_c}{(\tau^0)^2} \tag{2.5}$$

where E is the Young modulus of the material, G_c is the critical energy release rate, τ^0 is the maximum interfacial strength, and M is a parameter that depends on each model.

Within the cohesive zone at least 3 elements are required [26, 75], which usually requires the mesh size to be smaller than 0.3mm. Combined with the facts of overall panel size (usually 100mm*150mm) and dozens of delaminations, the model size could be huge, or even unaffordable.

The second issue is that the pattern of multiple delamination distribution over the laminate thickness is oversimplified. The common approach is to assume the distribution in cylindrical or, a closer simulation, conical shape from a section view [27, 31, 49, 82]. This kind of assumptions are far from reality, and the distributing pattern affects the ultimate failure mechanism because it dominates the form and position of initial failure, Suemasu, Irie [79]. Recently, a way to determine the distributing pattern through impact simulation becomes available [78, 80, 81, 83], but accuracy seems in need of further improvement in comparison with experimental results. Moreover, the comparison is merely performed on the level of overlapped delamination area with NDI, C-scan for instance, rather than the individual delaminations. In the meantime, the computation cost of impact simulation is extremely high, usually a couple of days or even weeks are required and the computational efficiency of this approach is impractical.

2.5.2.10 Calculation of buckling load

Based on the stress concentration perception, the key issue of CAI prediction is to degrade the stiffness of delaminated area. Usually, the degradation factor is designated as the ratio of the buckling load of the delaminated area with respect to its in-plane compressive failure load in an undamaged condition. It can be seen that the calculation of the buckling load plays an essential role in this CAI prediction method [20, 54, 84].

The stability-related problem covers a very wide range. Here, only the problem related to multiple sublaminates is reviewed. Substantial work has been devoted to this field by many researchers. In the early age, the case of one-dimensional or through-width delamination was studied. Simitses, Sallam [20] studied the influence of delamination size and sublaminate thickness to the buckling load based on Euler-Bernoulli beam theory. Shu and Mai [84] discovered the upper and lower bound of buckling load based on different assumptions of plane section. The upper bound solution could be obtained through the assumption that the section plane at delamination front remained plane and perpendicular to the centre line of the laminate, while the lower bound solution was obtained through the assumption that all sublaminates had the same length during deformation. Gu and Chattopadhyay [54] performed a detailed experimental study and employed a high-order laminate theory to investigate how the buckling load was affected by lay-up sequence and location of the delamination as well as its length.

The work above dealt with single delamination case and obtained the critical buckling load through direct derivation of governing equations. However, for CAI cases, single delamination is oversimplified, multiple delaminations must be considered [21]. However, to deal with multiple

delaminations, the analytical method which pursues closed-form solution over the entire area becomes infeasible when relatively complex models are encountered. In contrast, there is another method referred as Rayleigh-Ritz method which can cope with multiple delaminations more efficiently. Generally speaking, it consists of four steps [85]: (1) select a kinematically admissible transverse displacement function; (2) calculate the total potential energy of the delaminated plate; (3) apply the Trefftz criterion [72] to yield eigenvalue equations; (4) solve the eigenvalue equations and find the minimum eigenvalue as the buckling load. Through Rayleigh-Ritz method Suemasu [21] investigated the critical buckling load of plate bearing seven equally spaced, equal-length, through-width multiple delaminations. He employed Timoshenko beam theory to consider the shear deformation at the delamination front as Euler-Bernoulli's hypothesis was thought insufficient to describe the intensive deformation at delamination front. However, this investigation was applied only to the case of equally spaced, equal-length multiple delaminations which implied all sublaminates buckle simultaneously at the same compressive load. Additionally, no contact constraints were imposed in this work and sublaminates might overlap or penetrate with each other.

Although substantial work based on through–width delamination has been done, its contribution to CAI is limited. Through-width delamination cannot reflect the real delamination pattern induced by low-velocity impact, which is contained within the laminate rather than through width. For this case, deformation is not uniform over the width and significant stress concentration arises locally in some zone close to the delamination edge [79]. Therefore, cases of delaminations of this type must be always as a two-dimensional problem. Rayleigh-Ritz method again shows its versatility. The general process to calculate the buckling load of so delaminated

laminates using the Rayleigh-Ritz method is the same as it deals with the case of through-width delamination. However, a much more complex transverse displacement function is required, which is capable of coping with the entire delaminated area and its boundary conditions.

It is worth mentioning the actual delamination shape on each individual interface is often peanut shaped. However, construction of a transverse displacement function which can satisfy the boundary condition around a peanut shaped zone is too complex. Therefore, as a compromise, researchers had to assume a relatively simple shape, which was easy for constructing transverse displacement function but still possessed the basic characteristics of the impact-induced delamination. As a result, a circle or ellipse was selected, and the displacement function was assumed in the following form [82, 85].

$$w = \left[1 - \left(\frac{x}{a}\right)^2 - \left(\frac{y}{b}\right)^2\right]^2 (C_0 + C_1 x^2 + C_2 y^2) \tag{2.6}$$

where x and y are the in-plane coordinates, a and b are the major and minor semi axes of the delamination, respectively. The direction of the major axis may vary from interface to interface. C_0, C_1 and C_2 are the constants to be determined. However, three constants can only predict the buckling mode of sublaminate symmetric with respect to x and y axes. Therefore, the number of constants were increased to six by Xiong, Poon [38] as follows

$$w = \left[1 - \left(\frac{x}{a}\right)^2 - \left(\frac{y}{b}\right)^2\right]^2 (C_1 + C_2 x + C_3 y + C_4 xy + C_5 x^2 + C_6 y^2) \tag{2.7}$$

Even though, Jane and Yin [86] argued that six constants could not describe the deflection deformation accurately and therefore increased the number to nine as follows

$$w = \left[1 - \left(\frac{x}{a}\right)^2 - \left(\frac{y}{b}\right)^2\right]^2 \cdot \tag{2.8}$$

$$(C_1 + C_2x^2 + C_3xy + C_4y^2 + C_5x^4 + C_6x^3y + C_7x^2y^2 + C_8xy^3 + C_9y^4)$$

The calculation involving nine undetermined constants are extremely complex. On the other hand, thanks to the fast developing computation capability in recent decades, buckling load prediction of multiple delaminations through FE method becomes affordable. A lot of commercial FE packages, such as ABAQUS, ANSYS, Nastran, LS-Dyna, were made available in the past few decades, bringing significant convenience for structural analysis. Therefore, analytical or semi-analytical methods were less and less used. Suemasu, Irie [79] investigated the critical buckling load of a laminate containing as many as seven artificial circular delaminations through commercial FE package ABAQUS. Arman, Zor [87] investigated the effect of a single circular delamination around a circular open hole to the critical buckling load of woven fabric laminated composite plates through commercial FE package ANSYS and determined the critical delamination size due to a plummeting drop and the corresponding buckling load. Hwang and Liu [88] also employed ANSYS to investigate the buckling behaviour of laminates with multiple delaminations. They found if the largest delamination was near surface, other delaminations underneath had less influence to buckling behaviour. However, if short delamination appeared above the long delamination, various behaviours would be observed depending on the length ratio.

2.5.2.11 Soft inclusion

It was mentioned above that many researchers employed soft inclusion method to simulate the stress concentration phenomenon around the delamination front when the impacted laminate

was subjected to in-plane compressive load. The rationale of this method is that the delaminated area is easy to buckle and shows less stiff in-plane behaviour when it enters the post-buckling regime, like a soft inclusion, and stress redistribution is induced accordingly. In order to simulate this stress concentration phenomenon simply without extremely complex FE modelling, the stiffness in this delaminated area is degraded artificially. Based on the assumption of soft inclusion, a couple of methods of stiffness degradation were presented, which are reviewed as follows.

Uniform stiffness degradation

At the beginning, the whole delaminated area was simply assumed as one homogeneous softened part and a uniform degradation factor was applied to this area. The degradation factor was usually assigned as the ratio of critical buckling load of the delaminated area with respect to the in-plane compressive failure load of corresponding undamaged laminate [38, 89]. Xiong, Poon [38] gave an explanation for this method. He assumed the deforming process to be like this: initially, a linear stress-strain relationship exhibited when delaminated plate was compressed. However, when the critical buckling stress σ_B was reached the largest sublaminate buckled. After that, the compressive load sustained by this sublaminate became constant, and the process repeated until all sublaminates in the delaminated area buckled. This process can be schematically illustrated in Figure 2.22. The straight line 1 represents the mechanical behaviour of undamaged laminate. The horizontal line 2 represents the process in which successive buckling of remaining sublaminates. According to this figure, the degradation factor is determined as

$$d = \frac{\sigma_B}{\sigma_0} \tag{2.9}$$

where σ_B and σ_0 are the buckling stress of the biggest sublaminate and failure strength of undamaged laminate, respectively. Once the degradation factor is determined, elastic modules of the soft inclusion are determined by multiplying the modulus of undamaged material with this degradation factor.

Obviously, this explanation of the damaging process has some questionable points. Firstly, the bi-linear strain-stress curve in Figure 2.22 seems more appropriate to the case of through-width delamination. For the case of embedded delamination the curve is unlike this but resembles a straight line from beginning to final failure. Secondly, even using this soft inclusion method to simplify the case of through-width delamination, the stress-strain relationship of the simplified model with degraded stiffness will only develop along the straight line 3 in Figure 2.22, which means that the stress distribution of this simplified model can only reflex the true stress state at the second intersection point of curve 2 and 3 where ε_0 is reached. The remaining stress state of this simplified model in the loading process does not have the physical meaning. Thirdly, Xiong attributed final failure of the laminate to the loss of stability (global buckling). Actually, this damage mode may not take place necessarily, especially when anti-buckling devices are employed during the loading process. Nevertheless, this degradation approach was still widely employed for CAI prediction.

There is another problem to be considered further: the delamination size through laminate thickness is not uniform, which means sublaminates may buckle at diverse compressive loads individually. Therefore, which buckling load should appear in Equation (2.9) can be a problem.

Different researchers presented a range of methods to deal with this issue. Xiong, Poon [38] suggested using the buckling load of the sublaminate separated by the largest delamination to ensure that predicted CAI was conservative. Tang, Shen [2] presented a method to calculate the buckling sequence of all sublaminates and degraded each sublaminate depending on its own buckling load. This process will be reviewed in detail in Appendix C. Nilsson [40] presented an empirical equation of stiffness reduction coefficient related to the projected area of delamination. From the evaluation in that paper, it compares well with experiment.

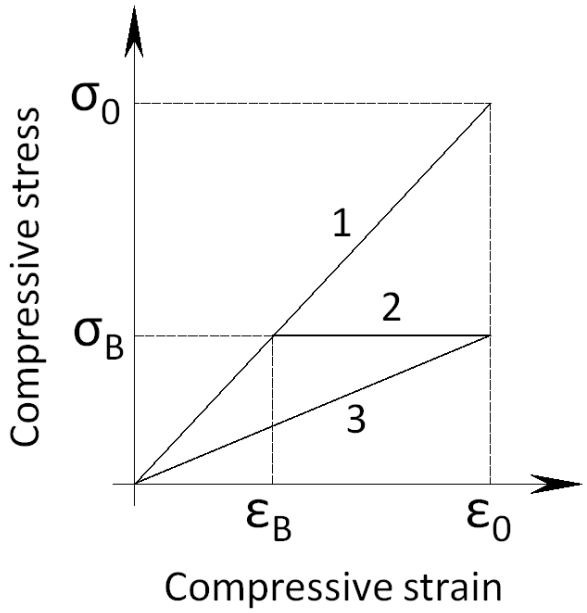

Figure 2.22 Material degradation for damaged region

Qi and Herszberg [39] employed the similar approach as Equation (2.9) to determine the degradation factor. However, they replaced the numerator of Equation (2.9) with the residual compressive strength of impacted laminate (CAI). The process was repeated to a number of groups of specimens subjected to different impact energies and they found the ratio ranged from

0.28 to 0.87 for a specific group. However, this method is impractical for predictive CAI evaluations, because the ratio obtained experimentally only applies to that specific group. Once the material system or lay-up sequence is changed, new experiments have to be conducted.

As an extreme simplicity, Chen attempted to model the delaminated area as an elliptical open hole, of which the major and minor axes were equal to the damage width (the maximum width of the delaminated area perpendicular to the loading direction) and the dent diameter, respectively. It tended to underestimate the CAI strength as it neglected the load carrying capability of the delaminated area completely.

Non-uniform stiffness degradation

Although algorithms of stiffness degradation mentioned above are diverse, the common characteristic is that a constant and uniform degradation factor is designated for the overall soft inclusion area (regarding Chen's criterion which simplifies the delaminated area as an open hole, the degradation coefficient can be considered as zero). However, this approach is questionable since the degradation effect in the delaminated area is neither uniform nor constant during the compression process [54]. In order to investigate this problem, Gu and Chattopadhyay [54] experimentally measured the stiffness distribution of the delaminated area. He sliced the impacted laminate into 10-mm-wide specimens and measured the elastic moduli. However, the compressive experiment designed in his work only measured the pure compression moduli which were dominated by the amount of fibre breakage. In actual CAI cases, the appearing moduli are more affected by stability loss of the overall delaminated plate. Single, sliced strip is not capable to reflex this behaviour.

Some other researchers have made significant contribution to investigate the stiffness distribution in foreign object impact (FOI) cases. Thanks to the fast developing technology, one cutting edge instrument called Digital Image Correlation (DIC) or Digital Speckle Photogrammetry (DSP) is capable of measuring the displacement field of a large surface of a specimen, which employs tracking and image registration techniques for accurate 2D and 3D measurements of changes in images through multiple digital cameras. Employing DIC and FE method, an approach referred as inverse method was developed by Sztefek and Olsson [90] to investigate the stiffness distribution in impact-damaging area. Briefly speaking, the rationale of inverse method is to minimize the difference between experimental displacement fields measured through DIC and corresponding numerical prediction on iterative updating of the material parameters in a FE model.

Firstly, Sztefek and Olsson [90] investigated the stiffness distribution in tension cases. As the strain gradients are predominantly caused by fibre breakage, the reduction in tensile stiffness was confined to a small region with fibre failure in the damage centre, and it was adequately accurate to discretize the stiffness within the damaged area into three concentric rings in which the stiffness decreased gradually from the outmost ring neighbouring the undamaged area to the central circle.

However, when employing DIC to compression cases, a difficulty was encountered. Due to local buckling of the delaminated zone, the readings from DIC only represented the deformation of the surface ply or a surface sublaminate. They were unable to represent the overall delaminated area. As a compromise, displacements in the delaminated regions were therefore excluded from the

analyses in compression. Instead, displacements over the undamaged material were used to determine the stiffness in the damage area. A disadvantage of this approach is that the spatial stiffness distribution can no longer be described since multiple sections within that area would result in non-unique solution but only one set of degraded material parameters. Additionally, it was found that the uniform degraded stiffness did not keep constant during the compressing process, but decreased nonlinearly. According to the conclusion from Sztefek and Olsson [90], a curve is obtained to simulate the stress concentration phenomenon of soft inclusion. For example, Craven [4] employed VUMAT to allow the stiffness of material within delaminated area to vary according to this curve in an FE model analysed using commercial package ABAQUS. However, this curve is not universally applicable. Many factors, such as material system, lay-up sequence, geometry and impact damage as well as boundary conditions, may affect this curve significantly. Therefore, Craven [4] suggested developing a library of curves from experimental data covering the majority combinations of impact energies, locations and laminate thickness/lay-up from an experimental test matrix. This would provide data for analysis of large structural components for all requirements at the design stage, in which the impacted area does not need to be simulated in detail but through the soft conclusion method. This idea may be applicable. However, it is not suitable for CAI case, which is the lowest experimental level in the building-block certification validation hierarchy. The benefit of this curve library would be more helpful if obtained from lower levels of experiments feeding higher levels of application.

It can be concluded that although researchers have realized the degradation factor should be neither uniform nor constant, a proper way to derive this parameter for CAI prediction is still not

yet available. This motivated the author to develop a more practical methodology to be presented in Chapter 6.

2.5.2.12 Stress distribution

Once the degraded stiffness of delaminated area has been determined, the next step is to obtain the stress distribution. Because in most CAI cases, catastrophic failure occurs over the central line across the width, where the residual width of intact laminate from the delamination front to the side edge of the laminate is minimum, leaving two broken halves inserting into each other in a broom shape. The stress distribution along this line should have a lot to do with the observed failure, which can be obtained analytically or numerically. For example, Qi and Herszberg [39] obtained the in-plane stress distribution using complex variable method by treating the impact damage as a circular soft inclusion in the case of an infinite plate subjected to remote in-plane loadings. Chen, Shen [91] developed a method by assuming the delaminated area as an elliptic open hole. Olsson, Iwarsson [92] presented a closed form solution for the stress distribution in an isotropic infinite plate with a circular isotropic inclusion. Tang, Shen [2] obtained the stress distribution through FE method.

It is worth mentioning that in most cases when analytical approach was employed to obtain stress distribution, the models assumed the laminate to be an infinite plate. Therefore, a finite-width correction was needed. For example, Qi and Herszberg [39] defined the residual strength of a plate with finite width was defined as

$$\sigma_r = \frac{\sigma_r^{\infty}}{Y} \tag{2.10}$$

where σ_r^{∞} is the residual strength of a plate with infinite width. Y is the correction factor defined as

$$Y = \left\{\frac{2 + (1 - 2R/W)^3}{3(1 - 2R/W)}\right\}^{\left(1-M_r^N\right)^M} \tag{2.11}$$

where N and M are constants, R is the radius of circular delamination and W the width of the plate.

Chen, Shen [1] employed the method of the finite width correction factor a elliptical hole.

$$Y = \left\{\frac{\lambda^2}{(1-\lambda)^2} + \left[\frac{1-2\lambda}{(1-\lambda)^2} - \frac{\lambda^2}{1-\lambda}\left(\frac{2a}{W}M\right)^2\right]\sqrt{1 + (\lambda^2 - 1)\left(\frac{2a}{W}M\right)^2}\right\}^{-1} \tag{2.12}$$

where

$$\lambda = \frac{b}{a}$$

$$M = \frac{\sqrt{1 - 8\left[\frac{3(1-2a/W)}{2 + (1-2a/W)^3} - 1\right]} - 1}{2\left(\frac{2a}{W}\right)^2}$$

where a and b are the major and minor semi axes of the elliptical open hole, respectively.

Xiong, Poon [38] presented another expression of finite width correction which was defined as the ratio of the stress concentration in a finite width plate to that of an infinite width plate. As the expression was quite lengthy, it is not presented here.

2.5.2.13 Failure criteria

Once the stress distribution had been obtained, diverse failure criteria were adopted to predict the CAI strength. Some researchers employed some well-known criteria. For example, Nilsson [40] employed point stress criterion and [89] employed the maximum strain criterion. Other researchers proposed their own criteria, which, however, had significant trace of Point Stress Criterion or Average Stress Criterion which were developed firstly as engineering approaches to predict tensile or compressive strength of specimens with open hole [93].

The point stress criterion assumes that the failure will occur when the stress $\sigma_y(x,0)$ at a certain small fixed distance d_0 ahead of the hole boundary reaches the tensile or compressive strength X of the material (Figure 2.23), which is expressed in the following equation:

$$\sigma_y(x,0)\big|_{x=R+d_0} = X \tag{2.13}$$

The average stress criterion assumes that the failure will occur when the average value of $\sigma_y(x,0)$ over some small fixed distance l_0 ahead of the hole boundary first reaches the tensile or compressive strength X of the material (Figure 2.23), which is expressed as follows

$$\frac{1}{l_0}\int_R^{R+l_0} \sigma_y(x,0)dx = X \tag{2.14}$$

The reason that researchers liked to develop their own failure criteria for CAI prediction from these classic criteria which were proposed to deal with open-hole cases is probably due to two factors. Firstly, the damage mechanism of CAI resembles that of open-hole cases, of which concentrated stress at the edge of the hole triggers final collapse of the entire laminate. Secondly, these criteria were developed at least two decades ago. At the time, high computation cost was

an issue using FE method involving non-linear material degradation. Instead, obtaining the stress distribution in an elastic state through analytical or empirical approach, the use of these criteria was perhaps more efficient. For example, Xiong, Poon [38] predicted the CAI strength through the criterion presented by Whitney and Nuismer [94], which assessed the failure by evaluating the stress state at a characteristic distance, d, from the boundary of the elliptical damage. Chen, Shen [1] and Tang also presented their own failure criteria, respectively. As their algorithms can be accessed, they will be evaluated through the experimental data of Appendix A and presented in Appendix B and Appendix C of this thesis.

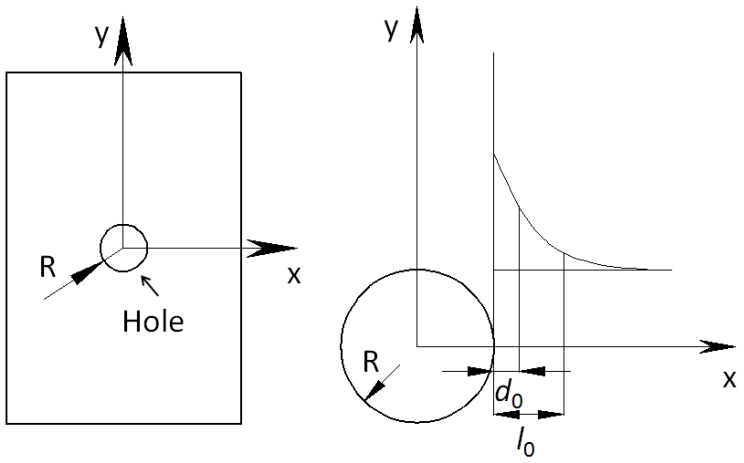

Figure 2.23 Schematic of parameters involved in Point Stress and Average Stress failure criteria

From above review, it is found that, to the best of the author's knowledge, all prediction methods based on soft inclusion assumption have a common calculating process: obtain the stress state in elastic deformation stage from simplified model, of which corresponding delaminated area is replaced with soft inclusion; then apply some exclusive failure criteria to predict CAI strength or

behavior. These methods are of low computation cost. However, a common and significant weakness of these methods is that an extra parameter, characteristic length or something similar, is required usually. This parameter is not independent on lay-up sequence and damage state, and extra experiments are required for each given case in order to obtain the characteristic length. In this case, the experimental cost is usually high. Partly, the reason of employing soft inclusion assumption through above strategy is due to the limitation of computing power at the time. Nowadays, the ability has been significantly improved. The value of such an approach will be explored in Chapter 6.

2.6 Conclusion

Two major perceptions of damage mechanisms of CAI and corresponding prediction methods have been reviewed briefly. It can be found that both perceptions are too categorical, emphasizing on a single damage mode only. Although the perceptions based on two different mechanisms have been present for decades, there are few publications, to the best of the author's knowledge, attempting to reconcile them. In the author's view, these two failure mechanisms might co-exist in an actual damage process of CAI, and they compete to dominate the damage process. Various factors, such as geometry size, boundary conditions, material system and impact damage status, etc. may favour one to another as the damage process evolves. It is clear that an appropriate understanding of the damage mechanism in diverse circumstances is essential for developing a CAI prediction method. Therefore, the objectives of this thesis are to investigate the damage mechanisms of CAI, and then to propose an appropriate prediction method based on this damage mechanism.

2.7 Summary

This chapter presents a brief review of CAI-related problems and points out the current issues of CAI study based on theoretical prediction methods. So far, a unanimous prediction method of CAI is still not available. One of the reasons is that the damage mechanism is not clearly understood. There are mainly two perceptions and corresponding prediction methods currently. As these prediction methods refer to a wide range of knowledge and techniques, the background of each of them is reviewed briefly. Finally, based on this review, the objectives of this thesis can be defined.

Chapter 3 Process and analysis of experimental results

3.1 Introduction

The experimental process, including drop-weight impact, non-destructive inspection (NDI) and compression after impact, were conducted at Aircraft Strength Research Institute (ASRI) in China by the author assisted by his colleagues before the PhD project started at Nottingham University. The experiments provided data as reference and resource for the PhD study, which is presented in Appendix A. However, the delamination distribution analysis based on the C-scan results, the experimental data processing and presentation have been carried out as a part of the PhD study.

The experiments involved 4 groups, 62 specimens in total, which were made up of 4 different material systems and subjected to a range of impact energy levels. The impact and compression tests were conducted routinely based on established test standards. The strength of the testing programme was the double-sided ultrasound scan conducted on the specimens after the impact tests which was considered essential for informing detailed delamination simulation. The single-sided scan cannot provide adequate information for such simulation due to the intrinsic weakness of ultrasound scan. Based on the experimental results, the relationship between the damage characteristics, such as the delamination area and impact energy, were investigated.

3.2 Double-sided scan

Before the drop-weight impact test, specimens were scanned by ultrasound C-scan to insure the initial perfect status. After the impact test, impact dents on the specimens were measured immediately. This was because the dent might recover gradually. Then the specimens were

scanned again to identify the range of delamination induced by impact. Conventionally, for large numbers of CAI tests, scan was required to be conducted on only one side of the specimen (usually the impact face) to get a general view of the delamination, such as the overall shape and size. For example, ASTM D7136 recommends measuring the overall delamination width, delamination length and maximum delamination diameter. However, these measurements are insufficient for deep investigation. In order to obtain more information, most specimens in this study were scanned on both faces.

The reason of scanning on both faces attributes to the intrinsic weakness of C-scan, which makes use of ultrasound to detect the defect underneath the surface of the specimen. Ultrasound waves reflect when they meet a delaminated interface. According to the speed of ultrasound wave transmitting through this medium and the time taken by the wave from emitting to returning, the depth of that defect can be calculated. However, if there is another defect exactly right underneath, the ultrasound wave will not reach it. Therefore the lower defect will be "shaded" and its existence cannot be detected directly. Figure 3.1(a) demonstrates the delamination distribution from the section view schematically. Routinely, scan is conducted on one side of the specimen, and only part of delaminations can be detected (the bold lines inside the section in Figure 3.1(b)) leaving the area underneath unknown (grey area in Figure 3.1(b)). In order to detect delamination distribution as much as possible, the other side of the specimen is scanned as well (Figure 3.1(c)). Even though, delaminations inside may still not be detected because of the "shadow" projected from delaminations closer to surfaces (red lines inside the section in Figure 3.1(d)). However, although the complete picture of delaminations cannot be

obtained fully even with double-sided scan, it offers significantly more information about the delamination state then single-sided scan.

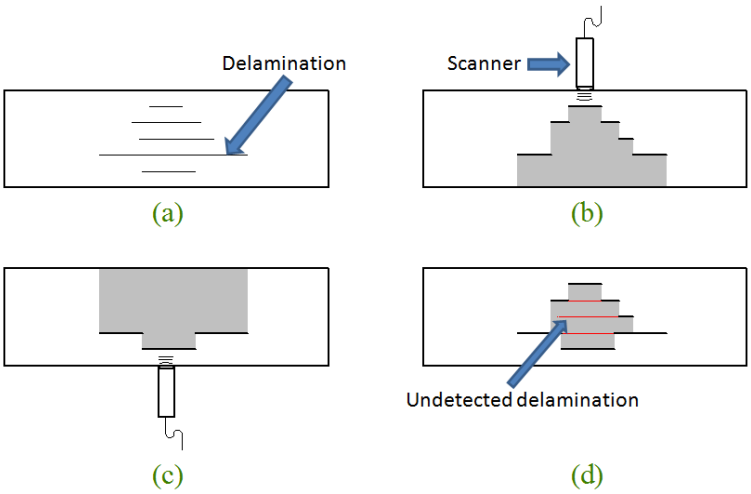

Figure 3.1 Schematic illustration of weakness of scanning inspection

The C-scan machine employed in this study was IUCS-II (Figure 3.2), which was developed by ASRI. IUCS-II consists of a scanner, a frame containing locator and vacuum cup, and a computer. The locator can be fixed on not only horizontal but inclined or even vertical surfaces by the vacuum cup. The scanner is swept over the surface by the operating staff manually. All scanning information is stored in the computer. The whole system is compact, light-weight and flexible. Therefore it is suitable for in-field operation. The precision of this system is 1mm in the in-plane direction and 0.1mm in depth.

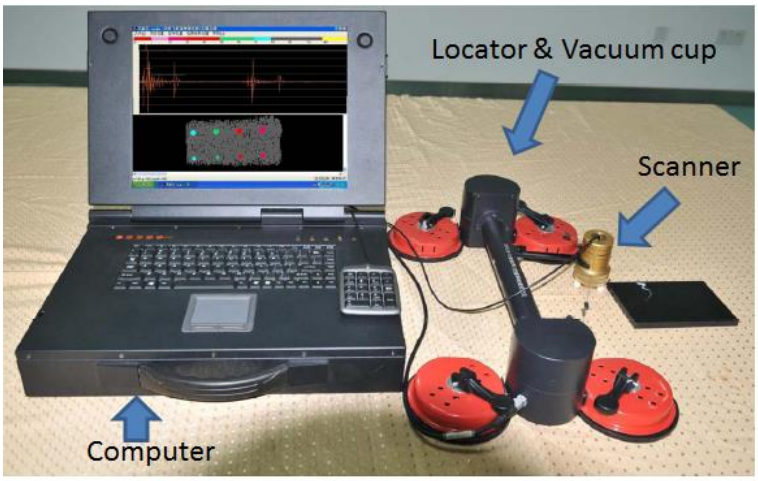

Figure 3.2 IUCS-II portable C-scan system

After the drop-weight test, specimens of group A1, A2, A3, B and D were scanned on both faces using this device. The others were single sided scanned only, of which the reasons will explained later. Firstly, the specimen was fixed in a frame with the impact face upwards and scanned. Then the specimen was reversed and scanned on the back face. Finally, these two sets of scanning information were combined properly and an integral set of scanning data describing the delamination distribution of an impacted laminate was formed.

3.3 Discussion

The quality of C-scan is affected by surface condition of the specimen significantly. For specimens bearing BVID, high quality of scanning image can be obtained usually. However, for specimens bearing severe impact damage, the humped or even exploded surface will hinder the scanning operation. The scan results of all specimens are presented in three categories as follows.

3.3.1 Three categories of scan result

The first type is featured by double-sided and complete scan, which covers group B and D. The second type is also scanned double-sided but incomplete due to the severe damage at the centre, including groups A1, A2 and A3. The third type is featured by only single-sided scan, including group A4, A5 and C. The reason for only single-sided scan on group A4 and A5 was due to the extremely poor condition of the back face of these specimens, like splitting fibres or even penetrated impact dent, where scan from that side was not practical. The reason of single-sided scan on group C was simply that they were not planned.

3.3.1.1 Double-sided and complete scan

The superimposed delamination images for all specimens of group B and D are presented from Figure 3.3 to Figure 3.8. The process of obtaining these figures was as follows. As the in-plane precision of the portable C-scan system IUCS-II was 1mm, a grid of 1mm density was generated. Each block represents a spot of detected delamination. A superimposed delamination shape could be obtained. In the meantime, the length, width and area of the delamination were also obtainable from these figures. The area was the space occupied by the delamination (equivalent to the sum of coloured blocks in quantity).

Three colours were used to distinguish the source of the detected delamination for each figure. Green meant at that location delaminations were detected from both impact-face and back-face scans. It is worth mentioning that this case reflects two possible scenarios. One is that the unique delamination at some interface is detected by impact-face and back-face scans simultaneously. The other is that delaminations present at different interfaces but incidentally are the same in-plane area. The black blocks represented delaminations detected from impact-face scan only,

and red blocks from back-face scan only. Theoretically speaking, one should have only green blocks along the profile of the overall delaminated zone because the same outlines of delamination area should be obtained no matter from the impact-face or the back-face scan. However, because of inevitable error in the manual-scanning operation, for example, slight misalignment of the specimen after turning the face, the two sets of blocks could not match each other precisely and therefore a few black and red blocks show on at the edge of the delamination area.

From these figures it is also observed that some blank zones appeared at the centre of the delamination areas. This resulted from unsuccessful scan due to severe damage there.

From these superimposed delamination images, the shape of superimposed delamination can be considered roughly as a circle with B5-4 as an exception, compared with other regular delamination shapes in the same test group as shown in Figure 3.7. This may be due to occasionally improper operation of the drop-weight impact test.

The superimposed delamination images presented above can be associated with individual interfaces, because each detected delamination spot contains not only the in-plane position of the plate but also the depth in the laminate thickness direction. Extract the delamination spots which have the same depth from the scan results, the outline of the delamination shape on an individual interface can be obtained. Due to the intrinsic weakness of C-scan, only the part of the delamination exposed to scan sensor can be detected.

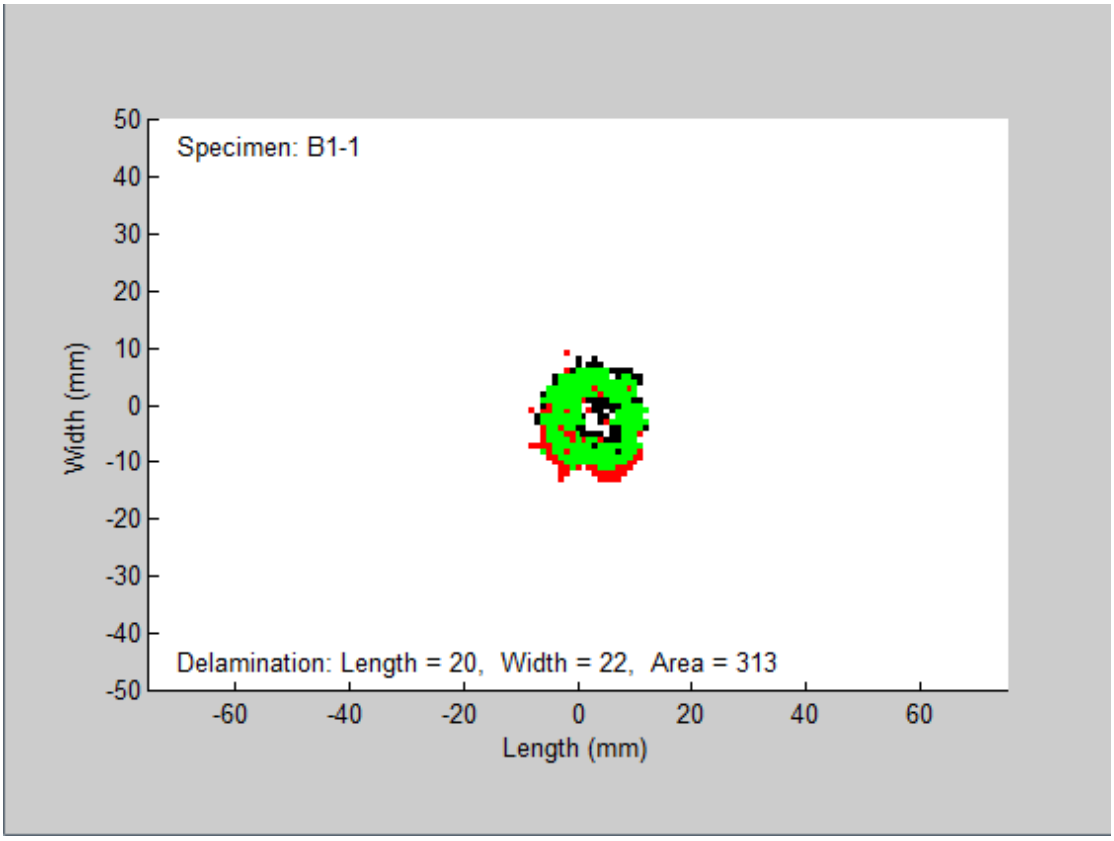
Specimen: B1-1
Delamination: Length = 20, Width = 22, Area = 313
Width (mm)
Length (mm)
50
40
30
20
10
0
-10
-20
-30
-40
-50
-60
-40
-20
0
20
40
60

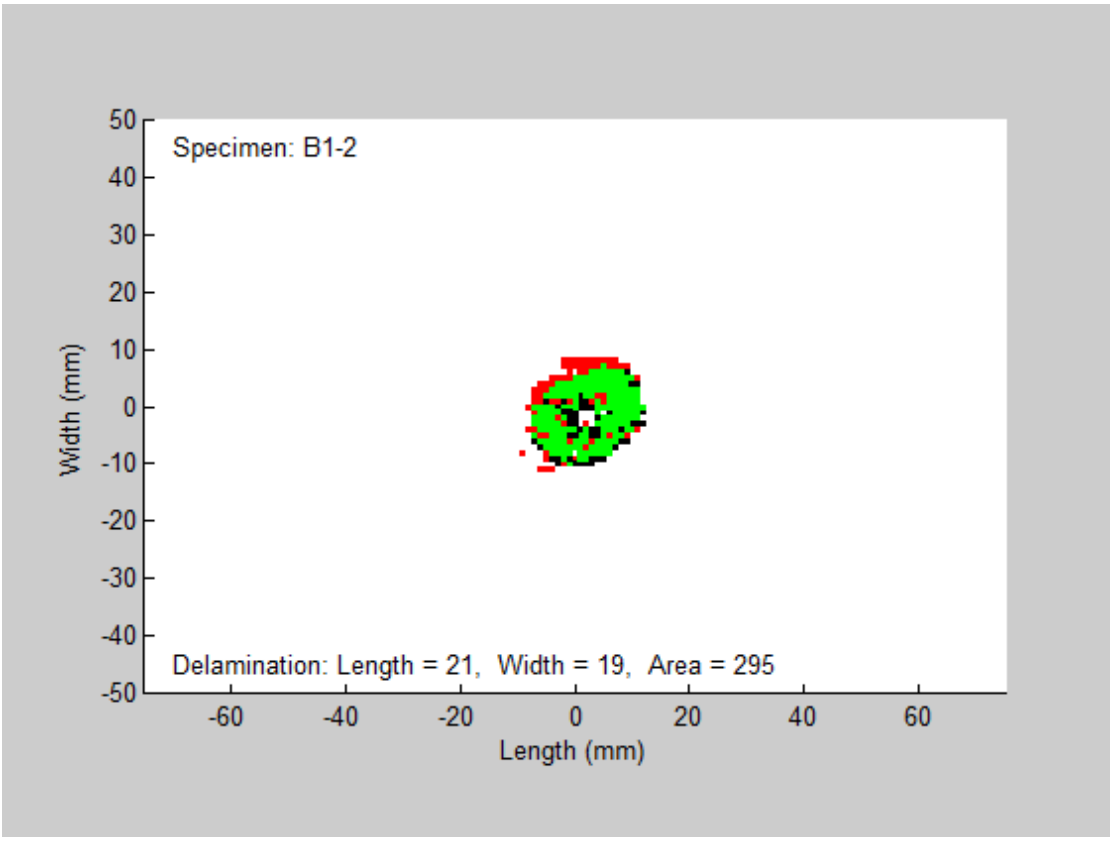
Specimen: B1-2
Delamination: Length = 21, Width = 19, Area = 295
Width (mm)
Length (mm)
50
40
30
20
10
0
-10
-20
-30
-40
-50
-60
-40
-20
0
20
40
60

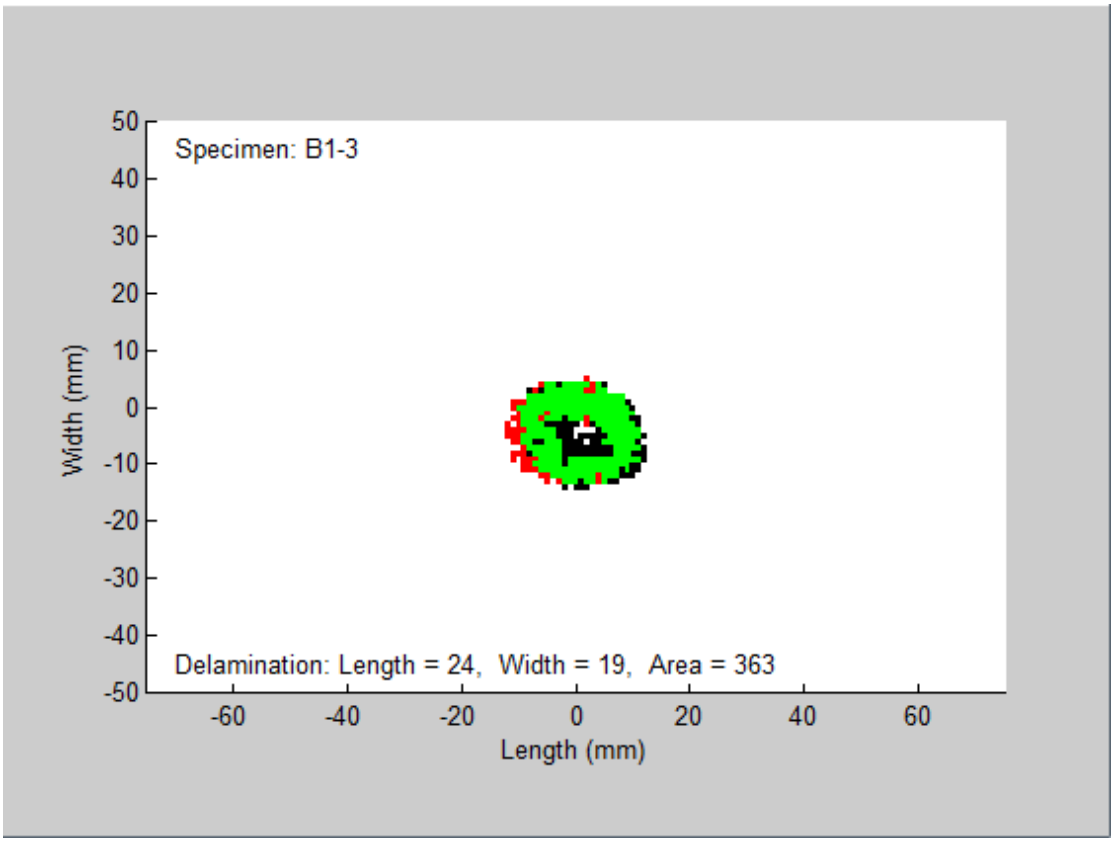
Specimen: B1-3
Delamination: Length = 24, Width = 19, Area = 363
Width (mm)
Length (mm)
50
40
30
20
10
0
-10
-20
-30
-40
-50
-60
-40
-20
0
20
40
60

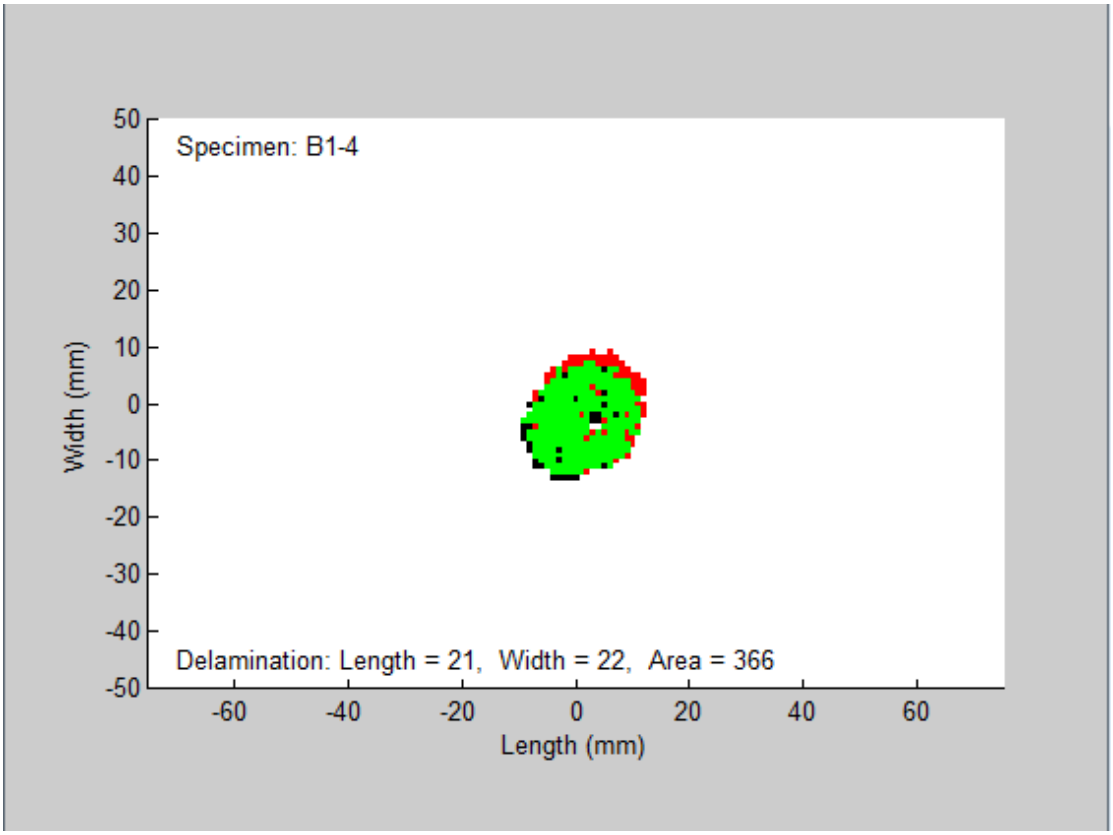
Specimen: B1-4
Delamination: Length = 21, Width = 22, Area = 366
Width (mm)
Length (mm)
50
40
30
20
10
0
-10
-20
-30
-40
-50
-60
-40
-20
0
20
40
60

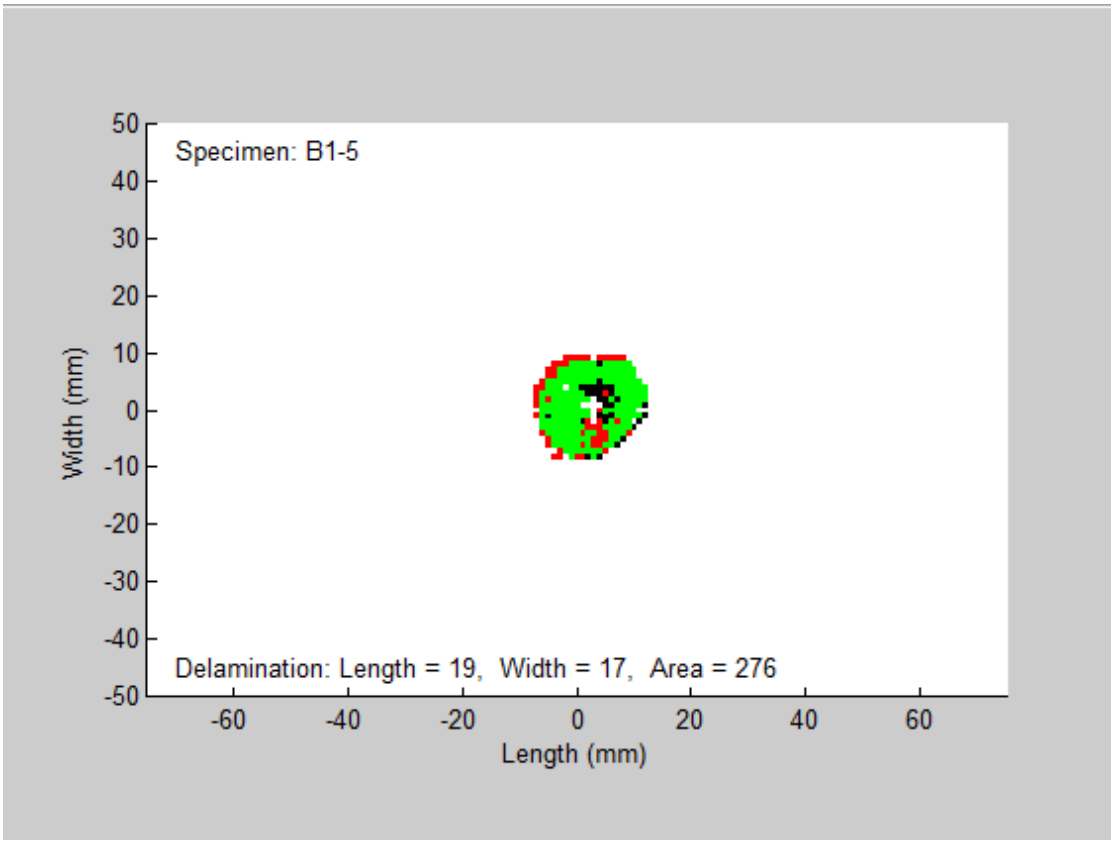

Figure 3.3 Superimposed delamination image of sub-group B1

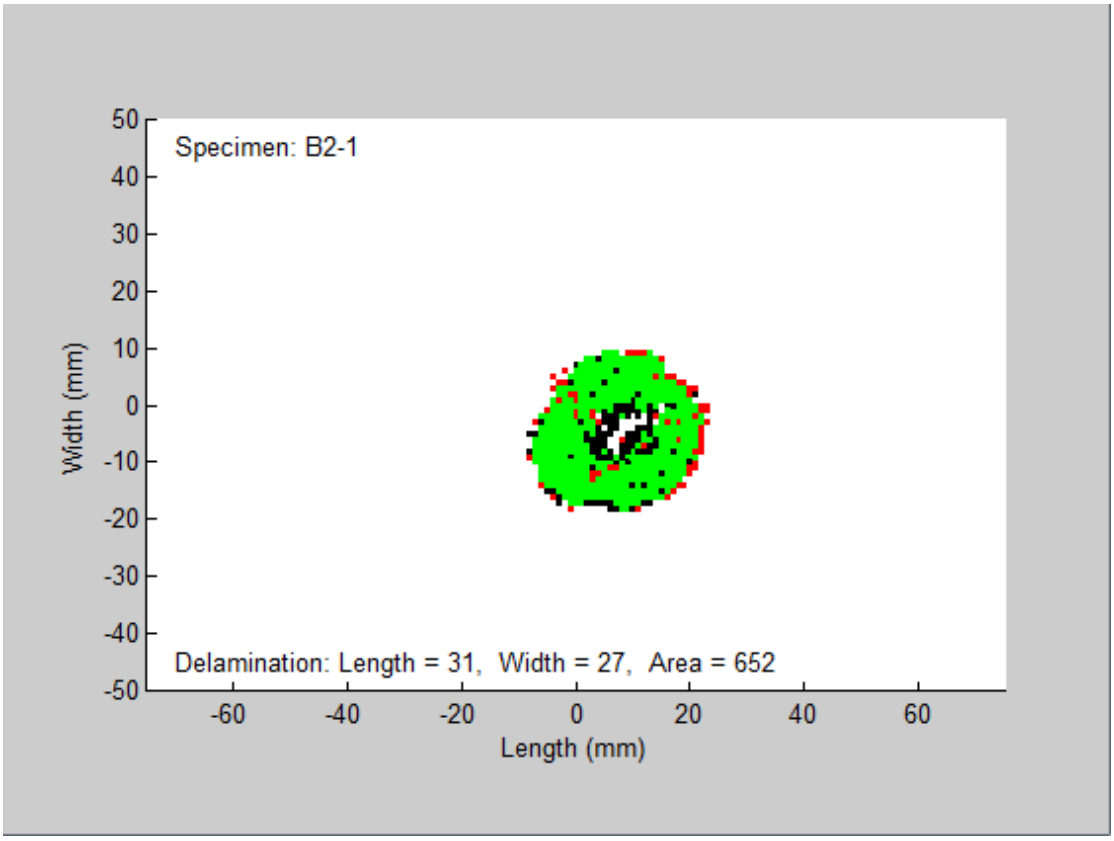
Specimen: B2-1
Delamination: Length = 31, Width = 27, Area = 652
Width (mm)
Length (mm)
50
40
30
20
10
0
-10
-20
-30
-40
-50
-60
-40
-20
0
20
40
60

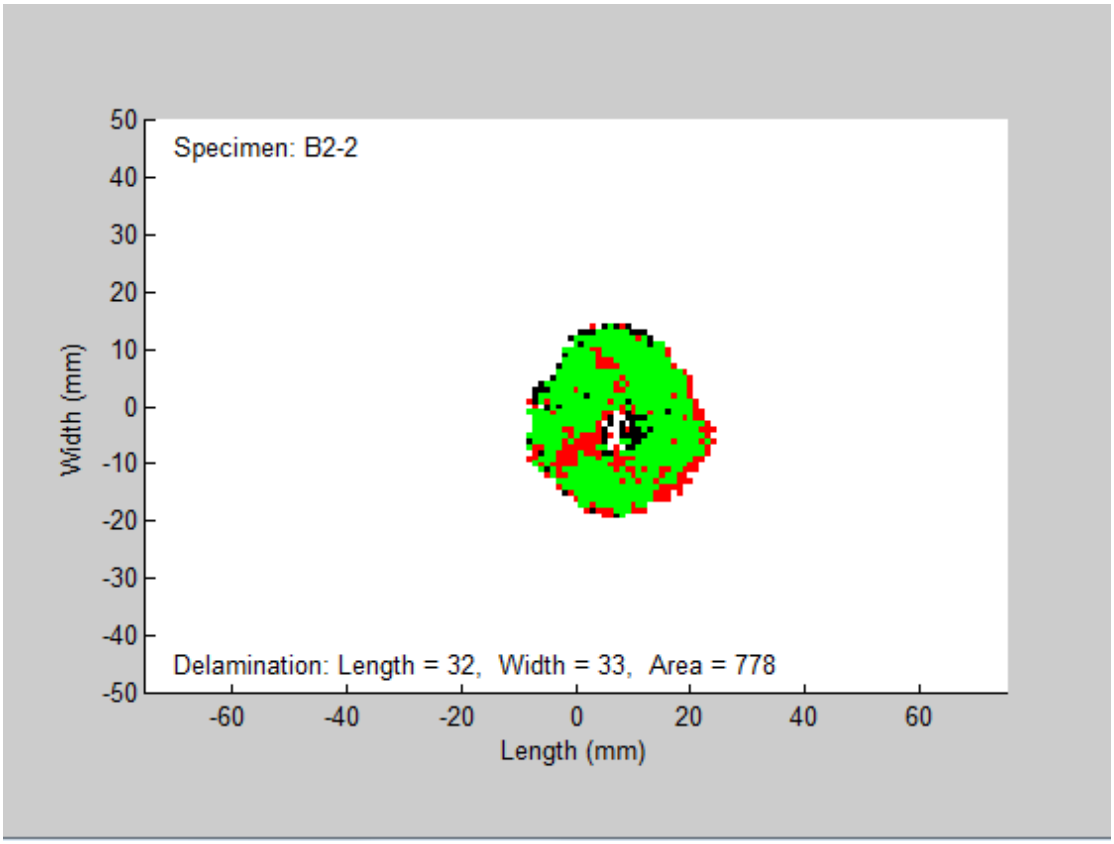
Specimen: B2-2
Delamination: Length = 32, Width = 33, Area = 778
Width (mm)
Length (mm)
50
40
30
20
10
0
-10
-20
-30
-40
-50
-60
-40
-20
0
20
40
60

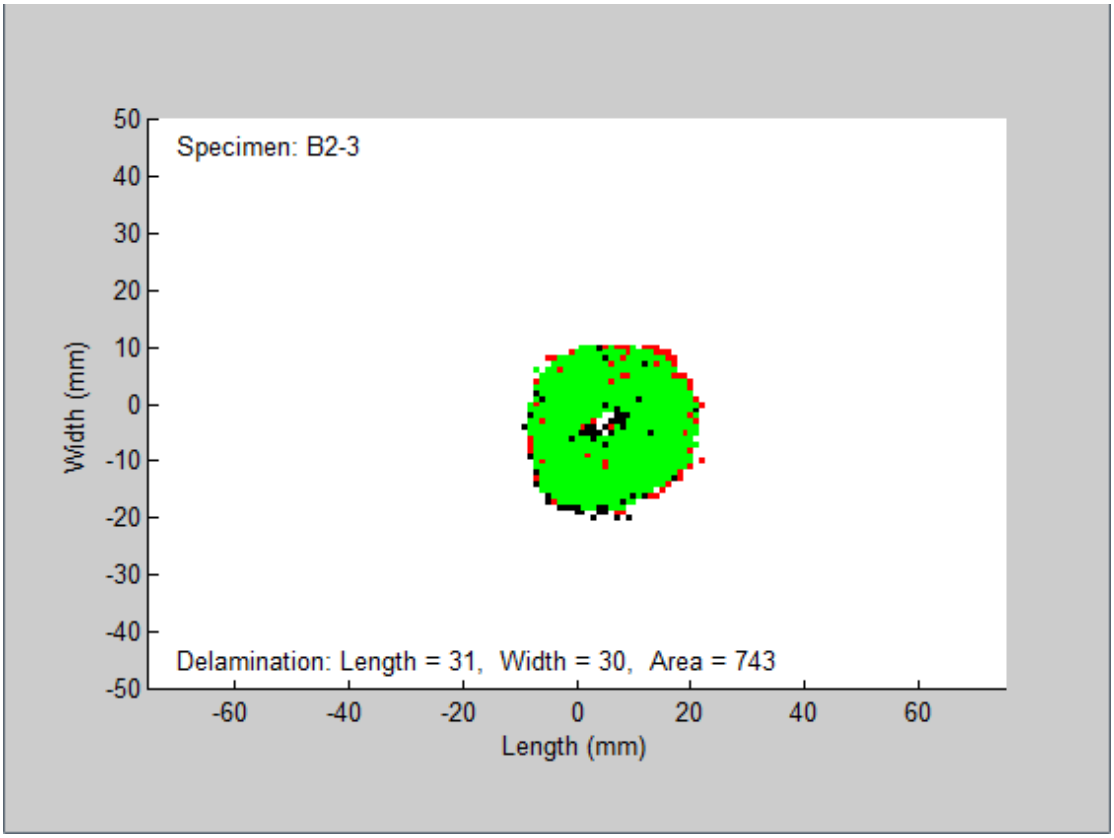
Specimen: B2-3
Width (mm)
Length (mm)
Delamination: Length = 31, Width = 30, Area = 743

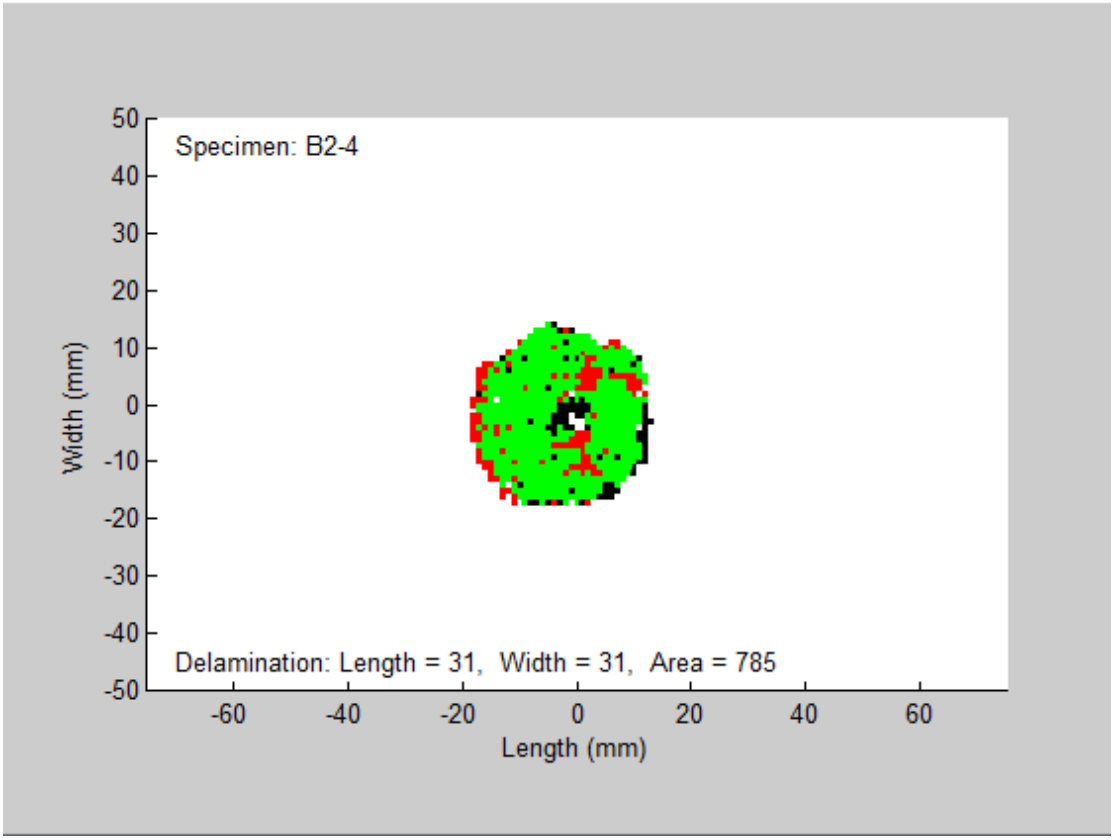
Specimen: B2-4
Width (mm)
Length (mm)
Delamination: Length = 31, Width = 31, Area = 785

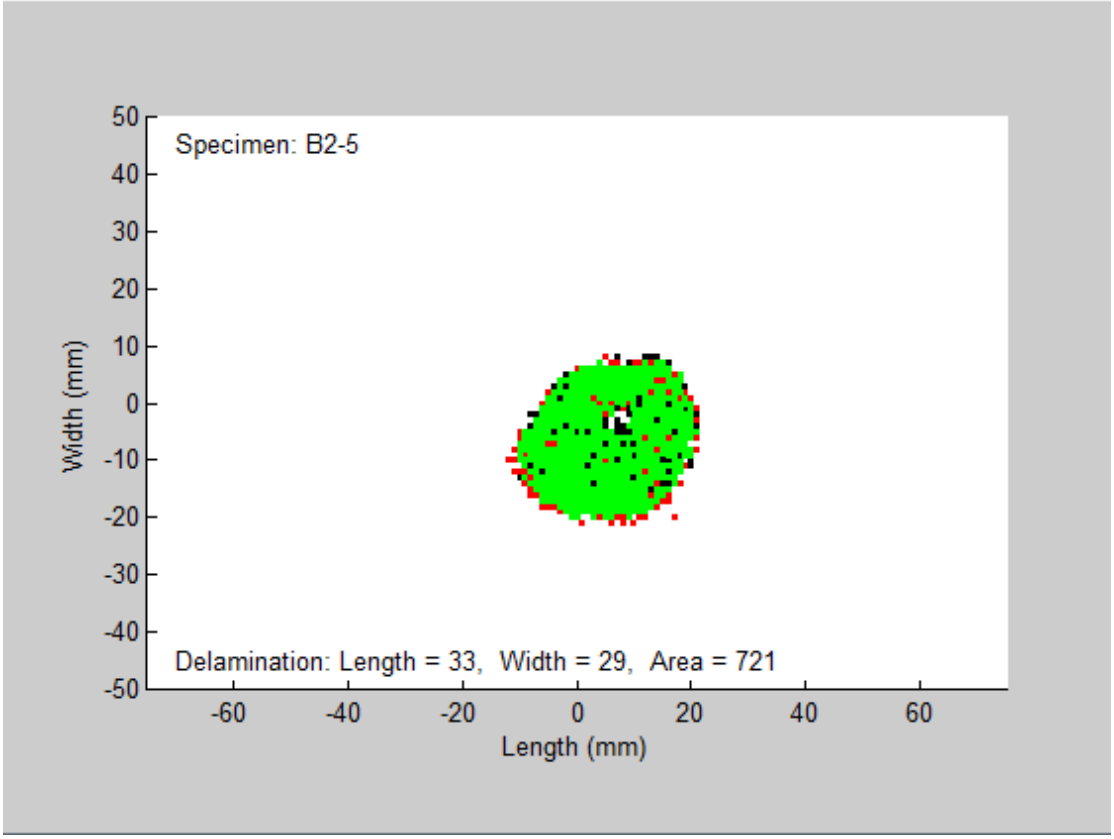

Figure 3.4 Superimposed delamination image of sub-group B2

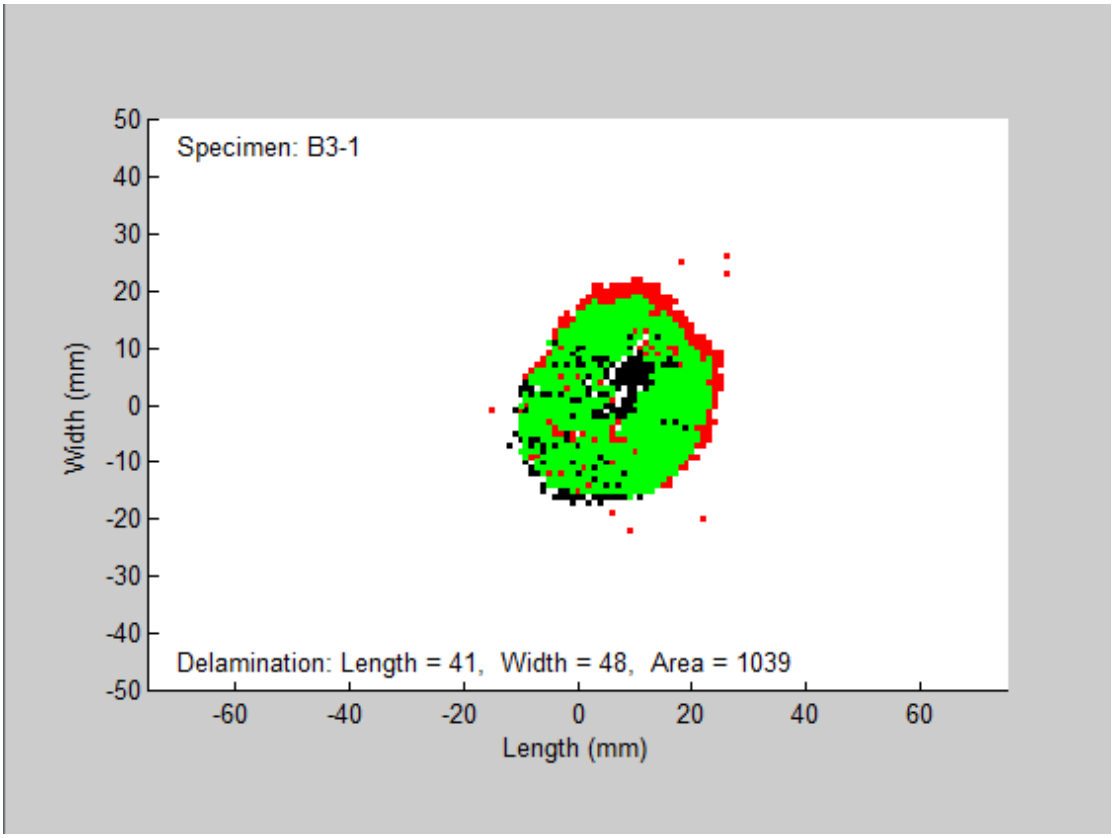
Specimen: B3-1
Delamination: Length = 41, Width = 48, Area = 1039
Width (mm)
Length (mm)
50
40
30
20
10
0
-10
-20
-30
-40
-50
-60
-40
-20
0
20
40
60

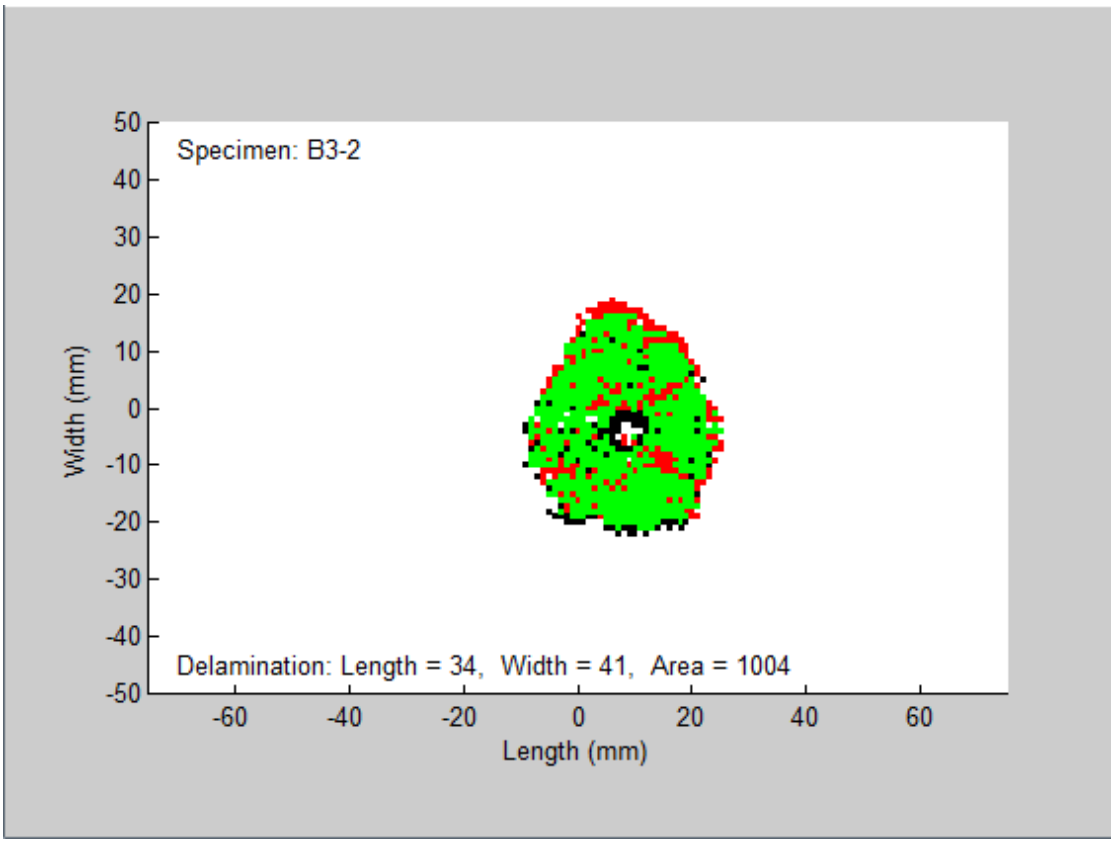
Specimen: B3-2
Delamination: Length = 34, Width = 41, Area = 1004
Width (mm)
Length (mm)
50
40
30
20
10
0
-10
-20
-30
-40
-50
-60
-40
-20
0
20
40
60

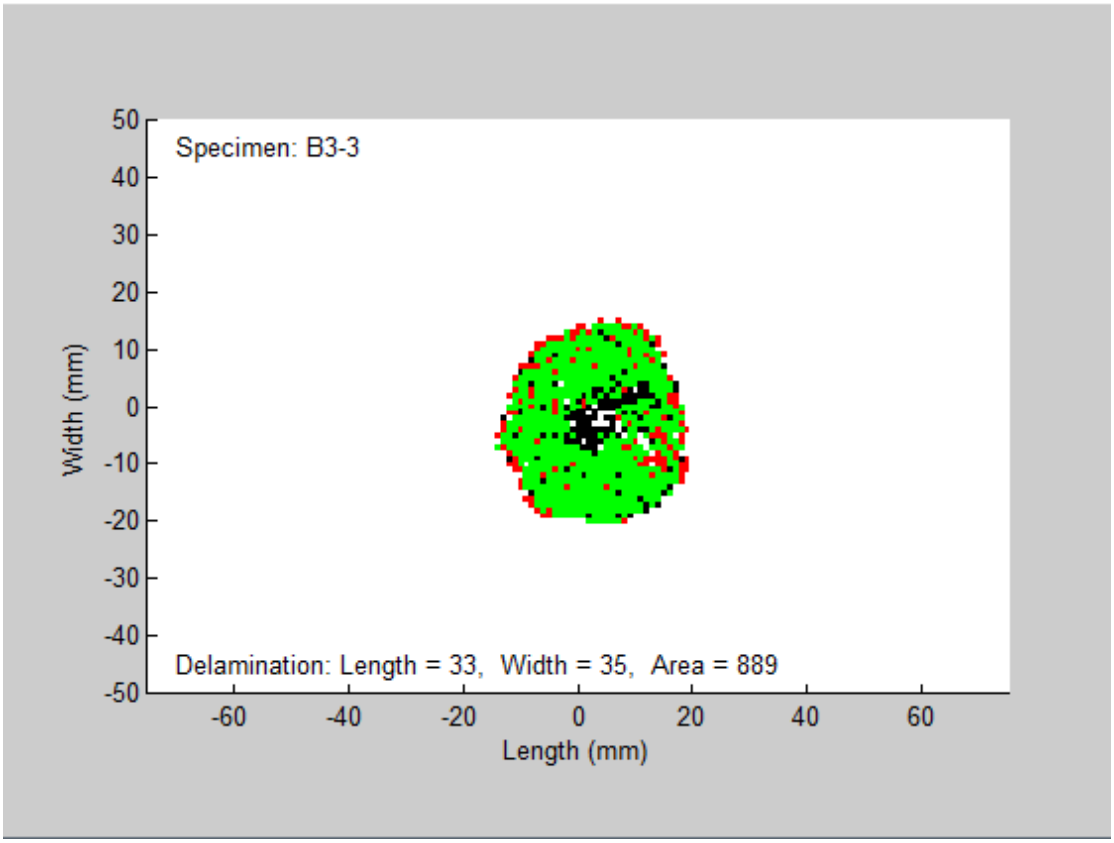
Specimen: B3-3
Delamination: Length = 33, Width = 35, Area = 889
Width (mm)
Length (mm)
50
40
30
20
10
0
-10
-20
-30
-40
-50
-60
-40
-20
0
20
40
60

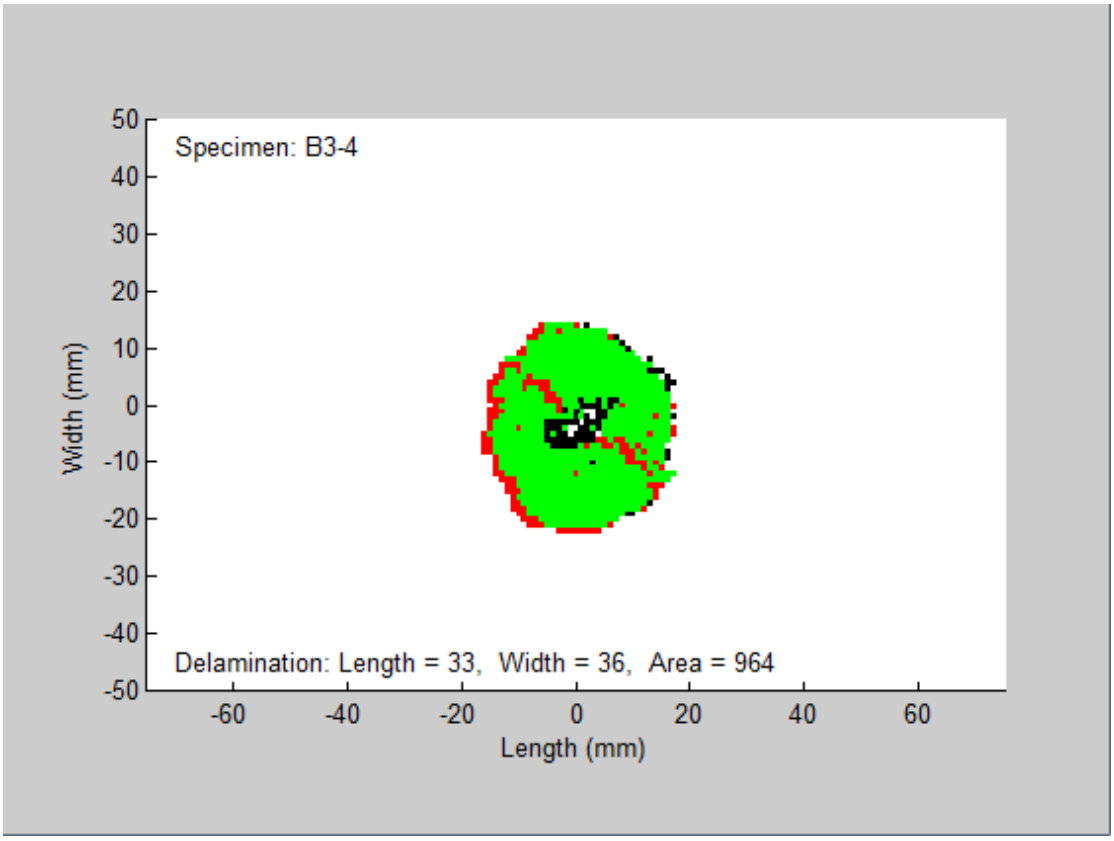
Specimen: B3-4
Delamination: Length = 33, Width = 36, Area = 964
Width (mm)
Length (mm)
50
40
30
20
10
0
-10
-20
-30
-40
-50
-60
-40
-20
0
20
40
60

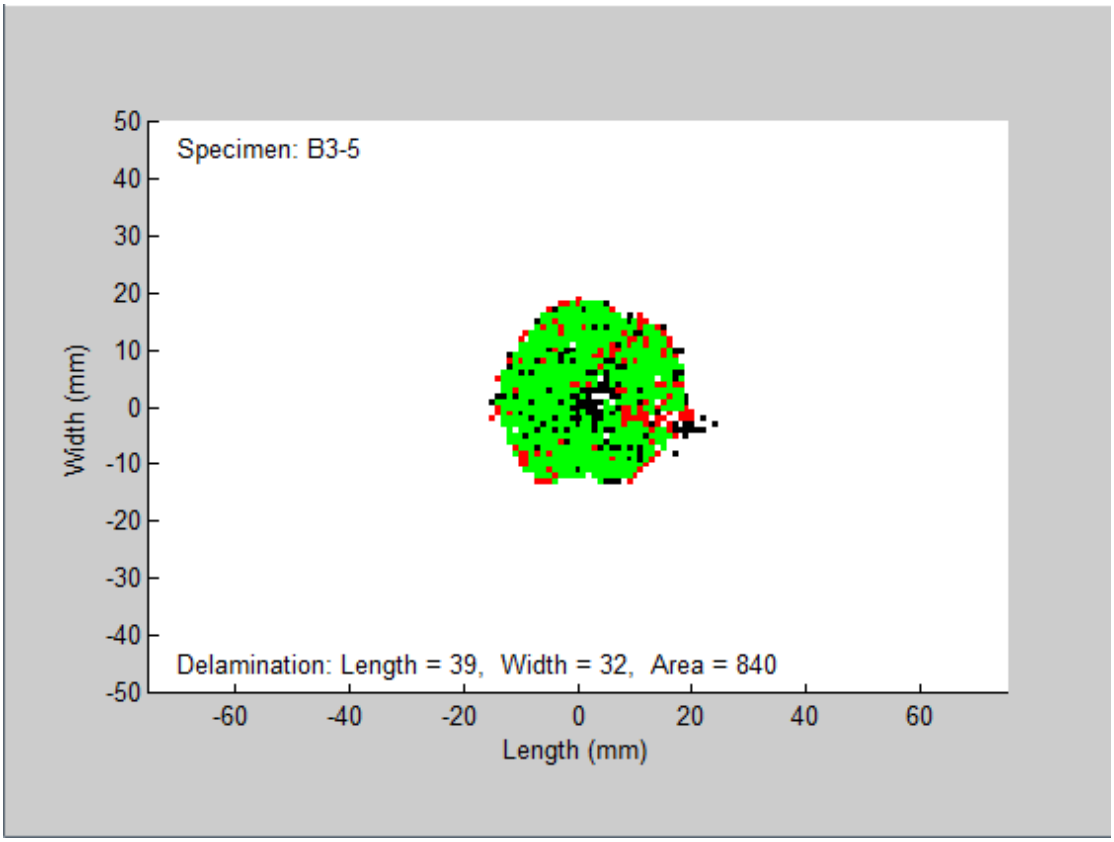

Figure 3.5 Superimposed delamination image of sub-group B3

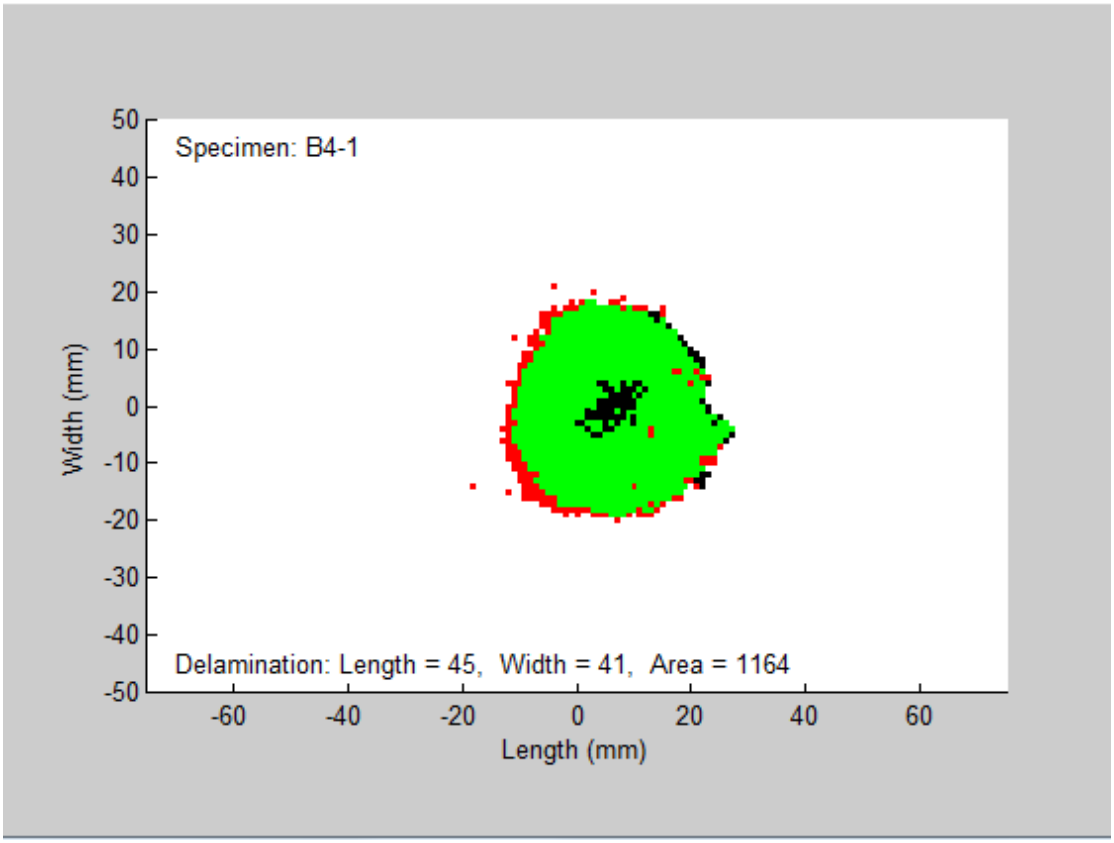
Specimen: B4-1
Delamination: Length = 45, Width = 41, Area = 1164
Width (mm)
Length (mm)
50
40
30
20
10
0
-10
-20
-30
-40
-50
-60
-40
-20
0
20
40
60

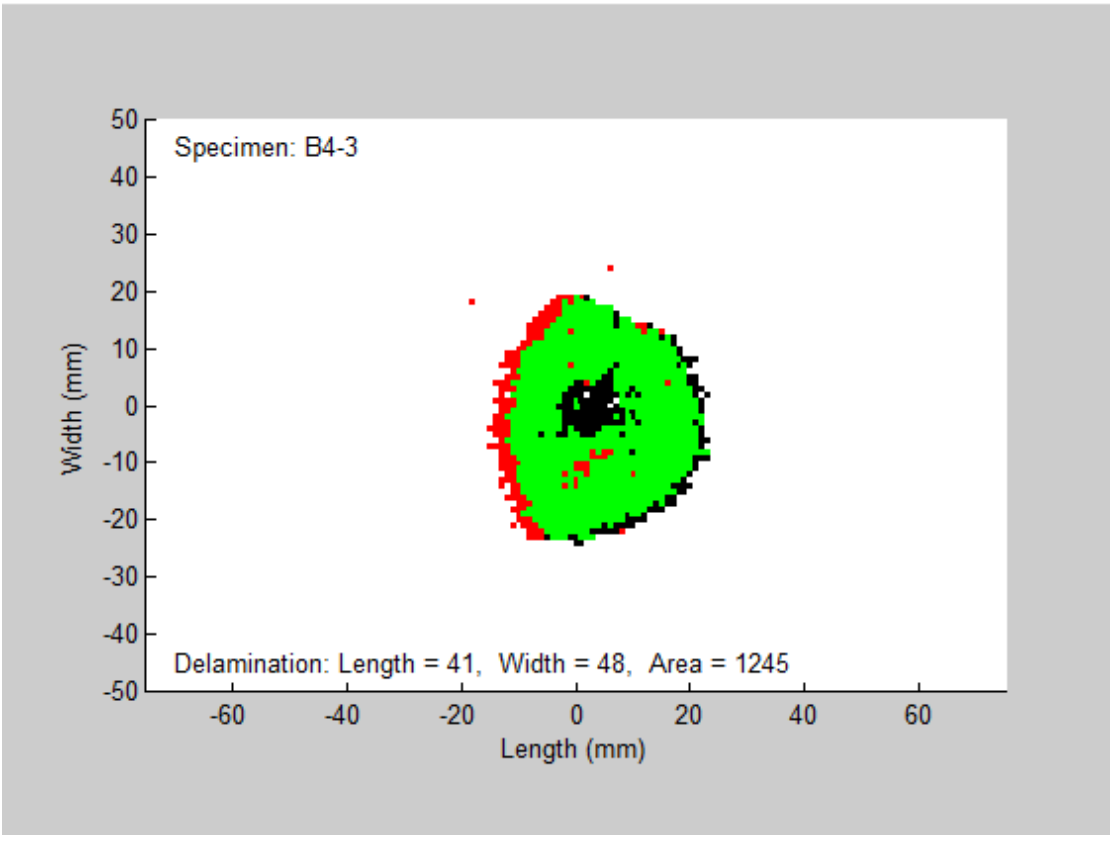
Specimen: B4-3
Delamination: Length = 41, Width = 48, Area = 1245
Width (mm)
Length (mm)
50
40
30
20
10
0
-10
-20
-30
-40
-50
-60
-40
-20
0
20
40
60

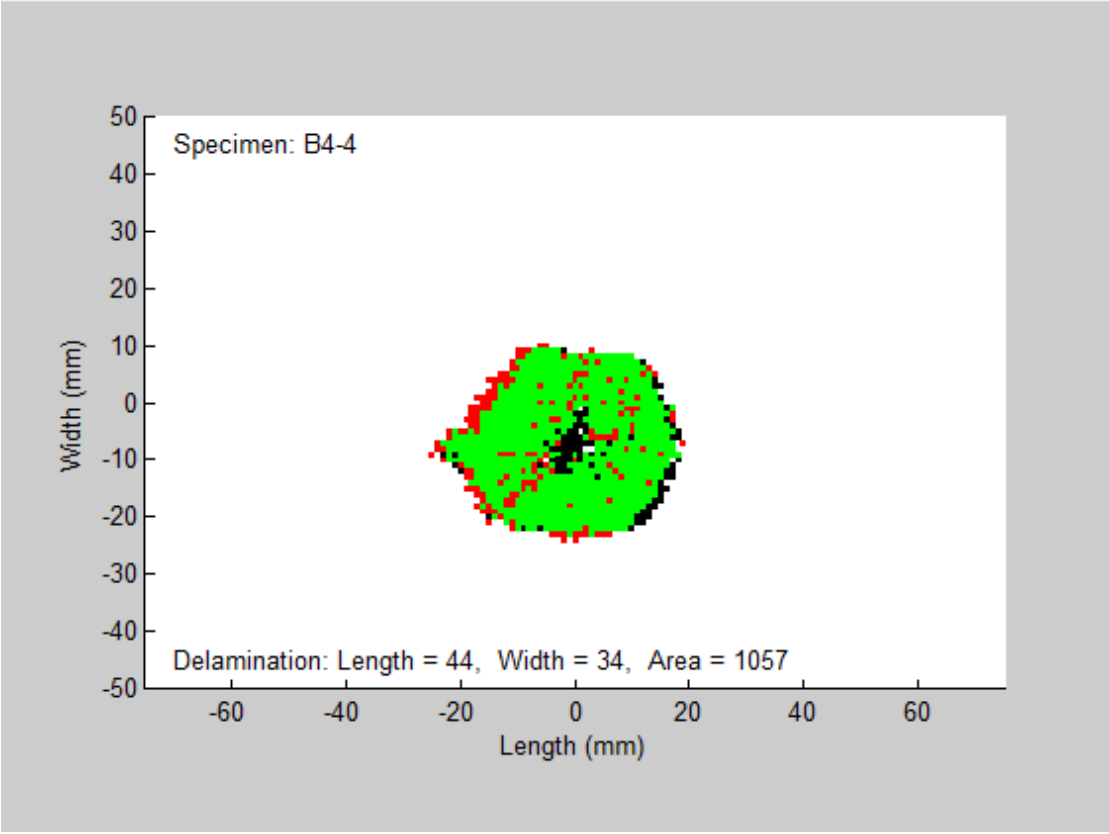

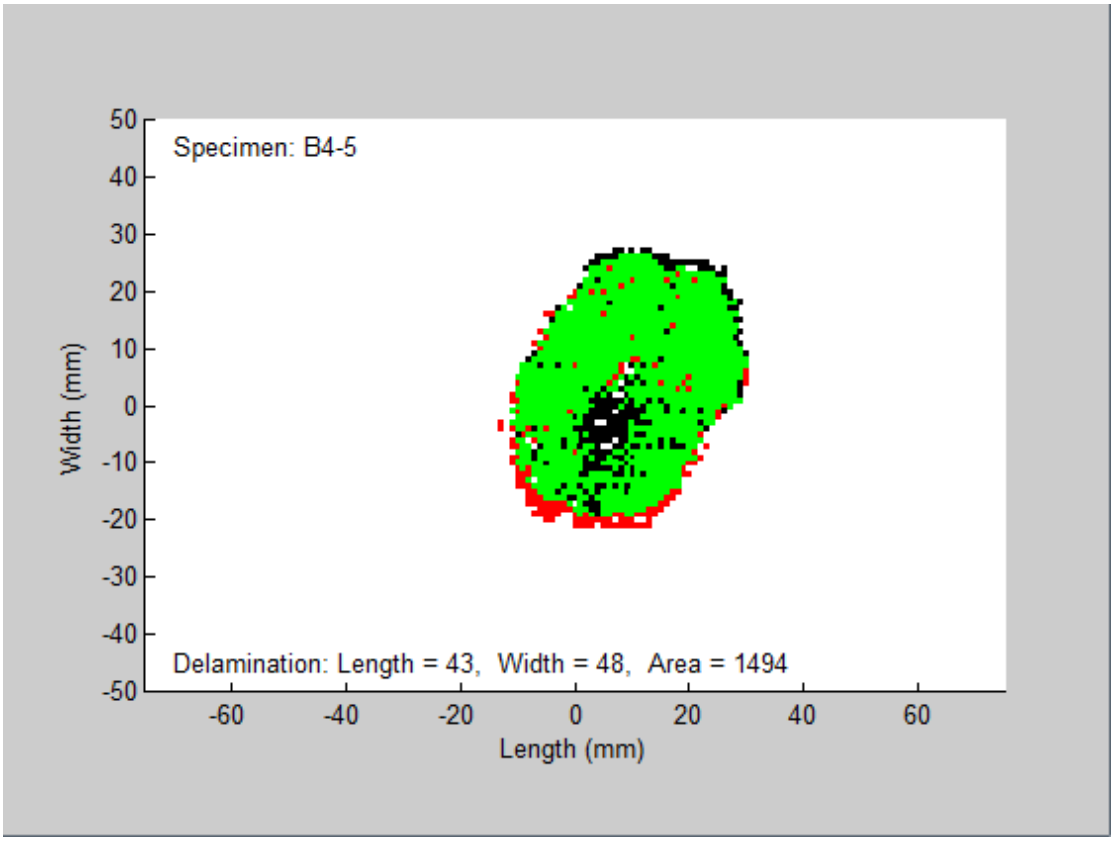

Figure 3.6 Superimposed delamination image of sub-group B4

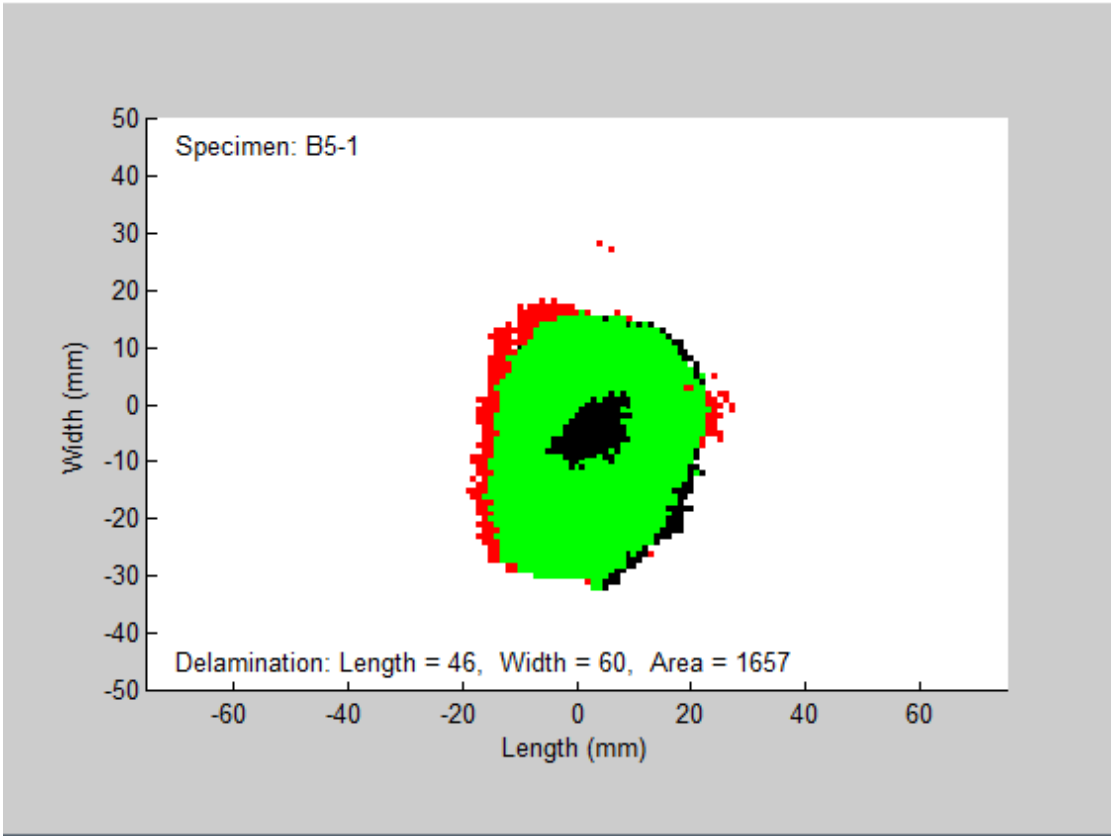
Specimen: B5-1
Delamination: Length = 46, Width = 60, Area = 1657
Width (mm)
Length (mm)
50
40
30
20
10
0
-10
-20
-30
-40
-50
-60
-40
-20
0
20
40
60

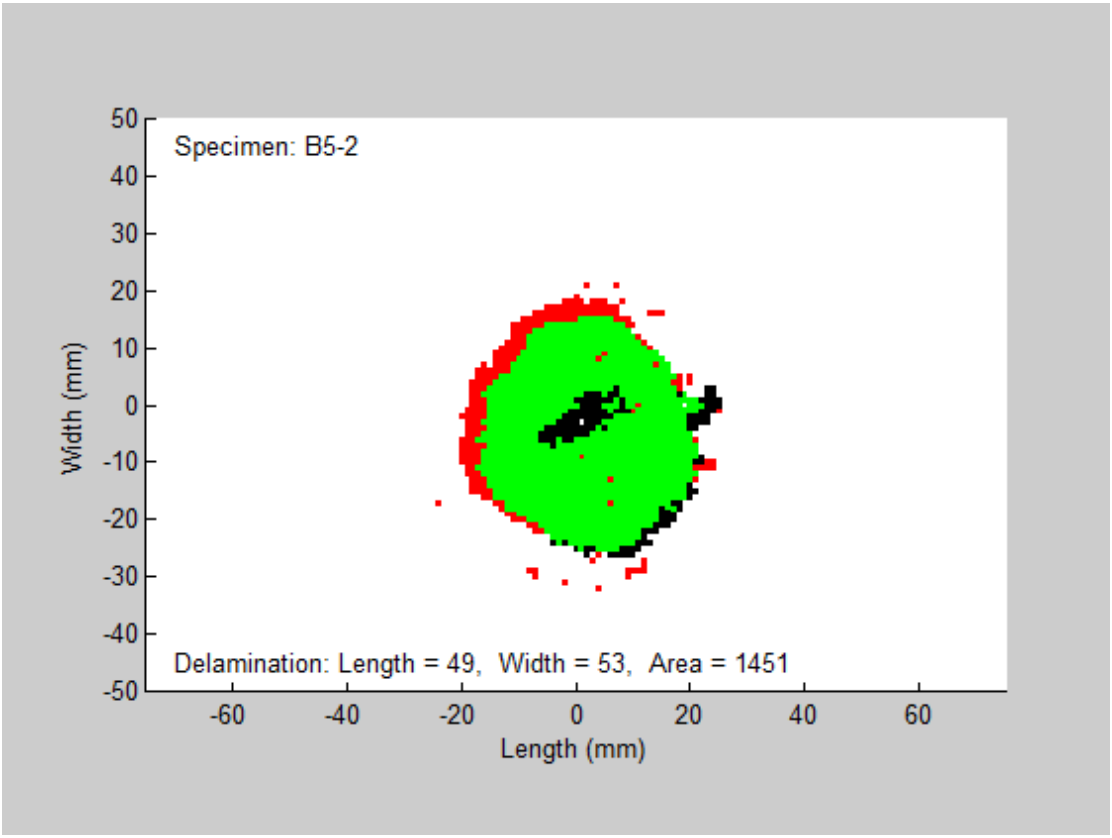
Specimen: B5-2
Delamination: Length = 49, Width = 53, Area = 1451
Width (mm)
Length (mm)
50
40
30
20
10
0
-10
-20
-30
-40
-50
-60
-40
-20
0
20
40
60

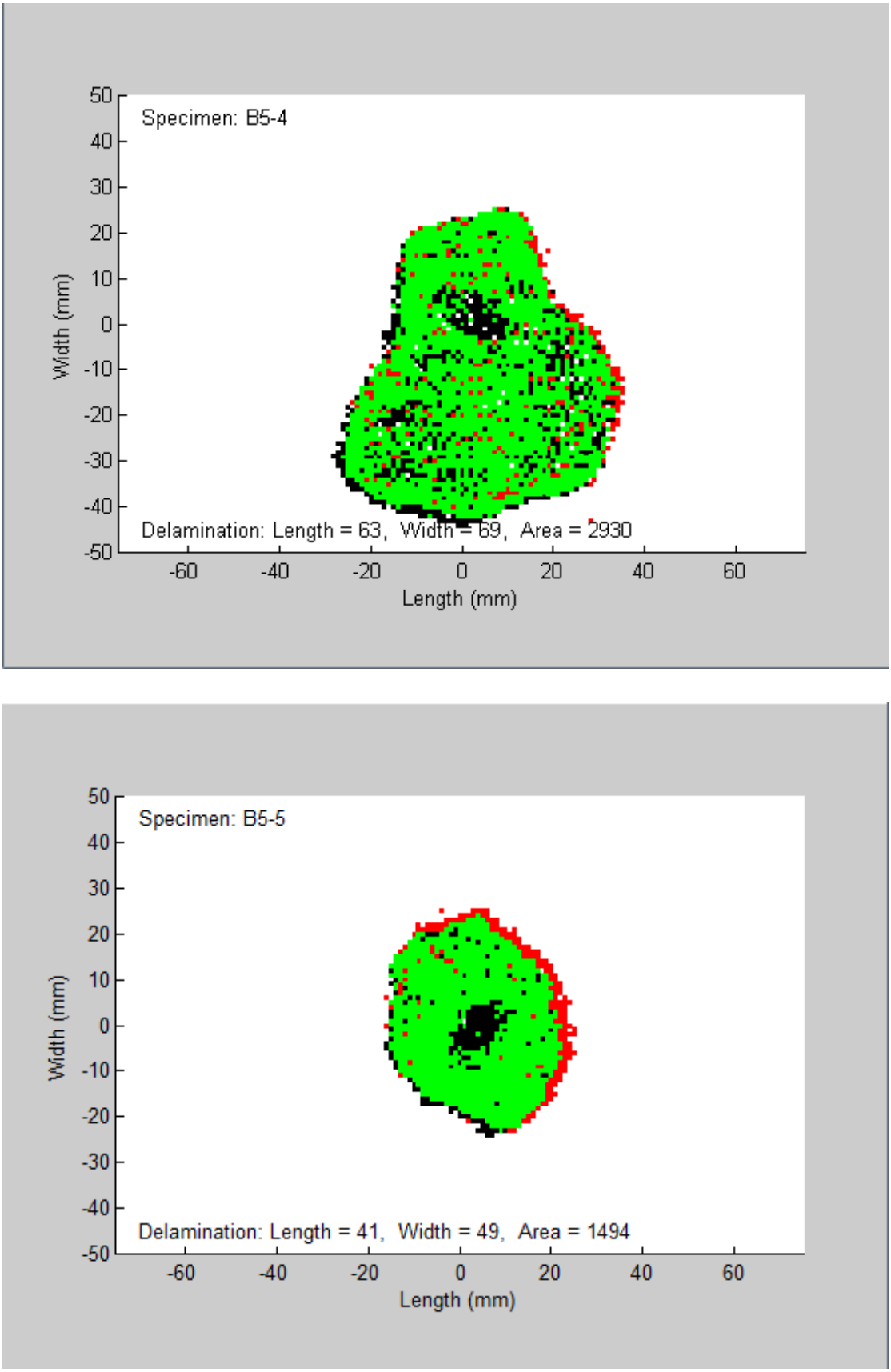

Figure 3.7 Superimposed delamination image of sub-group B5

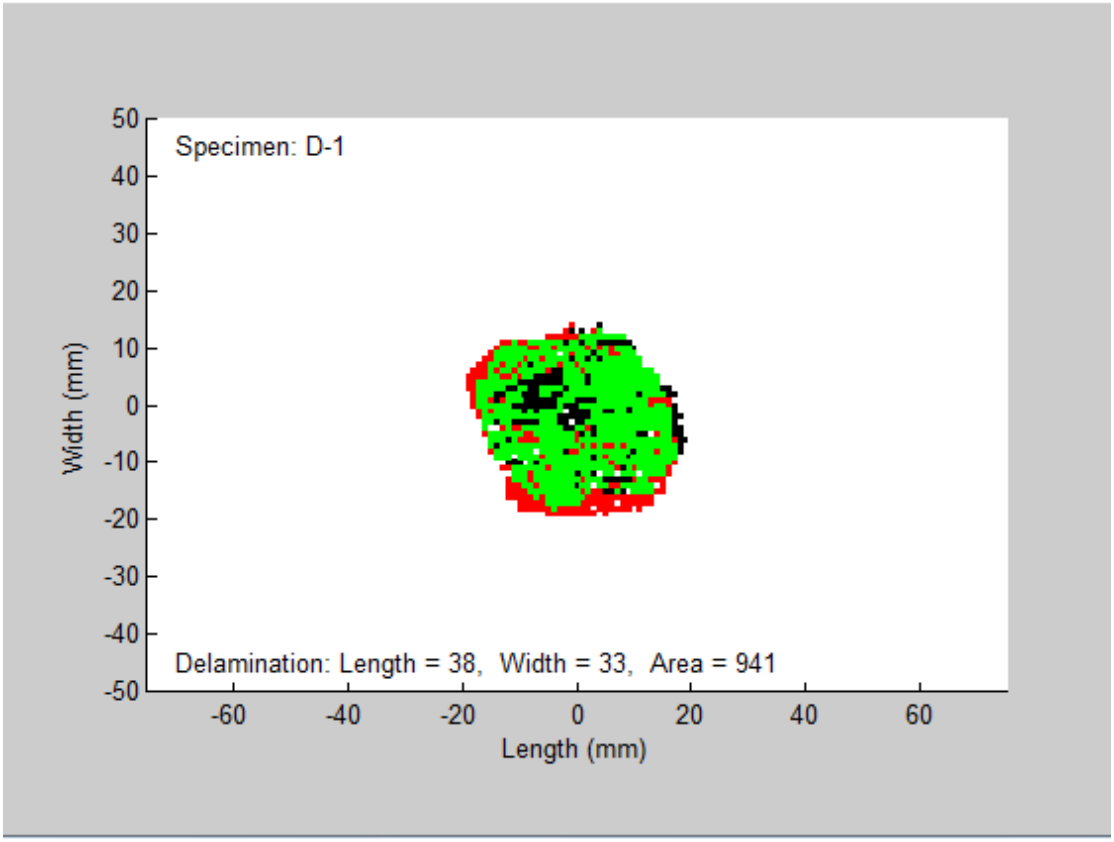
Specimen: D-1
Delamination: Length = 38, Width = 33, Area = 941
Width (mm)
Length (mm)
50
40
30
20
10
0
-10
-20
-30
-40
-50
-60
-40
-20
0
20
40
60

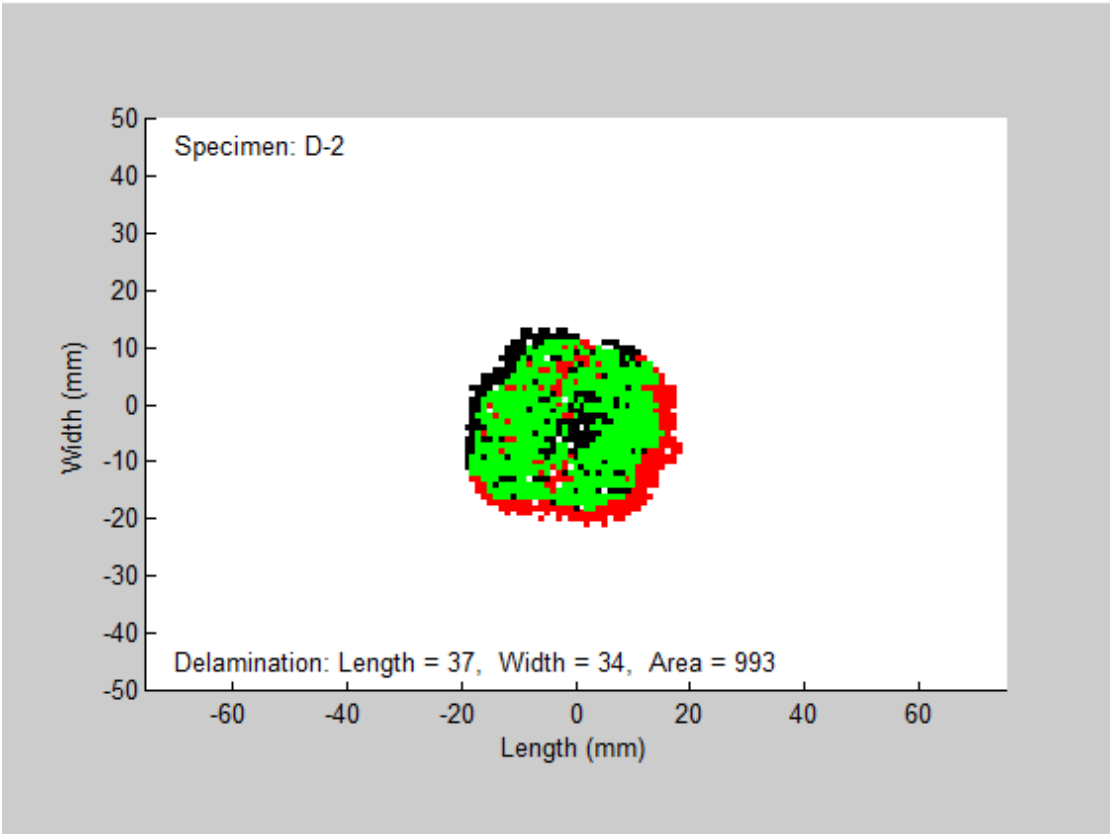
Specimen: D-2
Delamination: Length = 37, Width = 34, Area = 993
Width (mm)
Length (mm)
50
40
30
20
10
0
-10
-20
-30
-40
-50
-60
-40
-20
0
20
40
60

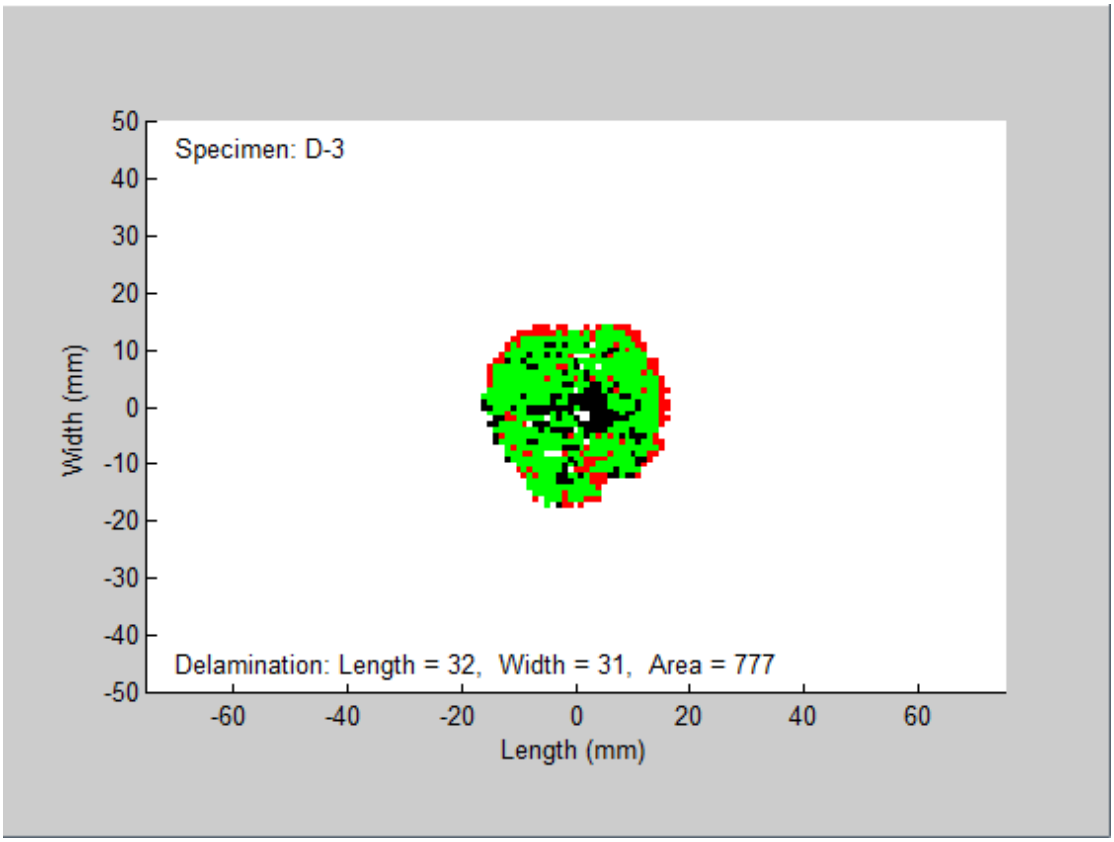
Specimen: D-3
Width (mm)
Length (mm)
Delamination: Length = 32, Width = 31, Area = 777

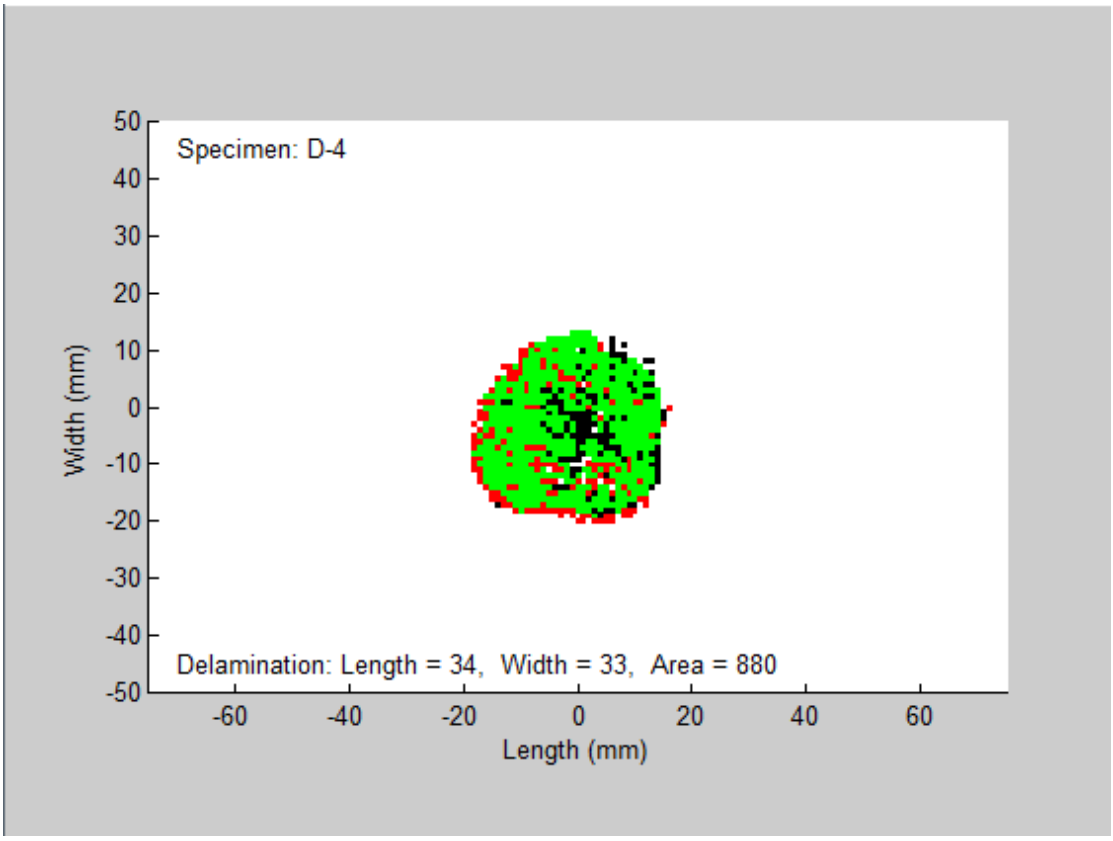
Specimen: D-4
Width (mm)
Length (mm)
Delamination: Length = 34, Width = 33, Area = 880

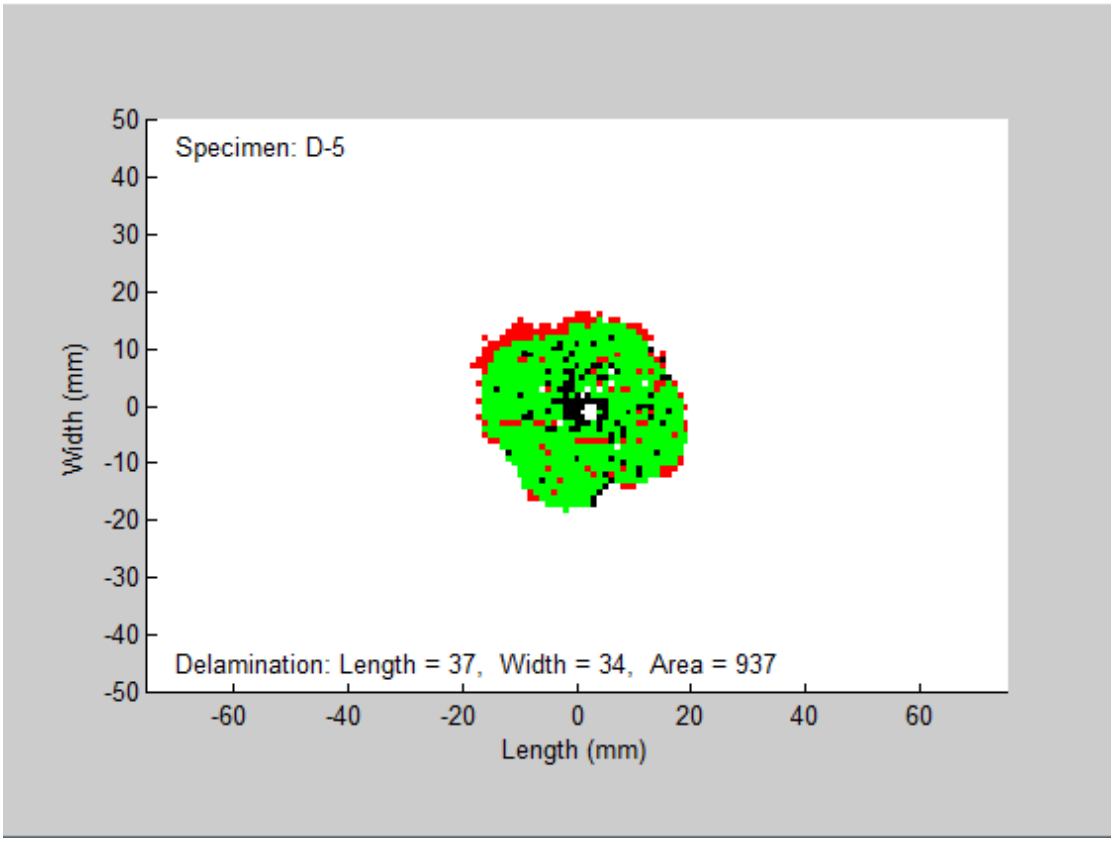

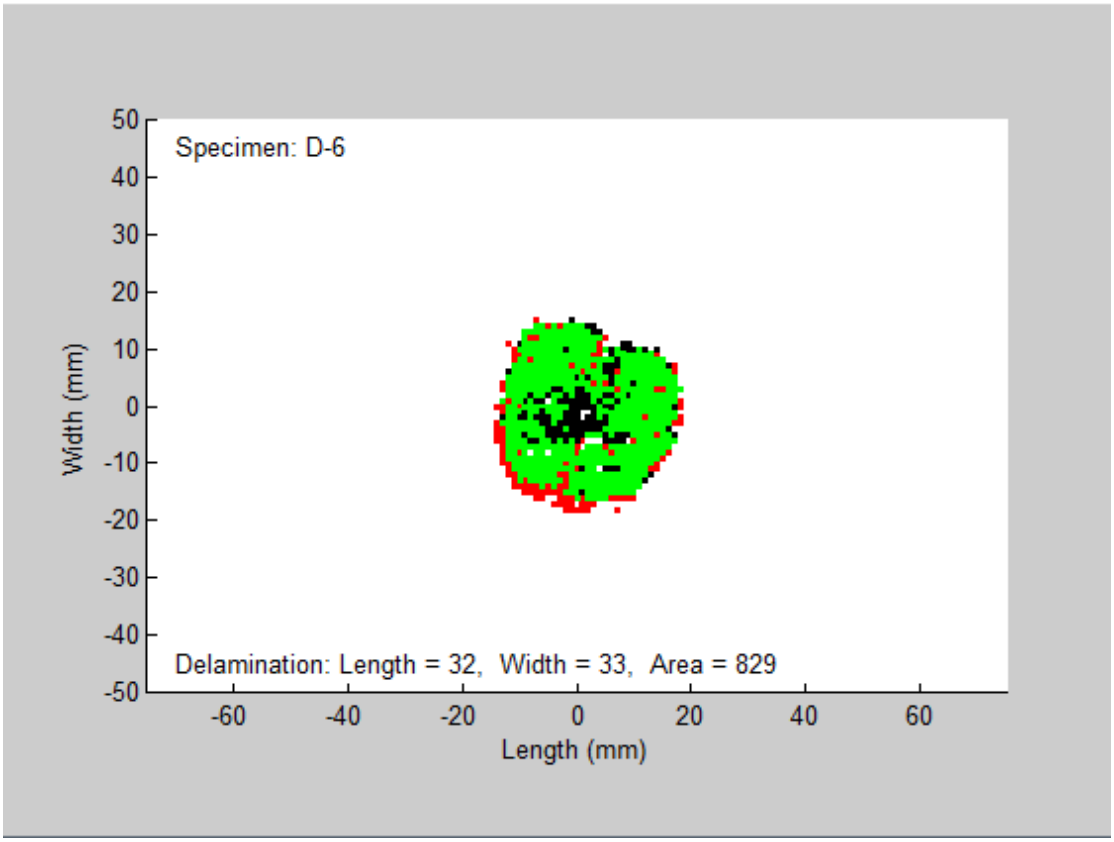

Figure 3.8 Superimposed delamination image of group D

Observing the delamination distributions on individual interfaces for all specimens, similar tendencies can be found. For instance, B4-1 is selected as a representative from this double-sided and complete scanning category, shown in Figure 3.9. The order of the interface number annotated at the bottom-right corner of each frame is counted from impact face to back face. This means that the bigger the interface number, the closer to the back face. To be consistent with the colouring convention above, black squares represent delamination detected from impact-face scan and red squares from back-face scan. Green squares represent at that positions delaminations were detected from both sides.

From Figure 3.9, two phenomena, which are also observed commonly in other specimens, need to be discussed. The first is that except on the interfaces close to the surface of the laminate, either the impact face or the back face, the detected delaminations on other interfaces are mainly in the form of a ring. This is due to the intrinsic weakness of C-scan, and the inner blank area is the blind zone of the scan masked by other delaminations right above. The other phenomenon is that these rings expand gradually from the interface close to one side of the laminate towards the interface closing to the mid-plane, and then shrinks gradually towards the interface close to the other side of the laminate. This is an important characteristic of delamination distribution through the laminate thickness direction induced by low velocity impact. The outline of the delamination distribution from the section view of the laminate is usually of a spindle shape, with the maximum delamination area at or close to the middle interface while the minimum at both ends. Because of this distribution pattern, the overall profile

of delamination distribution can be detected well by double-sided C-scan. However, according to the knowledge obtained from other techniques, such as deply [47], it is already known that the delamination shape on each individual interface is peanut shaped or double-fan shaped, which is bounded by the fibre orientations of upper and lower laminae in acute angle. Combining this knowledge with the overall profile of delamination distribution obtained from C-scan, the detailed delamination distribution state can be identified. On each individual interface the delamination is peanut shaped of which the position is bounded by the fibre orientation of upper and lower laminae which is illustrated in Figure 2.15. The delamination size on each interface is determined by the span of the scattered squares detected on that interface. This strategy will be employed for the simulation of delamination distribution when detailed FE models of CAI are constructed in Chapter 5. The second phenomenon is that on some interfaces close to the laminate surfaces, the delamination is presented in the form of scattered patches rather than a continuous area. This is probably due to the presence of transverse matrix cracks and fibre breakage. Usually, the delamination surface is parallel with the laminate surface, and is vertical to the longitudinal axis of the scan sensor accordingly. In this case, the ultrasound wave emitted by the sensor is able to reflect back to the sensor to report the existence of the delamination. However, when transverse matrix cracks and fibre breakage get involved, massive tiny but irregular crack faces induce diffused reflection of the ultrasound wave. Figure 3.10 displays the number variation of detected spots over the interfaces of the first specimen from each group. In each individual group, similar variation trends among specimens are observed. Following the same colouring convention, the black dash line with hollow circle markers represents the number of detected squares from impact-face scan, and red dot line with hollow square markers

represents that detected from back-face scan, and the green solid line with star markers represents the sum of detected squares from both scans. Investigating these curves, some tendencies can be summarised as follows: (1) the net total number of squares on individual interfaces usually increases gradually from the interface close to the impact face, then reaches the maximum at some interface usually somewhere between the mid-plane and back face, and then drops rapidly as the interface close to the back face; (2) delaminations detected from impact-face scan appear almost in all interfaces, while the delaminations detected from back-face scan mainly appear within the half thickness on the back-face side of the laminate and rarely any in the other half thickness. These tendencies are in agreement with the observation obtained from Figure 3.9 that the profile of the delamination distribution over laminate thickness is like a spindle, and the largest delaminations usually appear at a few interfaces from the mid-plane towards the back-face of the laminate.

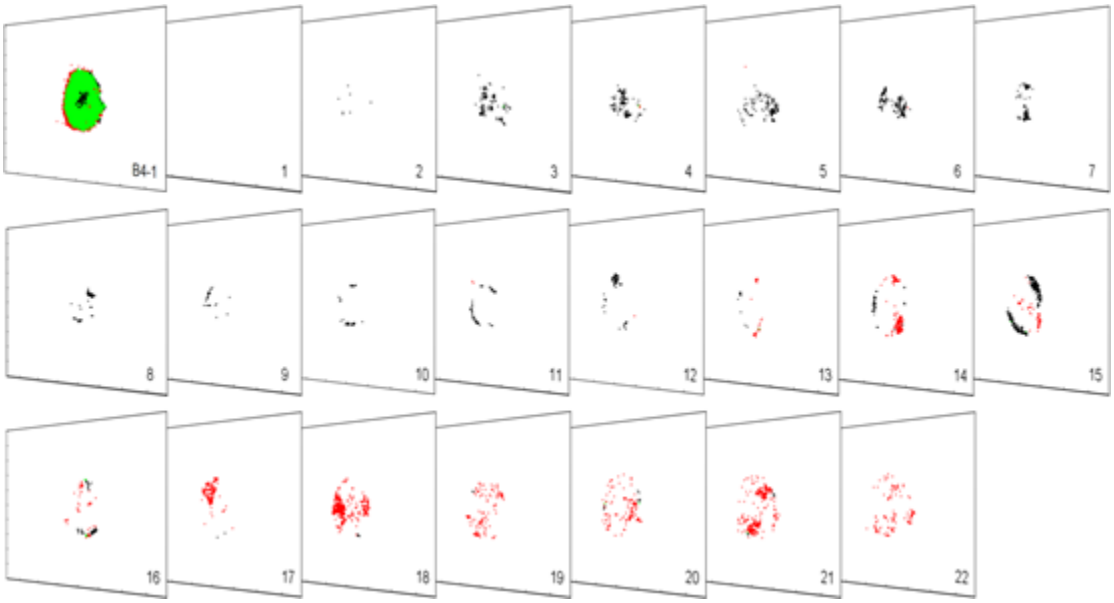

Figure 3.9 Schematic of detected delamination on each individual interface of B4-1 (green squares represent delamination detected from both face scans, black squares represent from impact-face scan only, red squares represent from back-face scan only)

3.3.1.2 Double-sided but incomplete scan

Group A1, A2 and A3 belong to this type. Similarly, the images of superimposed delamination for each specimen are presented from Figure 3.11 to Figure 3.13. Compared with the images of previous category, such as from Figure 3.3 to Figure 3.8, two differences are observed. One is that significant blank area appears at the centre of the superimposed delamination area. The other is that the green area has reduced significantly, replaced by mottled red and black squares. All these phenomena are the consequence of severe impact damage at the laminate surface. Usually, deep impact dent lies in the centre of the specimen surface on the impact side and a bulge appears on the opposite side accordingly, accompanied with split fibres from a few outmost laminae. In this case, scan cannot be conducted smoothly over these severely damaged areas, leaving the blank area and mottled delamination squares on the images.

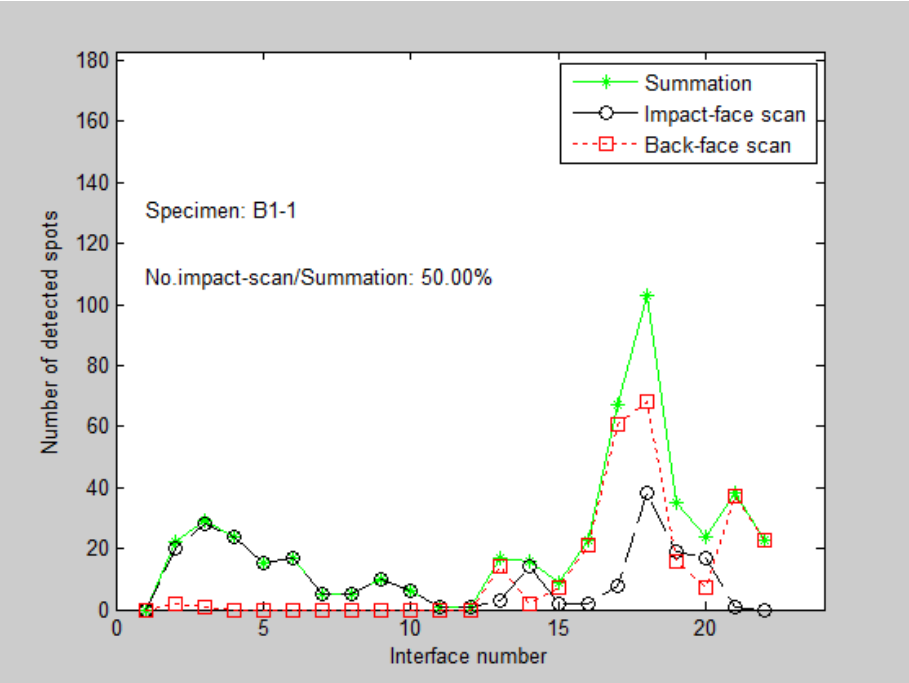
Summation
Impact-face scan
Back-face scan
Specimen: B1-1
No.impact-scan/Summation: 50.00%
Number of detected spots
Interface number
0
20
40
60
80
100
120
140
160
180
0
5
10
15
20

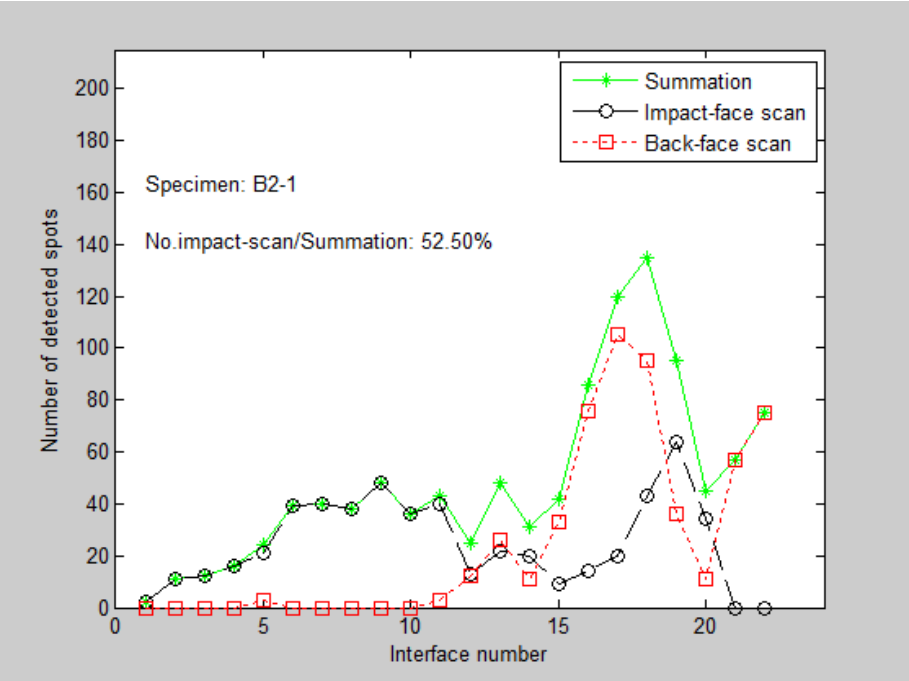
Summation
Impact-face scan
Back-face scan
Specimen: B2-1
No.impact-scan/Summation: 52.50%
Number of detected spots
Interface number
0
20
40
60
80
100
120
140
160
180
200
0
5
10
15
20

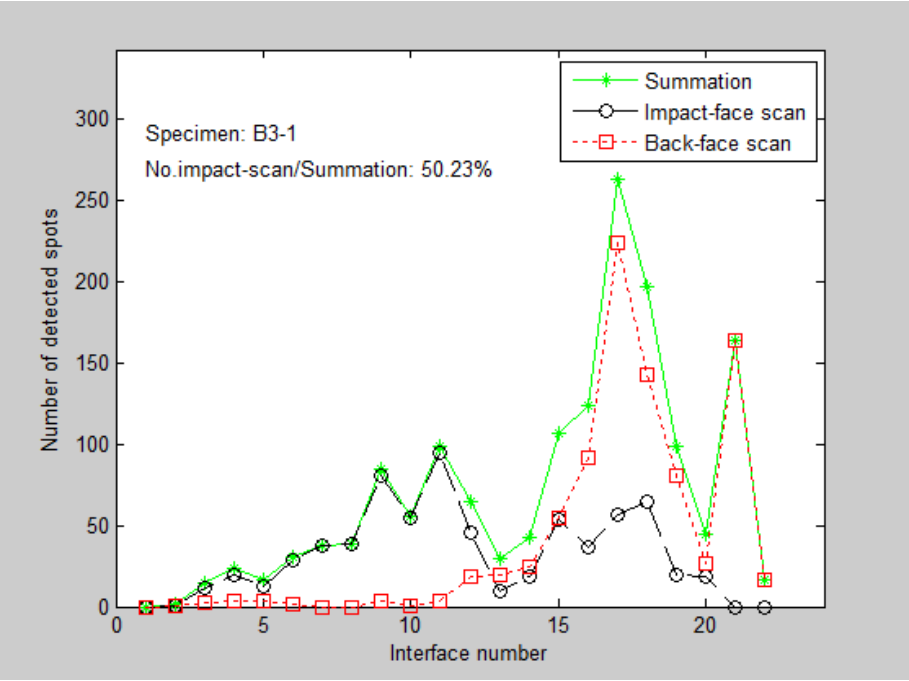
Summation
Impact-face scan
Back-face scan
Specimen: B3-1
No.impact-scan/Summation: 50.23%
Number of detected spots
Interface number
0
50
100
150
200
250
300
0
5
10
15
20

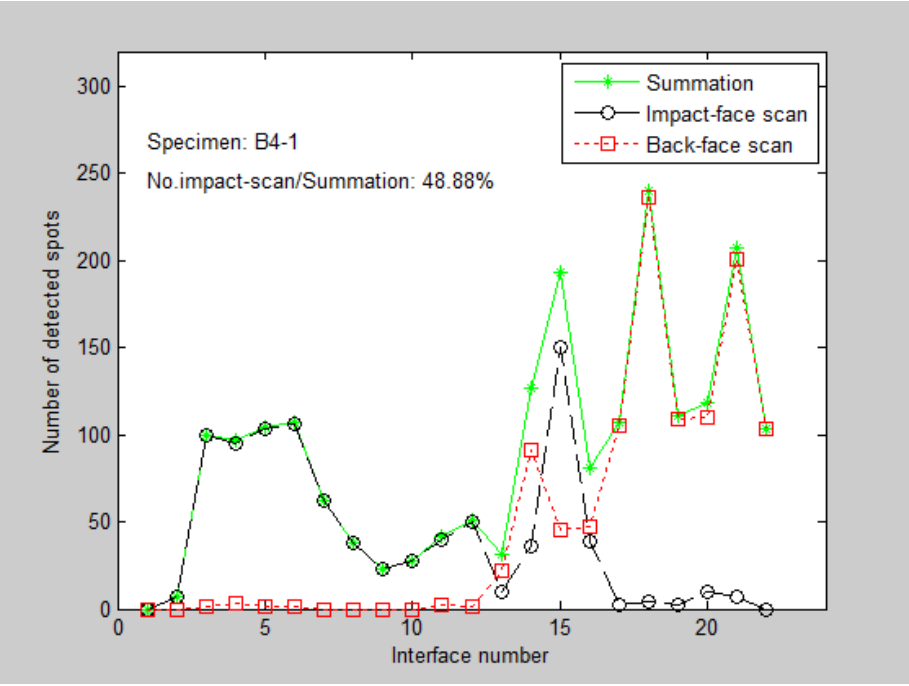
Summation
Impact-face scan
Back-face scan
Specimen: B4-1
No.impact-scan/Summation: 48.88%
Number of detected spots
Interface number
0
50
100
150
200
250
300
0
5
10
15
20

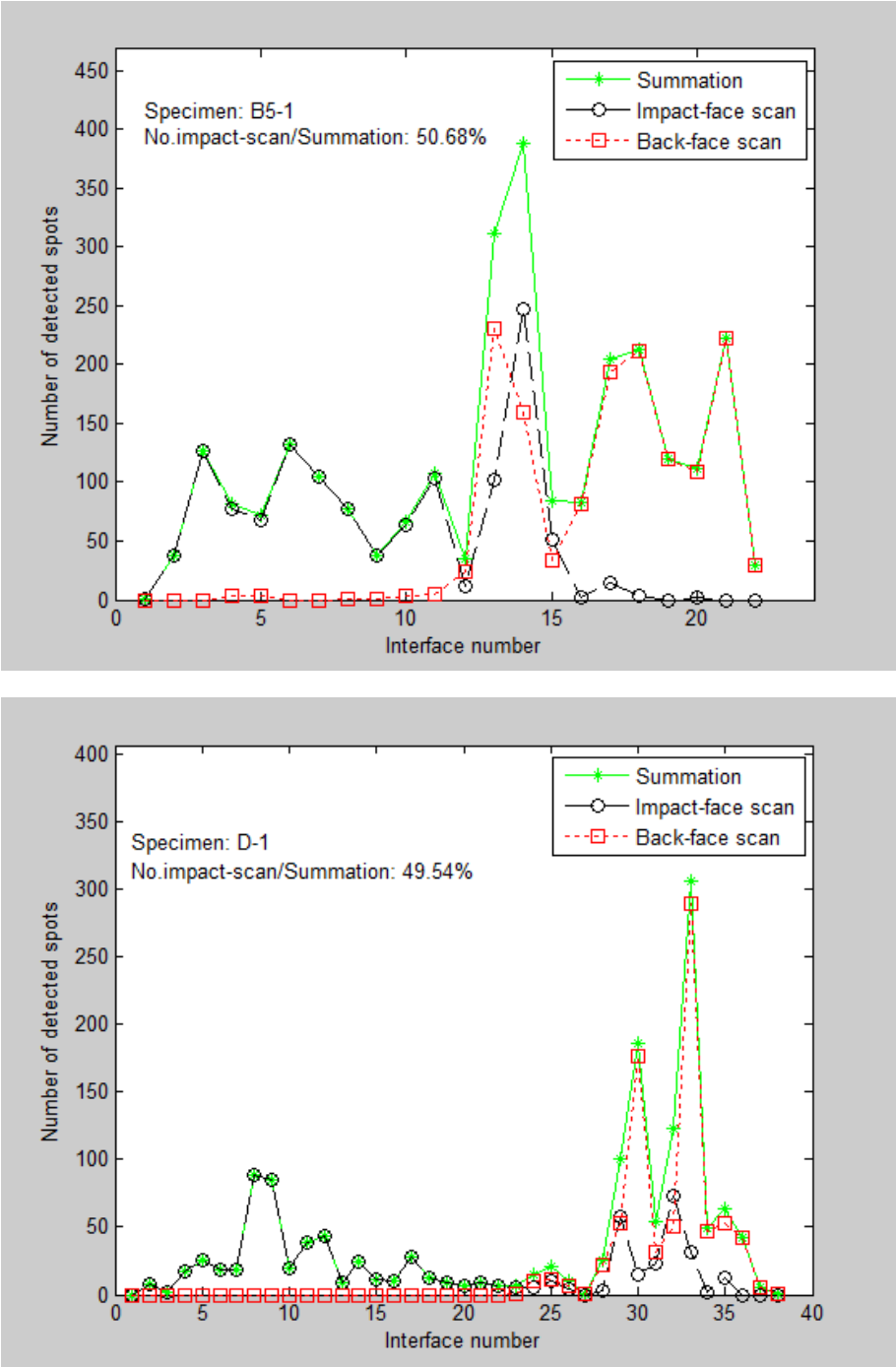

Figure 3.10 The variation of detected delamination squares against interfaces (Interface number ascends from impact face to back face)

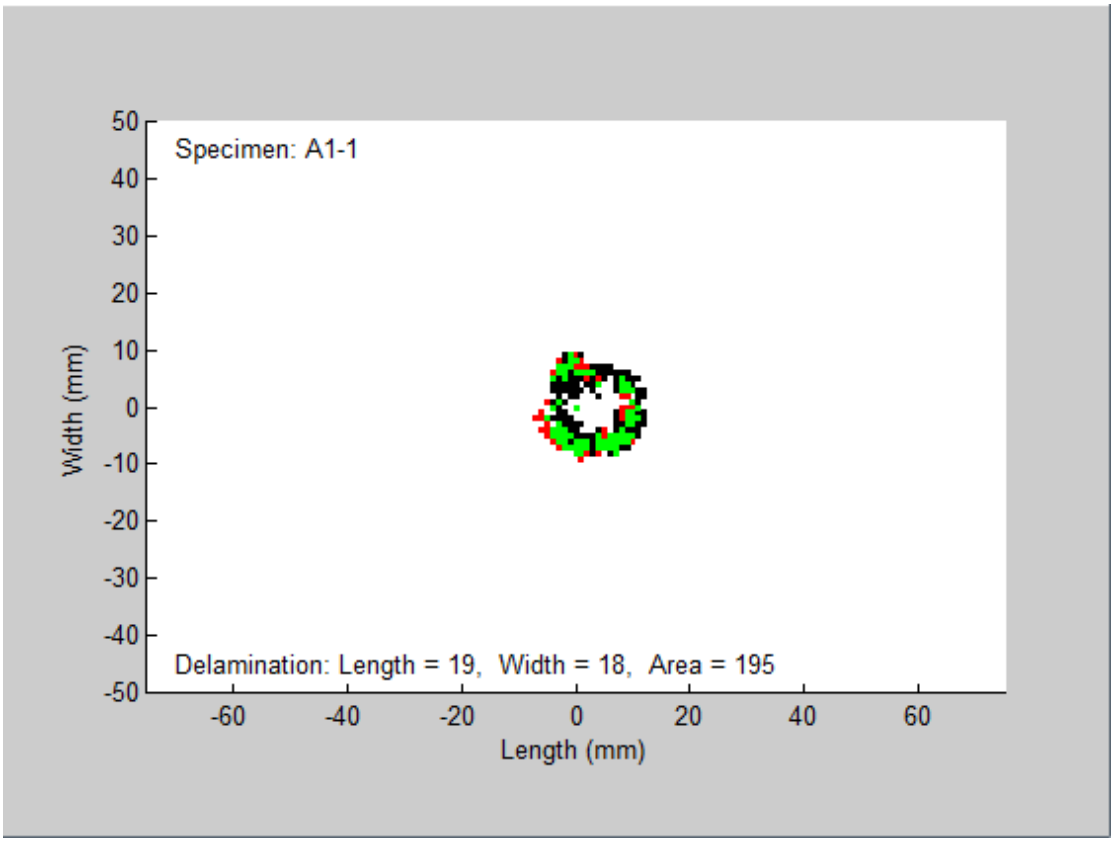
Specimen: A1-1
Delamination: Length = 19, Width = 18, Area = 195
Width (mm)
Length (mm)
50
40
30
20
10
0
-10
-20
-30
-40
-50
-60
-40
-20
0
20
40
60

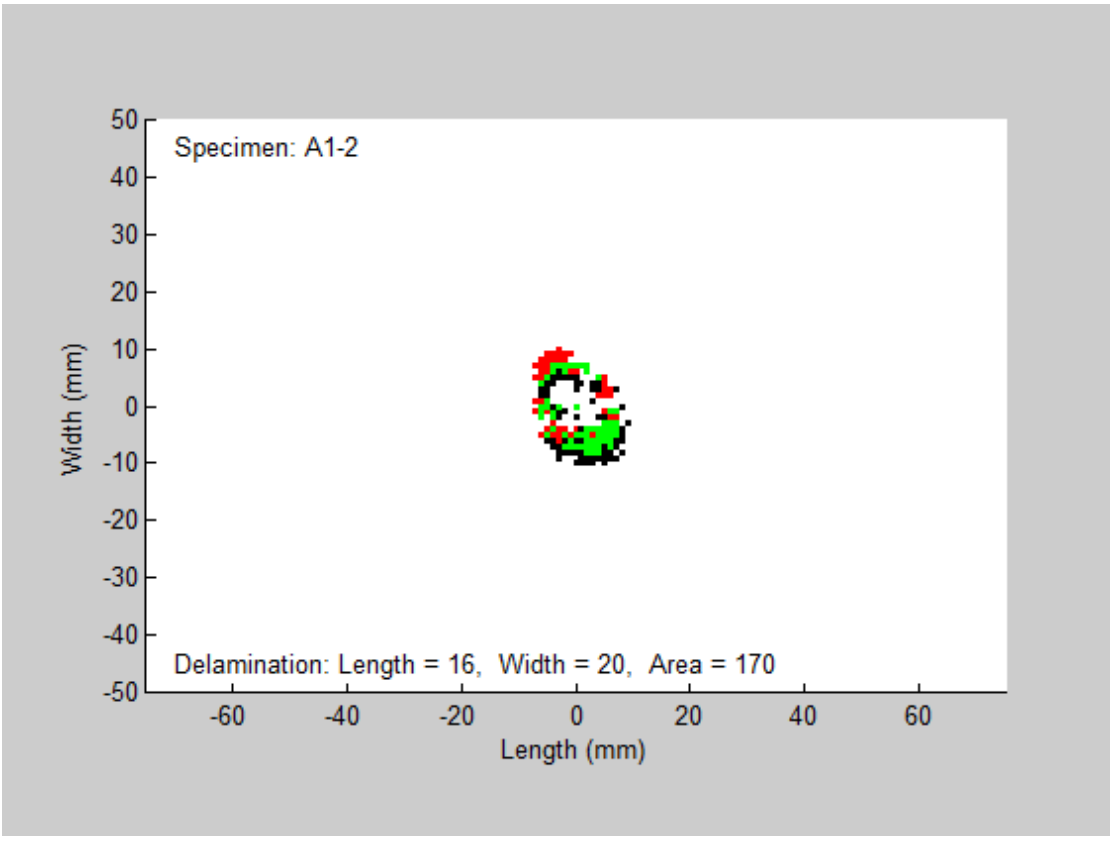
Specimen: A1-2
Delamination: Length = 16, Width = 20, Area = 170
Width (mm)
Length (mm)
50
40
30
20
10
0
-10
-20
-30
-40
-50
-60
-40
-20
0
20
40
60

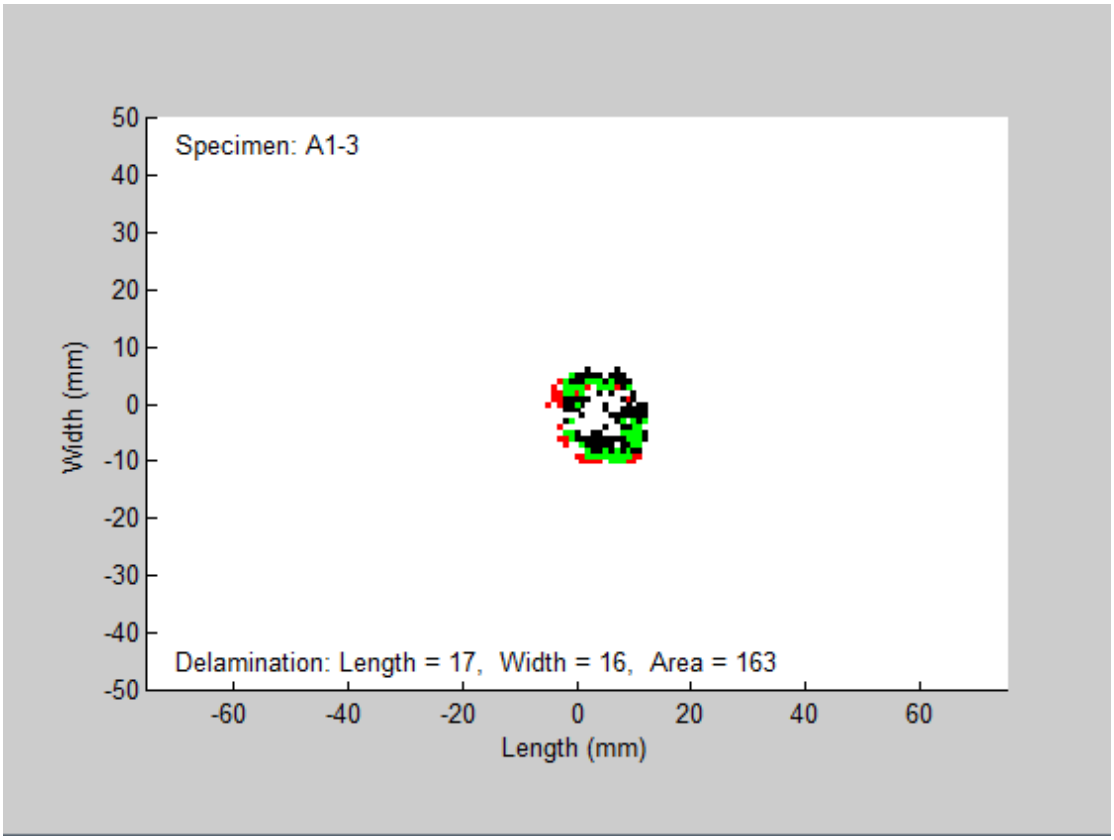
Specimen: A1-3
Delamination: Length = 17, Width = 16, Area = 163
Width (mm)
Length (mm)
50
40
30
20
10
0
-10
-20
-30
-40
-50
-60
-40
-20
0
20
40
60

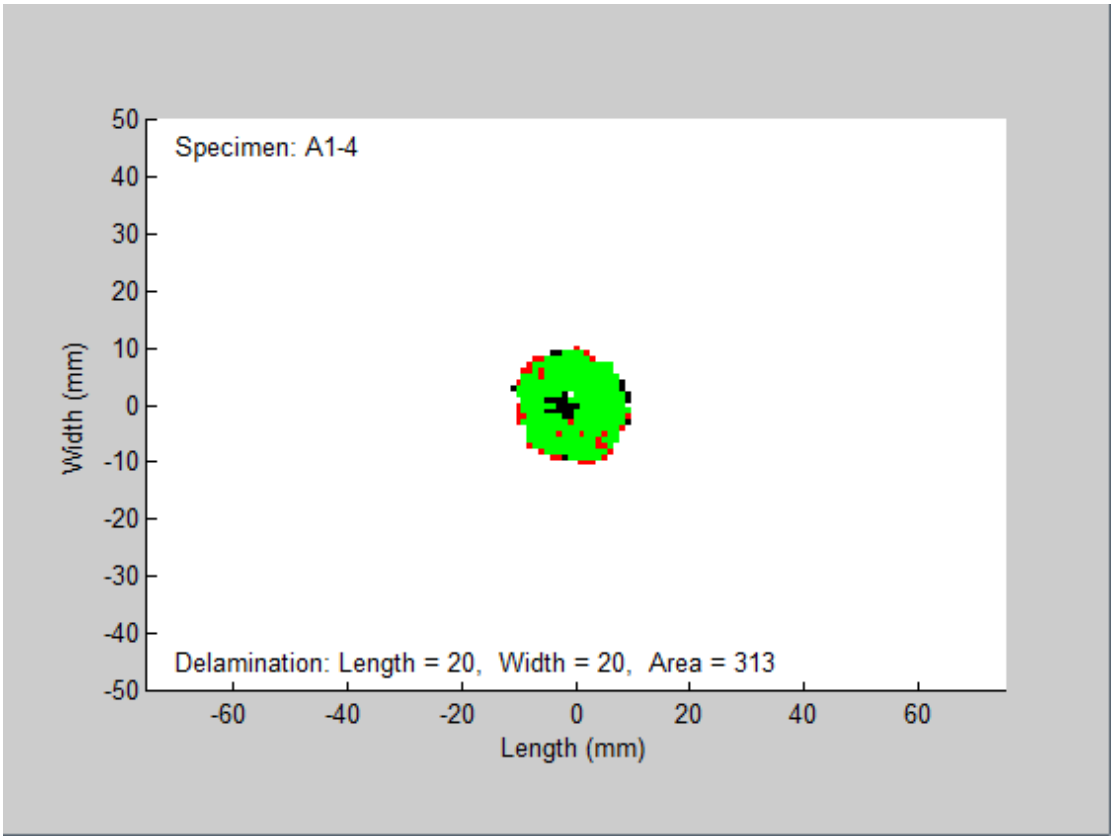
Specimen: A1-4
Delamination: Length = 20, Width = 20, Area = 313
Width (mm)
Length (mm)
50
40
30
20
10
0
-10
-20
-30
-40
-50
-60
-40
-20
0
20
40
60

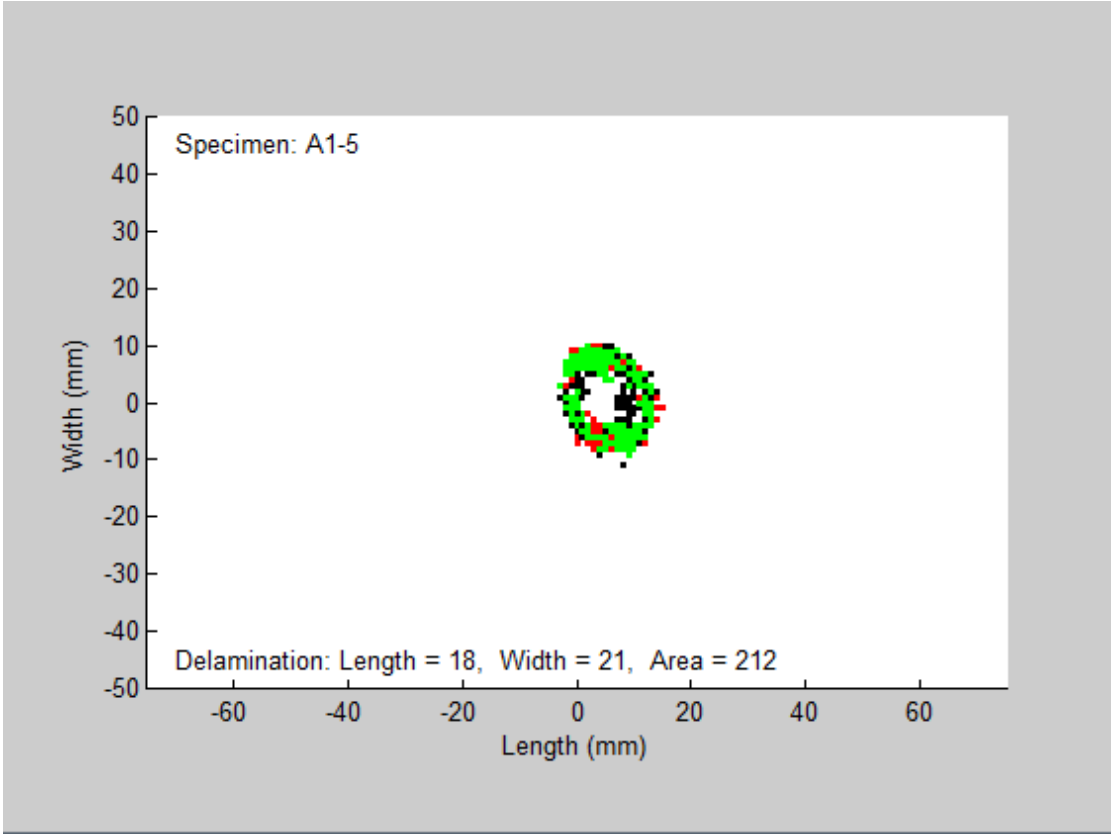

Figure 3.11 Superimposed delamination image of sub-group A1

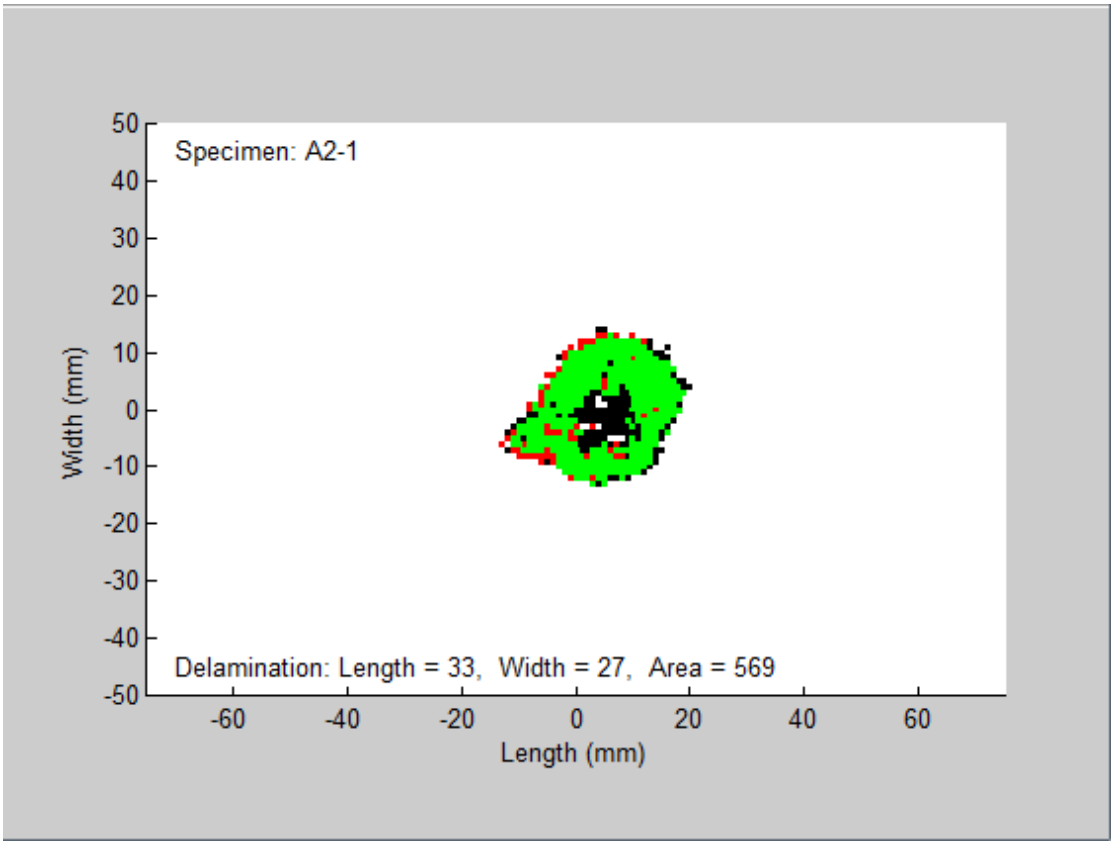
Specimen: A2-1
Delamination: Length = 33, Width = 27, Area = 569
Width (mm)
Length (mm)
50
40
30
20
10
0
-10
-20
-30
-40
-50
-60
-40
-20
0
20
40
60

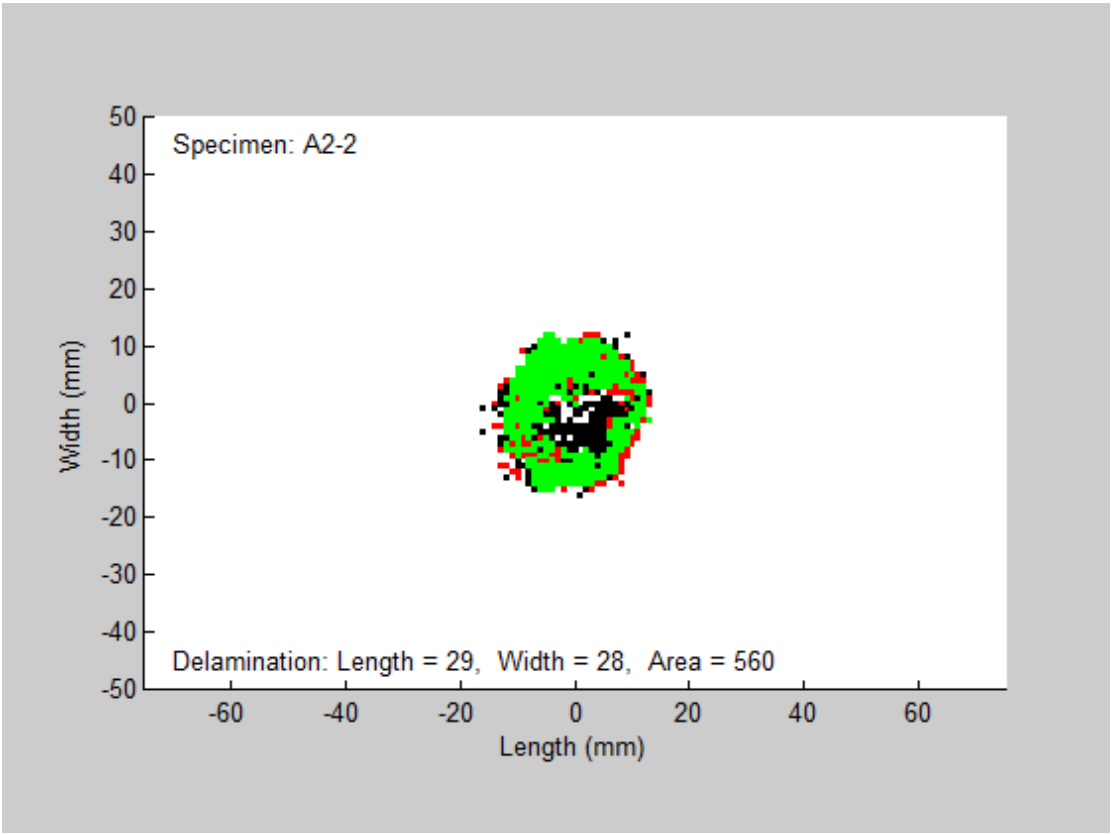
Specimen: A2-2
Delamination: Length = 29, Width = 28, Area = 560
Width (mm)
Length (mm)
50
40
30
20
10
0
-10
-20
-30
-40
-50
-60
-40
-20
0
20
40
60

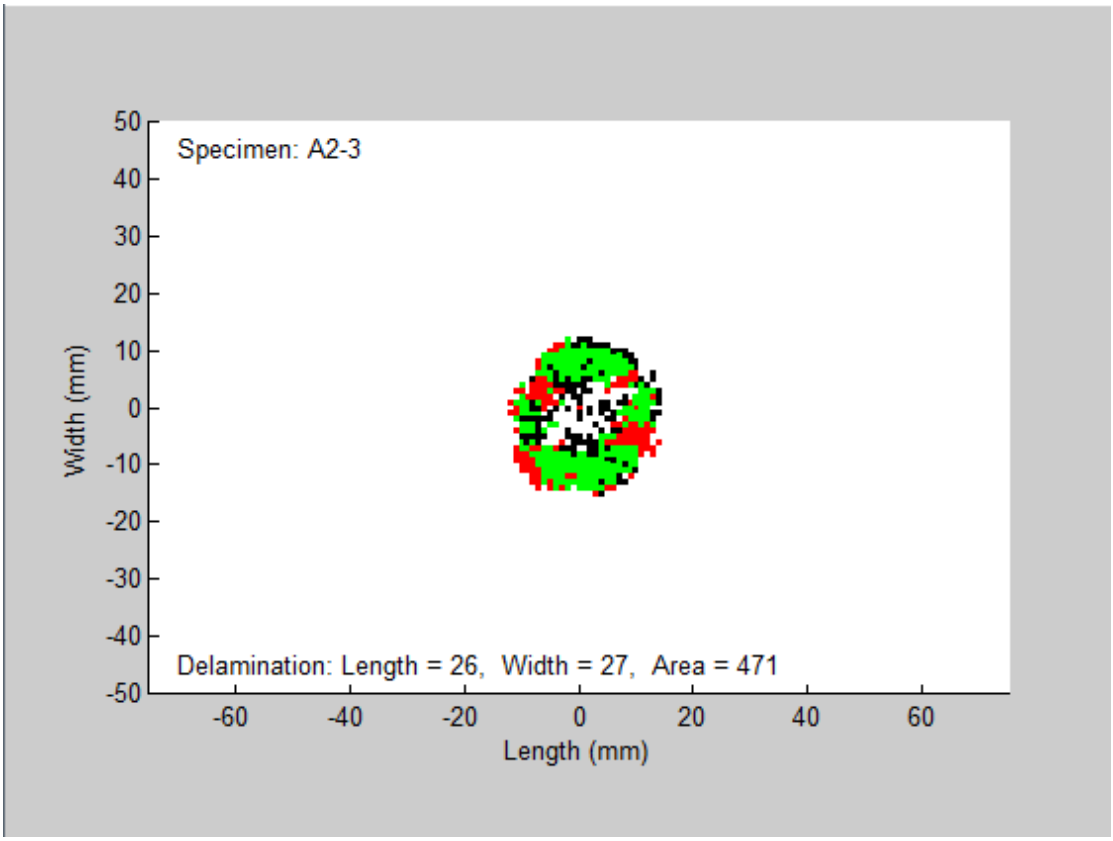
Specimen: A2-3
Delamination: Length = 26, Width = 27, Area = 471
Width (mm)
Length (mm)
50
40
30
20
10
0
-10
-20
-30
-40
-50
-60
-40
-20
0
20
40
60

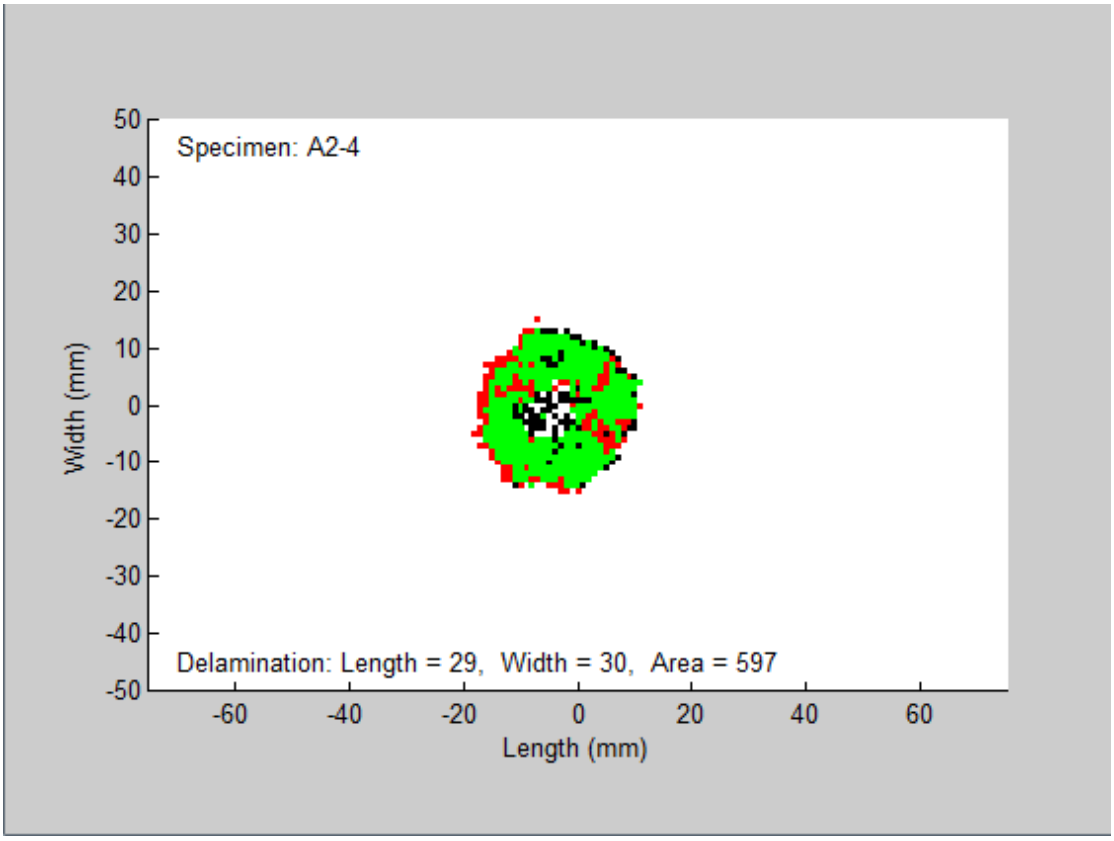
Specimen: A2-4
Delamination: Length = 29, Width = 30, Area = 597
Width (mm)
Length (mm)
50
40
30
20
10
0
-10
-20
-30
-40
-50
-60
-40
-20
0
20
40
60

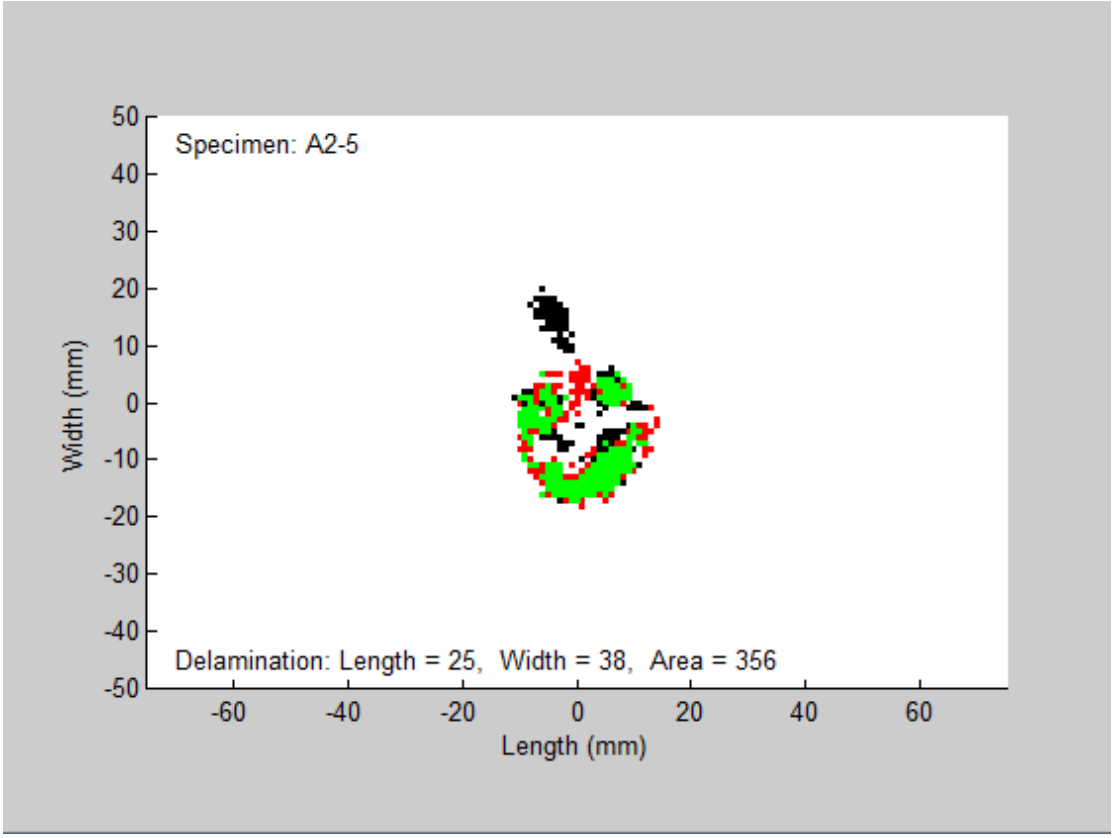

Figure 3.12 Superimposed delamination image of sub-group A2

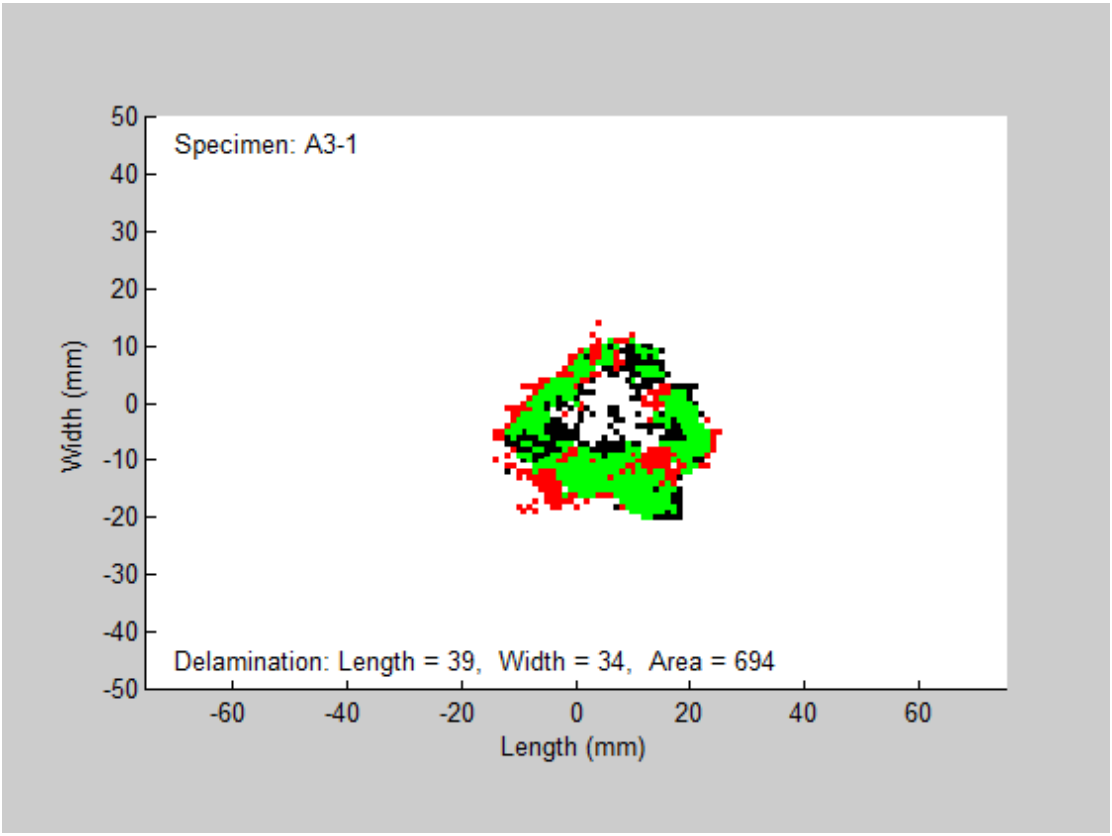
Specimen: A3-1
Delamination: Length = 39, Width = 34, Area = 694
Width (mm)
Length (mm)
50
40
30
20
10
0
-10
-20
-30
-40
-50
-60
-40
-20
0
20
40
60

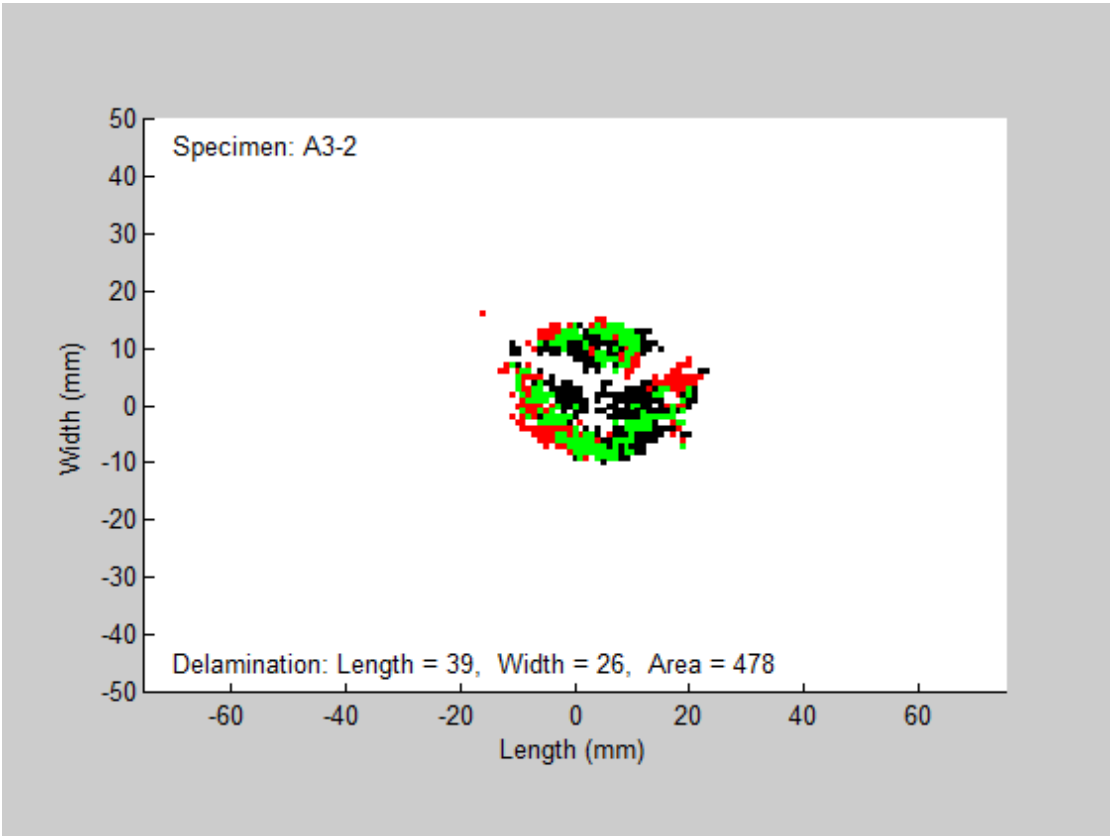
Specimen: A3-2
Delamination: Length = 39, Width = 26, Area = 478
Width (mm)
Length (mm)
50
40
30
20
10
0
-10
-20
-30
-40
-50
-60
-40
-20
0
20
40
60

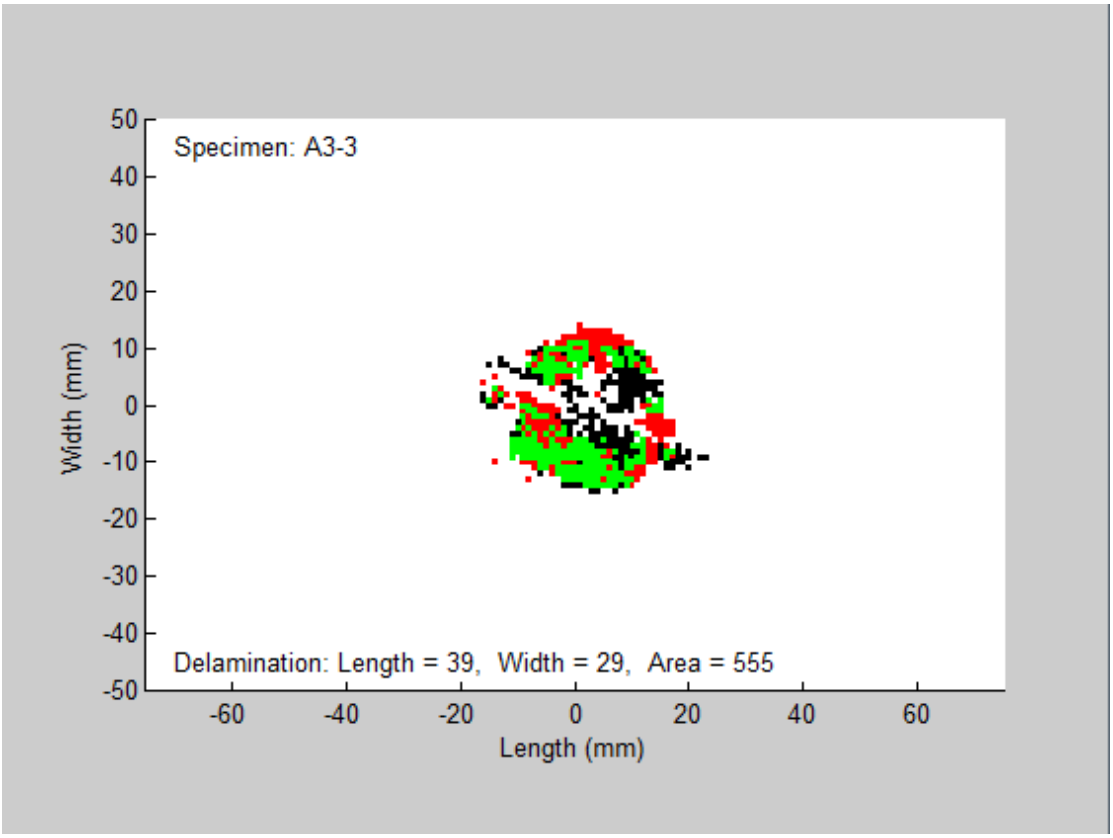
Specimen: A3-3
Delamination: Length = 39, Width = 29, Area = 555
Width (mm)
Length (mm)
50
40
30
20
10
0
-10
-20
-30
-40
-50
-60
-40
-20
0
20
40
60

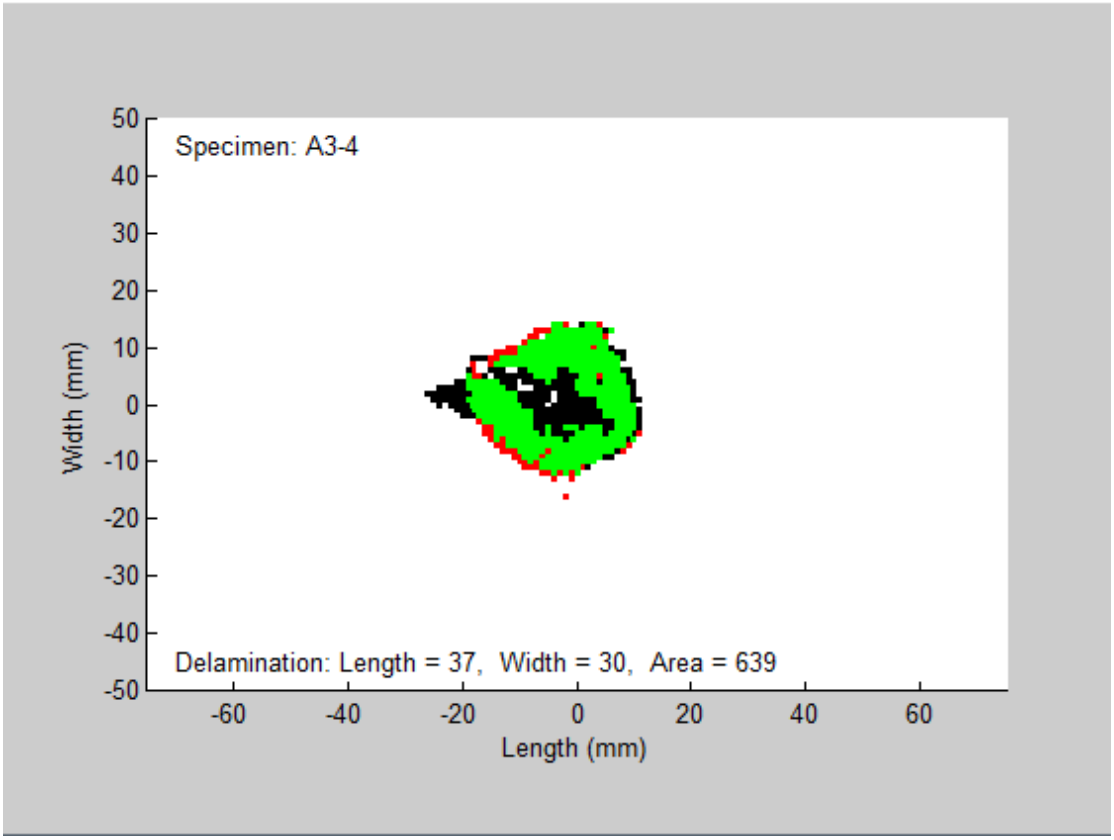
Specimen: A3-4
Delamination: Length = 37, Width = 30, Area = 639
Width (mm)
Length (mm)
50
40
30
20
10
0
-10
-20
-30
-40
-50
-60
-40
-20
0
20
40
60

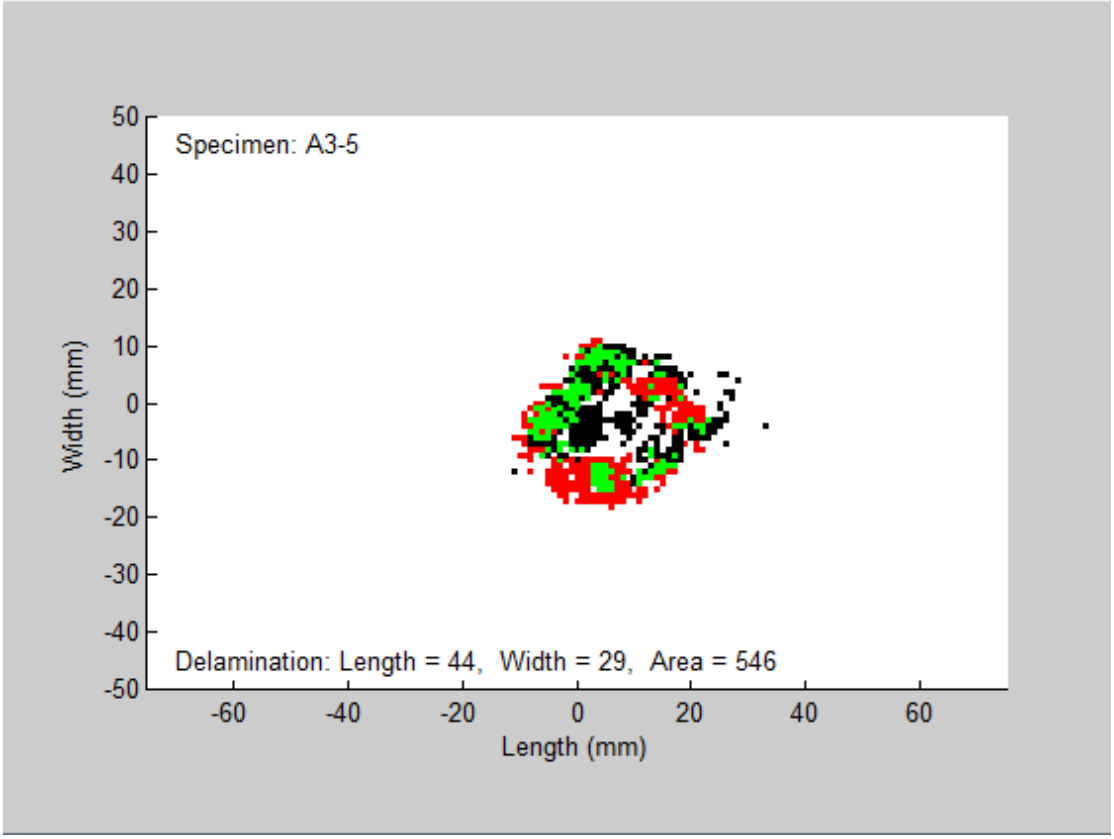

Figure 3.13 Superimposed delamination image of sub-group A3

A2-4 is selected as a representative (Figure 3.14) to demonstrate the decomposed delamination distribution on each individual interface. Similar tendencies are observed as the previous type. Therefore, it is not repeated here again.

The variation of detected delamination squares against interface numbers are plotted in Figure 3.15 for the first specimen of each group in this type. Again, similar characteristics to the previous category are found. For brevity, it is not discussed here again.

Although the scanning quality in this category is worse than that of the previous one, it is still valid for estimating the delamination distribution over the laminate thickness. This is because although the scanning result about the central part of the delamination area is absent largely, the

scanning operation was not affected significantly. Consequently, the remaining detected delamination squares on each interface can represent the outline of the delamination on that interface. Combined with the already-known tendency of delamination shape on individual interfaces, the detailed delamination distribution inside the laminate can be assumed reasonably.

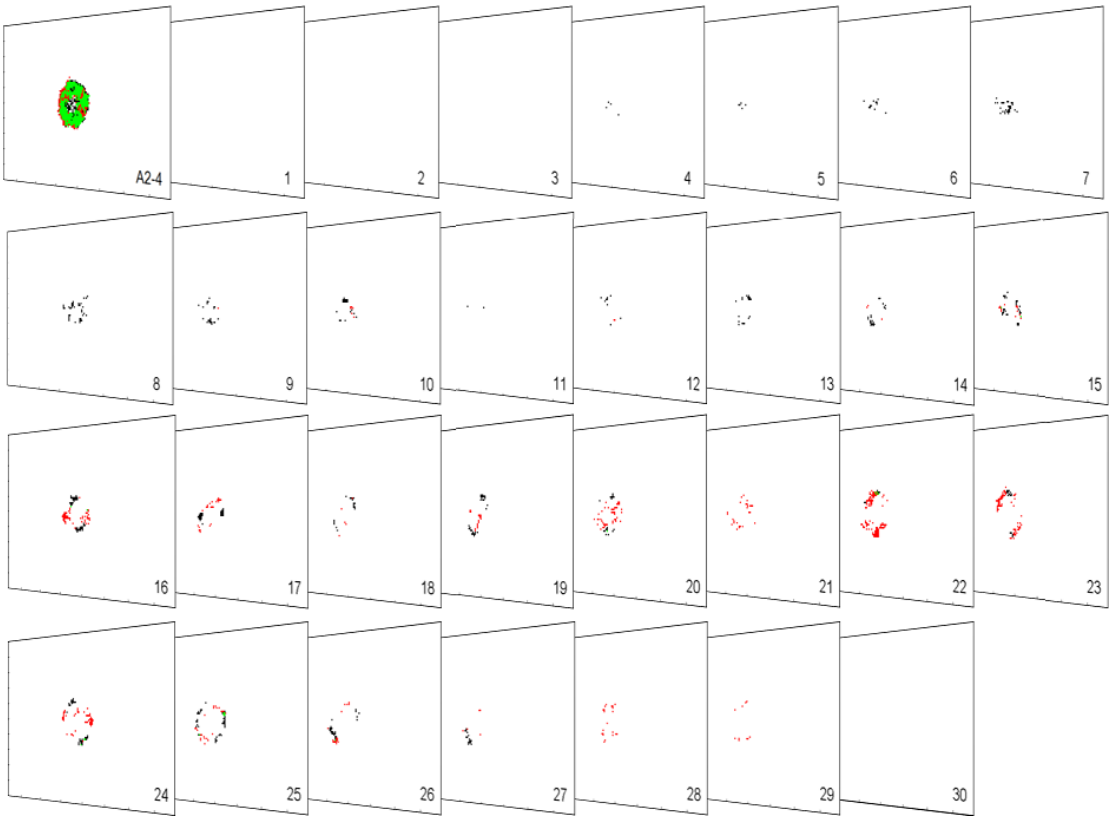

Figure 3.14 Schematic of detected delamination on each individual interface of A2-4 (green squares represent delamination detected from both faces, black squares represent from impact-face scan only, red squares represent from back-face scan only)

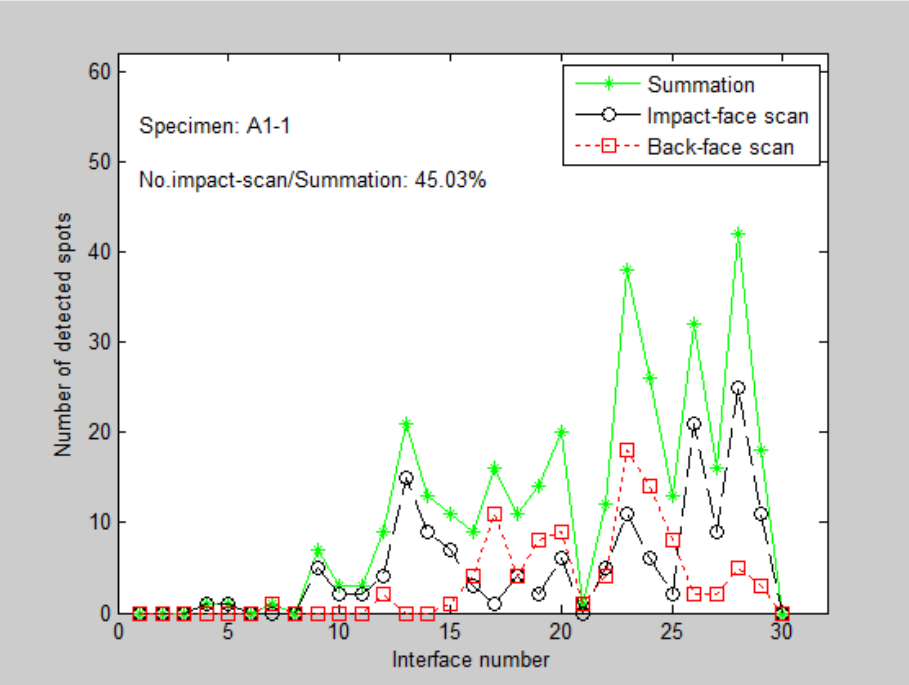
Summation
Impact-face scan
Back-face scan
Specimen: A1-1
No.impact-scan/Summation: 45.03%
Number of detected spots
Interface number
0
10
20
30
40
50
60
0
5
10
15
20
25
30

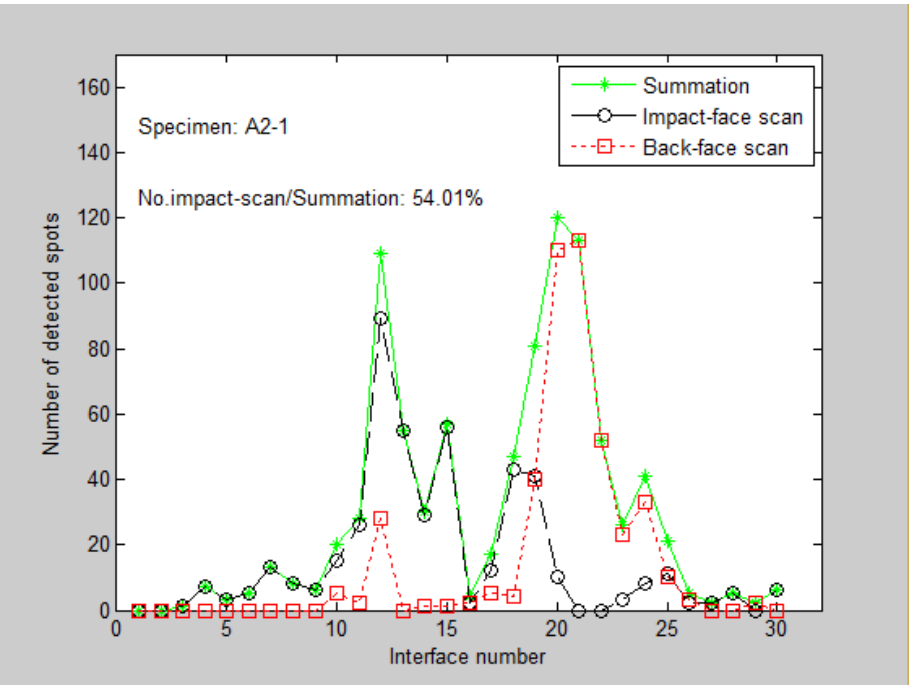
Summation
Impact-face scan
Back-face scan
Specimen: A2-1
No.impact-scan/Summation: 54.01%
Number of detected spots
Interface number
0
20
40
60
80
100
120
140
160
0
5
10
15
20
25
30

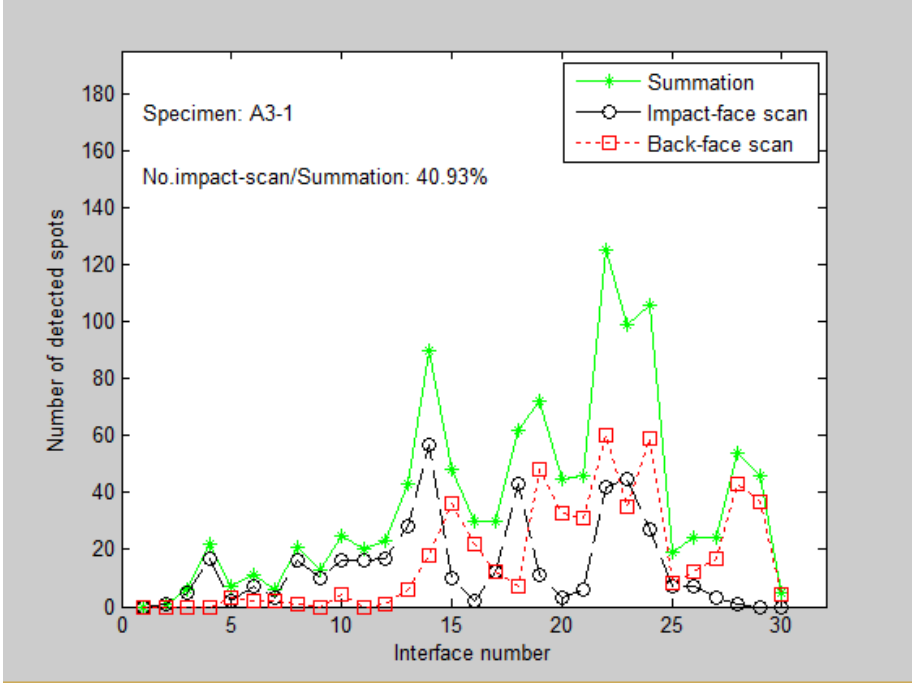

Figure 3.15 The variation of detected delamination squares against interfaces (Interface number ascends from impact face to back face)

3.3.1.3 Single face scan

In this category, only single face scan is conducted on the impact face. Group A4, A5 and C belong to this category. Among these groups are different. For group A4 and A5, the reasons of single face scan was due to the extremely poor surface condition on the back face. Exploded and split surface impeded the scan operation completely. For group C, the scanning followed the conventional routine which only required single face scan.

The superimposed delamination images of group A4 and A5 are demonstrated in Figure 3.16 and Figure 3.17 respectively. Larger blank areas, compared with previous category, are observed in the centre part of the delamination areas. As a relatively better case, A4-4 was scanned on both

sides. Even though, it is seen that on the back side only the perimeter zone was able to be scanned.

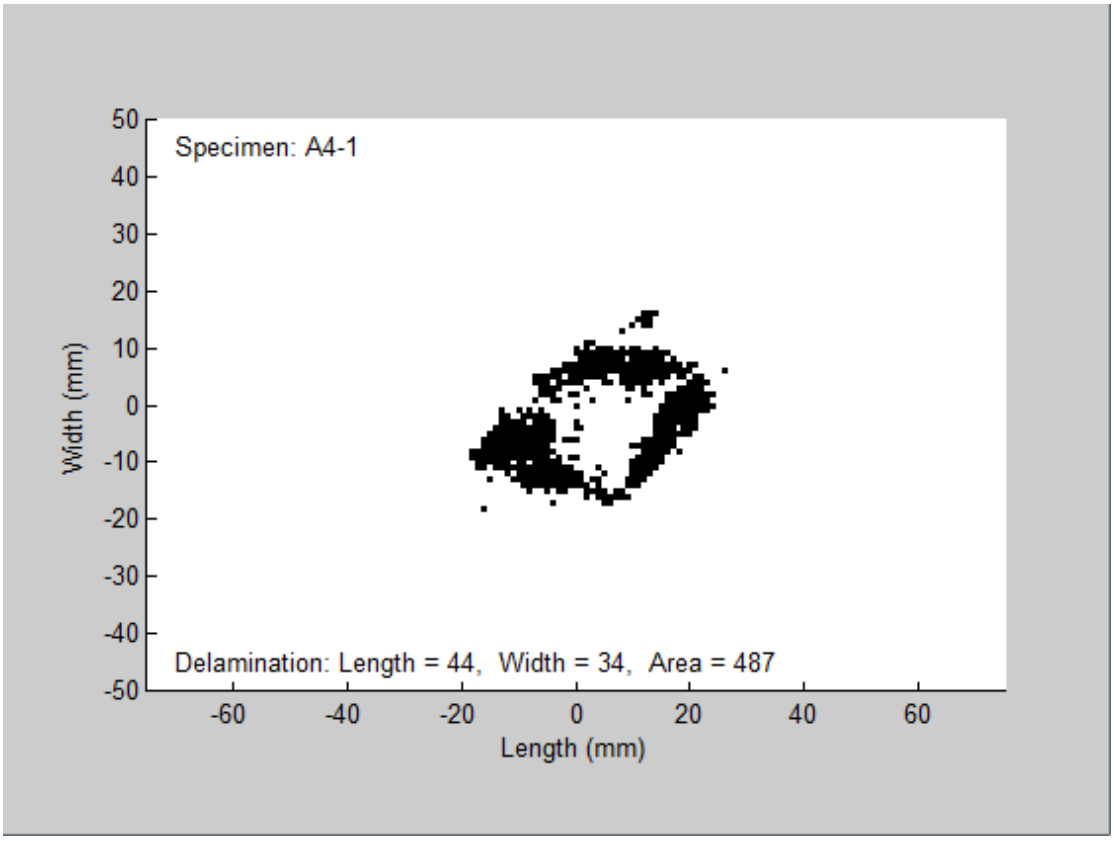
Specimen: A4-1
Delamination: Length = 44, Width = 34, Area = 487
Width (mm)
Length (mm)
50
40
30
20
10
0
-10
-20
-30
-40
-50
-60
-40
-20
0
20
40
60

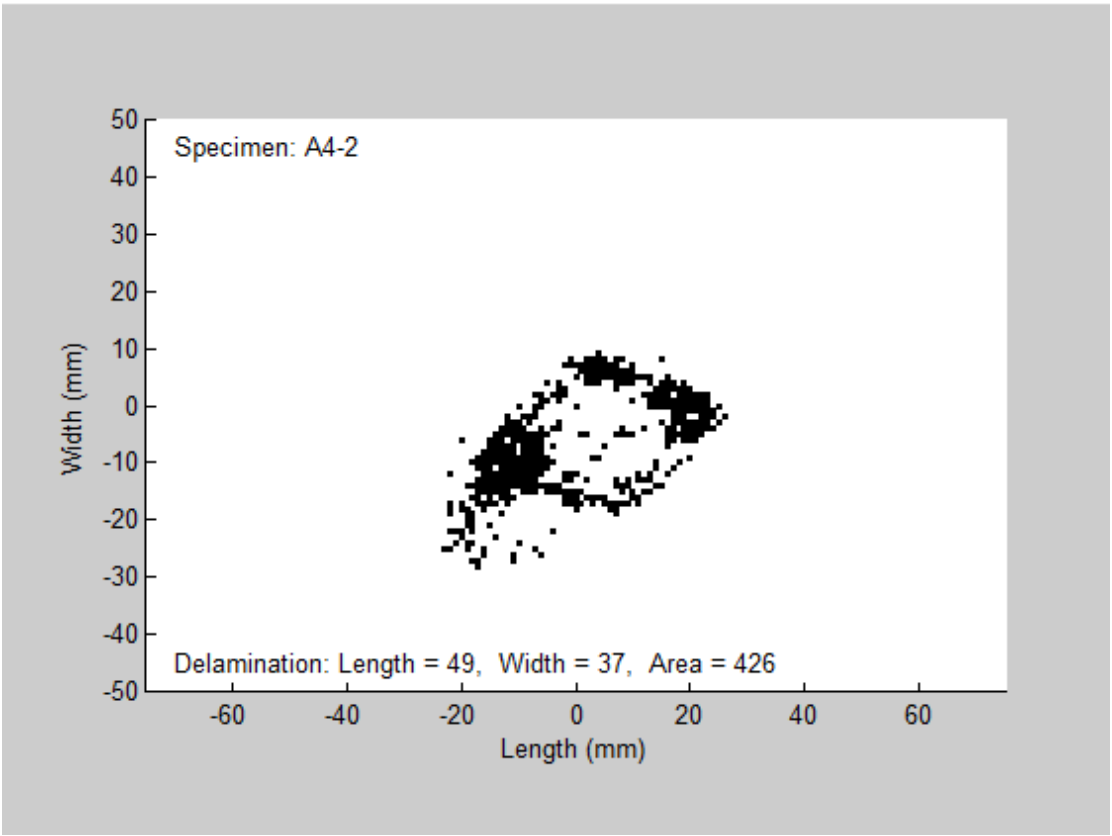
Specimen: A4-2
Delamination: Length = 49, Width = 37, Area = 426
Width (mm)
Length (mm)
50
40
30
20
10
0
-10
-20
-30
-40
-50
-60
-40
-20
0
20
40
60

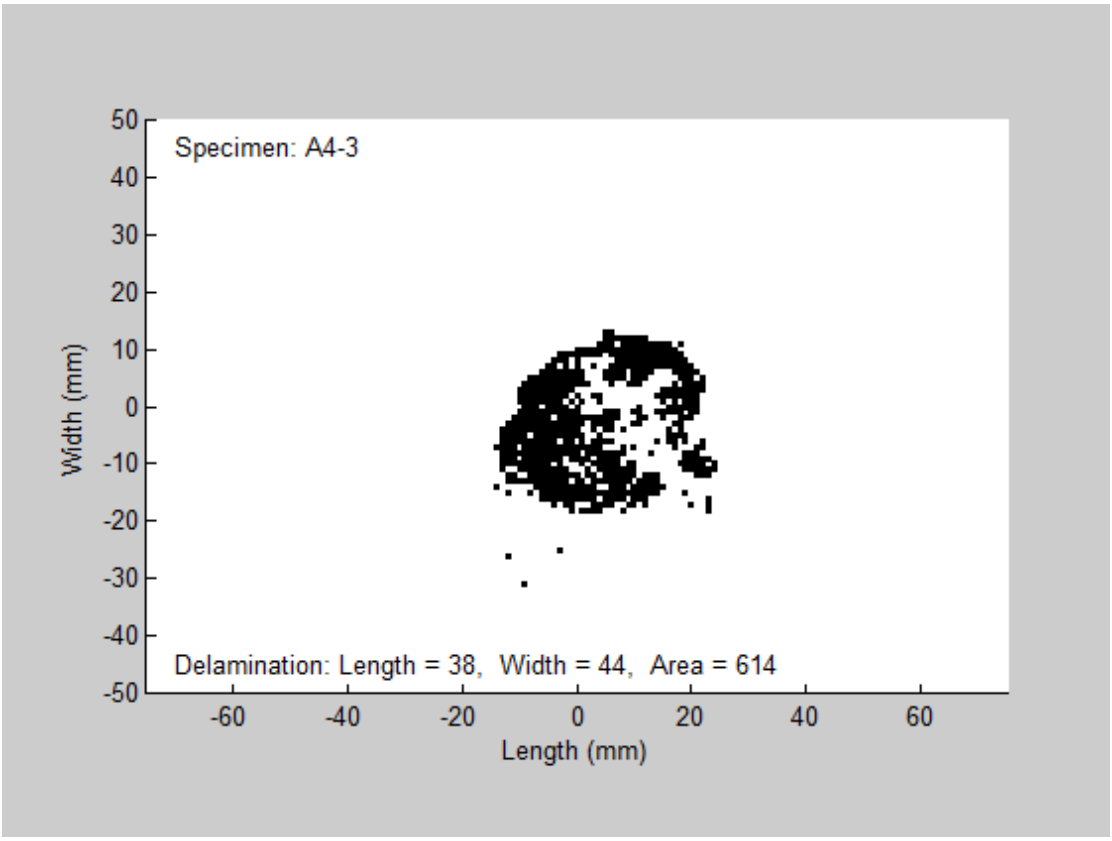
Specimen: A4-3
Delamination: Length = 38, Width = 44, Area = 614
Width (mm)
Length (mm)
50
40
30
20
10
0
-10
-20
-30
-40
-50
-60
-40
-20
0
20
40
60

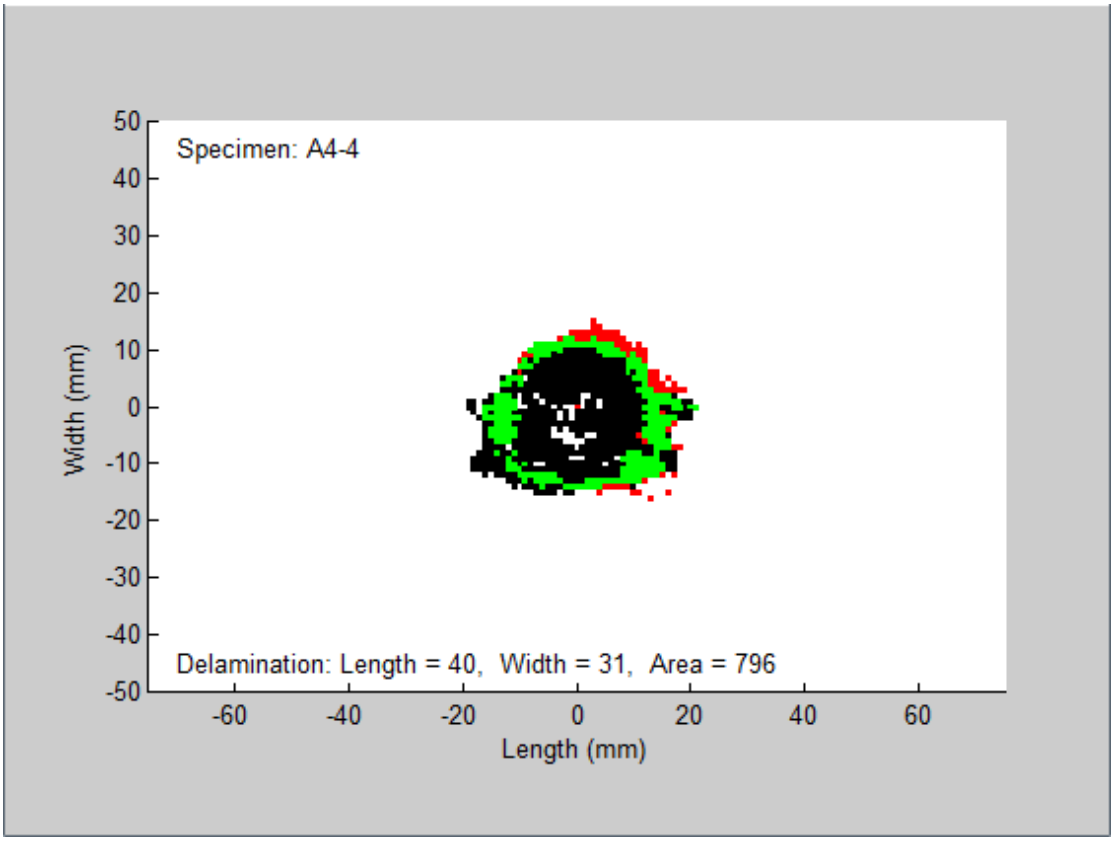
Specimen: A4-4
Delamination: Length = 40, Width = 31, Area = 796
Width (mm)
Length (mm)
50
40
30
20
10
0
-10
-20
-30
-40
-50
-60
-40
-20
0
20
40
60

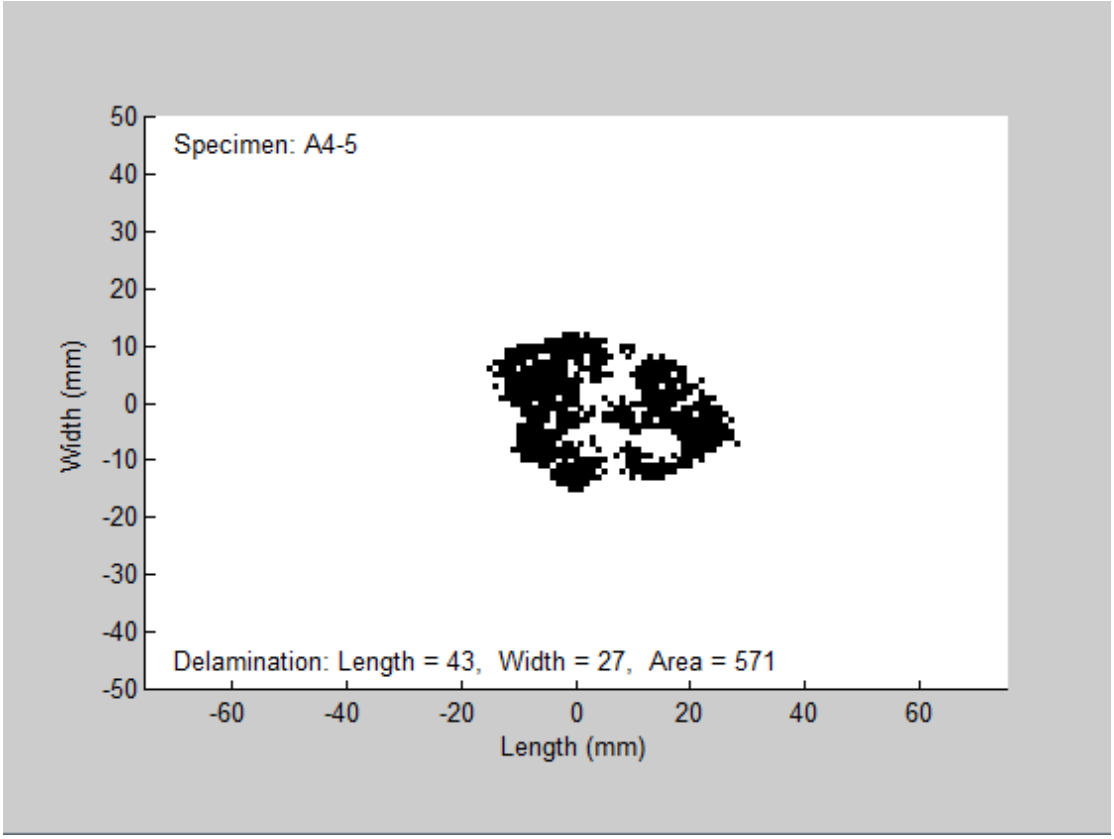

Figure 3.16 Superimposed delamination image of sub-group A4

The superimposed delamination images of group C are presented in Figure 3.18. Due to relatively lower impact energy, scan was conducted on the impact face successfully including the central area around the impact spot.

In this category, the overall profile of delamination distribution through laminate thickness direction cannot be identified because of the absence of essential information from back-face scan. Therefore, assumptions will have to be made on the delamination distribution when these cases are investigated later in Section 5.3.1.

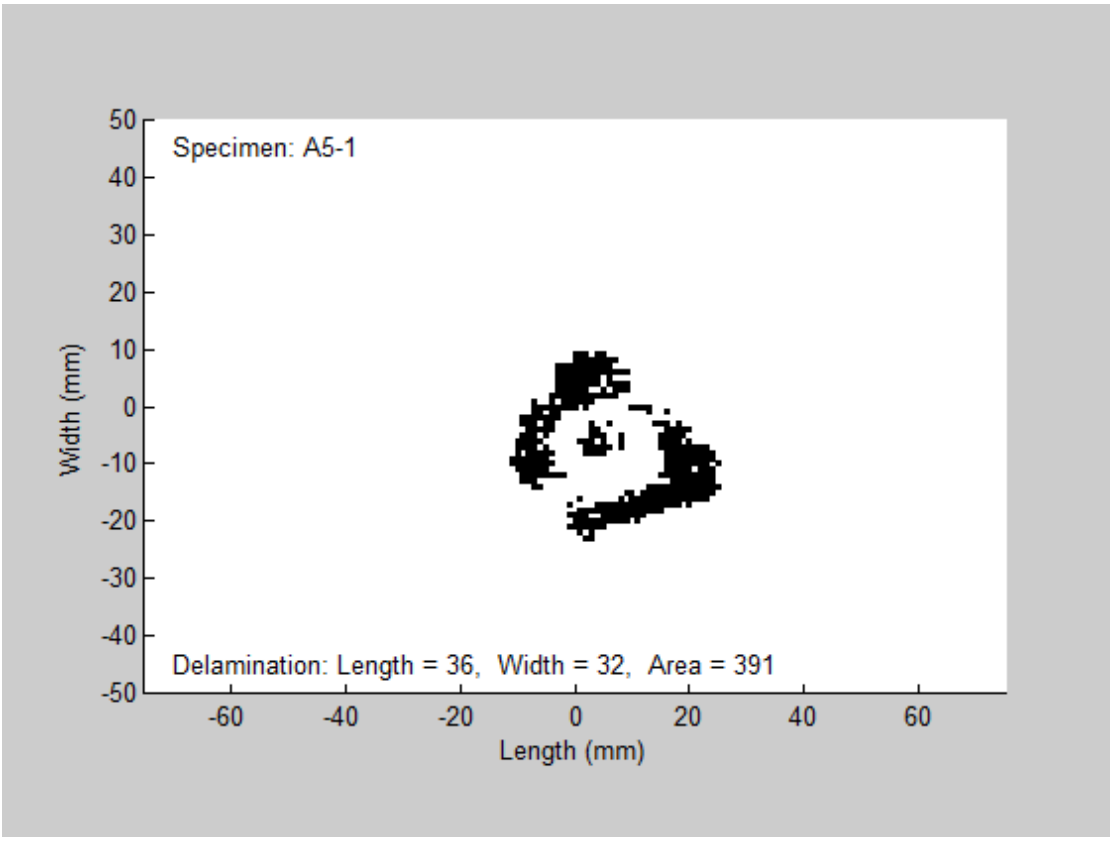
Specimen: A5-1
Delamination: Length = 36, Width = 32, Area = 391
Width (mm)
Length (mm)
50
40
30
20
10
0
-10
-20
-30
-40
-50
-60
-40
-20
0
20
40
60

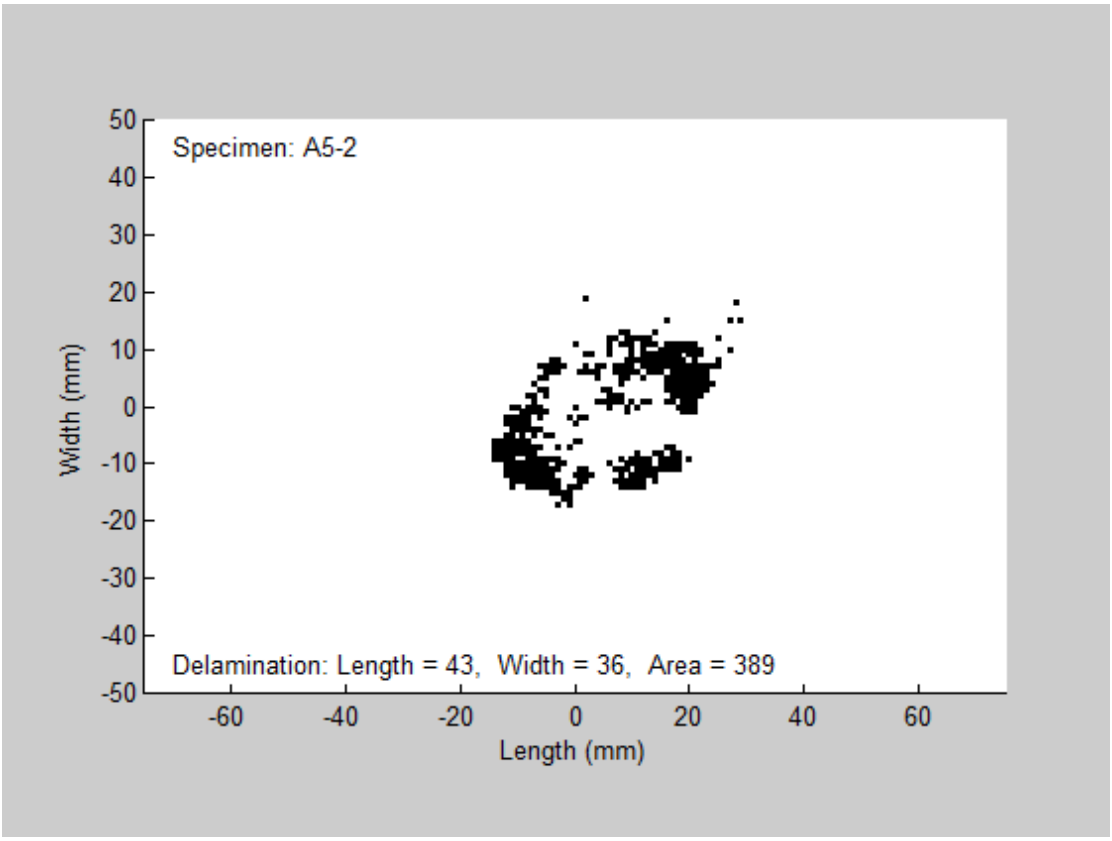
Specimen: A5-2
Delamination: Length = 43, Width = 36, Area = 389
Width (mm)
Length (mm)
50
40
30
20
10
0
-10
-20
-30
-40
-50
-60
-40
-20
0
20
40
60

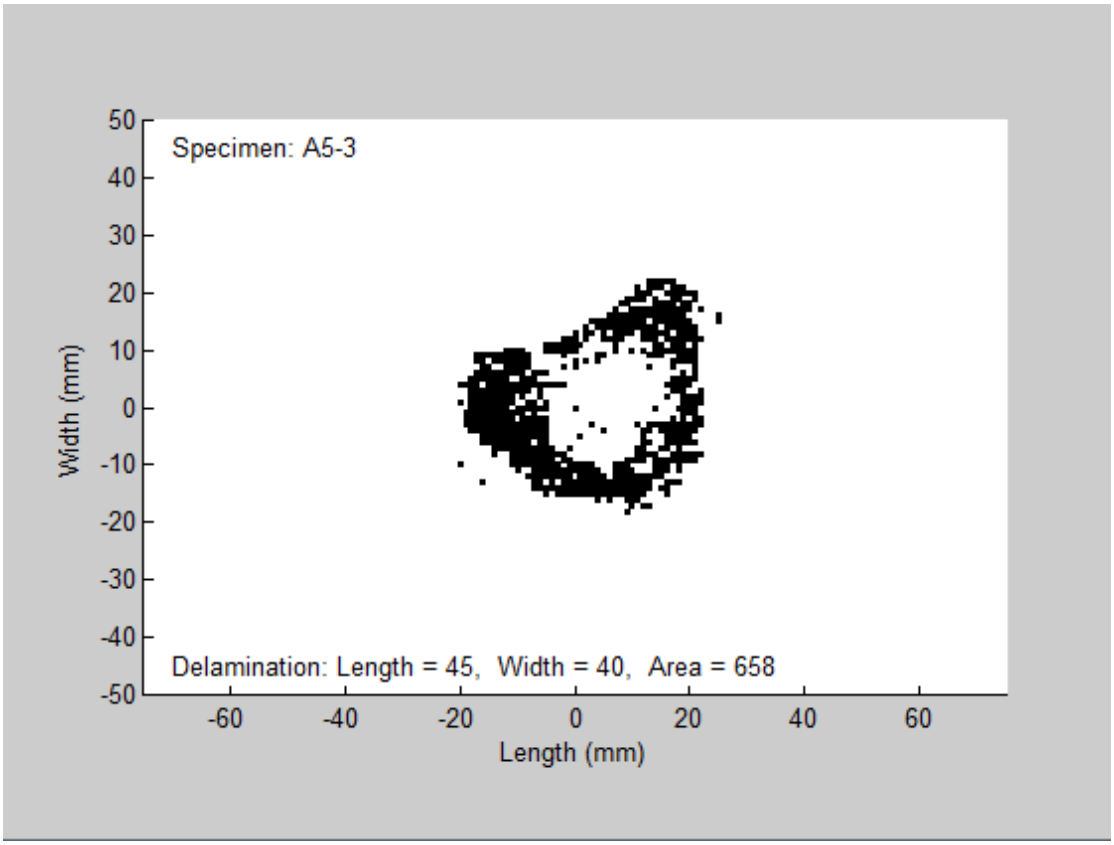
Specimen: A5-3
Delamination: Length = 45, Width = 40, Area = 658
Width (mm)
Length (mm)
50
40
30
20
10
0
-10
-20
-30
-40
-50
-60
-40
-20
0
20
40
60

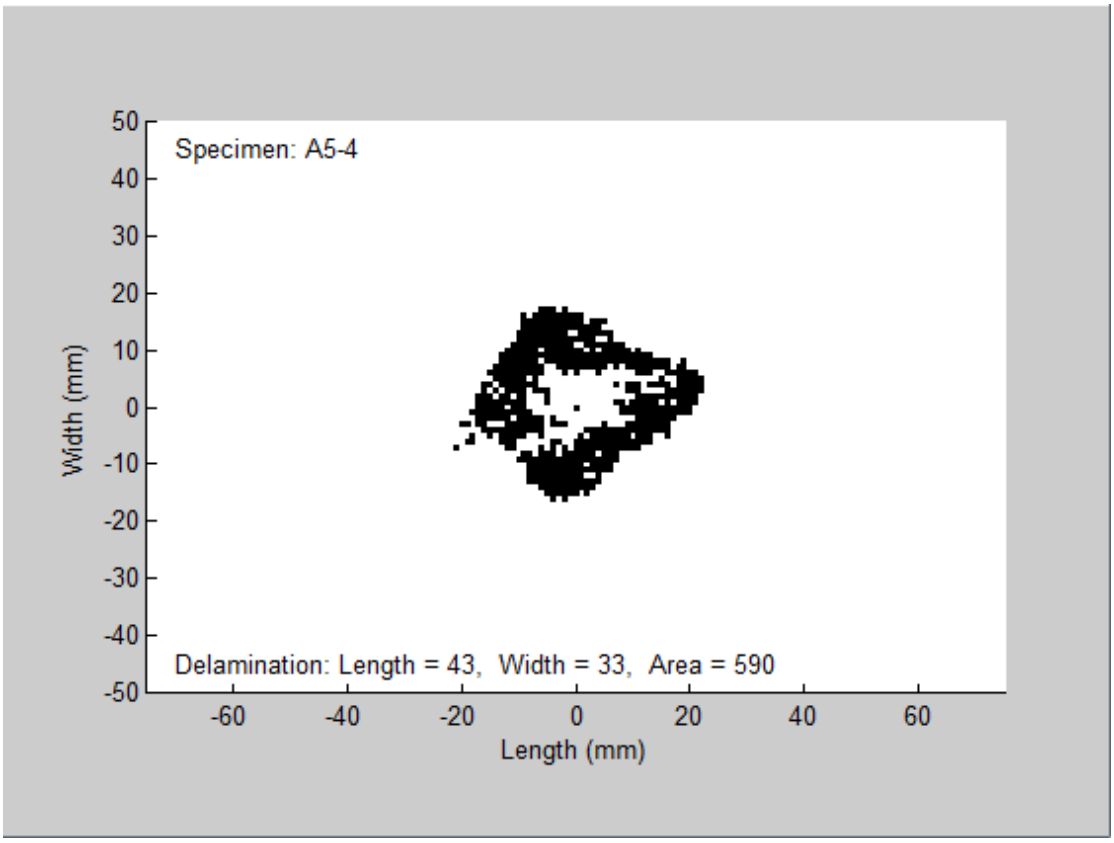
Specimen: A5-4
Delamination: Length = 43, Width = 33, Area = 590
Width (mm)
Length (mm)
50
40
30
20
10
0
-10
-20
-30
-40
-50
-60
-40
-20
0
20
40
60

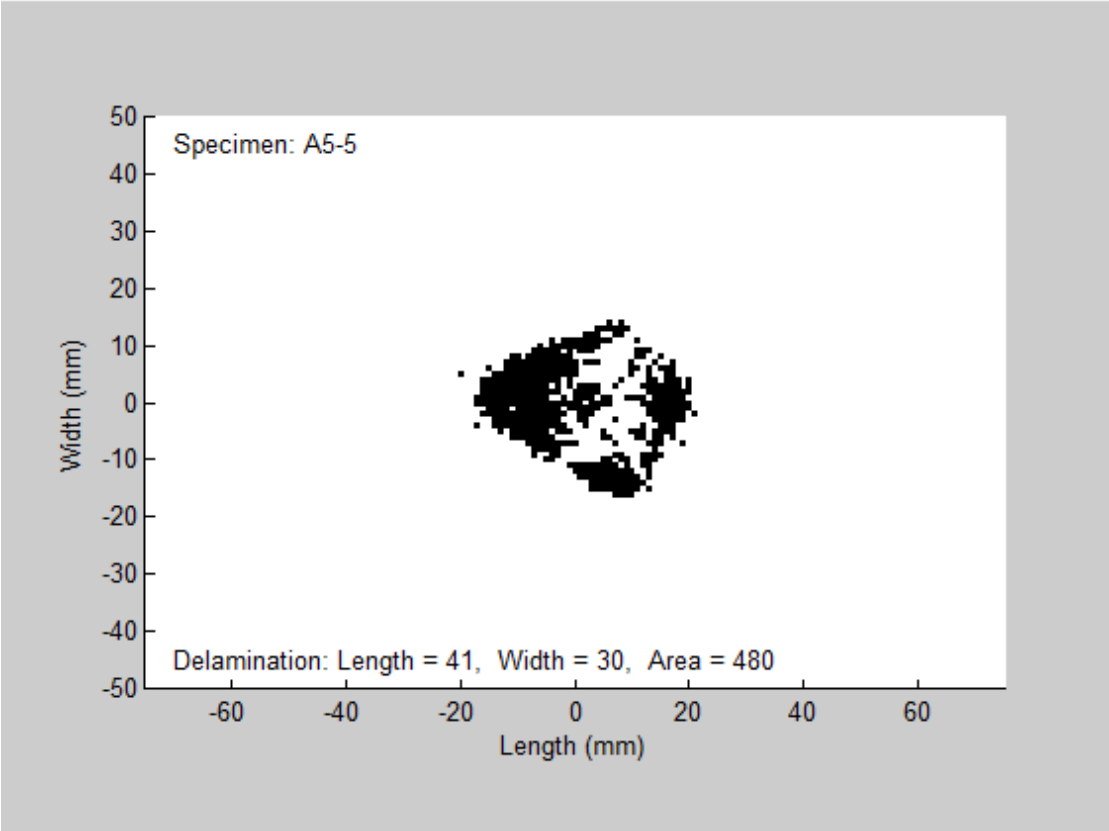

Figure 3.17 Superimposed delamination image of sub-group A5

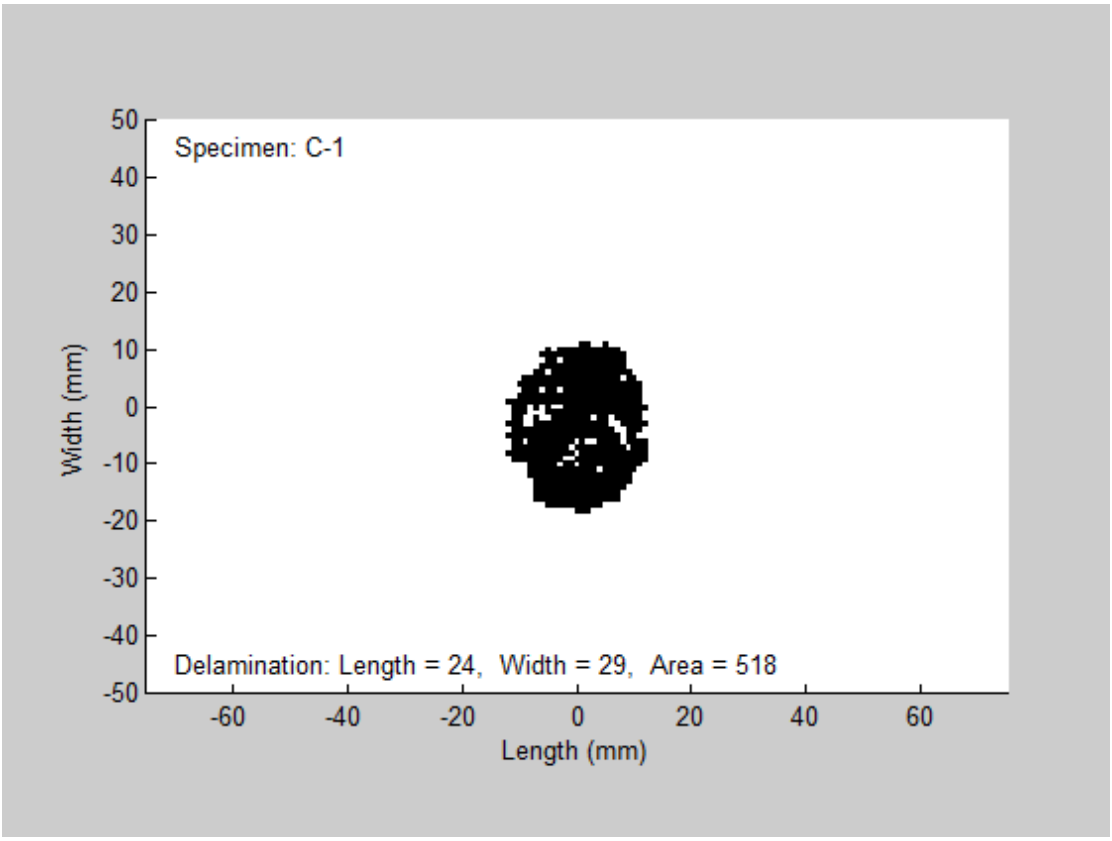
Specimen: C-1
Delamination: Length = 24, Width = 29, Area = 518
Width (mm)
Length (mm)
50
40
30
20
10
0
-10
-20
-30
-40
-50
-60
-40
-20
0
20
40
60

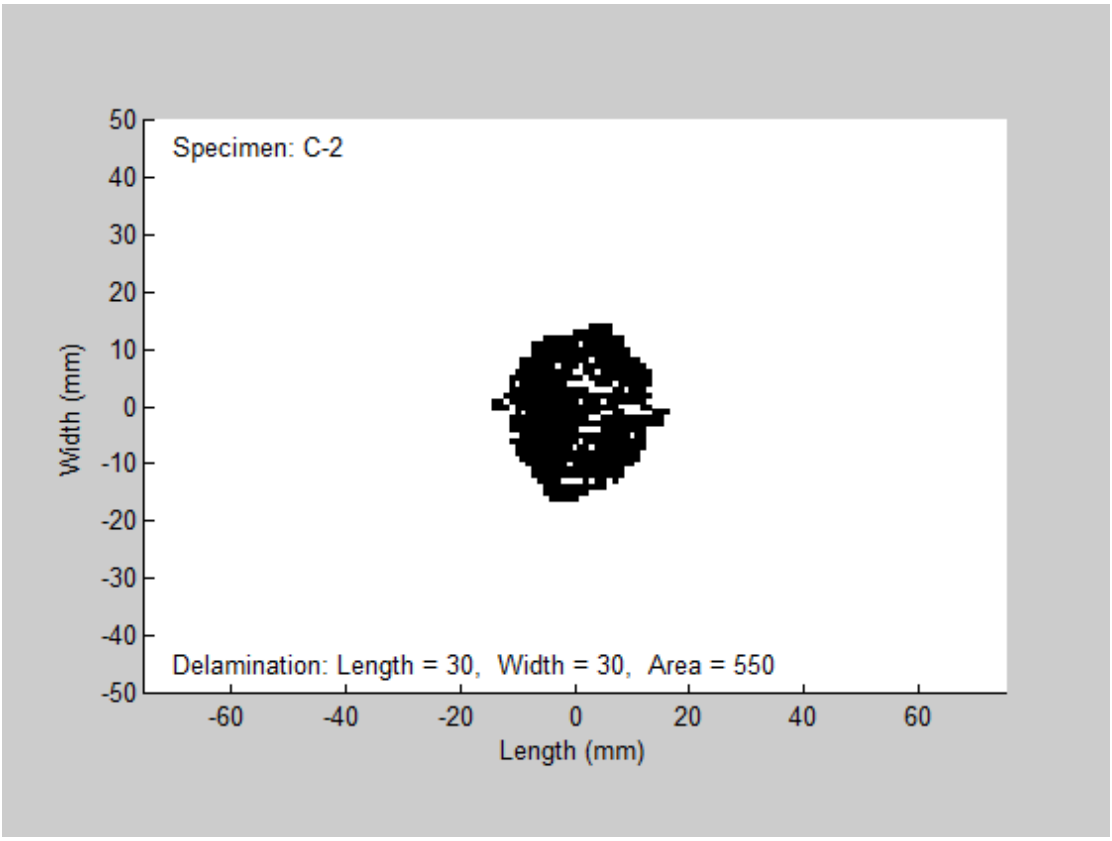
Specimen: C-2
Delamination: Length = 30, Width = 30, Area = 550
Width (mm)
Length (mm)
50
40
30
20
10
0
-10
-20
-30
-40
-50
-60
-40
-20
0
20
40
60

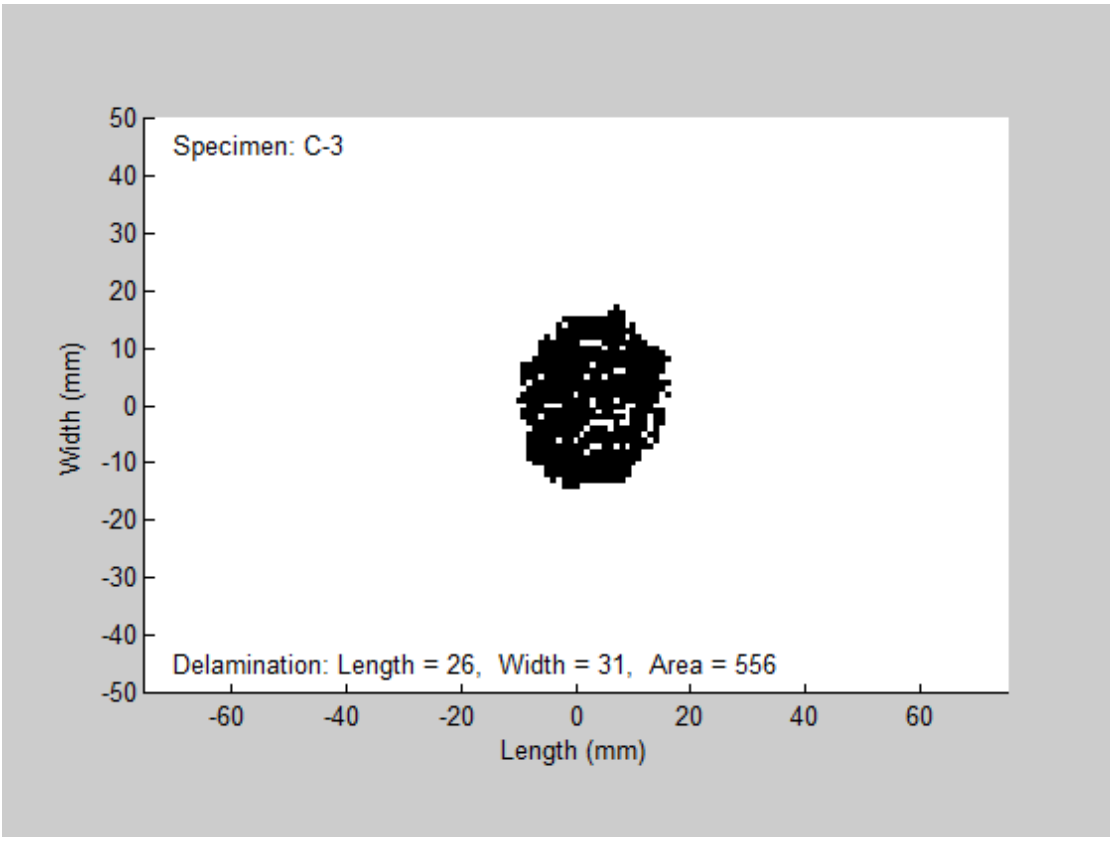
Specimen: C-3
Delamination: Length = 26, Width = 31, Area = 556
Width (mm)
Length (mm)
50
40
30
20
10
0
-10
-20
-30
-40
-50
-60
-40
-20
0
20
40
60

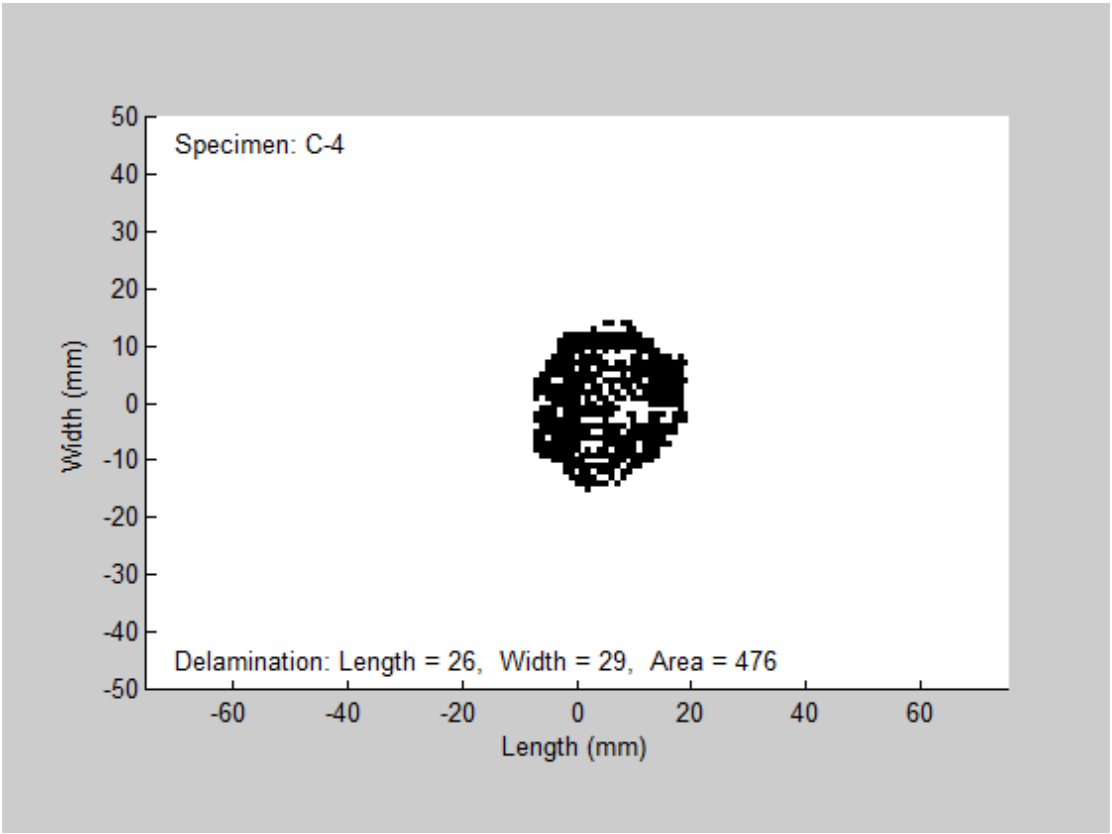
Specimen: C-4
Delamination: Length = 26, Width = 29, Area = 476
Width (mm)
Length (mm)
50
40
30
20
10
0
-10
-20
-30
-40
-50
-60
-40
-20
0
20
40
60

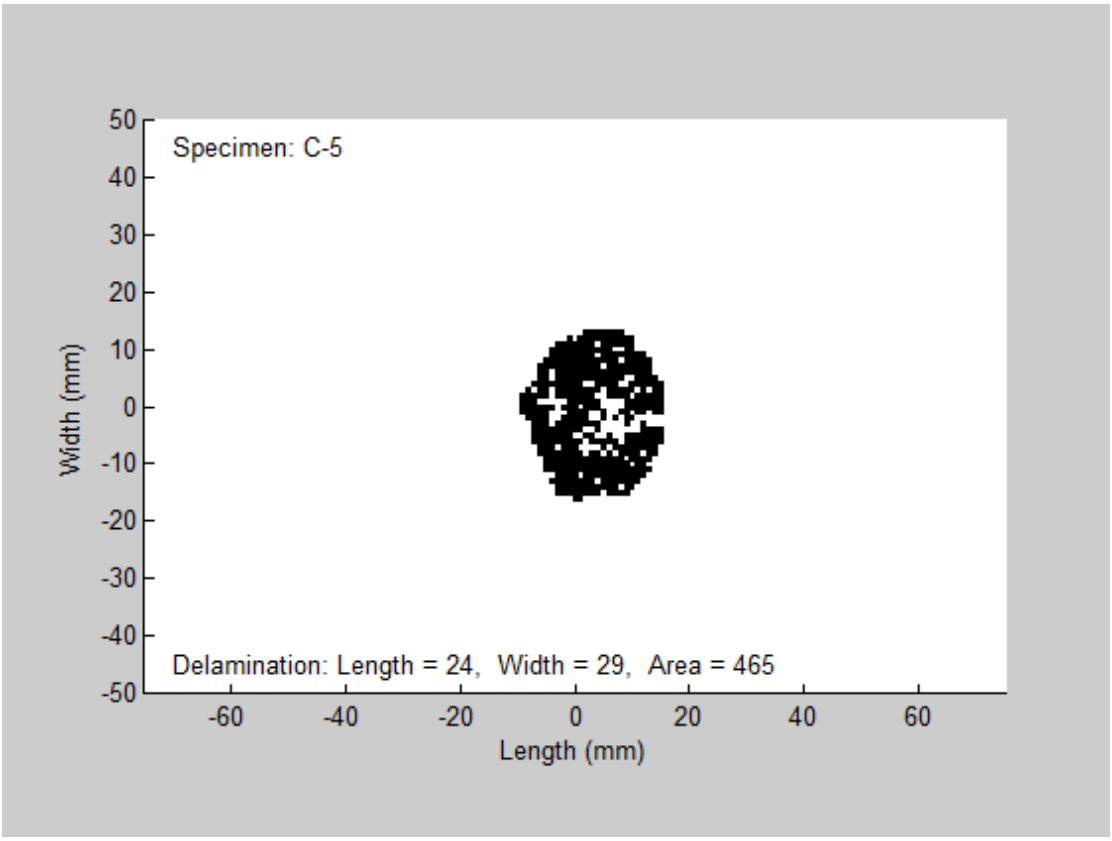

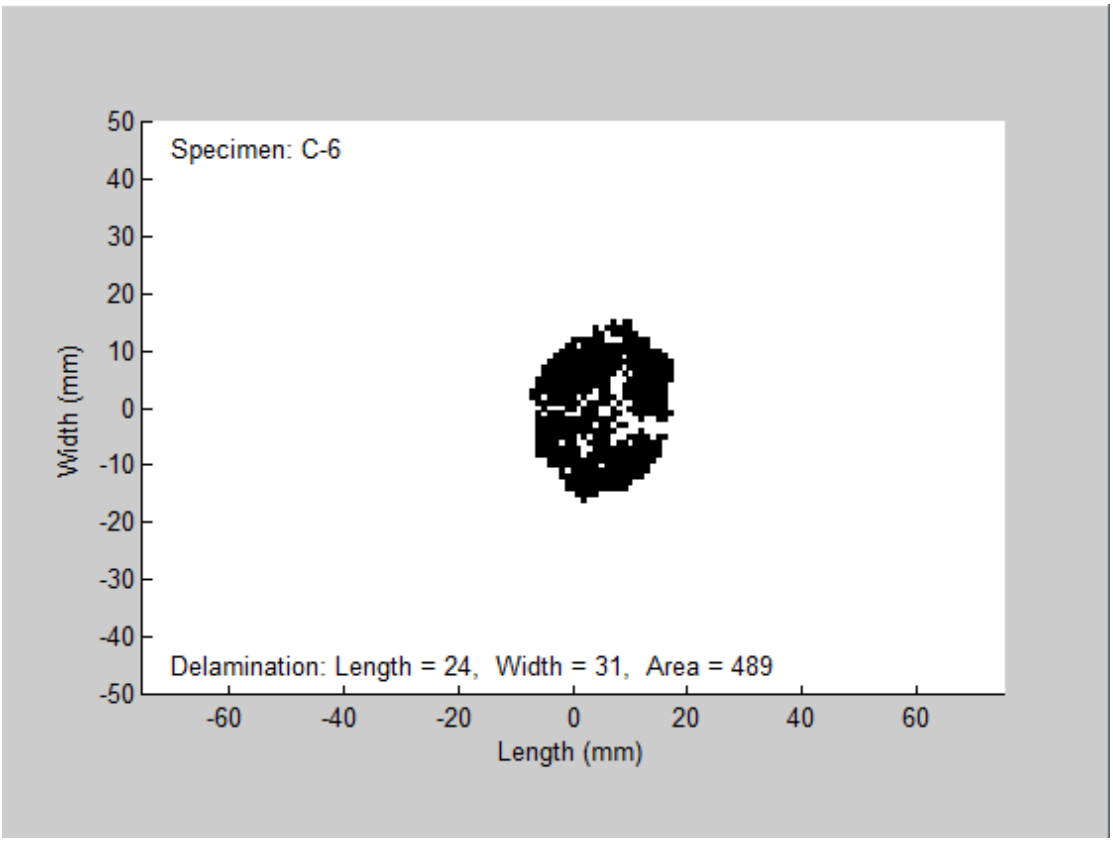

Figure 3.18 Superimposed delamination image of group C

3.3.2 Comparison

The superimposed delamination areas (the central blank areas, if present, are also counted as delaminations) are compared between group A and B (Figure 3.19). It is found that under the same impact energy level the delamination area of group A is always smaller than that of group B, although the CERRs of group A are smaller, which means delamination propagation is relatively easier to take place. This attributes to two factors. The first is that specimens in group A consist of 32 laminae, 8 more than those of specimens in group B. This means more interfaces were involved to absorb the impact energy, and the delamination area on each interface could reduce accordingly. The second factor is that another damage mode was involved. Comparing the impacted specimens between group A and B, especially when impact energy reached relatively high levels, deeper or even penetrated impact dents were observed in specimens of group A. In this case, fibre breakage was usually involved. This damage mode absorbed significant proportion of impact energy, which could have generated larger extent of delaminations. Additionally, it is found that the delamination area increased monotonivally as impact energy increased for specimens in group B, while the delamination area kept stable in specimens of group A when impact energy reached 50 and 60J. This implies that generating delamination was the dominant form of transferring impact energy in group B, while fibre breakage became an important form of transferring impact energy along with delamination in group A when impact energy reached a high level. It is reasonable to expect that there also exists a threshold of impact energy for specimens of group B, over which fibre breakage would appear along with delaminations and

transverse matrix cracks too. Shen, Yang [47] investigated this phenomenon and correlated it with depth of impact dent. He observed that below some specific dent depth (referred as “knee point” by him), the CAI strength decreased as the dent depth increased. However, over that knee point, the CAI value hardly varied. His explanation was that below the knee point, only transverse matrix cracks and delaminations were induced by impact. While over the knee point, fibre breakage got involved and became the dominant damage mode gradually as the impact energy increased. In this case, superimposed delamination area hardly increased and there was not much further reduction in the CAI strength either. Through investigating on a large number of experimental cases, Shen, Yang [47] proposed that the general value of the knee point was about 0.5mm. It can be seen that his conclusion applies to the specimens of group A basically, which was shown in Figure 3.20. However, the specimens of group B cannot be verified because of the lack of the experimental data over the knee point.

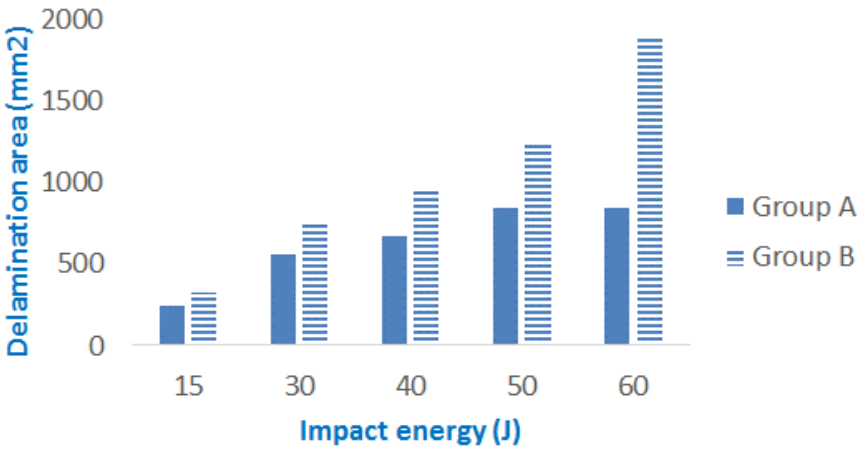

Figure 3.19 Comparison of superimposed delamination area between group A and B from Appendix A

3.4 Conclusion

Before the PhD course, the author conducted all the CAI tests as presented in this chapter assisted by his colleagues when he worked in ASRI China. The tests involved 4 groups, totally 62 specimens, which were made up of 4 different material systems, subjected to diverse impact energies. The overall test process was performed routinely according to corresponding test standards, and the test results were used as reference for theoretical prediction of CAI strength in the PhD study. It is worth mentioning that the result of non-destructive inspection performed on specimens through double-sided ultrasound scan served as an important source of experimental data and played a crucial role for the PhD study although the effort of conducting these experiments have not been counted as a part of the PhD programme.

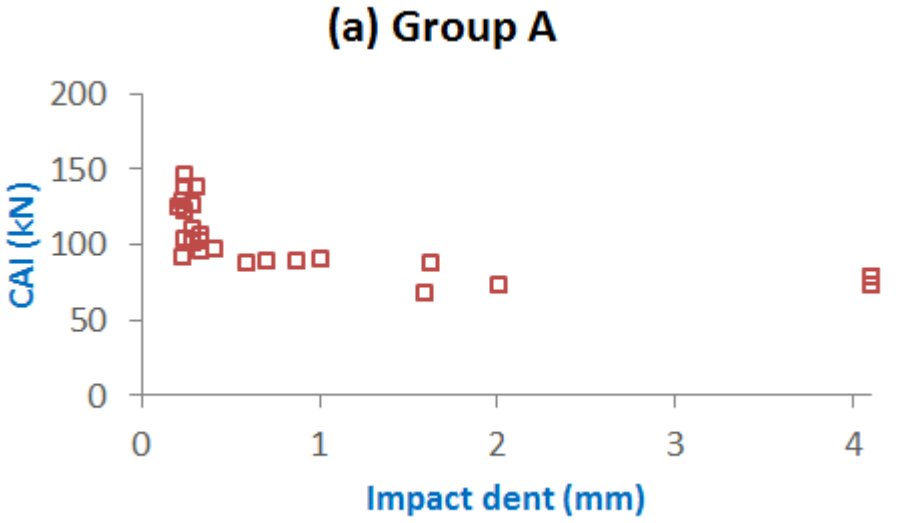
(a) Group A
200
150
100
50
0
CAI (kN)
0
1
2
3
4
Impact dent (mm)

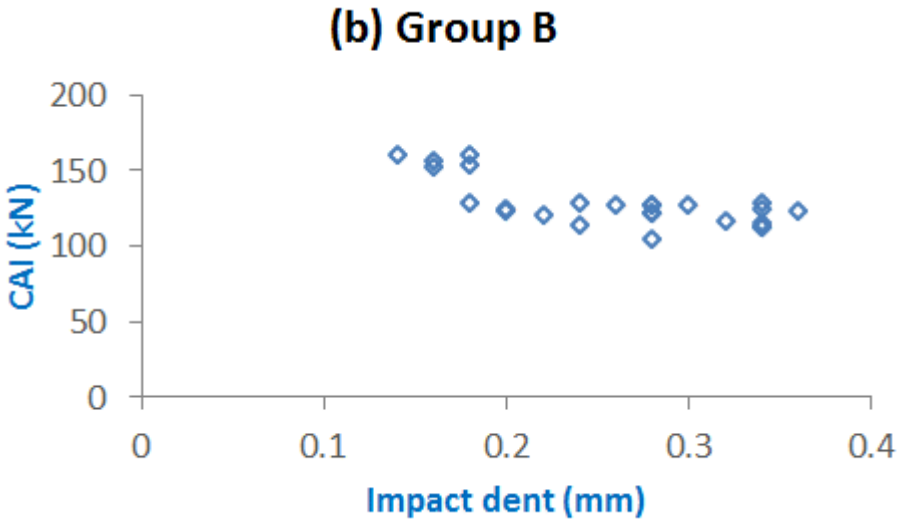
(b) Group B
200
150
100
50
0
CAI (kN)
0
0.1
0.2
0.3
0.4
Impact dent (mm)

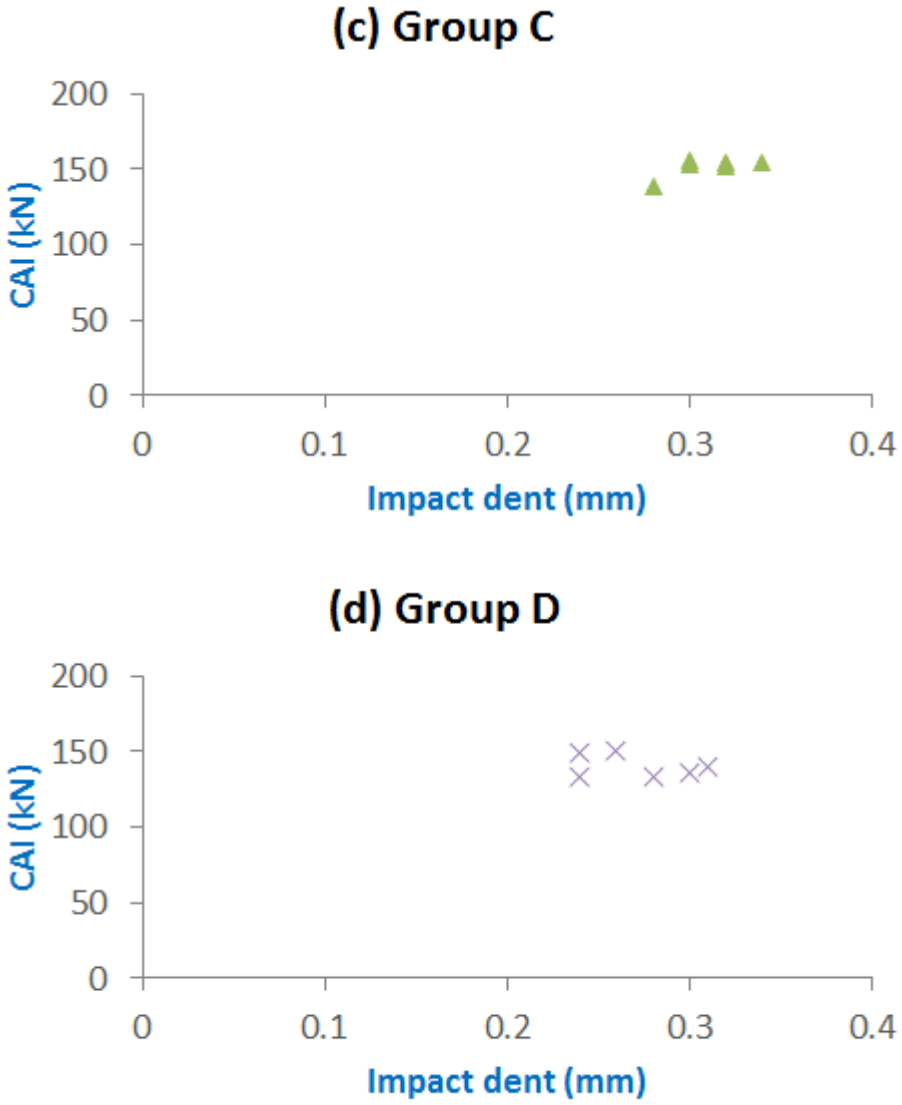

Figure 3.20 The correlation between CAI value and impact dent depth for (a) Group A, (b) B, (c) C and (d) D

Through investigating the inspection results, it is found that double-sided ultrasound scan is essential for determining the detailed delamination distribution state of CAI cases. This is because the overall profile of delamination distribution over the laminate thickness resembles a spindle with its maximum waistline on the interface close to the mid-plane of the laminate and narrows down gradually towards both surfaces of the laminate. This distribution feature makes

its profile detectable to the double-sided scan, although the delamination shape on each individual interface of the laminate could not be detected precisely due to the intrinsic weakness of ultrasound scan. Combined with the peanut-shaped delaminations formulated between laminae which are widely accepted [10], delamination distribution of a given CAI case can be reasonably idealised. This method would be very helpful for constructing detailed FE models of CAI later in this thesis.

Last but not the least, the relationship between superimposed delamination area and impact energy has been investigated. It is found that when delamination is the major damage mode induced by impact, the relationship is strong and monotonic increasing. When other damage modes get involved, such as fibre breakage, this relationship becomes weak, implying that the superimposed delamination area varies little as the impact energy increases once the impact energy exceeds a threshold.

Chapter 4 Investigation of progressive failure mechanisms of CAI

4.1 Introduction

In order to investigate the damage mechanism of CAI, extensive parametric study is conducted on detailed FE models which take both failure modes, delamination propagation and in-plane failure due to stress concentration, into account simultaneously. Through this analysis, a number of characteristic mechanisms of CAI are observed and multiplicity of delamination is found as the dominating factor to influence the damage process. The objective of this chapter is not to determine the damage mechanism of CAI ultimately because of the idealization made to models employed in parametric study. However, the knowledge obtained here is profoundly supportive for the investigation to follow in subsequent chapters.

4.2 Numerical error of cohesive elements

End notched flexure (ENF) test is usually employed to obtain the critical energy release rate of Mode II. The FE model is constructed, of which the specimen configuration is shown in Figure 4.1 schematically. The continuum shell elements SC8R are employed to simulate the upper and lower sublaminates, and the zero thickness cohesive elements COH3D8 are used to simulate the interface. The quadratic nominal stress criterion is employed for the delamination initiation simulation as shown in Equation (4.1).

$$\left(\frac{\langle t_n \rangle}{t_n^0}\right)^2 + \left(\frac{t_s}{t_s^0}\right)^2 + \left(\frac{t_t}{t_t^0}\right)^2 = 1 \tag{4.1}$$

where t_n, t_s, t_t represent the normal and the two shear tractions, respectively. The symbol <> used above represents the Macaulay bracket with the usual interpretation, which signifies that a pure compressive deformation or stress state does not initiate damage. t_n^0, t_s^0, t_t^0 represent the peak values of the nominal stress when the deformation is either purely normal to the interface or purely in the first or the second shear direction, respectively.

The power law Equation (2.3) is employed for the delamination propagation simulation. The FE model is rotated around its normal axis over 0°, 15°, 30° and 45°, respectively, which is shown in Figure 4.2. Theoretically, the load-displacement curves for these models should be the same, no matter how many degrees the model rotates. However, the curve varies over not only the rotation angles but also the value of the power in the power law, which is shown in Figure 4.3.

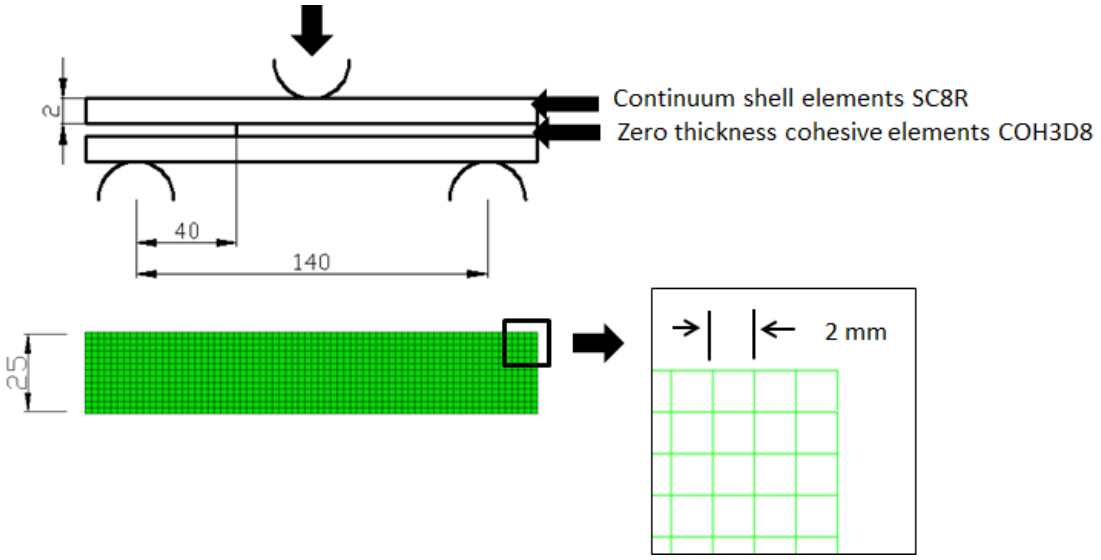

Figure 4.1 Schematic illustration of ENF model

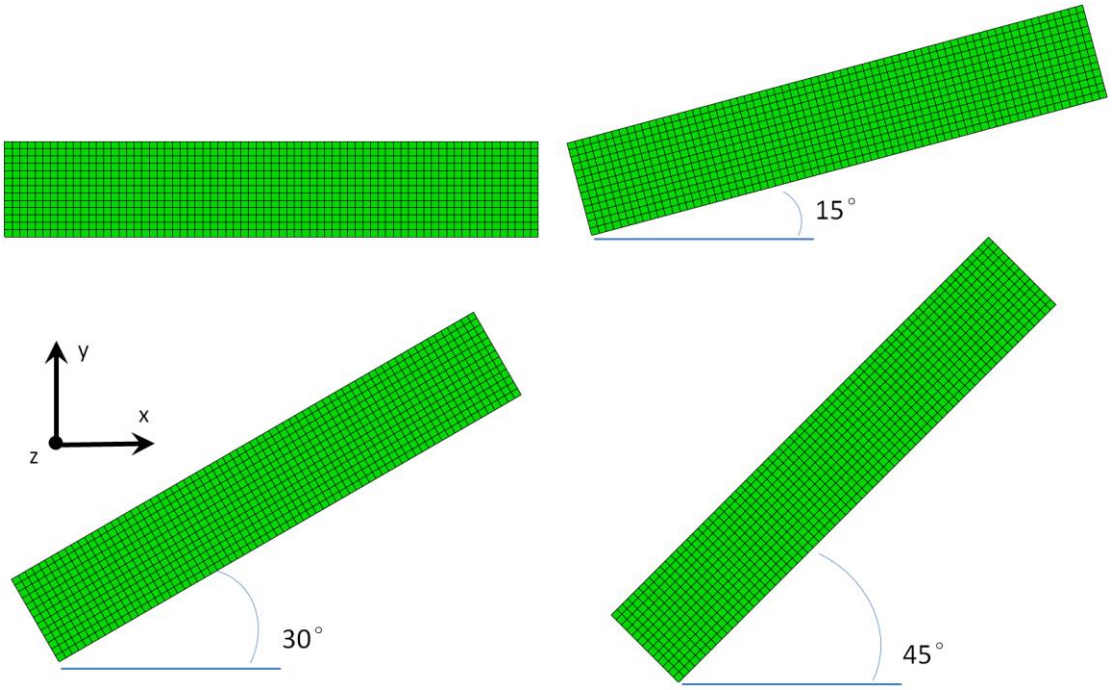

Figure 4.2 Diverse rotation of ENF model

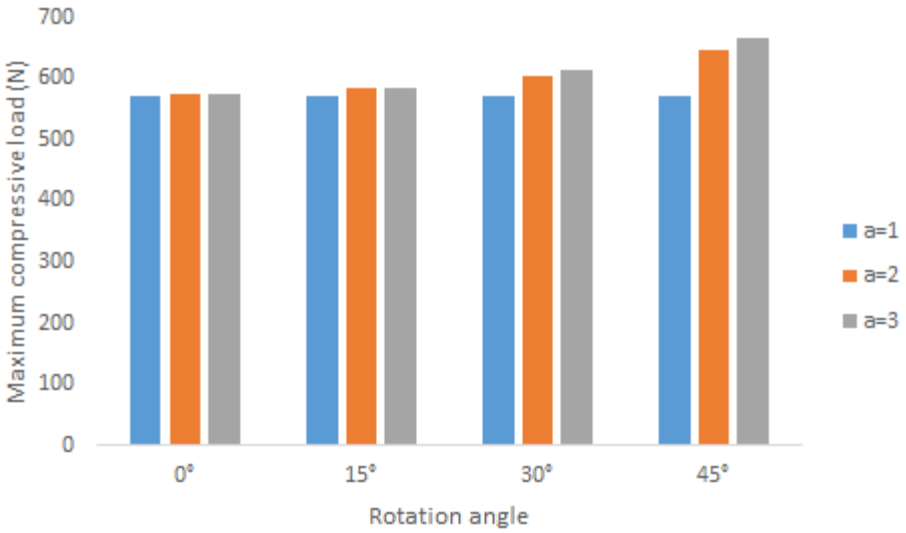

Figure 4.3 Variation of maximum compressive load due to different rotation angle θ and power value α

This problem attributes to the discrepancy between the coordinate system of cohesive element and the direction of delamination propagation. Assume (x, y, z) defines the coordinate system of

cohesive elements as shown in Figure 4.4, which is usually coincident with the global coordinate system. (x*, y*, z*) is defined at delamination front, of which z* is normal to the delamination plane and y* coincides with the tangent of the delamination front. Conventionally, the axis z aligns with axis z*, which ensures that the Mode I crack of cohesive element is consistent with the definition of Mode I crack in fracture mechanism. However, as the delamination propagates, axis x* deviates from axis x with an angle, as shown in Figure 4.4. Because the crack modes of cohesive elements are defined based on their own coordinate systems xyz rather than the coordinate system x*y*z* aligning with the propagating direction of delamination, the Mode II and III crack of cohesive element may not reflect the true fracture modes. For example, although the physical crack mode of the ENF model in Figure 4.2 is of pure Mode II, the crack mode of corresponding cohesive elements is accounted as mixed-mode of Mode II and III in ABAQUS. According to ABAQUS user's manual[1], the delamination propagates when the work done by the tractions and their conjugate relative displacements in the cohesive element exceeds the mixed-mode fracture energy, which is determined through Equation (4.2).

$$G_C = \frac{1}{\left(\left(\frac{m_1}{G_{IC}}\right)^{\alpha} + \left(\frac{m_2}{G_{IIC}}\right)^{\alpha} + \left(\frac{m_3}{G_{IIIC}}\right)^{\alpha}\right)^{\frac{1}{\alpha}}} \tag{4.2}$$

where

[1] For detail seen 31.5.6 Defining the constitutive response of cohesive elements using a traction-separation description, Abaqus analysis user's manual, Version 6.11

$$m_1 = \frac{G_I}{G_I + G_{II} + G_{III}}$$

$$m_2 = \frac{G_{II}}{G_I + G_{II} + G_{III}} \tag{4.3}$$

$$m_3 = \frac{G_{III}}{G_I + G_{II} + G_{III}}$$

where G_{I}, G_{II}, G_{III} are denoted as the work done by the tractions and their conjugate relative displacements in the normal, first, and second shear directions, respectively. G_{IC}, G_{IIC}, G_{IIIC} are the critical energy release rate (CEER) of Mode I, II and III, respectively.

The constitutive relationship of the cohesive element in linear elastic phase is usually defined as follows

$$\begin{Bmatrix} \mathrm{t_z} \\ \mathrm{t_x} \\ \mathrm{t_y} \end{Bmatrix} = \begin{bmatrix} \mathrm{k_{normal}} & 0 & 0 \\ 0 & \mathrm{k_{shear}} & 0 \\ 0 & 0 & \mathrm{k_{shear}} \end{bmatrix} \begin{Bmatrix} \delta_\mathrm{z} \\ \delta_\mathrm{x} \\ \delta_\mathrm{y} \end{Bmatrix} \tag{4.4}$$

In the ENF model,

$$m_1 = 0$$

The separation along axis x and y of the global coordinate system xyz has following relationship.

$$\cos\theta\, \delta_y = \sin\theta\, \delta_x$$

Additionally, G_{IIIC} is usually set to be equivalent to G_{IIC}.

$$G_{IIC} = G_{IIIC}$$

Therefore,

$$G_{\mathrm{II}} = \frac{K_{\mathrm{shear}}}{2}\delta_{\mathrm{x}}^2 \tag{4.5}$$

$$G_{\mathrm{III}} = \frac{K_{\mathrm{shear}}}{2}\delta_{\mathrm{y}}^2 \tag{4.6}$$

Substitute Equation (4.2)-(4.6) into (4.1), the expression of G_C is obtained in Equation (4.7)

$$G_C = \frac{G_{IIC}}{(((\cos\theta)^2)^\alpha + ((\sin\theta)^2)^\alpha)^{\frac{1}{\alpha}}} \tag{4.7}$$

For the cohesive element in the middle of the delamination front, the traction-separation curve is plotted in Figure 4.5, of which the value of the closed area equals to the mixed-mode fracture energy G_c. From the Figure 4.5 it can be seen that the greater the discrepant angle θ and the value of the power α, the greater the value of G_c deviating from the G_{IIC}, which accounts for the phenomenon of different maximum compressive load obtained from the same ENF model but diverse rotating angles.

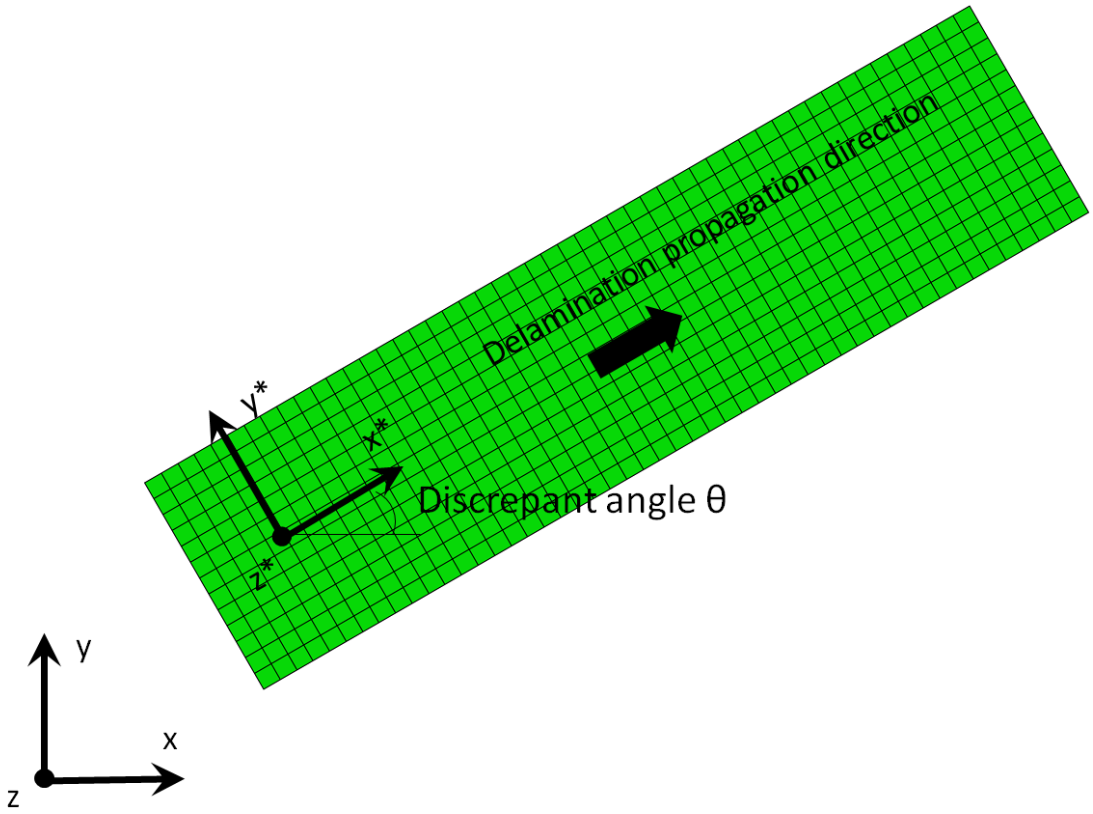

Figure 4.4 Definition of discrepant angle

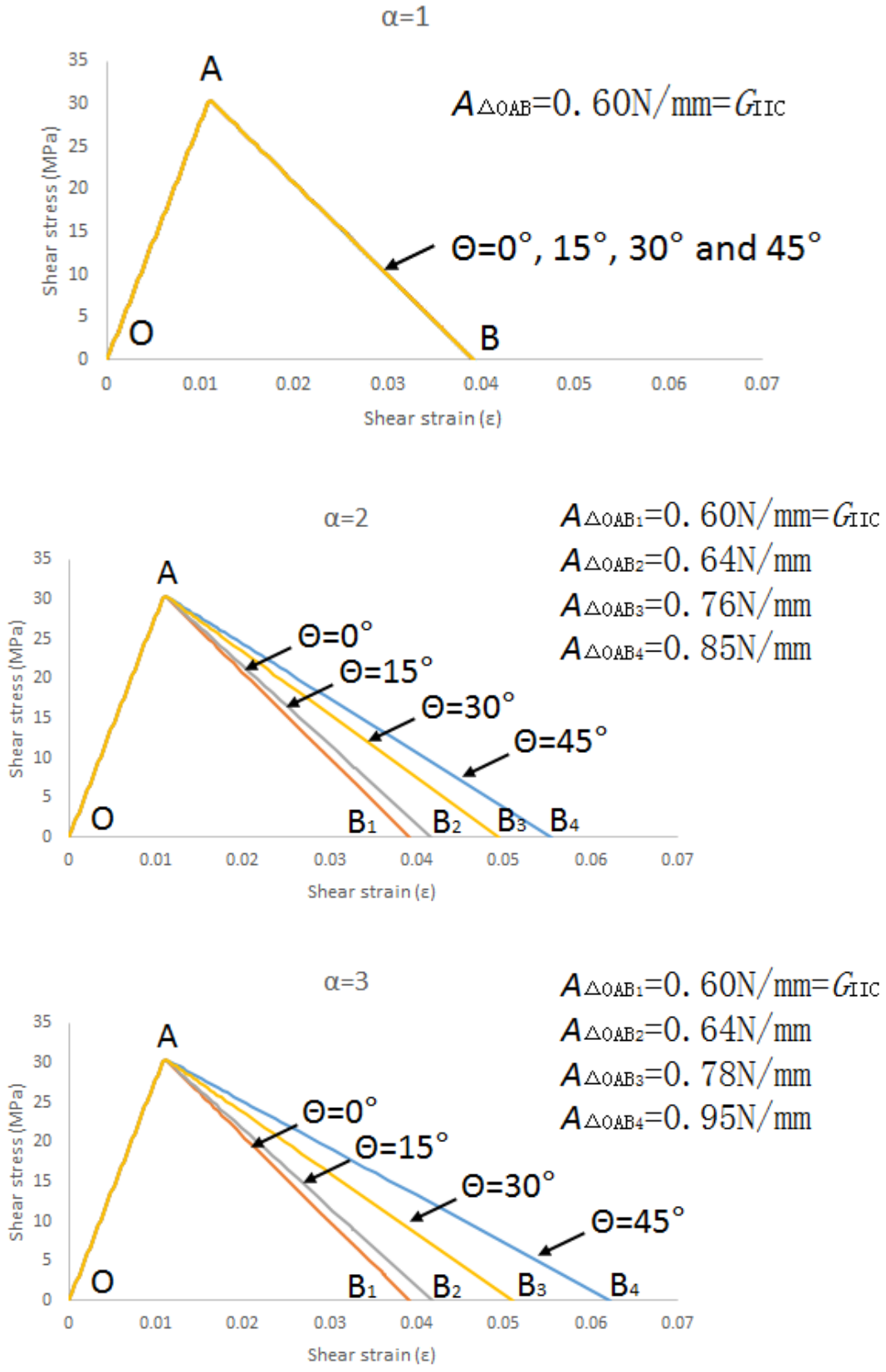

Figure 4.5 Variation of shear stress and strain curve due to different rotation angle θ and power value α

Therefore it is important to be aware of the effect of the Discrepant Angle especially when high value of α is employed for failure criterion of delamination propagation. To solve this problem ultimately, an adaptive coordinate fixed at each individual cohesive element is essential, which can adapt automatically to fit the delamination propagation direction when delamination front propagates through this cohesive element. However, this technique is not well established yet and hence not adopted here. In order to avoid the significant error, α=1 is assumed in this thesis.

4.3 Detailed FE model

Cohesive elements or VCCT probably is most commonly employed in simulating delamination propagation so far. Substantial amount of study outcomes about delamination propagation in CAI-related problems using these methods can be found in the literature. Among the published results the delamination patterns vary, from single delamination to multiple delaminations, from circular or rectangular [24], to peanut shaped, etc.. However, the common issue there, to the best of the author's knowledge, is that only delamination propagation is taken into account while in-plane failure of lamina is ignored by most people.

In this chapter, the purpose is to identify which failure mode, delamination propagation or in-plane failure due to stress concentration in the zones around the delamination front, is the dominant factor to determine the CAI strength (strictly speaking, the compressive strength of the parametric study model here) and the condition for either mode to become dominant. Similar method of detailed FE model construction which was employed before in other publications ([79] for instance) for investigating delamination propagation alone is adopted here. However, the

improvement is that in-plane failure criterion for individual lamina is implemented in this model as well. By altering the size, location and the number of delaminations, a parametric study is performed to help the understanding of the damage mechanism of CAI.

4.3.1 Construction method

Throughout the thesis, all FE models, including detailed FE models here and simplified FE models to be presented later, are constructed and analysed on the ABAQUS Version 6.11. For detailed FE models, assume there are n initial delaminations present at different positions over the laminate thickness (Figure 4.6, delaminated areas are exaggerated for the purpose of clear visibility). Consequently the laminate is partitioned into (n+1) sublaminates, each of which is meshed with a layer of continuous shell elements[1]. Contact conditions between neighbouring sublaminates are introduced in the delaminated area in order to avoid impractical interpenetration during deformation. Over the intact part between each two neighbouring sublaminates a layer of zero thickness cohesive elements is introduced for the purpose of simulating potential delamination propagation. A schematic section view of the laminate to illustrate the configuration is demonstrated in Figure 4.6, in which hatched strips represent initial delaminations and the thicker lines between sublaminates represent interfaces where delamination may propagate through.

[1] For detail seen 25.6.2 Choosing a shell element, Abaqus analysis user's manual, Version 6.11

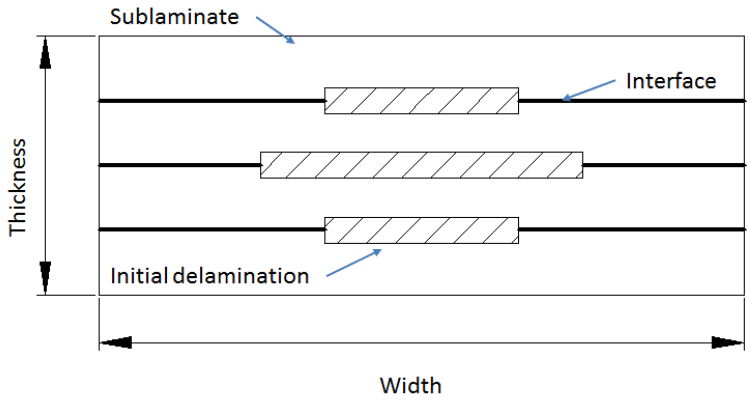

Figure 4.6 Schematic section view of laminate bearing delaminations

4.3.2 Geometry and boundary conditions

The in-plane dimensions of the FE model are 150mm in length and 100mm in width (Figure 4.7). Both edges along the width direction are referred as loading edges, on which equivalent but opposite displacements are prescribed to simulate the compressive load applied by test machine in a displacement control mode. The out-of-plane displacement on both loading edges is constrained and therefore the loading edges can expand freely in width direction due to Poisson's effect when the panel is compressed. Moreover, nodes on the top and bottom surfaces of the panel along the lines as shown in Figure 4.7 are constrained for the out-of-plane displacements, representing the two sliding edges aligning with compressive load direction, one on each side approximate 4mm off from the edge. This constraint is to simulate the anti-global-buckling device which consists of two pairs of slide plates with knife edges as required in test standard ASTM D7137.

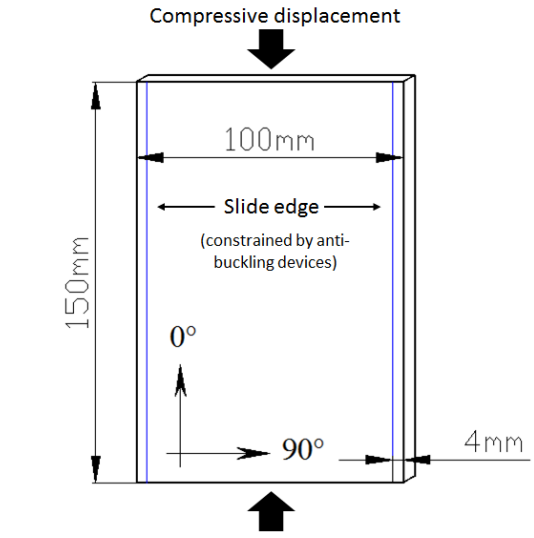

(a) Front view

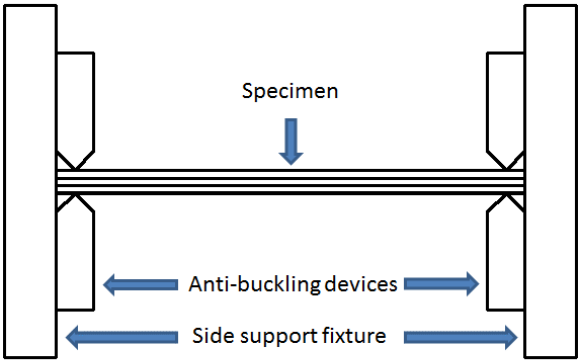

(b) Top view with side fixtures

Figure 4.7 Schematic of specimen details of the CAI model based on test standard ASTM D7137

4.3.3 Meshing strategy

Uniform 8-node hexahedron continuum shell element SC8R are employed for discretizing the laminate model, as shown in Figure 4.8(a), while matched 8-node hexahedron but zero thickness cohesive element COH3D8 are used for potential delamination interface. Although uniform-meshing strategy is not the most economical solution, it is adopted here based on two

considerations. The first reason is to provide a common basis for parametric study. In this chapter, successive alterations of numbers of layers, sizes and distribution types of initial delaminations have been considered. Identical meshes provide convenience for comparisons. The second reason is the concern of potential delamination propagation between sublaminates. In some of other publications, such as [49], only the mesh at initial delamination front was refined. Once delamination propagated beyond this area, mesh became coarse. As simulation of delamination propagation employing cohesive element is sensitive to mesh density, this meshing strategy tends to delay the delamination propagation numerically, as will be demonstrated in Section 4.7.2. The overall process of delamination propagation will be monitored if it takes place. Because the location and extent of potential delamination propagation is unknown, it is wise to have a uniform mesh over the entire domain despite the sacrifice of computation efficiency.

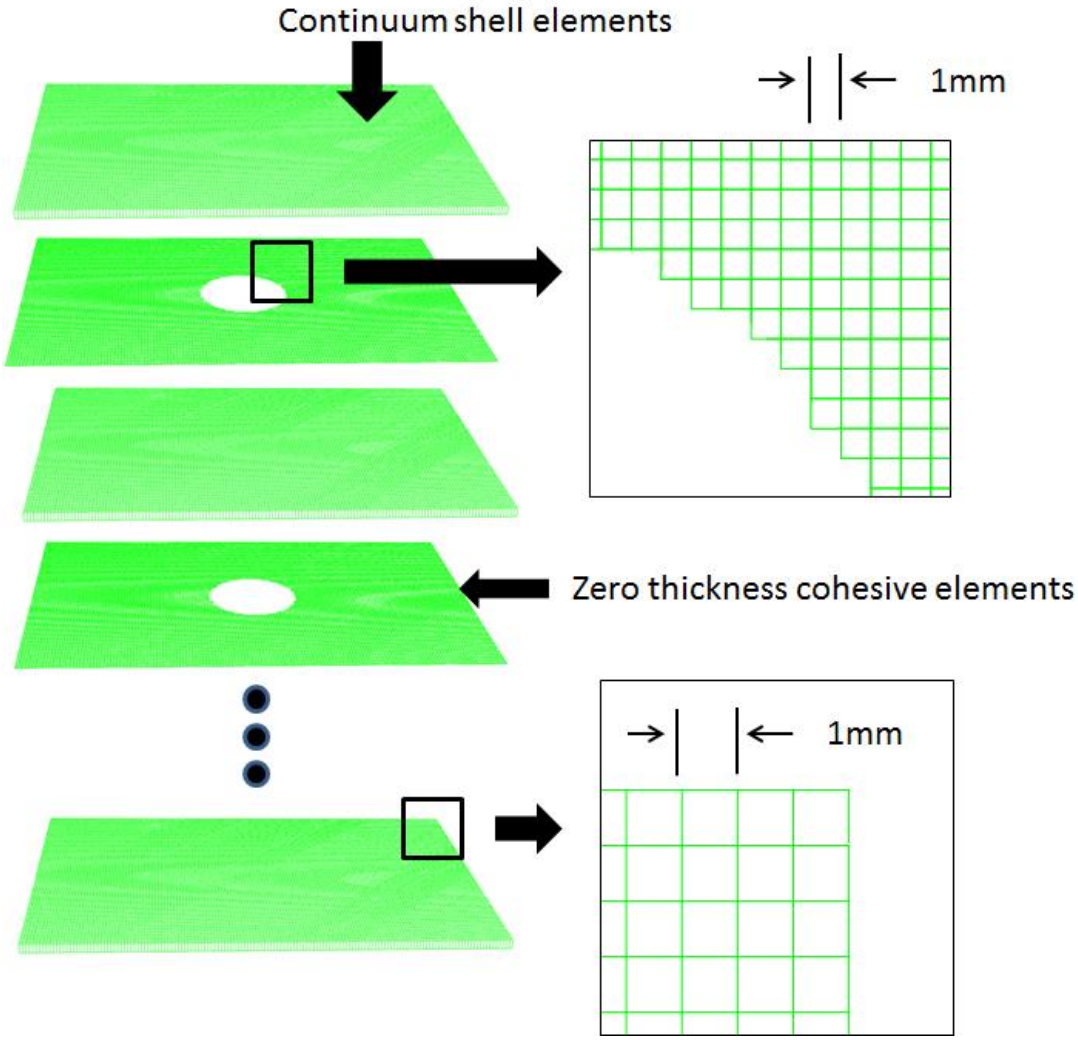

Figure 4.8 Mesh configuration of uniform-meshed model

4.4 Failure criteria

As mentioned above, one of the main objective of this thesis is to identify which failure mode, delamination propagation or in-plane failure due to stress concentration, is the dominant damage mechanism of CAI. To simulate potential delamination propagation, cohesive elements are employed. However, as discussed in Section 4.2, a significant error may arise when predicting the failure of cohesive element. This is due to inconsistence of coordinate system of cohesive

element and delamination propagation direction. It is found that the larger the value of the power α in Equation (2.3), the more the error. In order to eliminate this numerical error, the power is kept at 1 in the current and the following chapters. Therefore, the failure criterion of the interface is expressed in Equation (4.8).

$$\frac{G_I}{G_{Ic}} + \frac{G_{II}}{G_{IIc}} + \frac{G_{III}}{G_{IIIc}} \leq 1 \tag{4.8}$$

where G_{Ic}, G_{IIc} and G_{IIIc} are the CERR of Mode I, II and III, respectively, in which G_{Ic} and G_{IIc} have been obtained from relevant experiments, respectively. The value of G_{IIIc} is assigned to be equal to G_{IIc} conventionally.

In order to simulate in-plane failure of individual lamina, a built-in Hashin's failure criterion in ABAQUS is employed, which was first presented in [95]. For brevity, it is not repeated here.

4.5 Lamina and laminate

The unidirectional lamina employed in this chapter is IM7/8551-7 [96], of which the in-plane properties, nominal thickness and CERR are listed in Table 4.1.

The lay-up sequence is $[45/0/-45/90]_{3S}$, in which fibre orientation is with respect to the x axis with 0° and 90° illustrated in Figure 2.9(a). This is a lay-up sequence resulting in the so-called quasi-isotropic laminates as are widely used in aircraft structures. Besides, only a fixed thickness is employed. This is because the effect of thickness variation to damage mechanism can be reasonably reflected through altering the number of delaminations.

4.6 Parametric study coverage matrix

In this chapter, only delaminations are considered. Other damage modes, such as transverse matrix cracks and fibre breakage, are excluded. This simplification is reasonable because when impacted laminates are subjected in-plane compressive load, corresponding sublaminates tend to lose stability and deform into post-buckling regime at very early loading stage. The stiffness reduction and load carrying capacity due to delaminations are much more significant than those due to transverse matrix cracks and fibre breakage, Rolfes, Noack [97], Craven [4] and Dost [41]. Furthermore, the delamination on each interface is assumed to be circular shaped only, rather than double spiral fan-shaped which is more realistic. This is because the parametric study here is not aimed to predict CAI precisely but to investigate how the damage mechanisms are influenced by delamination patterns. A simplified approach can be justified. However, although the parametric study models are not as realistic as practical CAI cases, some important trends related to the damage mechanisms of CAI can still be validly revealed. The influence of delamination patterns to damage mechanism is investigated by altering the number, size and distribution pattern of delaminations. Multiple delaminations are assumed to be in a cylindrical, conical or spindle shaped, respectively, in terms of their distribution pattern over the laminate thickness as shown in Figure 4.9. According to these factors the parametric study coverage matrix contains three categories.

Table 4.1 Properties for the unidirectional lamina of IM7/8551-7[96] for parametric study

Fibre type	IM7
Matrix	8551-7
Longitudinal modulus E_1 (GPa)	165
Transverse modulus E_2 (GPa)	8.4
In-plane shear modulus G_{12} (GPa)	5.6
Major Poisson's ratio ν_{12}	0.34
Longitudinal tensile strength X_t (MPa)	2560
Longitudinal compressive strength X_c (MPa)	1590
Transverse tensile strength Y_t (MPa)	73
Transverse compressive strength Y_c (MPa)	185
In-plane shear strength S_{12} (MPa)	90
Ply thickness (mm)	0.1425
Mode I energy release rate G_{IC} (J/m^2)	200
Mode II energy release rate G_{IIC} (J/m^2)	610

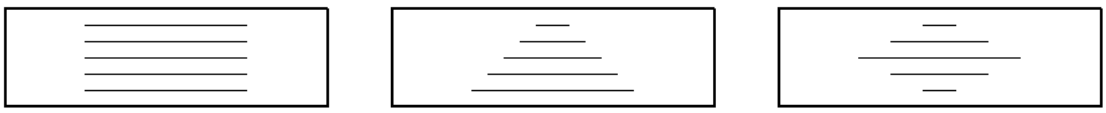

Figure 4.9 Multiple delaminations distributing in (a) cylindrical, (b) conical and (c) spindle shape

As the laminate employed in this chapter consists of 24 plies, there are 23 interfaces inside accordingly. In the first category, single delamination, of which the size in terms of radius varies over 10, 15, 20 25 and 40mm, and the location alters at 4th interface, 8th interface and

mid-plane, is considered. It involves 14 cases as listed in Table 4.2 in FE model names, the naming rule being illustrated in Figure 4.10(a). Different fonts are used in this table as well as in Table 4.3 and Table 4.4 for the purpose of distinguishing the diverse damage mechanisms to be described later in this chapter.

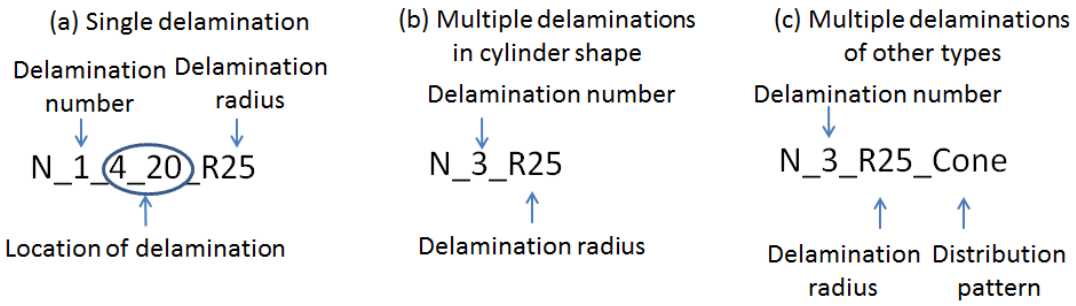

Figure 4.10 Naming rule of parametric study models of (a) single delamination, (b) multiple delaminations in a cylindrical shape and (c) multiple delaminations in a conical or spindle shape

Table 4.2 Parametric study coverage matrix of single delamination

(Roman: Type 1- superficial delamination propagation; **Bold**: Type 2- global failure)

	N_1_4_20_R25	N_1_4_20_R20	N_1_4_20_R15	N_1_4_20_R10
N_1_8_16_R40	**N_1_8_16_R25**	**N_1_8_16_R20**	**N_1_8_16_R15**	**N_1_8_16_R10**
N_1_12_12_R40	**N_1_12_12_R25**	**N_1_12_12_R20**	**N_1_12_12_R15**	**N_1_12_12_R10**

In the second category, multiple delaminations distributing in cylindrical shape over the laminate thickness are considered (Figure 4.9(a)). The size varies over 15, 20 25 and 40mm in term of radius, and the number of delaminations varies over 3, 5, 7, 11 and 23. These multiple

delaminations are of equal size, evenly spaced through the laminate thickness. There are 17 cases in this category as listed in Table 4.3 in terms of FE model names, following the naming rule as illustrated in Figure 4.10(b). As initial imperfection is required for post-buckling analysis through FE method, the deflection over the delaminated area is assigned as the initial imperfection, which is designated as 1% of the sublaminate thickness in respective models. Therefore, absolute value of initial deflection varies among these models, as shown in Figure 4.11.

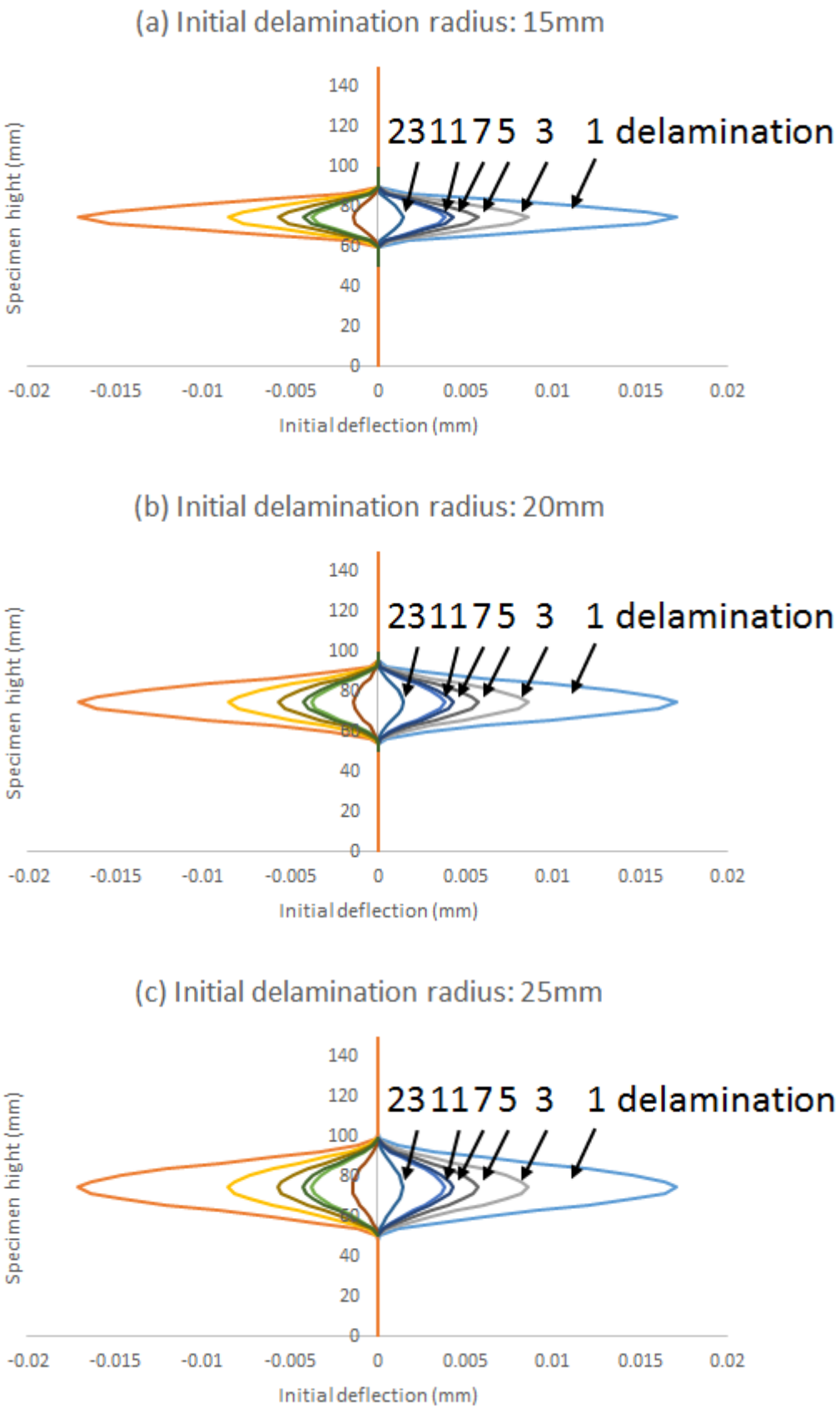

Figure 4.11 Initial deflections over parametric models with multiple delaminations in cylindrical distributing pattern

Table 4.3 Parametric study coverage matrix of multiple delaminations in cylindrical shape

(*Italic*: Type 3-delamination propagation; ***Bold and italic***: Type 4-stress concentration)

	N_3_R25	*N_3_R20*	*N_3_R15*
	N_5_R25	*N_5_R20*	*N_5_R15*
	N_7_R25	*N_7_R20*	*N_7_R15*
N_11_R40	*N_11_R25*	*N_11_R20*	*N_11_R15*
N_23_R40	***N_23_R25***	***N_23_R20***	***N_23_R15***

In the third category, delaminations are also equally spaced but delamination size alters linearly in a conical shape (Figure 4.9(b)) and double linearly in a spindle shape (Figure 4.9(c)). The maximum delamination radius varies between 20 and 25mm, while the minimum radius is fixed at 5mm for all patterns. The number of delamination varies over 3, 5, 7, 11 and 23. Table 4.4 lists all corresponding FE models with the naming rule illustrated in Figure 4.10(c).

Table 4.4 Parametric study coverage matrix of multiple delaminations in conical and spindle shape

(*Italic*: Type 3-delamination propagation; ***Bold and italic***: Type 4-stress concentration)

N_3_R25_Cone	*N_3_R20_Cone*	*N_3_R25_Spindle*
N_5_R25_Cone	*N_5_R20_Cone*	*N_5_R25_Spindle*
N_7_R25_Cone	*N_7_R20_Cone*	*N_7_R25_Spindle*
N_11_R25_Cone		*N_11_R25_Spindle*
N_23_R25_Cone		***N_23_R25_Spindle***

4.7 Parameter setting

Before performing formal analysis, some critical parameters of these parametric study models need to be determined first. These parameters must be set properly so that both numerical error and computation cost can be balanced at an acceptable level.

4.7.1 Loading period

Through the discussion in Section 2.5.2.4, it was concluded that, for detailed FE model in this thesis, ABAQUS/Explicit solver is the most appropriate choice. However, CAI test is considered as quasi-static test, and the loading speed of cross head of the universal testing machine is 1.25mm/min [12] according to the test standard. The computation cost will be unaffordable if the real loading period is applied. Fortunately, as ABAQUS manual stated:

> "For quasi-static simulations incorporating rate-independent material behavior, the natural time scale is generally not important. To achieve an economical solution, it is often useful to reduce the time period of the analysis or to increase the mass of the

model artificially. Both alternatives yield similar results for rate-independent materials."[1]

Here, the above recommended approach of reducing time period is adopted. N_1_12_12_R25 is selected as a benchmark test. The in-plane size of both continuous shell elements and cohesive elements is 1mm square. And the time period was attempted from 1.5, 3, 4.5 to 6s successively. All FE models collapsed with the same failure mode (the failure mode will be described in Section 4.8.1.3) and their load-displacement curves are plot in Figure 4.12. From these curves it can be found that the failure loads converge rapidly as the time period increases. The time period of 3, 4.5 or 6s would be the better choice in terms of accuracy. However, the time period is too long even for this single delamination model, more than 10 hours for calculation were needed on a desktop PC configured with i7 CPU and 12GB RAM. When the FE model with as many as 39 delaminations is analysed, the calculation period will be unaffordable. It is found that with a time period of 1.5s, the failure load is only 3.4% higher than that with 6s. Therefore, 1.5s is selected as the time period for all detailed FE models analysed in this thesis.

[1] Quoted from 11.7.1 Mass scaling, Abaqus analysis user's manual, Version 6.11

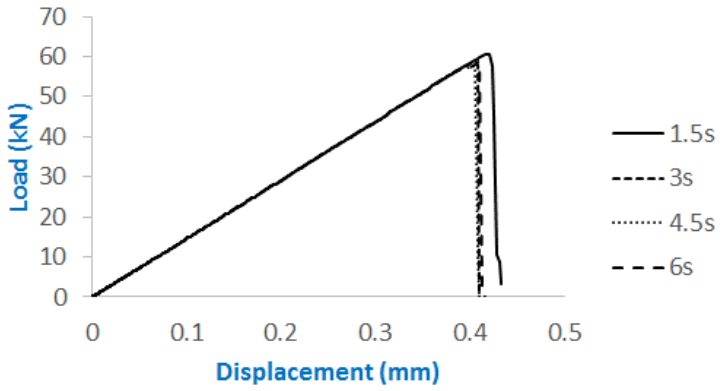

Figure 4.12 Load-displacement curve of FE model N_1_12_12_R25 solved by ABAQUS/Explicit at loading period of 1.5, 3, 4.5 and 6s respectively

4.7.2 Element size

It is known that the mesh size affects the accuracy significantly, which is more pronounced when it comes to the simulation of delamination propagation using cohesive elements. Turon, Davila [75] discovered that for typical graphite-epoxy or glass-epoxy composite materials, the length of the cohesive zone is smaller than 1 or 2mm. Therefore, the element size, in order to have at least two elements in the cohesive zone, should be smaller than 0.5mm. This refining requirement renders most practical problems with large structure intractable.

N_1_4_20_R25 is selected as the benchmark case for mesh sensitivity study, which is meshed with 6 different element sizes, 2, 1, 0.5, 0.25, 0.2 and 0.15mm, respectively. The damage process of these 6 models are similar, which is described in detail in Section 4.8.1.1. The difference is that delamination propagation initiates at different compressive loads as the element size varies. Figure 4.13 shows such critical compressive loads of each model with respect to that of the

model configured with mesh size of 0.15mm. It is found that the coarser the mesh, the harder the occurrence of delamination propagation in simulation can be triggered.

It is found that the results from the model with an element size of 1mm is on track to convergence. For the purpose of parametric study in this chapter, which aims to investigate the qualitative trends of damage mechanisms rather than simulating delamination propagation quantitively, the 1mm option offers a reasonable compromise.

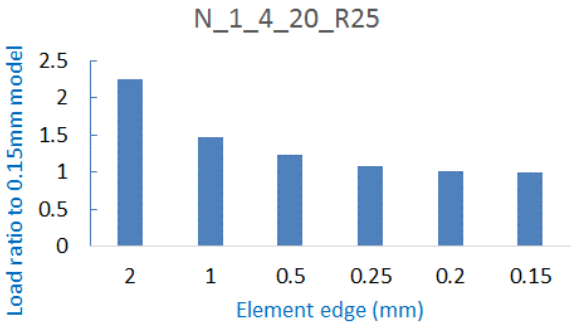

Figure 4.13 Comparison of compressive loads of initial delamination propagation among the same model but with different element sizes

4.7.3 FE model evaluation

The accuracy of the FE model is evaluated through comparing with the experimental results of two references. In the first reference, the specimen bears 7 uniform circular delaminations, which is shown schematically in Figure 4.14. The calculated CAI strength is 222MPa, a little lower than the average experimental result 241MPa, which is shown in Figure 4.15. Furthermore, the damage mechanism of the FE model is evaluated, which is coincident with the experiments due

to excessive delamination propagation. Figure 4.16(a) shows the ultrasonic C-scanning image taken after the compression test, while the simulation of delamination propagation in the FE model is shown in Figure 4.16(b). The red part in the centre of the Figure 4.16(a) is the propagated delamination and the chaotic yellow band in Figure 4.16(a) is the reflection of crushed band over the specimen. Because the strength values of the laminae are not given in the reference, the FE model can only simulate delamination propagation, which is shown in Figure 4.16(b).

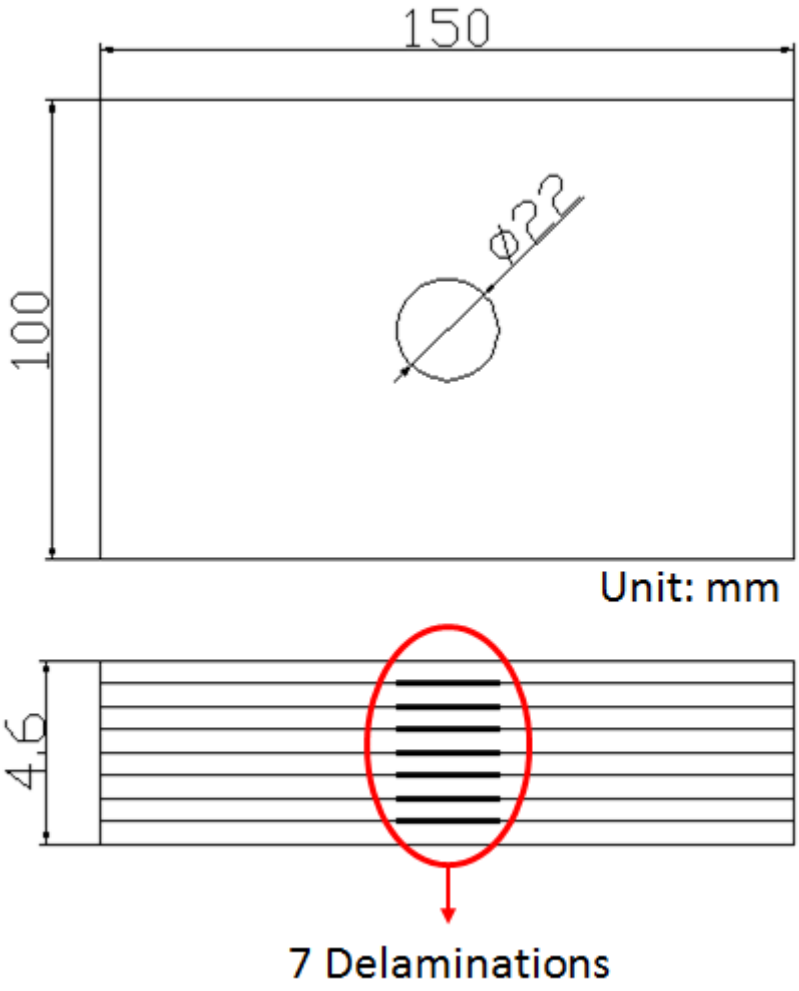

Figure 4.14 Specimen configuration with multiple delaminations

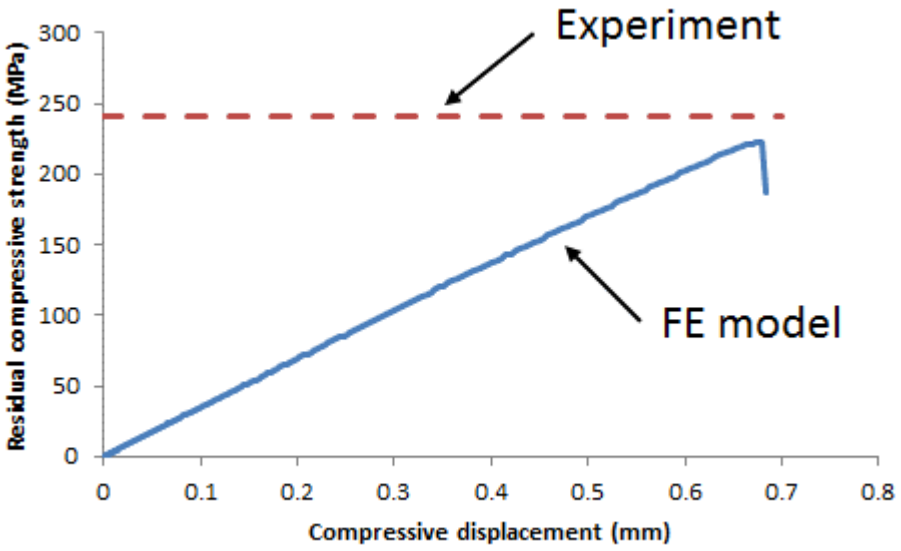

Figure 4.15 The comparison of residual compressive strength between FE model and experimental result from [31]

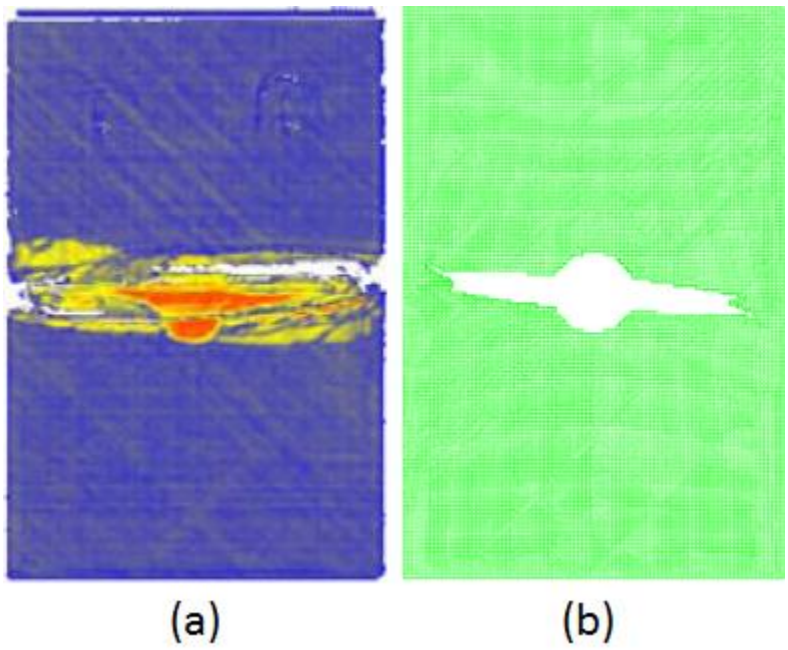

Figure 4.16 The comparison of final damage status between (a) C-scanning image and (b) FE simulation

In the second reference [23], a single circular delamination was placed inside a plate after 3, 5 or 7 prepreg layers, respectively, which is shown in Figure 4.17 schematically. The load-deflection curves for these three models obtained from experiments and FE simulations are shown simultaneously in Figure 4.18 for comparison. It can be seen that delamination buckling loads (the bifurcation point of each curve) over these three models are predicted accurately. However, the global buckling load obtained from FE model (around 140kN) is slightly greater than that from experiments (around 110kN). This is mainly due to the coarse mesh of cohesive elements which deters the delamination propagation numerically.

Based on above evaluation, it is seen that the error induced by this FE modelling strategy is acceptable. Therefore, it is adopted for following parametric study.

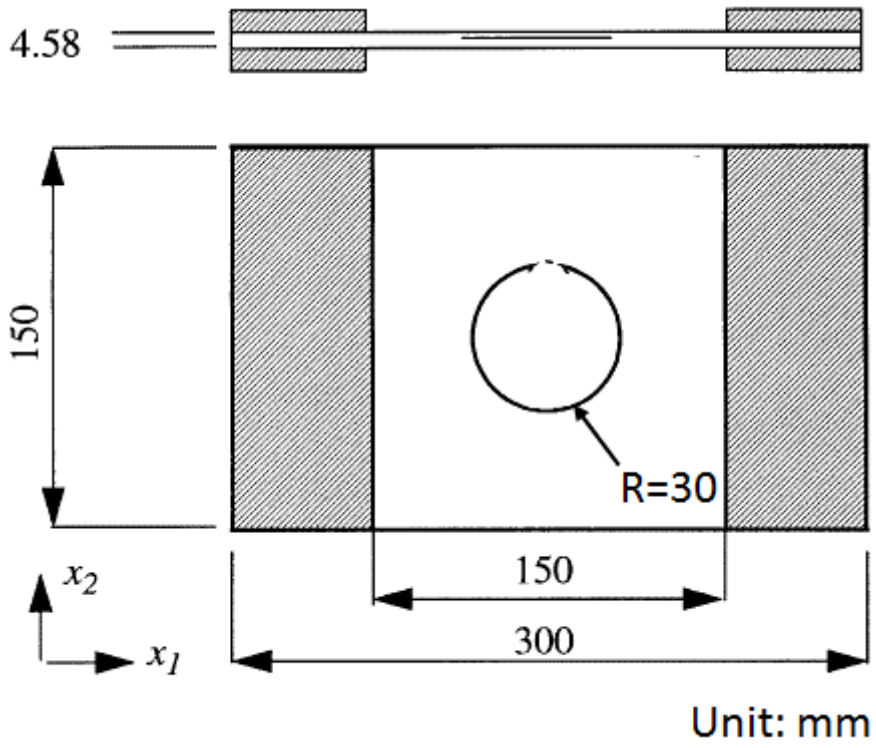

Figure 4.17 Schematic top and side view of the composite plate containing single circular delamination

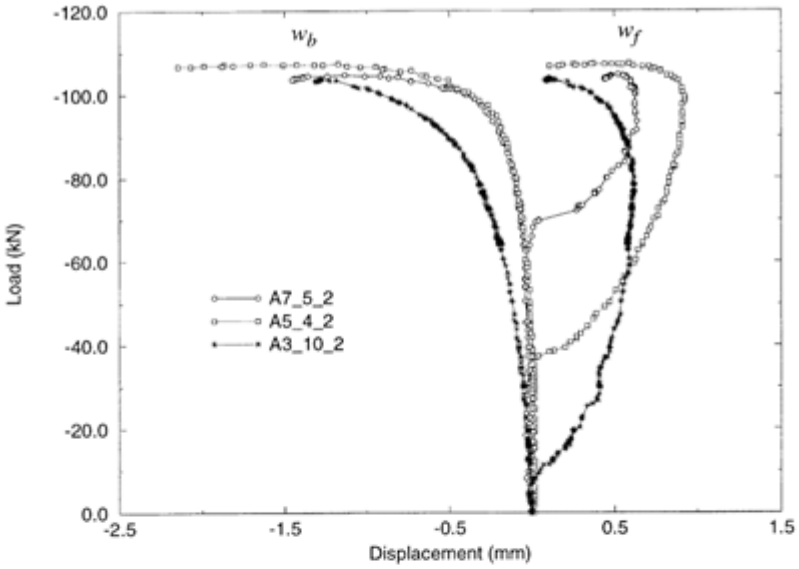

(a) experiments

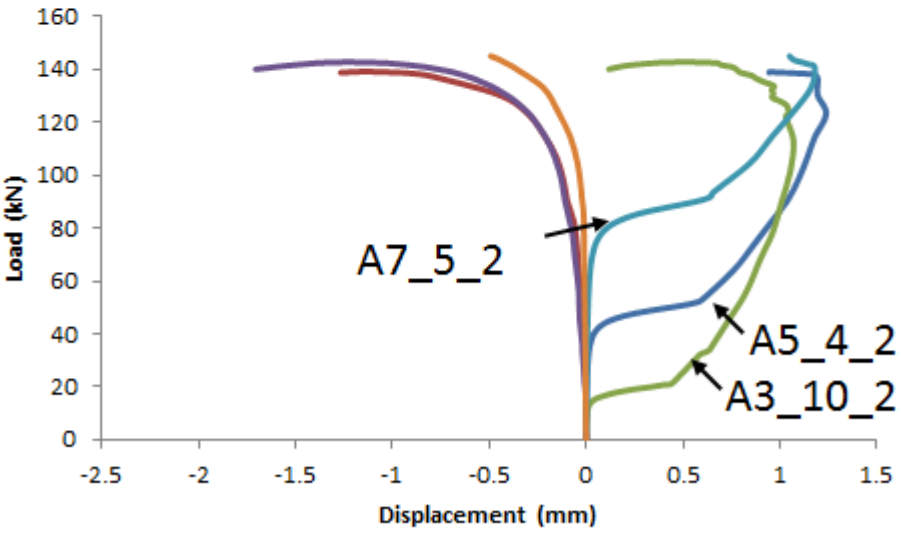

(b) FE simulations

Figure 4.18 Load-deflection curves for three circular delaminated plates, delaminated at layers 3, 5 and 7, respectively. (a) Experiments, (b) FE model

4.8 Discussion

For each model involved in the above parametric study covering matrices, the damage process is monitored. In order to explain the damage mechanism of each model clearly, some critical loading states of that model during the damage process are extracted for illustration. Basically, one critical loading state is that when fibre compressive failure in the 0° laminae firstly takes place. As the primary element to sustain compressive load, fibre failure in 0° laminae indicates that the collapse of the whole laminate will follow immediately. Another critical loading state is that when the maximum compressive load (referred as failure load) is reached. Investigating the damage state of the laminate at this load level helps to understand which kind of failure mode dictates the load sustainability of the whole laminate.

4.8.1 Single delamination

4.8.1.1 Delamination at fourth interface

N_1_4_20_R10 is analysed firstly. Figure 4.19(a) illustrates the deflection of the central points of both sublaminates during the loading process up to failure load. It is found that at the beginning, both sublaminates sustain the compressive load together. At about 51.47% failure load, the thinner sublaminate buckles and bends away, while the thicker sublaminate remains stable (marked with circle in Figure 4.19(a)). The bending deformation along longitudinal centre line at that moment is also shown in Figure 4.19(b), and only tiny separation is observed at the central position. When compressive load reaches 98.49% failure load, a drastic increase of deflection is observed on both sublaminates (marked with diamonds in Figure 4.19(a)). This is due to initiation

of delamination propagation. At that point, more significant bending deformation (Figure 4.19(c)) is observed compared with that at the point of bifurcation (Figure 4.19(b)). As the compressive load increases, the delamination propagation exacerbates. When failure load is reached, massive delamination is observed, which is shown in Figure 4.20(a), while no fibre failure is observed at the time. After that, drastic drop of the compressive does not appear. Instead, it fluctuates before its final plunge, which is shown in Figure 4.21(a). During the process, delamination propagates continuously to an excessive extent (Figure 4.20(b)). When compressive load reaches its final peak, fibre failure appears in the 0° laminae of the thicker sublaminate, which is marked with red grids in Figure 4.20(c), (d) and (e). This fibre failure develops rapidly over the laminate width, leading the collapse of the whole laminate. Therefore, in this case, the failure load is determined by delamination propagation while the collapse of the whole laminate is triggered by in-plane fibre failure.

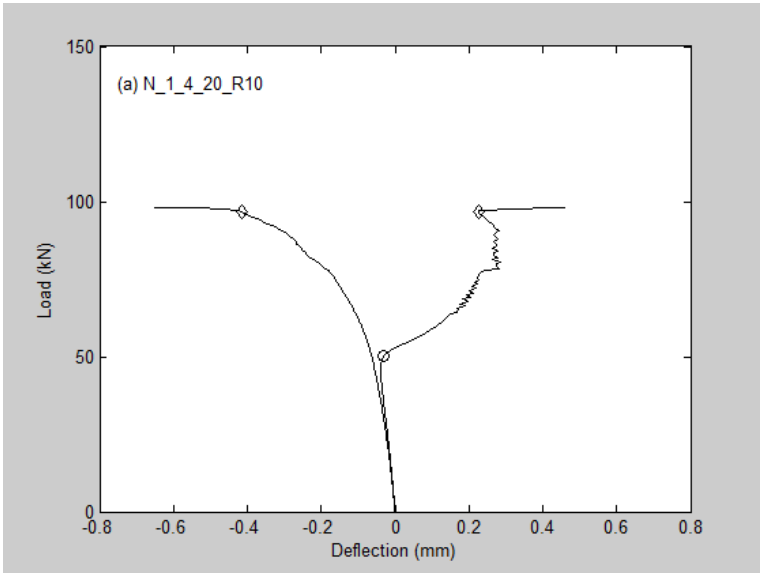
(a) N_1_4_20_R10
Load (kN)
Deflection (mm)
150
100
50
0
-0.8
-0.6
-0.4
-0.2
0
0.2
0.4
0.6
0.8

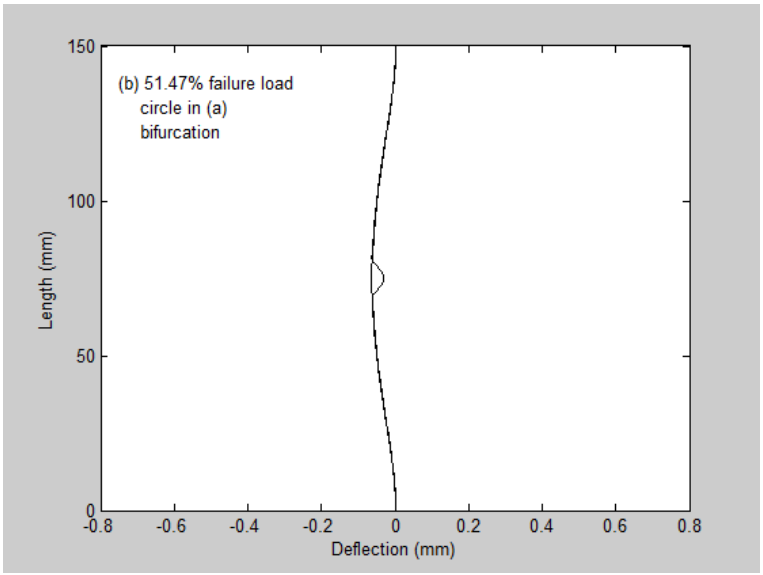
(b) 51.47% failure load
circle in (a)
bifurcation
Length (mm)
Deflection (mm)
150
100
50
0
-0.8
-0.6
-0.4
-0.2
0
0.2
0.4
0.6
0.8

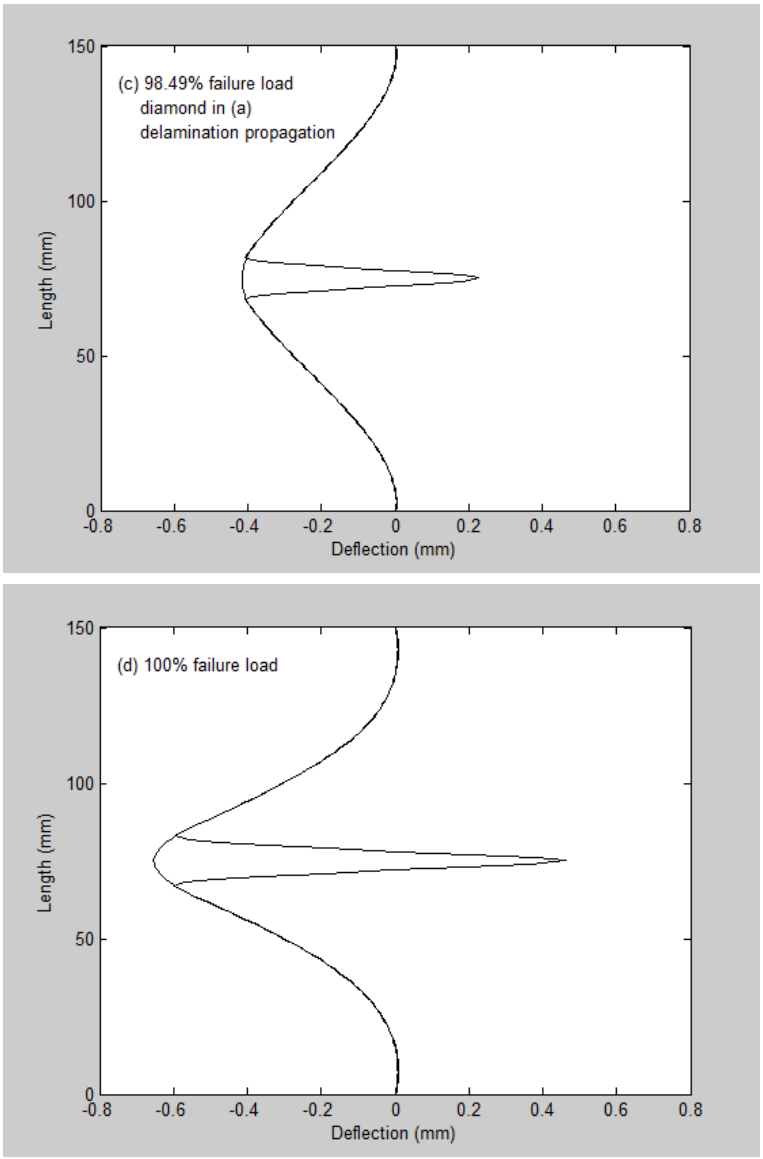

Figure 4.19 (a) deflection of central point of FE model N_1_4_20_R10 in loading process and bending deformation along the centre line in longitudinal direction at (b) 51.47%, (c) 98.49% and (d) 100% failure load respectively

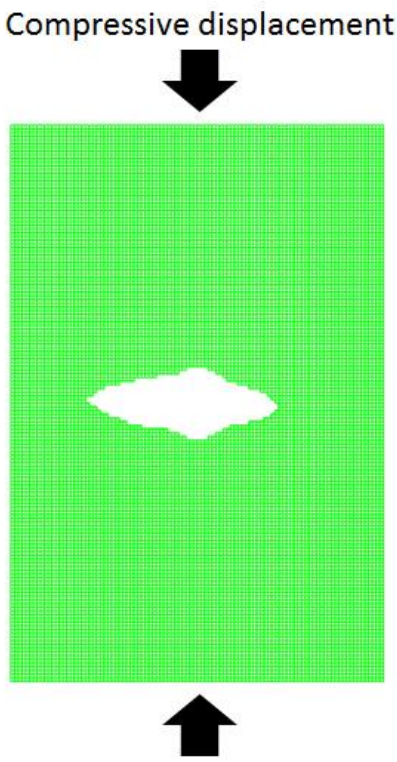

(a) Delamination propagation state when failure load is reached

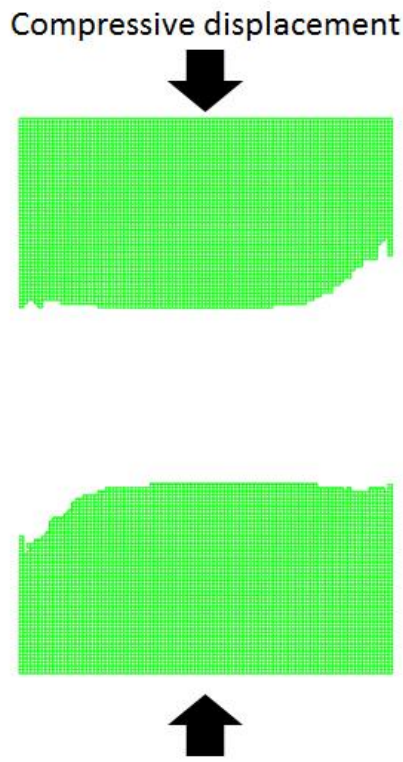

(b) Delamination propagation state when 2.73% drop of the failure load

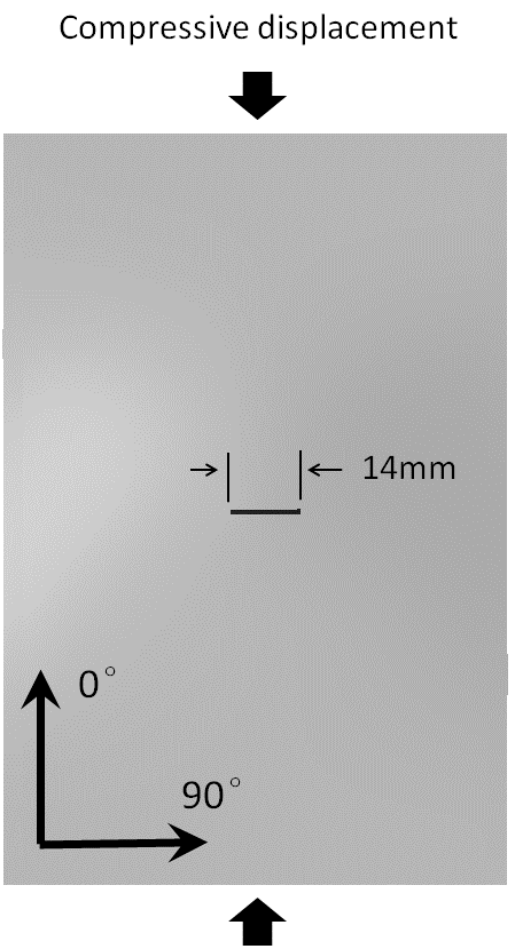

(c) Fiber failure state at the 2nd 0° lamina from front side when 2.73% drop of the failure load

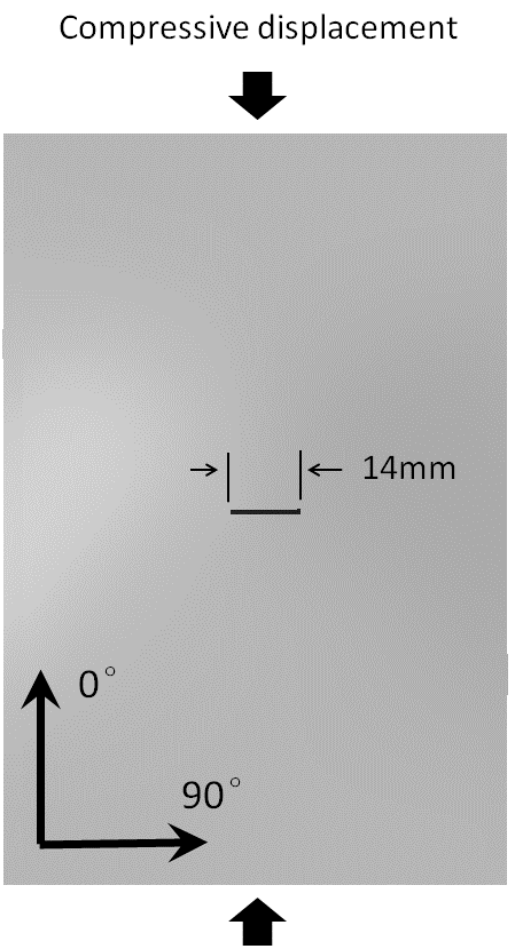

(c) Fiber failure state at the 2nd 0° lamina from front side when 2.73% drop of the failure load

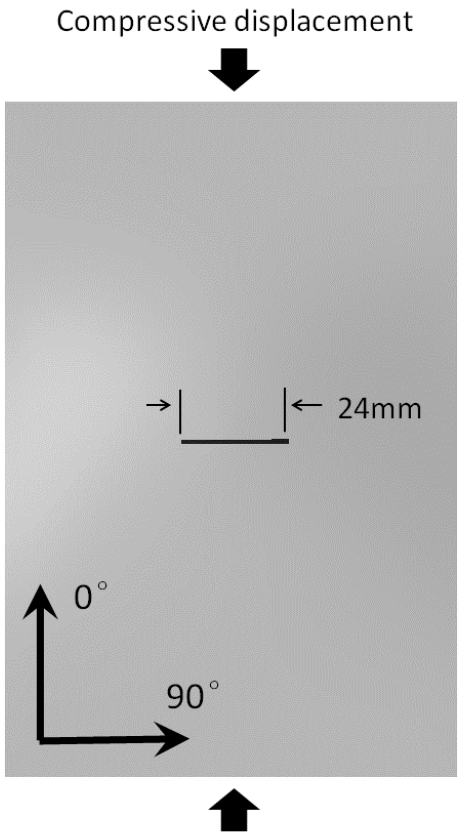

(e) Fiber compressive failure state at the 4th 0° lamina from front side when 2.73% drop of the failure load

Figure 4.20 Damage states of N_1_4_20_R10 at different load levels captured from ABAQUS window

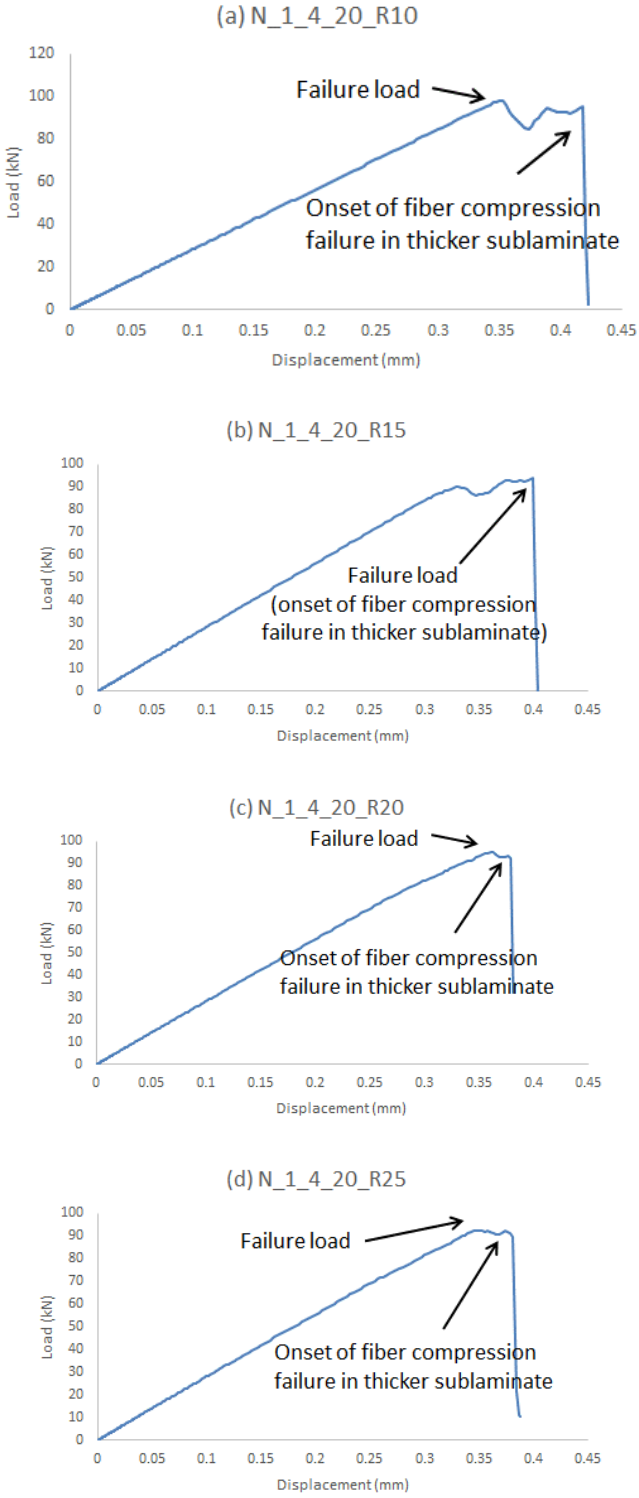

Figure 4.21 Load-displacement curves for FE models bearing single delamination at the forth interface

It is worth mentioning that although the damage state images of the FE model captured from ABAQUS window, such as Figure 4.20, are clear visually for damage mechanism illustration, they are not integrated and concise. With respect to above model, it is found that both failure modes,

delamination propagation and in-plane failure, initiate and develop over the central line across the width. Actually, from massive experiments, as well as simulations, the common final failure state of CAI specimens is observed like this. The laminate usually breaks along the centre line across the width where the residual width of intact laminate from the delamination front to the side edge of the laminate is minimum, leaving two broken halves inserting into each other in a broom shape (Figure 4.22 cited from original Fig. 3 of [98]). This implies that through monitoring the damage process of this region around the central line across the laminate width, damage mechanism can be revealed. Therefore, a series of schematic section views of this region reflecting damage states, for example, Figure 4.23, have the same effect as Figure 4.20 does. In Figure 4.23, the hatched areas represent initial delamination, grey parts represent interface failure, and black parts in the laminae of the laminate represent areas of fibre compressive failure. Figure 4.23(a) is equivalent to Figure 4.20(a), in which only delamination propagation is observed when failure load is reached. Figure 4.23(b) is the integration of from Figure 4.20(b) to (e), in which excessive delamination propagation as well as in-plane failure are observed at the moment when compressive load drops 2.73% from the failure load.

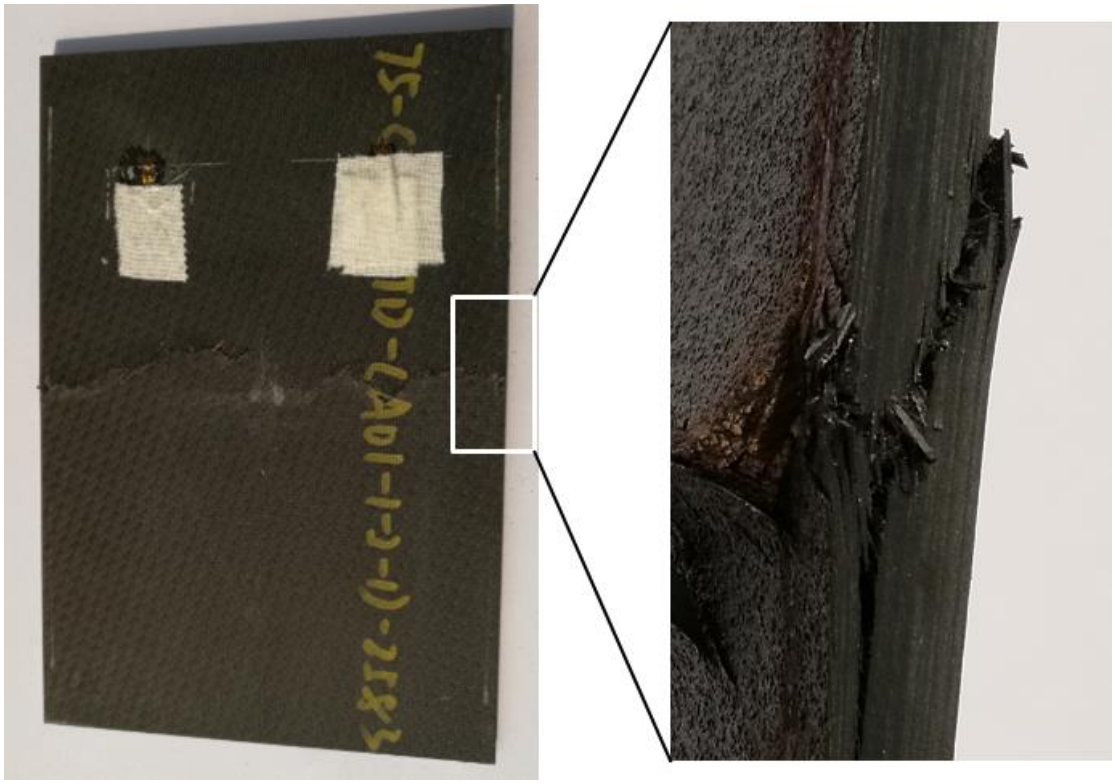

Figure 4.22 Failed CAI specimen configuration

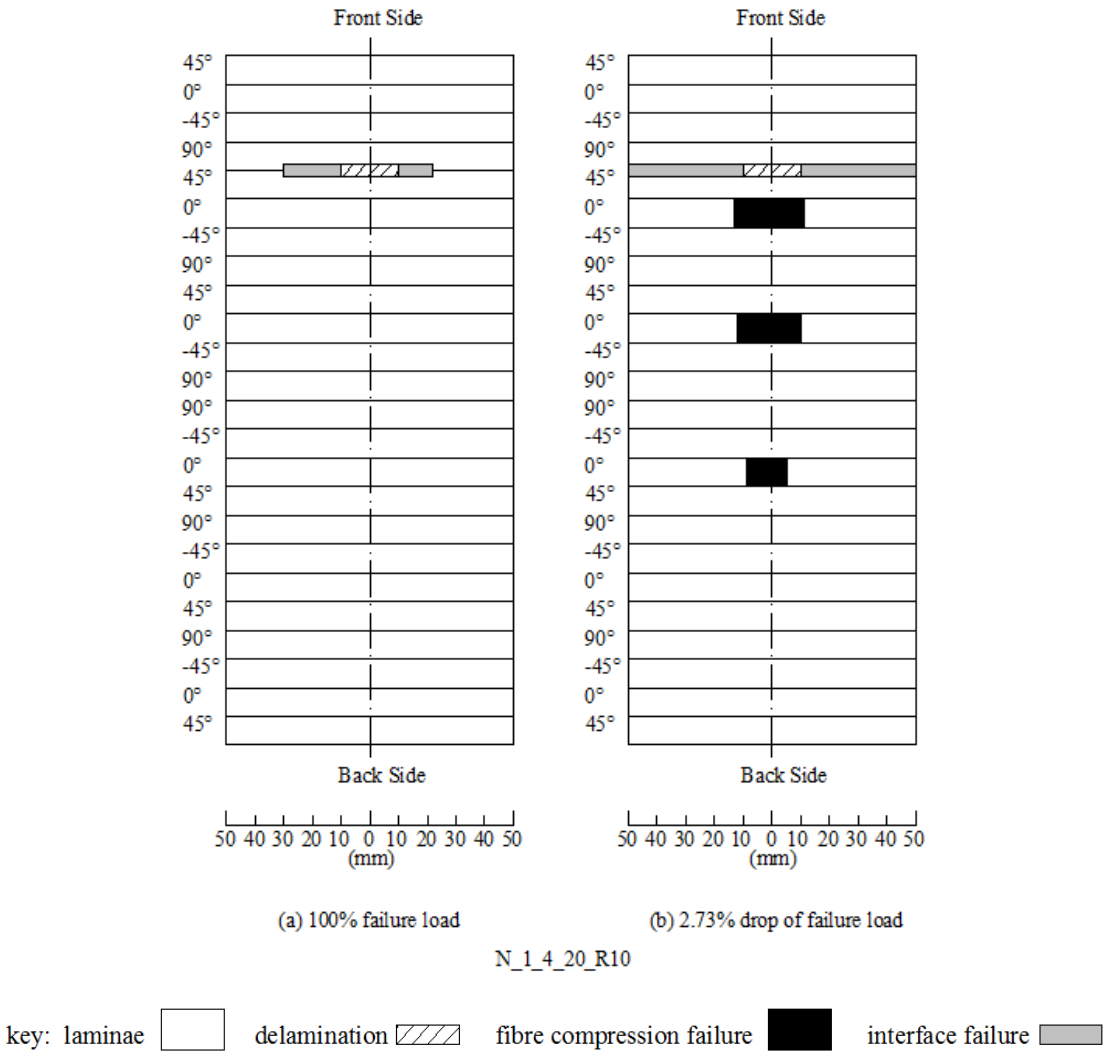

Figure 4.23 Schematic damage process of N_1_4_20_R10

N_1_4_20_R15 is analysed next. Figure 4.24 illustrates the deflection of the centre points of both sublaminates during the loading process up to the failure load. Similar to the case of N_1_4_20_R10, it is also found, at the beginning, both sublaminates sustain the compressive load together. But, as the size of initial delamination increases, at lower percentage of failure load compared with previous case, about 28.10%, the thinner sublaminate buckles and bends away, while the thicker sublaminate keeps stable (marked with circle in Figure 4.24). Similarly, drastic increase of deflection turns up at 89.03% failure load due to delamination propagation (marked

with diamond in Figure 4.24). When fibre failure takes place firstly in the thicker sublaminate, delamination has propagated extensively over the width, as shown in Figure 4.25. After that, the whole laminate collapses immediately afterwards.

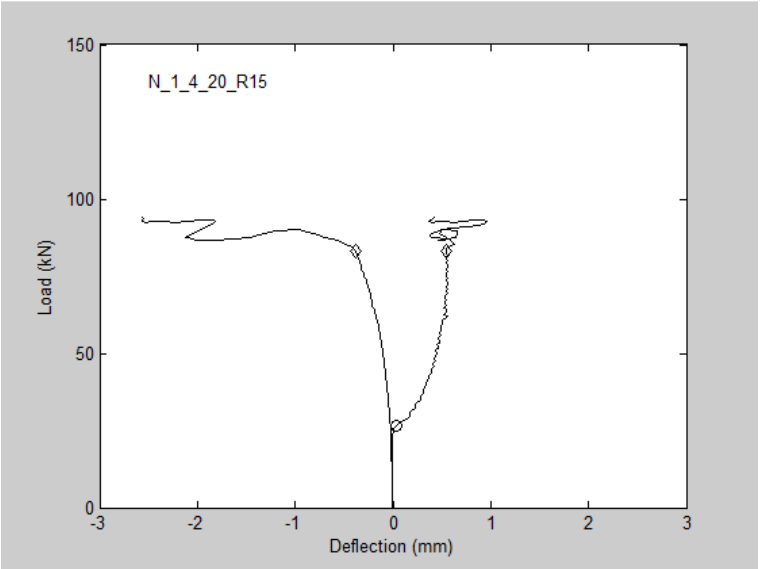

Figure 4.24 Deflection of centre points of FE model N_1_4_20_R15 in loading process

N_1_4_20_R20 is analysed thirdly. Figure 4.26 illustrates the deflection alteration of the central point of both sublaminates during the loading process until the failure load is reached. Similar to previous case in Figure 4.24, two characteristic points are observed as well. They are bifurcation at 16.68% failure load and initial delamination propagation at 80.33% failure load, which are marked with circle and diamond in Figure 4.26, respectively. When failure load is reached, fibre failure is observed in thinner sublaminate (Figure 4.27(a)). However, this seems not affecting the whole laminate significantly, and the compressed load is still sustained at high level. As the load increases, fibre failure in the thinner sublaminate develops through the width, which leads that

the thinner sublaminate cannot contribute to sustain load anymore and transfers the previously sustained load to thicker sublaminate which already sustains high level of load. Therefore, the damaging process is accelerated and fibre failure extensively develops in thicker sublaminate (Figure 4.27(b)). Immediately afterwards, the laminate collapses.

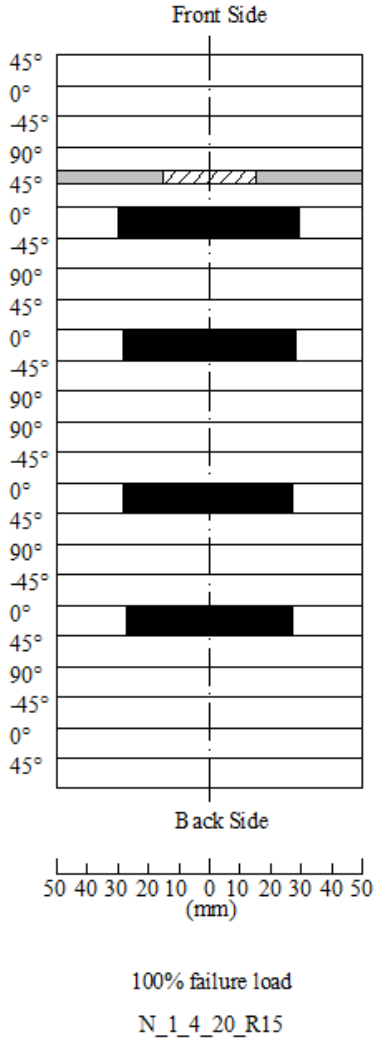

100% failure load

N_1_4_20_R15

Figure 4.25 Schematic damage state of N_1_4_20_R15 when failure load is reached

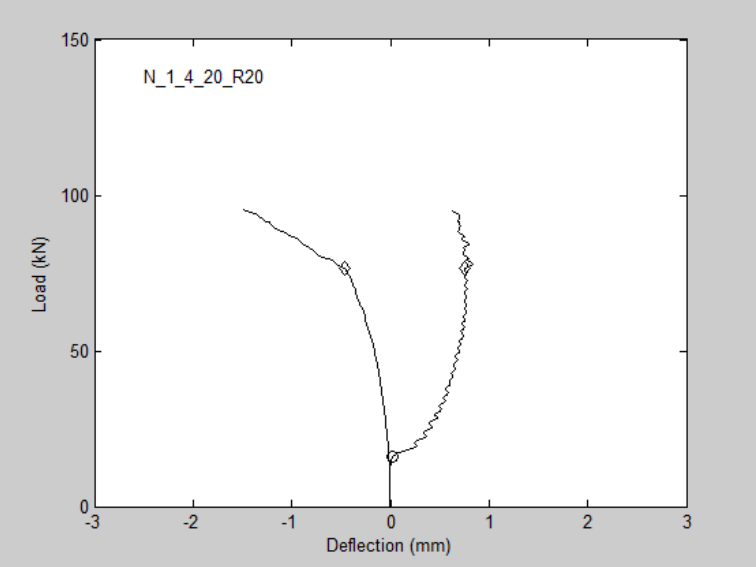

Figure 4.26 Deflection of central point of FE Model N_1_4_20_R20 in loading process

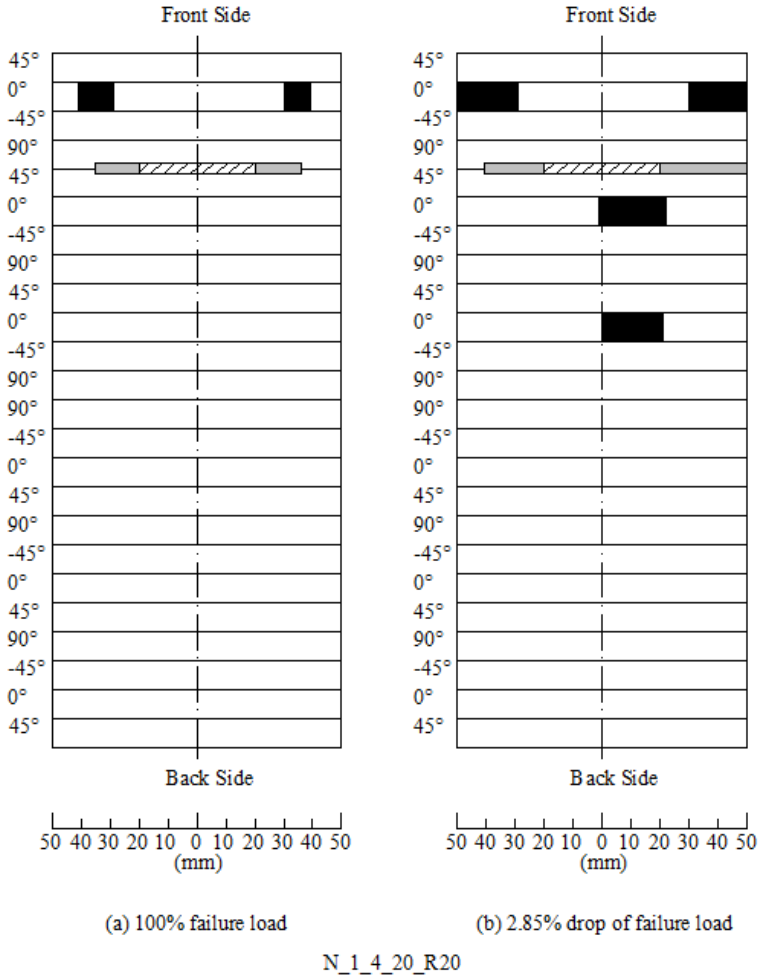

Figure 4.27 Schematic damage process of N_1_4_20_R20

Not surprisingly, the damage process of N_1_4_20_R25 is almost a repeat of previous cases in this sub-group. The deflection in Figure 4.28 shows these characteristic points during the loading process until failure load is reached: bifurcation in circle at about 11.48% failure load, initial delamination propagation in diamond at about 77.28% failure load. When the failure load is reached, only delamination propagation is observed (Figure 4.29(a)). As the compressive load increases continuously, fibre failure takes place at the propagated delamination front in thinner sublaminate (Figure 4.29(b)) and in the thicker sublaminate (Figure 4.29(c)), successively. Immediately after that, the laminate collapses.

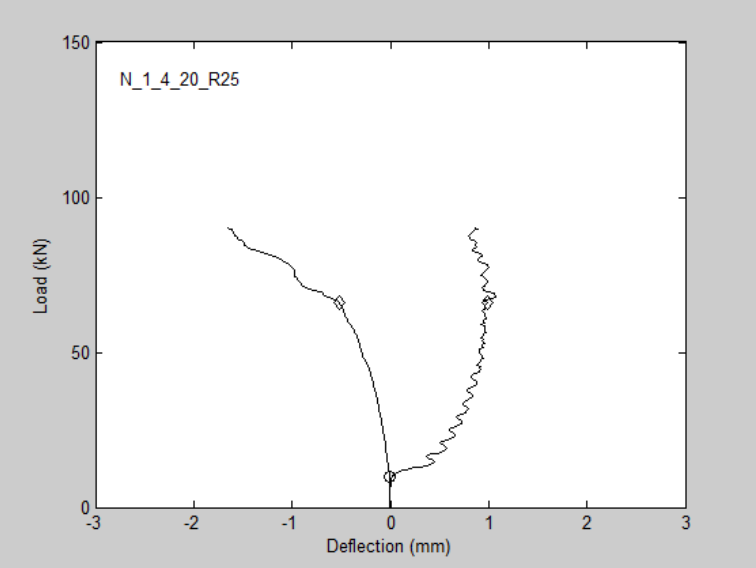

Figure 4.28 Deflection of central point of FE Model N_1_4_20_R25 in loading process

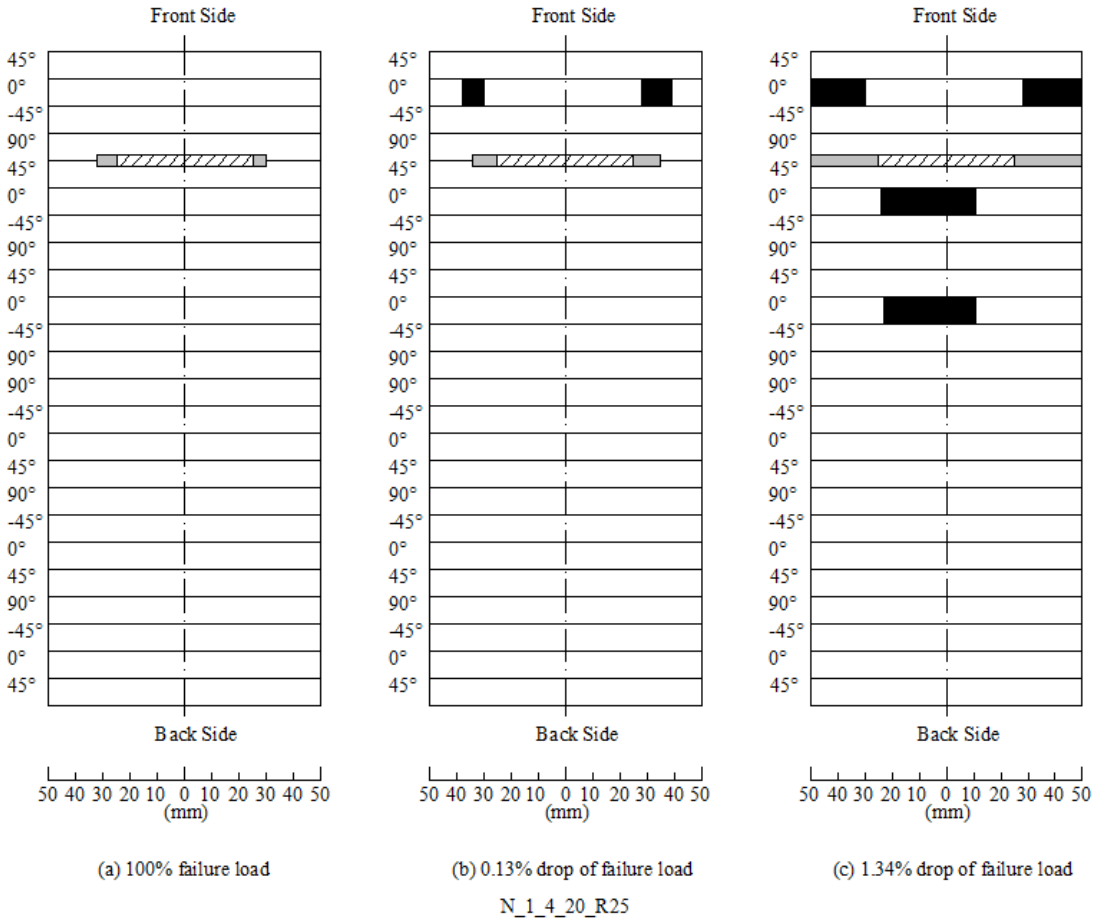

Figure 4.29 Schematic damage process of N_1_4_20_R25

As a conclusion, the failure loads of all the FE models in this sub-group are determined by delamination propagation, but the catastrophic failure of the entire laminate is a consequence of failure of thicker sublaminate. And it can also be found that the bigger size of initial delamination, the earlier thinner sublaminate buckles and bends away (51.47%, 28.10%, 16.68% and 11.48% of corresponding failure load, respectively).

4.8.1.2 Delamination at eighth interface

In this sub-group, the effect of initial delamination size to damage mechanism is exposed clearly. When the size is small, it has limited influence to the whole laminate, which collapses like an intact laminate. Take N_1_8_16_R15 for example, before failure load reaches, neither fibre damage nor interface failure is observed. However, at the failure, all 0° laminae fail through width abruptly, accompanied with failure of corresponding cohesive element through width as well (Figure 4.32(b)). When bigger initial delamination is induced, sequential failure on different locations of the laminate can be observed. For example, delamination propagation can be observed before fibre failure takes place in N_1_8_16_R25 (Figure 4.32(a)).

The distinct deflections of centre points of the models, of which the delamination size in terms of radius varies over 10mm to 25mm, in this sub-group also show this phenomenon. For N_1_8_16_R10 and N_1_8_16_R15, buckling occurs at relatively high load level, after which both sublaminates bend towards one side and collapse immediately (Figure 4.33(a) and (b)). For N_1_8_16_R20 and N_1_8_16_R25, buckling occurs at lower load level, and sublaminates bend towards opposite sides. After buckling sublaminates still deform in a relatively long process before final collapse (Figure 4.33(c) and (d)).

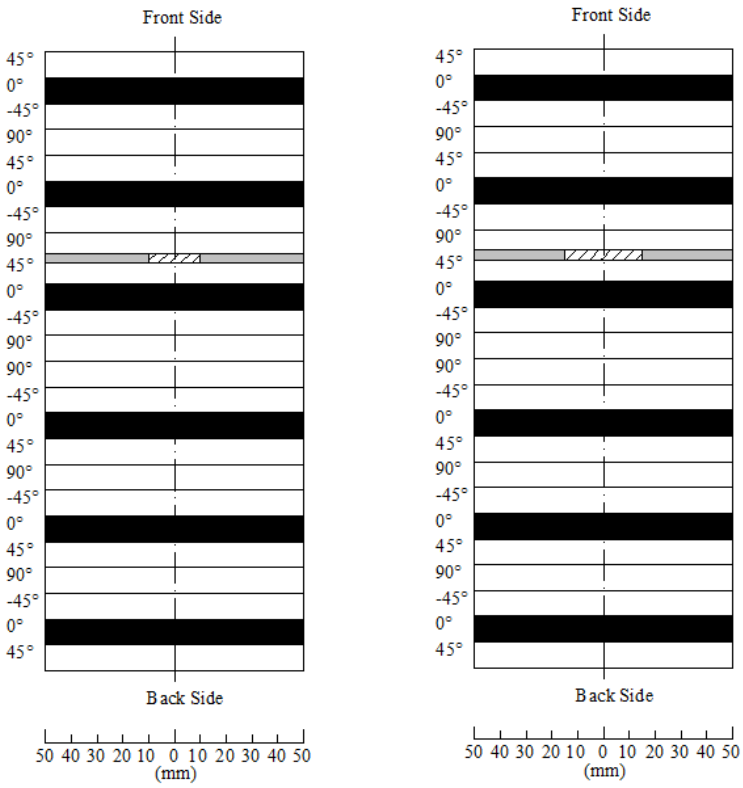

Figure 4.30 Schematic damage states of N_1_4_20_R10 and N_1_4_20_R15 when failure load is reached

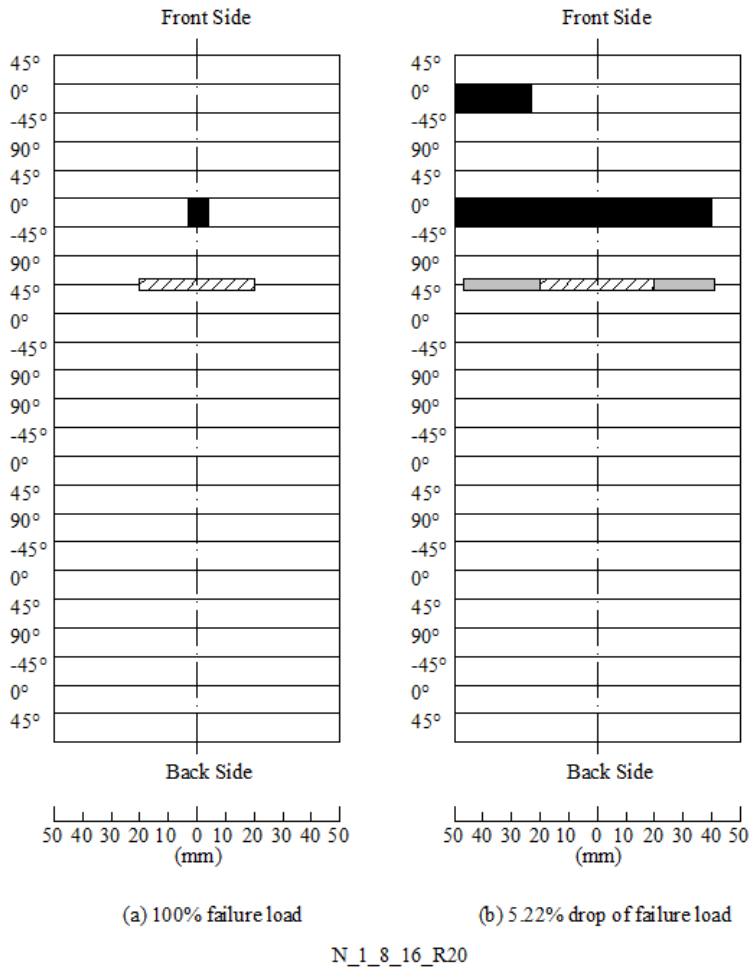

(a) 100% failure load (b) 5.22% drop of failure load

N_1_8_16_R20

Figure 4.31 Schematic damage process of N_1_8_16_R20

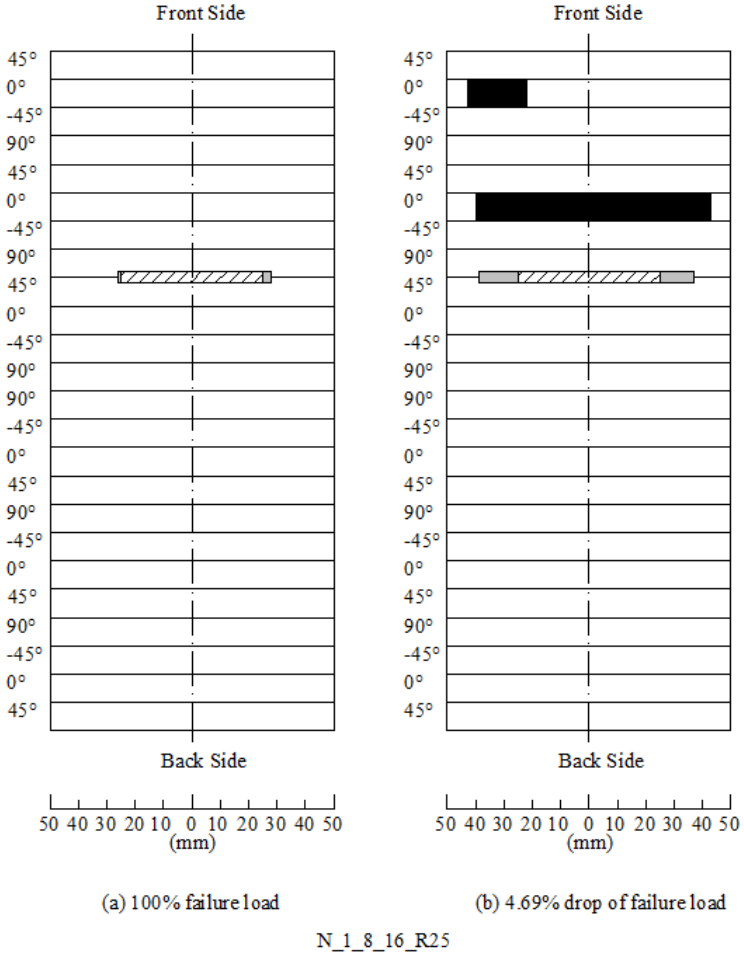

Figure 4.32 Schematic damage process of N_1_8_16_R25

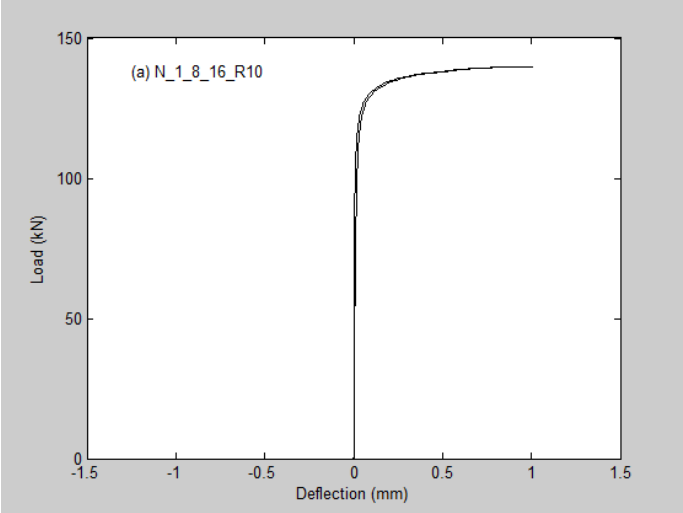
(a) N_1_8_16_R10
Load (kN)
Deflection (mm)
150
100
50
0
-1.5
-1
-0.5
0
0.5
1
1.5

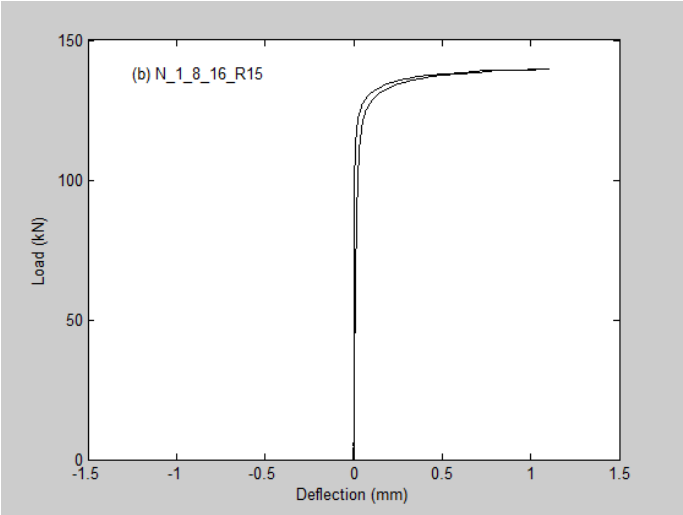
(b) N_1_8_16_R15
Load (kN)
Deflection (mm)
150
100
50
0
-1.5
-1
-0.5
0
0.5
1
1.5

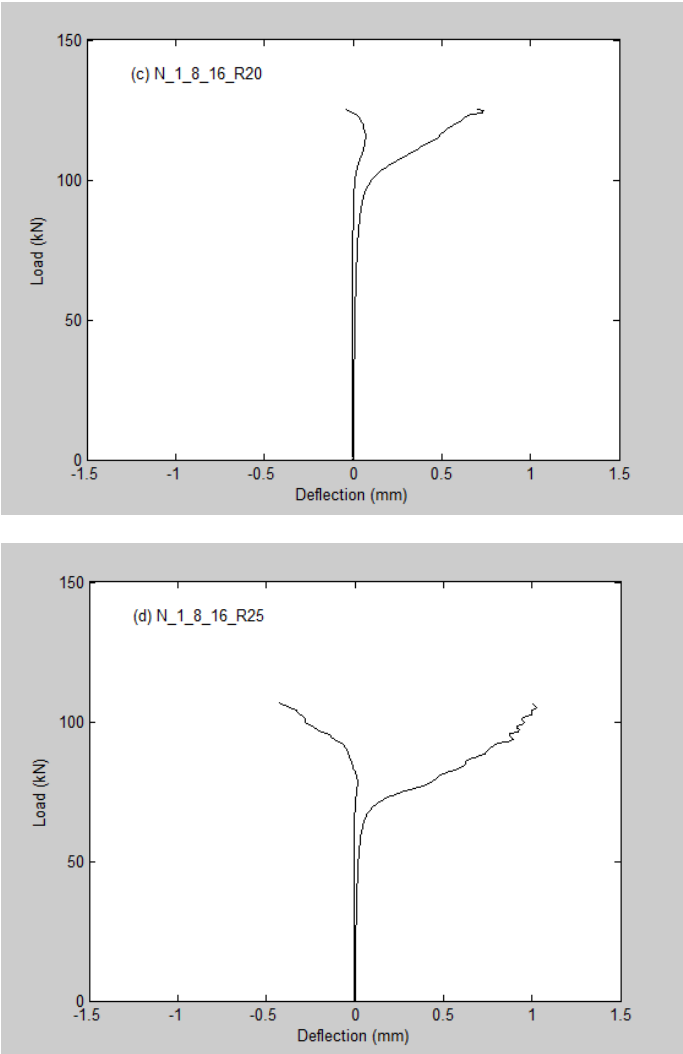

Figure 4.33 Correlation of compressive load and deflection at central point on both sublaminates of the FE models bearing single delamination in the eighth interface

When the delamination size increases to a relatively extreme condition, such as 40mm in radius, the damage process is found distinct from previous cases. Figure 4.34 shows the load-displacement curve of this model, which drops first when delamination begins to propagate. During the following long process, large extent of delamination propagation is observed before in-plane failure takes place and the whole laminate collapses.

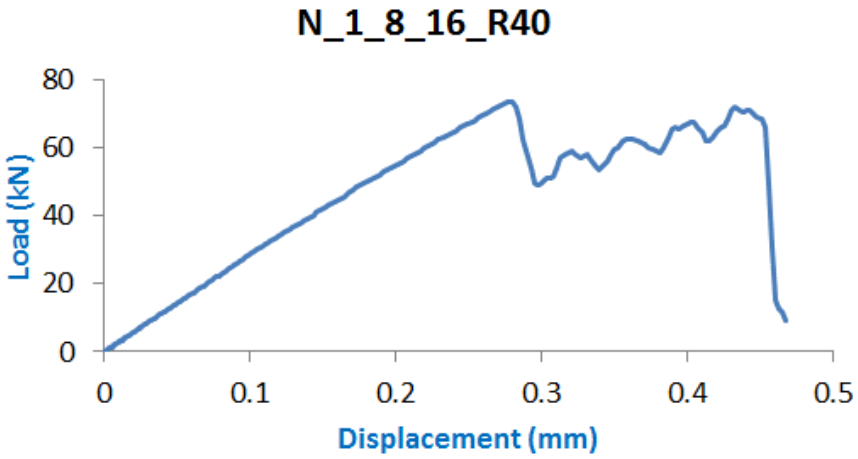

Figure 4.34 Load-displacement curve of N_1_8_16_R40

4.8.1.3 Delamination at mid-plane

N_1_12_12_R25 is analysed firstly. It can be found that neither fibre compression failure nor interface failure takes place until the failure load is reached (Figure 4.35(a)). However, after delamination begins to propagate, subsequent capability of sustaining compressive load is undermined. Before the entire model collapses, delamination has already propagated about 11mm towards both sides of the laminate (Figure 4.35(b)). After that, almost all 0° laminae fail through the width of the laminate and the plate collapses (Figure 4.35(c)). It is worth mentioning that in the final collapsing process the failure of cohesive element is considered as not due to excessive delamination propagation. Rather, it is as a consequence of in-plane failure in the neighbouring sublaminates. Because when the laminate catastrophically fails, it breaks into two halves which interpenetrate into each other in broom shape. This drastic deformation of laminate also causes the failure of cohesive element. The deflection variation of the central points of both sublaminates during the loading process is plotted in Figure 4.36. It can be seen that at beginning

sublaminates split at mid-plane and bend outwards, respectively. When the compressive load reaches about 95.8% failure load, deflections of both sublaminates abruptly decrease until the collapse of the entire laminate. This is due to switch from local buckling to global buckling, which can be confirmed through the deformation alteration along centre line along the length at these two load levels in Figure 4.37. Figure 4.38 shows the compressive stress distribution along the centre line along the width of the laminate at different loading stages. Each curve represents the ratio of average compressive stress of all 0° laminae with respect to compressive strength. It can be seen that before global buckling takes place, stress distributes pretty evenly (the solid curve in Figure 4.38). Once global buckling takes place, stress concentration arises but still not significant (the dash curve in Figure 4.38). As compressive load continues to increase, delamination propagation takes place and the position of concentrated stress moves along with the developing delamination front. Just before the laminate collapses, significant stress concentration is observed and peak compressive stress appears far away from the initial delamination front (the dot curve in Figure 4.38). Therefore, the damage mechanism of this model can be reasonably described as follows. Buckling deformation of delaminated area triggers stress concentration as well as delamination propagation. As delamination propagates, concentrated stress increases along with the moving delamination front. Once concentrated stress exceeds its material strength, in-plane failure initiates and spreads over the laminate width rapidly, leading collapse of the entire laminate. Therefore, failure load of this model is determined by delamination propagation. However, the collapse is caused by in-plane failure.

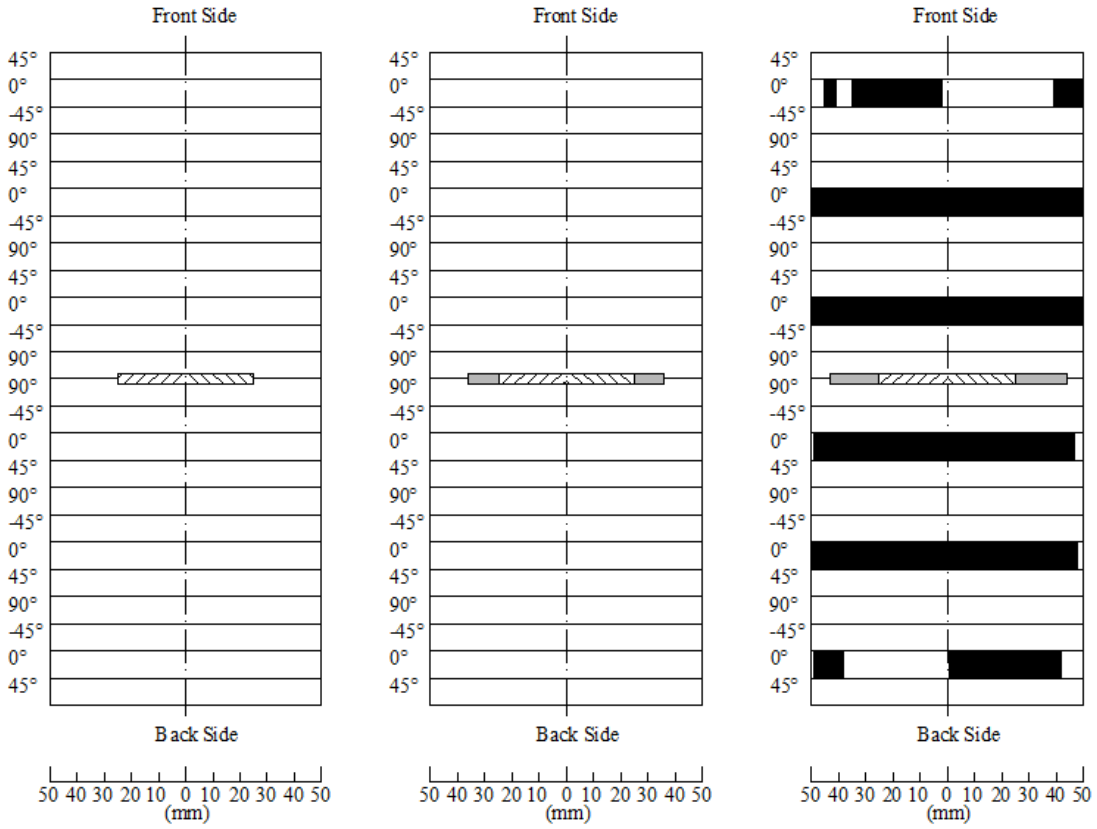

Figure 4.35 Schematic damage process of N_1_12_12_R25

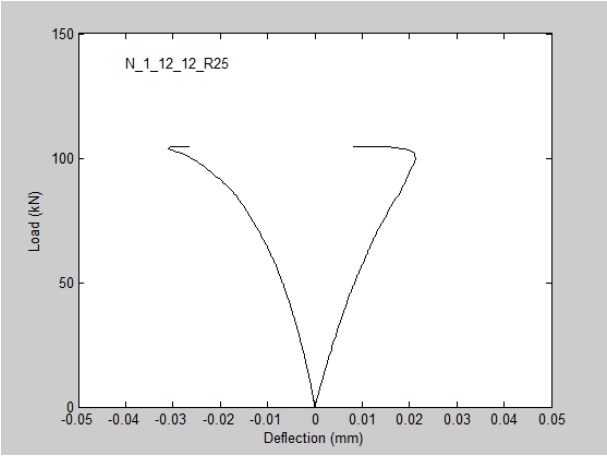

Figure 4.36 Deflection of central point versus load of N_1_12_12_R25

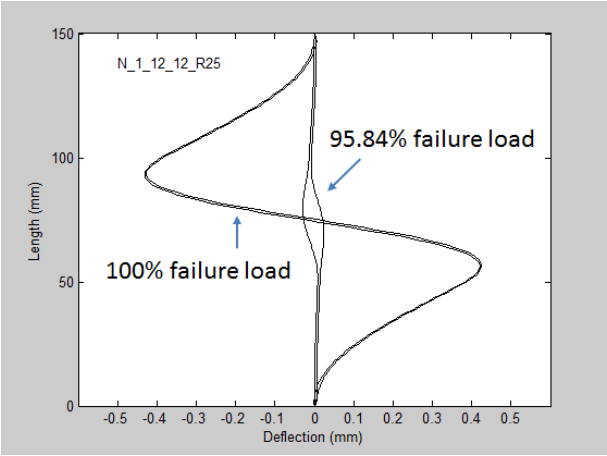

Figure 4.37 Deformation along centre line along the length at different load level of N_1_12_12_R25

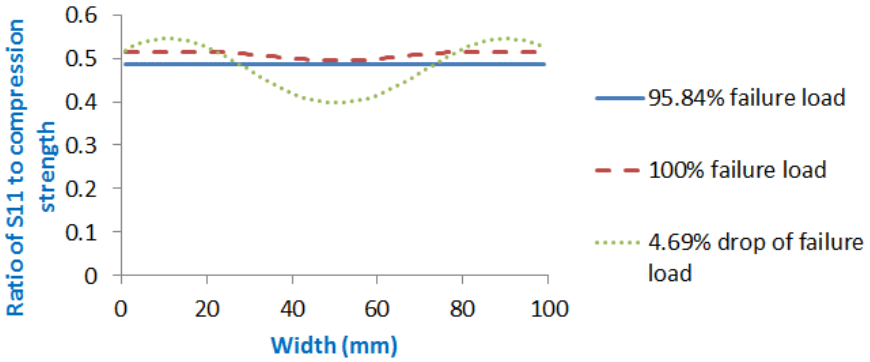

Figure 4.38 Ratio of compressive stress in 0° laminae to compressive strength versus laminate width at different load levels of N_1_12_12_R25

N_1_12_12_R20 is analysed next. Figure 4.39 demonstrates the failure process and it is similar to that of N_1_12_12_R25. However, the difference is that before catastrophic failure takes place, the propagation length of delamination is shorter than that of N_1_12_12_R25, about 7mm. The deflection variation of the central points of both sublaminates during the loading process is plotted in Figure 4.40. It can be seen that at beginning both sublaminates split at the mid-plane and bend outwards, respectively. When the compressive load reaches about 87.6% failure load, deflections of both sublaminates gradually move towards one side, rather than moving towards the mid-plane as in the case of N_1_12_12_R25 in Figure 4.36. However, this discrepancy does

not affect the overall deformation. The abrupt change of deflection is also the consequence of conversion from local buckling to global buckling. This can be confirmed through the deformation of centre line along the length in Figure 4.41. After global buckling, significant stress concentration is observed in the zones around the delamination front, which is shown by green curve in Figure 4.43. Compared with the stress distribution in model N_1_12_12_R25, it is found higher concentrated stress arises in the zones around the delamination front. In a word, the damage mechanism of this model is the same as that of N_1_12_12_R25.

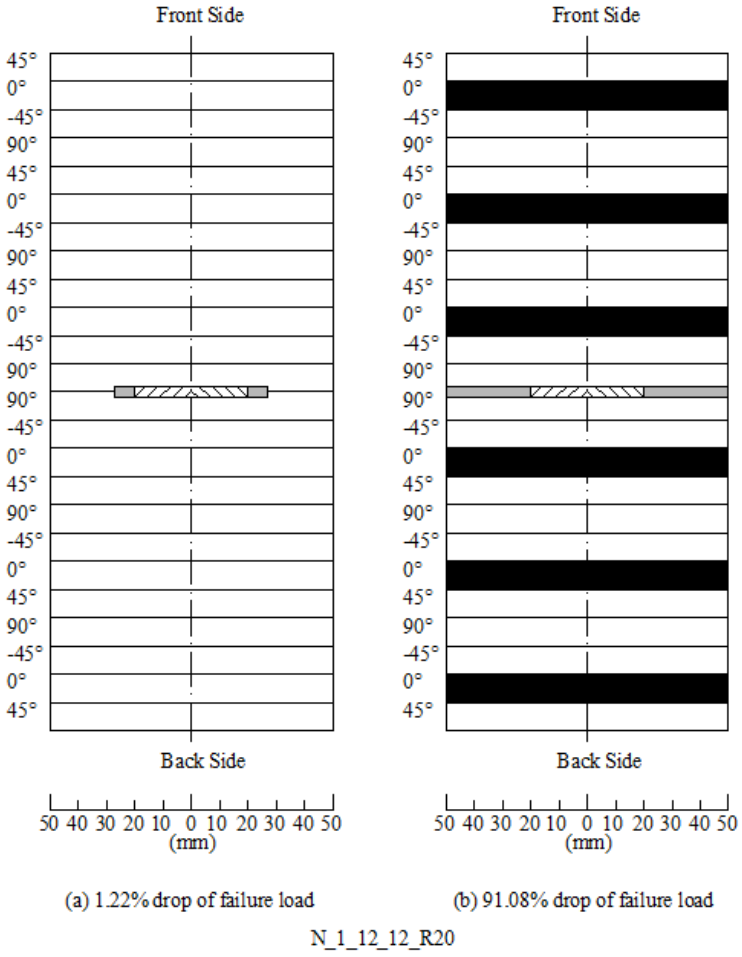

Figure 4.39 Schematic damage process of N_1_12_12_R20

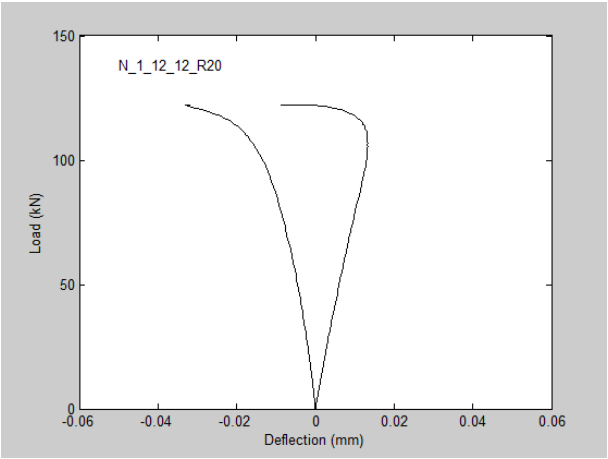

Figure 4.40 Deflection of central point of N_1_12_12_R20

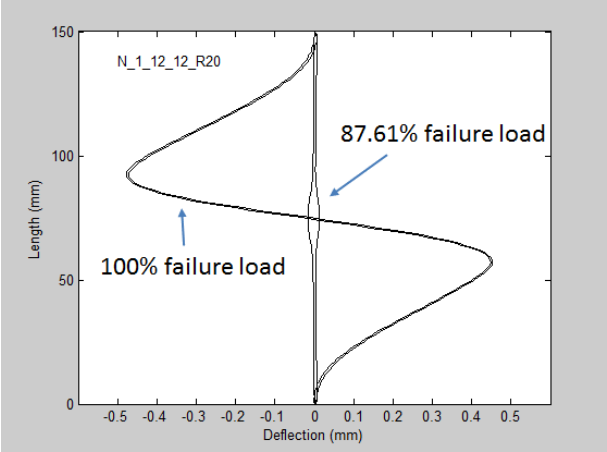

Figure 4.41 Deformation along centre line along the length at different load level of N_1_12_12_R20

N_1_12_12_R15 is analysed on the third case. Figure 4.42 demonstrates the damage process. As it is almost the same as that N_1_12_12_R20, it will not be described repeatedly. However, there are two points worth mentioning. The first is that the propagation length of delamination decreases further before catastrophic failure takes place, only about 1mm. The second is that the average stress distributing along the width is higher than previous two cases while the stress

concentration becomes less obvious (red curve in Figure 4.43). This indicates that as the delamination size decreases, delamination propagation is more and more difficult to take place and the laminate deforms more and more like an intact plate. It can be imaged that below a threshold size of delamination, delamination propagation would not take place and the laminate deforms and collapses as an intact plate.

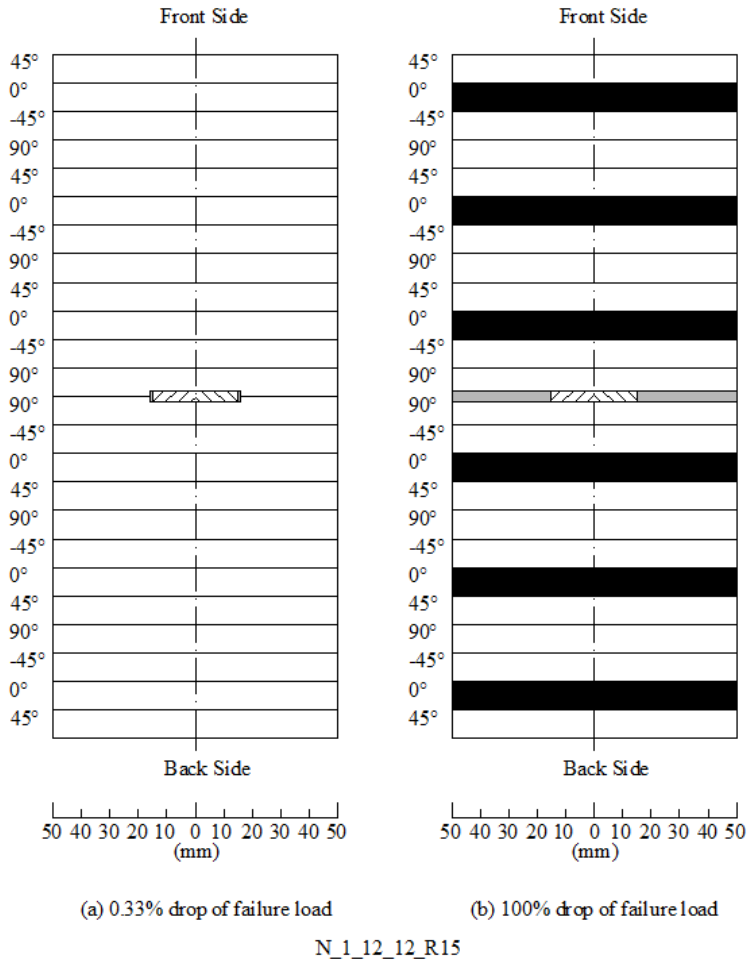

Figure 4.42 Schematic damage process of N_1_12_12_R15

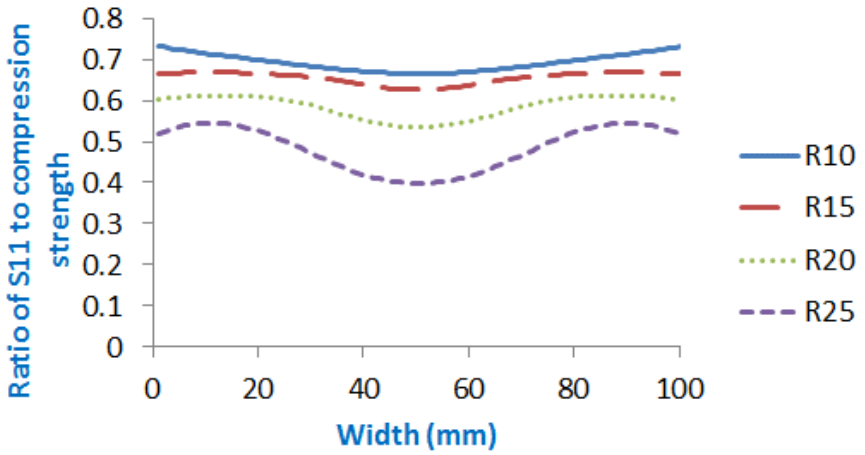

Figure 4.43 Ratio of compressive stress in 0° laminae to compressive strength versus laminate width at failure load among different models

Actually, the presumption above can be confirmed in model N_1_12_12_R10. Figure 4.44 demonstrates the damage process, from which delamination propagation is not observed all the way. Figure 4.45 shows the deflection variation of the central point of both sublaminates during the loading process. It is found that up to 71% failure load global buckling takes place. The deformation along the centre line along the length doesn't form a sinusoidal wave but a hump towards one side (Figure 4.46). The damage mechanism of this model is excessive bending due to global buckling, and delamination propagation is not observed at all.

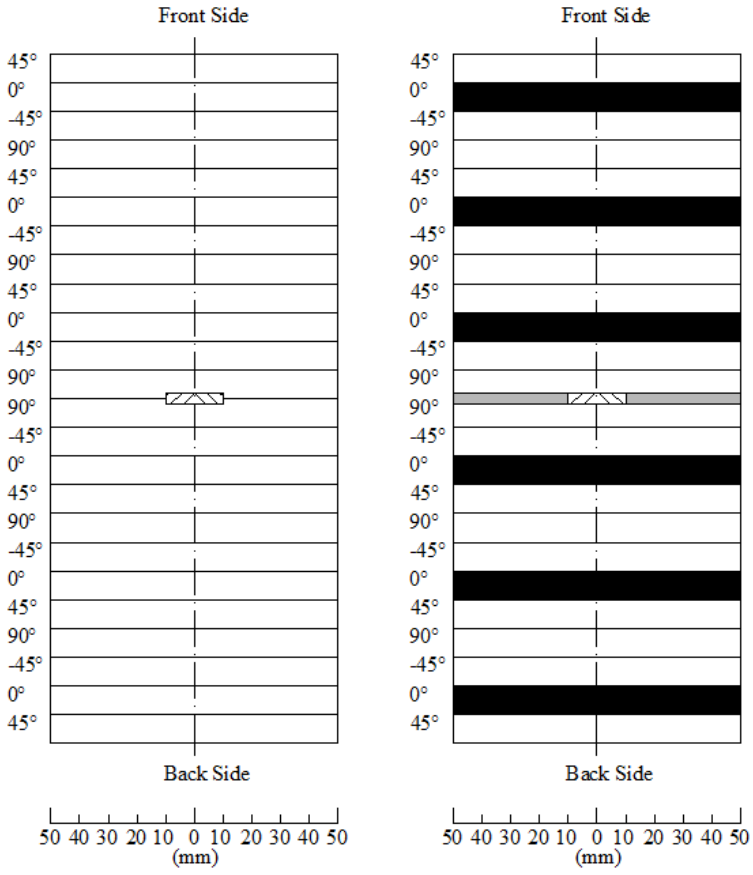

Figure 4.44 Schematic damage process of N_1_12_12_R10

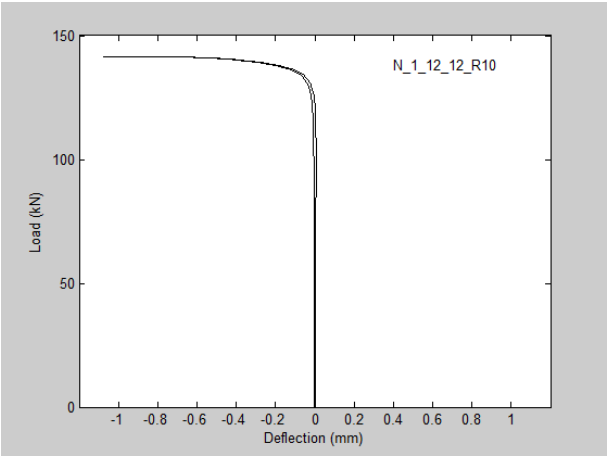

Figure 4.45 Deformation central points of both sublaminates in of N_1_12_12_R10

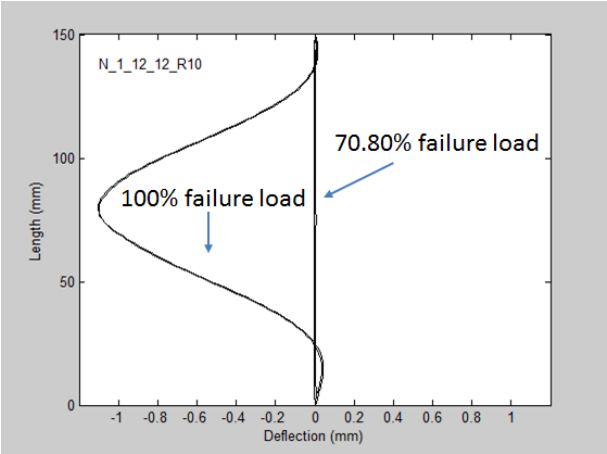

Figure 4.46 Deformation along centre line along the length at different load level of N_1_12_12_R10

As another extreme case, the delamination size in this sub-group is increased into 40mm in terms of radius. Figure 4.47 shows the load-displacement curve of N_1_12_12_R40, in which a long process of fluctuation is observed. This is due to large extent of delamination propagation before the final collapse of the whole laminate, which is quite similar to that of N_1_8_16_R40.

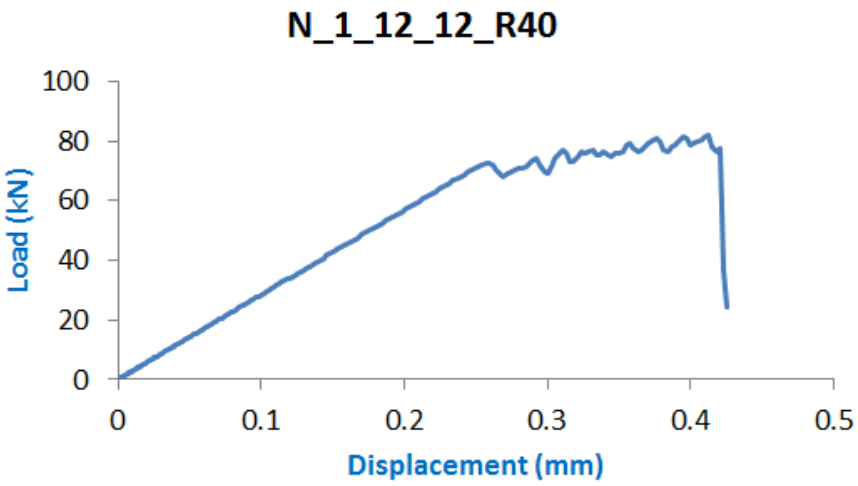

Figure 4.47 Load-displacement curve of N_1_12_12_R40

4.8.1.4 Comparison of failure load

Part of the failure loads in this group are compared in a bar chart of Figure 4.48. It is found the failure load of the sub-group of FE models bearing delamination in the mid-plane drops monotonously as the delamination size increases. This is attributed to the extent of delamination propagation. The larger extent of delamination propagation, the earlier and higher stress concentration arises, and, consequently, the earlier laminate collapses. In contrast, the sub-group bearing delamination in the eighth interface demonstrates a significant drop when initial delamination size increases from 15mm to 20 mm in terms of radius due to different damage mechanism. With smaller initial delamination, laminate is prone to fail integrally and shows higher load sustainability. The sub-group bearing delamination in the fourth interface has the lowest failure load. This is because two sublaminates sustain compressive load separately and the thinner sublaminate buckles and fails to withstand compressive load in the early stage. This also explains why the failure loads in this sub-group are very close to each other. Actually, although according to previous analysis that the failure load in this sub-group is determined by delamination propagation, the twenty-layer sublaminate plays the main role of sustaining the compressive load.

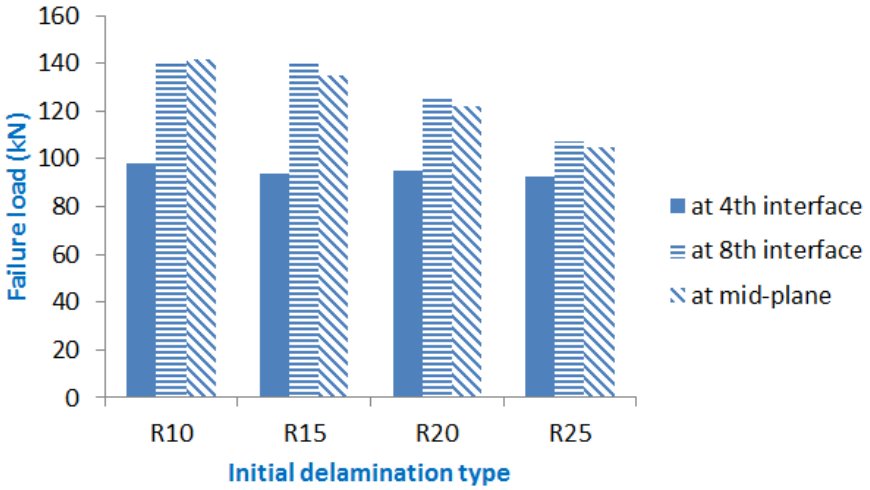

Figure 4.48 Comparison of failure load of FE models bearing single delamination

4.8.2 Uniform multiple delaminations

4.8.2.1 Three delaminations

For N_3_R15 there is neither fibre breakage nor delamination propagation at failure load. After the failure load, delamination in the mid-plane propagates about 10mm towards both side edges symmetrically and some tiny propagation, about 2mm, takes place in the other interfaces on the both sides (Figure 4.49(a)). All this happens at 2.09% drop of failure load. After that, at about 46.59% drop of failure load, massive fibre breakage is observed in the outmost 0° laminae expanding about 18mm and all interfaces fail (Figure 4.49(b)). These events happen abruptly and transiently, within only 0.0059mm increase of compressive displacement. Therefore, this delamination propagates in an unstable way before fibre breakage happens. The damage mechanism is concluded as delamination propagation determines failure load but in-plane failure triggers final collapse of the entire laminate.

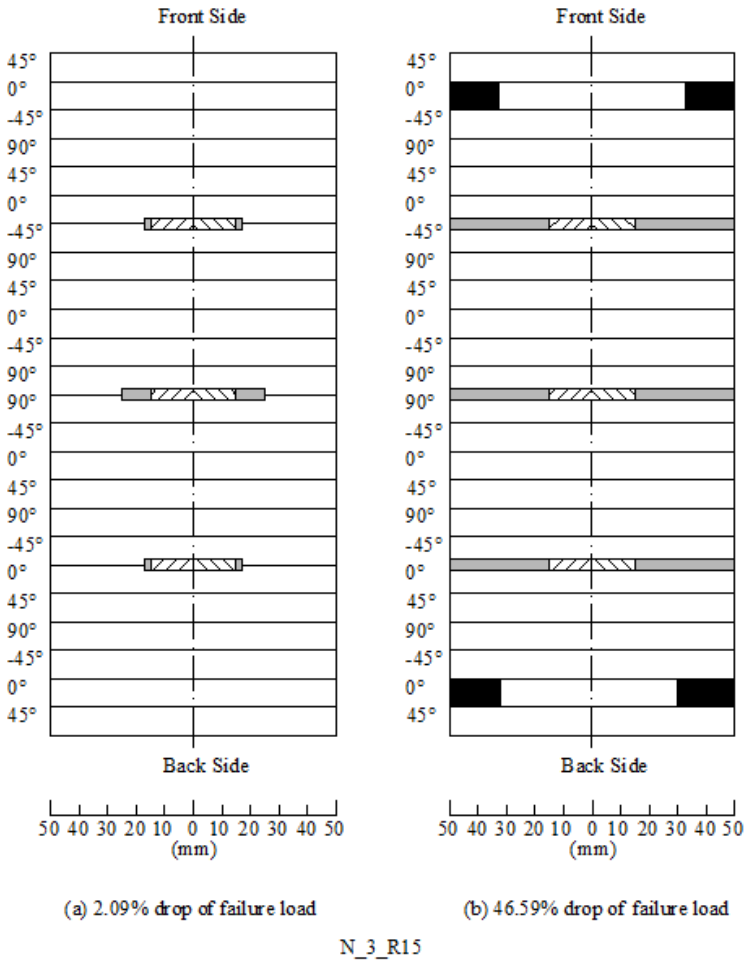

Figure 4.49 Schematic damage process of N_3_R15

The damage process of N_3_R20 is similar. Up to the failure load, neither fibre breakage nor delamination propagation is observed (Figure 4.50(a)). After that, delamination propagation initiates and develops until the load level drops 11.94% of failure load when initial fibre breakage takes place, followed by the collapse of the entire laminate collapses. Therefore, the damage mechanism is the same as that of previous case. However, the period between the failure load

and the fibre failure takes a little bit longer, and the compressive displacement from the failure load to the fibre failure is 0.0109mm, almost twice of the precious one.

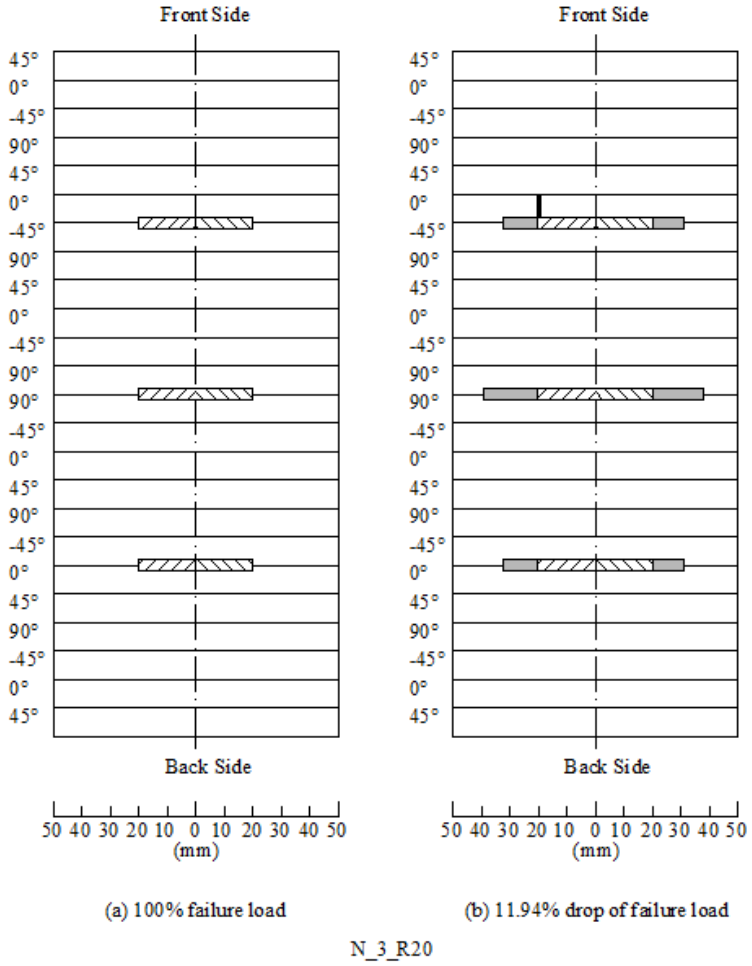

Figure 4.50 Schematic damage process of N_3_R20

The damage process of N_3_R25 is found a little different from previous two cases in this group. When failure load is reached, delamination in the central interface has already propagated about 8mm in one direction and 4mm in the opposite (Figure 4.51(a)). In the meantime, the compressive displacement between failure load and initial fibre breakage (of which the damage

state is demonstrated in Figure 4.51(b)) is about 0.027mm. This doubles the value of N_3_R20 which is already twice of that of N_3_R15. This suggests that the delamination propagation speed slow down as delamination size increases.

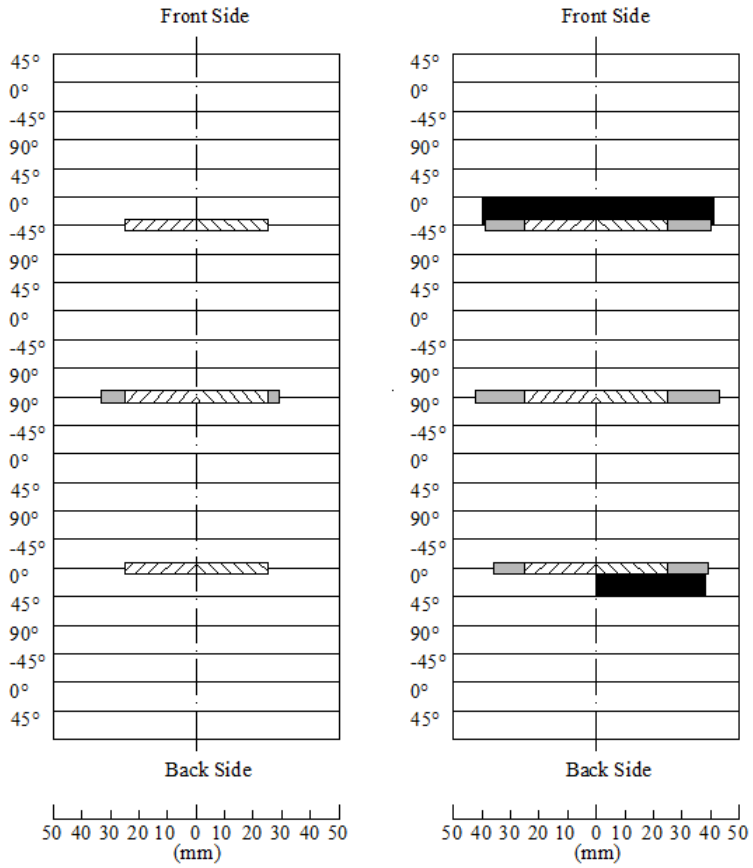

Figure 4.51 Schematic damage process of N_3_R25

4.8.2.2 Five delaminations

The damage process of N_5_R15 is similar to that of N_3_R15. Again, neither delamination propagation nor in-plane failure is observed up to the failure load. However, massive delamination propagation as much as 8mm emerges in each interface abruptly (Figure 4.52(a)) before in-plane failure initiates. Soon after, in-plane failure in a zone of maximum 20mm inwards from side edge is observed in all 0° laminae (Figure 4.52(b)). Therefore, it is estimated that delamination propagates more than 15mm before initial in-plane failure takes place.

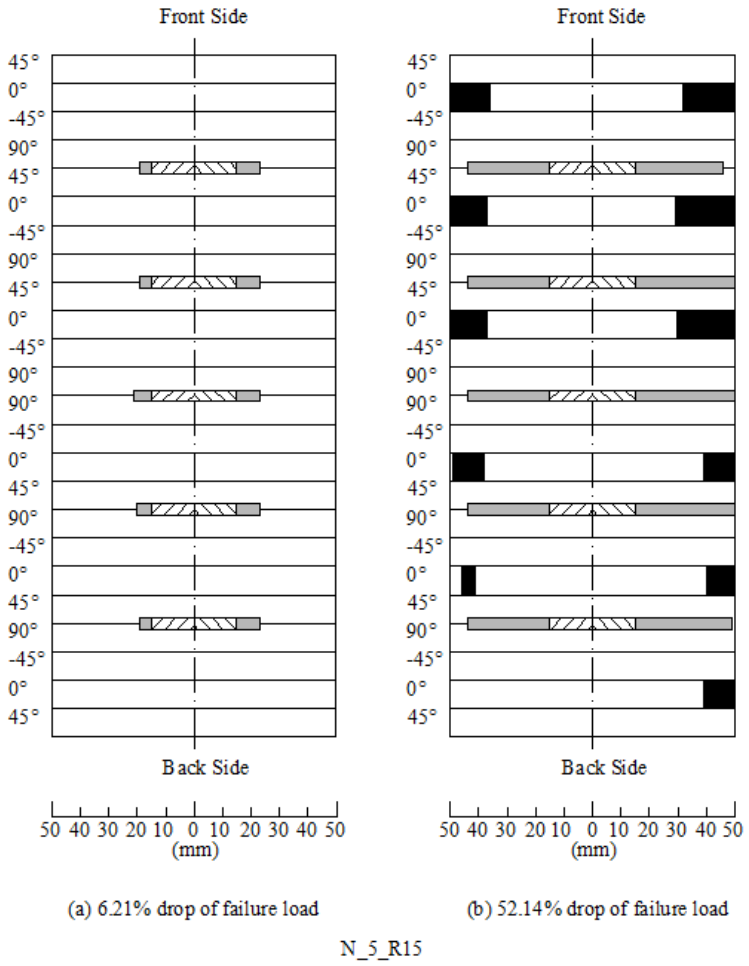

(a) 6.21% drop of failure load (b) 52.14% drop of failure load

N_5_R15

Figure 4.52 Schematic damage process of N_5_R15

The damage process of N_5_R20 and N_5_R25 almost repeat that of N_5_R15 and hence are not described except for their schematic representations in Figure 4.53 and Figure 4.54. However, it is worth mentioning that in this group the compressive displacement from failure loads to initial in-plane failure are 0.0048, 0.0049 and 0.005mm, respectively. The delamination propagation in this group is unstable. The size of the delamination has not shown any strong relationship to the propagation speed as was observed in the previous group.

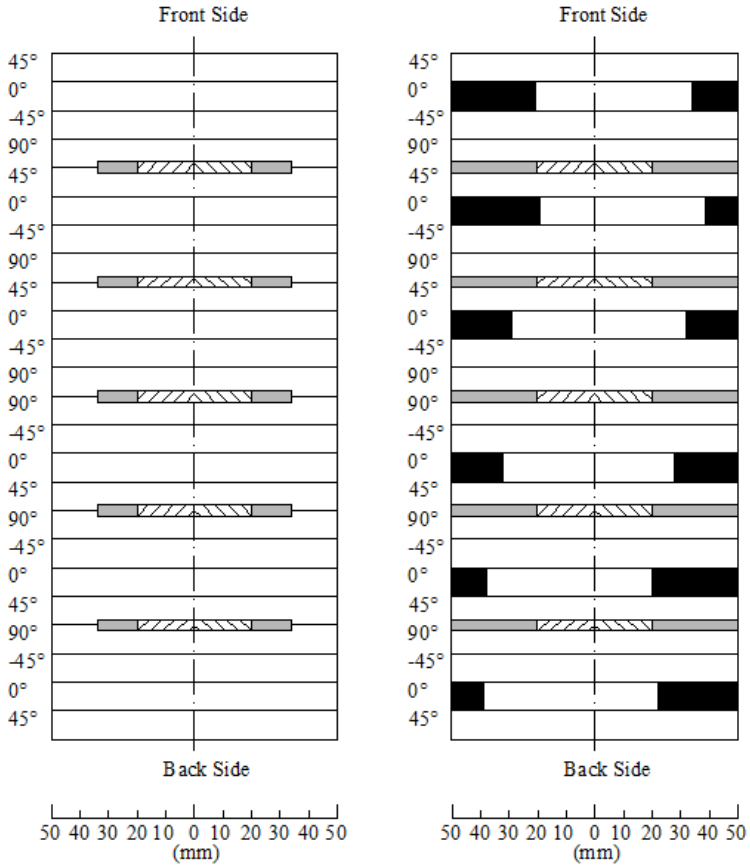

Figure 4.53 Schematic damage process of N_5_R20

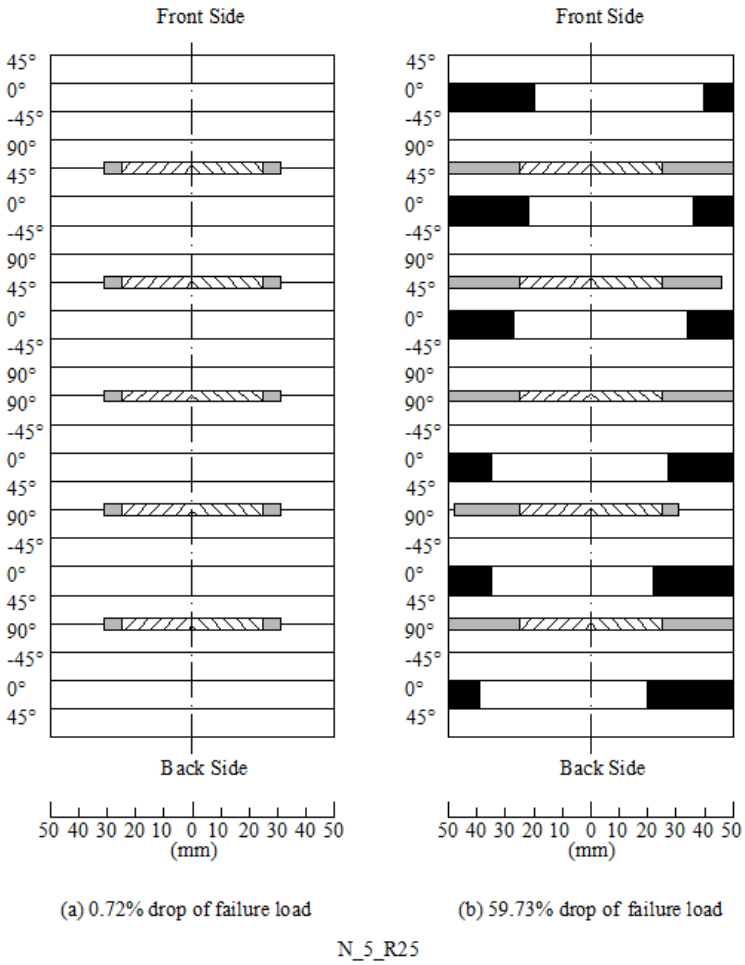

Figure 4.54 Schematic damage process of N_5_R25

4.8.2.3 Seven delaminations

For N_7_R15, delamination propagation is only observed in the central interface, about 3mm, up to the failure load (Figure 4.55(a)). After that, propagation initiates and develops successively in other interfaces. When in-plane failure is observed, delamination has already propagated by about 25mm in the outmost interfaces, (Figure 4.55(b)).

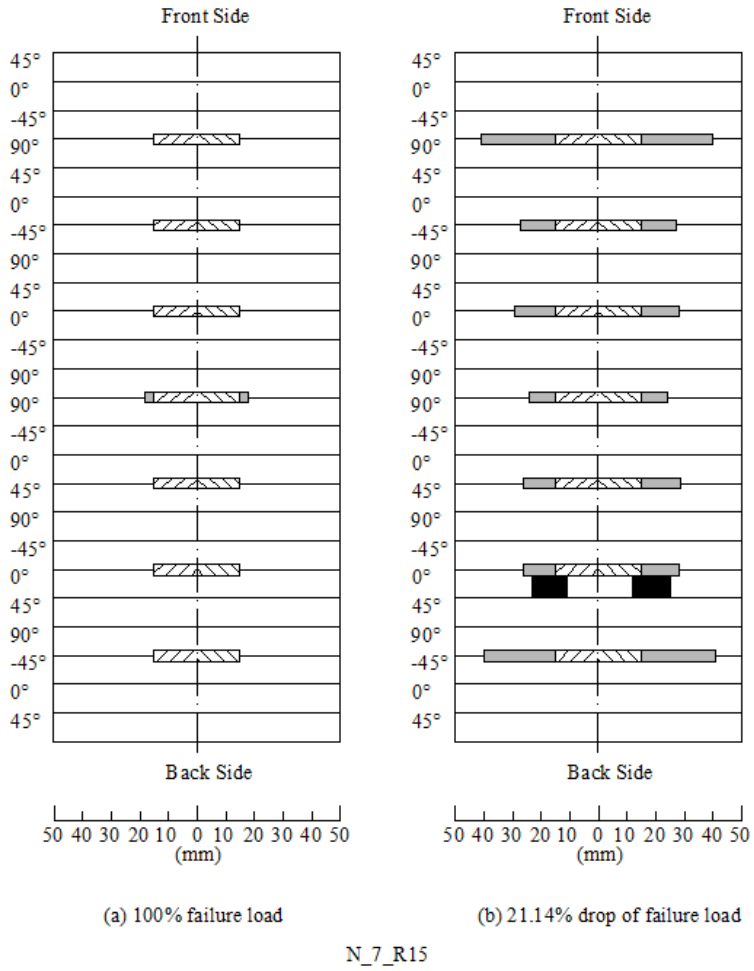

Figure 4.55 Schematic damage process of N_7_R15

N_7_R20 and N_7_R25 are found to have similar damage process as that of N_7_R15, which are shown in Figure 4.56 and Figure 4.57, respectively. However, as the number of delaminations increases, the number of plies in each sublaminate reduce and the effective properties of sublaminates differ from each other. As a result, the stresses born by each sublaminate vary. Therefore, in this group, initial in-plane failure is observed in some sublaminates, rather than all sublaminates in previous groups. In-plane failure is found around the initial delamination front rather than propagated delamination front. These phenomena reveal that as the number of delaminations increases, the extent of delamination propagation reduces gradually before

in-plane failure occurs. This is because with increasing number of delaminations, the thickness of each sublaminate reduces as well as the subsequent bending stiffness. The ERR built up at the delamination front reduces consequently. In the meantime, stress concentration picks up at the early stage in the loading process as the thinner sublaminates buckles easily shedding the stresses to the area next to the delaminated zone. In a word, in-plane failure due to stress concentration gradually becomes more dominant as the number of delamination increases.

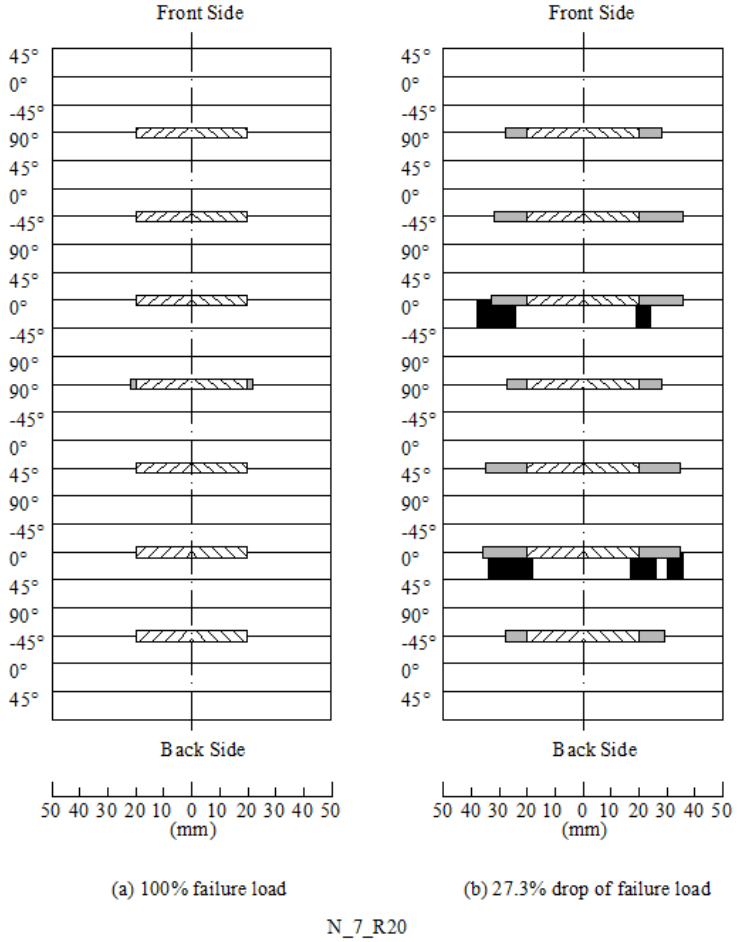

Figure 4.56 Schematic damage process of N_7_R20

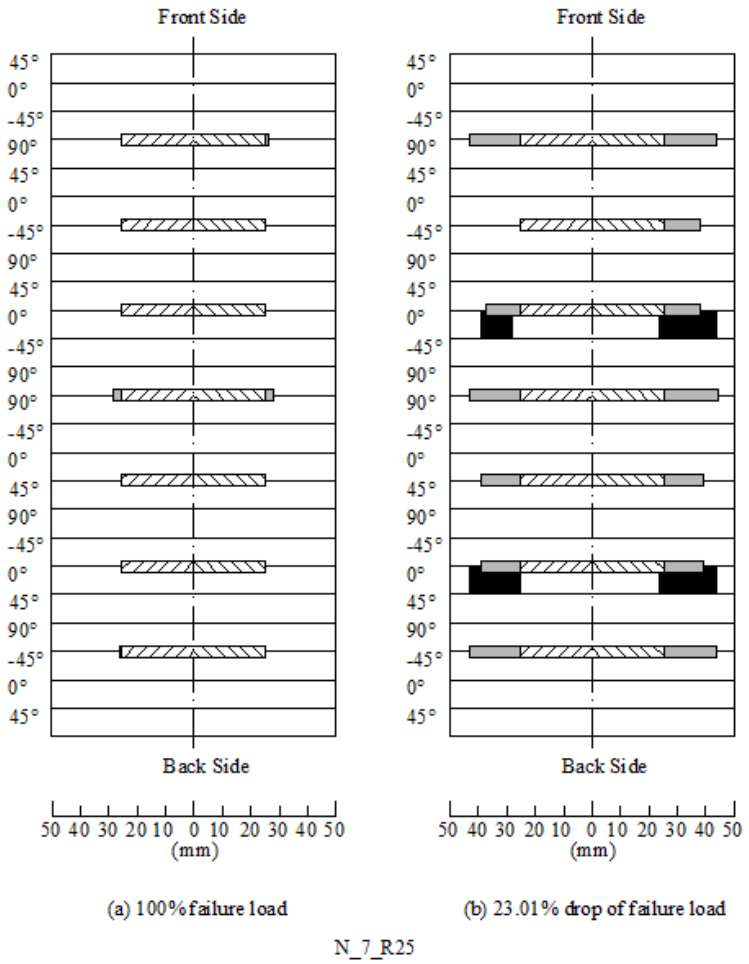

Figure 4.57 Schematic damage process of N_7_R25

4.8.2.4 Eleven delaminations

For N_11_R15, the damage process is schematically demonstrated in Figure 4.58. Only tiny amount of delamination propagation, about 3mm, has been observed up to the failure load. Soon after, without large extent of delamination propagation, initial failure is observed around the initial delamination front and the whole laminate collapses consequently. Similar damage process is also found in N_11_R20 and N_11_R25, which are shown in Figure 4.59 and Figure 4.60, respectively. From both of them less delamination propagation is found. This supports the

statement drawn above that the role of delamination propagation is fading away as the number of delaminations increases.

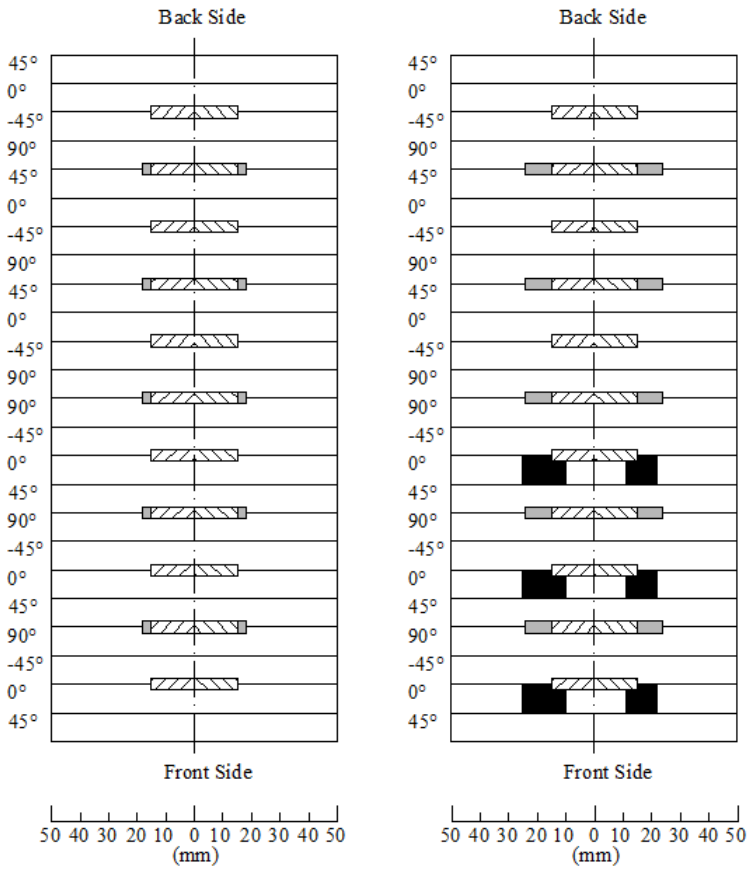

Figure 4.58 Schematic damage process of N_11_R15

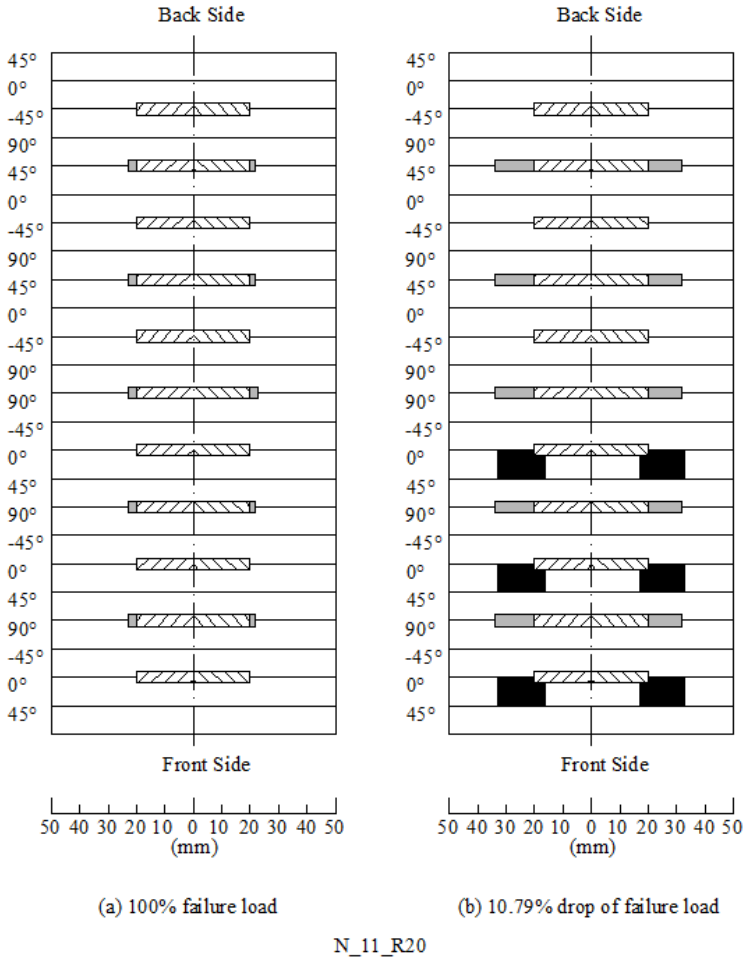

Figure 4.59 Schematic damage process of N_11_R20

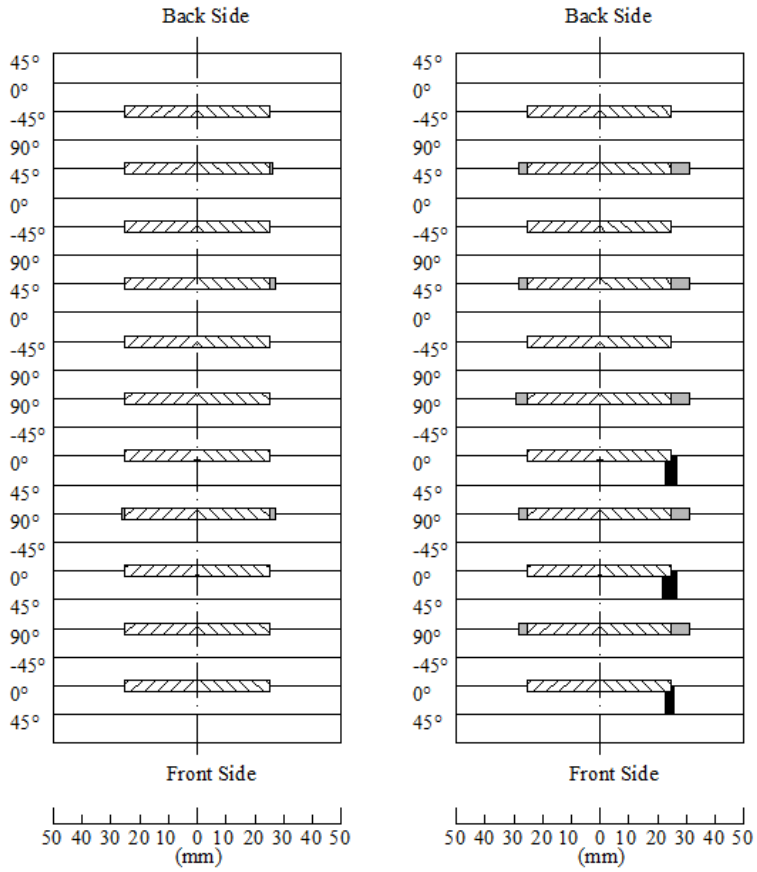

Figure 4.60 Schematic damage process of N_11_R25

There is an extreme case that the delamination size increases to 40mm in terms of radius. Figure 4.61 shows the damage process. It is found that during the whole process, delamination propagation is not observed, and the in-plane failure initiating around the delamination front leads the collapse of the whole laminate.

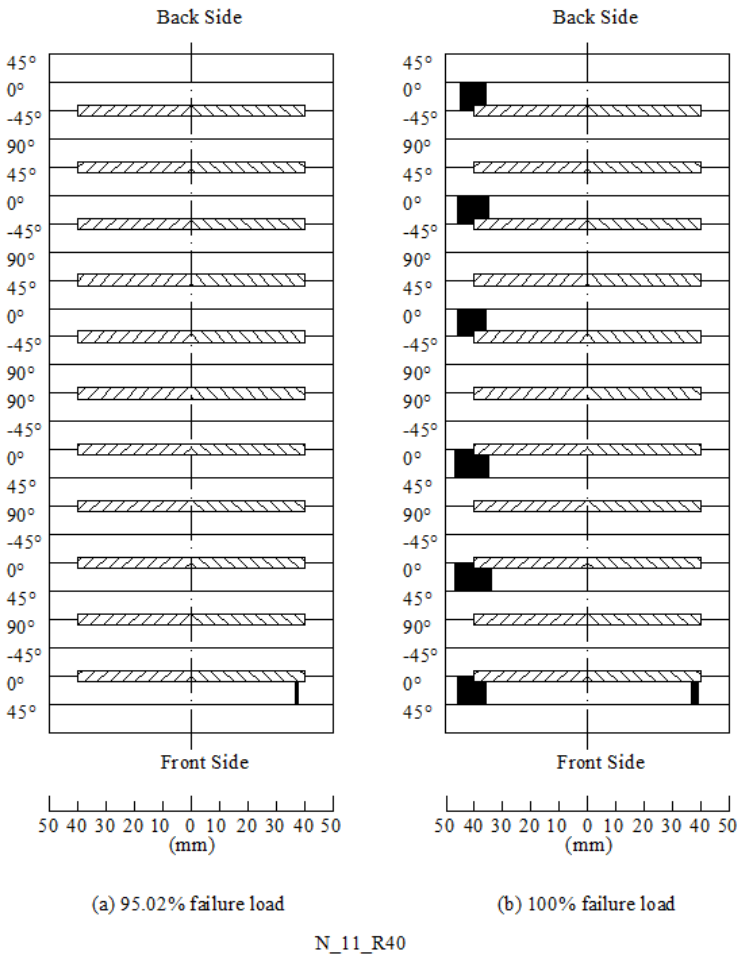

Figure 4.61 Schematic damage process of N_11_R40

4.8.2.5 Twenty-three delaminations

Finally, the number of delaminations increases to its limit. In this case, similar damage process to previous cases is observed again, which is shown from Figure 4.62 to Figure 4.64 schematically. However, only very small amount of delamination propagation is observed in this group up to failure load. Soon after, the laminate collapses. Additionally, in-plane failure is observed initiating at exactly the initial delamination front. All the observations made again confirm the conclusion that delamination propagation is less and less significant as the number of delaminations

increases. It is reasonable to expect that, below a threshold size of initial delamination, propagation will not take place before in-plane failure initiates and subsequent collapse of the entire laminate.

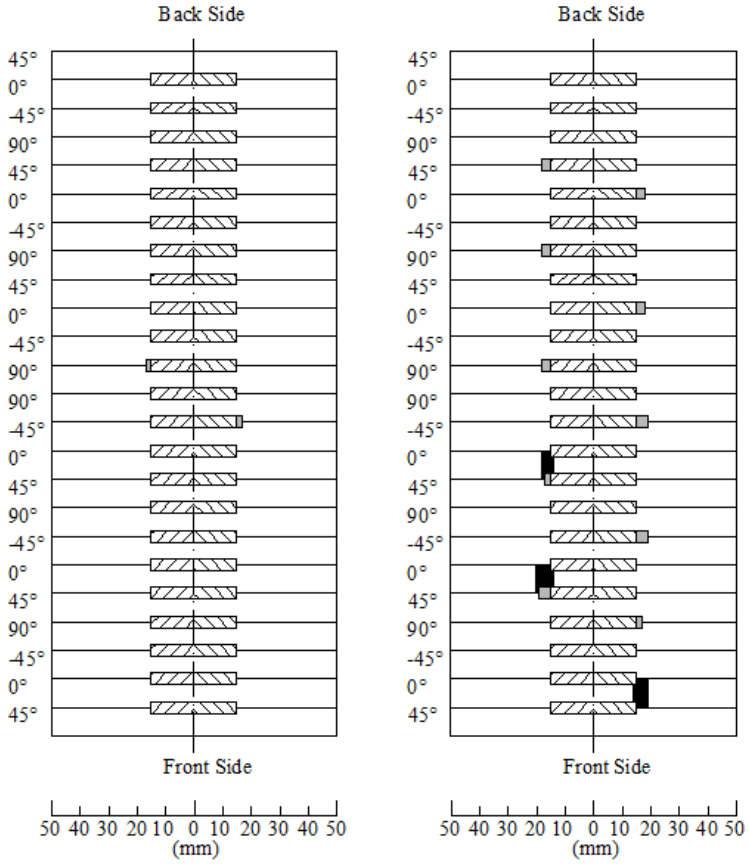

Figure 4.62 Schematic damage process of N_23_R15

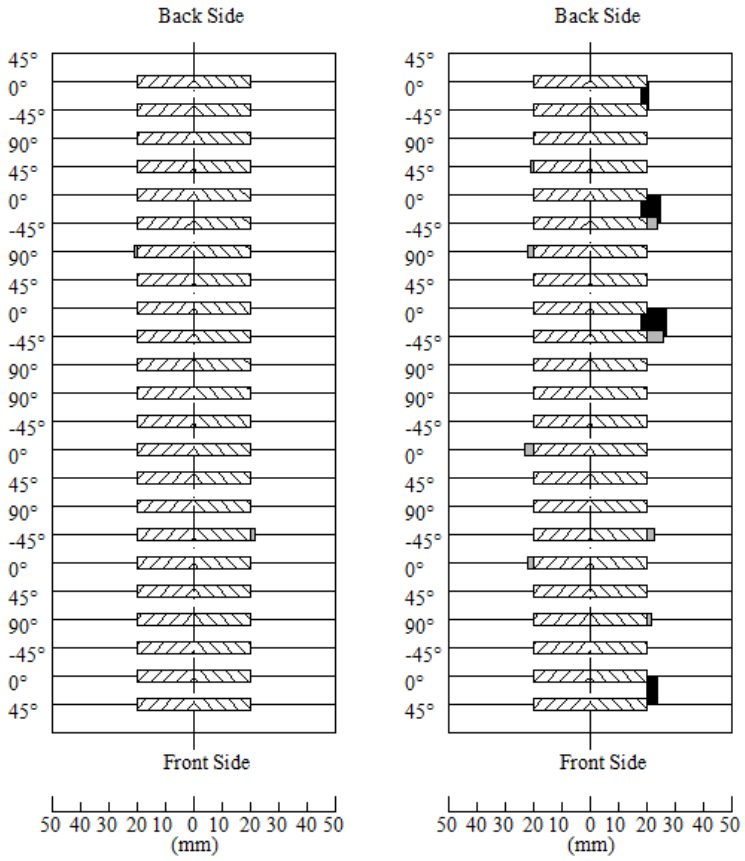

(a) 99.26% failure load (b) 100% failure load

N_23_R20

Figure 4.63 Schematic damage process of N_23_R20

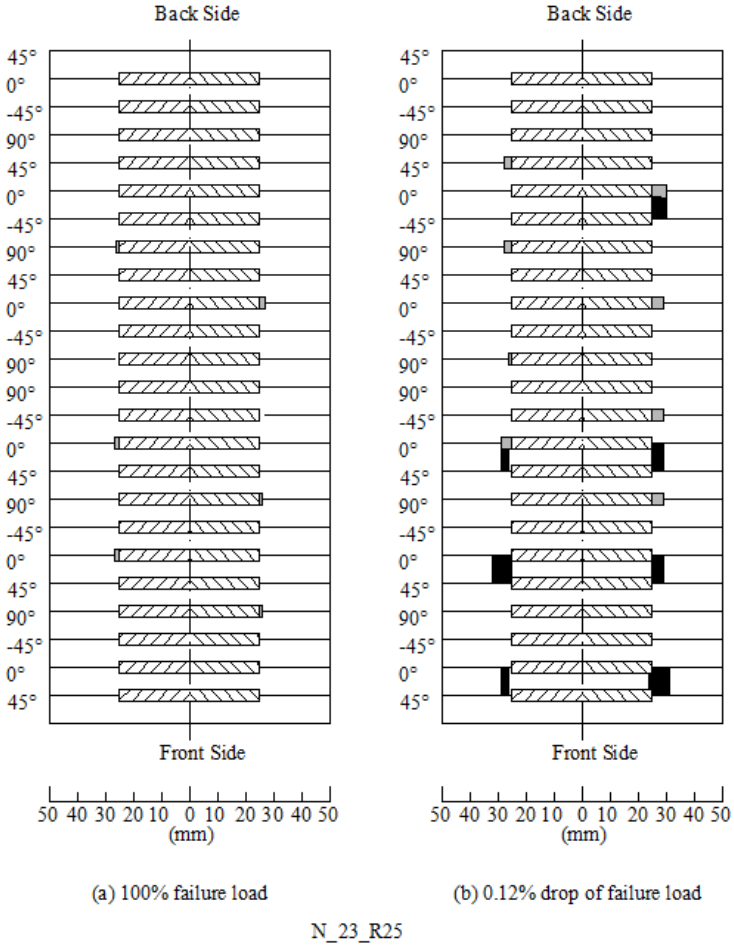

Figure 4.64 Schematic damage process of N_23_R25

There is another extreme case that the delamination size increases to 40mm in terms of radius. Figure 4.65 shows the damage process, which is almost the same of N_11_R40 that delamination propagation is not observed, and the in-plane failure initiating around the delamination front leads the collapse of the whole laminate.

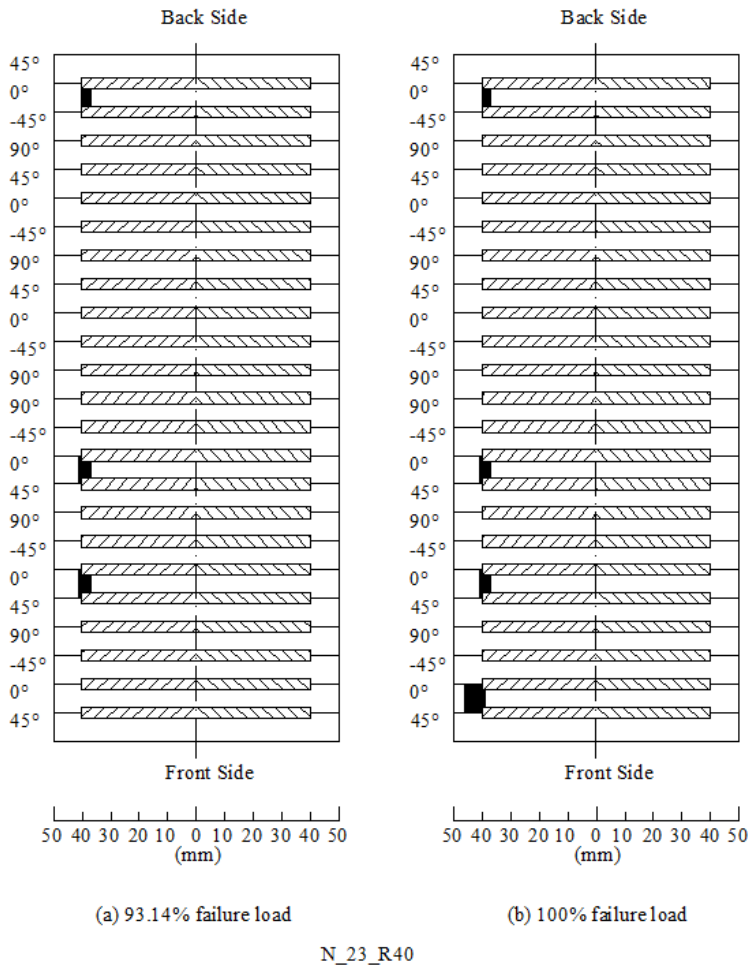

Figure 4.65 Schematic damage process of N_23_R40

4.8.3 Non-uniform multiple delaminations

4.8.3.1 Spindle shaped distribution

In this section, the model bearing multiple delaminations distributed in spindle shape in the thickness direction is investigated.

N_3_R25_Spindle is considered firstly. It is found that the failure is dominated my delamination propagation, which propagates over the width before collapse. . However, failure initiating at the

loading edge in this model rather than delaminated area leads invalid failure mode. Therefore, investigation is skipped.

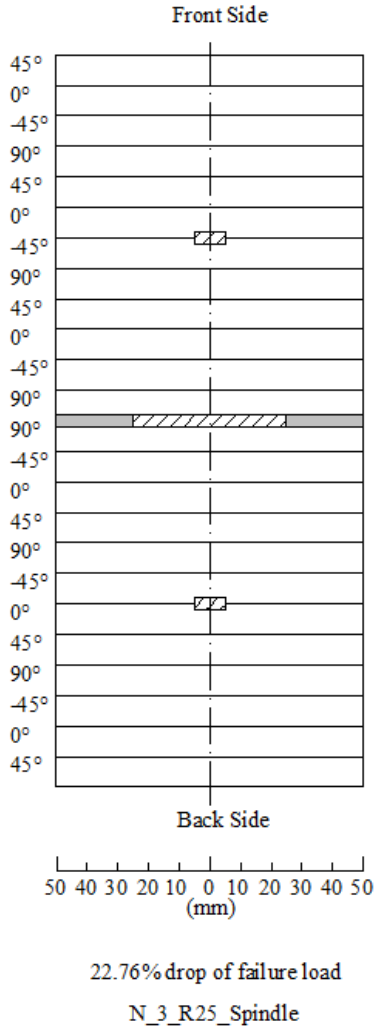

Figure 4.66 Schematic damage process of N_3_R25_Spindle

The damage process of N_5_R25_Spindle is schematically shown in Figure 4.67. It is found delamination propagation initiates at the outmost interfaces at failure load (figure on the left of Figure 4.67). Then extensive delamination propagation takes place in every interface, and finally

the laminate collapses due to in-plane failure spreading from side inwards (figure on the right of Figure 4.67). The damage process is similar to that of the model with same number of delamination but in cylindrical distribution.

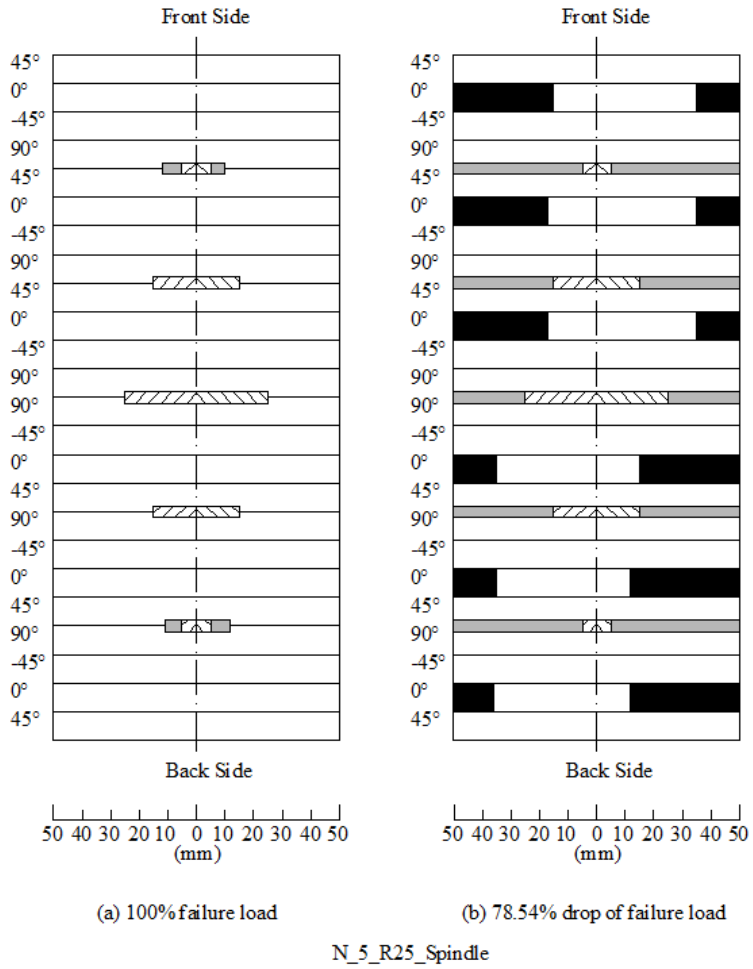

Figure 4.67 Schematic damage process of N_5_R25_Spindle

For N_7_R25_Spindle, delamination has propagated mainly in the mid-plane interface at failure load (figure on the left of Figure 4.68). Then in-plane failure initiates in all 0° laminae and the

laminate collapses (figure on the right of Figure 4.68). Its damage process is similar to that of N_5_R25_Spindle.

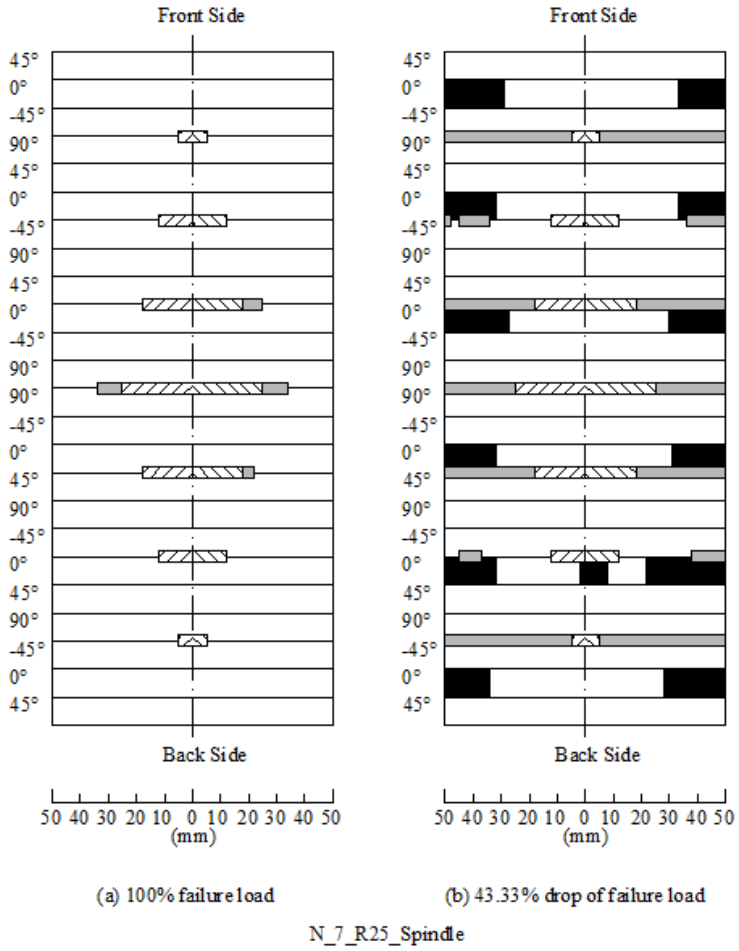

Figure 4.68 Schematic damage process of N_7_R25_Spindle

For N_11_R25_Spindle, delamination propagation takes place at the second outmost interfaces at failure load (figure on the left of Figure 4.69), which is followed by in few other interfaces before in-plane failure initiates in the zones around the delamination front of one interface (figure on the right of Figure 4.69), and then the collapse of the entire laminate.

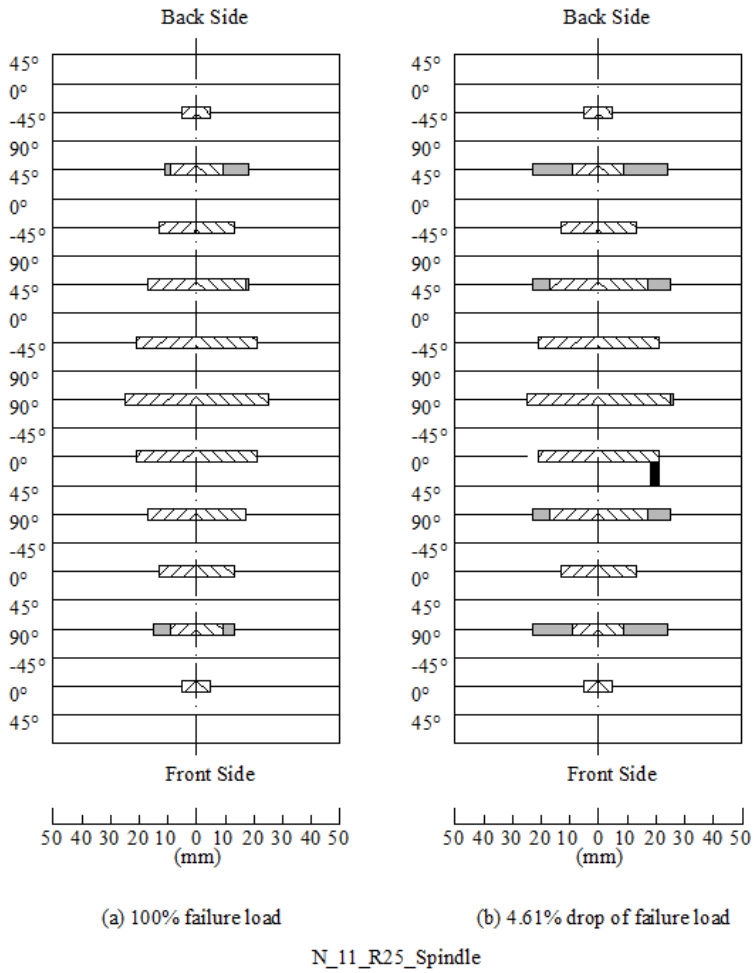

Figure 4.69 Schematic damage process of N_11_R25_Spindle

For N_23_R25_Spindle, delamination propagation of about 11mm is observed only in mid-plane interface at failure load, (figure on the left ofFigure 4.70). Beyond that only one delamination propagation is observed in another interface close to the mid-plane before the laminate collapses (figure on the right of Figure 4.70).

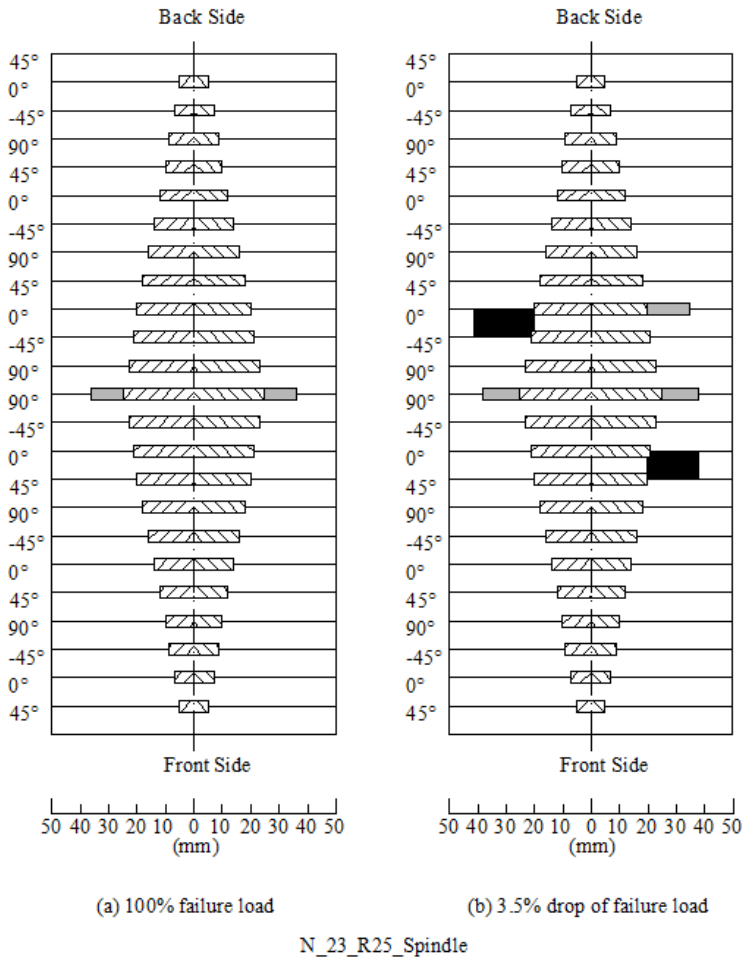

Figure 4.70 Schematic damage process of N_23_R25_Spindle

Figure 4.71 shows the deformation along the centre line along the length at failure load. It can be found that all laminates fail in global buckling, no matter what the number of delamination interface is, few or many. This aspect is different from that of cylindrical distribution, in which only local buckling occurs when number of delaminations increases. This is due to significant contrast of delamination sizes among outmost and mid-plane interfaces.

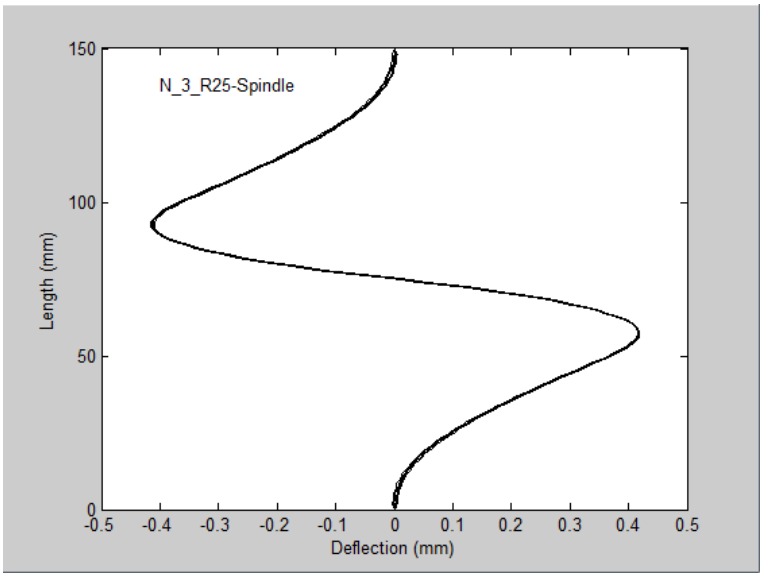
N_3_R25-Spindle
Length (mm)
Deflection (mm)
150
100
50
0
-0.5
-0.4
-0.3
-0.2
-0.1
0
0.1
0.2
0.3
0.4
0.5

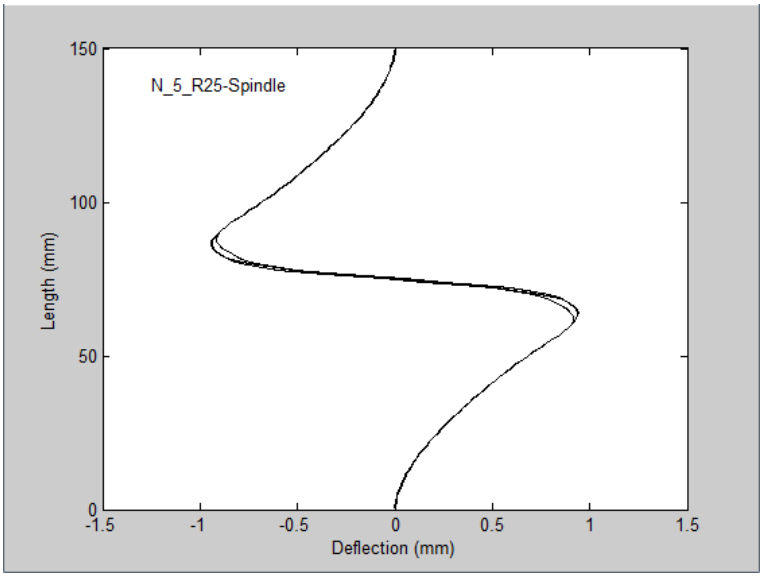
N_5_R25-Spindle
Length (mm)
Deflection (mm)
150
100
50
0
-1.5
-1
-0.5
0
0.5
1
1.5

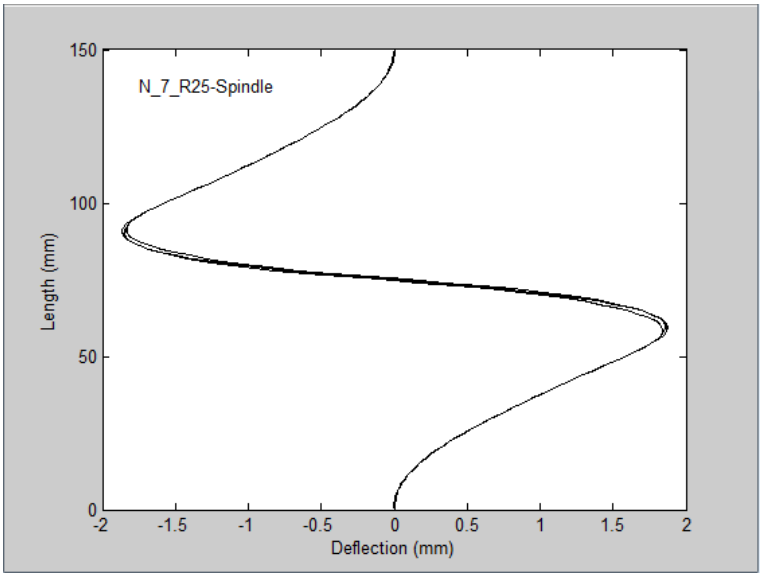
N_7_R25-Spindle
Length (mm)
Deflection (mm)
150
100
50
0
-2
-1.5
-1
-0.5
0
0.5
1
1.5
2

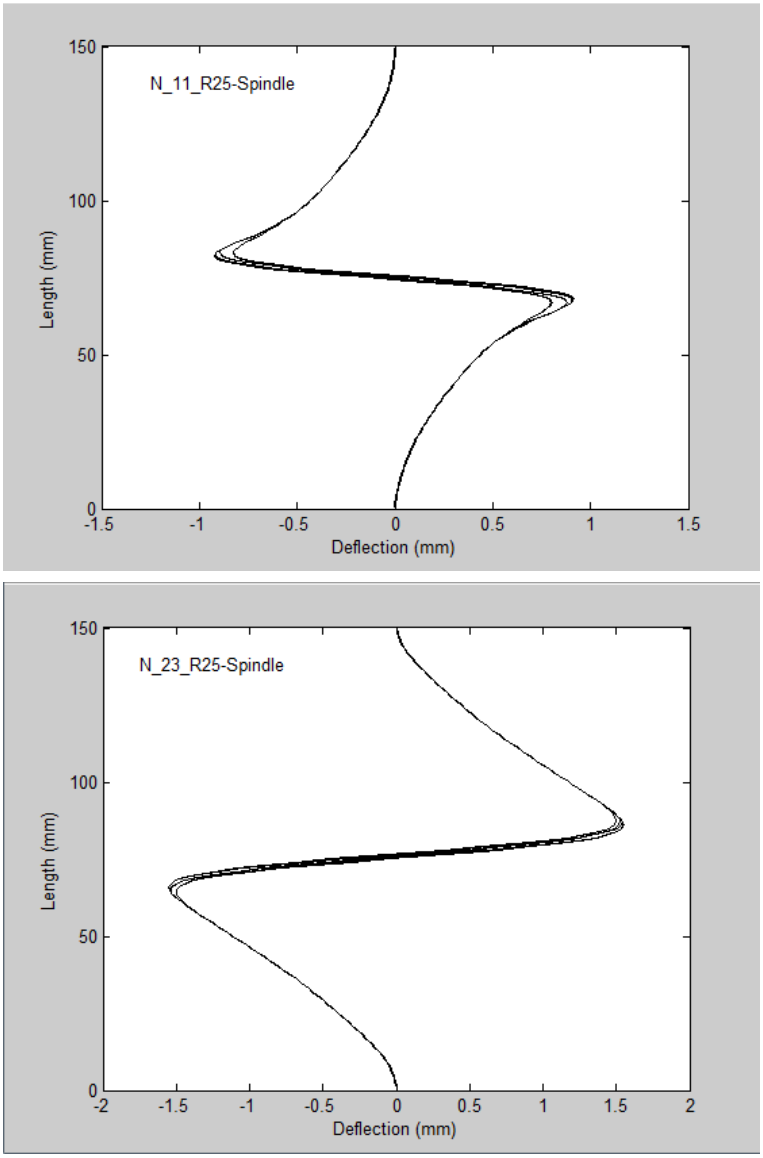

Figure 4.71 Deformation along longitudinal centre line of all models with delamination distribution in spindle shape

4.8.3.2 Cone shaped distribution

For the case with three delaminations, the damage processes are similar to each other. Figure 4.72 shows the deflection in the centre point of all sublaminates over the loading process. It is found that the outmost sublaminate on the largest delamination side loses stability first, then the middle and then the one on the other side successively. Figure 4.73 and Figure 4.74 show the

damage process of N_3_R20_Cone and N_3_R25_Cone, respectively. In both cases, some delamination propagation is observed before fibre breakage occurs. Afterwards, fibre breakage takes place and the whole laminate collapses subsequently.

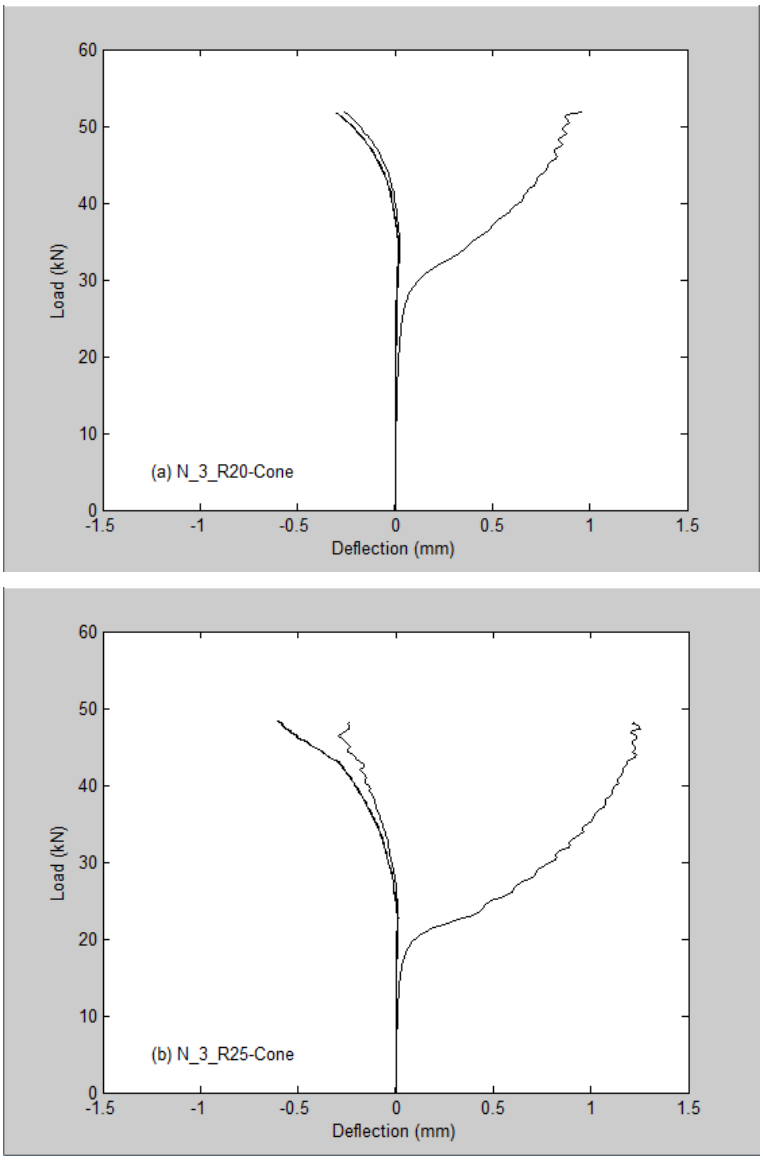

Figure 4.72 Deflection of central point versus compressive load for the model with three delaminations in cone-shape distribution of which the maximum radii are (a) 20mm and (b) 25mm

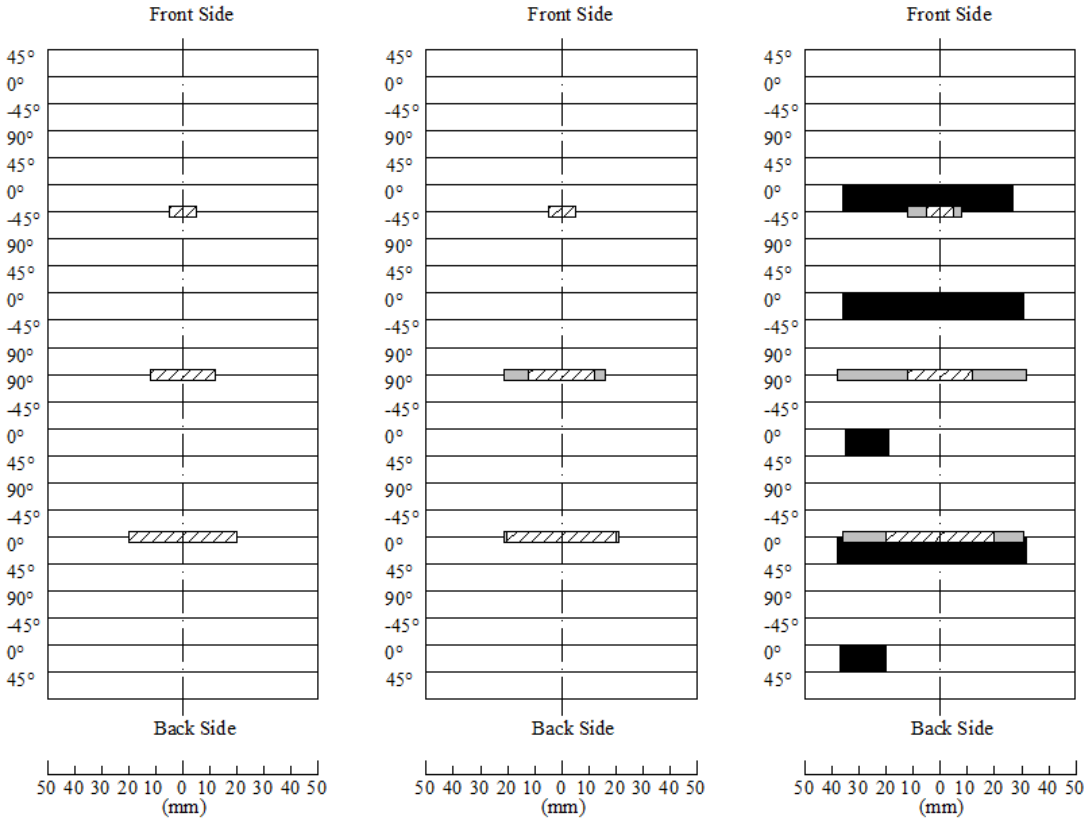

Figure 4.73 Schematic damage process of N_3_R20_Cone

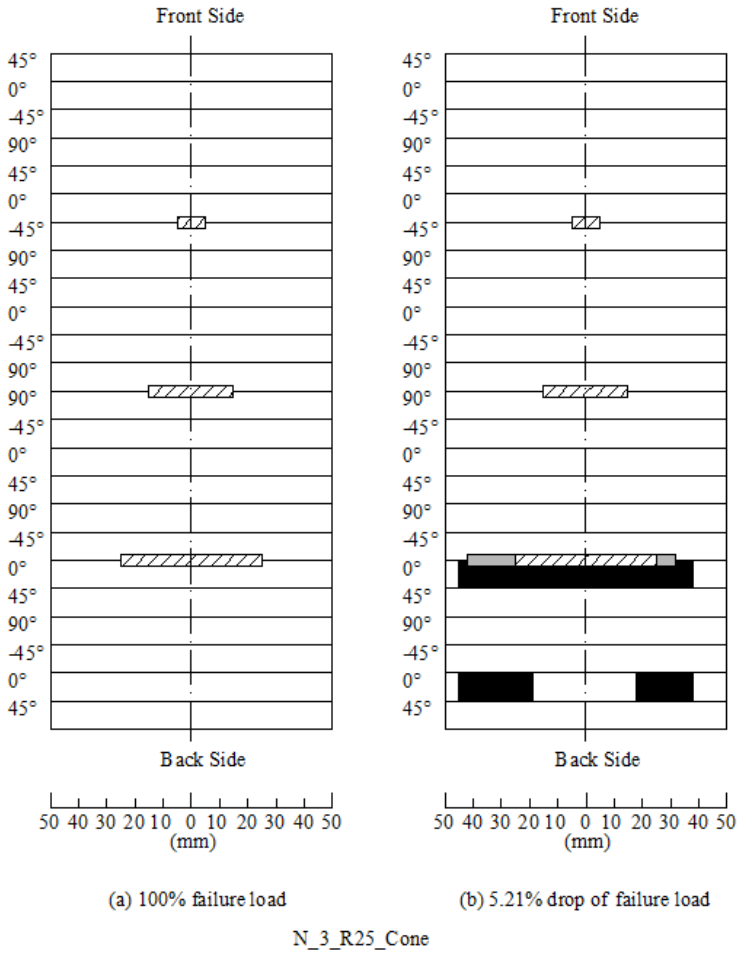

Figure 4.74 Schematic damage process of N_3_R25_Cone

In the sub-group of five delaminations, the damage mechanism is quite similar to that of previous sub-group. Figure 4.75 shows the deflection of central point of all sublaminates versus compressive load for both models. The phenomenon that successive buckling deformation of sublaminates from the largest delamination side to the smallest side is reproduced. Figure 4.76 and Figure 4.77 show the damage process of these two models, from which it can be clearly concluded that in this sub-group the failure load is determined by delamination propagation, while the whole laminate collapses due to in-plane failure.

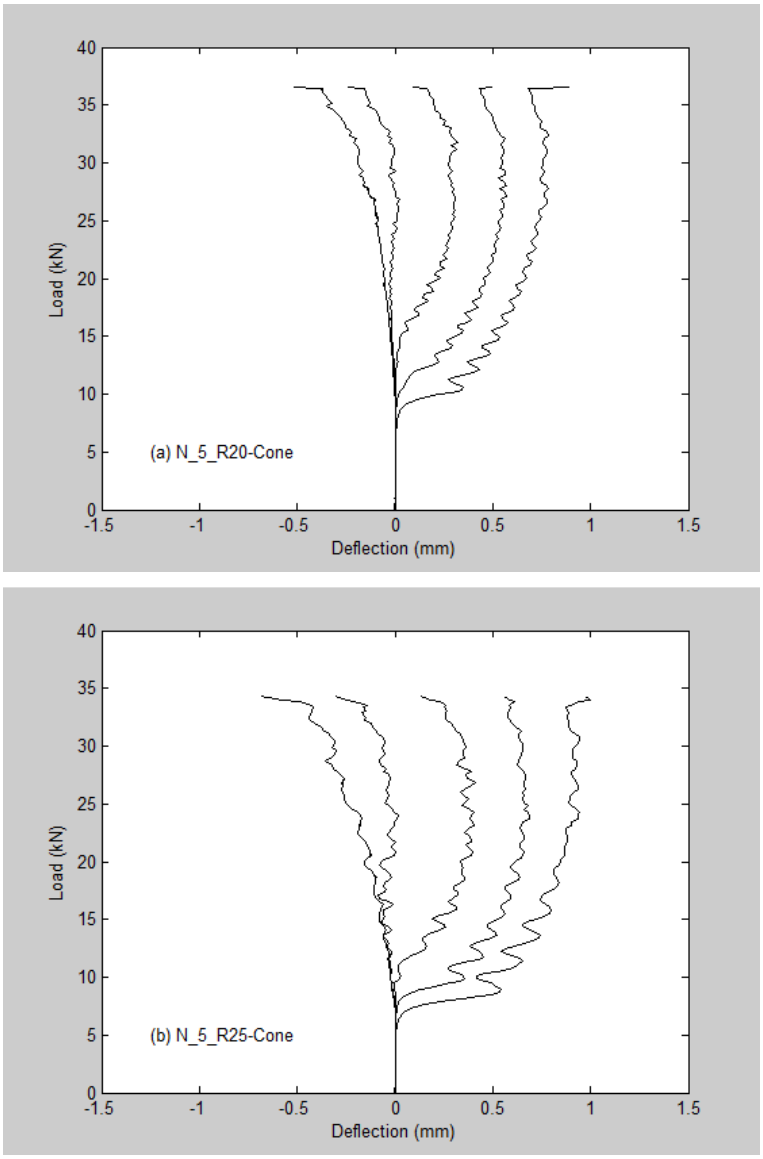

Figure 4.75 Deflection of central point versus compressive load of model with five delaminations in cone shape distribution of which the maximum radii are (a) 20mm and (b) 25mm

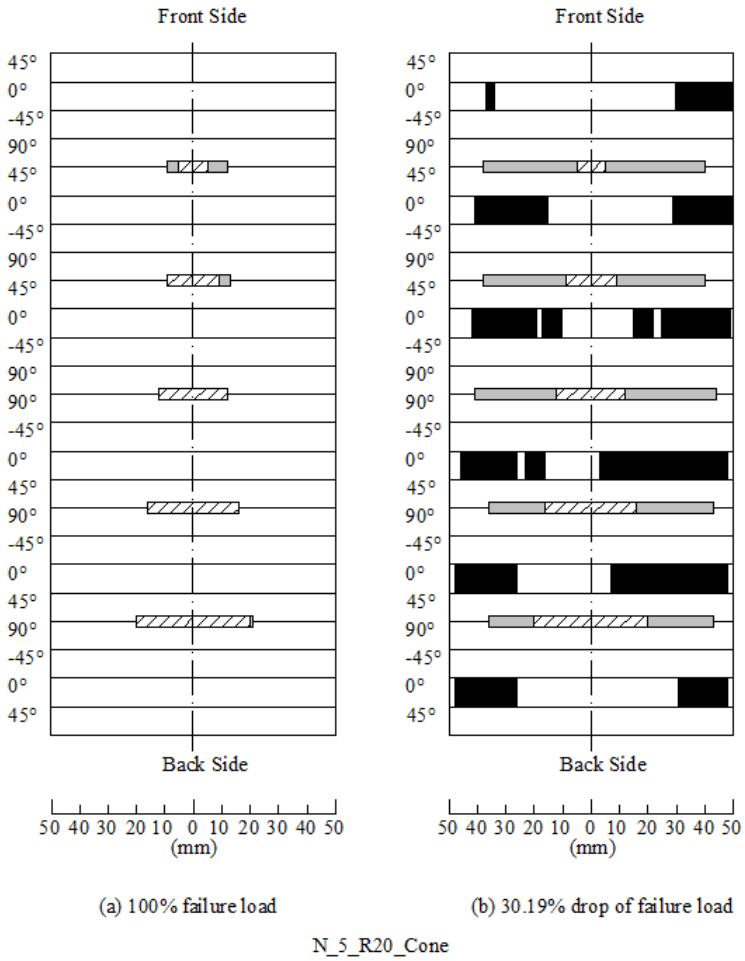

Figure 4.76 Schematic damage process of N_5_R20_Cone

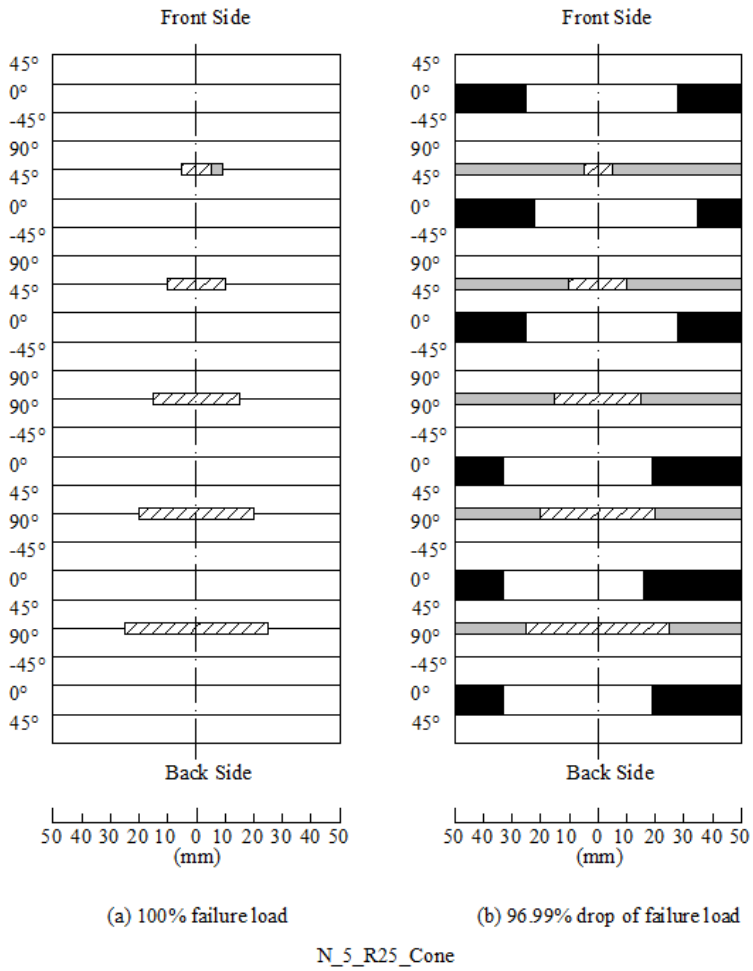

Figure 4.77 Schematic damage process of N_5_R25_Cone

In the sub-group of seven delamination, the damage mechanism is almost the same as the previous sub-groups. Successive buckling deformations of all sublaminates is observed through Figure 4.78. Figure 4.79 and Figure 4.80 show the damage process of both models.

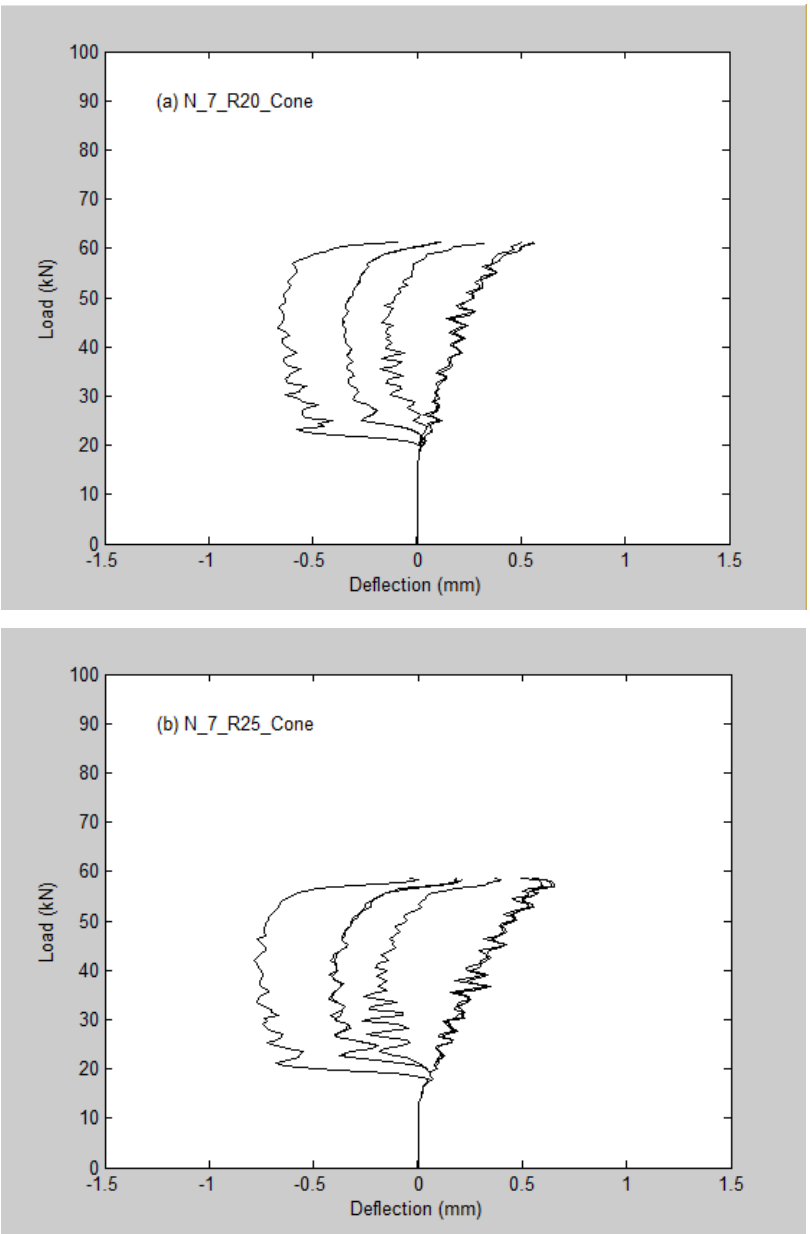

Figure 4.78 Deflection of central point versus compressive load of models with seven delaminations in cone shape distribution of which the maximum radii are (a) 20mm and (b) 25mm

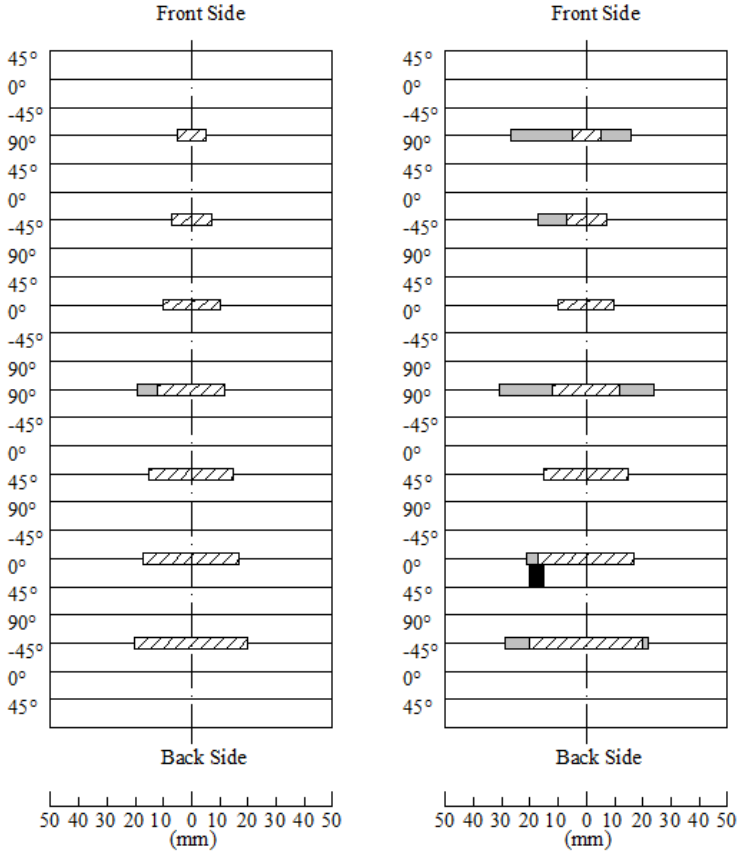

(a) 100% failure load (b) 5.83% drop of failure load

N_7_R20_Cone

Figure 4.79 Schematic damage process of N_7_R20_Cone

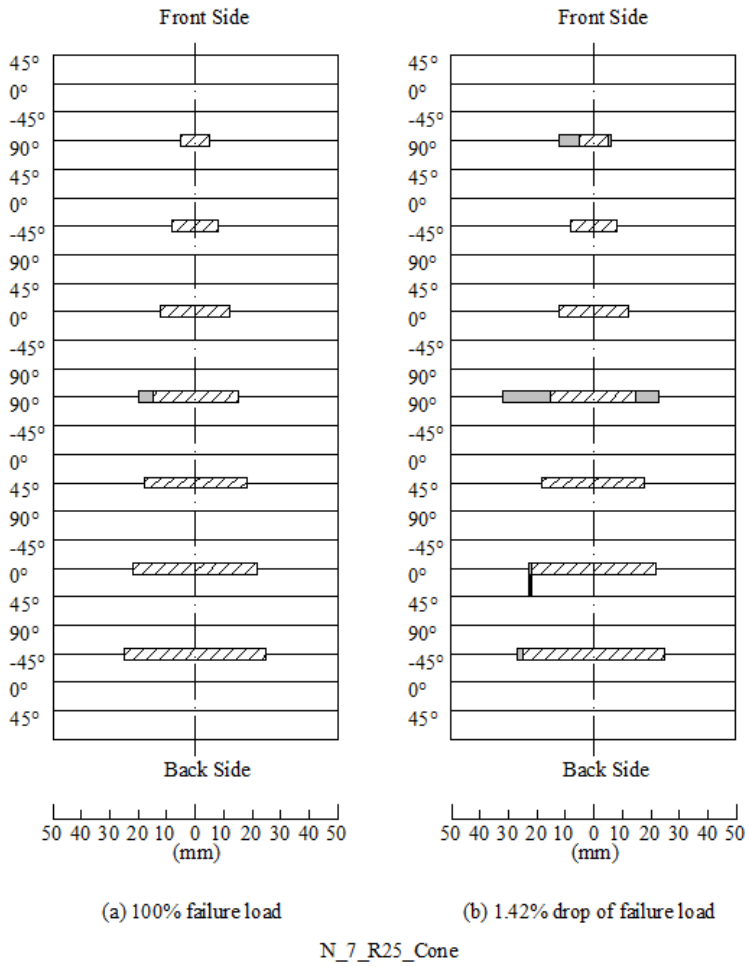

Figure 4.80 Schematic damage process of N_7_R25_Cone

Regarding N_11_R25_Cone and N_23_R25_Cone, again, successive buckling deformations of all sublaminates are observed through Figure 4.82 and Figure 4.84. Figure 4.81 and Figure 4.83 show the damage process of both models. However, it is worth mentioning that, unlike all other models in this group with cone shaped distribution pattern, in N_11_R25_Cone and N_23_R25_Cone delamination propagation has become so insignificant that in-plane failure can be concluded as the dominant failure mode.

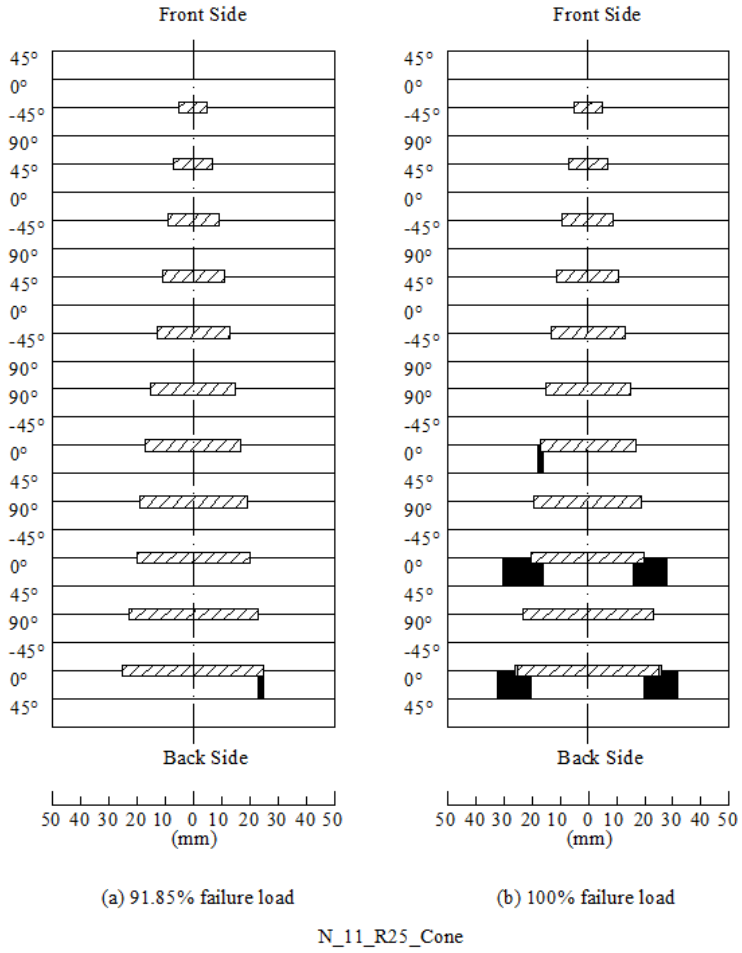

Figure 4.81 Schematic damage process of N_11_R25_Cone

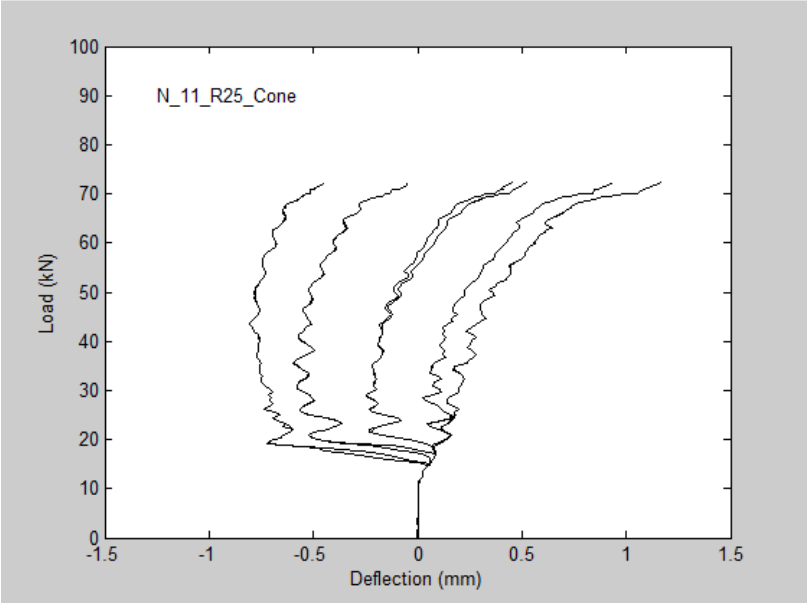

Figure 4.82 Deflection of central point versus compressive load of N_11_R25_Cone

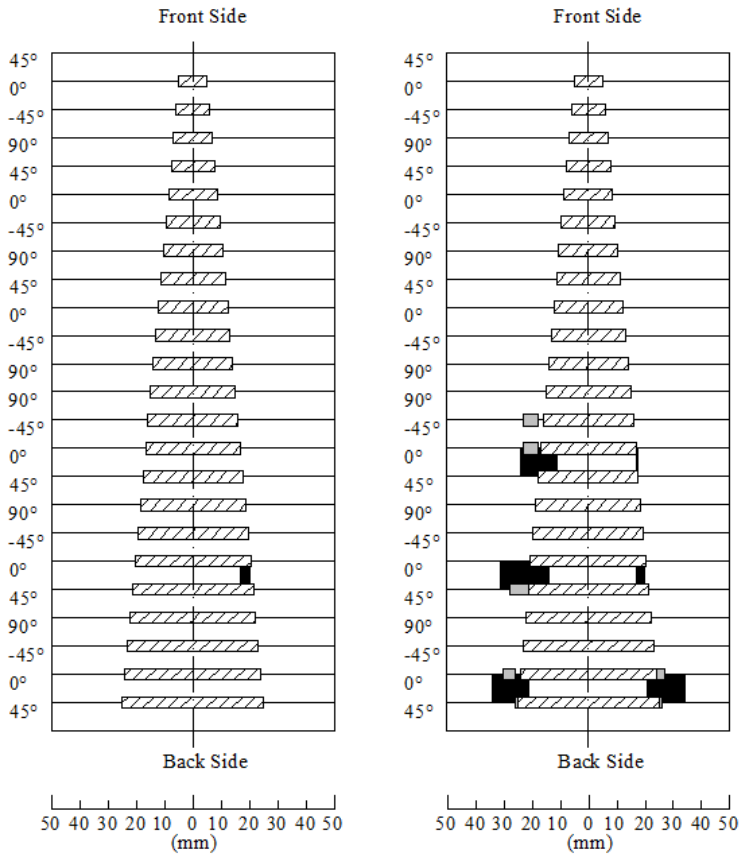

Figure 4.83 Schematic damage process of N_23_R25_Cone

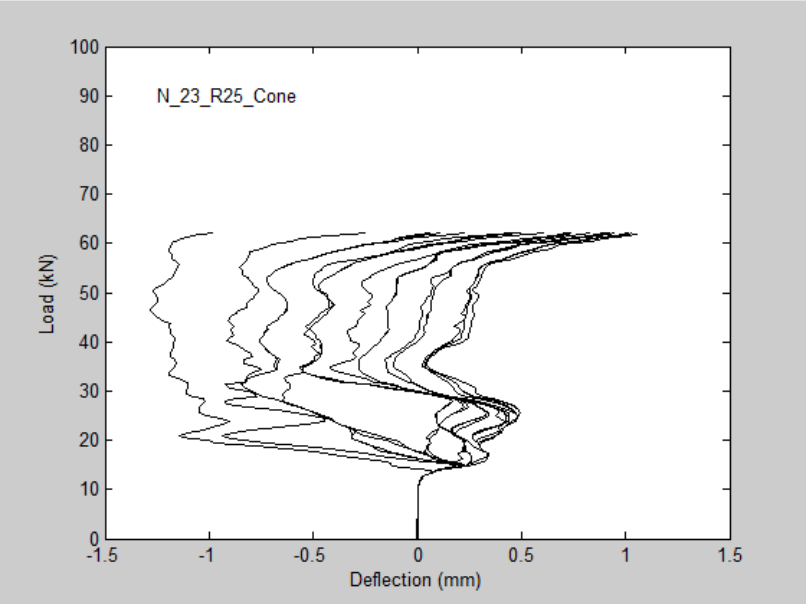

Figure 4.84 Deflection of central point versus compressive load for N_23_R25_Cone

4.8.4 Summary

4.8.4.1 Damage mechanism categorization

According to the analysis of all parametric study models involved in this chapter, it is found that the damage mechanisms can be categorised into four types, which are distinguished by font of Roman, **bold**, *italic* and ***bold & italic*** in Table 4.2, 5-3 and 5-4, respectively. (1) For the first type of damage mechanism, it is characterized with excessive delamination propagation. Models bearing single delamination located close to the laminate surface, or single and big delamination close to the mid-plane belong to this type; (2) the second type is characterised with global collapse of the whole laminate. Models with single small delamination close to the mid-plane belong to this type; (3) the third type is characterised by excessive delamination propagation followed by in-plane failure before the whole laminate collapses. Models in this type usually bear moderate number of

delaminations. When sublaminates buckle due to the in-plane compression, delamination propagation is triggered. In the meantime, buckling also lead stress redistribution and stress concentration arises in the zones around delamination front. As delamination propagates, concentrated stresses increase around the moving delamination front and eventually exceed the material strength. Then, fibre failure takes place as well as other types of material failure modes, and the process develops rapidly over the residual intact part along width direction. Consequently, the whole laminate collapses; (4) the final type is characterised by in-plane failure without significant delamination propagation. Models bearing excessive number of delaminations belong to this type. Similar to previous type, sublaminates buckle due to in-plane compression at the early stage. However, delamination propagation is hard to trigger because due to insufficient ERR because of reduced sublaminate thicknesses and hence their bending rigidities. Instead, fibre failure initiates in the zones around the delamination front as a result of stress concentration. Fibre failure develops along the width direction and the whole laminate collapses instantly.

The diverse damage mechanisms presented above reflect the diverse factors of delamination patterns. However, the investigation performed has served the purpose of understanding the contribution of individual factors.

4.8.4.2 Delamination multiplicity

From above results, it can be noticed that the altering delamination number influences the damage mechanism significantly. The mechanism is explained as follows. The occurrence of delamination propagation is dictated by ERR, which is completely a quantity defined at the

delamination front determined by a couple of factors such as overall compressive load, sublaminate deformation, sublaminate bending rigidity, etc.. ERR increases monotonically with the bending rigidity of sublaminates involved and bending curvature at the delamination front. In the case of single delamination located at the fourth interface, such as N_1_4_20_R10, significant bending deformation of the thinner sublaminate leads adequate ERR accumulated at the delamination front and consequent occurrence of delamination propagation. However, when the single delamination locates at the eighth interface or mid-plane, both sublaminates are too rigid which leads them retain stable up to relatively high compressive load. Once they buckle, the in-plane compressive stress exceeds the material strength rapidly, causing the whole laminate to collapse abruptly, for example, N_1_4_20_R20. On the other hand, when there are excessive delaminations, for example, 11 or 23 delaminations, corresponding sublaminate bending rigidities are undermined significantly due to the reduced sublaminate thicknesses. Although the sublaminates can bend to a great extent, it cannot build up sufficient ERR at the delamination front to trigger propagation before in-plane stresses around the delamination front exceed the material strength to trigger in-plane failure as a result of stress concentration. When there are moderate number of delaminations, the sublaminates can buckle locally to build up sufficient ERR for delamination propagation, like the models bearing 3, 5 or 7 delaminations here. This suggests in the case of multiple delaminations the existence of a specific range of the number of delaminations, which favour delamination propagation as the damage mechanism, with the exception of the case of single delamination located close to the surface. Accordingly, it implies that there exists a critical range of numbers of delaminations, beyond which delamination propagation is unlikely to take place. Although the range may vary from case to case due to

different delamination sizes, ply thicknesses, CERRs and etc.. The tendency remains largely valid in general.

This tendency can be further supported by the following analysis. Figure 4.85 shows the ratios of average compressive stress in 0° laminae along the centre line in width direction with respect to the laminar longitudinal compressive strength for all models in Table 4.3 as well as the models bearing single delamination in the mid-plane in Table 4.2 at the load level of respective failure loads. The 0° laminae are the primary element to sustain compressive load in CAI cases, and their behaviour will dominate the overall load sustainability of the laminate. It is found that for the models with single or three delaminations the stresses distribute relatively evenly in the undelaminated part and slightly drop at the delaminated area (except the one with three delaminations of a radius of 25mm). Apparently, due to the sparseness of the delaminations, sublaminates possess relatively high bending rigidity which allows little bending deform to cause in-plane stress redistribution. The laminate, although delaminated, sustains the compressive load almost as an integral. However, as the number of delaminations increases, the overall stress level drops but stress concentration becomes more and more significant around the delamination front. As sublaminates become thinner, they buckle locally at relatively low load level, which allows the in-plane stresses to redistribute to lead to in-plane crushing failure. Additionally, the thinner the sublaminates and the larger the delamination sizes, the higher the degree of stress concentration around the delamination front and the less compressive load the delaminated area sustains after buckling.

Distinct failure modes lead to different failure loads. In Figure 4.86, the failure loads of all models in Table 4.3 as well as the models bearing single delamination in the mid-plane are compared. An interesting observation is that the failure load does not decrease monotonically as the number of delamination increases. Instead, it drops sharply first then rebounds a little and the lowest failure load seems to correspond to the cases where delamination propagation dictates the final failure. Guided by the discussion made above regarding the damage mechanism, it can be concluded that the lowest values of the failure loads are of the consequence of excessive delamination propagation.

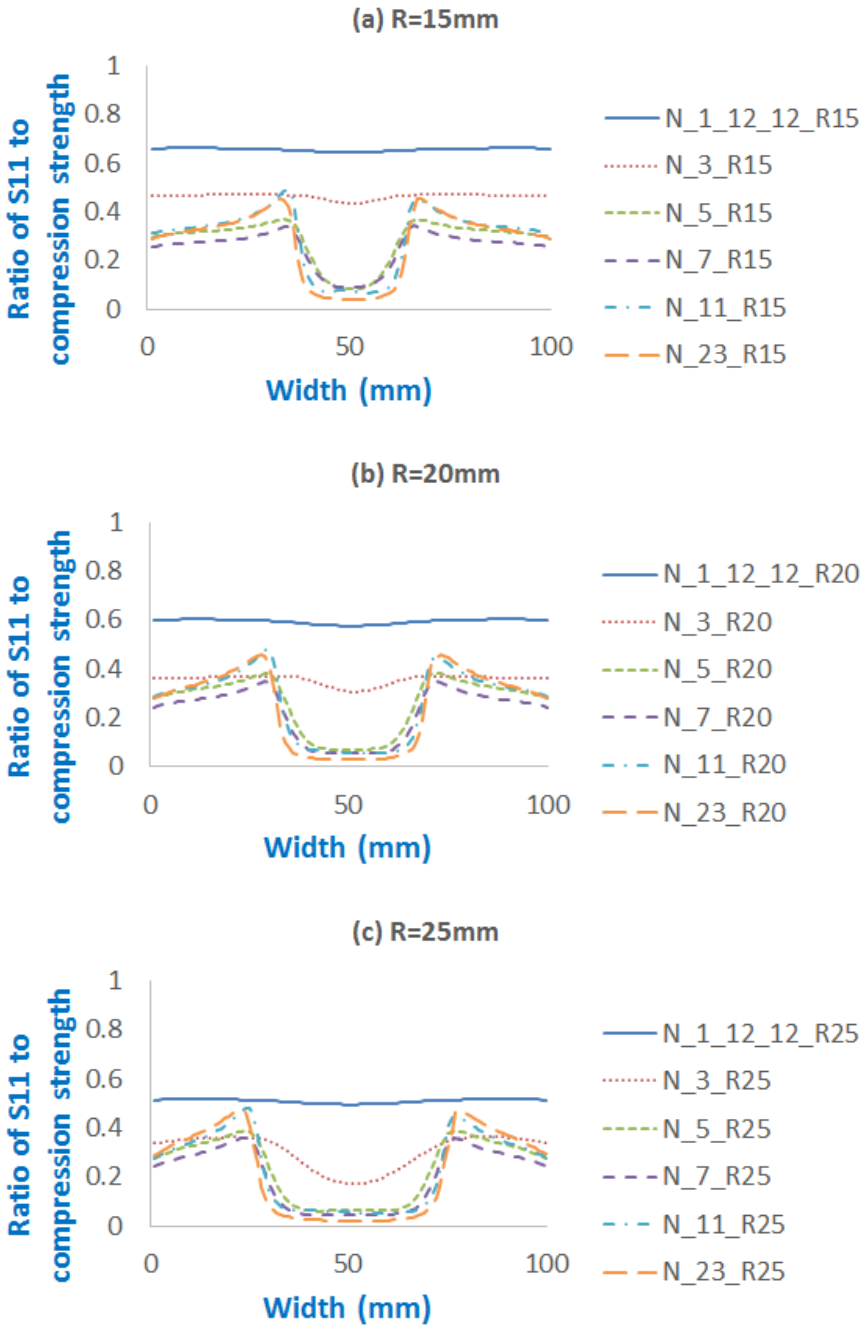

Figure 4.85 The ratio of compressive stress in 0° laminae to compressive strength over the laminate width at failure load among models of common delamination size ((a) R=15mm, (b) R=20mm, (c) R=25mm) but different numbers of delaminations

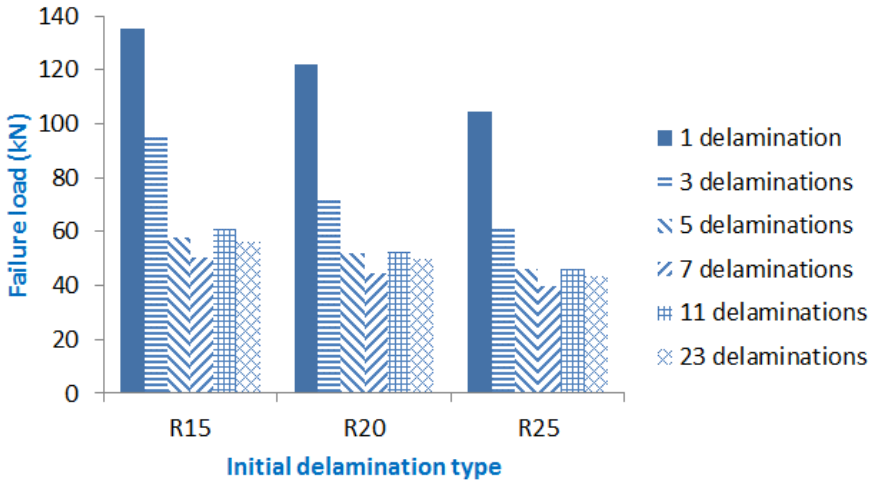

Figure 4.86 Comparison of failure load of FE models bearing multiple delamination

4.8.4.3 Delamination size

Generally, there is a tendency that the larger delamination size, the easier, i.e. the lower the load level, for the delamination propagation to take place. This is because larger delaminations allow sublaminates to bend more, which is helpful for higher ERR to build up at the delamination front. However, the extent of this tendency is limited and often masked by other factors, in particular the number of delaminations. For example, in the case of single delamination located at the eighth interface and mid-plane, when delamination radii increase to 40mm, delamination propagation was observed over the entire laminate width while in the case of 11 and 23 uniform delaminations, delamination propagation is not triggered when delamination radii increase to 40mm, for example, N_11_R40 and N_23_R40. This is because corresponding sublaminates successively deform into an advanced postbuckling regime during the loading process, given their low bending rigidities and large sizes preventing the ERR to build up to a sufficient amount to cause delamination propagation.

4.8.4.4 Delamination distribution

For cylindrical delamination distribution, its influence to damage mechanism has been investigated above. When the delamination sizes are not uniform over the laminate thickness, cases become more complex. Due to the compatibility of deformation of the whole laminate involving multiple sublaminates with diverse sizes and stiffness, the ultimate failure mode of either delamination propagation or in-plane failure does not necessarily occur at the seemingly most vulnerable point such as the delamination front of the maximum delamination. However, through parametric analysis, it has been found that the effects of delamination multiplicity are still present in the cases here. For example, compared with the case of 11 delaminations distributing in a conical shape (Figure 4.81), significant delamination propagation is observed before the laminate collapses when the delamination number reduces to 7 (Figure 4.79(b)).

It is also observed that with conical and spindle shaped delamination distributions, the models always produce higher failure load, compared with that of cylindrical distribution (Figure 4.87) when the maximum delamination radii of the conical and spindle cases are equal to that of cylindrical case. This is due to the fact that there is less total delamination area compared with that of cylindrical distribution, although they are marked with equal projected delamination area in normal direction to the laminate. In practical CAI cases, delamination distribution is usually not in a cylindrical shape but more likely to be in a conical or spindle shape. This simple observation suggests that the variation of sizes of delaminations distributed over the laminate thickness should be taken into account in proper CAI predictions, although it is usually ignored.

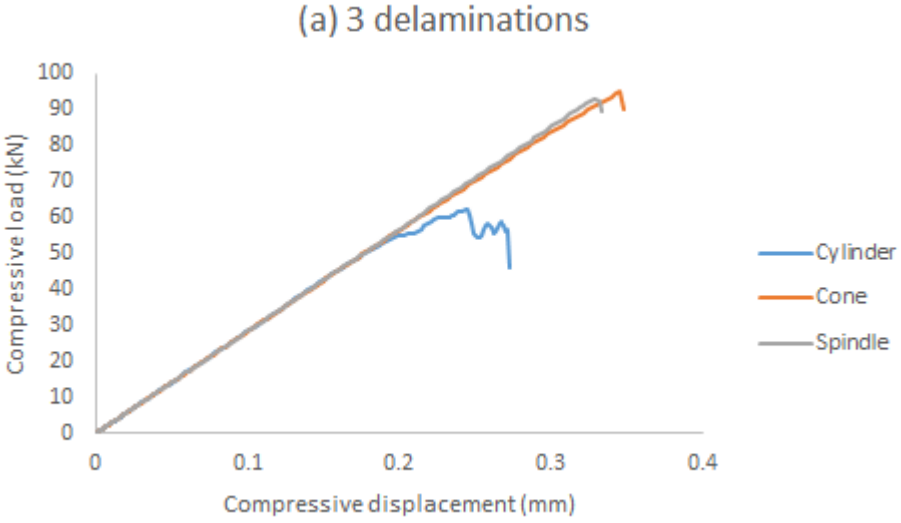
(a) 3 delaminations
Compressive load (kN)
100
90
80
70
60
50
40
30
20
10
0
0
0.1
0.2
0.3
0.4
Compressive displacement (mm)
Cylinder
Cone
Spindle

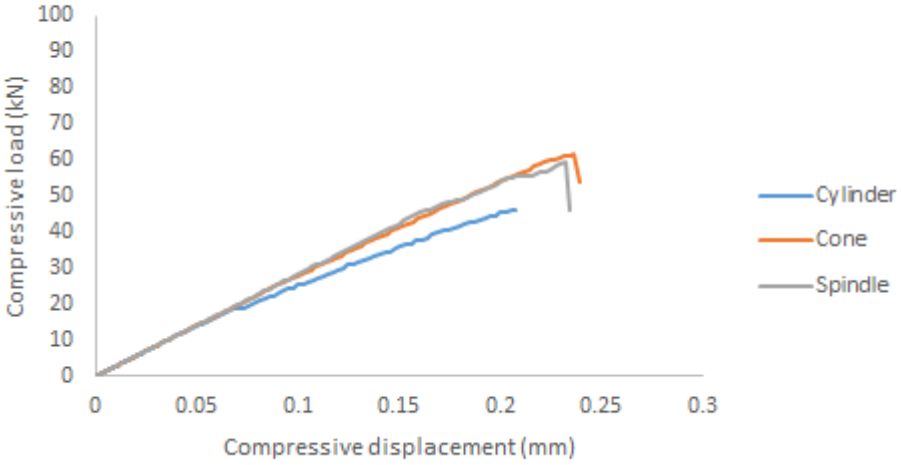
(b) 5 delaminations
Compressive load (kN)
100
90
80
70
60
50
40
30
20
10
0
0
0.05
0.1
0.15
0.2
0.25
0.3
Compressive displacement (mm)
Cylinder
Cone
Spindle

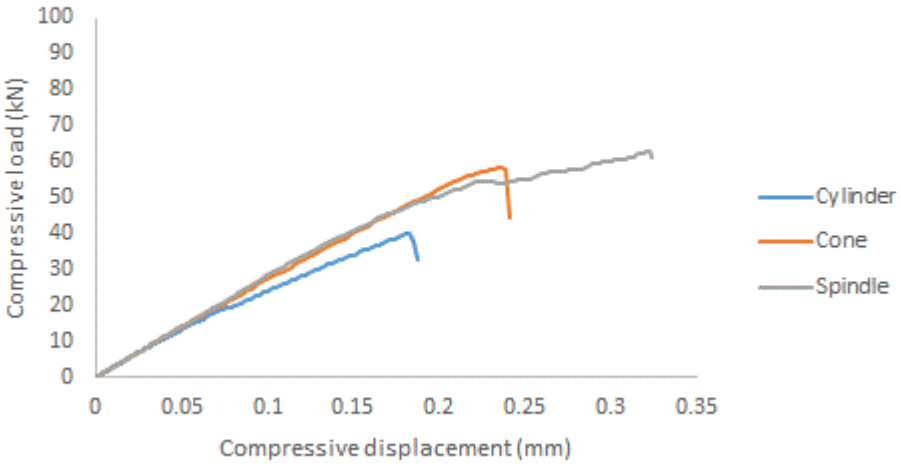
(c) 7 delaminations
Compressive load (kN)
100
90
80
70
60
50
40
30
20
10
0
0
0.05
0.1
0.15
0.2
0.25
0.3
0.35
Compressive displacement (mm)
Cylinder
Cone
Spindle

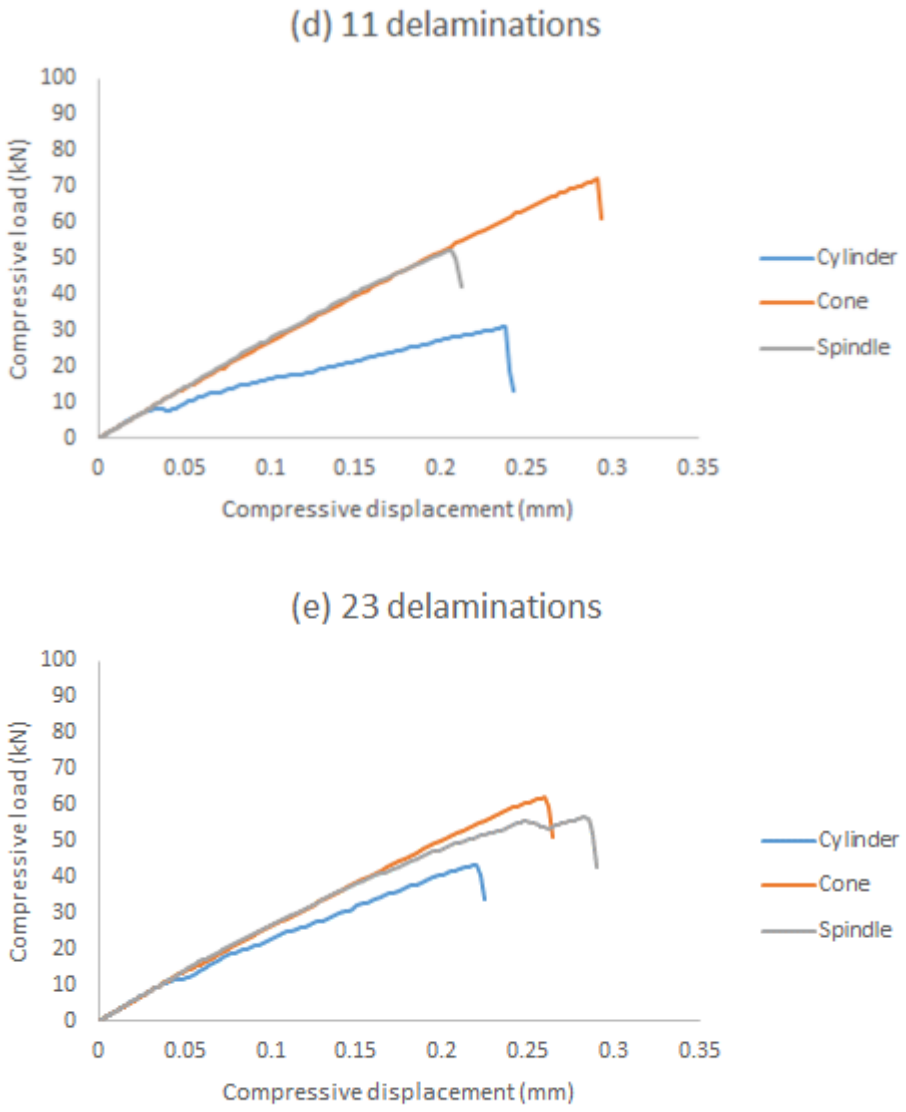

Figure 4.87 Comparison of failure loads among models with same biggest delamination size (R=25mm) but different distribution patterns

4.8.4.5 Suggestion to CAI investigation

Although the parametric study FE models in this paper are idealised, the obtained trends are of close relevance to the thorough understanding of the CAI damage mechanism. Through parametric study, it is found that the multiplicity of delamination is the major factor to influence

the form of damage mechanism. For a given case, there may exist a threshold number of delaminations, over which delamination propagation is unlikely to take place. Currently, the laminates used in aircraft structure usually consist of dozens of plies, and the lay-up sequences are so designed that successive laminae with same fibre orientation are voided. This means that a large number of interfaces exist over the laminate thickness, and almost the same number of delaminations will be induced by foreign object impact, resulting in low bending rigidity of each sublaminate. Additionally, transverse matrix cracks and fibre breakage induced by foreign object impact impair the bending rigidity further. Therefore, it is reasonable to expect that the required level of ERR at the delamination fronts would not be reached before in-plane failure due to stress concentration takes place, especially when the CAI cases bear small impact-induced damage such as BVID. Of course, this statement needs further confirmation through detailed CAI modelling which takes all relevant factors into account. It is also worth mentioning that this statement does not contradict to the experimental observation of delamination propagation as referred to in Table 2.2. In those reported cases, sublaminates consist of at least 2 or 3 laminae, which could be expected to build up adequate ERR to trigger delamination propagation. To the best of the author's knowledge, publications claiming observation of delamination propagation of CAI cases with common lay-up sequences are not found so far.

4.9 Conclusion

Damage mechanisms of CAI (strictly speaking, simplified or idealized CAI cases) are investigated through extensive parametric study using FE models, and important trends are obtained. Most previous methods from other publications considered only one failure mode, either delamination

propagation or in-plane failure due to stress concentration, which were too categorical. Therefore, as an improvement, the models in this paper take both failure modes into account, simultaneously. It is found that these two failure modes co-exist, and they compete to dominate the damage process depending on various factors, such as delamination multiplicity, size and distribution pattern. Diverse numbers of delaminations lead to different damage mechanisms. Delamination propagation is more likely to take place when the laminate bears moderate number of delaminations, neither too many nor too few. It suggests that there exists a threshold of characteristic number of delaminations for a given laminate, over which delamination propagation is unlikely to take place and in-plane failure due to stress concentration becomes the dominant damage mechanism. It is also found delamination size and distribution pattern make contribution to influence the damage mechanism, but their influences are less significant than that of delamination multiplicity. It is worth mentioning that non-uniform delamination sizes over laminate thickness lead significantly diverse failure load, compared with uniform delamination size, which should be taken into account in CAI investigations although it is usually omitted.

Finally, according to the trends obtained in this paper, it suggests that for CAI cases, especially bearing small impact-induce damage such as BVID, in-plane failure due to stress concentration could be the dominant failure mode and delamination propagation is unlikely to take place.

However, parametric study models employed in this chapter are rather idealized and hence differ from real CAI cases. The applicability of the conclusions obtained here need further verification. Therefore, more accurate detailed FE model which represents the reality better are needed for further investigation, which will be discussed in next chapter.

Chapter 5 CAI simulation based on C-scan delamination patterns

5.1 Introduction

In the previous chapter, some valuable conclusions about damage mechanisms of delaminated plate subjected to in-plane compression have been summarised. However, only based on the parametric study no solid conclusion about CAI can be made yet because the models in that chapter were idealised and differ from real CAI cases. In this chapter, the major objective is to present a method which can model CAI samples more realistically, and to investigate the damage mechanism subsequently.

In Section 5.2, the thoroughly modelling method is presented, which simulates the delamination distribution, transverse matrix cracks and fibre breakage in CAI samples by taking advantage of C-scan results as well as other experimental information. Through investigating these detailed FE models, the damage mechanism of CAI is concluded finally.

In Section 5.3, a further exploitation based on this modelling method is made, which proposes a method to predict the upper and lower limit of a given CAI test.

In Section 5.4, main conclusions about damage mechanisms are drawn, which lay the theoretical basis for a simplified CAI prediction method to be presented in the next chapter.

5.2 CAI FE model

From the parametric study in Chapter 4, it was found that in most models in that chapter further damage initiates in the form of delamination propagation but collapses in in-plane failure due to

stress concentration. It also suggested the tendency that, as the number of delamination increased beyond a threshold level, delamination propagation would be unlikely to take place and in-plane failure became the dominant failure mode. However, parametric study models alone are insufficient to prove this tendency since they are simplified and idealised from real CAI cases. It is essential to construct a detailed FE model which can simulate the damage induced by low velocity impact more realistically for the damage mechanisms investigation. In order to do so, modelling improvement needs to be done from three aspects at least, which are delaminations, transverse matrix crack, and fibre breakage.

5.2.1 Delaminations

In the parametric study the pattern of delamination distribution through laminate thickness is assumed to be in a cylinder-, cone- and spindle-shape, respectively, and the delamination on each interface is circular. This is not the real scenario inflicted by low velocity impact. Firstly, the pattern of delamination distribution over thickness is hardly in cylinder-shape and affected by many factors, such as laminate stiffness, lay-up sequence, impact energy, etc.. Moreover, it has been confirmed experimentally that the delamination shape on each interface is more likely peanut-shaped rather than circular. Therefore, these two issues need to be improved in the following.

5.2.1.1 Delamination distribution

C-scan results can be helpful to determine the detail of delamination distribution over thickness of a given CAI sample. Although the delaminations underneath the outmost ones cannot be

detected due to intrinsic weakness of C-scan, the profile of overall delamination distribution can still be captured through double-sided scan generally. This attributes to the outline of the delamination distribution induced by low-velocity impact, which usually has the maximum radius at or close to the middle surface and reduces gradually towards both panel sides, resembling a spindle. This exposes the profiles of most delaminations on individual interfaces to the scanning scanner for detection. Although it is possible that on some interfaces smaller delaminations are masked by neighbouring ones overshadowing them, the general tendency can be obtained as has been demonstrated in the literature [79] as well as the experimental observations in Figure 3.9. Since the overlapped delamination shape as well as delamination outline on each interface is circular roughly, Figure 3.9 for instance, assume the maximum diameter of delamination on each interface through following equation

$$d_{\mathrm{i}} = \sqrt{L_{\mathrm{i}} * W_{\mathrm{i}}} \tag{5.1}$$

where L_{i} and W_{i} are the maximum length and width covered by the detected spots on interface i, respectively. This algorithm may not be the best approach, and can be improved based on better scan result in future work.

Using above method, the thorough state of delamination distribution through laminate thickness direction of a given CAI panel can be reasonably determined provided that this panel is double-sided scanned. Applying this obtained distributing state to FE modelling, the simulation of delamination distribution in corresponding detail FE model is done. As an example, Figure 5.1 shows the simulated distribution for the samples B4-1-Spi listed in Table 5.1.

5.2.1.2 Delamination shape

It has been confirmed in many literature that the delamination shape on individual interface is not exactly circular but more like a peanut, Craven, Iannucci [29], Aoki, Kondo [31], Ovesy, Taghizadeh [28], which is bounded by fibres of neighbouring upper and lower plies in acute angle, Suemasu, Sasaki [49], Shen, Yang [47]. This is taken into account in the FE modelling, and the delamination simulation is shown in Figure 5.1, where the diameter of each delamination is determined through Equation (5.1).

As a supplement, in this chapter, corresponding detailed FE models with circular delaminations are also constructed, which are used for comparing the results later.

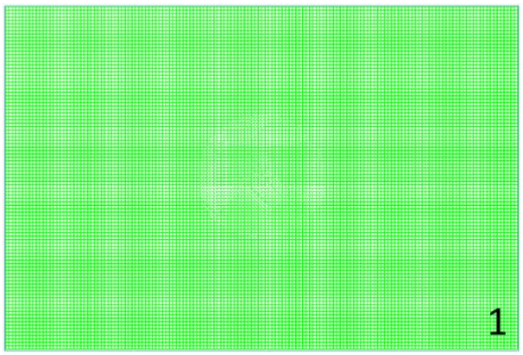
1

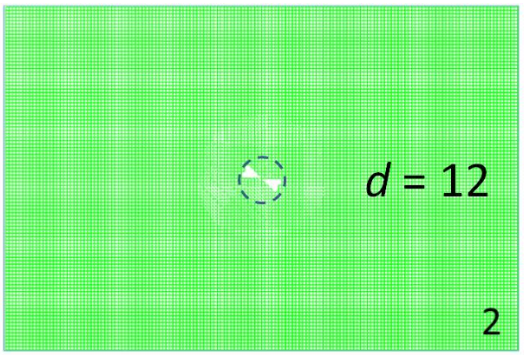
d = 12
2

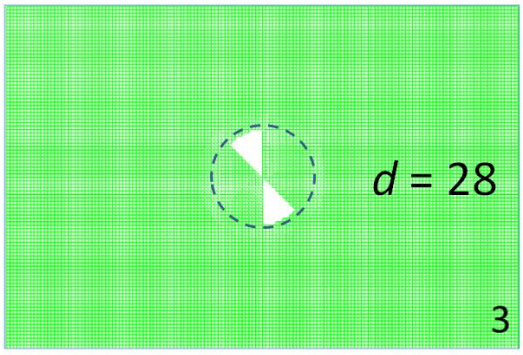
d = 28
3

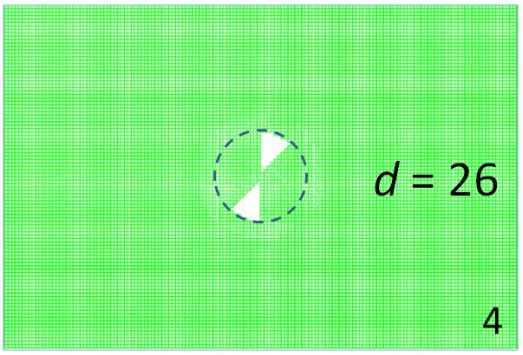
d = 26
4

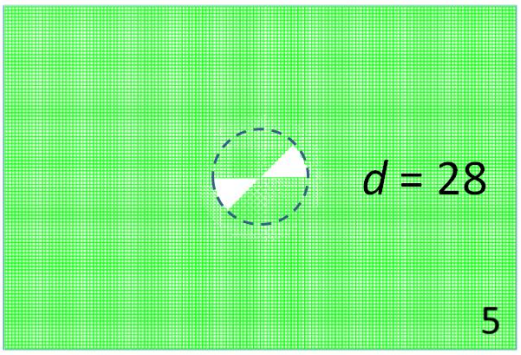
d = 28
5

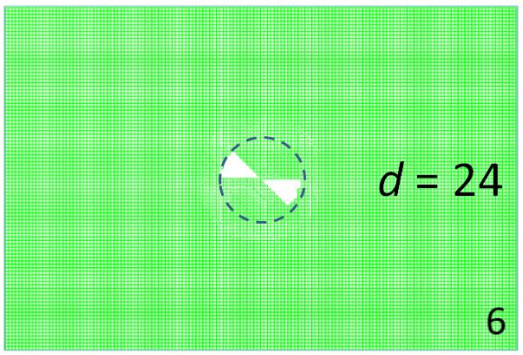
d = 24
6

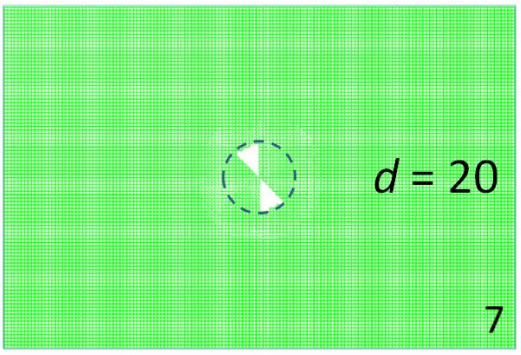
d = 20
7

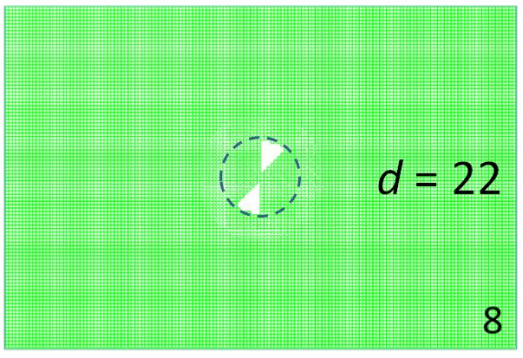
d = 22
8

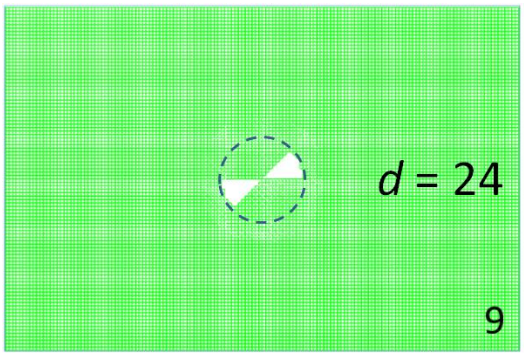
d = 24
9

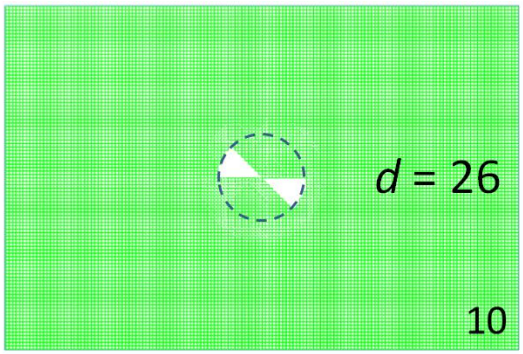
d = 26
10

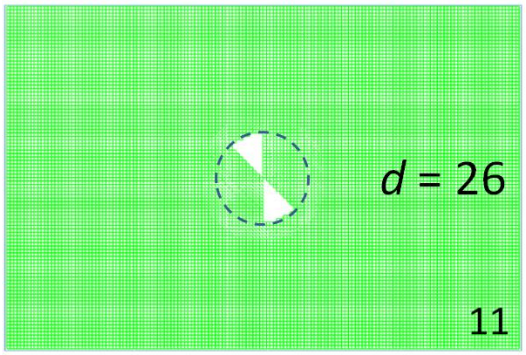
d = 26
11

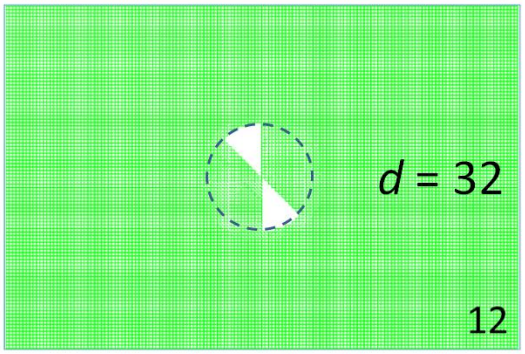
d = 32
12

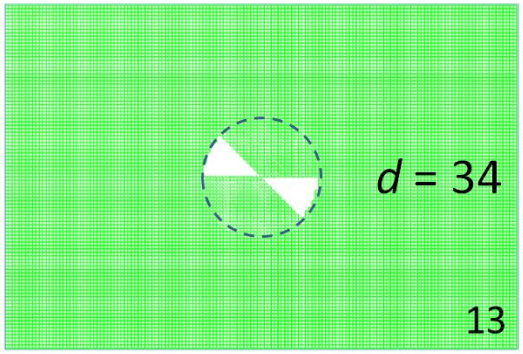
d = 34
13

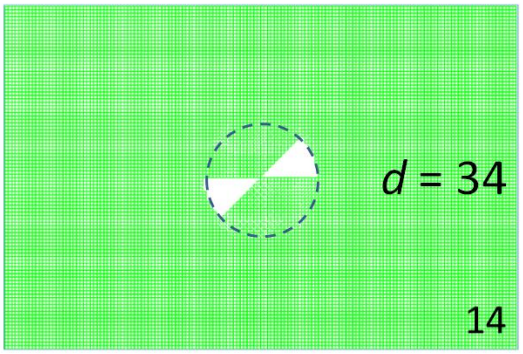
d = 34
14

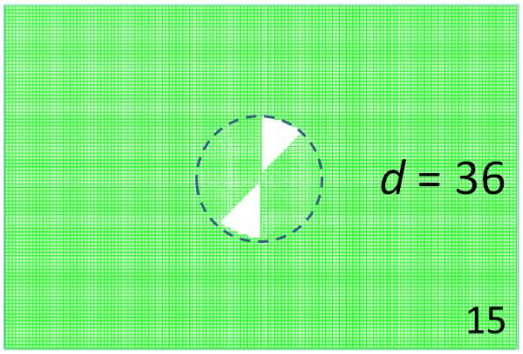
d = 36
15

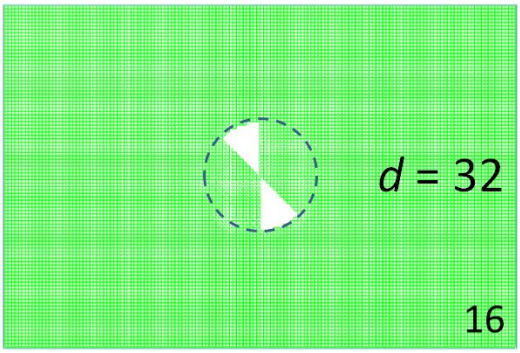
d = 32
16

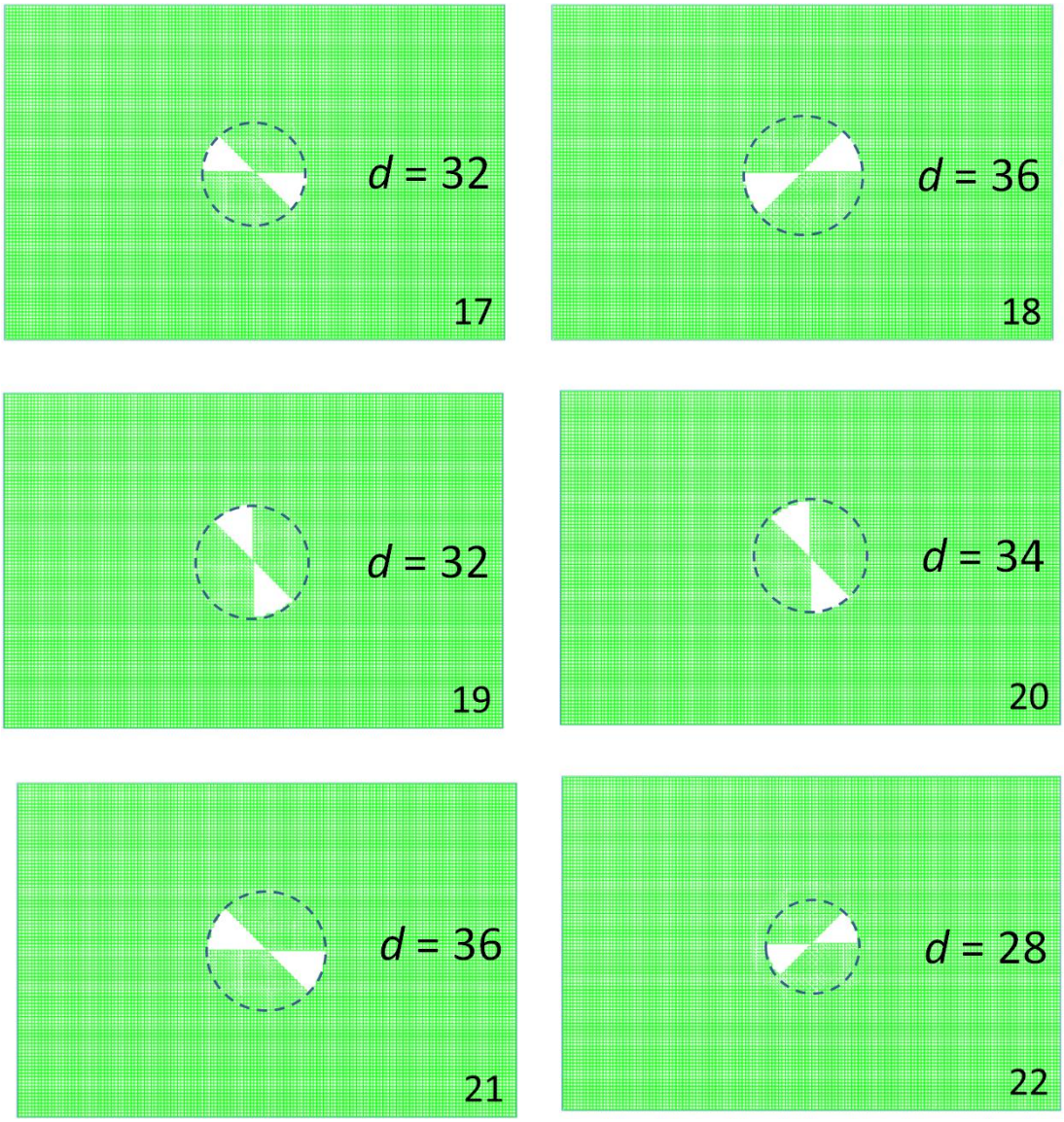

Figure 5.1 Schematic of initial delamination distribution of B4-1-Spi over interlaminar interfaces (interface number increasing from impact side to back side)

Table 5.1 Detailed FE models for each double-sided scanned sub-group

Circular delamination	Double spiral fan-shape delamination	Corresponding sample
A1-1-Cir	A1-1-Spi	A1-1
A2-1-Cir	A2-1-Spi	A2-1
A3-1-Cir	A3-1-Spi	A3-1
B1-1-Cir	B1-1-Spi	B1-1

B2-1-Cir	B2-1-Spi	B2-1
B3-1-Cir	B3-1-Spi	B3-1
B4-1-Cir	B4-1-Spi	B4-1
B5-1-Cir	B5-1-Spi	B5-1
D-1-Cir	D-1-Spi	D-1

5.2.2 Transverse matrix cracks

Damage induced by low velocity impact consists of not only delaminations but also transverse matrix cracks and fibre breakage. The distribution of transverse matrix cracks can be identified through destructive inspection methods. For example, it can be seen from the section view that the transverse matrix cracks exist between fibers within the laminae and connect with neighbouring ones through interlaminar delaminations (Figure 5.2) by sectioning over damaged zone and microscopy. On the other hand, from the front view of each laminar through deply technique [46], one main transverse matrix crack is usually observed across the impact-contacted point aligning with fibre direction, Shen, Yang [47]. Unfortunately, C-scan cannot distinguish transverse matrix cracks effectively from delaminations (ultrasound wave may reflect at the crack faces as well as at the delamination interfaces). Simulating the presence of transverse matrix crack for a specific case has to resort to some assumptions.

Suemasu, Sasaki [49] adopted the view that one main crack existed on each lamina and created real discontinuity within the layer of solid elements which modelled the lamina, and set transverse nonlinear spring elements connecting corresponding nodes to simulate the crack

behaviour, which had large spring constant only in compressive direction and zero in tensile direction. The configuration is shown in Figure 5.3. This approach is too complex. Zou, Reid [32] proposed a relatively simple model referred as damage representation, which replaced the cracked lamina in a laminate by a fictitious material whose properties were defined by the damage representation. Based on this method, the conventional laminate theory can be used to describe the overall behaviour of the cracked laminate. The properties were defined through following equations.

$$\begin{aligned} E_1 &= E_1^0 \\ E_2 &= E_2^0(1-\omega) \\ G_6 &= G_6^0(1-k\omega) \\ \nu_{12} &= \nu_{12}^0 \\ \nu_{21} &= \nu_{21}^0(1-\omega) \end{aligned} \tag{5.2}$$

where E_1, E_2, υ_{12} and υ_{21} are the longitudinal and transverse Young's moduli and Poisson's ratios, respectively, and G_6 is the in-plane shear modulus, in a damaged state. A superscript 0 refers to values in the undamaged state. ω is termed as the damage parameter, varies from 0 to 1. k is the parameter relative to the change of in-plane shear modulus and the transverse Young's modulus. The value of damage parameter ω reflects the influence of adjacent laminae. In the case of large area of delamination, this influence is quite limited. Therefore, Li, Reid [99] set the damage parameter to 1, and the properties reduced to

$$\begin{aligned} E_1 &= E_1^0 \\ E_2 &= 0 \\ G_6 &= 0 \\ \nu_{12} &= \nu_{12}^0 \\ \nu_{21} &= 0 \end{aligned} \tag{5.3}$$

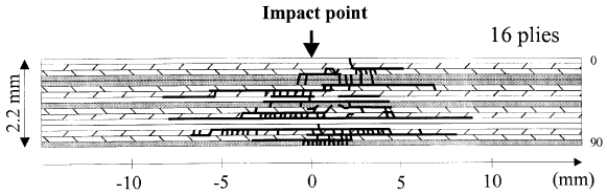

Figure 5.2 Schematic of transverse matrix cracks and delaminations [45]

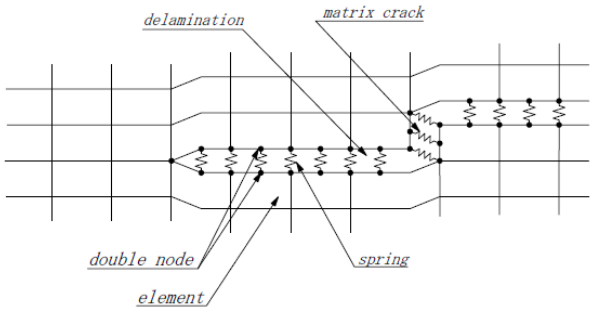

Figure 5.3 Strategy of transverse matrix crack simulation by Suemasu, Sasaki [49]

In this thesis, simulation of transverse matrix cracks takes advantage of above studying results and designates a strip of elements within each lamina along fibre orientation as the crack zone, of which elastic properties are prescribed through Equation (5.3). The length of the crack zone equals to the diameter of upper delamination.

5.2.3 Fibre breakage

Compared with large area of delamination, the effect of fibre breakage to CAI strength is usually insignificant. This is because firstly, the fibre breakage is mainly found within the impactor-contacting area on the specimen, of which the size is relatively small. In compression cases, the dominant factor influencing load sustainability is integral stability rather than material

strength. In this case, the delamination size is more dominant. Secondly, the fibre breakage may not be present in the impacted laminates when it is inflicted by relatively lower impact energy. Shen, Yang [47] suggested that there was probably no fibre breakage in the specimen of which impacting dent depth was lower than the threshold (referred as “knee point” by Shen, Yang [47]). Therefore, fibre breakage plays less significant role in CAI cases. Nevertheless, it is still simulated in the detailed FE models here. The affected depth is assumed to be equivalent to the impacting dent depth and the affected range is determined by the geometry of impactor tip as well as dent depth, which is schematically illustrated in Figure 5.4. The elastic properties of the continuous shell element involved in this area are degraded to near zero to simulate this damage.

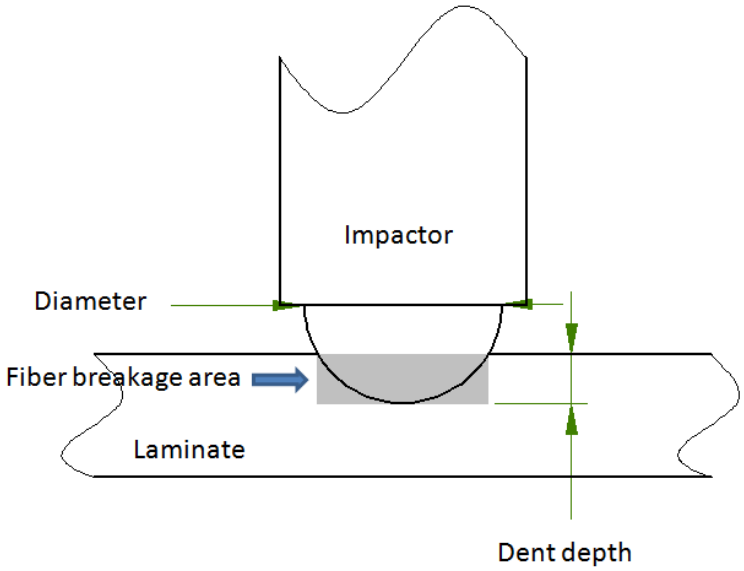

Figure 5.4 Schematic of fibre breakage area (Grey area. Not to scale for illustration purpose)

5.2.4 Damage mechanism investigation

From Chapter 3 it is known that specimens of sub-group A1, A2 and A3, the entire group of B were double-sided scanned. In this section, for these specimens detailed FE models with double spiral fan-shaped delaminations are constructed. The model names are listed in Table 5.1.

The overall failure status of all detailed FE models in this thesis (B4-1 is shown as an example in Figure 5.5) is in accordance with general experimental observation that the panel breaks through the width in the vicinity of the impact damage, leaving two broken halves inserting into each other in a broom shape.

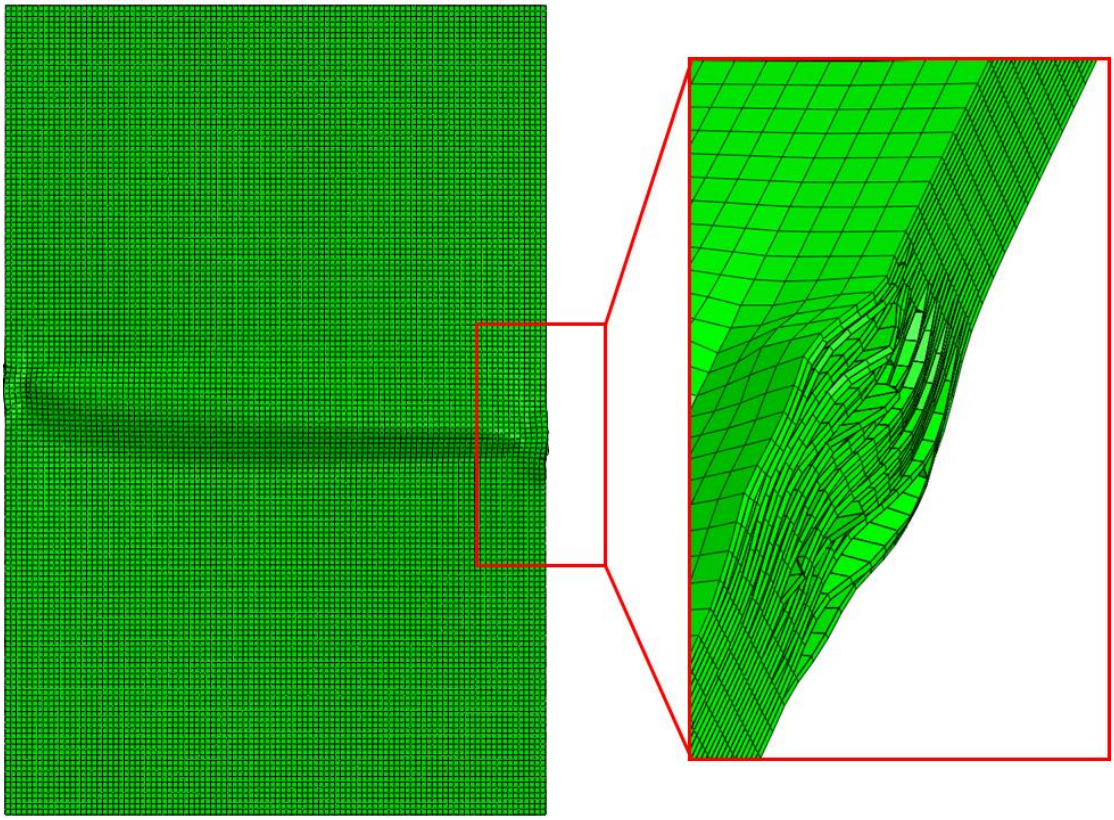

Figure 5.5 Ultimate failure state of detailed FE model B4-1

The damage mechanism of models with double spiral fan-shaped delaminations are investigated. It is found that all models fail due to the same damage mechanism. Fibres break around the delamination front and develop over the width leading the entire laminate collapses. During the entire loading process, delamination propagation is not observed.

Additionally, Figure 5.6 demonstrates the comparison between experiments and detailed FE model bearing double spiral fan-shaped delaminations. The strains are the compression strains averaged from four positions as shown in Figure 2.10 for each specimen. It can be seen that the values from models with double spiral fan-shaped delaminations, are little lower than experimental values generally. The reason is probably the delamination on each interface is slightly overestimated. Fortunately, the delamination assumption made in this thesis lead the prediction result conservative. However, more accurate identification of delamination on individual interface through high quality of C-scan result is needed in further investigation.

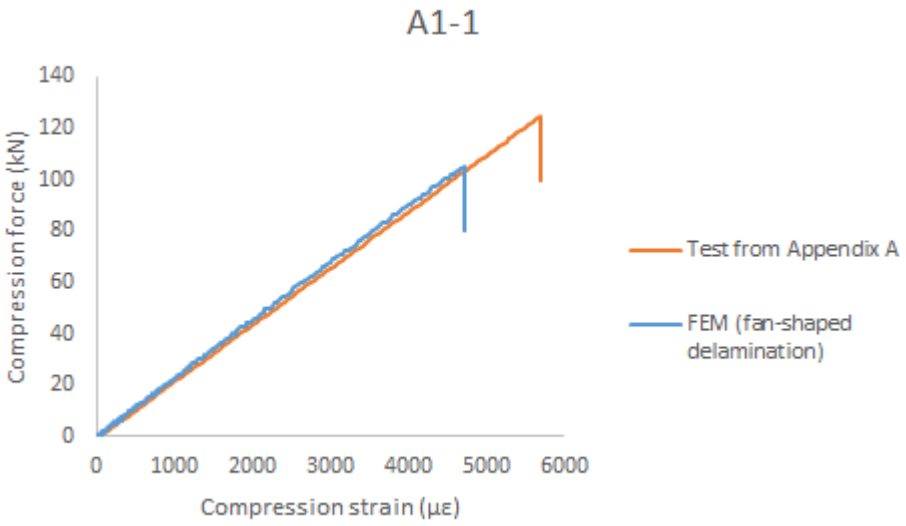
A1-1
Compression force (kN)
140
120
100
80
60
40
20
0
0
1000
2000
3000
4000
5000
6000
Compression strain (με)
Test from Appendix A
FEM (fan-shaped delamination)

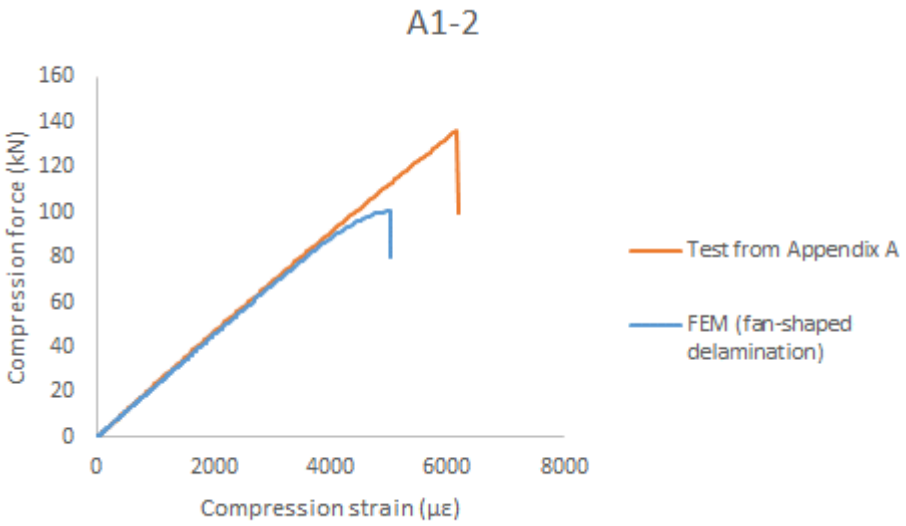
A1-2
Compression force (kN)
160
140
120
100
80
60
40
20
0
0
2000
4000
6000
8000
Compression strain (με)
Test from Appendix A
FEM (fan-shaped delamination)

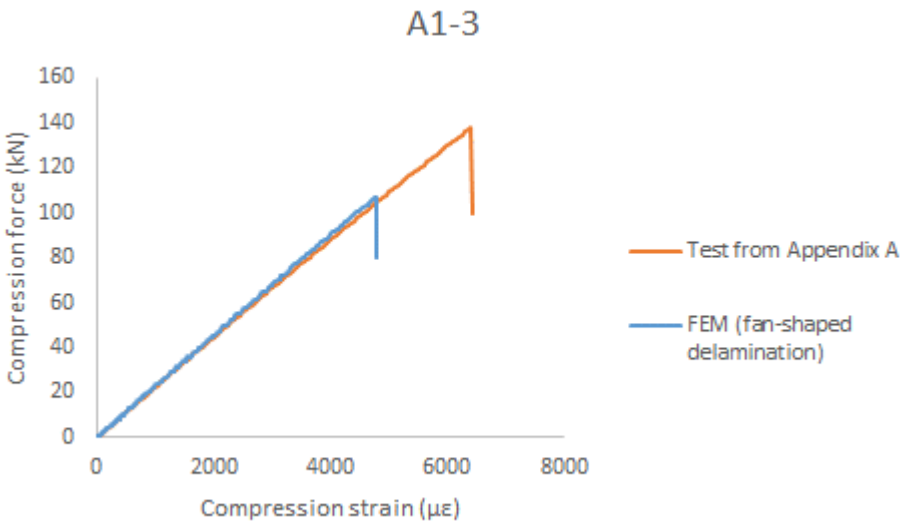
A1-3
Compression force (kN)
160
140
120
100
80
60
40
20
0
0
2000
4000
6000
8000
Compression strain (με)
Test from Appendix A
FEM (fan-shaped delamination)

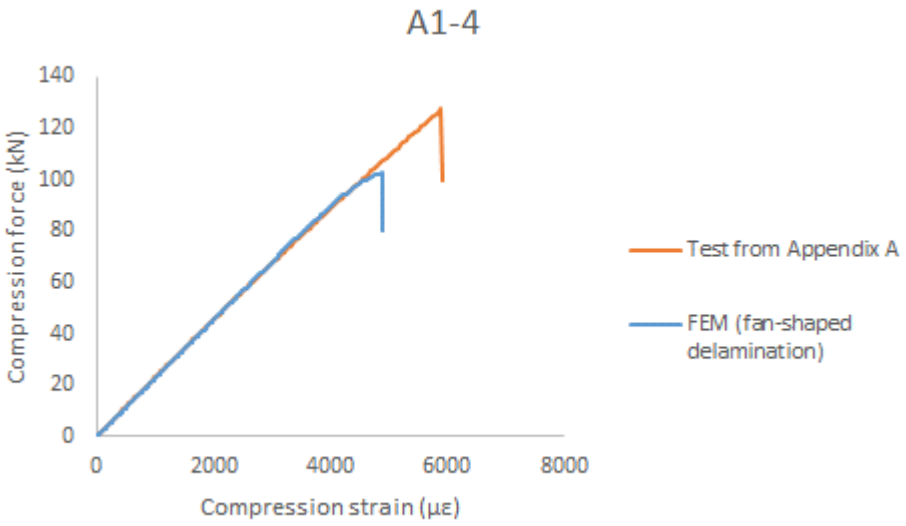
A1-4
Compression force (kN)
140
120
100
80
60
40
20
0
0
2000
4000
6000
8000
Compression strain (με)
Test from Appendix A
FEM (fan-shaped delamination)

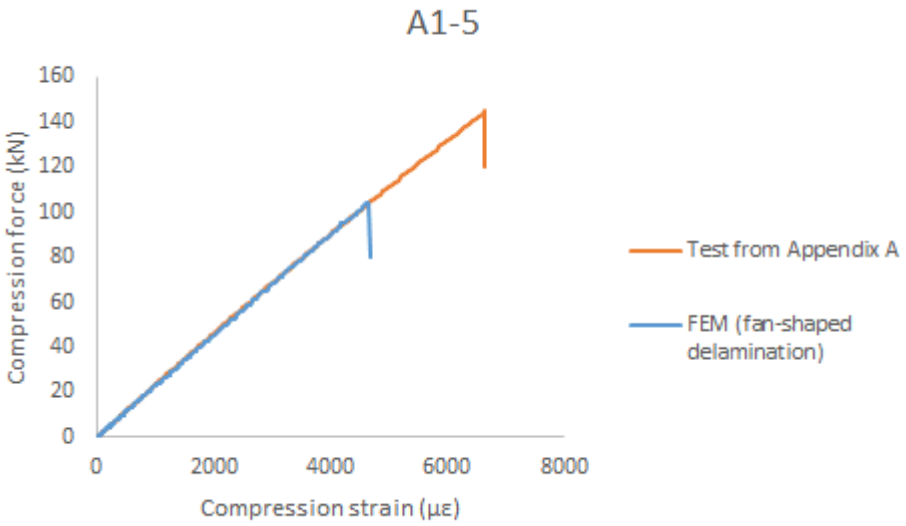
A1-5
Compression force (kN)
160
140
120
100
80
60
40
20
0
0
2000
4000
6000
8000
Compression strain (με)
Test from Appendix A
FEM (fan-shaped delamination)

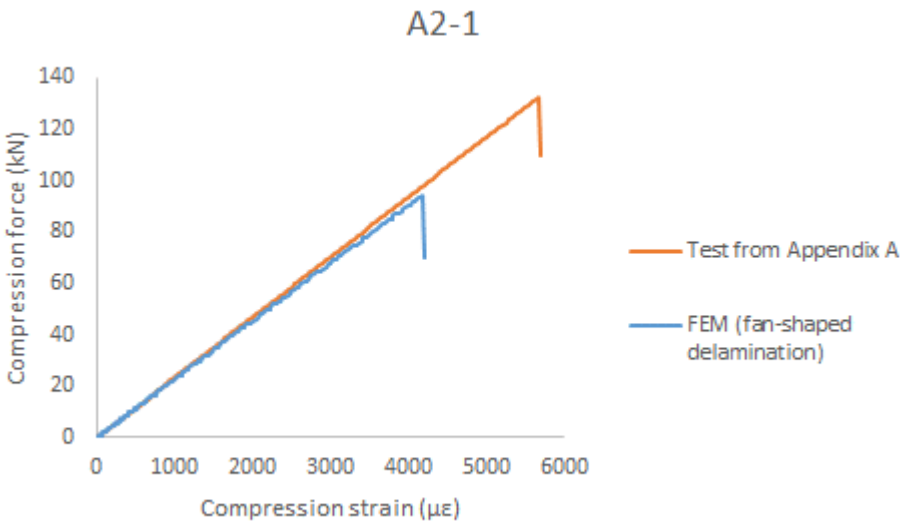
A2-1
Compression force (kN)
140
120
100
80
60
40
20
0
0
1000
2000
3000
4000
5000
6000
Compression strain (με)
Test from Appendix A
FEM (fan-shaped delamination)

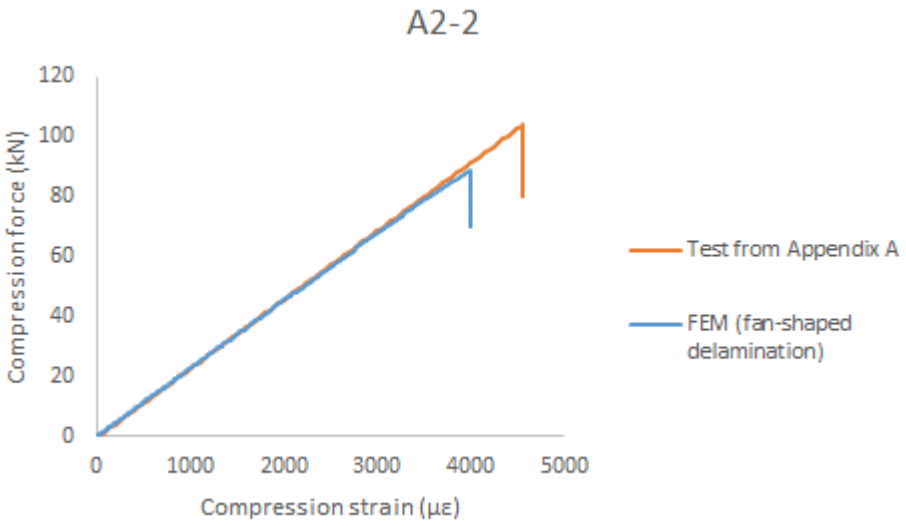
A2-2
Compression force (kN)
120
100
80
60
40
20
0
0
1000
2000
3000
4000
5000
Compression strain (με)
Test from Appendix A
FEM (fan-shaped delamination)

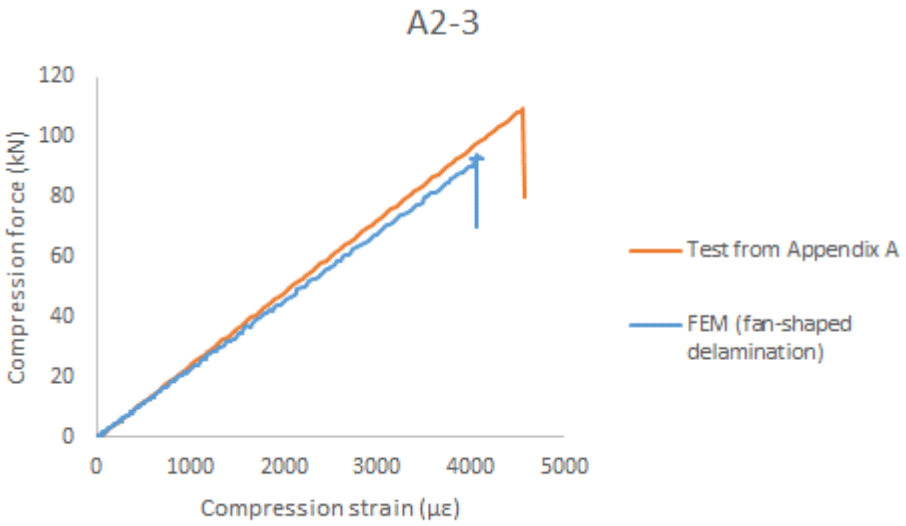
A2-3
Compression force (kN)
120
100
80
60
40
20
0
0
1000
2000
3000
4000
5000
Compression strain (με)
Test from Appendix A
FEM (fan-shaped delamination)

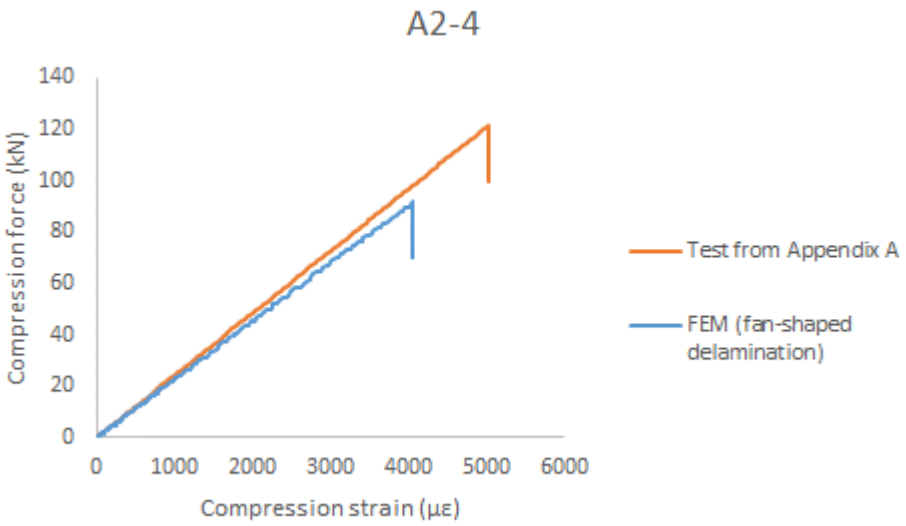
A2-4
Compression force (kN)
140
120
100
80
60
40
20
0
0
1000
2000
3000
4000
5000
6000
Compression strain (με)
Test from Appendix A
FEM (fan-shaped delamination)

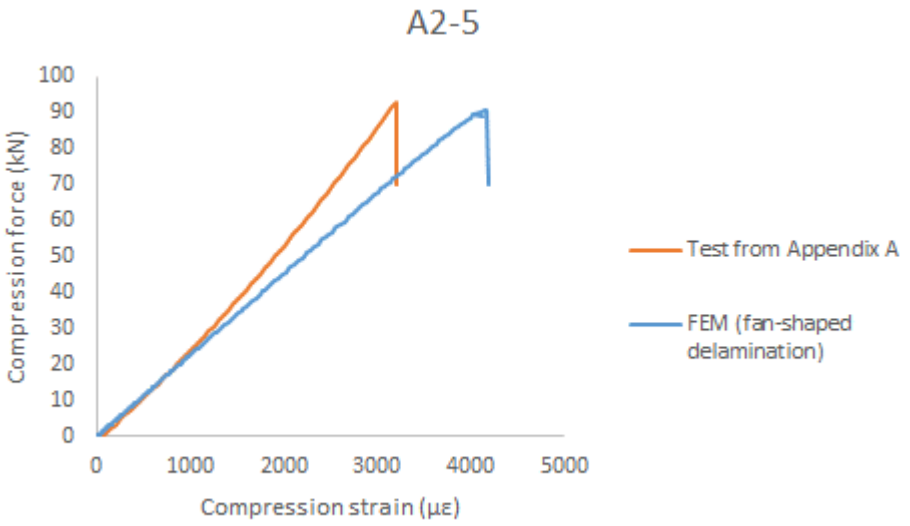
A2-5
Compression force (kN)
100
90
80
70
60
50
40
30
20
10
0
0
1000
2000
3000
4000
5000
Compression strain (με)
Test from Appendix A
FEM (fan-shaped delamination)

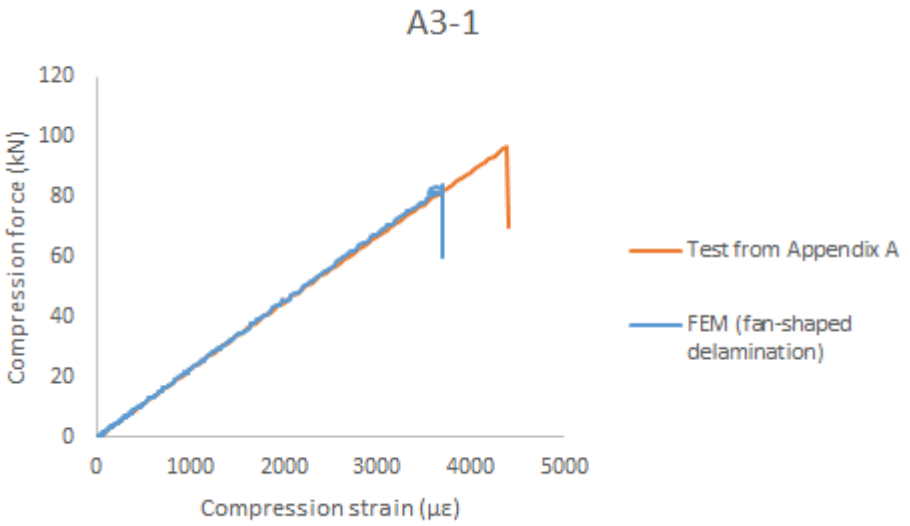
A3-1
Compression force (kN)
120
100
80
60
40
20
0
0
1000
2000
3000
4000
5000
Compression strain (με)
Test from Appendix A
FEM (fan-shaped delamination)

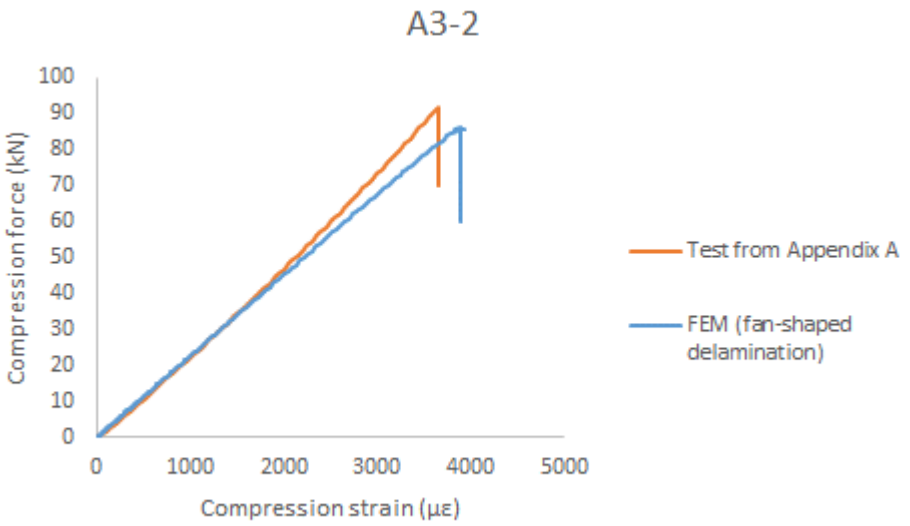
A3-2
Compression force (kN)
100
90
80
70
60
50
40
30
20
10
0
0
1000
2000
3000
4000
5000
Compression strain (με)
Test from Appendix A
FEM (fan-shaped delamination)

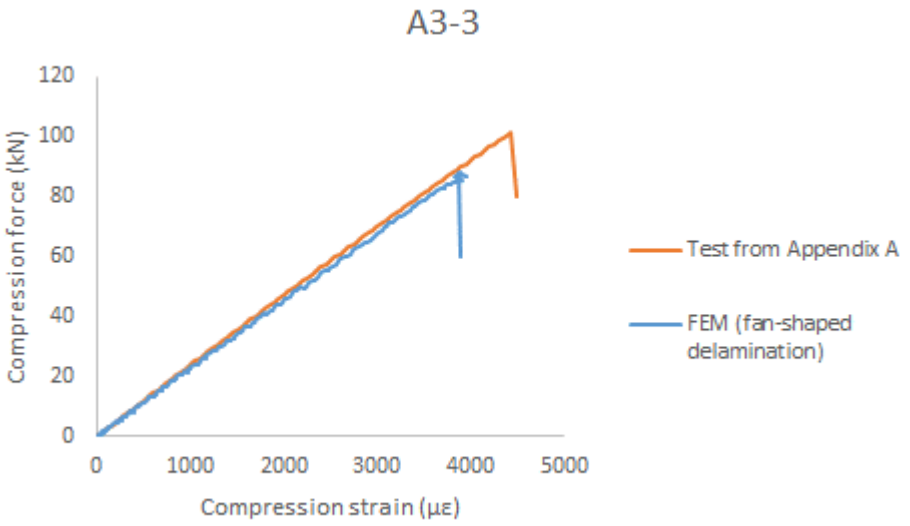
A3-3
120
100
80
60
40
20
0
Compression force (kN)
0
1000
2000
3000
4000
5000
Compression strain (με)
Test from Appendix A
FEM (fan-shaped delamination)

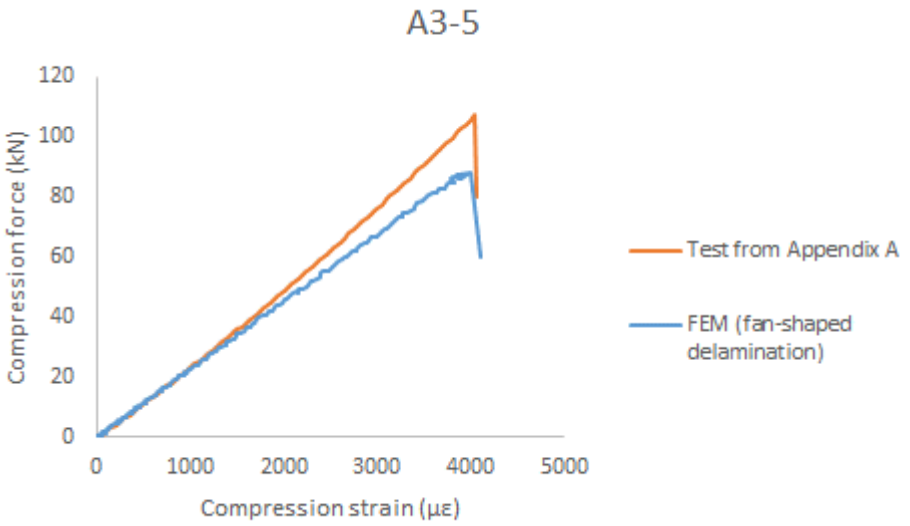
A3-5
120
100
80
60
40
20
0
Compression force (kN)
0
1000
2000
3000
4000
5000
Compression strain (με)
Test from Appendix A
FEM (fan-shaped delamination)

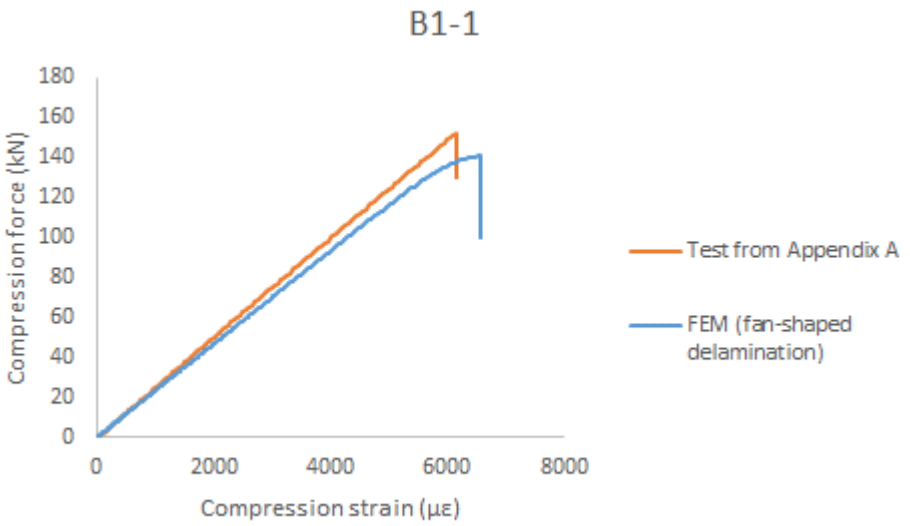
B1-1
180
160
140
120
100
80
60
40
20
0
Compression force (kN)
0
2000
4000
6000
8000
Compression strain (με)
Test from Appendix A
FEM (fan-shaped delamination)

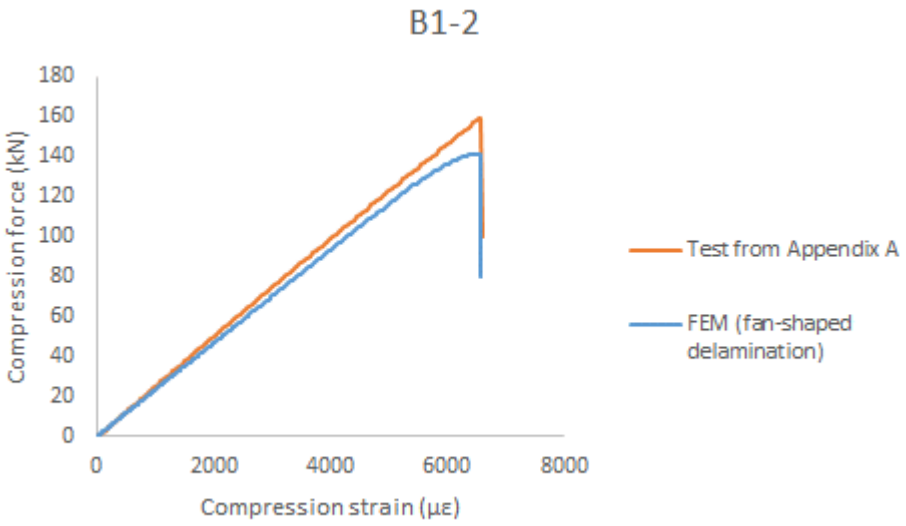
B1-2
Compression force (kN)
180
160
140
120
100
80
60
40
20
0
0
2000
4000
6000
8000
Compression strain (με)
Test from Appendix A
FEM (fan-shaped delamination)

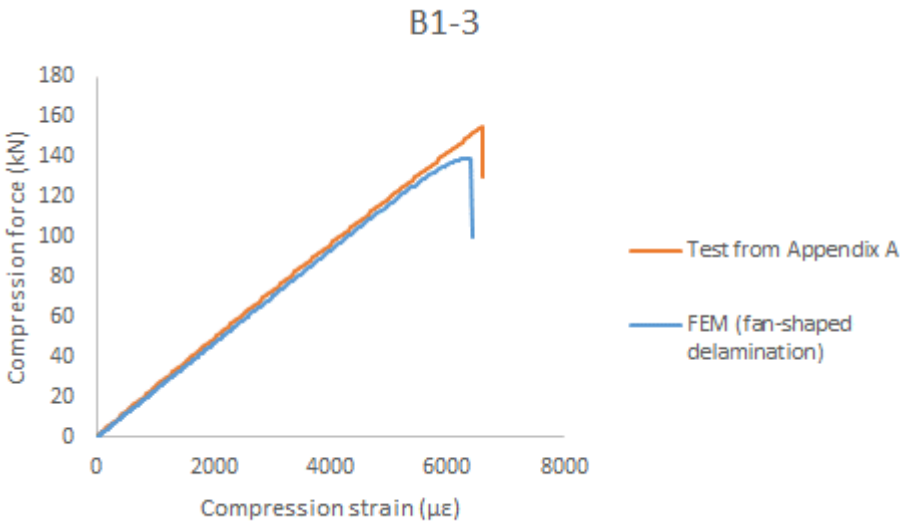
B1-3
Compression force (kN)
180
160
140
120
100
80
60
40
20
0
0
2000
4000
6000
8000
Compression strain (με)
Test from Appendix A
FEM (fan-shaped delamination)

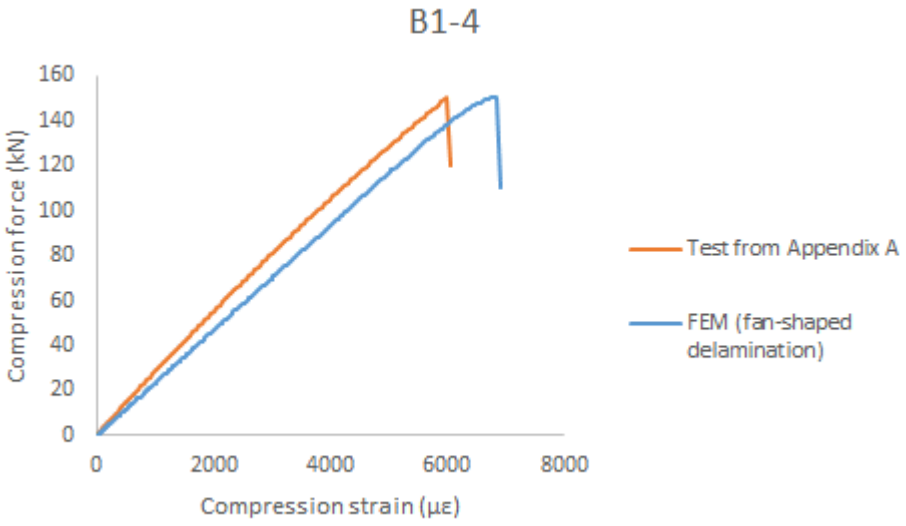
B1-4
Compression force (kN)
160
140
120
100
80
60
40
20
0
0
2000
4000
6000
8000
Compression strain (με)
Test from Appendix A
FEM (fan-shaped delamination)

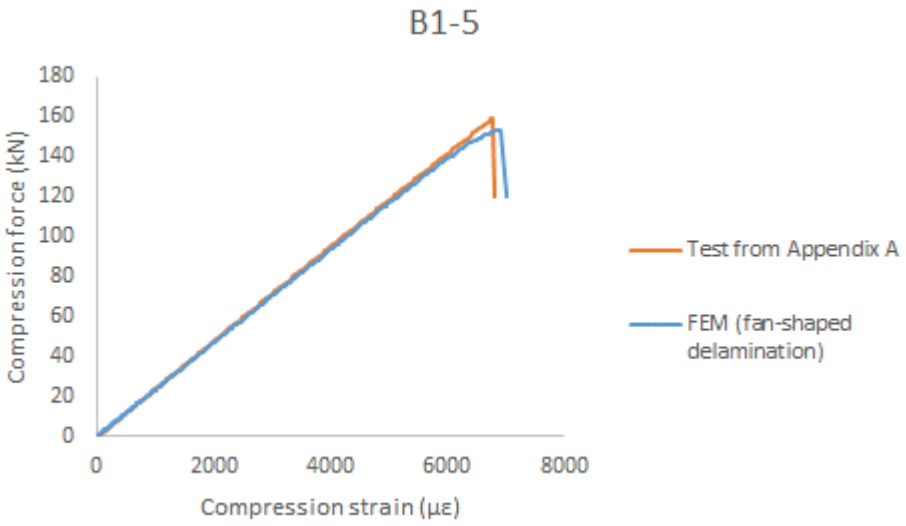
B1-5
Compression force (kN)
180
160
140
120
100
80
60
40
20
0
0
2000
4000
6000
8000
Compression strain (με)
Test from Appendix A
FEM (fan-shaped delamination)

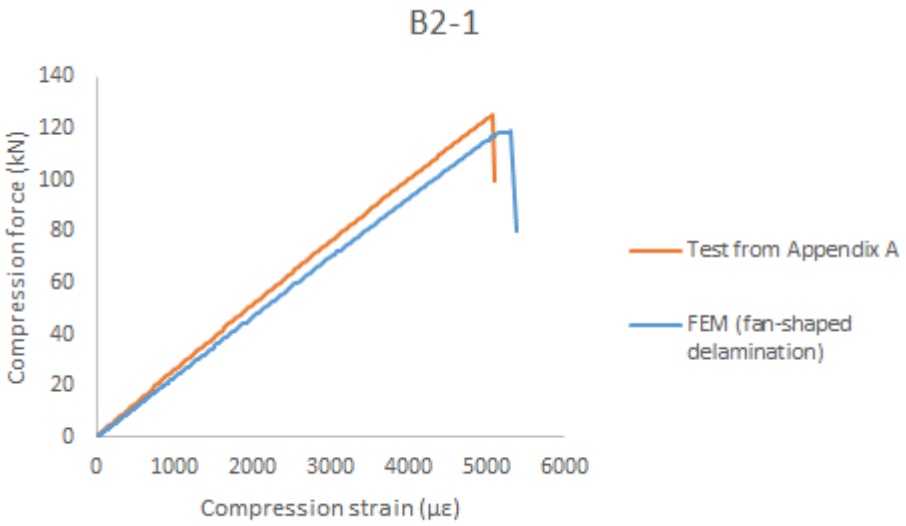
B2-1
Compression force (kN)
140
120
100
80
60
40
20
0
0
1000
2000
3000
4000
5000
6000
Compression strain (με)
Test from Appendix A
FEM (fan-shaped delamination)

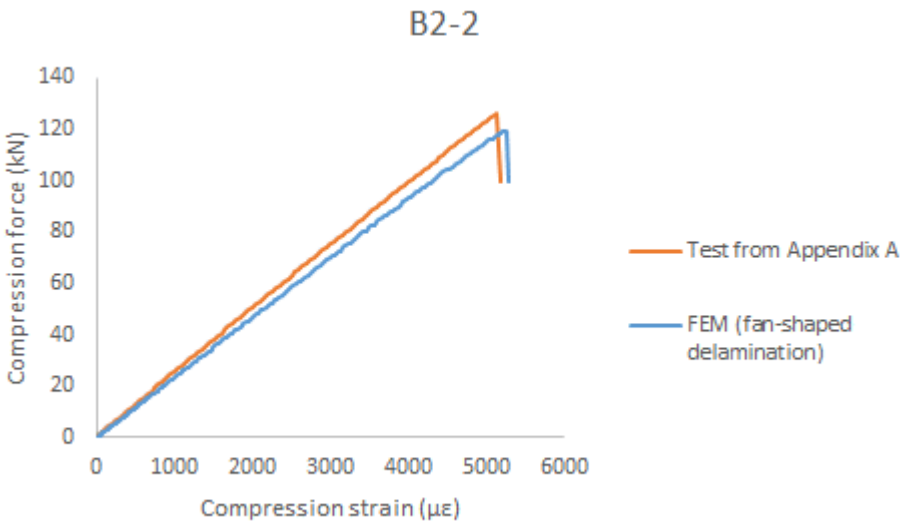
B2-2
Compression force (kN)
140
120
100
80
60
40
20
0
0
1000
2000
3000
4000
5000
6000
Compression strain (με)
Test from Appendix A
FEM (fan-shaped delamination)

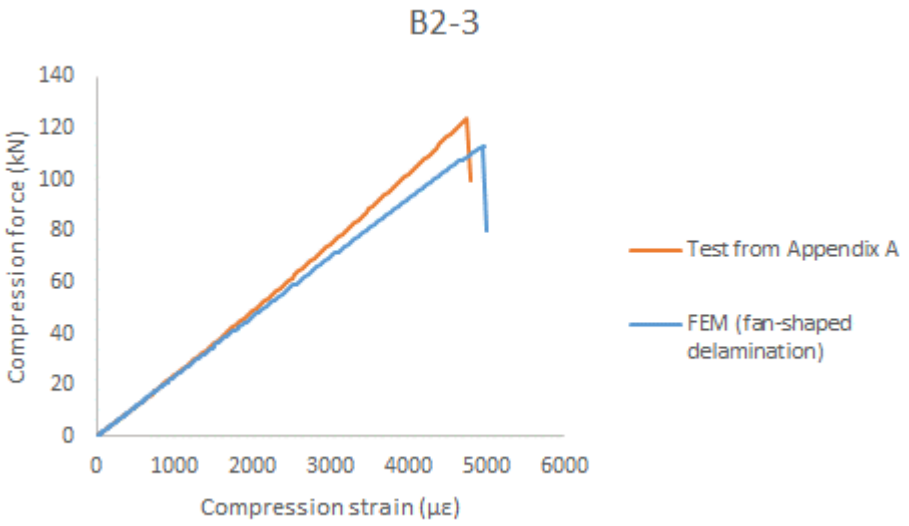
B2-3
Compression force (kN)
140
120
100
80
60
40
20
0
0
1000
2000
3000
4000
5000
6000
Compression strain (με)
Test from Appendix A
FEM (fan-shaped delamination)

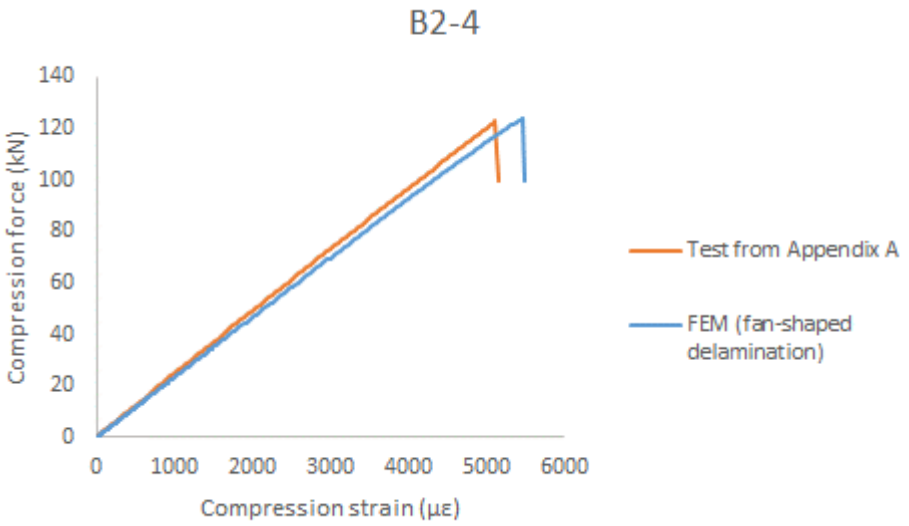
B2-4
Compression force (kN)
140
120
100
80
60
40
20
0
0
1000
2000
3000
4000
5000
6000
Compression strain (με)
Test from Appendix A
FEM (fan-shaped delamination)

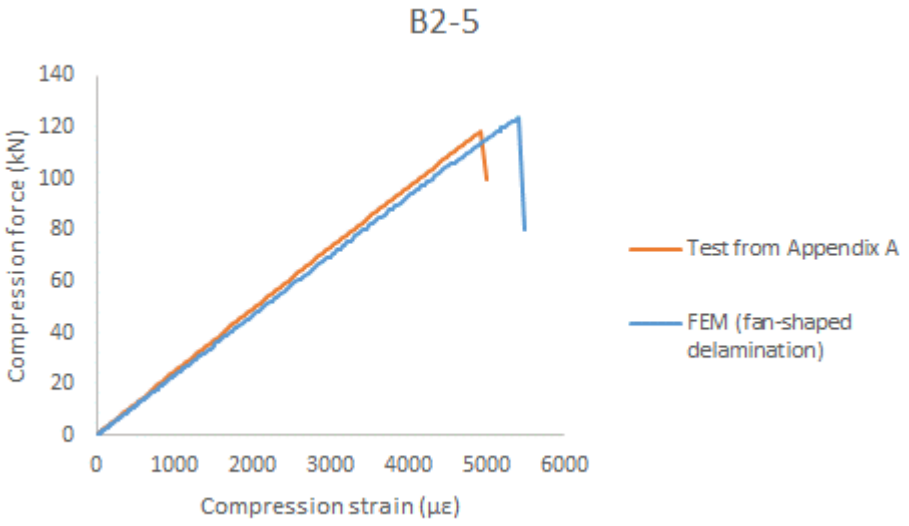
B2-5
Compression force (kN)
140
120
100
80
60
40
20
0
0
1000
2000
3000
4000
5000
6000
Compression strain (με)
Test from Appendix A
FEM (fan-shaped delamination)

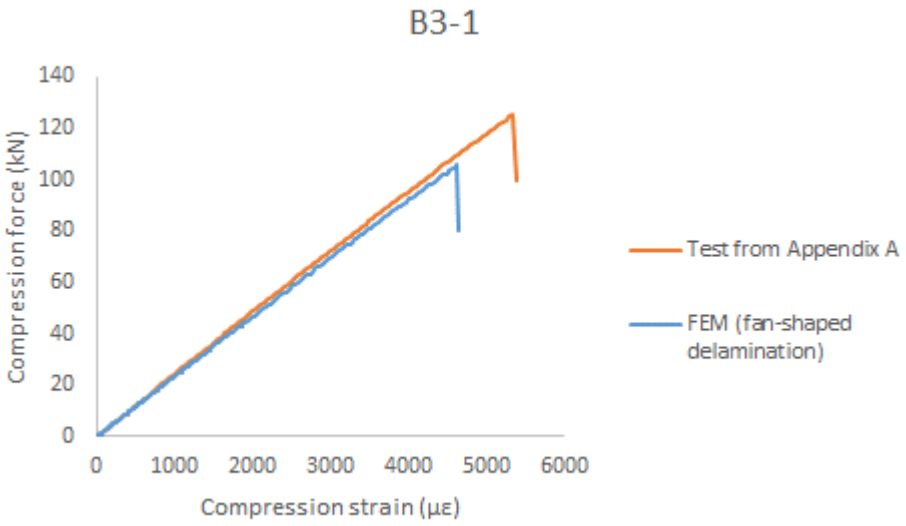
B3-1
Compression force (kN)
140
120
100
80
60
40
20
0
0
1000
2000
3000
4000
5000
6000
Compression strain (με)
Test from Appendix A
FEM (fan-shaped delamination)

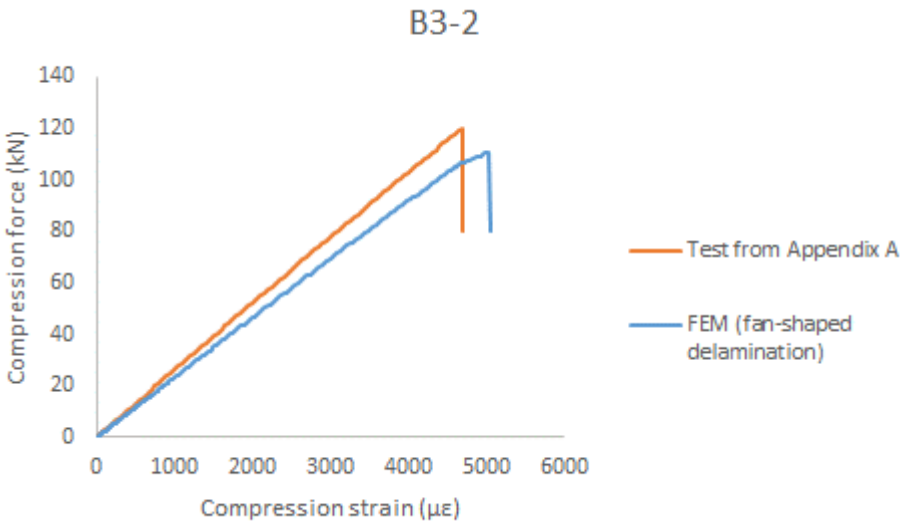
B3-2
Compression force (kN)
140
120
100
80
60
40
20
0
0
1000
2000
3000
4000
5000
6000
Compression strain (με)
Test from Appendix A
FEM (fan-shaped delamination)

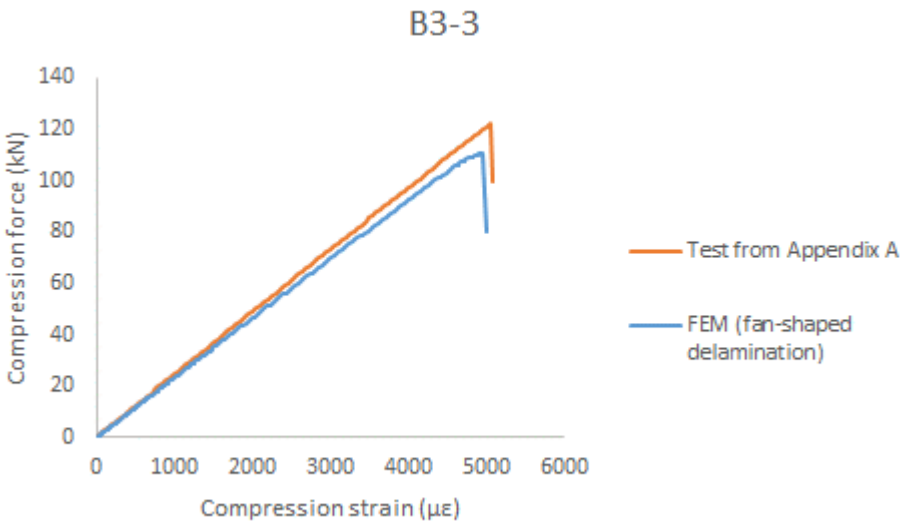
B3-3
Compression force (kN)
140
120
100
80
60
40
20
0
0
1000
2000
3000
4000
5000
6000
Compression strain (με)
Test from Appendix A
FEM (fan-shaped delamination)

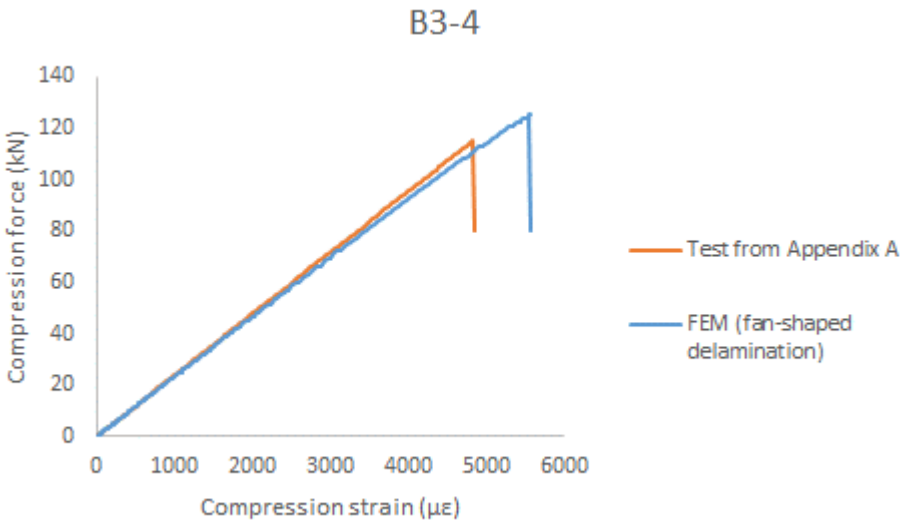
B3-4
Compression force (kN)
140
120
100
80
60
40
20
0
0
1000
2000
3000
4000
5000
6000
Compression strain (με)
Test from Appendix A
FEM (fan-shaped delamination)

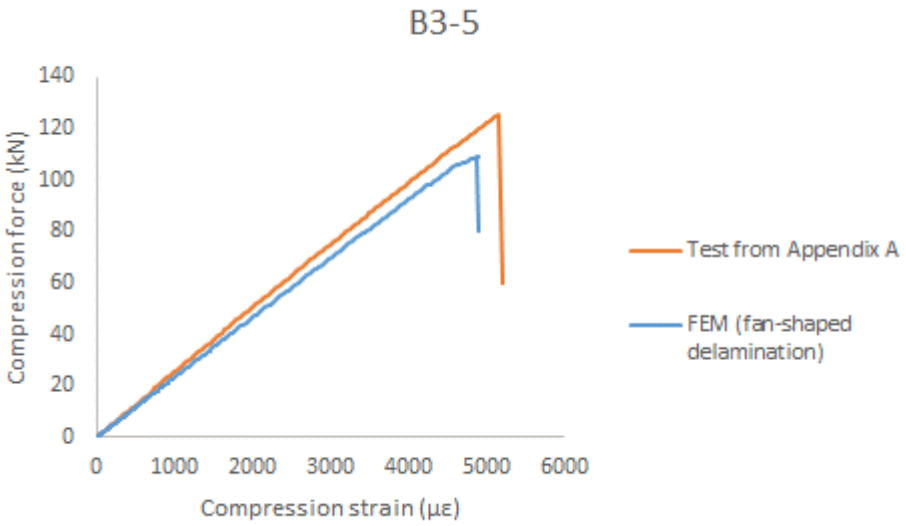
B3-5
Compression force (kN)
140
120
100
80
60
40
20
0
0
1000
2000
3000
4000
5000
6000
Compression strain (με)
Test from Appendix A
FEM (fan-shaped delamination)

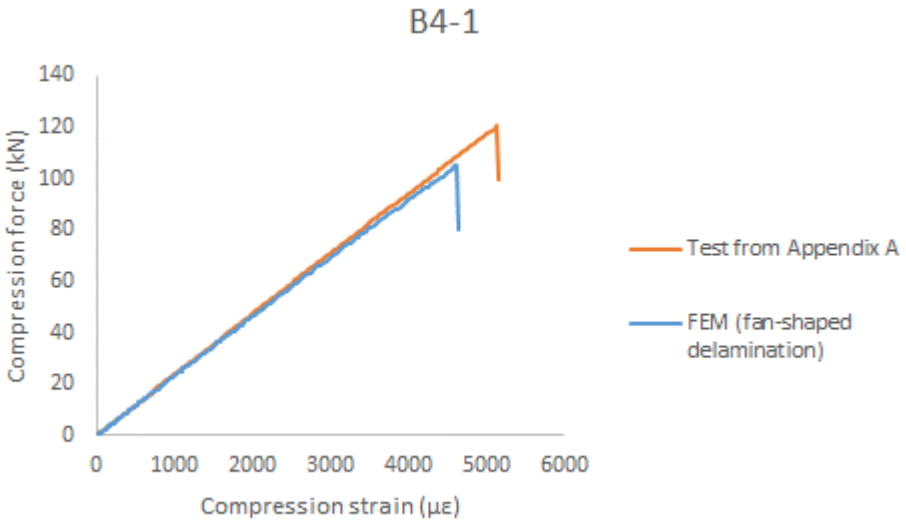
B4-1
Compression force (kN)
140
120
100
80
60
40
20
0
0
1000
2000
3000
4000
5000
6000
Compression strain (με)
Test from Appendix A
FEM (fan-shaped delamination)

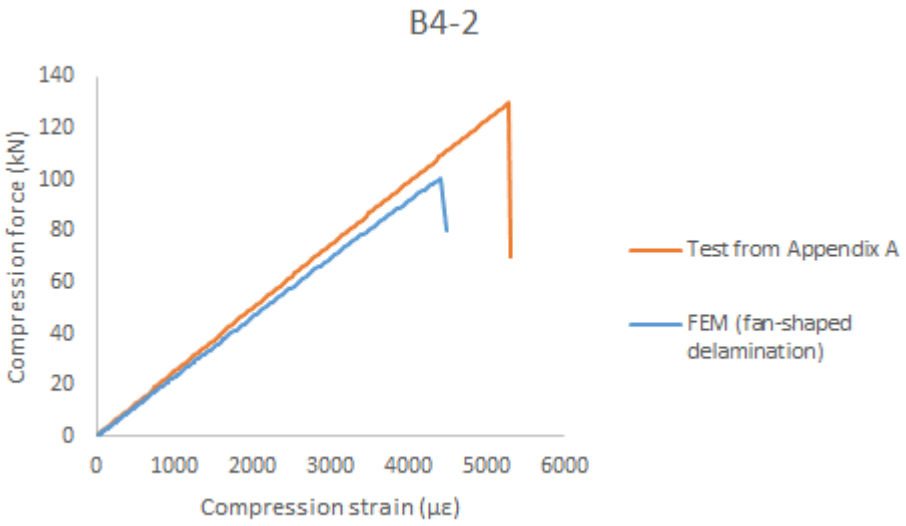
B4-2
Compression force (kN)
140
120
100
80
60
40
20
0
0
1000
2000
3000
4000
5000
6000
Compression strain (με)
Test from Appendix A
FEM (fan-shaped delamination)

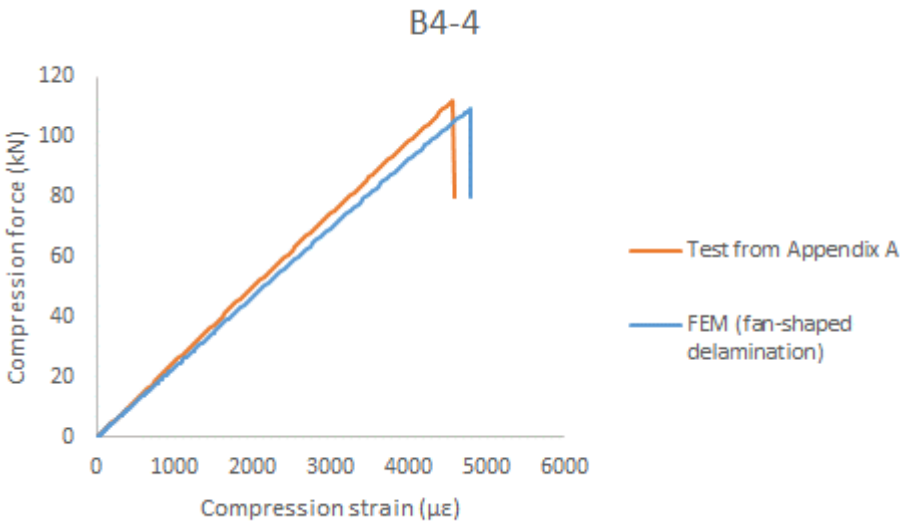
B4-4
Compression force (kN)
120
100
80
60
40
20
0
0
1000
2000
3000
4000
5000
6000
Compression strain (με)
Test from Appendix A
FEM (fan-shaped delamination)

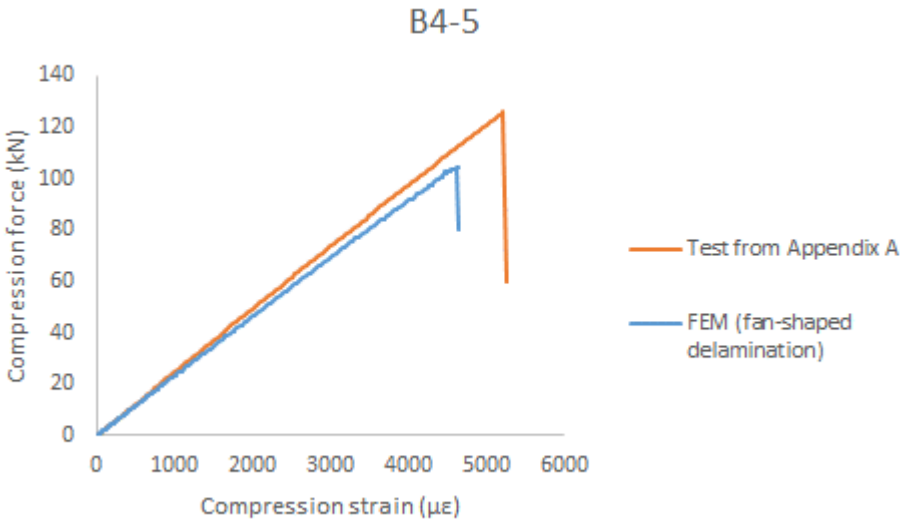
B4-5
Compression force (kN)
140
120
100
80
60
40
20
0
0
1000
2000
3000
4000
5000
6000
Compression strain (με)
Test from Appendix A
FEM (fan-shaped delamination)

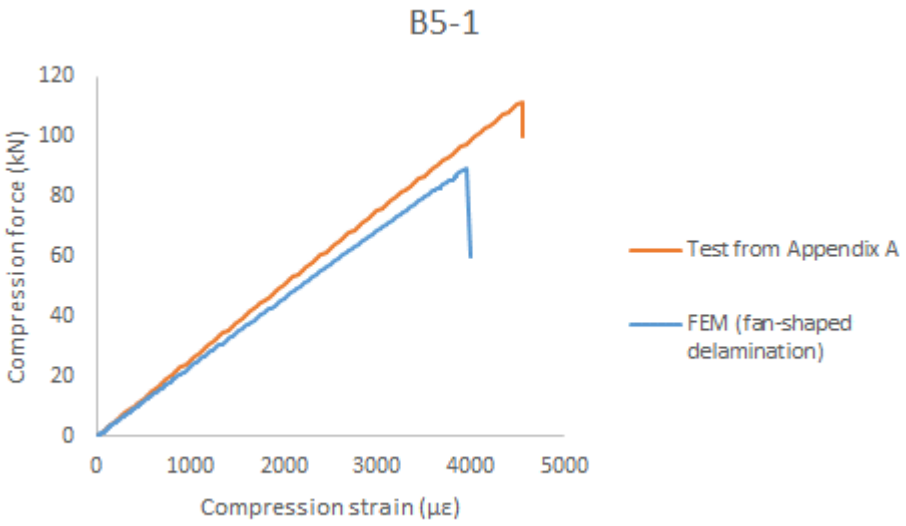
B5-1
120
100
80
60
40
20
0
Compression force (kN)
0
1000
2000
3000
4000
5000
Compression strain (με)
Test from Appendix A
FEM (fan-shaped delamination)

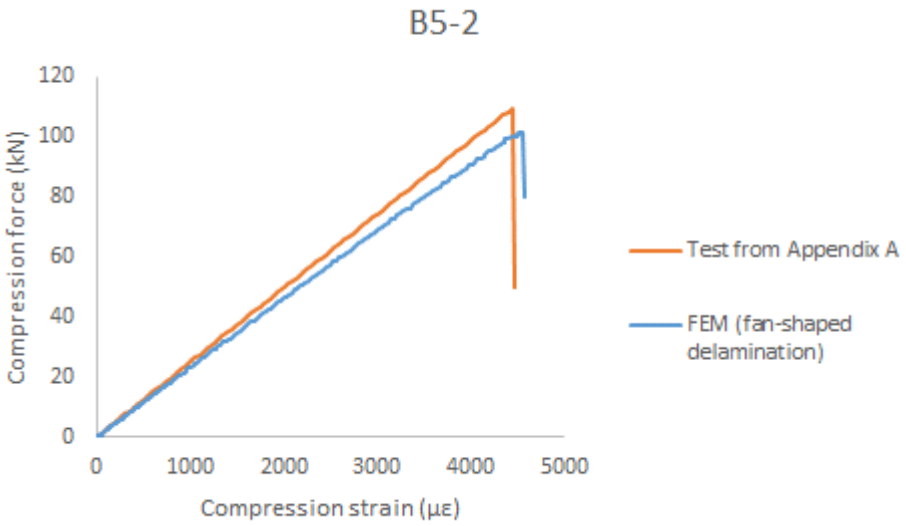
B5-2
120
100
80
60
40
20
0
Compression force (kN)
0
1000
2000
3000
4000
5000
Compression strain (με)
Test from Appendix A
FEM (fan-shaped delamination)

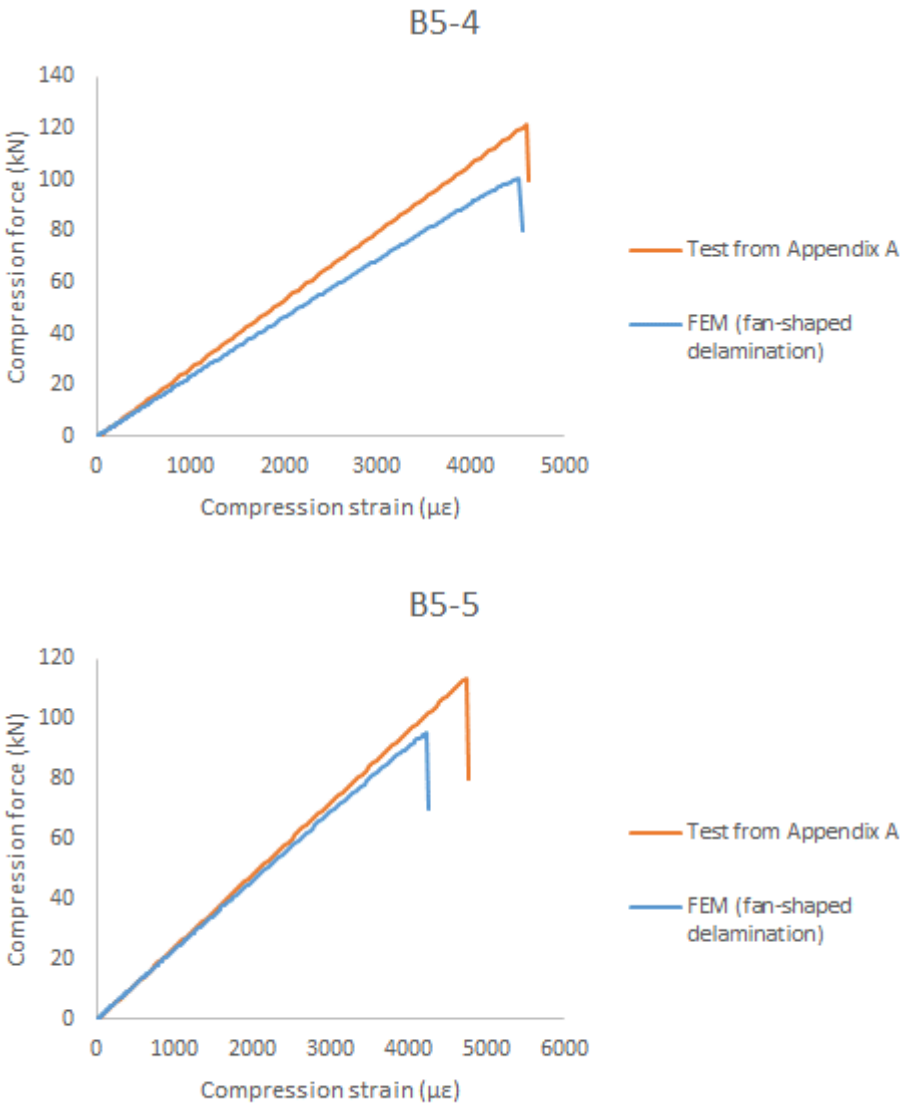

Figure 5.6 Comparison between experimental results and detailed FE models with circular and double spiral fan-shaped delaminations

5.2.5 Likelihood of delamination propagation

Although no delamination propagation is observed from all detailed FE models, it cannot guarantee this reflects the real damage mechanism because of relatively coarse mesh. As mentioned in Section 4.7.2, the element in-plane size is 1mm, which is too coarse and has the effect to deter propagation simulation using cohesive elements.

Nevertheless, there are two evidences from different aspects to support this conclusion. The first one is through the damage state investigation of the cohesive elements at the delamination front. The Damaging State Function (DSF), mentioned in Section 4.2, is employed here again. DSF reflects how large the margin is from the current state of cohesive element to its failure. The value of DSF varies between 0 and 1, where 0 means free of stress and 1 means initiation of failure. For each model in Table 5.1, the highest value of DSF of every single interface before fibre failure (after fibre failure DSF may exceed 1, but that is the consequent failure of neighbouring collapsed plies), from both the circular and double spiral fan-shaped delamination patterns, is extracted to form the curves in Figure 5.7. It can be seen that all DSF values are below 1, while the values from models with double spiral fan-shaped delaminations are significantly lower than that of counterpart models with circular delaminations. This proves the conclusion obtained in Section 4.8.4.3 from parametric study that the smaller delamination size, the less likelihood delamination propagation takes place again. However, these far-below-one DSF values in double spiral fan-shaped model can still not confirm that delaminations do not propagate in corresponding real CAI cases because the error of DSF between current models with coarse mesh and models with sufficiently refined meshes is unknown.

The second evidence is as follows. A phenomenon through Figure 4.86 is observed that with the same projected delamination area, the failure load of models bearing 11 delaminations are even higher than that of models with 7 delaminations. The reason is that larger extent of delamination propagation takes place in the models with 7 delaminations, which undermines the overall stiffness of the plate and accelerates stress concentration more significantly, leading earlier collapse of the whole plate consequently. This reveals the fact that delamination propagation can

impair the compressive load sustainability, and the larger extent of delamination propagation the lower ultimate compressive load to sustain. This principle helps to confirm the damage mechanism of CAI here. For example, reduce the CERR of A3-1-Spi, B4-1-Spi and B5-1-Spi artificially 2, 3 and 4 times to let delamination propagation to take place in different extents (as an example, B4-1-Spi is selected to show the diverse extents of delamination propagation when failure load is reached from Figure 5.8 to Figure 5.10 due to different reduced CERRs), successive drop of failure load is obtained accordingly in Figure 5.11. Therefore, if large extent of delamination propagation takes place in corresponding real CAI cases, the experimental CAI strength would not be higher than the predicted values from the model with original CERR but fall among the predicted values from models with reduced CERRs.

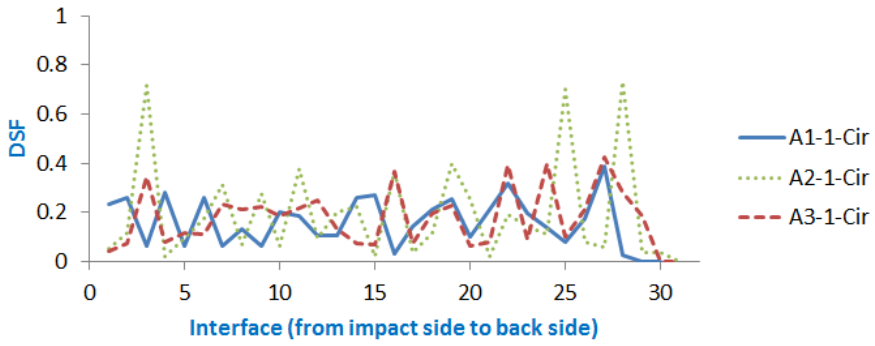

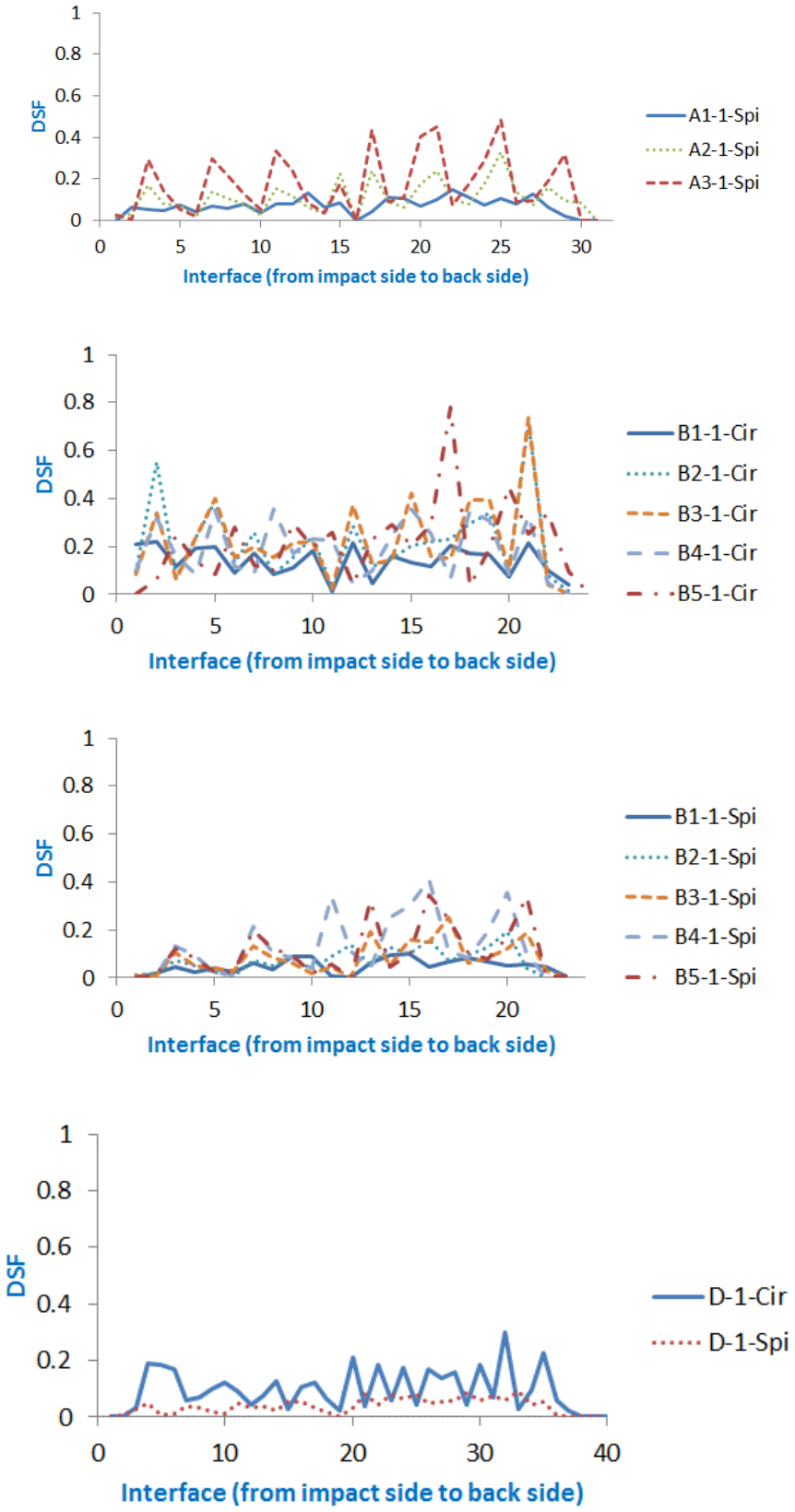

Figure 5.7 Maximum damage state function (DSF) of every single interface of all models in Table 5.1

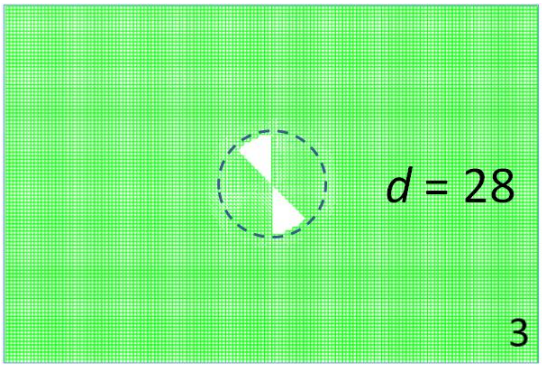
d = 28
3

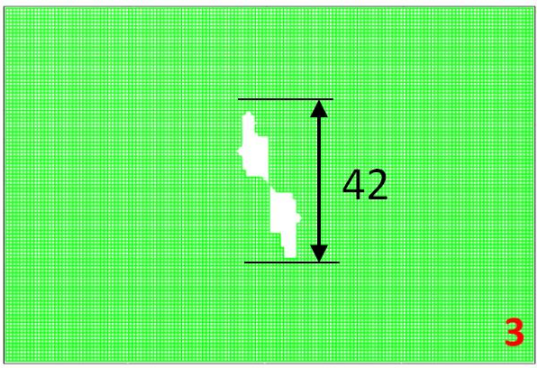
42
3

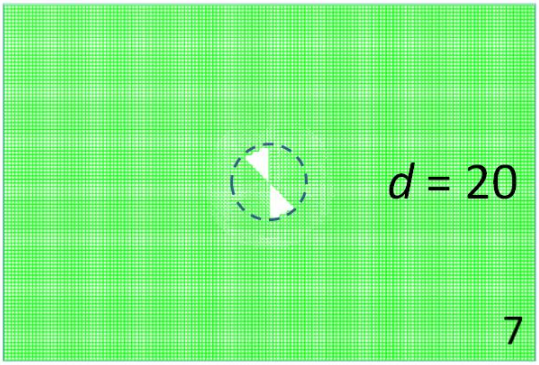
d = 20
7

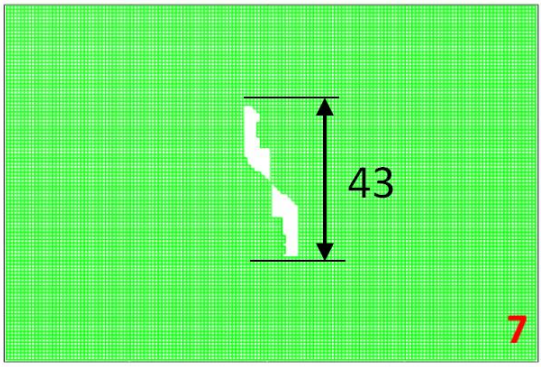
43
7

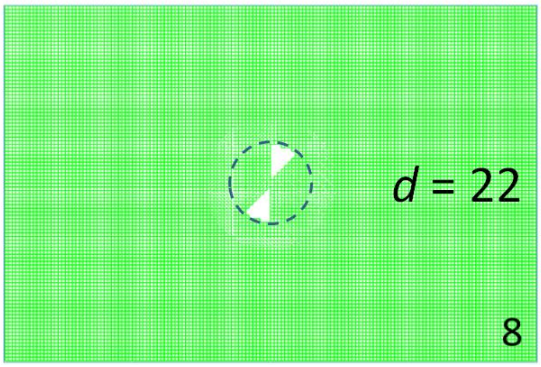
d = 22
8

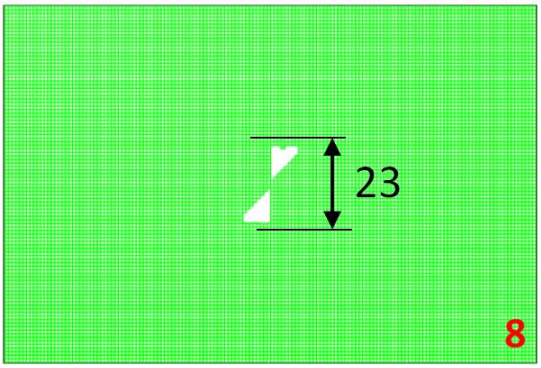
23
8

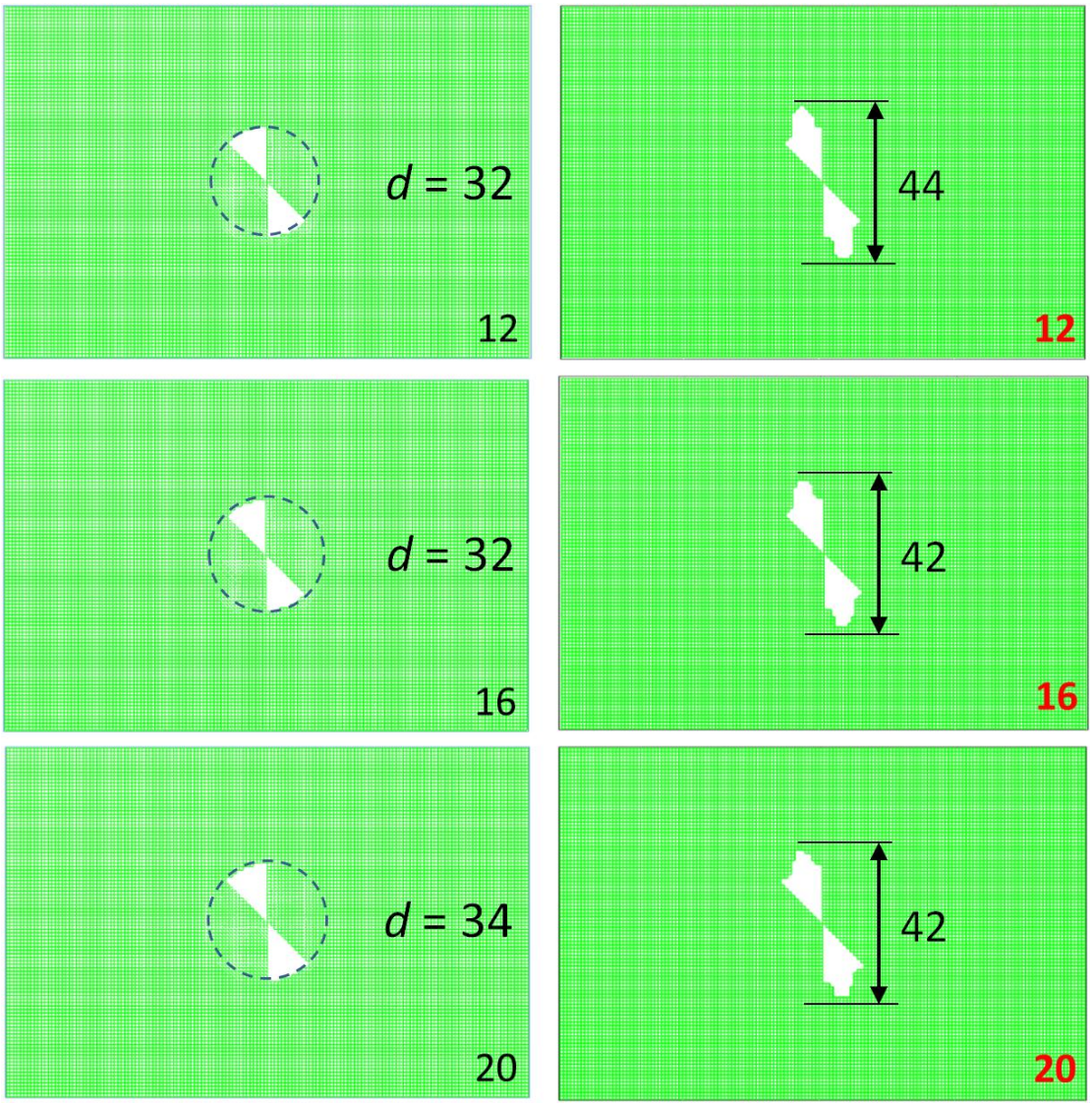

Figure 5.8 The state of delamination propagation of B4-1 configured with 1/2 CERR (highlighted in interfaces marked with red numbers, mm)

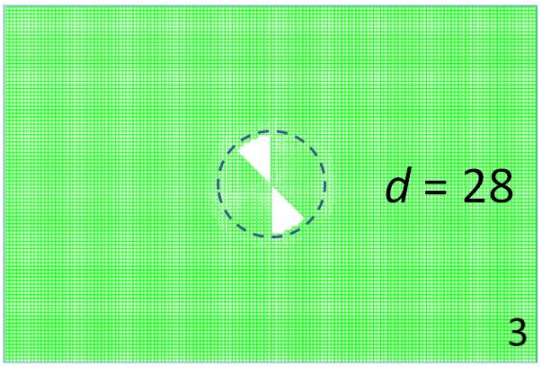
d = 28
3

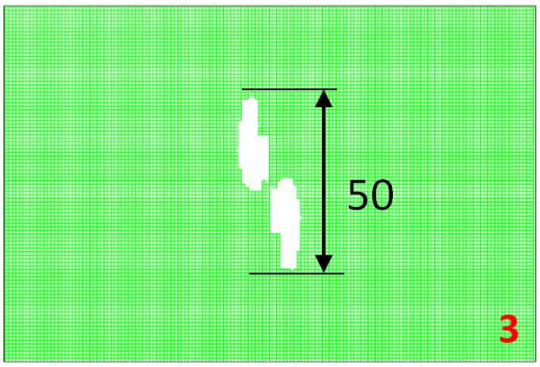
50
3

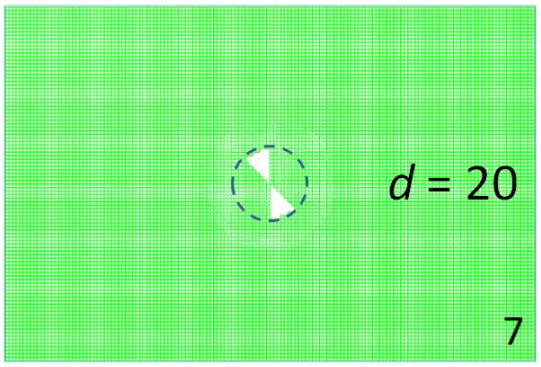
d = 20
7

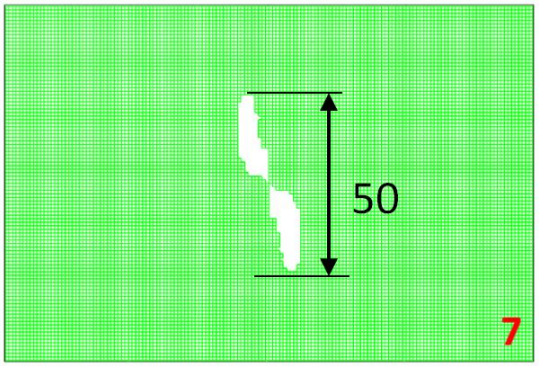
50
7

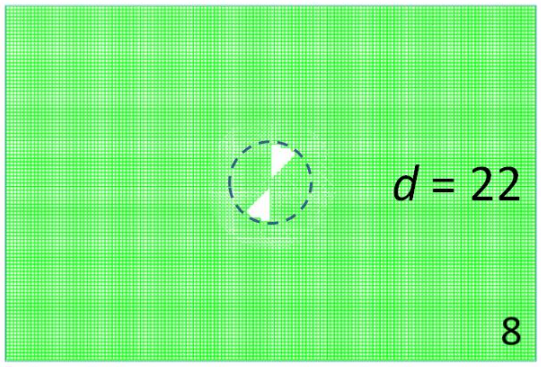
d = 22
8

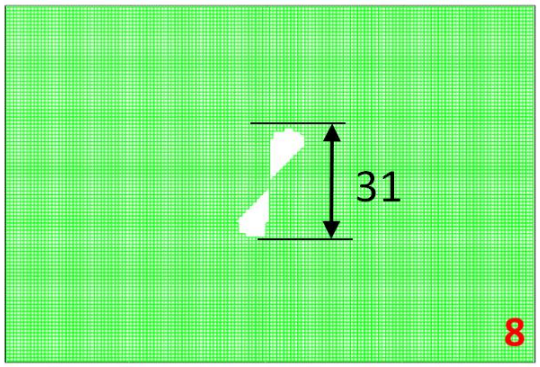
31
8

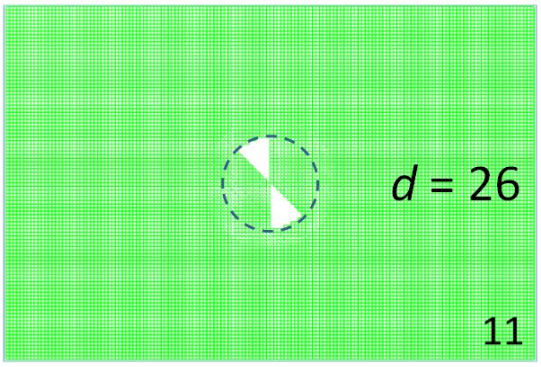
d = 26
11

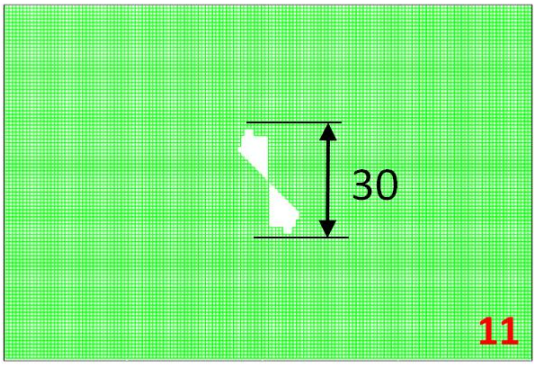
30
11

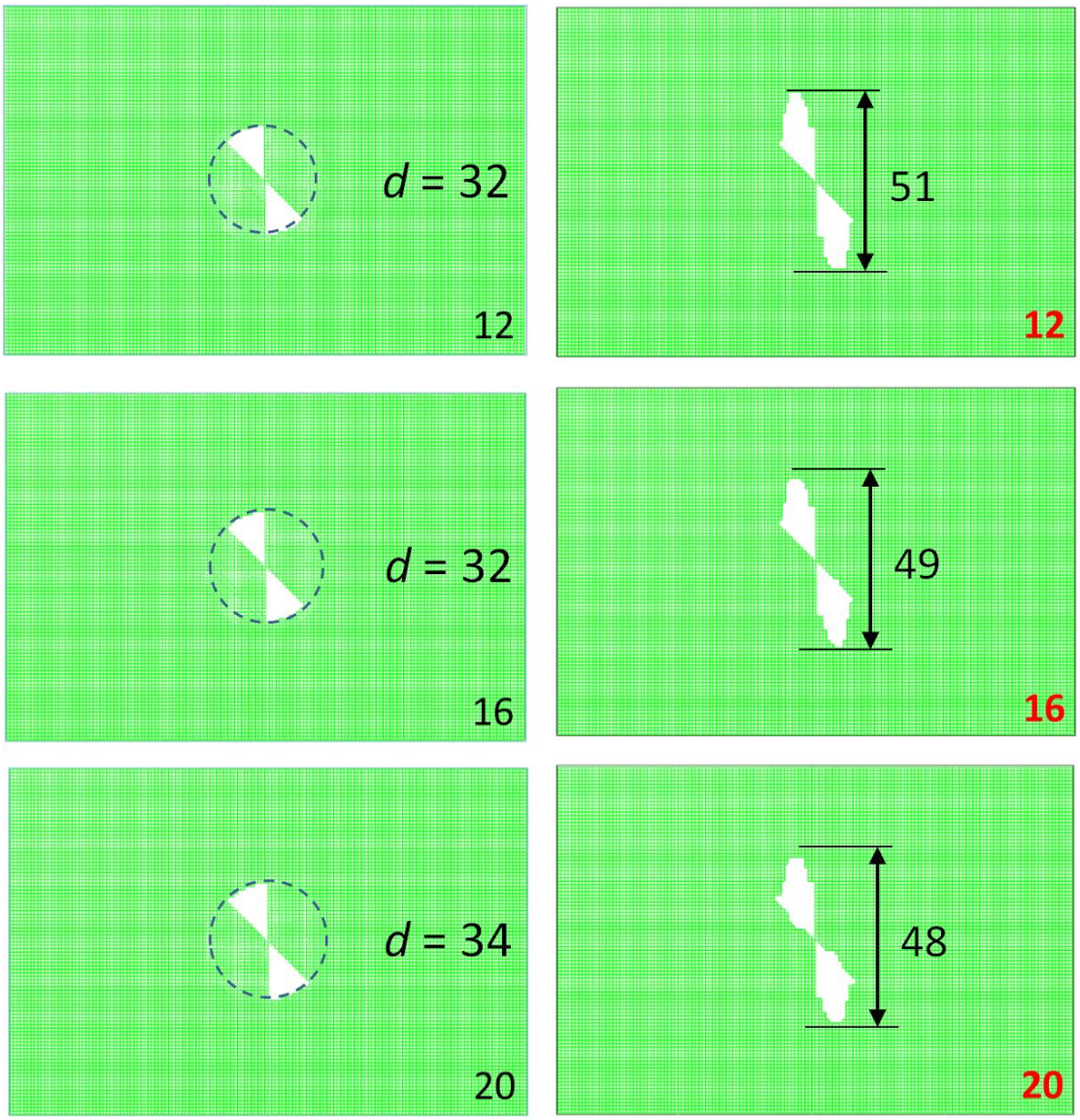

Figure 5.9 The state of delamination propagation of B4-1 configured with 1/3 CERR (highlighted in interfaces marked with red numbers, mm)

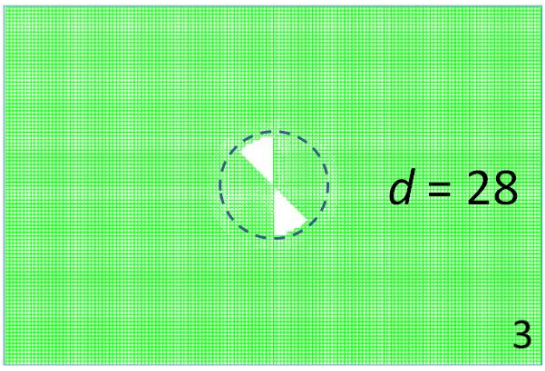
d = 28
3

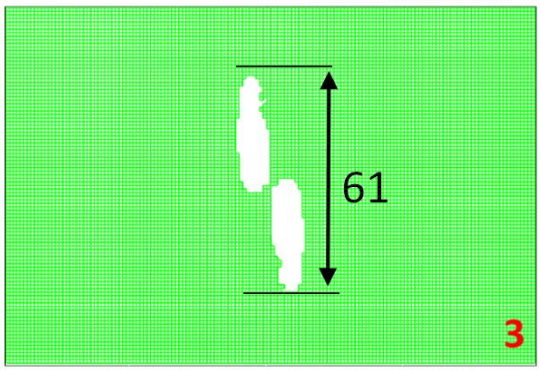
61
3

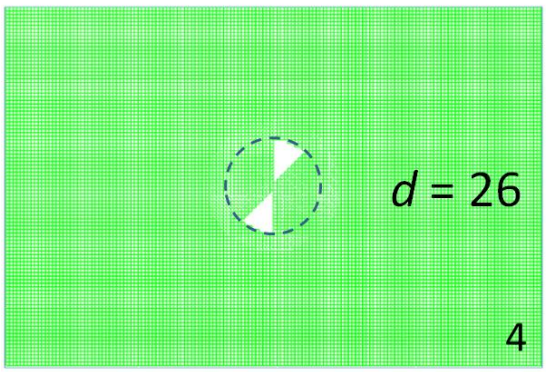
d = 26
4

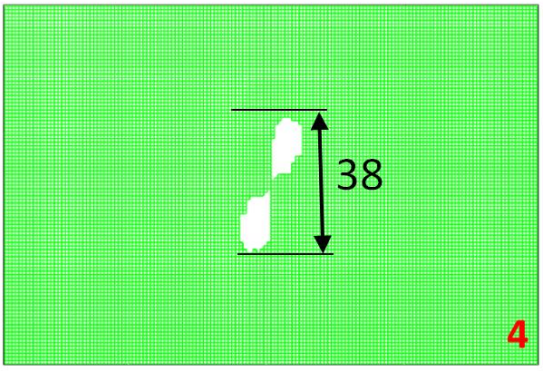
38
4

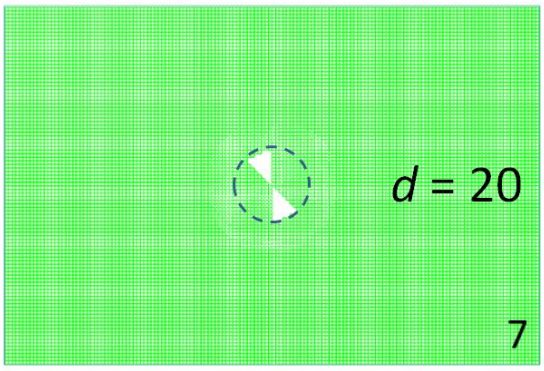
d = 20
7

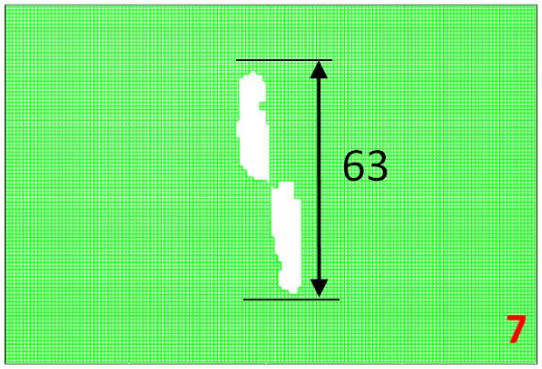
63
7

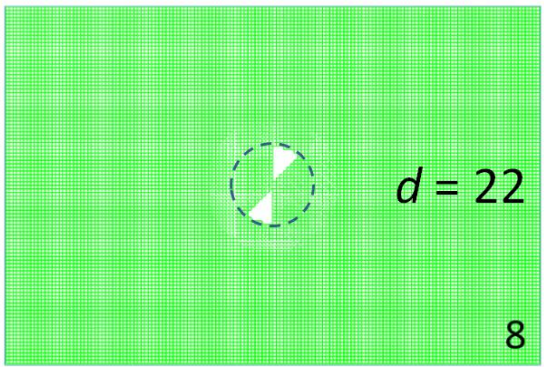
d = 22
8

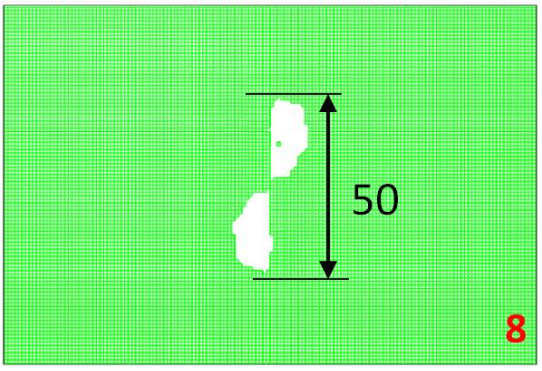
50
8

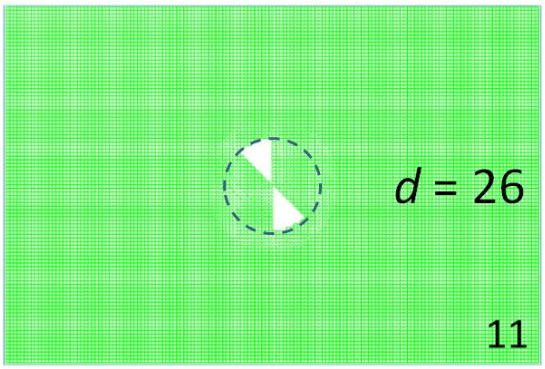
d = 26
11

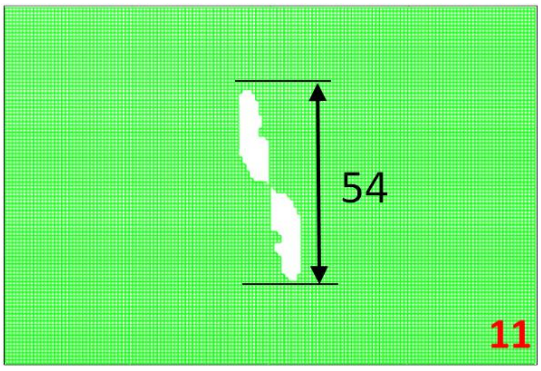
54
11

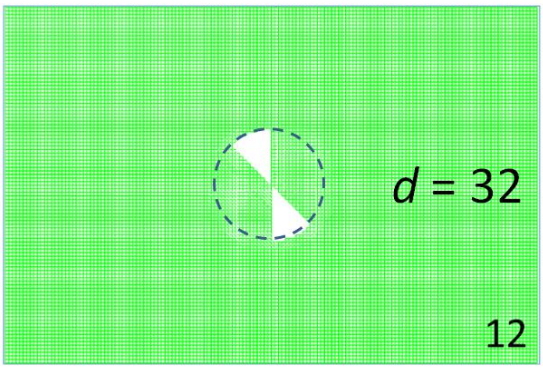
d = 32
12

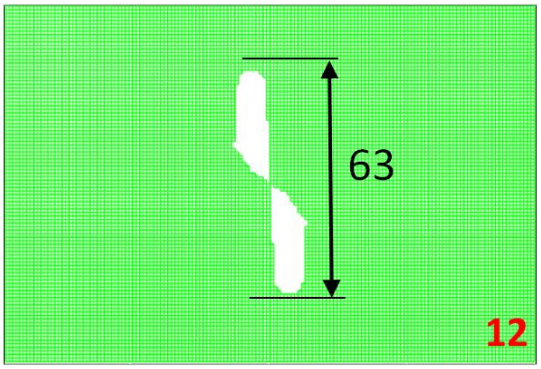
63
12

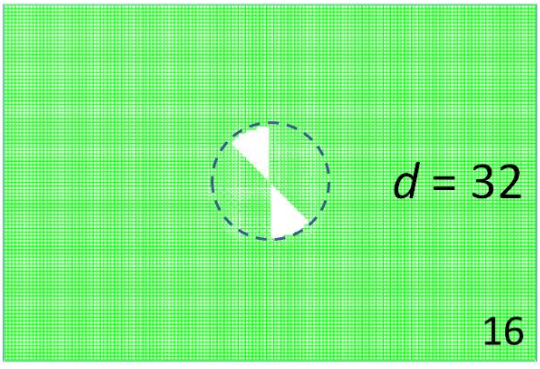
d = 32
16

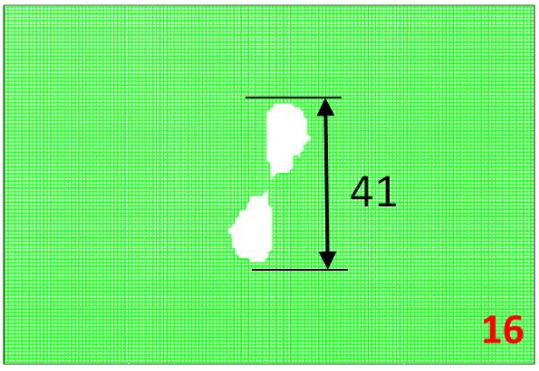
41
16

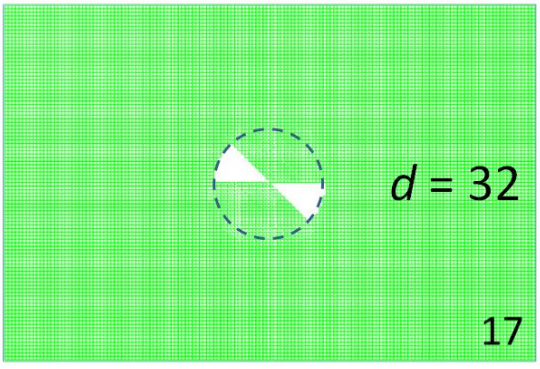
d = 32
17

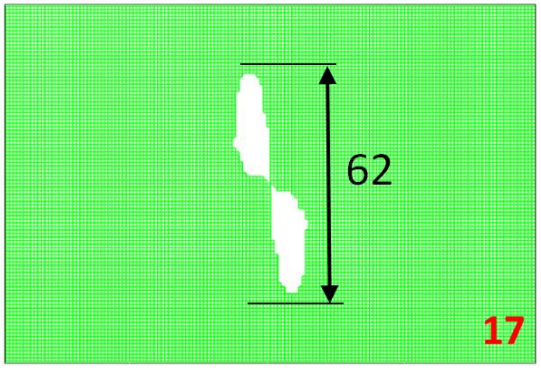
62
17

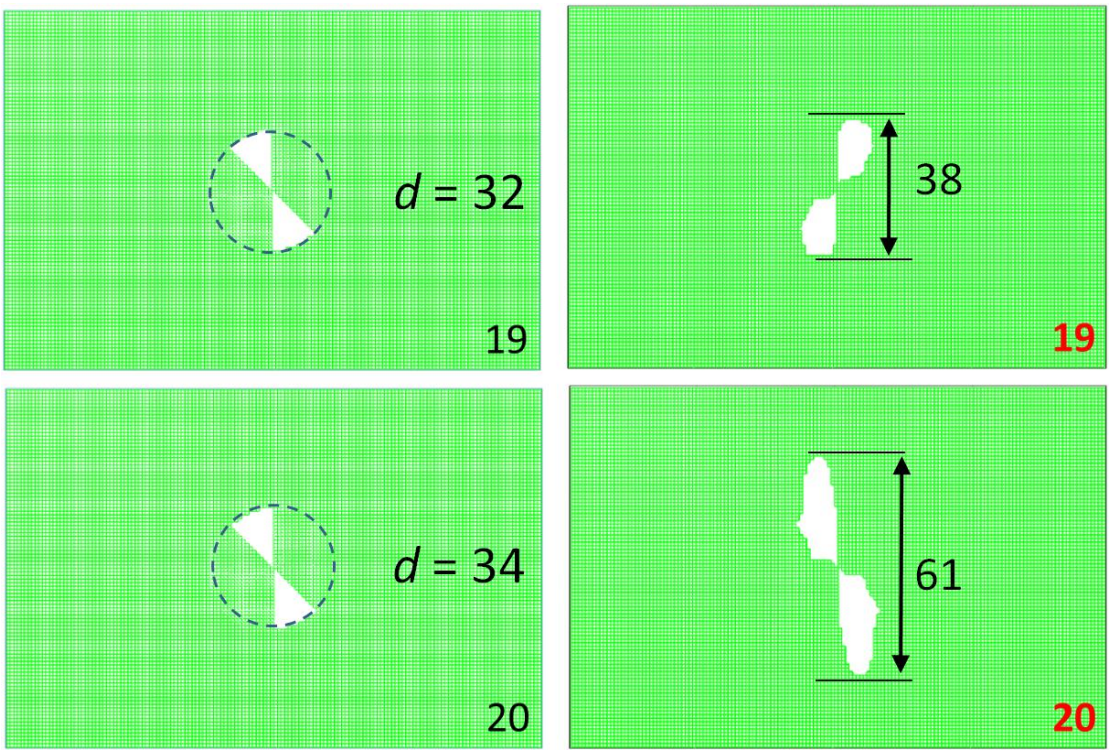

Figure 5.10 The state of delamination propagation of B4-1 configured with 1/4 CERR (highlighted in interfaces marked with red numbers, mm)

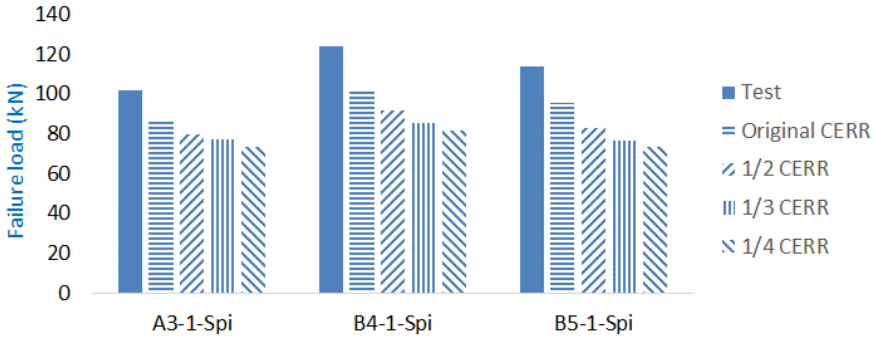

Figure 5.11 Failure loads comparison among test, detailed FE model with original, 1/2, 1/3 and 1/4 CERR

For the rest experimental samples which are not evaluated through the detailed FE modelling due to insufficient knowledge of delamination distribution over thickness through single-faced scan, similar conclusion can still be made. Regarding group A4 and A5, similar projected

delamination area (Figure 3.19) but deeper or even penetrated impact dent were observed (Table A.3(d) and (e)) compared with group A3. This means that more fibres were broken and more matrix material were smashed due to impact, which would impair the bending stiffness of sublaminates further and impede delamination propagation to take place accordingly. Regarding group C, with the same lay-up sequence and similar mechanical properties (Table A.1) of group D, but subjected to lower impact energy (Table A.3(l)) and induced smaller projected delamination area (Figure 3.8 versus Figure 3.18), it is reasonable to expect that delamination propagation is unlikely to take place either.

According to above arguments, it is reasonable to expect that these detailed FE models bearing double spiral fan-shaped delaminations listed in Table 5.1 capture the genuine damage mechanism of corresponding tests generally. It also suggests that all these experimental samples in this thesis collapsed mainly due to in-plane failure initiating around the delamination front and delamination propagation is unlikely to take place (at least not in large extent).

5.2.6 A conclusion on the CAI damage mechanisms

Based on the discussion above, it is appropriate to conclude that the damage mechanisms for all the CAI experiments as presented in Appendix A of this thesis are as follows. When an impact damaged laminate is subjected to the in-plane compressive load, the delaminated laminae in the damaged area buckle and this leads to stress redistribution around the damage area. Stress concentration arising around the delamination front triggers in-plane failure and subsequent collapse of the entire laminate. During the process, delamination propagation does not take place.

This conclusion has the potential for wider applicability beyond the current CAI cases because the experimentally tested samples supporting this conclusion have following representative characteristics, although extensive verification is needed as future work.

Firstly, the material systems of these experimental samples represent the leading edge composite systems currently utilized for primary structure of modern aircrafts, especially configured with toughened matrices. They have similar properties with those material systems, for example, Torayca T800H/3900-2 utilized for Boeing B777 and B787 Dreamliner [100], HexPly M21/IMA for Airbus A350 XWB, respectively [101].

Secondly, they have representative lay-up sequences. Although in practical use the lay-up sequence may vary according to specific design requirements, they have to obey the basic principle that laminae with same fibre orientation should avoid being laid up together [77]. This will render a large number of delaminations induced by foreign object impact, potentially on each interface involved in the laminate which is the key factor (founded through parametric study in Chapter 4) to impede delamination propagation.

Thirdly, the range of impact damage involved in this thesis covers full range of practical significance, from BVID to nearly full penetration.

Fourthly, they have the representative geometry, 150mm in length and 100mm in width. An alternative according to NASA Reference Publication 1092 [18], 254mm in length and 127mm in width, has become less commonly used now as it requires more material.

5.2.7 Practical suggestions

The coarse mesh employed in this chapter is a compromise, since the model with sufficiently refined mesh is usually computationally unaffordable. It can be easily estimated that the node number of current model with 48 plies is almost 1.5 million. If the element size decreases 4 or 5 times, even applied to the delaminated area only, the model size would be incredible. On the other hand, this extremely refined mesh is unnecessary and a huge waste if delamination propagation does not occur or only in tiny extent. Since it is reasonable to expect that delamination propagation does not take place (at least not extensively) in most CAI cases with BVID, a practical suggestion for CAI prediction while avoiding unaffordable computation cost can be given as follows, which is also summarized in flowchart Figure 5.12.

When evaluating the CAI strength of a given laminate configuration, one can conduct the CAI test to a specimen which has experienced the most serious impact damage state within the test plan (e.g. by overlapped delamination area). Then the corresponding detailed FE model can be constructed and analysed with coarse mesh presented in this chapter. One can only encountered one of the three cases. The first case is that delamination propagation is observed from the FE modelling. This negates the applicability of this modelling method at this impact damage level because even with this coarse mesh delamination propagation has been predicted, higher extent of delamination propagation would be investable in corresponding real CAI cases. The second case is that although delamination propagation is not observed in the FE model, the predicted CAI strength is significantly higher than the experimental value. This also restricts the applicability of this modelling method at this impact damage level because higher extent of delamination propagation would be expected in real CAI cases. If either of above cases is encountered, the CAI experiment with a less severe impact damage within the test plan needs to be conducted and the

FE analysis process repeat until the third case is met. The third case is that delamination propagation is not observed in the FE model and the predicted CAI strength is lower and close to the experimental value. In this case, the FE model captures the real damage mechanism generally, and the specimens with smaller delamination area can be simulated through this FE modeling method with sufficient level of confidence.

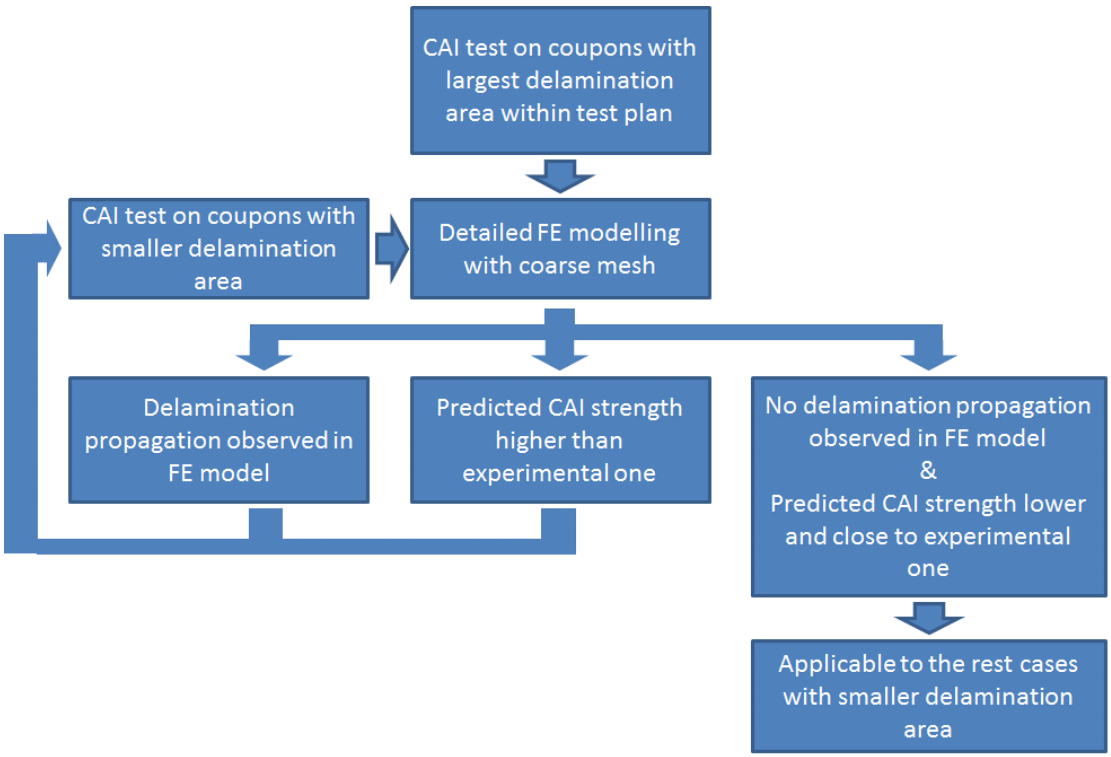

Figure 5.12 Flowchart of applying detailed FE model with coarse mesh to predict CAI

5.3 CAI prediction

Through above method, CAI strength can be predicted mostly at the conservative side. This is because the assumption of delamination distribution is inclined to overestimation. Meanwhile,

an idea emerges that what is the consequence if delamination distribution in detailed FE model is determined from C-scan result directly? The predicted CAI strength will be overestimated too much or only slightly? These will be explored in the following sections.

5.3.1 Manipulation of scan data

As discussed in Section 3.3, the C-scan results can be categorized into 3 types. The first type is featured by double-sided and complete scan. Group B and D belong to this type. The second type is featured by double-sided but incomplete scan. Sub-group A1, A2 and A3 belong to this type. The third type is featured by single-sided scan. Sub-group A4, A5 and group C belong to this type.

For the first type, the scan results can be input into the detailed FE models directly for CAI simulation. For the second type, however, because of severe damage on the surface over the impactor-contacted area, C-scan could not be properly conducted over that part, leaving a blind area of C-scan data. If this kind of scan data was fed directly into the CAI simulation without any manipulation, the detailed FE model would be considered having a much less damaged zone and CAI strength would be overestimated consequently. For the third type, it will be a shame if the scan data were not utilized simply because of their single-sided nature. In real field application of non-destructive inspection, single-sided scan is the most likely case as the back face is usually inside the structure and hence inaccessible. Therefore, manipulations are needed to recover some delamination spots according to the known delamination distribution from scan and to make such scanned results useful for the CAI predictions.

For the second scan type, it is assumed that the number of artificial spots on each interface is determined by the number of real spots on that interface detected from scan and the

superimposed delamination area of the whole laminate. Because on each individual interface the number of detected spots can vary significantly depending on which side the scan was taken from (from Section 3.3.1 it is found that spots detected from the impacted face distribute almost on all interfaces through laminate thickness, while spots from back face mainly appears on the latter half thickness of the laminate), the numbers of artificial spots are estimated from impact and back face separately through following equations.

$$N_{\mathrm{i}}^{\mathrm{impact-artifical}} = \frac{S_{\mathrm{blank}}}{S_{\mathrm{superimposed}}} N_{\mathrm{i}}^{\mathrm{impact-real}}$$
$$N_{\mathrm{i}}^{\mathrm{back-artifical}} = \frac{S_{\mathrm{blank}}}{S_{\mathrm{superimposed}}} N_{\mathrm{i}}^{\mathrm{back-real}} \quad (5.4)$$

where $N_{\mathrm{i}}^{\mathrm{impact-artifical}}$ the estimated number of artificial spots on interface i from impact face,

$N_{\mathrm{i}}^{\mathrm{back-artifical}}$ the estimated number of artificial spots on interface i from back face,

S_{blank} the blank heart area,

$S_{\mathrm{superimposed}}$ the superimposed delamination area detected by C-scan,

$N_{\mathrm{i}}^{\mathrm{impact-real}}$ the number of real spots detected from impact face scan on interface i,

$N_{\mathrm{i}}^{\mathrm{back-real}}$ the number of real spots detected from back face scan on interface i.

Once the number of spots on each interface is determined, the artificial spots are randomly distributed in the blank area through the random function in Matlab.

For the third type of scan data, the entire spots from back face need to be assumed because only impact face is scanned. As impact energy, laminate thickness, lay-up sequence, etc. will affect the delamination distribution significantly, it is wise to assume the trend of the distribution of

delamination spots from the back face based on other specimens which possess similar characteristics through following equation.

$$N_{\mathrm{i}}^{\mathrm{back-artifical}} = \frac{N_{\mathrm{i}}^{\mathrm{back-ref}}}{N_{\mathrm{all}}^{\mathrm{back-ref}}} N_{\mathrm{all}}^{\mathrm{impact}} \tag{5.5}$$

where $N_{\mathrm{i}}^{\mathrm{back-artifical}}$ the estimated number of artificial spots on interface i from back face,

$N_{\mathrm{i}}^{\mathrm{back-ref}}$ the number of spots detected from back face scan on interface i of reference,

$N_{\mathrm{all}}^{\mathrm{back-ref}}$ the total number of spots detected from back face scan of reference,

$N_{\mathrm{all}}^{\mathrm{impact}}$ the total number of spots detected from impact face scan of this specimen.

Here, the trend of distribution for group C follows the average distribution tendency of group D as reference because these two groups have the same lay-up sequence, sub-group A4 and A5 follow sub-group A3 as reference because only A3 is the most close to them. Additionally, for sub-group A4 and A5 there is still an issue that a significant part of the central area failed to be scanned from impact face. Similar manipulation as dealing with the second type through first equation of Equation (5.4) has to be conducted to reconstruct the delamination spots from impact face.

5.3.2 FE model with C-scan result

The strategy of constructing detailed FE model with C-scan results here is the same as before. The only difference is that delamination is not over a continuous area anymore. As analysed in Section 3.3, the C-scan data consists of massive spots, each of which represents a unit square area (1mm^2) of delamination. These spots are identified by their unique coordinates including

in-plane coordinate and depth in laminate thickness. According to the location of spots detected from C-scan, corresponding cohesive elements are absent to represent the existence of delamination. From section view of the detailed FE model, the delamination distribution may be like Figure 5.13, in which hatched rectangles represent initial delaminations. The bold lines in between sublaminates represent interfaces where delamination may propagate through.

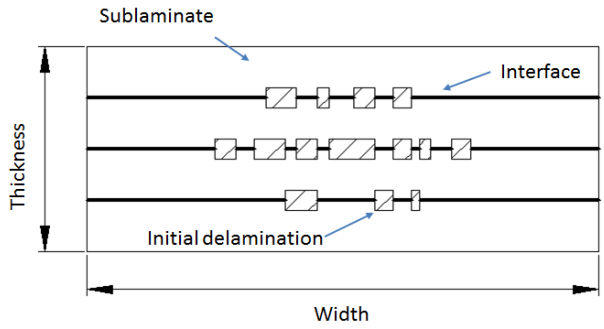

Figure 5.13 Schematic section view of laminate bearing scanned delaminations

5.3.3 Comparison

Figure 5.14 compares the CAI strength between experiments and detailed FE models bearing double spiral fan-shaped delaminations and scanned delaminations for all specimens, respectively. It is found that both patterns of detailed FE models have relatively good agreement with experiments. Moreover, in most cases, the predicted CAI from models of scanned delaminations and double spiral fan-shaped delaminations produced the higher and lower estimate of the experimental result, respectively. This phenomenon is explained like this. As discussed before, double spiral fan-shaped delaminations may still slightly overestimate the

delamination status in reality. On the other side, scanned delaminations actually only reflex the profile of overall delamination distribution and the delamination inside is ignored, which lead underestimate of the reality. Therefore, it is reasonable to suggest that using these two patterns of detailed FE models to define the upper and lower bounds of CAI strength, respectively.

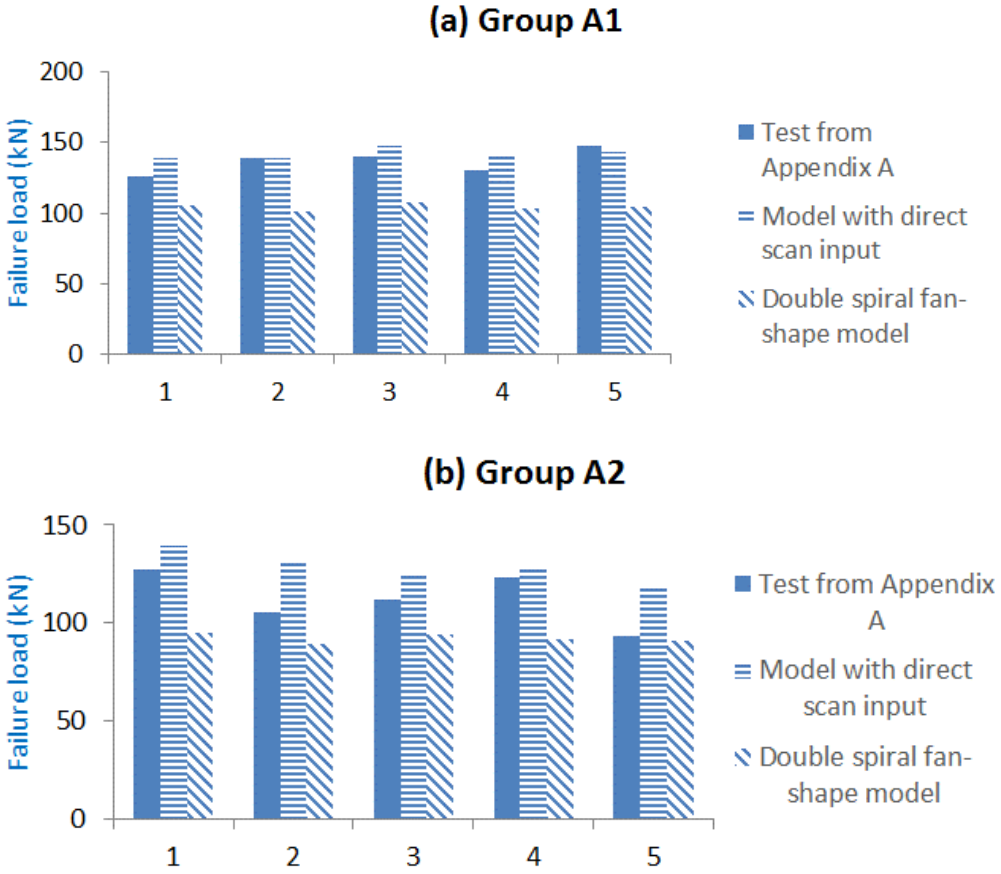

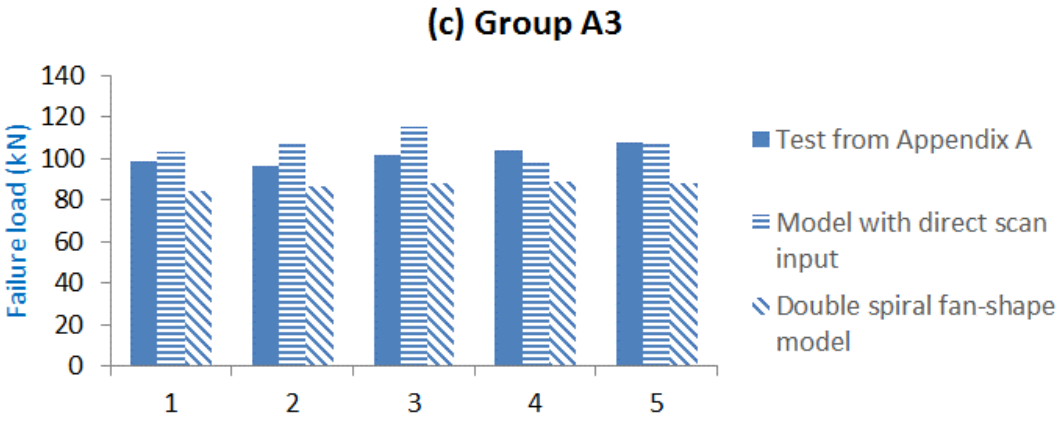
(c) Group A3
Failure load (kN)
140
120
100
80
60
40
20
0
1
2
3
4
5
Test from Appendix A
Model with direct scan input
Double spiral fan-shape model

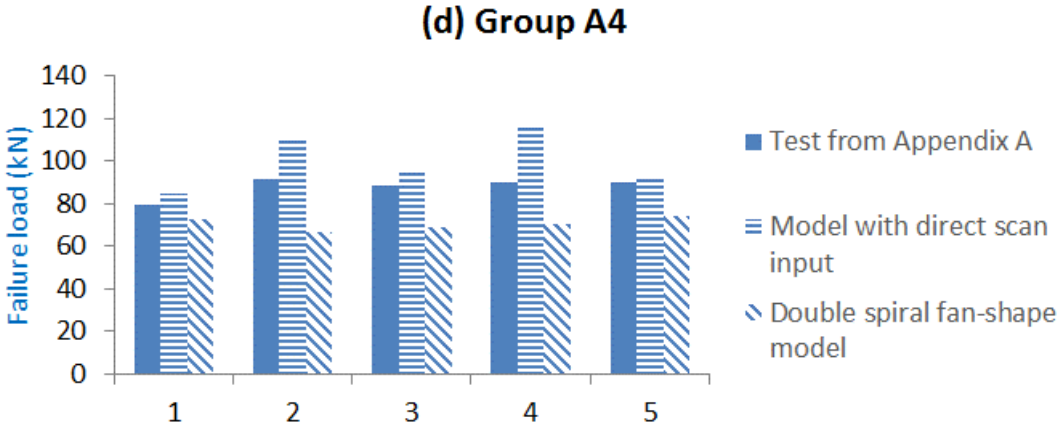
(d) Group A4
Failure load (kN)
140
120
100
80
60
40
20
0
1
2
3
4
5
Test from Appendix A
Model with direct scan input
Double spiral fan-shape model

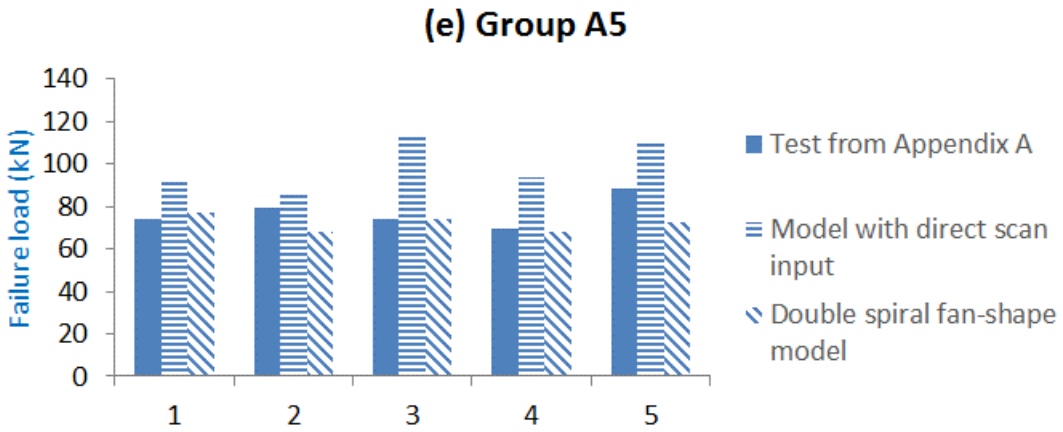
(e) Group A5
Failure load (kN)
140
120
100
80
60
40
20
0
1
2
3
4
5
Test from Appendix A
Model with direct scan input
Double spiral fan-shape model

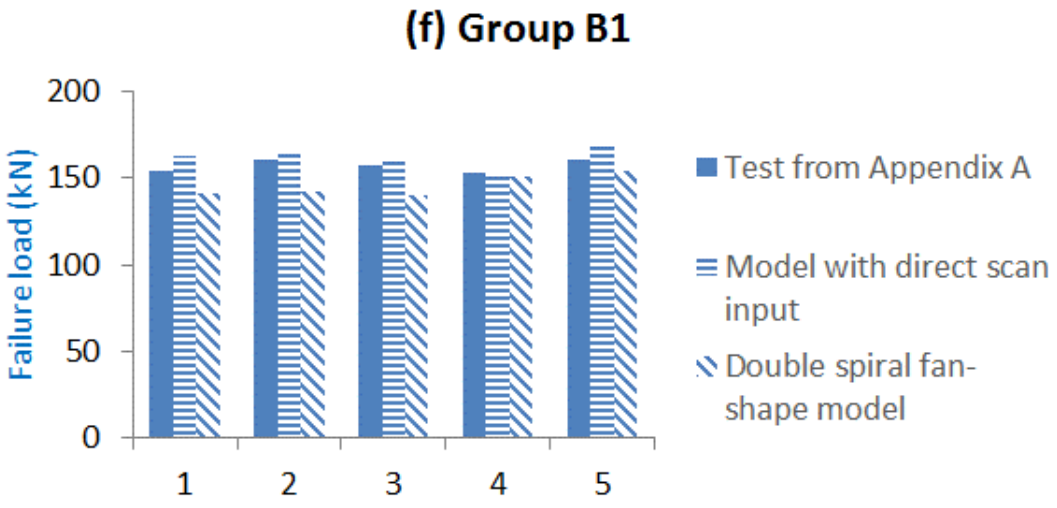
(f) Group B1
Failure load (kN)
200
150
100
50
0
1
2
3
4
5
Test from Appendix A
Model with direct scan input
Double spiral fan-shape model

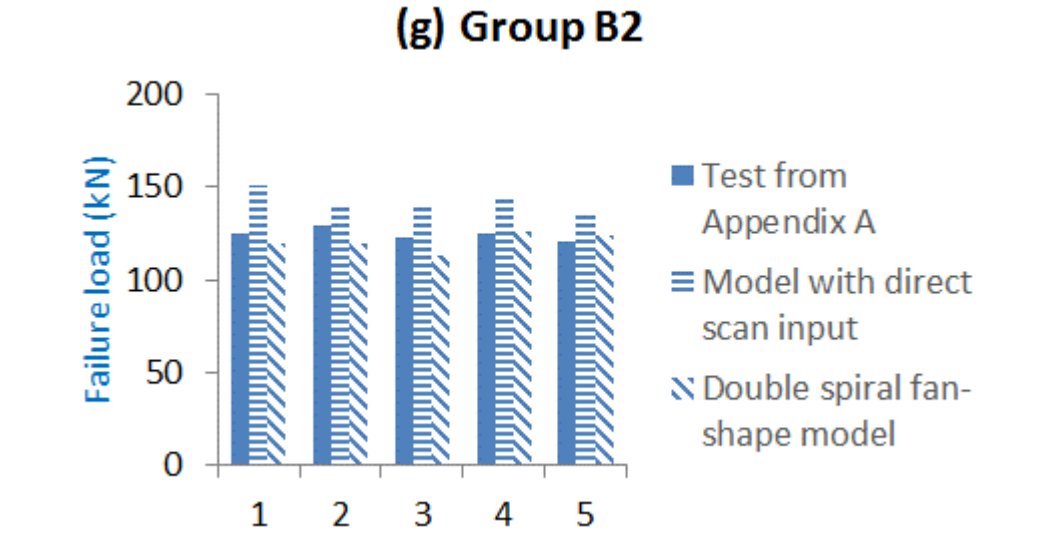
(g) Group B2
Failure load (kN)
200
150
100
50
0
1
2
3
4
5
Test from Appendix A
Model with direct scan input
Double spiral fan-shape model

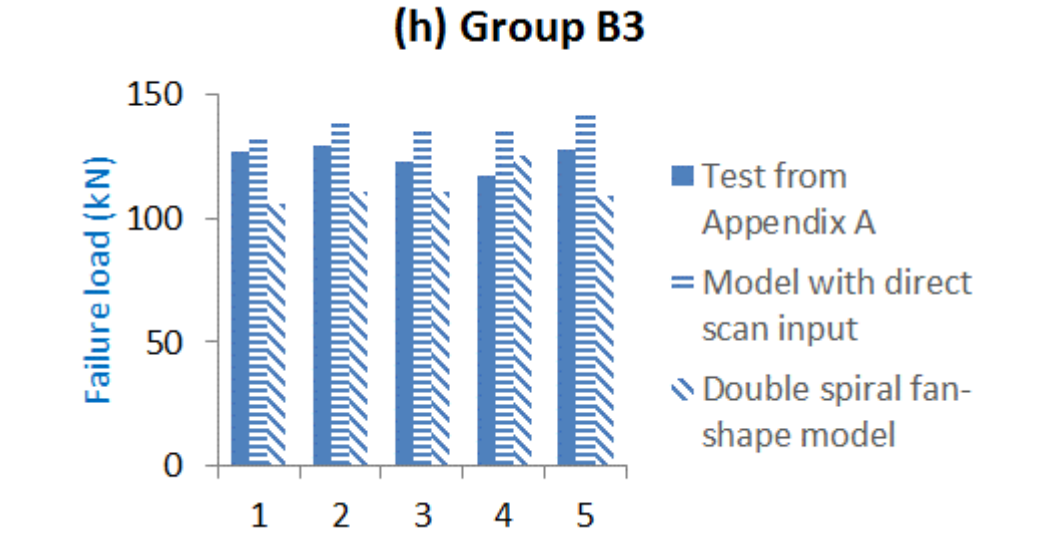
(h) Group B3
Failure load (kN)
150
100
50
0
1
2
3
4
5
Test from Appendix A
Model with direct scan input
Double spiral fan-shape model

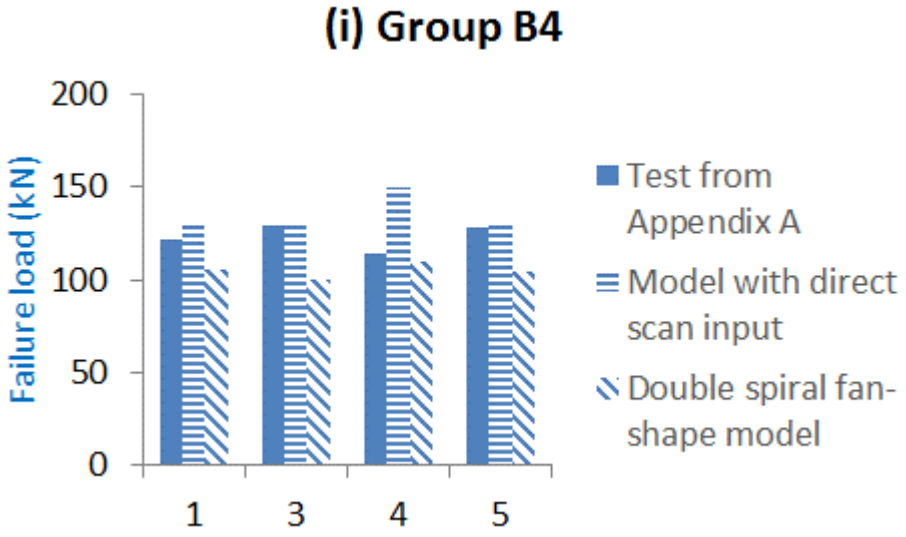
(i) Group B4
Failure load (kN)
200
150
100
50
0
1
3
4
5
Test from Appendix A
Model with direct scan input
Double spiral fan-shape model

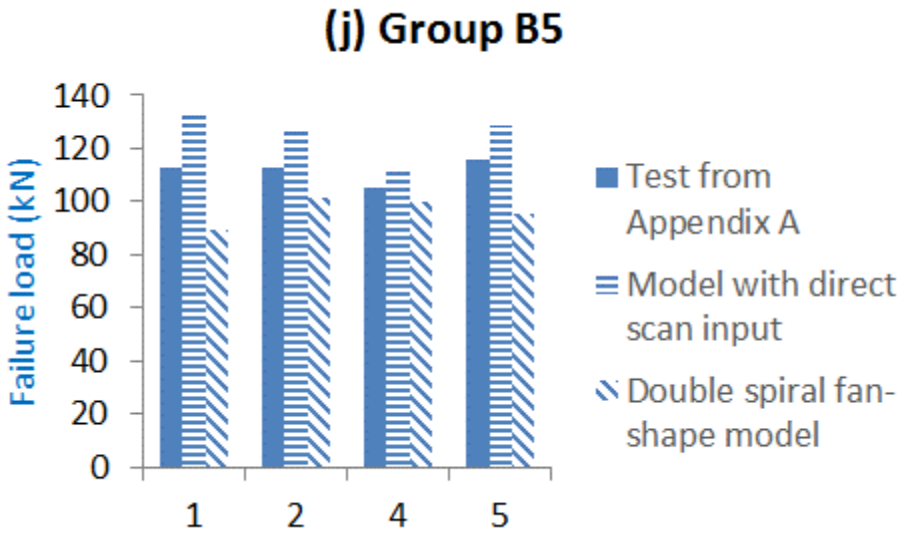
(j) Group B5
Failure load (kN)
140
120
100
80
60
40
20
0
1
2
4
5
Test from Appendix A
Model with direct scan input
Double spiral fan-shape model

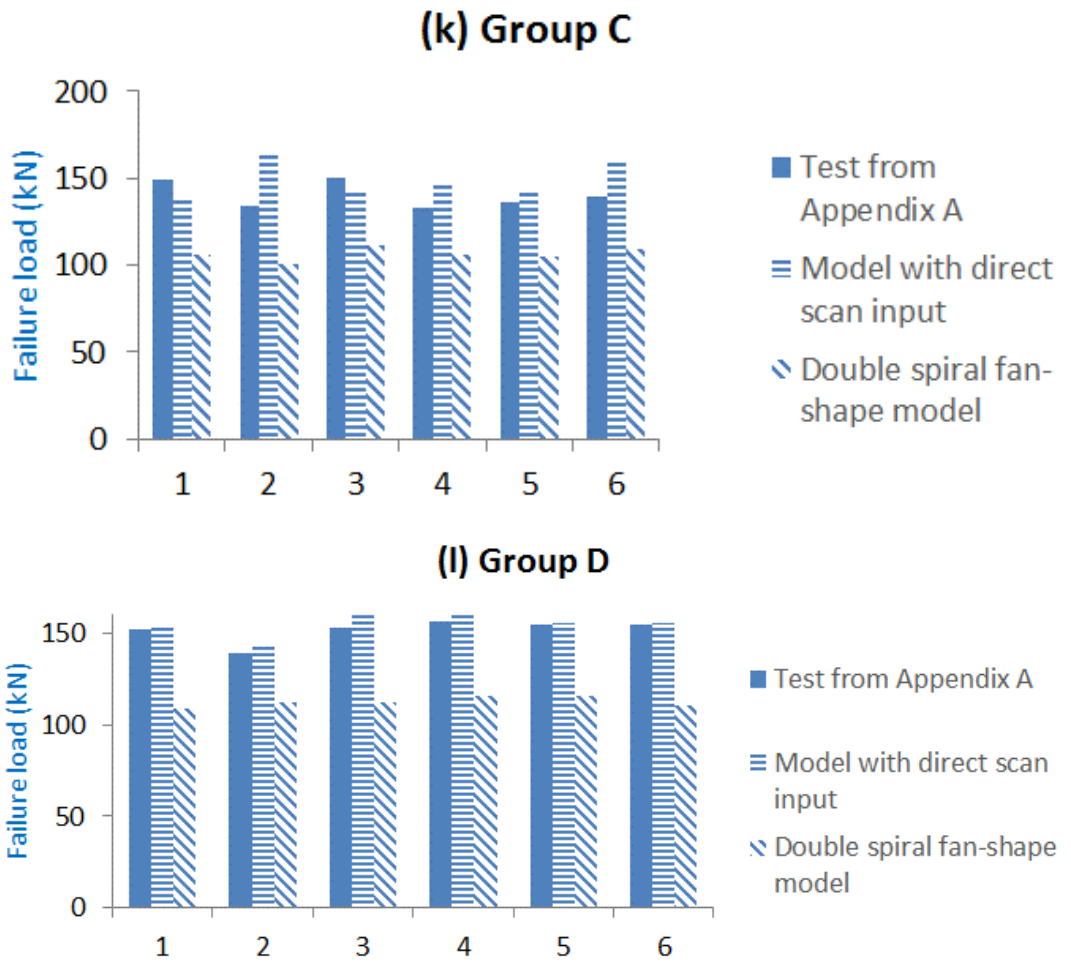

Figure 5.14 CAI comparison between experiments and detailed FE models with scanned and double spiral fan-shaped delaminations

5.3.4 Summary of prediction procedure

From above analysis, a method of CAI prediction through detailed FE models can be summarized. Briefly, the procedure is as follows:

1. Construct the detailed FE model, which possesses equal layers of continuous shell element to that of the actual specimen under consideration. Between any two neighbouring layers a layer of cohesive elements is introduced. Select proper in-plane and interlaminar failure criteria for the shell elements and cohesive elements, respectively.

2. According to double-sided C-scan results and lay-up sequence, introduce the delaminations distributed in accordance with the profile from scan result and in the pattern of double spiral fan-shape. Incorporate the effects of transverse matrix cracks and fibre breakage.

3. Determine the applicable range of this method based on the strategy presented in Figure 5.12, and predict CAI strength. As this method tends to overestimate induced impact damage, the predicted CAI strength is conservative usually.

4. Construct the detailed FE model in the same way but delamination distribution is defined by double-sided C-scan results after appropriate manipulation as described in Section 5.3.1.

5. Run the analysis for this detailed FE model and the corresponding CAI prediction can be considered as upper bound.

Although the prediction method presented above has a relatively good accuracy, the computation cost is high. Every single model usually takes more than 30 hours on a computer of Intel i7 3.2GHz CPU and 12GB RAM configuration. Actually, once the investigation of damage mechanism has revealed that the failure mode of delamination propagation almost irrelevant in CAI cases considered here for typical aerospace application, the presence of cohesive element seems redundant and layers of shell element can also be reduced to one layer which keeps the features of composite cross section. This would reduce computation cost significantly. The challenge then will be transferred to an appropriate way of employing one layer of shell elements to mimic the phenomenon of stress concentration which is induced by post-buckling deformation of multiple sublaminates in an acceptable manner. This will be discussed in the next chapter.

5.4 Summary

In this chapter, two main achievements have been made. The first achievement is that the damage mechanism of CAI has been concluded. CAI fails due to in-plane failure arising from the stress concentration for typical aerospace composites of toughened matrices. The failure mode in the form of delamination propagation can be ignored. But it is worth stressing that this conclusion is only verified for toughened material system and the sample with 150mm in length and 100m in width so far. Further widespread verification is needed. The second achievement is that a CAI prediction method through detailed FE model has been established. This method takes account of damage modes of realistic features and makes use of C-scan results appropriately. It is able to produce upper and lower bounds reasonably. In the meantime, its applying strategy is also presented. However, this method is relatively computationally costly. Taking benefit from the conclusion about the damage mechanism of CAI obtained in this chapter, an economic method which is suitable for design process will be presented and discussed in the next chapter.

Chapter 6 Simplified methodology

6.1 Introduction

In this chapter, a simplified CAI prediction method is presented, based on reasonable physical consideration with acceptable accuracy and low computation cost. The advantages of this method is that, firstly, it does not need an extra parameter anymore such as characteristic length which has to be determined through massive experiments. Secondly, it takes the experimentally measured delamination distribution due to impact as input, which is more realistic than the manual read from the superimposed C-scan image or more efficient than that from the complex impact simulation. Another work in this chapter is that the overall distribution of degraded stiffness over delaminated area is investigated through an improved inverse method presented by the author.

6.2 CAI strength prediction

Based on the damage mechanisms of CAI as concluded in Section 5.2.6 that damaged laminates tend to collapse due to in-plane failure which initiates around the delamination front as a consequence of stress concentration and significant delamination propagation is unlikely to take place, it provides the physical justification for the prediction method to be focused on the effects of stress concentration where the soft inclusion assumption becomes appropriate. The benefits of employing soft inclusion assumption are attractive. As the damage mode of delamination propagation can be safely avoided for the application concerned and only the phenomenon of stress concentration at delamination front needs to be considered, dozens of overlapped layers

of shell elements simulating delaminated sublaminate and the cohesive elements simulating potential delamination propagation in the detailed FE model can be waived. Instead, only one layer of shell elements with degraded stiffness in corresponding delaminated area can be employed. Consequently, high computational cost incurred by solving problems of geometric nonlinearity associated with structural instability, the contact of multiple interfaces, and the damage growth at multiple sites [27] in detailed FE model can also be avoided. It is therefore reasonable to employ the soft inclusion assumption to develop the simplified prediction method in this thesis.

6.2.1 Weaknesses of conventional soft inclusion method

As a simplified prediction method, there exists some weaknesses of the soft inclusion assumption. Firstly, replacing layers of shell and cohesive elements with only one layer of shell elements, simultaneously, removes the capability of simulating stress concentration induced by buckled sublaminates. The mechanism of stress concentration induced by degrading stiffness artificially (soft inclusion) is quite different from actual cause of complex post-buckling deformation of multiple sublaminates. Therefore, it is not easy to simulate properly, while it is crucial for the CAI strength prediction.

Secondly, the conventional CAI strength prediction methods based on soft inclusion assumption obtain the stress distribution around soft inclusion area at elastic deformation range as the first step, followed by the application of failure criteria to predict the CAI strength. Partly, the reason of this strategy is due to the limited computing power at that time. It would be much more costly if nonlinear and progressive damage analysis had been incorporated. Although the previous

methods were simple and fast, the most significant weakness was that they usually required extra parameters, such as characteristic length, for these failure criteria, in addition to the most common mechanical properties. This incurs extra cost and consequently impedes its prevalence. Nowadays, the computing power has grown significantly. The approach to be proposed in this thesis to address the issue of requiring extra parameter is to simulate the entire damage process of CAI through the simplified FE model based on soft inclusion assumption.

Thirdly, according to investigation from other publications, it is found that most CAI strength prediction methods based on soft inclusion assumption employed a single degradation factors over the entire soft inclusion zone. This is too rough, because from other publications, for example, [50] as well as experimental observations from double-sided scan in Section 3.3, it is already known that the outline of delamination distribution through laminate thickness direction is not cylindrical but conical or spindle. The single degradation factor over the entire soft inclusion zone turned a blind eye on this fact, which, actually, is critical to affect the failure process and final CAI strength accordingly. As an illustration, Figure 6.1 and Figure 6.2 demonstrate the overall and individual compressive stress distribution over the cross section along the width direction of B3-Ave-Spi listed in Table 5.1 when failure load is reached, respectively. It can be seen that, in the 23rd lamina which is close to back face of the laminate, stress concentration is very severe, and the stress at delamination front is very close to its strength limit. However, in other laminae the degree of stress concentration is less significant. This is due to the non-uniform delamination size through laminate thickness, and the diverse severities of stress concentration over the laminate thickness will affect the failure sequence among laminae. However, if the single degradation factor is employed, it is prone to enforces

failure occurring simultaneously among laminae with the same fibre orientation, which is less realistic and compromises the predicting accuracy consequently.

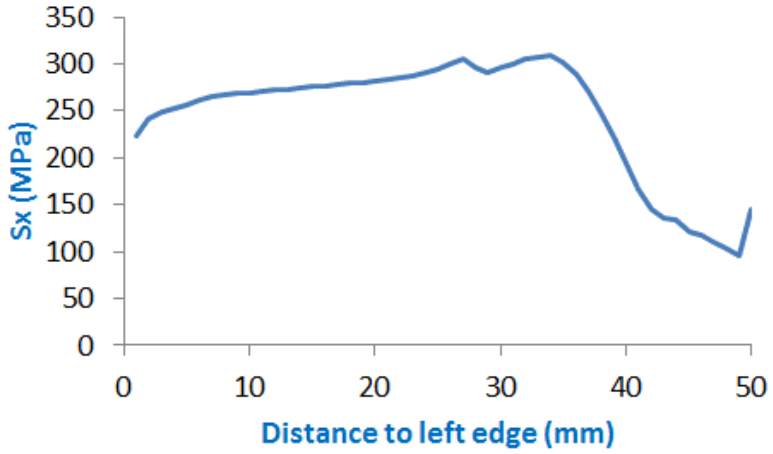

Figure 6.1 Average compressive stress along centre width of B3-Ave-Spi at failure load

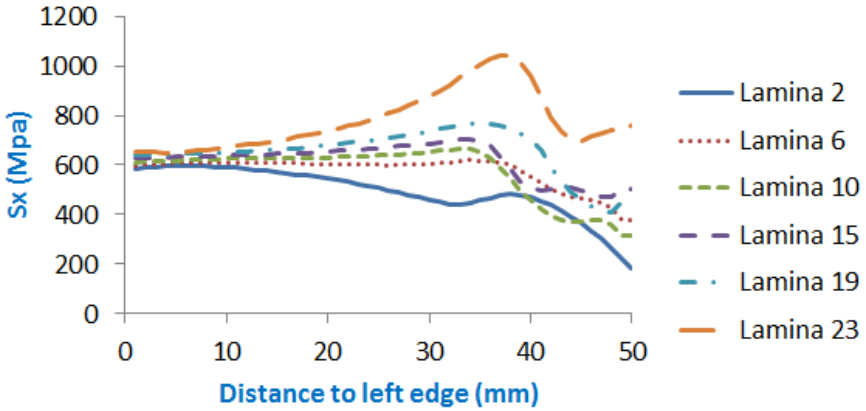

Figure 6.2 Compressive stress along centre width in each 0° lamina of B3-Ave-Spi at failure load (the smaller laminar number the closer to impact side)

6.2.2 Simplified method

Considering the issues listed in Section 6.2.1, the simplified method presented by Tang, Shen [2] stands out from most other similar methods because it degrades the stiffness sequentially by taking the variation of delamination sizes through laminate thickness into account. However, as discussed in Appendix C, there are also some weaknesses in Tang's method. The first is that the weight function of DI criterion (Damage Influence criterion) presented by Tang was based on empiric knowledge and cannot be applied widely. Therefore, the author is inspired to apply in-plane failure criterion, such as Hashin's failure criterion, to the simplified FE model created through Tang's method. Secondly, the degradation factor for specific sublaminate is prescribed to be the ratio of buckling stress of that sublaminate with respect to compressive strength of the overall laminate. Obviously, this strategy is not convincible. If the a_{ij} in Equation (C.2) are prescribed as the compliance of the whole laminate rather than the delaminated sublaminate, a modified theory is obtained. The modification is minor, but the physical representation of the problem has obviously been improved significantly. In the previous strategy, the calculated buckling load is the load when corresponding sublaminate is separating from the remaining part of the laminate and subjected to compressive load independently. In the modified strategy, the buckling load is the load the whole laminate sustains when the corresponding sublaminate buckles. Consequently, the degradation factor for the sublaminate is the ratio of the stress the whole laminate takes when this sublaminate buckles with respect to the whole laminate's compressive strength.

It is worth mentioning that although in the simplified model here, delamination simulation is not needed any more, the size of each individual delamination still needs to be known as it determines the dimension of sublaminate on corresponding lamina which are essential for the

calculation of buckling load and degradation factor accordingly. Therefore, this simplified method adopts the same strategy to determine the delamination state which is employed by detailed CAI modelling in Section 5.2.1 based on double-sided scan results.

After the modification, this modified prediction method is employed to calculate the CAI strength for all double-sided scanned specimens involved in this thesis. As an example, Figure 6.3 shows the compressive stress in each 0° lamina in the corresponding simplified FE model when subjected to the compressive load which is immediately prior to the failure load of B3-Ave-Spi. It can be seen that although the stress distribution is not entirely consistent with that from detailed FE model, it captures the phenomenon of diverse stress concentration states in different laminae which will trigger in-plane failure sequentially at different locations. In the meantime, it is found that stress over the soft inclusion area of the simplified FE model is generally lower than that of detailed FE model, which implies the degradation factor through this method is overestimated. However, this makes predicted CAI strength conservative. Furthermore, comparing the predicted CAI strength with experimental results for all specimens which have been double-sided scanned, it is found that the accuracy is acceptable (Figure 6.4). In the meantime, because of its significantly reduced computational demand compared with that of detailed FE model, the requirement for computer configuration is not necessarily to be very high. Usually, calculation can be done on ordinary desktop PC or laptop and the average calculation time is about 2 hours. Combining all these merits mentioned above, this modified Tang's method is recommended for CAI strength predictions.

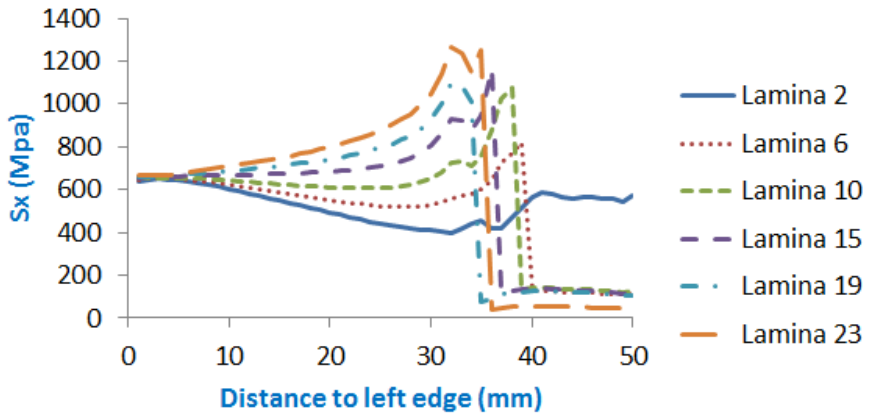

Figure 6.3 Compressive stress along centre width in each 0° lamina of corresponding simplified FE model of B3-Ave-Spi at failure load (the smaller laminar number the closer to impact side)

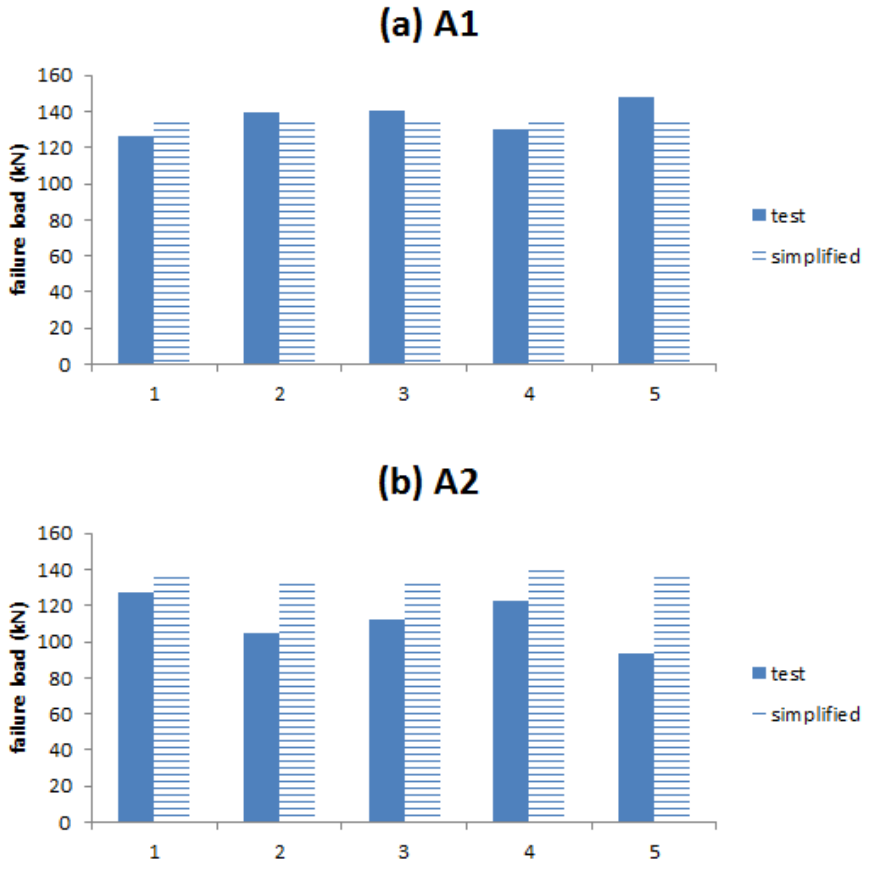

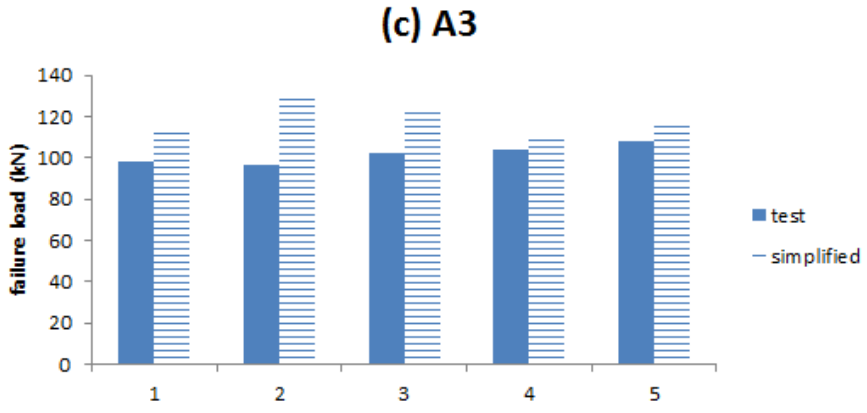
(c) A3
failure load (kN)
140
120
100
80
60
40
20
0
1
2
3
4
5
test
simplified

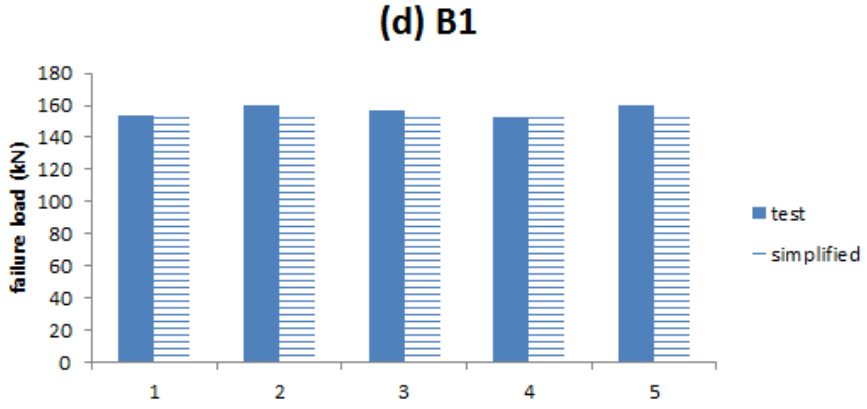
(d) B1
failure load (kN)
180
160
140
120
100
80
60
40
20
0
1
2
3
4
5
test
simplified

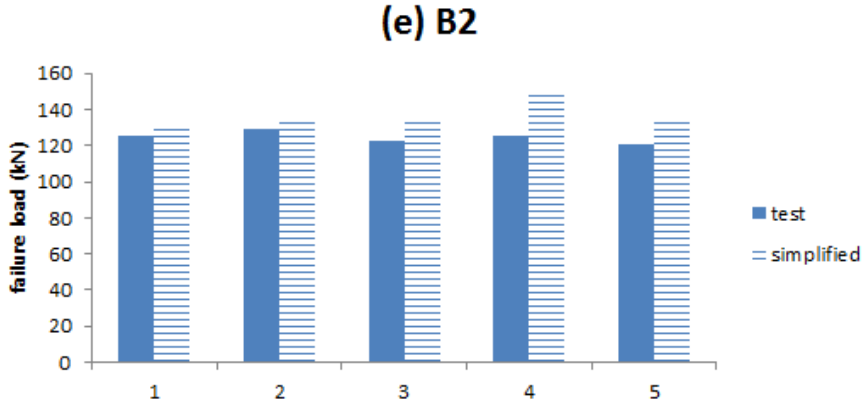
(e) B2
failure load (kN)
160
140
120
100
80
60
40
20
0
1
2
3
4
5
test
simplified

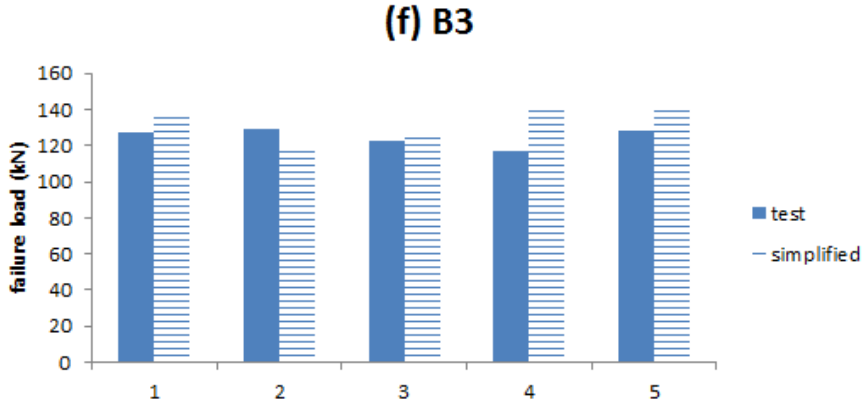
(f) B3
failure load (kN)
160
140
120
100
80
60
40
20
0
1
2
3
4
5
test
simplified

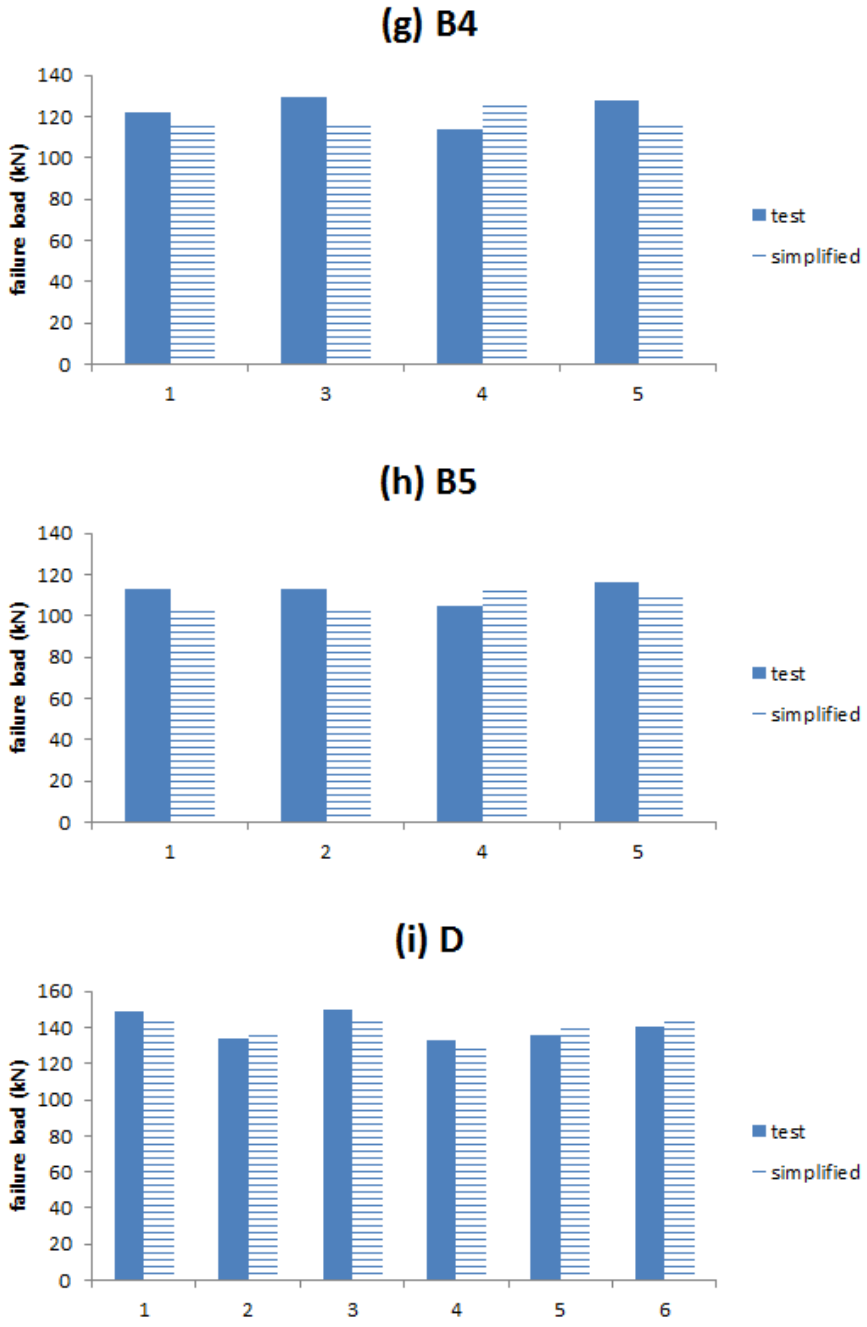

Figure 6.4 CAI comparison between experiments and predictions through modified Tang's method

6.2.3 Main procedure of the simplified method

A simplified method to predict CAI strength has been formulated. As a summary, the procedure is presented briefly as follows.

1. Determine the size of every single delamination over the laminate thickness using double-sided scan as described in detail in Section 3.3;

2. Determine the degradation factor for every single lamina according to the modified Tang's method presented in this chapter;

3. Construct the simplified FE model with the degradation factors and apply the designated in-plane failure criterion;

4. Run the analysis of this simplified FE model until failure to obtain CAI strength.

However, it should be pointed out that if the predicted CAI strength is significantly higher than the experimental value, it would be reasonable to suspect that this simplified prediction model might have failed to capture the correct damage mechanism of corresponding CAI test, in which significant delamination propagation may have taken place. In this case, this simplified prediction method is no longer applicable.

6.3 Improved inverse method

In the last section, a simplified prediction method of CAI strength, which is based on the soft inclusion assumption, has been presented. It employs diverse degradation factors and applies them to different scopes among laminae to degrade the stiffness of the delaminated area, with the purpose of emphasizing sequential failure among laminae within the laminate. But for each individual lamina, the degradation factor is still uniform over that delaminated area and constant during the whole loading process. However, study from Sztefek and Olsson [90] revealed that the degraded stiffness is neither uniform over the delaminated area nor constant during the

loading process. How should the stiffness degradation be described realistically? Unfortunately, Sztefek and Olsson [53] didn't solve this issue completely, which only captured the altering phenomenon of degradation factor during the loading process but still had to use a uniform degradation factor to describe the whole delaminated area. Therefore, there is a room for improvement.

The inverse method, which is presented originally by Sztefek and Olsson [90], is used to identify the constitutive parameters of the concerned area by iteratively updating the material parameters of FE model to match the displacement field of structure obtained from experiment. Sztefek and Olsson [90] investigated the stiffness distribution of impacted laminate in tension case firstly, and found that it is adequately accurate to discretize the stiffness within the damaged area into several concentric rings in which the stiffness decreases gradually from the outmost ring neighbouring to undamaged area to the centre. However, this method is not very successful to be applied to compression case. The reason is that, quoted as, “compression loading results in local delamination buckling of the damage zone, so that measured strain variations no longer correspond to true variations in material stiffness” [53]. Therefore, only a uniform set of constitutive parameters was obtained to represent the whole delaminated area. Obviously, one set of material parameters seems too coarse. In this section, this method is improved and a range of constitutive parameters can be obtained over the delaminated area.

6.3.1 Improvement

Unlike the original inverse method, in which only one set of degraded material parameters were proposed to represent the overall delaminated area, the current improved one can obtain sets of

degraded material parameters varying from section to section over the delaminated area. In order to achieve this objective, the delaminated area is firstly sliced into a number of strips along the compression direction (Figure 6.5), each of which will be designated with an exclusive degradation factor after the evaluation. It is assumed that in each sliced section the Poisson's Ratio is not affected but all other material parameters, such as Young's Modulus and shearing module, are degraded by a uniform degradation factor. Furthermore, because the quasi isotropic lay-up sequence is widely employed in the aerospace industry, it is reasonable to assume the general relationship between strain and stress over each sliced section is governed by following equations

$$\begin{aligned} \varepsilon_{xi} &= \frac{1}{\lambda_i E_i}\left(\sigma_{xi} - \nu_i \sigma_{yi}\right) \\ \varepsilon_{yi} &= \frac{1}{\lambda_i E_i}\left(\sigma_{yi} - \nu_i \sigma_{xi}\right) \end{aligned} \tag{6.1}$$

where ε_{xi} and ε_{yi} are the representative strain of sliced section i in x and y direction, respectively. Here, x and y represent the in-plane direction along and transverse to compressive load, respectively. E_i, ν_i, G_i and $\lambda_i$are the representative Young's Modulus, Poisson's Ratio, shear module and degradation factor of sliced section i, respectively. σ_{xi} and σ_{yi} are the representative stress of sliced section i, respectively.

Rearranging above equations, one gets

$$\begin{aligned} U_i &= \frac{L_i}{\lambda_i E_i}\left(\sigma_{xi} - \nu_i \sigma_{yi}\right) \\ V_i &= \frac{W_i}{\lambda_i E_i}\left(\sigma_{yi} - \nu_i \sigma_{xi}\right) \end{aligned} \tag{6.2}$$

where U_i and V_i are the relative displacements of two ends of the sliced section i in x and y direction, respectively. L_i and W_i are the length and width of the sliced section i, respectively.

The relationship between displacement and degradation factor has been established, which will be used in the present improved inverse method later.

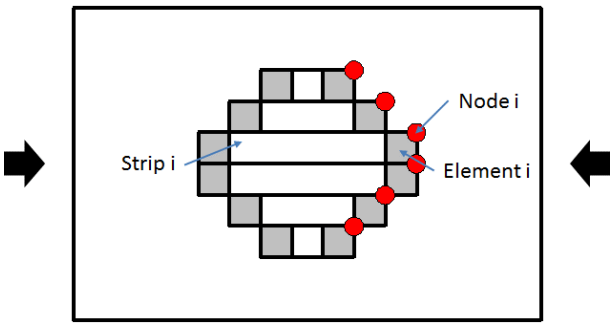

Figure 6.5 Partition of delaminated area for improved inverse method

6.3.2 Main elements of programme

This improved inverse method is coded in Matlab and consists of a main programme and several subroutines. The flowchart is presented in Figure 6.6. In the meantime, as this method needs results which are continuously updated from FE analysis, a code in python scripts has been written which is called to communicate between Matlab and ABAQUS.

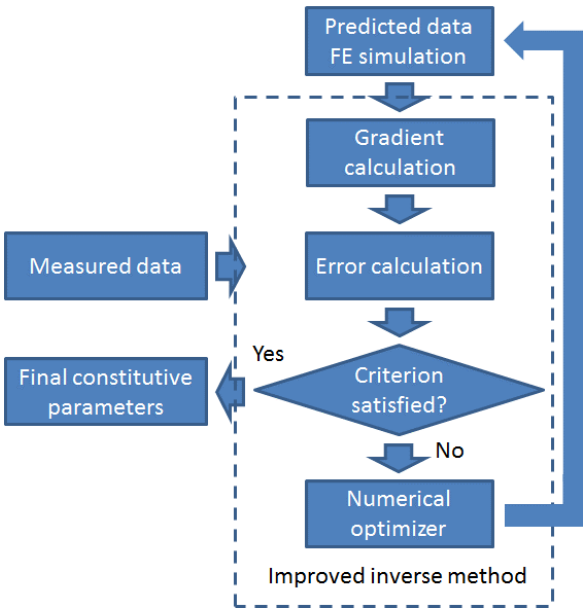

Figure 6.6 Flowchart of improve inverse method

Firstly, one of the subroutines collects measured data from experimental result as input. In this thesis, as no proper experimental data is available, the results from the detailed FE models with double spiral fan-shaped delaminations are employed instead. The “measured data” includes the displacement of nodes at the delamination front which are marked red in Figure 6.5 and stress state of corresponding element which are filled grey in Figure 6.5 as well. Moreover, the length and width of each slice are also collected.

Once the input has been prepared, ABAQUS is called to create a simplified FE model, which has exactly the same in-plane meshing strategy of corresponding detailed FE model but consists of only one layer of shell elements in thickness direction. The corresponding delaminated area of detailed FE model is referred as soft inclusion area in this simplified FE model, which is prescribed with a uniform degradation factor initially. Then ABAQUS is called again to run the analysis of this simplified FE model and displacements of specified nodes as marked red in Figure 6.5 are

collected, which is referred as predicted data, for gradient and error calculation in the following procedures.

Because the approach of searching for matched degradation factor here is based on gradient optimisation technique referred as steepest decent method, the gradient of mean squared error function with respect to each individual degradation factor is essential for error evaluation and searching direction determination. Firstly, error function is defined as

$$f(x) = \frac{1}{N}\sum_{i=1}^{N}\left[\left(\frac{u_{iexp} - u_{iFE}}{u_{max}}\right)^2 + \left(\frac{v_{iexp} - v_{iFE}}{v_{max}}\right)^2\right] \tag{6.3}$$

where N is the number of nodes involved for comparison. U_{iexp} and V_{iexp} are the displacements at node i of detailed FE model in x and y direction as input, respectively. U_{max} and V_{max} are the maximum displacements in x and y direction among them, respectively. U_{iFE} and V_{iFE} are the displacements of node i in x and y direction from the present simplified FE model, respectively.

In order to obtain the expression of gradient, relationship between error function and individual degradation factors is needed. However, Sztefek and Olsson [90] failed to obtain the explicit relationship, and the gradient was presented in an empirical expression through a parametric study. In this thesis, based on the assumption of isotropic material characteristics through Equation (6.2), an explicit expression of the gradient of error function with respect to each individual degradation factor λ_i can be obtained and presented as

$$\nabla f(x) = \left[\frac{\partial f(x)}{\partial u_{1FE}}\frac{du_{1FE}}{d\lambda_1} + \frac{\partial f(x)}{\partial v_{1FE}}\frac{dv_{1FE}}{d\lambda_1}, \cdots \frac{\partial f(x)}{\partial u_{iFE}}\frac{du_{iFE}}{d\lambda_i} + \frac{\partial f(x)}{\partial v_{iFE}}\frac{dv_{iFE}}{d\lambda_i}, \cdots \frac{\partial f(x)}{\partial u_{NFE}}\frac{du_{NFE}}{d\lambda_N} + \frac{\partial f(x)}{\partial v_{NFE}}\frac{dv_{NFE}}{d\lambda_N}\right]^T \tag{6.4}$$

Based on the definition of steepest decent method, the error is defined as the module of the gradient as defined in Equation (6.4). If the error is less than the tolerance, calculation terminates and the current set of degradation factors are employed to describe the stiffness degradation state. Otherwise, calculation goes on.

Denote the updated degradation factor as $\lambda_i^{(k+1)}$ of the (k+1)-th iteration. It can then be expressed a

$$\lambda_i^{(k+1)} = \lambda_i^{(k)} - \alpha^{(k)}\left(\nabla f(x)\right)_i \tag{6.5}$$

where $\lambda_i^{(k)}$ is the degradation factor of previous iteration k. $\left(\nabla f(x)\right)_i$ is the gradient with respect to sliced section i, which determines the searching direction of next iteration. $\alpha^{(k)}$ is the optimized incremental factor.

Substituting the updated degradation factor $\lambda_i^{(k+1)}$ into Equation (6.1), which is then substituted into error function Equation (6.3), the error function in terms of updated degradation factor is obtained. The function of numerical optimiser is to seek for the critical updated degradation factor, which makes the error function minimum. Once it is found, the updated degradation factor is also determined through Equation (6.5), which is applied to the simplified FE model for a new iteration. This procedure is repeated until the tolerance is met.

6.3.3 Application

This improved inverse method is applied to detailed FE model B3-Ave-Spi, which is defined in Table 5.1, as a test case. The tolerance is set as 1e-3. According to the nature of steepest decent

method, convergence is at a high rate initially but the rate drops as the iteration goes on. As an example, Figure 6.7 illustrates the convergence rate when searching for the degradation factor for model B3-Ave-Spi at 5.5% failure load when the initial uniform degradation factor is set as 0.8.

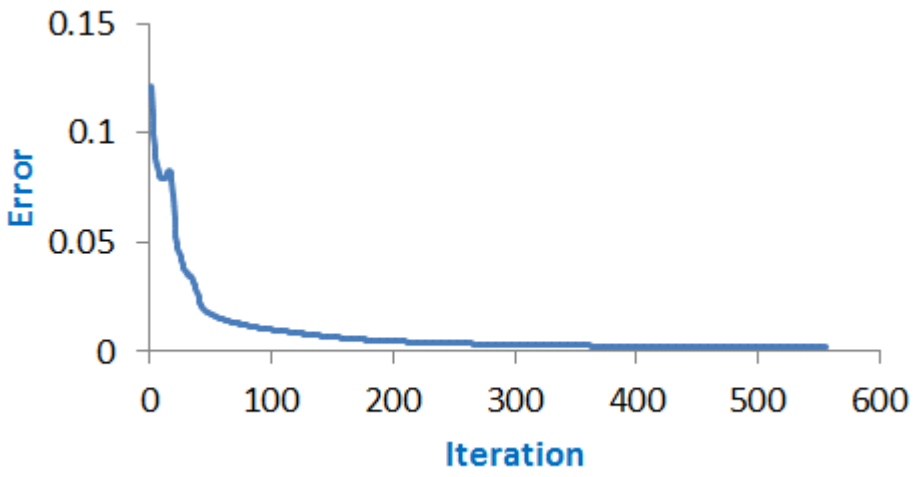

Figure 6.7 Convergence rate of degradation factor initiating at 0.8 for B3-Ave-Spi at 5.5% failure load

Figure 6.8 displays the degradation factor distribution from left edge of specimen to centre in width direction at different load levels for all models listed in Table 5.1 with double spiral fan-shaped delamination. The following observations can be made. Firstly, the degradation factor distributes non-uniformly at any given load level. The more close to delamination front, the more close to reach the value of unit which means no stiffness degradation. Secondly, at different load level, the degradation factor of the same sliced section varies. Degradation factors drop mostly as the compressive load increases. However, in the zone close to delamination front in some cases, the degradation factor may increases even exceeding unit as the compressive load increases. This is because the stiffness in the soft inclusion area has to vary in this way in order to meet the

required displacement field. Thirdly, the degradation factor varies from specimen to specimen at the load levels before failure takes place. This at least particularly illustrates the difficulties to obtain an empirical and universally applicable degradation factor for general cases.

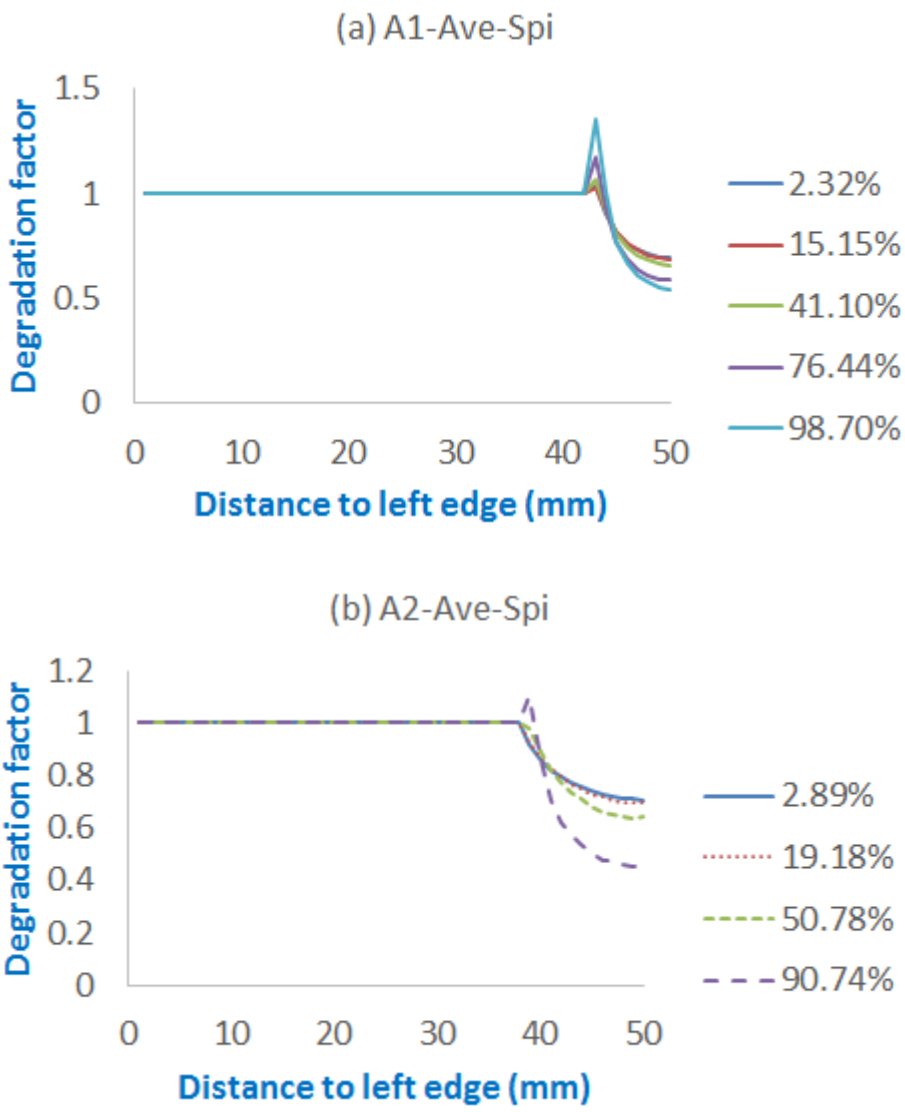

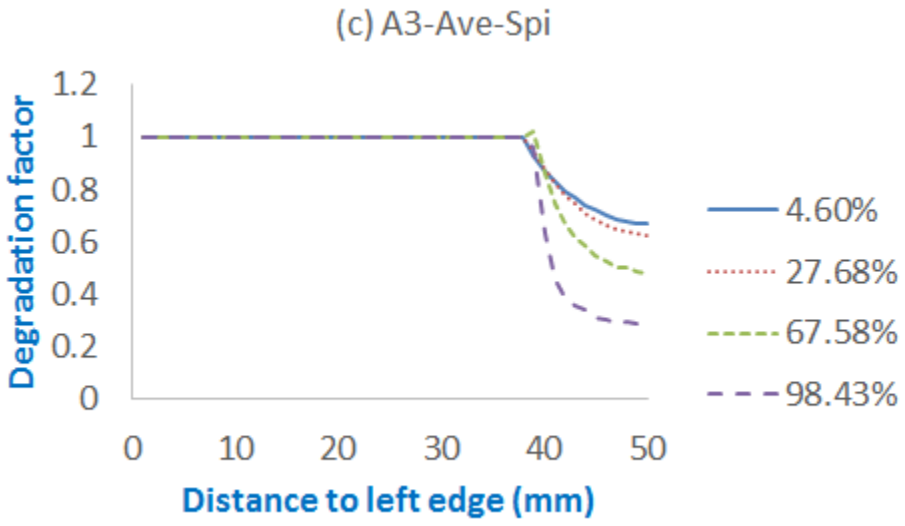
(c) A3-Ave-Spi
Degradation factor
1.2
1
0.8
0.6
0.4
0.2
0
0
10
20
30
40
50
Distance to left edge (mm)
4.60%
27.68%
67.58%
98.43%

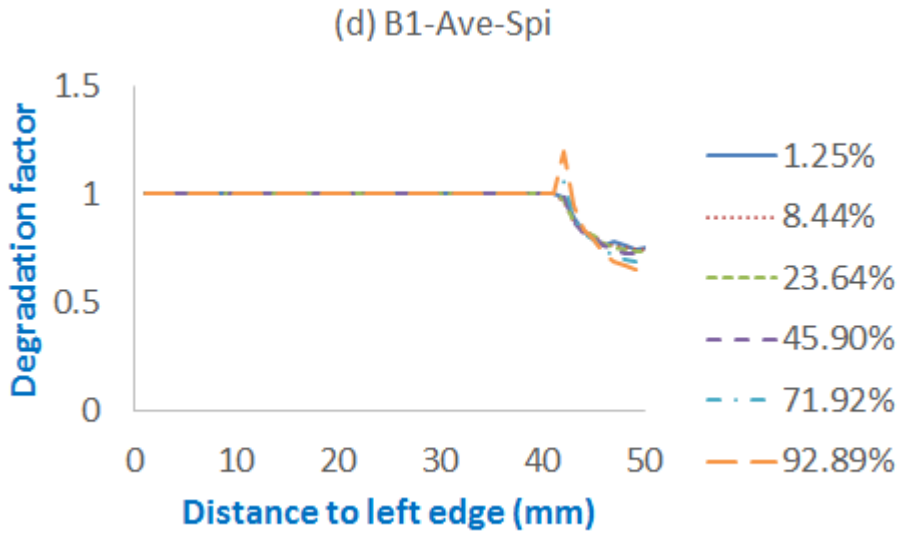
(d) B1-Ave-Spi
Degradation factor
1.5
1
0.5
0
0
10
20
30
40
50
Distance to left edge (mm)
1.25%
8.44%
23.64%
45.90%
71.92%
92.89%

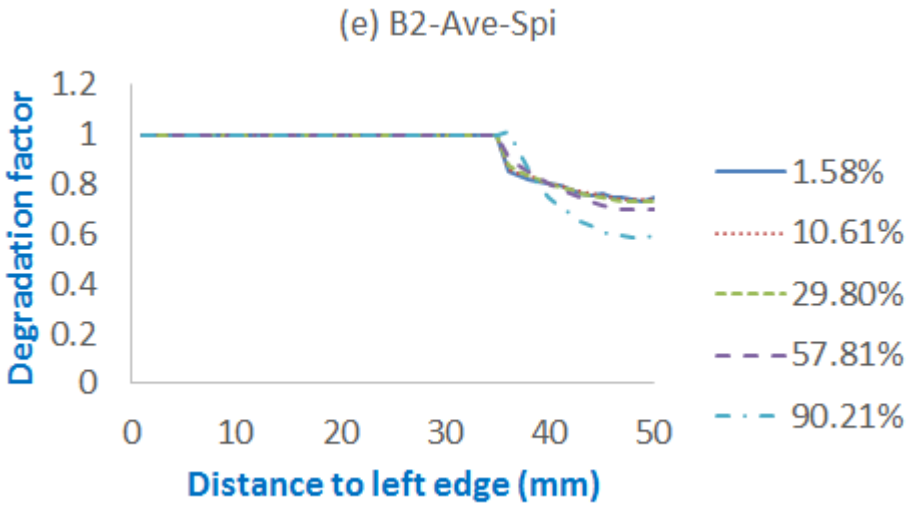
(e) B2-Ave-Spi
Degradation factor
1.2
1
0.8
0.6
0.4
0.2
0
0
10
20
30
40
50
Distance to left edge (mm)
1.58%
10.61%
29.80%
57.81%
90.21%

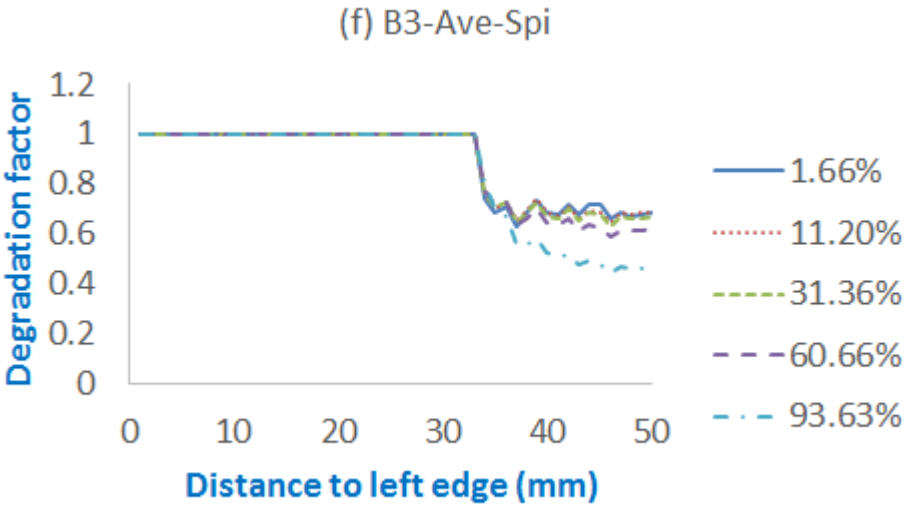
(f) B3-Ave-Spi
Degradation factor
1.2
1
0.8
0.6
0.4
0.2
0
0
10
20
30
40
50
Distance to left edge (mm)
1.66%
11.20%
31.36%
60.66%
93.63%

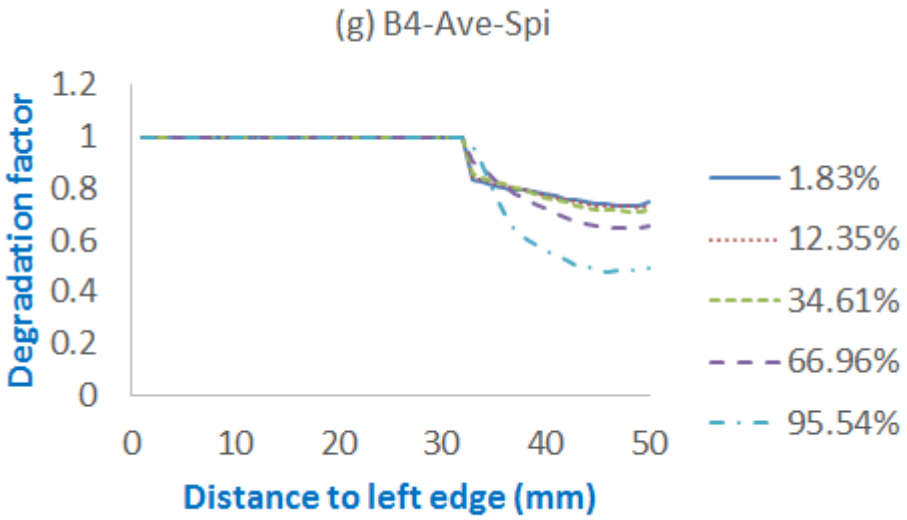
(g) B4-Ave-Spi
Degradation factor
1.2
1
0.8
0.6
0.4
0.2
0
0
10
20
30
40
50
Distance to left edge (mm)
1.83%
12.35%
34.61%
66.96%
95.54%

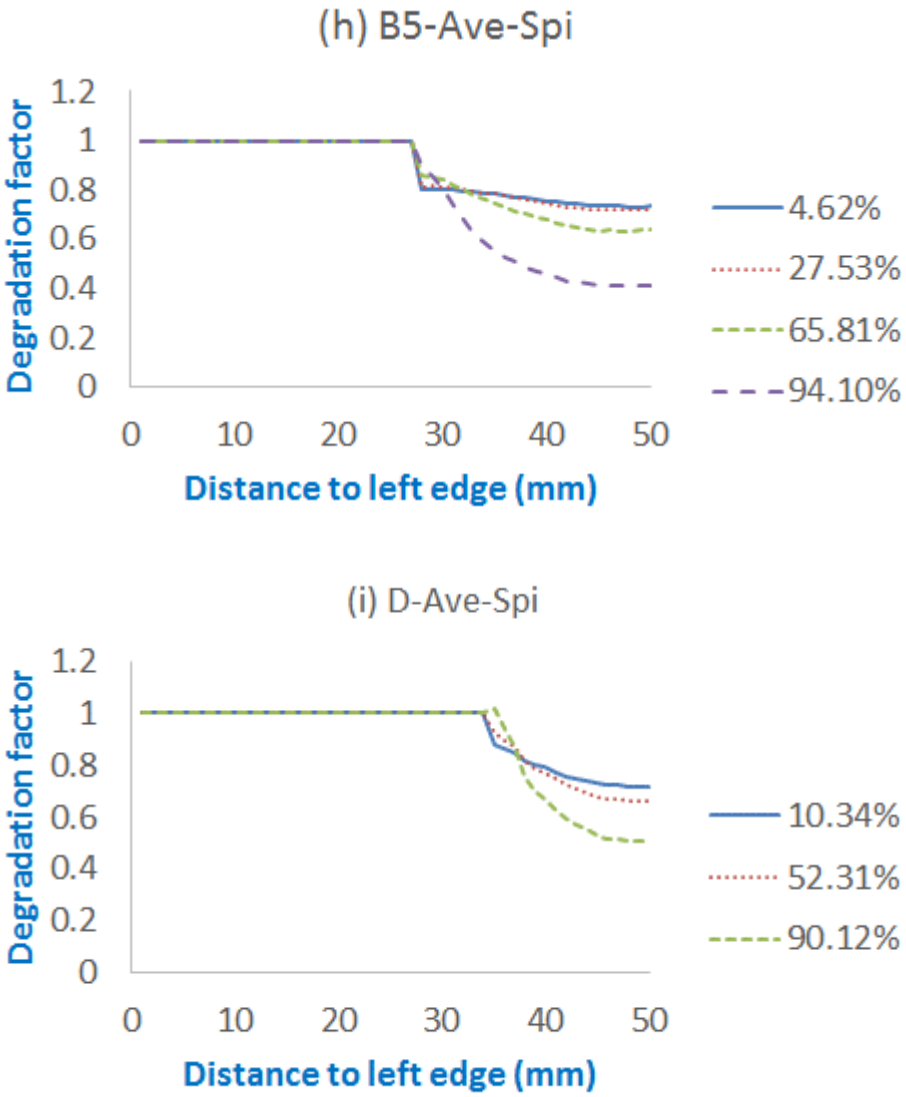

Figure 6.8 Stiffness degradation at different loading levels for all models in Table 6-1 with double spiral fan-shaped delamination

From above demonstration, it has been revealed that the degradation factor is neither uniform over the delaminated area nor constant during the loading process. Therefore, the idealised way to reflex the soft inclusion effect of delaminated area through simplified FE model is to assign the corresponding area with appropriate degradation factor at different load levels which is determined through this improved inverse method. This is to obtain the overall tendency of the variation of the degradation factor through improved inverse method first, then dynamically customise the stiffness of soft inclusion area of simplified FE model to be consistent with this

tendency. Through this strategy, the simplified FE model is capable of demonstrating similar mechanical behaviour of real damaged structure.

However, it is not efficient to apply this strategy to CAI cases. This is because if the variable degradation factors are needed for CAI simulation, the same CAI tests have to be conducted first to produce these variable degradation factors through the improved inverse method. In other words, it forms a closed cycle from the starting point to the results. Additionally, from Figure 6.8 it is found the degradation factors, even those when respective failure loads are approaching, are diverse from case to case dictated by many factors, such as the material systems, impact energies, etc.. Therefore, it is very difficult to obtain an empirical and universally applicable tendency of the degradation factor variation for various CAI cases. As the lowest experimental level in the building-block experimental hierarchy for aircraft certification[10], it is still practical to employ constant degradation factor in simplified FE model to predict CAI strength.

Actually, the significant benefit of employing soft inclusion method through this method can only make sense when the tendency of variation is obtained through simpler and lower level of structural analysis to inform more complex and higher-level one. This idea is also presented by [29, 90]. For example, one obtains the variable degradation factor at a coupon level, and assigns this to the specific area in a FE model to simulate the mechanical behaviour of impact-damaged stiffened panels. In this case, the impact-affecting area of the FE model of the stiffened panel only needs to have a single layer of shell elements rather than dozens of overlapped shell and cohesive elements.

[10] Schematically illustrated in Figure 2, FAA AC 20-107B, 2009.

6.4 Conclusion

Firstly, a simplified prediction method of CAI strength is presented, which is developed from conventional methods based on soft inclusion assumption while overcomes some critical weaknesses. This method does not need extra characteristic parameter, which was essential for previous methods but costly to be measured. In the meantime, this method adopts the double-sided scan result as the input of delamination state, and takes account of the fact of sequential failure among laminae due to diverse delaminated areas through the laminate thickness direction. This method provides good precision and is of low computation cost

Secondly, an improved inverse method is presented. Compared with the original one which employed only one set of degraded stiffness to describe the mechanical behaviour of the overall delaminated area, this method is able to capture the varying tendency of stiffness degradation over the delaminated area in CAI cases. Through this method, it is found that stiffness degradation is neither uniform over the delaminated area nor constant during the compressing process. Furthermore, the degradation factor varies from case to case at the load level when the laminate collapses. This implies that it is very difficult to obtain an empirical and universally applicable degradation factor for general CAI cases. Therefore, it will be more efficient to obtain the varying tendency of stiffness degradation from simple laminate through this method and apply this tendency to complex structures.

Chapter 7 Conclusion

7.1 Introduction

This chapter presents the major conclusions of this thesis and identifies the contributions to the related research field. Suggestions for future improvements are also presented.

7.2 Conclusion

For the CAI cases of toughened material system, laminates of standard dimensions, i.e. is utilized and the plate is 150mm length times 100mm width with moderate thickness, the general damage mechanism is as follows. When impacted laminate is subjected to in-plane compressive load, the delaminated area buckles and leads stress redistribution. Concentrated stress arising around the delamination front triggers in-plane failure and subsequent collapse of the entire laminate. In most cases, delamination propagation is unlikely to take place during the loading process. Therefore, the prediction method based on soft inclusion assumption is physically acceptable and computationally efficient.

To predict CAI based on soft inclusion assumption, assigning appropriate degradation factors to different laminae over the laminate thickness to capture the severities of stress concentration is crucial. This reflects the reality that in-plane failure takes place sequentially among laminae due to non-uniform delamination distribution over the laminate thickness.

Double-sided ultrasound scan results have been found to be extremely helpful for determining delamination state of CAI cases in detail. Combined with the knowledge of general tendency of

the delamination shape on each individual interface induced by impact, a reasonable idealisation of the delamination distribution through the thickness of a given CAI sample can be determined. This is essential for detailed FE modelling of CAI.

For the cases that delaminated plate subjected to in-plane compression, the multiplicity of delamination is the dominant factor determining the failure mode: (1) with few and large sized delaminations close to the mid-plane or few delaminations close to either surface, delaminations are likely to propagate extensively with unsustainable load drop; (2) with few and small delaminations close to the mid-plane, laminates tend to collapse due to global buckling; (3) with moderate numbers of delaminations, delamination propagation may be observed as well as in-plane failure in the zones around the delamination front due to stress concentration and it is the in-plane failure that leads ultimate failure of the panel straightaway; (4) with excessive number of delaminations, in-plane failure is the dominant mechanism responsible for immediate catastrophic failure of the panel.

Through improved inverse method presented by the author, it is found that the stiffness degradation is neither uniform over the delaminated area nor constant during compression process in the CAI case. However, a universally degrading tendency cannot be obtained and, therefore, the advantage of this method cannot be taken fully for CAI predictions. However, this method has the potential of connecting the detailed FE analysis at coupon level and simplified FE model of a complex structure.

7.3 Research contribution

The CAI damage mechanism of laminates using toughened material systems have been studied systematically. It can be concluded that in most cases impacted laminate fails due to in-plane failure initiating around the delamination front, and delamination propagation is unlikely to take place, in particular, when delaminations are found on most of the interfaces. This is the underlying justification for developing a computationally efficient method to predict CAI which only takes in-plane failure into account.

A method of detailed FE modelling of CAI is presented. This model takes all major damage modes, such as delaminations, transverse matrix cracks and fibre breakage, into account. It incorporates two possible failure modes simultaneously, delamination propagation and in-plane failure, and allows them to compete with each other to dominate the damage process. It employs C-scan result as damage input. This modelling method is more realistic than previous methods. In the meantime, the application strategy of this method is also presented.

A method to predict CAI strength based on soft inclusion assumption is presented. It overcomes some crucial weaknesses of previous methods, employs C-scan result as damage input, and it is effective in problem solving and efficient in computation.

An improved inverse method is presented, which has the potential to efficiently simulate the mechanical behaviour of a complex structure containing a zone of damage through a simplified FE model.

A deficiency of cohesive element is spotted. It roots from the discrepancy of coordinate systems of cohesive elements and crack propagation direction, and may bring additional numerical error if used improperly.

7.4 Future work

Through the research as presented in this thesis, the following directions have been identified as future work which would advance the understanding of the nature of the problem and the ability to solve it effectively and efficiently.

To overcome the deficiency of cohesive element, the discrepancy of coordinate systems of cohesive elements and crack propagation direction. This could eliminate the numerical error when employing power law as the failure criterion for mixed mode problems.

To improve the evaluation of damage state induced by foreign object impact through thorough investigation of deply technique, and in the meantime, to improve the accuracy of assumed delamination distribution determined by C-scan.

To improve the degradation method to obtain a more accurate stress state. Besides, to improve the meshing strategy on the simplified model.

To find a practical approach to connect the detailed FE analysis at coupon level and simplified FE model of a complex structure through the improved inverse method as presented in this thesis.

References

1. Chen, P., Z. Shen, and J. Wang, *A new method for compression after impact strength prediction of composite laminates.* Journal of Composite Materials, 2002. **36**(5): p. 589-610.
2. Tang, X., Z. Shen, P. Chen, and M. Gaedke. *Methodology for residual strength of damaged laminated composites*. in *Proc. 38th AIAA/ASME/ASCE/AHS/ASC Structures, Structural Dynamics and Materials Conference*. 1997.
3. Craven, R., L. Iannucci, and R. Olsson, *Delamination buckling: A finite element study with realistic delamination shapes, multiple delaminations and fibre fracture cracks.* Composites Part A: Applied Science and Manufacturing, 2010. **41**(5): p. 684-692.
4. Craven, R., *Modelling of impact damage in composites*. 2009, Imperial College London.
5. Prichard, J.C., *Post-impact compression behaviour of continuous fibre composite materials*. 1991.
6. Olsson, R., *Mass criterion for wave controlled impact response of composite plates.* Composite: Part A, 2000. **31**.
7. Olsson, R., *Analytical model for delamination growth during small mass impact on plates.* International Journal of Solids and Structures, 2010. **47**: p. 2884-2892.
8. FAA, *Composite aircraft structure*, U.S.D.o. Transportation, Editor. 2009.
9. Sánchez-Sáez, S., E. Barbero, R. Zaera, and C. Navarro, *Compression after impact of thin composite laminates.* Composites Science and Technology, 2005. **65**(13): p. 1911-1919.
10. Bouvet, C., S. Rivallant, and J. Barrau, *Low velocity impact modeling in composite laminates capturing permanent indentation.* Composites Science and Technology, 2012. **72**: p. 1977-1988.
11. Craven, R., S. Pindoria, and R. Olsson, *Finite element study of compressively loaded fibres fractured during impact.* Composites Science and Technology, 2009. **69**: p. 586-593.
12. ASTM, *Standard Test Method for Measuring the Damage Resistance of a Fiber-Reinforced Polymer Matrix Composite to a Drop-Weight Impact Event*. 2012.
13. ASTM, *Standard Test Method for Compressive Residual Strength Properties of Damaged Polymer Matrix Composite Plates*. 2012.
14. Yan, L., X. An, J.-l. Cai, D. Zhang, and X. Yi, *Study on Damage Equivalence of Composite Laminates Subjected to Low-velocity Impact and Quasi-static Indentation.* Journal of Aeronautical Materials, 2011. **31**(3): p. 5.
15. Boeing, *Advanced composite compression test*. 1988, Boeing Specification Support Standard BSS 7260: Seattle, Washington.
16. Airbus, *Determination of Compression Strength After Impact*, in *Airbus Test Method AITM1-0010* 2005.
17. SACMA, *SACMA Recommended Methods SRM 2R-94*. 1994, Suppliers of Advanced Composites Materials Association.

18. NASA-Langley, *Standard Tests for Toughened Resin Composites*, in *NASA Reference Publication 1092*. 1983: Hampton, Virginia.
19. Chai, H., C.D. Babcock, and W.G. Knauss, *One dimensional modelling of failure in laminated plates by delamination buckling.* International Journal of Solids and Structures, 1981. **17**(11): p. 1069-1083.
20. Simitses, G., S. Sallam, and W. Yin, *Effect of delamination of axially loaded homogeneous laminated plates.* AIAA journal, 1985. **23**(9): p. 1437-1444.
21. Suemasu, H., *Effects of multiple delaminations on compressive buckling behaviors of composite panels.* Journal of Composite Materials, 1993. **27**(12): p. 1172-1192.
22. Lee, J., Z. Gürdal, and O. Griffin Jr, *Buckling and postbuckling of circular plates containing concentric penny-shaped delaminations.* Computers & structures, 1996. **58**(5): p. 1045-1054.
23. Nilsson, K.F., L.E. Asp, J.E. Alpman, and L. Nystedt, *Delamination buckling and growth for delaminations at different depths in a slender composite panel.* International Journal of Solids and Structures, 2001. **38**(17): p. 3039-3071.
24. Whitcomb, J.D. and K. Shivakumar, *Strain-energy release rate analysis of plates with postbuckled delaminations.* Journal of Composite Materials, 1989. **23**(7): p. 714-734.
25. Whitcomb, J.D., *Analysis of a laminate with a postbuckled embedded delamination, including contact effects.* Journal of Composite Materials, 1992. **26**(10): p. 1523-1535.
26. Reeder, J.R., K. Song, P.B. Chunchu, and D.R. Ambur, *Postbuckling and growth of delaminations in composite plates*. 2002, AIAA.
27. Suemasu, H., W. Sasaki, T. Ishikawa, and Y. Aoki, *A numerical study on compressive behavior of composite plates with multiple circular delaminations considering delamination propagation.* Composites Science and Technology, 2008. **68**(12): p. 2562-2567.
28. Ovesy, H., M. Taghizadeh, and M. Kharazi, *Post-buckling analysis of composite plates containing embedded delaminations with arbitrary shape by using higher order shear deformation theory.* Composite Structures, 2012. **94**(3): p. 1243-1249.
29. Craven, R., L. Iannucci, and R. Olsson, *Homogenised non-linear soft inclusion for simulation of impact damage in composite structures.* Composite Structures, 2011. **93**(2): p. 952-960.
30. Suemasu, H., W. Sasaki, Y. Aoki, and T. Ishikawa. *Compressive behavior of impact damaged composite laminates*. in *In Proc. 16th Int. Conf. on Composite Materials, Kyoto, Japan 8â€“13 July 2007*. 2007.
31. Aoki, Y., H. Kondo, and H. Hatta, *Effect of delamination propagation on mechanical behaviour in compression after impact.* ICCM16, Kyoto, Japan, 2007.
32. Zou, Z., S. Reid, and S. Li, *A continuum damage model for delaminations in laminated composites.* Journal of the Mechanics and Physics of Solids, 2003. **51**(2): p. 333-356.
33. De Freitas, M. and L. Reis, *Failure mechanisms on composite specimens subjected to compression after impact.* Composite Structures, 1998. **42**(4): p. 365-373.
34. Nilsson, K.F., J.C. Thesken, P. Sindelar, A.E. Giannakopoulos, and B. Stoåkers, *A theoretical and experimental investigation of buckling induced delamination growth.* Journal of the Mechanics and Physics of Solids, 1993. **41**(4): p. 749-782.
35. Ruan, J., F. Aymerich, J. Tong, and Z. Wang, *Optical Evaluation on Delamination Buckling of Composite Laminate with Impact Damage.* Advances in Materials Science and Engineering, 2014. **2014**.
36. Tang, X. and J. Liu, *Theory manual of CDTAC 1.0*. 1998, Aircraft Strength Research Institute.

37. Soutis, C. and P. Curtis, *Prediction of the post-impact compressive strength of CFRP laminated composites.* Composites Science and Technology, 1996. **56**(6): p. 677-684.
38. Xiong, Y., C. Poon, P. Straznicky, and H. Vietinghoff, *A prediction method for the compressive strength of impact damaged composite laminates.* Composite Structures, 1995. **30**(4): p. 357-367.
39. Qi, B. and I. Herszberg, *An engineering approach for predicting residual strength of carbon/epoxy laminates after impact and hygrothermal cycling.* Composite Structures, 1999. **47**(1–4): p. 483-490.
40. Nilsson, E., *Residual Strength Prediction of Composite Laminates Containing Impact Damage.* Interface, 2005. **6**(7): p. 8.
41. Dost, E., *Effect of stacking sequence on impact damage resistance and residual strength for quasi-isotropic laminates*, in *American society for testing and materials*. 1991: Philadelphia.
42. Dost, E.F., L.B. Ilcewicz, W.B. Avery, and B.R. Coxon, *Effect of stacking sequence on impact damage resistance and residual strength for quasi-isotropic laminates*. Composite materials: fatigue and fracture ed. T.K. O'Brien. Vol. 3. 1991, Philadelphia: American society for testing and materials. 24.
43. Yang, X., Z. Shen, Y. Yan, and B.-s. Liu, *New methodology for evaluating toughness of composite laminates-investigation of damage resistance.* Chinese Journal of Aeronautics, 2003. **16**(2): p. 73-79.
44. Guild, F.J., J.C. Prichard, and P. Hogg, *A model for the reduction in compression strength of continuous fiber composites after impact damage.* Polymer composites, 2001. **24**(4): p. 333-339.
45. Sjögren, A., A. Krasnikovs, and J. Varna, *Experimental determination of elastic properties of impact damage in carbon fibre/epoxy laminates.* Composites Part A: Applied Science and Manufacturing, 2001. **32**(9): p. 1237-1242.
46. Tang, X., Z. Shen, and J. Liu, *The Deply technic for damage detection of composite laminat.* Acta Materiae Compositae Sinic, 1986. **3**: p. 5.
47. Shen, Z., S. Yang, and P. Chen, *Knee point phenomenon composites withstanding to impact and its physical meaning.* Acta Materiae Compositae Sinica, 2008. **25**(5): p. 125-133.
48. Olsson, R., *Analytical prediction of damage due to large mass impact on thin ply composites.* Composites Part A: Applied Science and Manufacturing, 2015. **72**: p. 184-191.
49. Suemasu, H., W. Sasaki, Y. Aoki, and T. Ishikawa. *Compressive behavior of impact damaged composite laminates*. in *In Proc. 16th Int. Conf. on Composite Materials, Kyoto, Japan 13 July 2007*. 2007.
50. Liu, D., *Impact-induced delamination—a view of bending stiffness mismatching.* Journal of Composite Materials, 1988. **22**(7): p. 674-692.
51. Li, S., S. Reid, P. Soden, and M. Hinton, *Modelling transverse cracking damage in thin, filament-wound tubes subjected to lateral indentation followed by internal pressure.* International journal of mechanical sciences, 2005. **47**(4): p. 621-646.
52. Ishikawa, T., S. Sugimoto, M. Matsushima, and Y. Hayashi, *Some experimental findings in compression-after-impact (CAI) tests of CF/PEEK (APC-2) and conventional CF/epoxy flat plates.* Composites Science and Technology, 1995. **55**(4): p. 349-363.

53. Sztefek, P. and R. Olsson, *Nonlinear compressive stiffness in impacted composite laminates determined by an inverse method.* Composites Part A: Applied Science and Manufacturing, 2009. **40**(3): p. 260-272.
54. Gu, H. and A. Chattopadhyay, *An experimental investigation of delamination buckling and postbuckling of composite laminates.* Composites Science and Technology, 1999. **59**(6): p. 903-910.
55. Pinho, S.T., L. Iannucci, and P. Robinson, *Physically-based failure models and criteria for laminated fibre-reinforced composites with emphasis on fibre kinking: Part I: Development.* Composites: Part A, 2006. **37**: p. 63-73.
56. Gaudenzi, P., P. Perugini, and A. Riccio, *Post-buckling behavior of composite panels in the presence of unstable delaminations.* Composite Structures, 2001. **51**(3): p. 301-309.
57. Williams, J., *On the calculation of energy release rates for cracked laminates.* International Journal of Fracture, 1988. **36**(2): p. 101-119.
58. Wang, S. and C.M. Harvey, *Mixed mode partition theories for one dimensional fracture.* Engineering Fracture Mechanics, 2012. **79**: p. 329-352.
59. Chai, H. and C.D. Babcock, *Two-dimensional modelling of compressive failure in delaminated laminates.* Journal of Composite Materials, 1985. **19**(1): p. 67.
60. Krueger, R., *Virtual crack closure technique: history, approach, and applications.* Applied Mechanics Reviews, 2004. **57**(2): p. 109-143.
61. Klug, J., X. Wu, and C. Sun, *Efficient modeling of postbuckling delamination growth in composite laminates using plate elements.* AIAA journal, 1996. **34**(1): p. 178-184.
62. Benzeggagh, M. and M. Kenane, *Measurement of mixed-mode delamination fracture toughness of unidirectional glass/epoxy composites with mixed-mode bending apparatus.* Composites Science and Technology, 1996. **56**: p. 439-449.
63. HB, *Testing Method for Mode II Interlaminar Fracture Toughness of Carbon Fiber Reinforced Plastics*. 1996.
64. Gong, X.-J. and M. Benzeggagh, *Mixed mode interlaminar fracture toughness of unidirectional glass/epoxy composite.* ASTM SPECIAL TECHNICAL PUBLICATION, 1995. **1230**: p. 100-123.
65. Zou, Z., S. Reid, P. Soden, and S. Li, *Mode separation of energy release rate for delamination in composite laminates using sublaminates.* International Journal of Solids and Structures, 2001. **38**(15): p. 2597-2613.
66. Bazhenov, S., *Interlaminar and intralaminar fracture modes in 0/90 cross-ply glass/epoxy laminate.* Composites, 1995. **26**(2): p. 125-133.
67. Wang, S. and Y. Zhang, *Buckling, post-buckling and delamination propagation in debonded composite laminates Part 2: Numerical applications.* Composite Structures, 2009. **88**(1): p. 131-146.
68. Asp, L.E., S. Nilsson, and S. Singh, *An experimental investigation of the influence of delamination growth on the residual strength of impacted laminates.* Composites Part A: Applied Science and Manufacturing, 2001. **32**(9): p. 1229-1235.
69. Hitchen, S. and R. Kemp, *The effect of stacking sequence on impact damage in a carbon fibre/epoxy composite.* Composites, 1995. **26**(3): p. 207-214.
70. De Moura, M., J. Gonçalves, A. Marques, and P. De Castro, *Prediction of compressive strength of carbon–epoxy laminates containing delamination by using a mixed-mode damage model.* Composite Structures, 2000. **50**(2): p. 151-157.

71. Zou, Z., S. Reid, S. Li, and P. Soden, *General expressions for energy–release rates for delamination in composite laminates.* Proceedings of the Royal Society of London. Series A: Mathematical, Physical and Engineering Sciences, 2002. **458**(2019): p. 645-667.
72. Raju, I.S., J.H. Crews, and M.A. Aminpour, *Convergence of strain energy release rate components for edge-delaminated composite laminates*. 1987, NASA: Hampton, Virginia, USA. p. 41.
73. Rybicki, E.F. and M. Kanninen, *A finite element calculation of stress intensity factors by a modified crack closure integral.* Engineering Fracture Mechanics, 1977. **9**(4): p. 931-938.
74. Whitcomb, J.D., *Three-dimensional analysis of a postbuckled embedded delamination.* Journal of Composite Materials, 1989. **23**(9): p. 862-889.
75. Turon, A., C.G. Davila, P.P. Camanho, and J. Costa, *An engineering solution for mesh size effects in the simulation of delamination using cohesive zone models.* Engineering Fracture Mechanics, 2007. **74**(10): p. 1665-1682.
76. Guiamatsia, I., J. Ankersen, L. Iannucci, and M. Fouinnetteau, *Enriched finite elements for the efficient prediction of impact-induced damage in composite laminates.* Composites Science and Technology, 2013. **79**: p. 87-96.
77. MIL-HDBK-17-3F, *Composite material handbook*, D.o. defence, Editor. 2002.
78. Tan, W., B.G. Falzon, L.N. Chiu, and M. Price, *Predicting low velocity impact damage and Compression-After-Impact (CAI) behaviour of composite laminates.* Composites Part A: Applied Science and Manufacturing, 2015. **71**: p. 212-226.
79. Suemasu, H., T. Irie, and T. Ishikawa, *Buckling and post-buckling behavior if composite plates containing multiple delaminations.* Journal of Composite Materials, 2009. **43**(2): p. 191-202.
80. Rivallant, S., C. Bouvet, and N. Hongkarnjanakul, *Failure analysis of CFRP laminates subjected to compression after impact: FE simulation using discrete interface elements.* Composites Part A: Applied Science and Manufacturing, 2013. **55**: p. 83-93.
81. González, E., P. Maimí, P. Camanho, A. Turon, and J. Mayugo, *Simulation of drop-weight impact and compression after impact tests on composite laminates.* Composite Structures, 2012. **94**(11): p. 3364-3378.
82. Kim, H. and K.T. Kedward, *A method for modeling the local and global buckling of delaminated composite plates.* Composite Structures, 1999. **44**(1): p. 43-53.
83. Yan, H., C. Oskay, A. Krishnan, and L.R. Xu, *Compression-after-impact response of woven fiber-reinforced composites.* Composites Science and Technology, 2010. **70**(14): p. 2128-2136.
84. Shu, D. and Y.-W. Mai, *Buckling of delaminated composites re-examined.* Composites Science and Technology, 1993. **47**(1): p. 35-41.
85. Shivakumar, K. and J. Whitcomb, *Buckling of a sublaminate in a quasi-isotropic composite laminate.* Journal of Composite Materials, 1985. **19**(1): p. 2-18.
86. Jane, K.C. and W.L. Yin, *Refined buckling and postbuckling analysis of two-dimensional delaminations—II. results for anisotropic laminates and conclusion.* International Journal of Solids and Structures, 1992. **29**(5): p. 611-639.
87. Arman, Y., M. Zor, and S. Aksoy, *Determination of critical delamination diameter of laminated composite plates under buckling loads.* Composites Science and Technology, 2006. **66**(15): p. 2945-2953.
88. Hwang, S.-F. and G.-H. Liu, *Buckling behavior of composite laminates with multiple delaminations under uniaxial compression.* Composite Structures, 2001. **53**(2): p. 235-243.

89. Dost, E., L.B. Ilcewicz, and J.H. Gosse. *Sublaminate stability based modeling of impact-damaged composite laminates*. in *Proc. of the 3rd technical conference of American society composites*. 1988.
90. Sztefek, P. and R. Olsson, *Tensile stiffness distribution in impacted composite laminates determined by an inverse method.* Composites Part A: Applied Science and Manufacturing, 2008. **39**(8): p. 1282-1293.
91. Chen, P., Z. Shen, and J. Wang, *Damage tolerance analysis of cracked stiffened composite panels.* Journal of Composite Materials, 2001. **35**(20): p. 1815-1843.
92. Olsson, R., J. Iwarsson, L.G. Melin, A. Sjögren, and J. Solti, *Experiments and analysis of laminates with artificial damage.* Composites Science and Technology, 2003. **63**(2): p. 199-209.
93. Toubal, L., M. Karama, and B. Lorrain, *Stress concentration in a circular hole in composite plate.* Composite Structures, 2005. **68**(1): p. 31-36.
94. Whitney, J. and R. Nuismer, *Stress fracture criteria for laminated composites containing stress concentrations.* Journal of Composite Materials, 1974. **8**(3): p. 253-265.
95. Hashin, Z., *Failure criteria for unidirectional fiber composites.* Journal of applied mechanics, 1980. **47**(2): p. 329-334.
96. Kaddour, A. and M. Hinton, *Input data for test cases used in benchmarking triaxial failure theories of composites.* Journal of Composite Materials, 2012. **46**(19-20): p. 2295-2312.
97. Rolfes, R., J. Noack, F.R. Valdepenas, M. Taeschner, and R. Zimmermann. *Fast Analysis Tools for Concurrent/Integrated Engineering of Composite Airframe Structures*. in *Optimization in Industry...: Presented at the Conference, Optimization in Industry*. 2001. American Society of Mechanical Engineers.
98. Prichard, J. and P. Hogg, *The role of impact damage in post-impact compression testing.* Composites, 1990. **21**(6): p. 503-511.
99. Li, S., S.R. Reid, and Z. Zou, *Modelling damage of multiple delaminations and transverse matrix cracking in laminated composites due to low velocity lateral impact.* Composites Science and Technology, 2006. **66**(6): p. 827-836.
100. Shivakumar, K., S. Lingaiah, H. Chen, P. Akangah, G. Swaminathan, and L. Russell, *Polymer nanofabric interleaved composite laminates.* AIAA journal, 2009. **47**(7): p. 1723-1729.
101. HEXCEL. *Composite trends from HEXCEL*. 2013; Available from: http://www.hexcel.com.
102. Ashton, J.E., *Approximate solution for unsymmetrically laminated plates.* Journal of Composite Materials, 1969. **3**.

Appendix A Experimental data

The experimental process, including drop-weight impact, non-destructive inspection (NDI) and compression after impact, were conducted at Aircraft Strength Research Institute (ASRI) in China by the author assisted by his colleagues before the PhD project started at Nottingham University. The experiments provided data as reference and resource for the PhD study, which is presented in this appendix.

A.1 Material systems and laminates

There are four different types of material systems involved in these tests. The in-plane mechanical properties, interfacial CERR and nominal ply thickness are listed in Table A.1, respectively. Properties of four types of unidirectional lamina

Table A.1 Properties of four types of unidirectional lamina

Material group	A	B	C	D
Longitudinal modulus E_1 (GPa)	150	145	140	130
Transverse modulus E_2 (GPa)	11	10	11	13
In-plane shear modulus G_{12} (GPa)	4.07	5.00	5.02	6.02
Major Poisson's ratio v_{12}	0.31	0.312	0.296	0.33
Longitudinal tensile strength X_T (MPa)	3100	2700	2632	2852
Longitudinal compressive strength X_C (MPa)	1200	1520	1406	1303
Transverse tensile strength Y_T (MPa)	60	68	56	65
Transverse compressive strength Y_C (MPa)	210	234	245	201
In-plane shear strength S_{12} (MPa, Max)	130	118	124	144
In-plane shear strength S_{12} (MPa, 0.2% offset)	54.6	53.4	61.8	67.3
Transverse shear strength S_{13} (MPa)	93	115	116	106
Ply thickness (mm)	0.128	0.19	0.1225	0.125
Mode I energy release rate G_{Ic} (J/m^2)	515	798	623	505
Mode II energy release rate G_{IIc} (J/m^2)	872	1030	992	897

Table A.2 Laminate definition and impact energy (The impact energy density is defined as the ratio of impact energy with respect to laminate thickness)

Material group	Specimen	Quantity	Lay-up	Nominal thickness (mm)	Impact energy (J)	Impact energy density (J/mm)
A	A1	5	$[45/0/-45/90]_{4S}$	4.096	15	3.66
	A2	5			30	7.32
	A3	5			40	9.77
	A4	5			50	12.21
	A5	5			60	14.65
B	B1	5	$[45/0/-45/90]_{3S}$	4.56	15	3.29
	B2	5			30	6.58
	B3	5			40	8.77
	B4	5			50	10.96
	B5	5			60	13.16
C	C	6	$[45/0/-45/90]_{5S}$	4.9	22	4.49
D	D	6	$[45/0/-45/90]_{5S}$	5	33	6.6

Accordingly, there were four groups of specimens manufactured, which were referred as A, B, C and D, respectively. For groups of A and B, there were 25 specimens in each group, which were divided into five sub-groups further, and for groups of C and D, there were 6 specimens in each group, as listed in Table A.2. Regarding lay-up sequence, the fibre orientation of 0° lamina was aligned with compressive direction.

A.2 Experiment results

Table A.3 list relevant data of every single specimen, including measured size, impacting energy, impacting dent depth, failure load and failure stress (the ratio of the failure load to the section area).

Table A.3 Test results

(a) Prescribed impact energy: 15J, lay-up: $[45/0/-45/90]_{4S}$

Specimen	Width (mm)	Thickness (mm)	Impact energy (J)	Impact dent (mm)	Failure load (kN)	Failure stress (MPa)
A1-1	100	4.13	15.2	0.2	126	306
A1-2	100.1	4.18	14.9	0.3	139	333
A1-3	100	4.15	14.9	0.24	140	337
A1-4	100.1	4.19	15.1	0.22	130	310
A1-5	100.1	4.2	15.1	0.24	148	351
			Average			327
			Standard deviation			18.98
			Coefficient of variance (%)			5.80

(b) Prescribed impact energy 30J ($[45/0/-45/90]_{4S}$)

Specimen	Width (mm)	Thickness (mm)	Impact energy (J)	Impact dent (mm)	Failure load (kN)	Failure stress (MPa)
A2-1	100	4.11	30.8	0.28	127	309
A2-2	100.1	4.09	30.7	0.24	105	256
A2-3	100.1	4.09	30.6	0.28	112	275
A2-4	100.1	4.09	30.8	0.24	123	300
A2-5	100.1	4.10	30.6	0.22	93	227
			Average			273
			Standard deviation			33.29
			Coefficient of variance (%)			12.18

(c) Prescribed impact energy 40J ($[45/0/-45/90]_{4S}$)

Specimen	Width (mm)	Thickness (mm)	Impact energy (J)	Impact dent (mm)	Failure load (kN)	Failure stress (MPa)
A3-1	99.88	4.11	40.7	0.4	98	240
A3-2	99.96	4.12	40.4	0.32	96	234
A3-3	99.96	4.12	38.7	0.28	102	248
A3-4	99.91	4.11	40.5	0.32	104	254
A3-5	99.93	4.11	40.3	0.32	108	263
			Average			248
			Standard deviation			11.41
			Coefficient of variance (%)			4.60

(d) Prescribed impact energy 50J ($[45/0/-45/90]_{4S}$)

Specimen	Width (mm)	Thickness (mm)	Impact energy (J)	Impact dent (mm)	Failure load (kN)	Failure stress (MPa)
A4-1	100.2	4.10	51.6	Through	79	193
A4-2	100.1	4.08	51.6	1	91	224
A4-3	100.1	4.09	51.5	0.58	89	216
A4-4	100.1	4.12	51.3	0.7	90	217
A4-5	100.2	4.12	51.2	0.86	90	218
			Average			214
			Standard deviation			11.93
			Coefficient of variance (%)			5.58

(e) Prescribed impact energy 60J ($[45/0/-45/90]_{4S}$)

Specimen	Width (mm)	Thickness (mm)	Impact energy (J)	Impact dent (mm)	Failure load (kN)	Failure stress (MPa)
A5-1	100.1	4.11	61.9	Through	74	179
A5-2	100.2	4.10	51.5	Through	79	193
A5-3	100.2	4.10	51.6	2	74	180
A5-4	100.1	4.08	51.5	1.58	69	170
A5-5	100.1	4.10	60.9	1.62	88	215
			Average			187
			Standard deviation			17.47
			Coefficient of variance (%)			9.32

(f) Prescribed impact energy 15J ($[45/0/-45/90]_{3S}$)

Specimen	Width (mm)	Thickness (mm)	Impact energy (J)	Impact dent (mm)	Failure load (kN)	Failure stress (MPa)
B1-1	100.1	4.63	15	0.18	154	331
B1-2	100.1	4.64	15.1	0.18	160	345
B1-3	100.1	4.64	15	0.16	157	339
B1-4	100.1	4.64	14.9	0.16	153	329
B1-5	100.1	4.63	15.2	0.14	160	346
			Average			338
			Standard deviation			7.81
			Coefficient of variance (%)			2.31

(g) Prescribed impact energy 30J ($[45/0/-45/90]_{3S}$)

Specimen	Width (mm)	Thickness (mm)	Impact energy (J)	Impact dent (mm)	Failure load (kN)	Failure stress (MPa)
B2-1	100.1	4.66	30.5	0.2	125	269
B2-2	100.1	4.67	30.6	0.18	129	275
B2-3	100.1	4.64	30.7	0.2	123	264
B2-4	100.1	4.63	30.5	0.34	125	269
B2-5	100.2	4.65	30.6	0.22	121	259
			Average			267
			Standard deviation			6.02
			Coefficient of variance (%)			2.25

(h) Prescribed impact energy 40J ($[45/0/-45/90]_{3S}$)

Specimen	Width (mm)	Thickness (mm)	Impact energy (J)	Impact dent (mm)	Failure load (kN)	Failure stress (MPa)
B3-1	100	4.59	40.5	0.28	127	277
B3-2	100.2	4.63	40.3	0.34	129	278
B3-3	100.2	4.63	40.4	0.36	123	264
B3-4	100.1	4.63	40.6	0.32	117	252
B3-5	100.1	4.66	40.8	0.3	128	275
			Average			269
			Standard deviation			11.12
			Coefficient of variance (%)			4.13

(i) Prescribed impact energy 50J ($[45/0/-45/90]_{3S}$)

Specimen	Width (mm)	Thickness (mm)	Impact energy (J)	Impact dent (mm)	Failure load (kN)	Failure stress (MPa)
B4-1	100	4.64	51.22	0.28	122	263
B4-2	100	4.66	51.6	0.28	127	273
B4-3	100.1	4.67	51.1	0.24	129	277
B4-4	100.1	4.66	51.3	0.24	114	245
B4-5	100	4.68	51.2	0.26	128	274
			Average			266
			Standard deviation			13.07
			Coefficient of variance (%)			4.91

(j) Specimen B with prescribed impact energy 60J ([45/0/-45/90]3S)

Specimen	Width (mm)	Thickness (mm)	Impact energy (J)	Impact dent (mm)	Failure load (kN)	Failure stress (MPa)
B5-1	100	4.62	60.5	0.34	113	245
B5-2	100.1	4.63	60.9	0.34	113	241
B5-3	100	4.66	61	0.28	122	262
B5-4	100.2	4.66	61.3	0.28	105	226
B5-5	100.3	4.65	61.5	0.34	116	248
			Average			244
			Standard deviation			12.97
			Coefficient of variance (%)			5.31

(k) Specimen C with prescribed impact energy 22J ([45/0/-45/90]5S)

Specimen	Width (mm)	Thickness (mm)	Impact energy (J)	Impact dent (mm)	Failure load (kN)	Failure stress (MPa)
C-1	100.2	4.91	21.7	0.32	152	309
C-2	100.2	4.89	21.8	0.28	139	285
C-3	100.2	4.92	21.6	0.30	153	311
C-4	100.2	4.91	22.0	0.30	156	317
C-5	100.2	4.89	21.9	0.32	154	314
C-6	100.2	4.86	22.0	0.34	154	317
			Average			309
			Standard deviation			12.11
			Coefficient of variance (%)			3.92

(l) Specimen D with prescribed impact energy 33J ([45/0/-45/90]5S)

Specimen	Width (mm)	Thickness (mm)	Impact energy (J)	Impact dent (mm)	Failure load (kN)	Failure stress (MPa)
D-1	100.1	5.05	33.7	0.24	149	295
D-2	100.1	4.99	34.0	0.24	134	268
D-3	100.1	5.04	33.6	0.26	150	298
D-4	100.1	5.11	33.0	0.28	133	260
D-5	100.1	5.06	33.7	0.30	136	268
D-6	100.1	5.04	33.9	0.31	140	278
			Average			278
			Standard deviation			15.57
			Coefficient of variance (%)			5.61

Appendix B FD criterion

FD (fibre damage) criterion is presented by Chen, Shen [1], who attempted to model the delaminated area as an elliptical open hole, of which the major and minor axes are equal to the damage width (the maximum width of delaminated area perpendicular to loading direction) and dent diameter respectively. They presented a failure criterion assuming that failure occurred when the stress in the 0° degree plies in a composite laminate over a characteristic distance away from the notch was equal to or greater than the longitudinal ultimate compressive strength of corresponding unidirectional laminate. It is expressed as

$$\frac{1}{l_0}\int_{a}^{a+l_0}\sigma_y^0(x,0)dx = X \tag{B.1}$$

where, l_0 is a lay-up independent material constant, a is half width of delaminated area perpendicular to load direction, σ_y^0 is the stress on 0° degree lamina of which the fiber orientation aligns with the loading direction, x is the distance from the delamination front, and X is the longitudinal ultimate strength of the corresponding unidirectional lamina.

This criterion has a significant trace of Average Stress Criterion mentioned in Section 2.5.2.13. Actually, this criterion was firstly presented to predict the failure strength of open-hole cases by Chen and then extended to CAI cases. Chen assumed that the collapse of the entire laminate was due to fiber failure in 0° degree laminae initiating close to the notch (open hole, cut or impact damage) and the constant l_0 is a characteristic length which was independent to lay-up and the form of notch. Therefore, Chen named this criterion as FD (fibre damage) criterion.

When this method is applied to CAI prediction, it probably underestimates the CAI behaviour by approximating delaminated area having a degree of capability sustaining some compressive load by an open hole. Additionally, any variation such as material, lay-up or impact energy would lead to different l_0, which needed to be repeatedly adjusted to match the tests. This hindered the wide application of this failure criterion on CAI cases. A comparison with the experimental results provided in Appendix A of this thesis is presented here. Because no precise value of l_0 is available for the laminates referred to in this thesis, it is selected at 2.4, 4.4 and 6.4, respectively, over the recommended range from 2.426 to 6.44 [1]. Figure B.1 shows the comparison between predicted results and test results. The discrepancy is significant, mainly due to the variation of the characteristic length l_0.

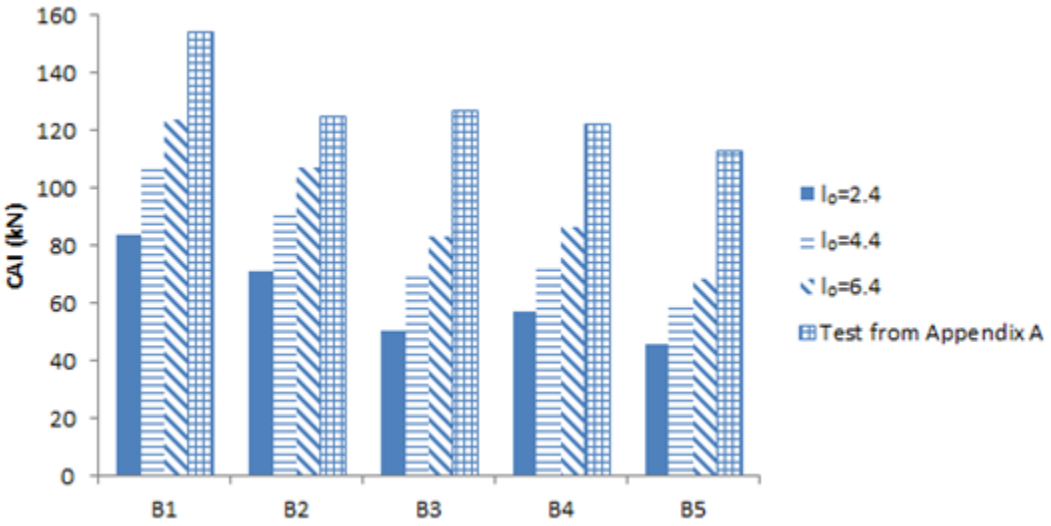

Figure B.1 CAI comparison between test and prediction through Chen's failure criterion with different characteristic length

Appendix C DI criterion

C.1 Introduction

Tang, Shen [2] presented a failure criterion referred as DI (Damage Influence) criterion, which was developed from Point Stress Criterion. This criterion was recorded as an internal document of ASRI in Chinese, of which some critical photocopies are attached at the end of this appendix (Figure C.5). This criterion was once evaluated by German Aerospace Center (DLR), and good agreement was reported [97]. However, they pointed out the difficulty of locating characteristic distance in CAI cases and therefore presented a monotonously increasing function referred as weight function, with which the weighted stress distributes like the upper curve with a valley point d_0 as sketched in Figure C.1. They described that when the weighted stress at d_0 reached compressive strength, the final failure occurred. It is expressed as

$$\min\left(\sigma_y(x,0)\cdot w(x,0)\right)=X \tag{C.1}$$

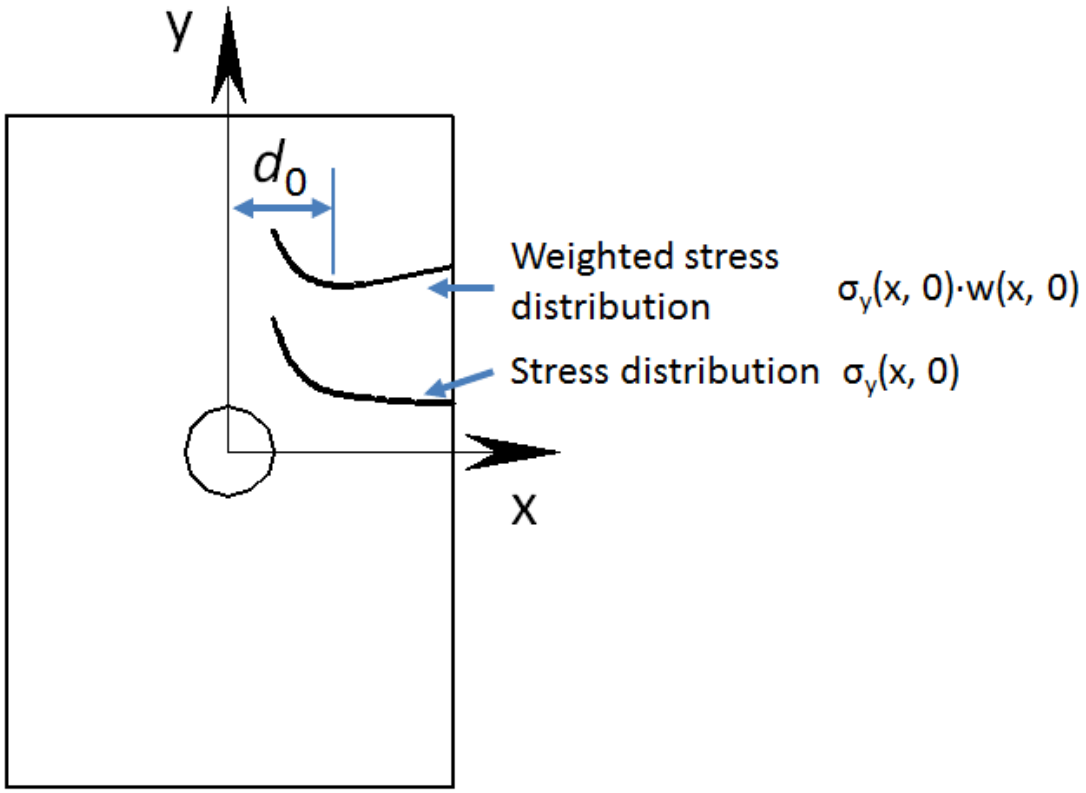

Figure C.1 Schematic of stress and weighted stress distribution with d_0 in Tang's method

The stress distribution was obtained through simplified FE model which consisted of only one layer of shell elements and the stiffness of corresponding delaminated area was degraded through a complex approach. In multiple-delamination cases such as CAI, Tang postulated the degradation coefficient for each sublaminate was

$$d_{\mathrm{k}} = \frac{N_{\mathrm{k}}/t_{\mathrm{k}}}{\sigma^0} \tag{C.2}$$

where N_{k} and t_{k} are the critical buckling load and thickness of the k^{th} sublaminate, respectively. σ_0 is the compressive strength of undamaged laminate.

C.1.1 Evaluation of N_{k}

N_k is the critical buckling load of the k^{th} sublaminate which is obtained through the following procedure, assuming that none of the delaminated lamina has buckled (Figure C.2(a)) at beginning.

Step 1

Carry out the buckling analysis for sublaminate Sub_1^{left} (it consists of only the 1^{st} layer from the surface on the left) and defined the buckling load as N_1^{left}. Repeat the same process for sublaminate Sub_1^{right} (it consists of all layers from 2^{nd} to n^{th}) and obtain the buckling load as N_1^{right} (Figure C.2(b)). The buckling analyses are based on the assumption that sublaminates on both sides of the delamination of a shape identical to the delamination, i.e. ellipse, with their edges fully clamped. The details of the analyses will be presented later.

Step 2

Considering the procedure as presented in Step 1 as the analyses for delamination 1, repeat the same procedure as in Step 1 for the each of the subsequent delaminations. A series of buckling loads (N_1^{left}, N_1^{right};… N_k^{left}, N_k^{right};… N_n^{left}, N_n^{right}) are obtained. Find the minimum of them and identify the sublaminate it is associated with. This sublaminate buckles as the load to the laminate increases to this level (Figure C.2(c)).

Step 3

Treat the remaining unbuckled sublaminates (Figure C.2(d)) in the same way as the laminate in Step 1 and 2, another buckling load can be obtained with another sublaminate buckled. Eventually every sublaminate will be associated with a buckling load. The buckling load obtained

for the sublaminate will be used to evaluate the stiffness degradation factor as introduced in Equation (C.2) for this sublaminate.

C.1.2 Calculation of N_k

In order to calculate the buckling load of elliptical delaminated sublaminate whose long axis lies at an angle of θ from global X axis, the deflection function is assumed in its local (material) coordinates x and y as

$$\omega(x,y) = \left(1 - \left(\frac{x}{a}\right)^2 - \left(\frac{y}{b}\right)^2\right)^2 (C_1 + C_2x^2 + C_3y^2 + C_4xy + C_5x + C_6y) \quad (C.3)$$

where a, b are the long and short half axes respectively. The total potential energy of the delaminated sublaminate is

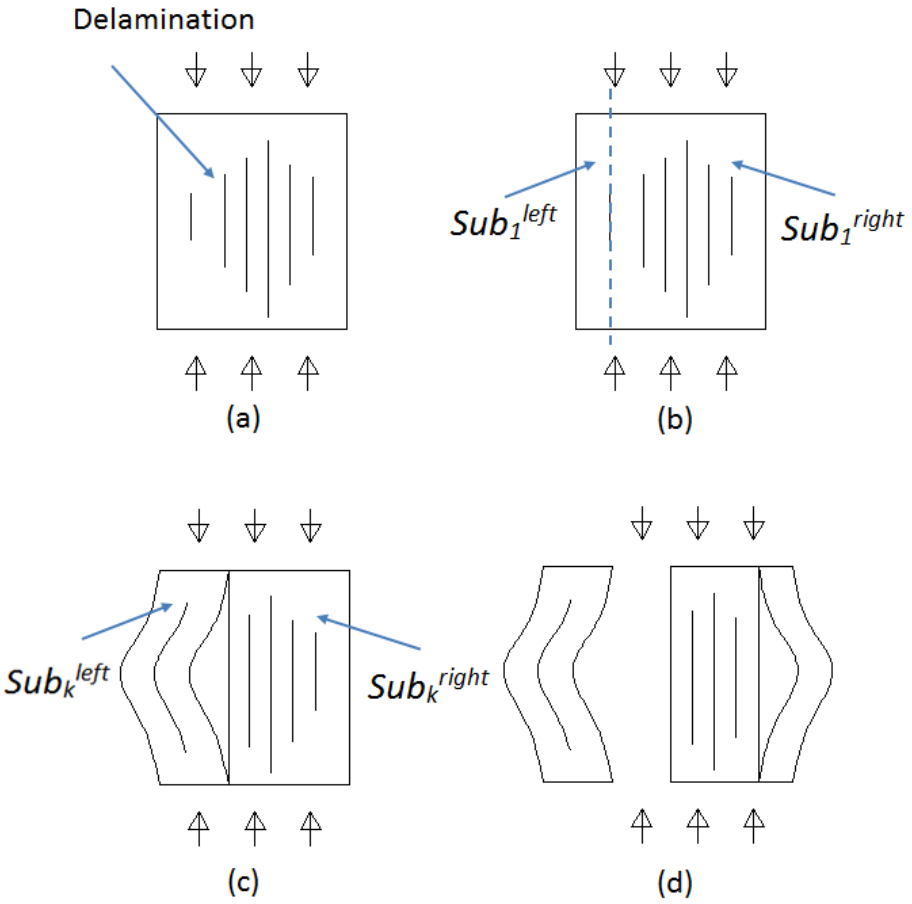

Figure C.2 Process demonstration of N_k definition (side view of the delaminated plate)

$$\Pi_p = \frac{1}{2}\int_{-a}^{a}\int_{-b\sqrt{1-(x/a)^2}}^{b\sqrt{1-(x/a)^2}}\left(\begin{Bmatrix}\frac{\partial^2\omega}{\partial x^2}\\ \frac{\partial^2\omega}{\partial y^2}\\ 2\frac{\partial^2\omega}{\partial x\,\partial y}\end{Bmatrix}^T [D]\begin{Bmatrix}\frac{\partial^2\omega}{\partial x^2}\\ \frac{\partial^2\omega}{\partial y^2}\\ 2\frac{\partial^2\omega}{\partial x\,\partial y}\end{Bmatrix} - \begin{Bmatrix}\frac{\partial\omega}{\partial x}\\ \frac{\partial\omega}{\partial y}\end{Bmatrix}^T \begin{bmatrix}N_1 & N_{12}\\ N_{12} & N_2\end{bmatrix}\begin{Bmatrix}\frac{\partial\omega}{\partial x}\\ \frac{\partial\omega}{\partial y}\end{Bmatrix}\right) dydx\Pi_p =$$

$$\frac{1}{2}\int_{-a}^{a}\int_{-b\sqrt{1-(x/a)^2}}^{b\sqrt{1-(x/a)^2}}\left(\begin{Bmatrix}\frac{\partial^2 w}{\partial x^2}\\ \frac{\partial^2 w}{\partial y^2}\\ 2\frac{\partial^2 w}{\partial x\,\partial y}\end{Bmatrix}^T \begin{bmatrix}\bar{D}_{11} & \bar{D}_{12} & \bar{D}_{16}\\ \bar{D}_{21} & \bar{D}_{22} & \bar{D}_{26}\\ \bar{D}_{61} & \bar{D}_{62} & \bar{D}_{66}\end{bmatrix}\begin{Bmatrix}\frac{\partial^2 w}{\partial x^2}\\ \frac{\partial^2 w}{\partial y^2}\\ 2\frac{\partial^2 w}{\partial x\,\partial y}\end{Bmatrix} - \begin{Bmatrix}\frac{\partial w}{\partial x}\\ \frac{\partial w}{\partial y}\end{Bmatrix}^T \begin{bmatrix}N_1 & N_{12}\\ N_{12} & N_2\end{bmatrix}\begin{Bmatrix}\frac{\partial w}{\partial x}\\ \frac{\partial w}{\partial y}\end{Bmatrix}\right) dydx \quad \text{(C.4)}$$

where

$$[\bar{\mathrm{D}}] = [\mathrm{D}] - [\mathrm{B}][\mathrm{A}]^{-1}[\mathrm{B}] \tag{C.5}$$

A, **B**, **D** are the extension, coupling and bending stiffness matrix of the sublaminate according to the classical laminate theory, respectively; N_1, N_2, N_{12}, the membrane forces in the sublaminate in its local coordinate system. This is the approximate bending stiffness matrix for unsymmetrical laminate [102]. Since membrane strains in the delaminated sublaminate in its material coordinates can be expressed as

$$\begin{Bmatrix} \varepsilon_1 \\ \varepsilon_2 \\ \gamma_{12} \end{Bmatrix} = \begin{bmatrix} a_{11} & a_{12} & a_{16} \\ a_{12} & a_{22} & a_{26} \\ a_{16} & a_{26} & a_{66} \end{bmatrix} \begin{bmatrix} \cos^2\theta & \sin^2\theta & 2\sin\theta\cos\theta \\ \sin^2\theta & \cos^2\theta & -2\sin\theta\cos\theta \\ -\sin\theta\cos\theta & \sin\theta\cos\theta & \cos^2\theta - \sin^2\theta \end{bmatrix} \begin{Bmatrix} N_{\mathrm{X}} \\ N_{\mathrm{Y}} \\ N_{\mathrm{XY}} \end{Bmatrix} \tag{C.6}$$

where a_{ij} are the compliance of the delaminated sublaminate in its material coordinates. Because under uniaxial compression,

$$N_{\mathrm{Y}} = N_{\mathrm{XY}} = 0 \tag{C.7}$$

membrane strains in the delaminated sublaminate in its material coordinates can be given as

$$\begin{Bmatrix} \varepsilon_1 \\ \varepsilon_2 \\ \gamma_{12} \end{Bmatrix} = \begin{Bmatrix} \rho_1 \\ \rho_2 \\ \rho_{12} \end{Bmatrix} N_{\mathrm{X}} \tag{C.8}$$

where

$$\begin{cases} \rho_1 = \mathrm{a}_{11}\cos^2\theta + \mathrm{a}_{12}\sin^2\theta - \mathrm{a}_{16}\sin\theta\cos\theta \\ \rho_2 = \mathrm{a}_{12}\cos^2\theta + \mathrm{a}_{22}\sin^2\theta - \mathrm{a}_{26}\sin\theta\cos\theta \\ \rho_{12} = \mathrm{a}_{16}\cos^2\theta + \mathrm{a}_{26}\sin^2\theta - \mathrm{a}_{66}\sin\theta\cos\theta \end{cases} \tag{C.9}$$

Thus

$$\begin{Bmatrix} N_1 \\ N_2 \\ N_{12} \end{Bmatrix} = \begin{bmatrix} A_{11} & A_{12} & A_{16} \\ A_{12} & A_{22} & A_{26} \\ A_{16} & A_{26} & A_{66} \end{bmatrix} \begin{Bmatrix} \varepsilon_1 \\ \varepsilon_2 \\ \gamma_{12} \end{Bmatrix} = \begin{Bmatrix} n_1 \\ n_2 \\ n_{12} \end{Bmatrix} N_X \tag{C.10}$$

where

$$\begin{cases} n_1 = A_{11}\rho_1 + A_{12}\rho_2 + A_{16}\rho_{12} \\ n_2 = A_{12}\rho_1 + A_{22}\rho_2 + A_{26}\rho_{12} \\ n_{12} = A_{16}\rho_1 + A_{26}\rho_2 + A_{66}\rho_{12} \end{cases} \tag{C.11}$$

Substituting Equation (C.10) into Equation (C.4), the variational principle leads to an eigenvalue problem

$$([K] - N_X[K_g])\{C\} = 0 \tag{C.12}$$

where [K] and $[K_g]$ are the stiffness and geometric stiffness matrices, respectively. {C} is a vector containing constants in Equation (C.3) to be determined. The lowest eigenvalue for N_X gives the critical load for the sublaminate under consideration.

C.2 CAI prediction

After degradation factors are determined, stress distribution of this simplified model with soft inclusion can be calculated. The weighted stress distribution is also obtained through weight function presented below

$$w(x,0) = 1 + \left(2\left(1 - \frac{t_{max}}{T}\right)\right)^{\left(1-\frac{t_{max}}{T}\right)} \sqrt{\frac{2x}{W}} \tag{C.13}$$

where t_{max} is the thickness of the thickest sublaminate through which laminae share the same degradation factor. T and W are thickness and width of the entire laminate, respectively.

Tang's method is coded in Delphi 7 and evaluated in Figure C.3 based on part of the experimental results mentioned in Appendix A, where comparison of CAI strengths are shown, and a good agreement between experiments and predictions from B1-1 to B4-1. However, there is a significant discrepancy at B5-1. The reason is that the minimum value of the weighted stress fails to be spotted between the crest and the right end of the weight-stress curve (Figure C.4(e)). Actually, it can be seen that as the larger the delamination size, the more drastic alteration of stress distribution in the undamaged part of laminate arises, and the less significance of the minimum weighted stress. Unfortunately, in the literature, there is no explanation about this issue.

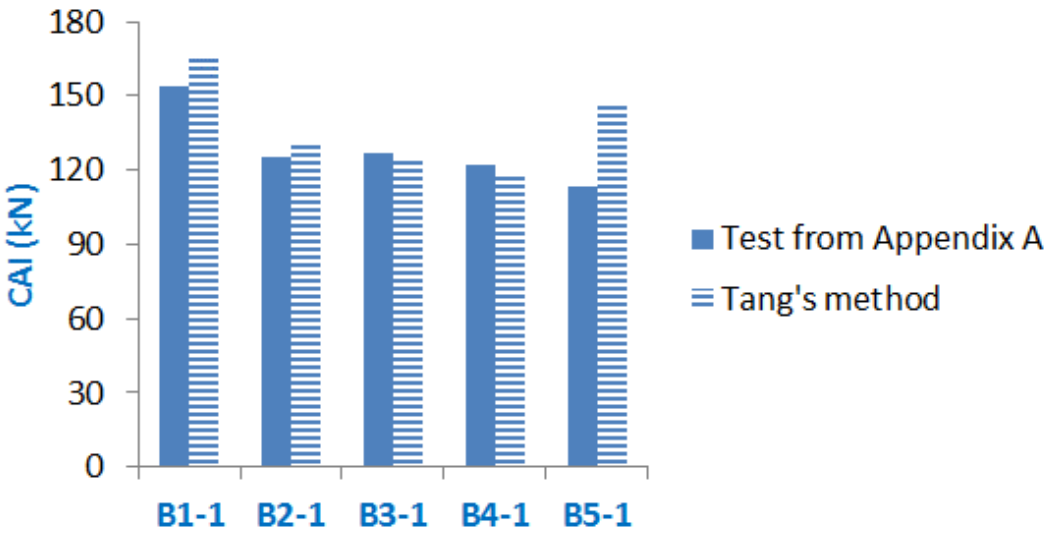

Figure C.3 CAI comparison between experiment and Tang's method

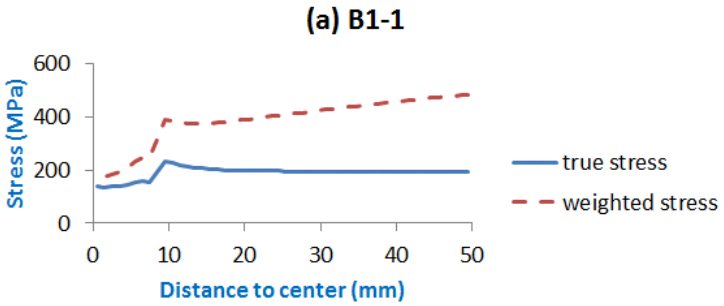
(a) B1-1
Stress (MPa)
600
400
200
0
0
10
20
30
40
50
Distance to center (mm)
true stress
weighted stress

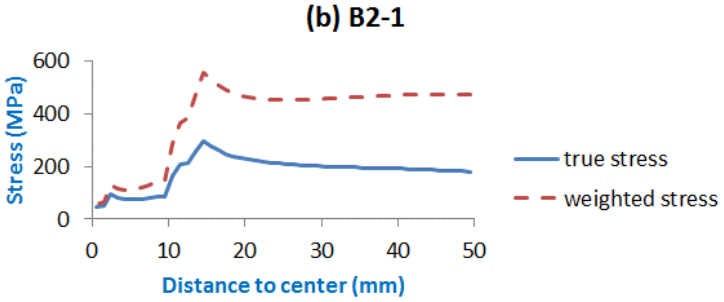
(b) B2-1
Stress (MPa)
600
400
200
0
0
10
20
30
40
50
Distance to center (mm)
true stress
weighted stress

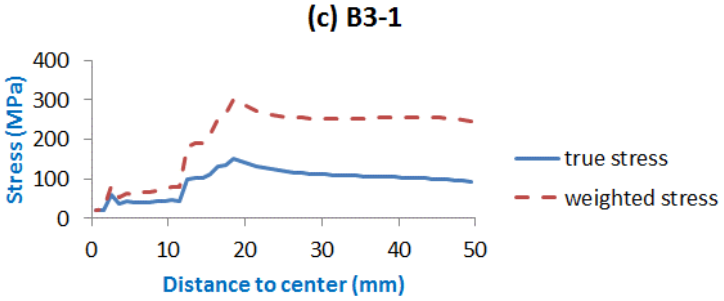
(c) B3-1
Stress (MPa)
400
300
200
100
0
0
10
20
30
40
50
Distance to center (mm)
true stress
weighted stress

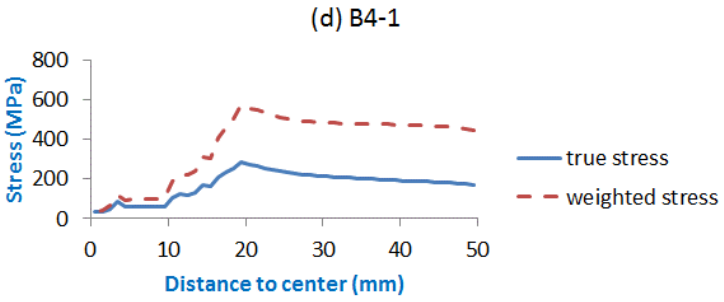
(d) B4-1
Stress (MPa)
800
600
400
200
0
0
10
20
30
40
50
Distance to center (mm)
true stress
weighted stress

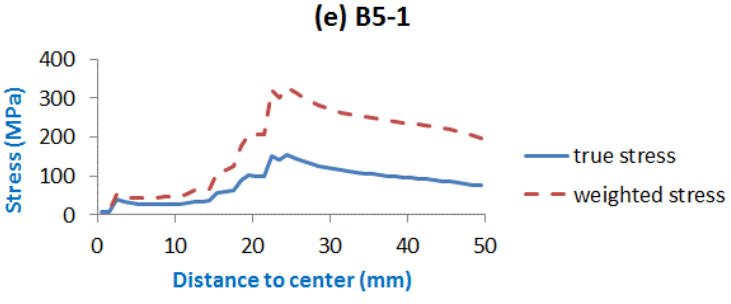
(e) B5-1
Stress (MPa)
400
300
200
100
0
0
10
20
30
40
50
Distance to center (mm)
true stress
weighted stress

Figure C.4 Real and weighted stress distribution from center to side edge through Tang's method

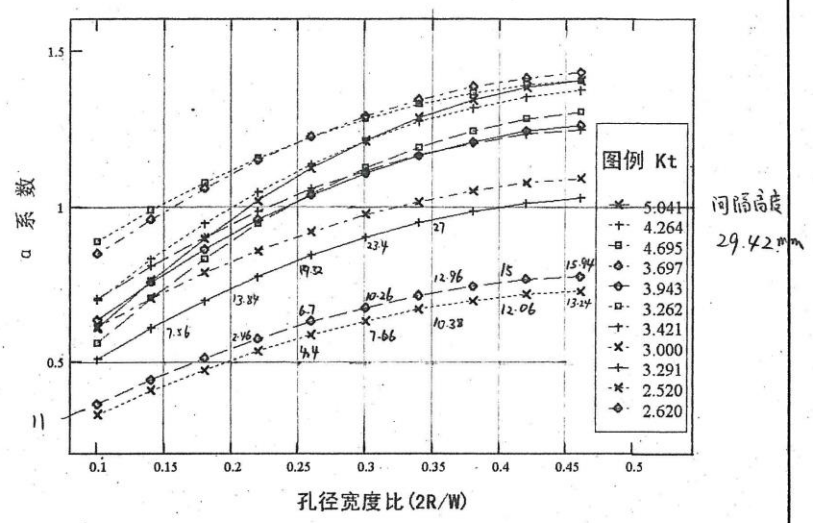

图 11　由层压板刚度性能模拟的 α 系数与 $2R/W$ 的关系曲线

6　带冲击损伤层压板压缩剩余强度估算方法

实验与理论研究表明，含冲击损伤复合材料层压板的压缩破坏模式一般是由分层区域的局部屈曲控制的[20-23]。目前主要有二种分析思路，来分析层压板的冲击压缩强度。一是基于层间应变能释放率(G_c)的分层扩展方法；二是把冲击分层在出现局部屈曲后模氮为软化夹杂进行强度分析。前一种方法中,具有代表性的工作是 Cairns[24,25]所进行的分析。后者则以 Boering 公司的 Dost 等人[26-28]开展的研究为代表。但他们均只考虑具有单一形式的子层情况。对于损伤形式呈空间分布呈且有不对称的冲击损伤而言，这种单一子层的处理方式就有其固有的局限性，例如只能针对预先设计的分层形式(等直径的预埋分层)，或仅能用于准各向同性铺层等。从方法的实现与实用方面比较，基于软化夹杂的方法更具有吸引力。但必须从损伤表征、子层屈曲分析、破坏判据选择上等方面作进一步的研究与改进。“软化夹杂”的分析思路一般主要包括这样五个步骤：

1) 分层区域的屈曲分析；
2) 将屈曲的分层区域模氮为软化夹杂(soft inclusion)；
3) 对含有软化夹杂的层压板进行应力分布计算；
4) 进行有限宽度修正；

5) 利用破坏判据得到最终的剩余强度数据值。

6.1 冲击分层的屈曲分析

已有许多文章介绍了分层屈曲的分析方法[24,29-32]。这些方法均将分层区域模拟为具有一定厚度的图形或椭圆形子层(sublaminate)进行分析，但大都只改虑一个子层。由于冲击损伤引起分层，出现在不同的层间，方向和尺寸也不相同，因此用多子层的屈曲分析方法更为合适。

考虑图 13 的带冲击损伤层压板。沿 A-A 剖面如图 14 所示，假设所有层间分层可以用一椭圆近似表征，其局部坐标为 *oxyz*；原点与层压板的整体坐标系 *OXYZ* 的原点重合。每个分层的方向角 θj 用 X 与 x 间的夹角表示。

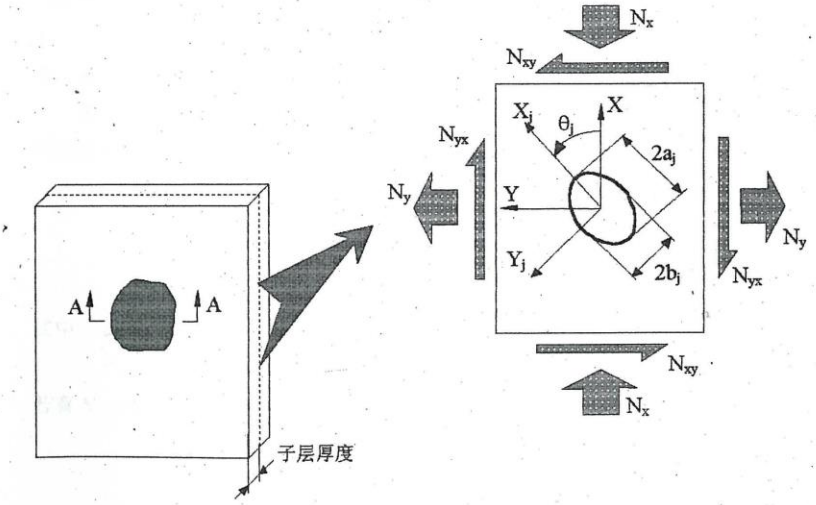

图 13 子层屈曲分析示意图

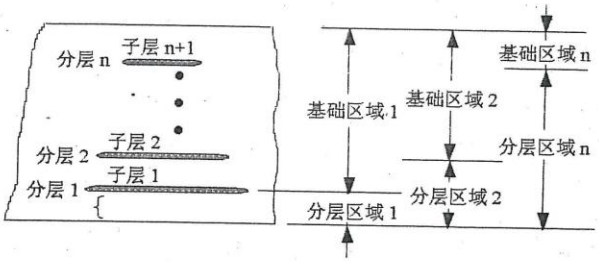

图 14　分层区域与基础区域的定义

这时术语“子层”表示由相邻二个分层(或分层与层压板的表面)之间所包含的铺层(组)。除了最外两个子层(图中的 1 与 n + 1 所标示的子层)外，各子层的屈曲均受到相邻子层的约束。这样，如图所示，每个分层把层压板分隔为“分层区域”与“基础区域”。分层区域与基础区域均由一个或若干个子层组成，表示可能出现局部屈曲的区域。分层区域与基础区域相对而言的，因此分层区域与基础区域相比或者要厚或者要薄。

每一组分层区域与基础区域的屈曲应变按类似于 Shivakumar 和 Whitcomb[30] 的做法求解。其中采限了下列不同的处理方法：

1)　分层区域的假设应变场

$$\begin{Bmatrix}\varepsilon_x\\ \varepsilon_y\\ \gamma_{xy}\end{Bmatrix}=\begin{bmatrix}a_{11} & a_{12} & a_{16}\\ a_{12} & a_{22} & a_{26}\\ a_{16} & a_{26} & a_{66}\end{bmatrix}\begin{bmatrix}\cos^2\theta & \sin^2\theta & 2\cos\theta\sin\theta\\ \sin^2\theta & \cos^2\theta & -2\cos\theta\sin\theta\\ -\cos\theta\sin\theta & \cos\theta\sin\theta & \cos^2\theta-\sin^2\theta\end{bmatrix}\begin{Bmatrix}N_X\\ N_Y\\ N_{XY}\end{Bmatrix} \tag{22}$$

式中：a_{ij} 表示沿分层局部坐标下的分层区域的柔度系数；

N_X，N_Y，N_{XY} 表示沿层压板整体坐标系下分层区域所受的载荷；

若有 $N_X=N_{XY}=0$，则(22)式可表示为：

$$\begin{Bmatrix}\varepsilon_x\\ \varepsilon_y\\ \gamma_{xy}\end{Bmatrix}=\begin{Bmatrix}\rho_x\\ \rho_y\\ \rho_{xy}\end{Bmatrix}\cdot N_X \tag{23}$$

其中

$$\begin{cases}\rho_x=a_{11}\cos^2\theta+a_{12}\sin^2\theta-a_{16}\cos\theta\sin\theta\\ \rho_y=a_{12}\cos^2\theta+a_{22}\sin^2\theta-a_{26}\cos\theta\sin\theta\\ \rho_{xy}=a_{16}\cos^2\theta+a_{26}\sin^2\theta-a_{66}\cos\theta\sin\theta\end{cases} \tag{24}$$

因此，用总体坐标系下的面内载荷 N_X 表示的局部坐标系下面内载荷为

$$\begin{Bmatrix} N_x \\ N_y \\ N_{xy} \end{Bmatrix} = \begin{bmatrix} A_{11} & A_{12} & A_{16} \\ A_{12} & A_{22} & A_{26} \\ A_{16} & A_{26} & A_{66} \end{bmatrix} \begin{Bmatrix} \varepsilon_x \\ \varepsilon_y \\ \gamma_{xy} \end{Bmatrix} = \begin{Bmatrix} n_x \\ n_y \\ n_{xy} \end{Bmatrix} \cdot N_X \tag{25}$$

其中

$$\begin{aligned} n_x &= A_{11}\rho_x + A_{12}\rho_y + A_{16}\rho_{xy} \\ n_y &= A_{12}\rho_x + A_{22}\rho_y + A_{26}\rho_{xy} \\ n_{xy} &= A_{16}\rho_x + A_{26}\rho_y + A_{66}\rho_{xy} \end{aligned} \tag{26}$$

2) 分层区域的刚度系数计算方法

由于分层区域内的子层一般呈不对称铺层方式，因此需要计算分层区域的[A]，[B]，[D]等刚度矩阵(在局部坐标系下)。计算时，我们假设在分层区域刚刚出现屈曲时，所有的子层的曲率均相同。这样就可以按照经典层压板理论计算[A]，[B]，[D]。

3) 临界屈曲应变的求解

采用 Rayleigh-Ritz 法求临界屈曲载荷，选择下面的挠度函数

$$w(x,y) = \left(1 - \left(\frac{x}{a}\right)^2 - \left(\frac{y}{b}\right)^2\right)^2 \cdot \left(C_1 + C_2x^2 + C_3y^2 + C_4xy + C_5x + C_6y\right) \tag{27}$$

分层区域的总势能表示为：

$$\Pi_p = \frac{1}{2}\int_{-a}^{a}\int_{-b\sqrt{1-(x/a)^2}}^{b\sqrt{1-(x/a)^2}} \left(\begin{Bmatrix} w_{,xx} \\ w_{,yy} \\ 2w_{,xy} \end{Bmatrix}^T \begin{bmatrix} \bar{D}_{11} & \bar{D}_{12} & \bar{D}_{16} \\ \bar{D}_{12} & \bar{D}_{22} & \bar{D}_{26} \\ \bar{D}_{16} & \bar{D}_{26} & \bar{D}_{66} \end{bmatrix} \begin{Bmatrix} w_{,xx} \\ w_{,yy} \\ 2w_{,xy} \end{Bmatrix} - \begin{Bmatrix} w_{,x} \\ w_{,y} \end{Bmatrix}^T \begin{bmatrix} N_x & N_{xy} \\ N_{xy} & N_y \end{bmatrix} \begin{Bmatrix} w_{,x} \\ w_{,y} \end{Bmatrix} \right) dydx \tag{28}$$

其中，第一项是由弯曲引起的应变能，第二项表示面内载荷所做的功。$\bar{D}_{ij}$ 为折减弯由刚度[33]，定义为：

$$[\bar{D}] = [D] - [B][A]^{-1}[B] \tag{29}$$

由势能驻值原理，导出以矩阵形式表示的特征方程为

$$\left([K] - N_X[K_g]\right)\{C\} = 0 \tag{30}$$

其中，$\{C\} = \lfloor C_1\ C_2\ C_3\ C_4\ C_5\ C_6 \rfloor^T$

这里，[K]为分层区域的刚度矩阵，具体为

$$[K] = \bar{D}_{11}[K_1] + \bar{D}_{22}[K_2] + 2\left(\bar{D}_{12} + 2\bar{D}_{66}\right)[K_3] + 2\bar{D}_{16}[K_{16}] + 2\bar{D}_{26}[K_{26}] \tag{31}$$

$$[K_1]=\frac{2b\pi}{a^3}\begin{bmatrix} 4 & 0.5a^2 & 0.5b^2 & 0 & 0 & 0 \\ & 1.35a^4 & 0.05a^2b^2 & 0 & 0 & 0 \\ & & 0.15b^4 & 0 & 0 & 0 \\ & sym & & 0.25a^2b^2 & 0 & 0 \\ & & & & 2.5a^2 & 0 \\ & & & & & 0.5b^2 \end{bmatrix} \tag{32}$$

$$[K_2]=\frac{2a\pi}{b^3}\begin{bmatrix} 4 & 0.5a^2 & 0.5b^2 & 0 & 0 & 0 \\ & 0.15a^4 & 0.05a^2b^2 & 0 & 0 & 0 \\ & & 1.35b^4 & 0 & 0 & 0 \\ & sym & & 0.25a^2b^2 & 0 & 0 \\ & & & & 0.5a^2 & 0 \\ & & & & & 2.5b^2 \end{bmatrix} \tag{33}$$

$$[K_3]=\frac{\pi}{3ab}\begin{bmatrix} 8 & a^2 & b^2 & 0 & 0 & 0 \\ & 1.1a^4 & 0.5a^2b^2 & 0 & 0 & 0 \\ & & 1.1b^4 & 0 & 0 & 0 \\ & sym & & 0.9a^2b^2 & 0 & 0 \\ & & & & 3a^2 & 0 \\ & & & & & 3b^2 \end{bmatrix} \tag{34}$$

$$[K_{16}]=\frac{b\pi}{a}\begin{bmatrix} 0 & 0 & 0 & 0 & 0 & 0 \\ & 0 & 0 & 0.8a^2 & 0 & 0 \\ & & & 0.4b^2 & 0 & 0 \\ & & sym & 0 & 0 & 0 \\ & & & & 0 & 2 \\ & & & & & 0 \end{bmatrix} \tag{35}$$

$$[K_{26}]=\frac{a\pi}{b}\begin{bmatrix} 0 & 0 & 0 & 0 & 0 & 0 \\ & 0 & 0 & 0.4a^2 & 0 & 0 \\ & & 0 & 0.8b^2 & 0 & 0 \\ & & sym & 0 & 0 & 0 \\ & & & & 0 & 2 \\ & & & & & 0 \end{bmatrix} \tag{36}$$

[Kg]为子层的几何刚度矩阵，具体为

$$[K_g]=n_x[K_{g1}]+n_y[K_{g2}]+n_{xy}[K_{g3}] \tag{37}$$

$$[K_{g1}]=\frac{b\pi}{60a}\begin{bmatrix} 40 & 0 & 4b & 0 & 0 & 0 \\ & 3a^4 & 0 & 0 & 0 & 0 \\ & & b^4 & 0 & 0 & 0 \\ & sym & & a^2b^2 & 0 & 0 \\ & & & & 12a^2 & 0 \\ & & & & & 4b^2 \end{bmatrix} \tag{38}$$

$$[K_{g2}]=\frac{a\pi}{60b}\begin{bmatrix} 40 & 4a^2 & 0 & 0 & 0 & 0 \\ & a^4 & 0 & 0 & 0 & 0 \\ & & 3b^4 & 0 & 0 & 0 \\ & sym & & a^2b^2 & 0 & 0 \\ & & & & 4a^2 & 0 \\ & & & & & 12b^2 \end{bmatrix} \tag{39}$$

$$[K_{g3}]=\frac{b\pi}{60a}\begin{bmatrix} 0 & 0 & 0 & -4 & 0 & 0 \\ & 0 & 0 & a^2 & 0 & 0 \\ & & & b^2 & 0 & 0 \\ & sym & & 0 & 0 & 0 \\ & & & & 0 & 8 \\ & & & & & 0 \end{bmatrix} \tag{40}$$

求解特征方程(30)后得到的最小特征值就是分层区域的屈曲临界载荷。

由于我们考虑的是含有多分层的一般情况，因此，由不同的屈曲临界应变。我们采取迭代的算法，每次求出所有分层区域(包括基础区域)中的嗳小屈曲临界载荷。一旦某一分层区域出现了局部屈曲，则从层压板铺层中，消除屈曲区域所包含的铺层，然后再对剩余的层压板分层继续迭代，求出下一个最小屈曲临界载荷“重复这一过程，直到所有区域都求出了相应的最小临界屈曲载荷为止。这样就求得一组分层区域与之对应的最小临界区域载荷 $N_X^{(j)}$。

6.2 屈曲分层区域的软化处理

我们得到的是多分层区域的一组临界屈曲载荷(应力)，因此不能直接采用文献[26]中介绍的针对单一子层形式的有效刚度折减方法。本文采用的软化的基本思想是，首先假设，一旦分层区域，出现局部屈曲后便呈现 Euler 屈曲行为，此时屈曲的区域承受的载荷便保持不变(即屈曲载荷)。(这一假设的合理性已被文献[26]中的几何非线性有限元分析予以证实)。

设层压板的无损伤压缩强度为 σ_0，则我们把每个屈曲分层区域的临界屈曲应力在层压板无损伤强度中所占的比例，定义为该屈曲分层区域的刚度退化系数；

$$R^{(j)}=\frac{N_X^{(j)}/t_j}{\sigma_0}=\frac{\sigma^{(j)}}{\sigma_0} \tag{41}$$

其中：$N_X^{(j)}$ 为对应分层区域 j 的最小临界屈曲载荷；

t_j 为该分层区域的厚度。

Figure C.5 Photocopies of Tang's criterion recorded as ASRI's internal document in Chinese